
**ELECTROCHEMICAL
CORROSION TESTING**

Mansfeld/Bertocci, *editors*

ASTM STP 727

**AMERICAN SOCIETY FOR
TESTING AND MATERIALS**

ELECTROCHEMICAL CORROSION TESTING

A symposium
sponsored by ASTM
Committee G-1 on Corrosion of Metals
AMERICAN SOCIETY FOR
TESTING AND MATERIALS
San Francisco, Calif. 21-23 May 1979

ASTM SPECIAL TECHNICAL PUBLICATION 727
Florian Mansfeld, Rockwell International
Science Center, and Ugo Bertocci, National
Bureau of Standards, editors

ASTM Publication Code Number (PCN)
04-727000-27



AMERICAN SOCIETY FOR TESTING AND MATERIALS
1916 Race Street, Philadelphia, Pa. 19103

Copyright © by AMERICAN SOCIETY FOR TESTING AND MATERIALS 1981
Library of Congress Catalog Card Number: 80-68949

NOTE

The Society is not responsible, as a body,
for the statements and opinions
advanced in this publication.

Foreword

The Symposium on Progress in Electrochemical Corrosion Testing was held 21–23 May 1979 in San Francisco, Calif. The symposium was sponsored by ASTM Committee G-1 on Corrosion of Metals. Dr. Florian Mansfeld, Rockwell International Science Center, served as symposium chairman; Dr. Ugo Bertocci, National Bureau of Standards, served as vice-chairman. Drs. Mansfeld and Bertocci also served as editors of this publication.

Related ASTM Publications

Corrosion of Reinforcing Steel in Concrete, STP 713 (1980), \$22.50,
04-713000-27

Corrosion and Degradation of Implant Materials, STP 684 (1979), \$37.75,
04-684000-27

Stress Corrosion Cracking—The Slow Strain-Rate Technique, STP 665
(1979), \$39.75, 04-665000-27

Intergranular Corrosion of Stainless Alloys, STP 656 (1978), \$24.00,
04-656000-27

Atmospheric Factors Affecting the Corrosion of Engineering Metals, STP
646 (1978), \$24.50, 04-646000-27

Corrosion Fatigue Technology, STP 642 (1978), \$32.00, 04-642000-27

Chloride Corrosion of Steel in Concrete, STP 629 (1977), \$21.25,
04-629000-27

Stress Corrosion—New Approaches, STP 610 (1976), \$43.00, 04-610000-27

A Note of Appreciation to Reviewers

This publication is made possible by the authors and, also, the unheralded efforts of the reviewers. This body of technical experts whose dedication, sacrifice of time and effort, and collective wisdom in reviewing the papers must be acknowledged. The quality level of ASTM publications is a direct function of their respected opinions. On behalf of ASTM we acknowledge with appreciation their contribution.

ASTM Committee on Publications

Editorial Staff

Jane B. Wheeler, *Managing Editor*
Helen M. Hoersch, *Associate Editor*
Helen P. Mahy, *Senior Assistant Editor*
Allan S. Kleinberg, *Assistant Editor*

Contents

Introduction	1
Scanning Reference Electrode Techniques in Localized Corrosion— H. S. ISAACS AND BRIJESH VYAS	3
Potential Dependence of Localized Corrosion in Iron— JAROMÍR TOUŠEK	34
A Method for Quantifying the Initiation and Propagation Stages of Crevice Corrosion—T. S. LEE	43
A Strain-Control Technique for Assessing the Corrosion-Fatigue Sensitivity of Stainless Steels—C. AMZALLAG, B. MAYONOBE, AND P. RABBE	69
Potential and Strain-Rate Effects in Slow Strain-Rate Stress Corrosion Cracking of Type 304 Stainless Steel in 35 Percent Magnesium Chloride at 120°C— K. J. KESSLER AND H. KAESCHE	84
Corrosion and Electrochemical Behavior of Iron-Chromium-Nickel Alloys in Concentrated Sulfuric Acid Solutions—H. S. TONG	96
Electrochemical Impedance Techniques in Corrosion Science— D. D. MACDONALD AND M. C. H. MCKUBRE	110
Alternating-Current Impedance Measurements Applied to Corrosion Studies and Corrosion-Rate Determination—I. EPELBOIN, C. GABRIELLI, M. KEDDAM, AND H. TAKENOUTI	150
A Corrosion Monitor Based on Impedance Method— S. HARUYAMA AND T. TSURU	167
Impedance Measurements on Organic Coatings on Mild Steel in Sodium Chloride Solutions—J. D. SCANTLEBURY, K. N. HO, AND D. A. EDEN	187

Digital Faradaic Impedance Measurements on Corroding Copper in Acid Solutions—W. H. SMYRL	198
Evaluation of Electrochemical Techniques for Monitoring of Atmospheric Corrosion Phenomena—FLORIAN MANSFELD	215
Practical Experience with an Electrochemical Technique for Atmospheric Corrosion Monitoring—VLADIMIR KUCERA AND JAN GULLMAN	238
An Electrochemical Technique to Measure Diffusible Hydrogen in Metals (Barnacle Electrode)—J. J. DELUCCIA AND D. A. BERMAN	256
Cyclic Polarization Measurements—Experimental Procedure and Evaluation of Test Data—ROBERT BABOIAN AND G. S. HAYNES	274
Application of Potentiokinetic Hysteresis Technique to Characterize the Chloride Corrosion of High-Copper Dental Amalgams—N. K. SARKAR	283
Direct Measurement of the Corrosion Current for Oxygen-Reduction Corrosion—JOHN POSTLETHWAITE	290
Electrochemical Behavior of Carbon Steel in Fused Salts—C. M. CHEN AND G. J. THEUS	303
Galvanic Corrosion of Copper Alloys—YUICHI ISHIKAWA, NOBUYOSHI HOSAKA, AND SUSUMU HIOKI	327
Electrochemical Investigation of Cavitation-Corrosion Damages of a Pump Casing—YUICHI ISHIKAWA, TOSHINORI OZAKI, SUMIO SUDO, AND SUSUMU HIOKI	339
A Method of Evaluating Polarization Curves for Stainless Steel via a Simple Passivation Model—S.-O. BERNHARDSSON AND ROLF MELLSTRÖM	352
Effect of Large Voltage Modulations on Electrodes Under Charge-Transfer Control—UGO BERTOCCI AND J. L. MULLEN	365
Progress in Mini-Potentiostat Development for Corrosion Testing—H. A. NEWBORN, D. C. BRATLIE, AND C. R. CROWE	381

A Microprocessor-Based Corrosion Measurement System—

W. M. PETERSON AND HOWARD SIEGERMAN

390

Summary

407

Index

409

Introduction

Electrochemical techniques are finding increased use not only in corrosion research but in practical applications, especially in the chemical and petroleum industries. This is due to a better understanding of the basic mechanisms and kinetics of the electrochemical reactions that determine the corrosion behavior of different material/electrolyte combinations, the availability of improved electrochemical techniques for the study of corrosion phenomena, and the demonstration by numerous investigators that such techniques can be applied successfully for corrosion monitoring and control.

ASTM Subcommittee G01.11 on Electrochemical Measurements in Corrosion Control has a long history in the development of practices for the use of electrochemical methods. An example is ASTM Recommended Practice for Standard Reference Method for Making Potentiostatic and Potentiodynamic Anodic Polarization Measurements (G5-78), which is used worldwide for calibration of electrochemical instrumentation in laboratory work. More recent documents produced by Subcommittee G01.11 include a practice for conducting polarization-resistance measurements and a procedure for the use of potentiodynamic polarization techniques in the evaluation of the susceptibility to localized corrosion.

In order to review the state of the art and discuss new techniques, Subcommittee G01.11 organized the Symposium on Progress in Electrochemical Corrosion Testing, which was held in San Francisco in May 1979. The response to the call for papers was excellent with truly international participation by speakers from the United States, Czechoslovakia, France, West Germany, Japan, England, Sweden, and Canada. The participants in the symposium were in many cases those who are responsible to a large extent for the progress in electrochemical corrosion testing.

The topics discussed ranged from various aspects of localized corrosion phenomena (such as pitting, crevice corrosion, corrosion fatigue, and stress corrosion cracking) to the use of a-c impedance techniques and a number of special areas usually not discussed in detail despite their practical importance (such as atmospheric corrosion and the development of improved equipment for electrochemical corrosion studies). The session on the background and application of a-c impedance techniques has special importance, since it allowed for the first time a thorough discussion of the possibilities this approach brings to corrosion research and corrosion monitoring.

It is hoped that this volume will serve a large segment of the corrosion community by providing background information to the newcomers in the field,

2 ELECTROCHEMICAL CORROSION TESTING

giving detailed discussions of special topics to the more experienced corrosionists, and establishing a general survey of the state of the art in electrochemical corrosion testing. The organizers of this symposium were gratified by the very active participation of the audience during the presentation of the papers, and hope that this volume will encourage increased use of electrochemical techniques in the continuing struggle to reduce the enormous costs of corrosion.

Florian Mansfeld

Rockwell International Science Center, Thousand Oaks, Calif. 91360; symposium chairman and co-editor

Ugo Bertocci

National Bureau of Standards, Washington, D.C. 20234; symposium vice-chairman and co-editor

H. S. Isaacs¹ and Brijesh Vyas²

Scanning Reference Electrode Techniques in Localized Corrosion

REFERENCE: Isaacs, H. S. and Vyas, Brijesh, "Scanning Reference Electrode Techniques in Localized Corrosion," *Electrochemical Corrosion Testing, ASTM STP 727*, Florian Mansfeld and Ugo Bertocci, Eds., American Society for Testing and Materials, 1981, pp. 3-33.

ABSTRACT: The principles, advantages, and implementations of scanning reference electrode techniques are reviewed. The technique locates the position of localized corrosion, and can be used to monitor the development of corrosion and changes in the corrosion rate under a wide range of conditions. Data related to pitting, intergranular corrosion, welds, and stress-corrosion cracking are presented.

KEY WORDS: stainless steel, welds, pitting, intergranular corrosion, stress corrosion cracking

The definition of localized corrosion is usually restricted to specific types of attack often related to the presence of chlorides. This definition may be broadened to incorporate all other cases where corrosion at specific areas of the metal surface takes place. General corrosion rates in most systems have been measured, and design allowance can be made for the metal losses during the expected life of the system. Problems arise when the corrosion becomes localized, and the penetration rate of the metal is orders of magnitude greater than the predicted general corrosion; in many cases, localized corrosion is only identified after failure. Localized forms of corrosion, therefore, take a far greater toll than the incorrect choice of materials that give unacceptable general corrosion.

During localized corrosion [1,2]³ the electrochemical dissolution is well separated from the cathodic reactions. This makes an *in situ* study of the anodic and cathodic reactions amenable to direct measurement in contrast with general corrosion where the reactions can take place in close proximity. The aim of this investigation is to separate clearly the anodic and cathodic

¹Metallurgist and associate metallurgist, respectively, Brookhaven National Laboratory, Upton, N.Y. 11973.

²Member, Technical Staff, Bell Laboratories, Murray Hill, N.J. 07974; formerly at Brookhaven National Laboratory, Upton, N.Y. 11973.

³The italic numbers in brackets refer to the list of references appended to this paper.

4 ELECTROCHEMICAL CORROSION TESTING

reactions without interfering with the processes taking place or altering them to an extent whereby they no longer relate to conditions during exposure. *In situ* measurements, such as mapping of potentials in solution or the physical separation of anodic and cathodic areas and the measurement of the currents flowing between them, have been successfully used to identify the processes during corrosion.

Other methods, such as weight loss or penetration rates, have also been used, but these require periodic removal of the metal from the corroding environment. The periodic removal can alter the progress of corrosion or initiate changes in the processes involved. Thus the measurements do not necessarily represent a single progression of the reaction, but possibly the integrated effect of a repetitive process. During pitting, for example, the pits may repassivate on removal from the corrosive environment and reinitiate on subsequent exposure. In the case of stress-corrosion cracking, the uncorroded area may act as the cathode and, when cathodic polarization is limiting, interaction between the growth rates of the various cracks would be expected. However, when the anodic process is slow or when the cathode is at the crack wall, no interaction between the cracks would occur. The identification of these effects would require a large number of samples because of the required statistics, and even then it would be extremely difficult to extract the rate processes or the electrochemistry taking place.

In a large number of studies, sections of samples have been used to separate the anodic and cathodic processes [3-6]. In an early work related to the water-line corrosion [3], the corroding section of the sample was separated from the partially immersed cathodic portion. The currents between the shorted pieces gave rates that correlated well with the observed weight losses. The behavior of welds has been studied using similar techniques [4]. The welds were sectioned or masked to give representative parts parallel with the weld direction. Separate sections of plates have also been used to investigate pitting corrosion [5]. Measurements were conducted on the relation and variations of current between the different sections during pitting corrosion, and demonstrate the existence of a marked dependence between pit size and its stability.

Areas around a weld have been studied separately using a liquid drop drawn across the sample. The potential variations and the polarization characteristics as a function of the drop position were measured [7]. In another study [8] an insulating coating over a weld area was perforated with a microhardness indenter, and a liquid drop was placed over the perforation. The potential and the polarization characteristics of the underlying deformed and wetted metal were measured.

The flow of current from the anodic to the cathodic areas can be also determined without sectioning samples. In an early work on water-line corrosion, Evans and Agar [9] calculated the current from the measured equipotential lines associated with the flow of current during the corrosion of zinc.

A scanning reference electrode technique (SRET) was used to measure the potential variation in the solution. An agreement of within 10 percent was obtained between the measured corrosion rates from weight loss and the calculations from the equipotential surfaces.

Jaenicke and Bonhoeffer [10,11], Copson [12], and Rozenfeld [13] have measured the potential distribution around galvanic couples and calculated the corrosion rates and the surface current density distributions. Measurements of potential distribution during corrosion of bismuth-cadmium and zinc-aluminum alloys were also studied [11]. More recent measurements of couples of iron and copper have been conducted by Hildebrand and Schwenk [14].

Theory

Aqueous corrosion of metals is an electrochemical process involving anodic oxidation of the metal and cathodic reduction of species from the solution. During localized corrosion, the two processes usually take place at well-separated areas. The flow of electrons within the metallic phase does not involve significant ohmic potential differences because of the high conductivity of the metal. The flow of current within the aqueous phase, carried by ions, is associated with small potential changes between the anodic and cathodic areas.

Figure 1 shows a schematic of the flow of current in the electrolyte from a localized anodic to the surrounding cathodic areas and equipotentials set up around the localized electrode. By scanning a "passive" reference probe with a fine capillary tip parallel and in close proximity to the metal surface, the potential distribution in the liquid can be measured. The potential changes are most rapid over the localized electrode; a potential maximum or minimum is observed over its center. In the SRET work presented here, the sign convention adopted is opposite to that generally used in order to show anodic areas as potential peaks and cathodic areas as minima. Thus the SRET is an *in situ* technique used to locate the anodic and cathodic sites and study the electrochemical processes during localized corrosion without altering the processes taking place, changing the local environment over the corrosion site, or influencing the rate of corrosion.

The distribution of potential and current can be theoretically determined from the Laplace equation

$$\nabla^2 E = 0 \quad (1)$$

and Ohm's Law

$$i = -K \nabla E \quad (2)$$

where E , i , and K are the potential, current density, and solution conductivity,

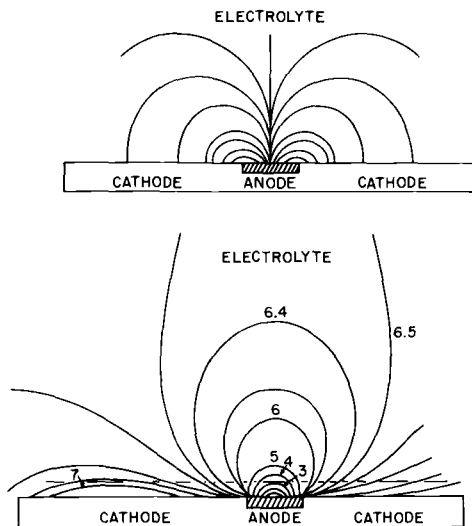


FIG. 1—Schematic drawing of a local corrosion cell showing (a) current paths in the electrolyte flowing from the anode to the cathode, and (b) equipotential lines in the electrolyte.

ity, respectively. The boundary conditions for the solution of these equations depends on the polarization characteristics of the anodic and cathodic areas. If either area has a high polarization characteristic, low currents will flow in solution; hence, there will be little potential variations between anode and cathode. A greater variation of potential will occur with high currents. The product of the polarization resistances ($\Delta V/\Delta i$) and the electrolyte conductivity has the dimension of length

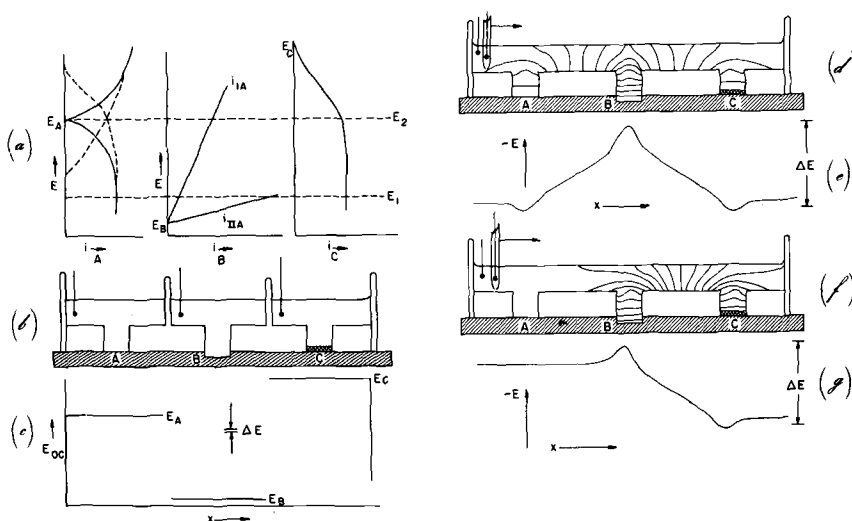
$$L = K \frac{\Delta V}{\Delta i} \quad (3)$$

and has been used to determine the potential variations in corroding systems [15-19].

It should be emphasized that the SRET does not directly measure the potential variations of the metal surface, but responds to current variations in solution. These currents are more dependent on the polarization characteristics of the metal surface than the surface potential. This can be demonstrated by the following hypothetical examples.

Three Evans-type polarization curves are shown in Fig. 2a. In A, anodic and cathodic partial polarization curves are given by the dashed lines representing the reactions on a passive metal surface (for example, iron in a chloride solution below its pitting potential). The full lines represent the net polarization curves. In B, anodic polarization curves representing anodic

behavior of a localized anodic cell (for example, a large pit) for two different conditions are shown; one (I) has a greater polarization characteristic than the other (II). The third Evans-type diagram, *C*, could be for a noble metal (for example, a platinum coating on iron). The cathodic curves in Fig. 2*a*, *A* and *C*, could arise from oxygen reduction and, if equal in area, would show the same currents when limiting concentration polarization is reached. These three areas are considered to be present on a single metal surface separated by an insulating coating as in Figs. 2*b*, 2*d*, and 2*f*, where the "iron" forms the base of a shallow container holding a highly conducting chloride-containing electrolyte. In Fig. 2*b* the solutions in contact with areas *A*, *B*, and *C* are separated from each other and have the respective Evans-type diagrams shown in Fig. 2*a*. Each area is at its open circuit potential; measurements of the potential as a function of the position in the solution can be represented by Fig. 2*c*. If these separations are removed, two conditions can arise depending on the anodic behavior of area *B*. If the lower polarization is considered, the polarization of the three areas would be close to potential E_1 in Fig.



- (a) Polarization diagrams for each exposed area.
A—Passive surface supporting anodic and cathodic reactions.
B—Local "pitting" anode with either high (I) or low (II) polarization.
C—Metal-coated area supporting only a cathodic reaction.
- (b) Areas exposed to separate solutions.
 (c) Open-circuit potentials in solutions between "iron" and the reference electrodes.
 (d) Equipotential lines in solution when area *B* has low polarization (II).
 (e) Potential variations on scanning across the sample for case (d).
 (f) Equipotential lines in solution when area *B* has high polarization (I).
 (g) Potential variations on scanning across the sample for case (f).

FIG. 2—Schematic variations of the potential in a solution above a partially coated "iron" surface.

2a. The currents from the anodic area *B* would flow to both *A* and *C*; the potentials developed in the solution are shown by equipotential lines in Fig. 2d. If the potential were measured at a fixed distance from the metal surface above the coating using the SRET, the potential variations would be similar to the curve shown in Fig. 2e. The magnitude of these potential variations cover a range ΔE , which is much smaller than the potential range shown in Fig. 2c.

Under conditions where the anodic area *B* has the larger polarization (1), the potential of the three areas would be close to E_2 in Fig. 2a. This potential is equal to E_A , the open circuit potential of area *A*; under this condition no currents will flow to or from *A*. The equipotential lines for this condition are shown in Fig. 2f. The shape of the potential variations from the SRET is shown in Fig. 2g. It should be noted that no potential variations are observed when scanning above area *A*; the potential measurements would not be capable of distinguishing whether the probe is directly over the area *A* or the coatings adjacent to it. A similar condition could be achieved if area *A* is placed between *B* and *C*. If the coating were thin, it would once again not distinguish between the presence of a coating or the passive metal surface under the scanning reference electrode from the potential variations. This analysis demonstrates clearly that the SRET only responds to potential variations in the solution, which are associated with the flow of current, and does not relate directly to the potentials of the metal surfaces or the coating.

Experimental Technique

The potential fields generated in the electrolyte due to local corrosion sites can be measured by scanning a microtip reference electrode over a horizontally exposed surface facing up. The equipment built at Brookhaven National Laboratory is shown schematically in Fig. 3 [20,21]. The microtip reference electrode is held by a mechanical stage attached to low-friction, linear bearings for smooth motion in the *X*- and *Y*-direction, and driven by two stepping motors. The mechanical stage can be automatically programmed to scan both in the *X*- and *Y*-directions parallel to the specimen surface. The length of the *X*-direction can be varied up to 26 mm and, at each end of the *X*-scan, the *Y*-direction can be shifted to a set value (from 30 to 200 μm). An area of the surface is thus scanned by a rectangular wave. The linear speed of the scan in the *X*-direction can be varied from 0.1 to 300 mm/s.

Alternatively, potential fields on cylindrical samples can be obtained by keeping the probe stationary while rotating the sample [22,23]. The microtip reference electrode measures the potential variations along the circumference of the sample as the potential field around the sample rotates with the sample. A schematic of such an instrument is shown in Fig. 4 [23]. A motor is used to rotate a cylindrical metal specimen in the electrolyte so that the rotational motion of the sample is synchronized to produce a signal that is pro-

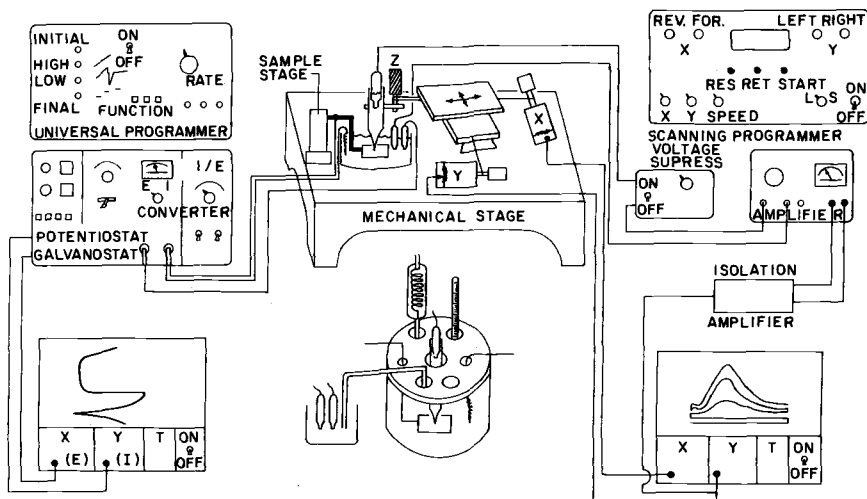


FIG. 3—Schematic of the scanning reference electrode technique for flat samples (Ref 21).

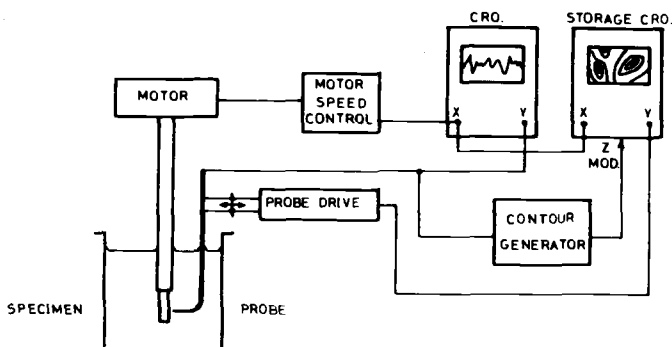


FIG. 4—Schematic of the scanning reference electrode technique for a cylindrical rotating sample (Ref 23).

portional to the angular position of the sample with respect to the probe. The microtip reference electrode is made to scan in the vertical direction (parallel to the cylindrical axis). If the signal of the sample rotation is fed to the X-direction and the signal of the scan of the probe to the Y-direction, the surface scan of the cylindrical specimen is obtained. The size of the area examined on the specimen surface can be controlled by regulating the length over which the microtip reference electrode moves along the axis of the sample and controlling the time per revolution of the specimen.

The most important parameter in the measurement of the potential fields is the distance between the microtip reference electrode and the specimen surface; this must be held constant during a given experiment. This is achieved

by attaching the specimen to a stage with three independent rotations when flat specimens are studied. Mechanical vibrations are kept to a minimum by attaching the mechanical stage to a cast-iron stand placed on a vibration-free table. In the case of a rotating specimen, it is necessary that the motor, rotating shaft, and the specimen lie on the same axis so that there is no eccentricity of the rotation. The whole apparatus should be made as rigid as possible [22].

The potential field in the electrolyte during localized corrosion is the difference in the potential measured by the microtip reference electrode and a reference electrode placed more than 10 mm away from the sample surface. The two signals are fed into a differential electrometer and the resultant potential amplified to the desired amount. The potential fields can be plotted on an *X-Y* recorder by feeding the signal from the *X*-position of the motor to the *X*-amplifier of the recorder the sum of the *Y*-position of the motor and the amplified potential difference to the *Y*-amplifier of the recorder. Thus one obtains a two-dimensional plot of the potential-field variations at a plane parallel to the sample surface. The signals can be also recorded on a storage oscilloscope and photographed. Alternatively, the amplified potential difference can modulate the intensity of the cathode-ray tube of an oscilloscope [20] or plot the equipotential lines from an analyzer [23].

A third scanning technique [24] incorporates two adjacent reference electrode probes to determine the currents flowing from the pits. Two scans are required for each measurement. One scan, having two probes close together displaced horizontally, gives the potential fields parallel to the specimen surface. In the other scan, the probes are displaced vertically to determine the field perpendicular to the surface. The vector sum of the fields indicates the magnitude and direction of the current flow, and summation over the active area is used to estimate the total currents from the anodic to the cathodic areas. This technique integrates only the current flowing across the plane of the potential measurement and does not include the currents flowing below the probes. These latter currents can be a significant fraction of the total current. Figure 5 shows the two fields normal and parallel to the surface over a pit on stainless steel.

Calibration

In order to obtain a quantitative value of the local corrosion currents, it is necessary to obtain a relation between the potential peak and the local current. This may be obtained theoretically by Eqs 2 and 3 [15] or determined experimentally. Owing to the lack of data relating the polarization characteristics of the systems studied, this relation was determined using a model electrochemical cell consisting of a localized anode in a large cathode.

A platinum sheet, 25 μm thick, was sandwiched between two copper blocks 10 mm wide and 10 mm long. The platinum was electrically insulated from the copper by two Mylar sheets 125 μm thick. The platinum was made the

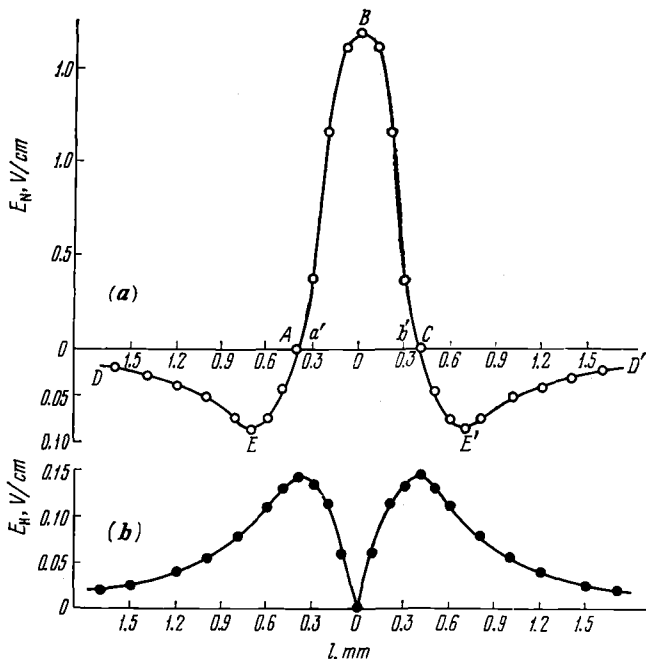


FIG. 5—Potential fields in solution over a pit in (a) the normal and (b) the horizontal directions in a 0.05 M $FeNH_4(SO_4)_2$ + 1 M NH_4Cl solution (Ref 24).

anode, and the copper the cathode. Platinum does not dissolve in the electrolyte and hence maintains its structural shape. The probe was scanned parallel to the surface of this model cell, across the anode and the cathode, at various sample-to-probe distances, d , in electrolytes of different conductance.

The peaks obtained for an applied anodic current of $1 \mu A$ through the platinum in 0.001 N sulfuric acid (H_2SO_4) as a function of d are shown in Fig. 6. If the probe is too far from the specimen surface, then either the signal is lost or the peaks are small and broad. As d decreases, the peak height increases and the width of the peak decreases giving a clear location of the local corrosion site. As anticipated, these results are consistent with the potential field generated from a local region shown in Fig. 1. For a clear determination of the corrosion site, therefore, the probe should be held close to the sample surface. The distance between the probe and metal surface, however, should not be less than the outer-tip diameter of the probe, or else it will disturb the potential distribution in the electrolyte [25]. For kinetic studies, a constant value of d must be maintained to obtain a meaningful relation between the peak height and the local current.

The effect of electrolyte conductivity on the peak height is shown in Fig. 7. The peak heights, with $d = 25 \mu m$ and anodic currents varied over two or-

12 ELECTROCHEMICAL CORROSION TESTING

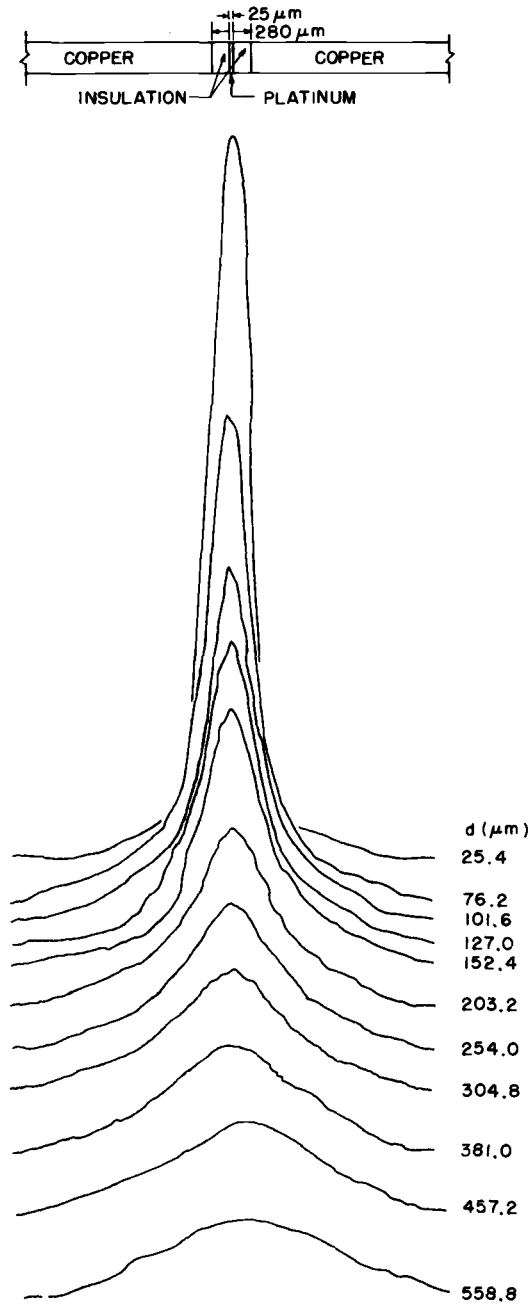


FIG. 6—Potential peaks for various distances (d) between the microtip reference electrode and the sample surface for an applied anodic current of $1\ \mu\text{A}$ through a platinum anode in $10^{-3}\ \text{N}\ \text{H}_2\text{SO}_4$.

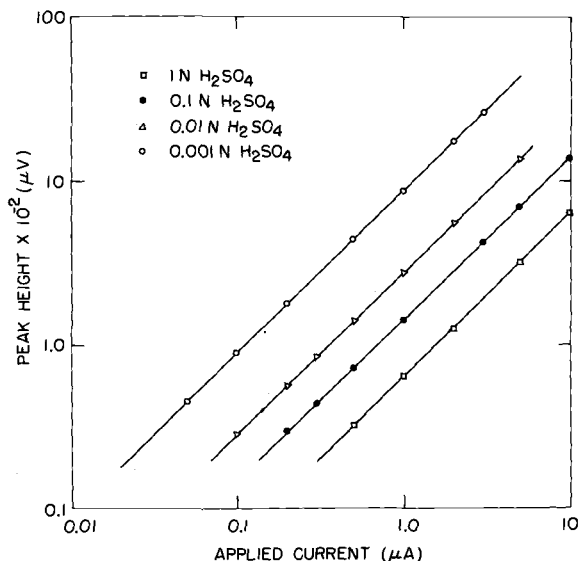


FIG. 7—Peak height versus applied anodic current in 1 N, 0.1 N, 0.01 N, and 0.001 N H_2SO_4 .

ders of magnitude, increased with decrease in electrolyte conductivity. Also, for a given electrolyte conductivity, there is a linear relationship between the peak height and the magnitude of the applied current. The peak heights thus give a direct measure of the intensity of the corrosion currents originating from the anodic sites.

Finally, the effect of the local area on the magnitude and shape of the peak is shown in Fig. 8. The peak height over the local region increases with increase in area due to the increase in the local current up to an area where the anode becomes large (~ 0.5 mm) and cannot be treated as a local region. It is observed that the maximum in the peak lies over the center of the local area. The peak shape thus gives an indication of the area of the local region.

Sensitivity and Resolution

The sensitivity (the ability to unambiguously determine very small corrosion currents originating from localized regions) and the resolution (the ability to distinguish between two anodic sites close to each other) of the SRET are governed mainly by the distance between the probe and specimen surface and the conductivity of the solution, as discussed previously. In a given experiment, however, the choice of the electrolyte may be limited by the type of localized corrosion to be studied. Additionally, the distance d is limited to the diameter of the probe tip. A decrease in the probe-tip diameter increases the sensitivity and resolution of the technique. A very fine tip, however, has a

very high impedance that increases the electrical noise and decreases the response time. Therefore proper compromise should be made for the choice of the probe-tip diameter.

The resolution of the SRET is dependent not only on the proximity of two corroding sites, but the magnitude of the corrosion current from each site. A schematic of the potential peaks obtained from two adjacent points for various corrosion conditions is shown in Fig. 9. If the corrosion currents from the two anodic sites are low, the potential peaks are small and broad. Hence, these can be resolved only if d is small. If the potential field from the two corroding sites is large, one does not obtain separate distinguished peaks, but two small peaks on a large broad peak. If one of the sites corrodes much faster than the other site, however, one observes only a change in the slope of the larger potential peak at the point of the other corrosion site. Thus, in each case, the location of the corrosion sites can be easily and accurately identified, but a quantitative measure of the corrosion rate at each site becomes difficult.

Applications

Pitting Corrosion

Pitting corrosion is a highly localized form of corrosion attack of passive metal surfaces and is generally directly related to the presence of chlorides or bromides. The development of pitting is sensitive to almost all variables associated with the interface between the metal and the electrolyte. These variables include the chloride concentration, the presence of other anions that may act as pitting inhibitors, the composition of the metal, its surface preparation and history, and the electrochemical potential [24,26-31]. The potential has been shown to be decisive in the initiation and propagation of pitting. If the potential is held below a critical value (usually termed the "pitting potential") pits do not develop. If the potential rises to or above the critical range, pitting initiates and can then continue to propagate below this potential [29]. If the potential is decreased sufficiently, the pitting eventually stops, and if held at low potentials, the pits lose the high chloride concentrations and the metal surface within the pit passivates.

The pitting behavior of stainless steels was investigated by Rosenfeld and Danilov [24] using the adjacent reference electrode technique. Their measurements were carried out in a solution containing about 0.05 *M* ferric ammonium sulfate [$\text{FeNH}_4(\text{SO}_4)_2$] and 1.0 or 0.56 *M* ammonium chloride (NH_4Cl). They could detect pits 30 to 60 s after contact with the solution. Initially, the rates of dissolution of all the pits were similar; with time, however, some of the pits stopped corroding or showed decreased rates. Microscopic observation of the pits showed that they were covered by a film or shielding layer resulting from the attack of the metal by chloride ions pene-

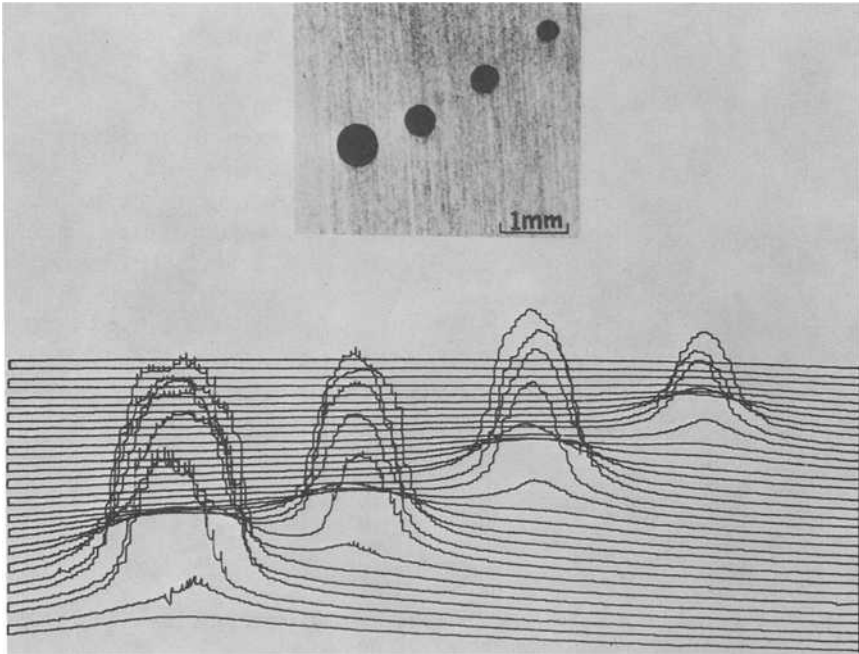


FIG. 8—Potential variation on copper held at open-circuit potential in $0.1\text{ N H}_2\text{SO}_4$ produced by the four circular markings of varying size. The inset shows the photomicrograph of the copper sample.

trating the oxide film. Destroying the shielding layer led to passivation. The authors considered the rupture of the shield assisted the diffusion of the “passivator” into the pit. The process of passivation took a relatively long time (on the order of tens of minutes) after disruption of the shield. The time for deactivation of the pits increased with the size of the pits. The deactivation process was probably a result of a diffusion process, but it is not possible to separate whether it was the result of increased diffusion of the high-chloride concentration from the pit or the diffusion of bulk solutions into it, since the time dependence of both processes are similar.

The currents from the pit were related to the square root of time. The current densities therefore decreased and, assuming a hemispherical pit, the surface area varied linearly with time. This result is in agreement with work by other investigators [26,27].

The SRET has been used to study the pitting of Type 304 stainless steels in a ferric chloride solution [20,30] composed of 0.4 M ferric chloride (FeCl_3) and adjusted to pH 0.9 [29]. The change in the number of active pits was studied as a function of time and surface preparation. On exposing the steel to the solution, the potential of the specimen increased rapidly above the

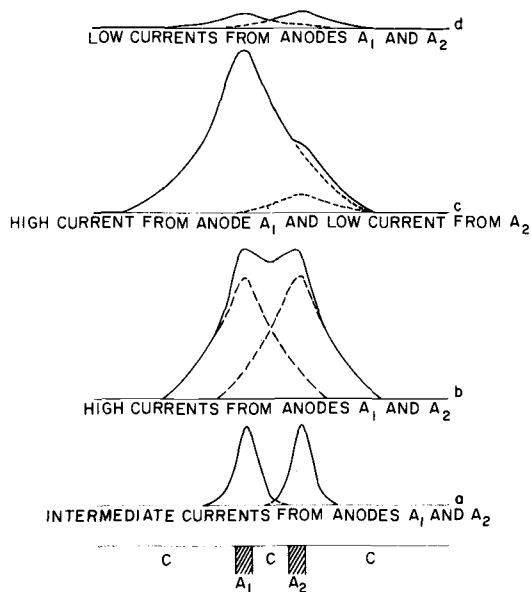


FIG. 9—Schematic of potential peaks from two adjacent anodic sites showing the effect anodic current from each site on the resolution of the SRET.

pitting potential with the generation of active pits. With time, the potential of the specimen decreased as the active pits grew and the number decreased. However, small potential increase was observed when pits passivated. The active and repassivated pits were separated using the SRET. The active pits were always covered by a film and contained a dark-green solution. Figure 10 shows a sequence of scans represented by potential surfaces for an electropolished surface at the times shown. Each peak is associated with the currents from active pits. On the first scan, initiated 1 min after exposure, fourteen pits could be identified. The number of active pits decreased until only one pit was active after 86 min. When the final pit was subjected to a jet of solution, it repassivated. The anodic currents polarizing the cathodic reaction then ceased, the potential rose rapidly above the pitting potential, and the sequence of events observed on first contacting the specimen with the chloride solution was repeated.

It was suggested that the film over the active pits was the passive oxide film originally on the metal surface that was undermined by the pitting process [20]. This possible explanation was investigated by varying the surface preparation of the stainless steel prior to pitting. The number of active pits was again studied as a function of time; a semilogarithmic plot was used to determine the half-life of the pits (Fig. 11). The surface preparations studied were electropolishing or abrasion and the effects of subsequent oxidation or ca-

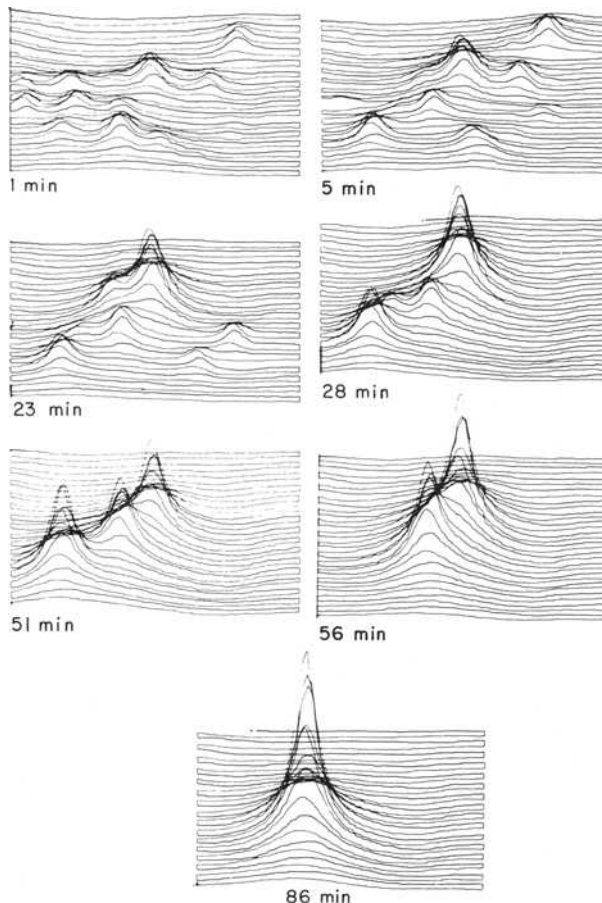


FIG. 10—Potential scans above an electropolished Type 304 stainless steel surface in 0.4 M FeCl_3 . The periods after exposure to the electrolyte are shown (Ref 20).

thodic polarization. The results were highly dependent on surface treatment. Air oxidation of electropolished surface at temperatures above 100°C for 24 h increased the half-lives of the pits. These changes are shown in Fig. 11, which includes the variations in the number of active pits for surfaces oxidized at 110, 165, and 240°C , and with cathodically polarized electropolished surfaces. Table 1 shows the half-lives for these and other treatments.

The results were found to be consistent with the changes in the properties of the original oxide layer over the pit before it was undermined by the pitting process. The thicker the oxide, the greater was the protection afforded to the growing pit and the longer the pits remained active. When the metal was abraded, stresses in the oxide film led to short half-lives (< 1 s). The half-life

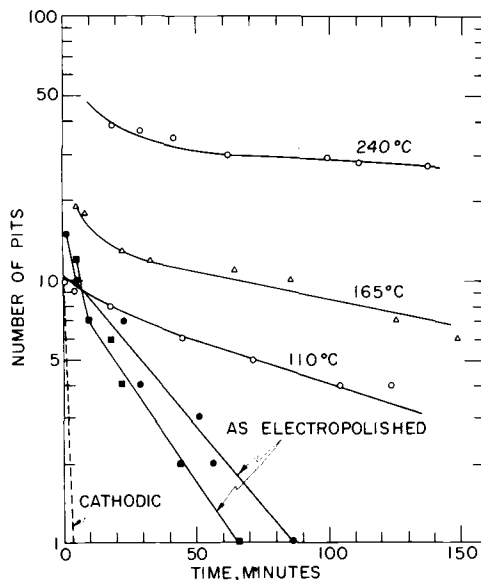


FIG. 11—Influence of surface treatment on the behavior of active pits with time for electropolished surfaces (Ref 28).

TABLE 1—Variations of pit half-life with surface preparation.

Surface Treatment	Pit Half-Life, min ^a
Electropolished and cathodically polarized	< 1
As electropolished	22
Electropolished and oxidized at 110°C for 24 h	90
Electropolished and oxidized at 165°C for 24 h	150
Electropolished and oxidized at 240°C for 24 h	430
Electropolished and oxidized at 250°C for 2 h	480
Electropolished and oxidized at 300°C for 22 h	340
Electropolished and oxidized at 375°C for 2 h	270
Abraded with 600-grade SiC	< 1
Abraded and oxidized at 250°C for 8 h	5

^aMaximum variation of 20 percent.

of pits on abraded surfaces was low (~5 min) even after oxidation at 250°C in comparison with similarly oxidized electropolished surfaces that gave a half-life of 480 min.

The pitting of stainless steels during the early development of the pits was interpreted in terms of maintaining the presence of high chloride concentrations within the pit and reducing the loss of chloride by diffusion into the lower-concentration bulk solution. The presence of the oxide film over the

pits hampers the diffusion of chloride that builds up as a result of ionic conduction. These two factors (the presence of the oxide film and the flow of chloride into the pit) suggest that improved pitting resistance of alloys may be accomplished either by reducing the rate of dissolution of the alloy in the concentrated environment within the pit or changing the properties of the passive oxide layer. The ideal passive oxide film for pitting resistance would be thin, highly stressed, and easily disrupted when undermined by pitting. These properties of the film contrast with those usually considered to give improved corrosion resistance.

The additions of nitrate to the ferric chloride solution inhibits pitting corrosion. The effect of nitrate was consistent with an influence on properties of the oxide film on steels [20]. At a critical concentration of 0.075 *M* sodium nitrate (NaNO_3) in the ferric chloride solution, pitting was not inhibited, but the pits that initiated did not propagate for more than a few minutes. It was suggested that the nitrate weakened the film, which was easily disrupted when undermined and led to repassivation.

Pitting of stainless steel was also studied in sodium chloride solutions under potentiostatic conditions using the SRET. The peak heights over the pitting areas were summed; the sum was found to be linearly related to the applied current. In ferric chloride solutions, the logarithm of the summed peak heights was plotted against the corrosion potential of the specimen. The slope of this plot was similar to that observed during cathodic polarization of the steel in ferric chloride inhibited with 1 *M* NaNO_3 to prevent pitting. The agreement between the slopes indicated that under open circuit conditions the cathodic polarization characteristics could be determined from the variation of the potential peaks, since they are a measure of the polarizing current [20].

Gainer and Wallwork [23] used the rotating cylinders to study the effects of surface abrasion and metallurgical features on the pitting corrosion of mild steels in 10^{-5} *N* sodium chloride (NaCl). The potential variation caused by difference in current flow was greatest for coarse abrasion on 280 grit paper. A 600 grit and $<1 \mu$ diamond-paste finishes gave similar results with smaller potential fluctuations. The differences observed on the coarsely abraded surface indicate a high density of active pits ($\sim 2.5 \times 10^3/\text{cm}^2$); their activity was probably associated with the greater true cathodic area available on the rougher surface. The number of active sites decreased with time, and the intensity of corrosion of the remaining active sites increased. The formation of pits around active sites were found to be related to presence of inclusions and scratches.

Intergranular Corrosion

Intergranular corrosion (IC) is defined as the localized attack, in certain corrosive media, at the grain boundaries of steels. This form of corrosion is

particularly severe in sensitized stainless steels. In austenitic stainless steels, sensitization is caused by (1) heat treating the alloy in the temperature range of 500 to 850°C for a few hours and quenching; (2) cooling slowly through the same temperature range, and (3) welding [32,33]. It is generally believed that sensitization leads to the precipitation of chromium-rich carbides at the grain boundaries and the depletion of chromium adjacent to the boundary [34]. This depletion has been observed by scanning transmission electron microscopy [35]. The depletion of chromium at the grain boundary leads to IC of stainless steels in certain environments.

The SRET has been used to determine the accelerated corrosion of grain boundary region in sensitized Type 304 stainless steel. Figure 12a is a potential scan during the IC of a large grain size (diameter ~ 3 mm), sensitized (600°C for 24 h) Type 304 stainless steel in 2.5 N sulfuric acid (H_2SO_4) at room temperature at a potential of -200 mV versus saturated calomel elec-

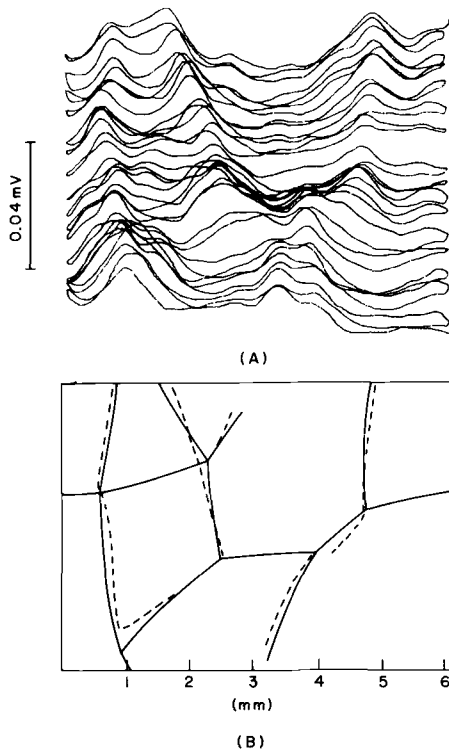


FIG. 12—Potential scan of the grain boundaries attacked on a large grain size, sensitized Type 304 stainless steel held at -200 mV in 2.5 N H_2SO_4 . (a) area scan of the potential fields measured by the SRET; (b) line drawing of the grain boundaries etched on metallographic observation of the sample (dark lines). Also drawn are the lines across the peaks in Fig. 12a (dotted lines).

trode (SCE). Figure 12b is a line drawing of the etched boundaries on metallographic observation after the test showing a clear relation between the etched boundaries (dark lines) and the peak maximum in Fig. 12a (dotted lines). The potential peaks in Fig. 12a were observed only in the case of sensitized Type 304 stainless steel; solution-annealed (1100°C for 3 h) samples exhibited no potential peaks and no grain boundary etching in this solution.

The dependence of intergranular corrosion on the electrochemical potential of Type 304 stainless steel in 2.5 N H₂SO₄ can be determined by slowly increasing the potential (0.3 V/h) of the sample in the anodic direction and scanning the surface simultaneously. In the potential region where sensitized Type 304 stainless steel is susceptible to IC, peaks are observed on scanning; in the potential region, where the material does not undergo IC, no peaks are observed. This is shown schematically in Fig. 13. The material is susceptible to IC between -280 to +80 mV versus SCE and then again in the transpassive region (>820 mV versus SCE). This result is consistent with the observation of IC of this steel in the Strauss test and the nitric acid test.⁴

In order to obtain a semiquantitative relation between the corrosion current flowing and the resulting potential field in the electrolyte due to intergranular corrosion, experiments were run in 1 N H₂SO₄ + 0.05 M potassium thiocyanate (KCNS) using the back-scan procedure [36,37]. The sample is held at -500 mV in the electrolyte for 5 min, then instantaneously raised

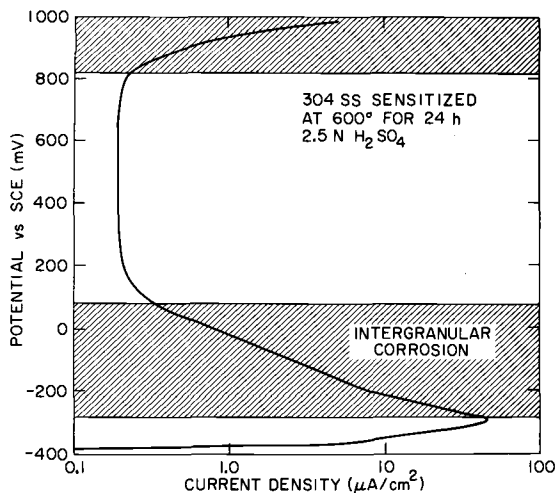


FIG. 13—Anodic polarization for the large grain size, sensitized Type 304 stainless steel in 2.5 N H₂SO₄. Also shown are potential zones over which the material is susceptible to intergranular attack.

⁴See ASTM Recommended Practices for Detecting Susceptibility to Intergranular Attack in Stainless Steels (A 262-79).

to +200 mV. The sample is cathodic at -500 mV and passive at +200 mV (versus SCE). The sample is held at +200 mV for 2 min, then decreased in the reverse direction from +200 to -500 mV at a rate of 3 V/h. In the case of solution-annealed samples, the surface was passive to -100 mV, when the currents became cathodic. In the case of sensitized samples, however, large anodic currents were observed, and the polarization curve showed an anodic peak. The anodic peak is a result of the active dissolution of the sensitized grain boundaries.

Figure 14 shows a polarization curve for Type 304 stainless steel sensitized at 600°C for 4 h obtained by the back-scan technique. An active peak is observed in the potential region -380 to -30 mV. In this region increased grain-boundary dissolution takes place. This is observed as potential peaks in Fig. 15. The peak height of one of the peaks is plotted against the applied potential in Fig. 14. It is observed that the shape of the peak height versus the current-density curve is similar to the potential versus the current-density curve. This demonstrates that the active current flows from the grain boundaries of the sensitized stainless steel, and the peak height is proportional to the total current. There is a direct correlation between the current and peak height. In the case of solution-annealed samples, no anodic corrosion current was observed nor were any potential peaks measured.

Grubitsch and Zirkl [38] have used the SRET to determine IC in precipitation-hardened aluminum-copper alloys. On heat treatment at 150°C for 1 h, CuAl₂ is precipitated at the grain boundaries of the alloy; this results in a precipitate-free zone adjacent to it. The grain boundary region is preferen-

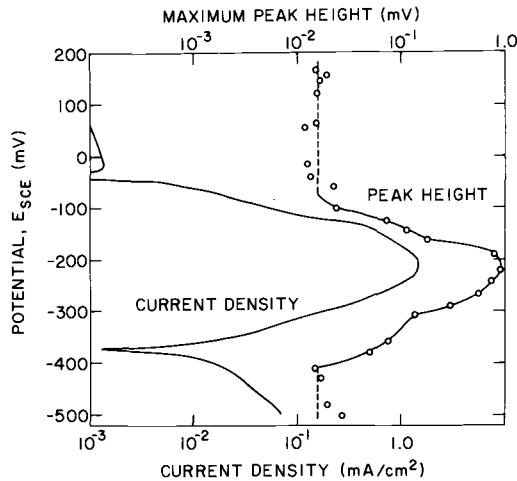


FIG. 14—Polarization curve of coarse-grained, sensitized Type 304 stainless steel in 1 N H_2SO_4 + 0.05 M KCNS at room temperature, and the peak height from one of the grain boundaries versus the applied potential.

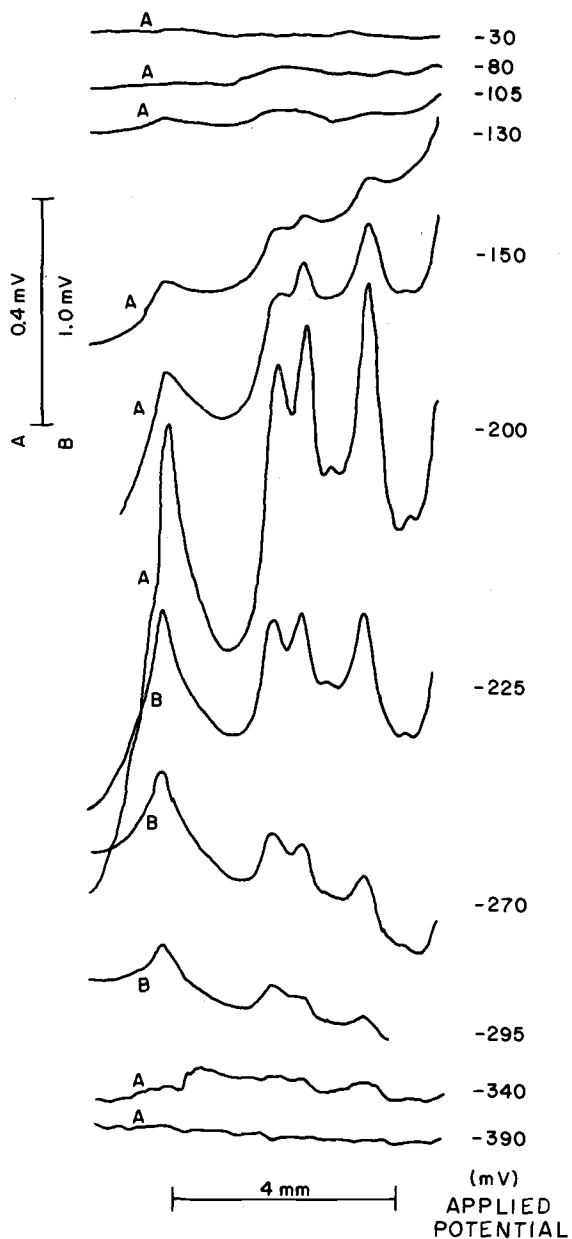


FIG. 15—Potential peaks obtained from different grain boundaries of sensitized Type 304 stainless steel during scanning in 1 N H_2SO_4 + 0.05 M KCNS at various applied potentials.

tially attacked in a large number of chloride-containing acidic solutions. However, when the alloy is solution treated (that is, no precipitation or the copper-free zone is formed) at 500°C for 12 h, it is not susceptible to IC.

Welds

In welding it is assumed that corrosion behavior of the weld metal and the parent metal is similar. This is not always the case, however, particularly when austenitic stainless steels are considered. The weldment (that is, the weld metal and the adjacent parent metal affected by the heat of the welding) may be susceptible to varying degrees of preferential attack. The weld metal may corrode more or less than the parent metal owing to differences in composition or metallurgical condition [33]. In addition, the heat-affected zone adjacent to the weld may be preferentially attacked as a result of metallurgical changes caused by the heating cycles [32]. The factors that can influence the type and degree of preferential attack depend on (1) composition and structure of base and weld metal, (2) metallurgical changes in the parent metal due to welding, (3) welding process and procedure, (4) size of material welded, and (5) the type of the environment [39].

The SRET has been successfully used to identify the preferential attack of Type 304 stainless steel weldments. The type of preferential attack observed are (1) attack of the ferrite in the weld matrix, (2) fusion boundary corrosion, and (3) intergranular corrosion of the sensitized material in the heat-affected zone of the base metal. Figure 16 shows the potential peaks measured on Type 304 stainless steel weldment, prepared by manually shielded arc gas welding Type 308 weld metal in 2.5 N H₂SO₄ at room temperature at various potentials. The weldment was slowly polarized (0.3 V/h) in the anodic direction from -500 mV to +1 V versus SCE and, simultaneously, the microtip reference electrode was scanned over the face of weldment. The potential regions exhibiting the different types of preferential attacks are shown in Fig. 17.

At more negative potentials, where the sample is cathodic, the weld material exhibits larger cathodic current densities than the parent metal. At a potential of -420 mV, however, where the overall current is cathodic, the weld exhibits preferential anodic dissolution (Fig. 16). The preferential attack of the weld extends into the anodic region, and the rate of attack increases with increase in anodic current. The preferential attack of the weld stops when the metal is passivated. In the transpassive region, however, the weld again corrodes preferentially, and the rate of attack increases with increase in the current.

The fusion boundary is preferentially attacked at potentials close to the maximum in the anodic peak. The preferential corrosion of the fusion boundary is shown as large peaks at the ends of the broad peak produced by corrosion of the weld, as shown in Fig. 16 for applied potentials -330, -300

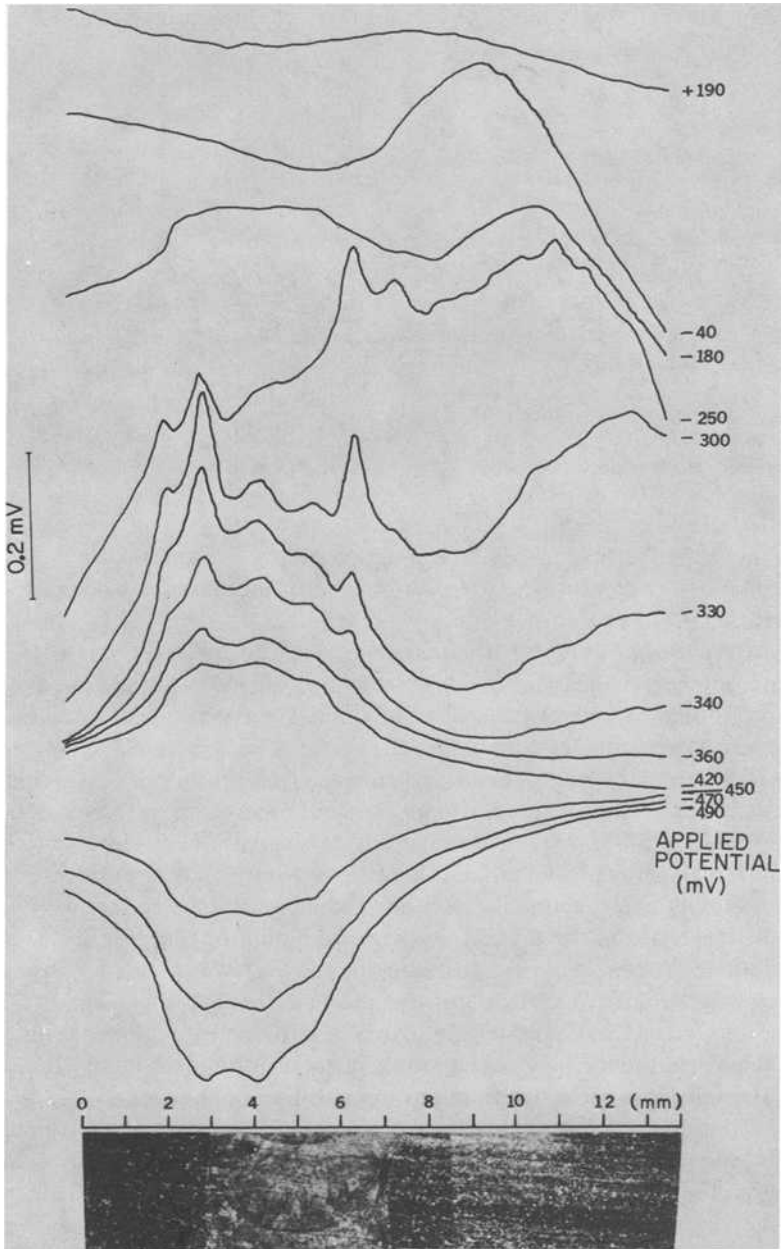


FIG. 16—Line scan across a Type 304 stainless steel weldment in 2.5 N H₂SO₄ at room temperature at various applied potentials showing preferential attack of (a) the weld metal, (b) fusion boundary, and (c) heat-affected zone.

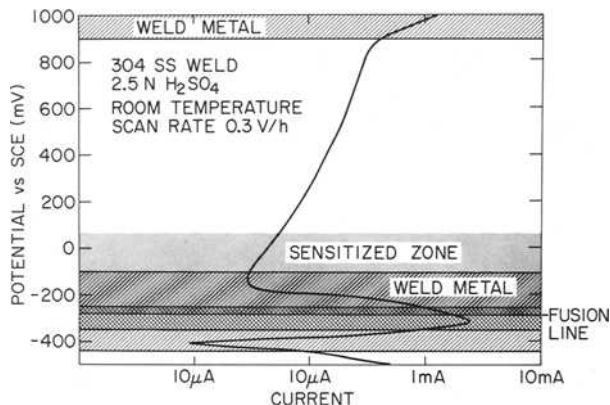


FIG. 17—Polarization curve for Type 304 stainless steel weldment showing the potential regions over which the different types of preferential attack occur.

and -250 mV versus SCE. As the sample passivates and the total current of the sample decreases, the corrosion of the fusion boundary decreases drastically.

In Fig. 16, at an applied potential of -250 to -40 mV versus SCE, the development of a peak in the base metal is observed. This peak is due to the intergranular attack of the sensitized zone. The peak increases as the polarization current decreases; that is, the metal is passivated. The single, large peak is a result of the preferential corrosion of a large number of grain boundaries in the sensitized zone. The peak is observed from -310 to $+100$ mV, beyond which the complete weldment is passivated. The position of this maximum changes with potential. This results from changes in position of the most susceptible regions in the sensitized zone with potential.

Micrographs of the attacked regions were obtained in order to determine the effect of the local microstructure on the various modes of preferential attack (Fig. 18). The microstructure in the weld center consists of a network of ferrite platelets in an austenitic matrix. In the active region, the increased corrosion of the ferrite gives rise to the peak over the weld metal. It is known that ferrite is more active than austenite at the lower potential [40,41]. The corrosion of the ferrite gives rise to the anodic peak of the weld, although the total current of the sample is cathodic. The waves on this peak are caused by the presence of the root of the run in the weld. At the fusion boundary, the ferrite is not in the form of fine platelets, but is present as large, separate particles. This increased ferrite content at the boundary gives rise to the enhanced corrosion of the fusion boundary. No sigma phase was observed at the fusion boundary. On each side of the weld, the parent material is in the solution-annealed state, and no grain-boundary etching was observed. At a distance of 2 to 3 mm from the weld fusion line, the grain boundaries are

etched. This increased corrosion from the sensitized grain boundaries gives rise to the broad peak over this region.

Similar differences in the corrosion of the weld and the parent metal have been observed for ferritic 17 percent chromium steels in chloride-containing solutions [38]. It has been found that the type of preferential attack depends on the impressed applied current and the electrolyte (for example, the chloride concentration, pH, and the presence of organic solvents). Hildebrand and Schwenk [14] have measured the increased anodic activity in the heat-affected zones of austenitic stainless steel welds. Using an SRET, they were able to plot the potential field arising from corrosion of the sensitized region in heat affected zones in $10^{-3} N$ alcoholic hydrochloric acid (HCl).

Sensitization in the heat-affected zone adjacent to the weld is probably the most common cause of intergranular corrosion and intergranular stress-corrosion cracking in stainless steels in service. In order to determine the susceptibility of a given weldment to these forms of localized attack, it is necessary to develop a test that will give (1) the location of the sensitized zone, and (2) a quantitative measure of the degree of sensitization. The SRET meets these requirements and has been successfully used to give the location and degree of sensitization of the weldments for various welding process variables. The details of the test are given elsewhere [21]. In summary, the test consists of

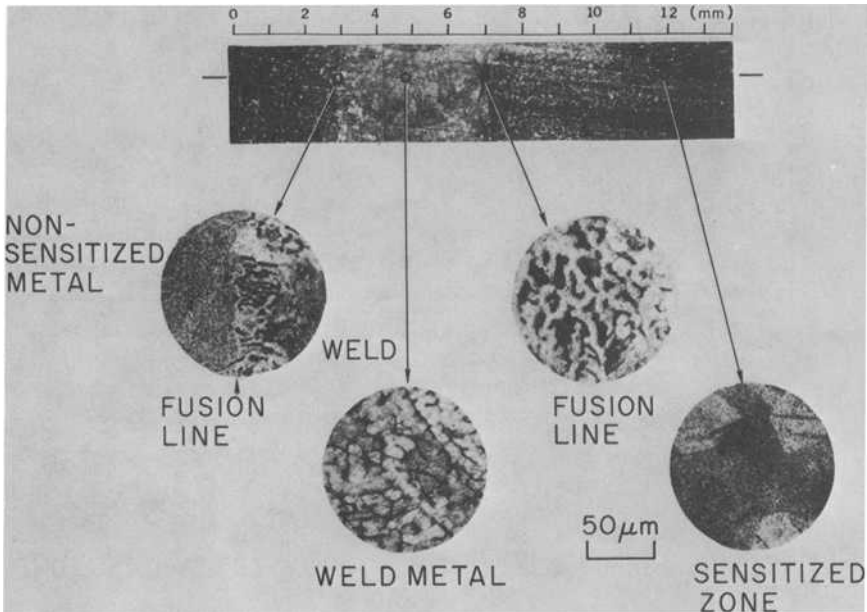


FIG. 18—Micrographs of Type 304 stainless steel weldment showing the attacked structure in the weld metal, fusion line, nonsensitized parent metal, and the sensitized boundaries in the heat-affected zone.

scanning across the weldment while it is polarized by the back-scan technique (described earlier). A representative scan for Type 304 stainless steel weldment over the heat-affected zone is shown in Fig. 19. The location and width of potential peak gives an indication of the location and width of the sensitized zone (as observed in the etched sample in Fig. 19); the peak height is proportional to the degree of sensitization. This technique is more sensitive than accepted chemical methods of evaluating stainless-steel welds for their resistance to intergranular corrosion.

Stress-Corrosion Cracking

Stress-corrosion cracking (SCC) in metal systems is concerned with the nucleation and propagation of cracks in stressed metals induced by the environ-

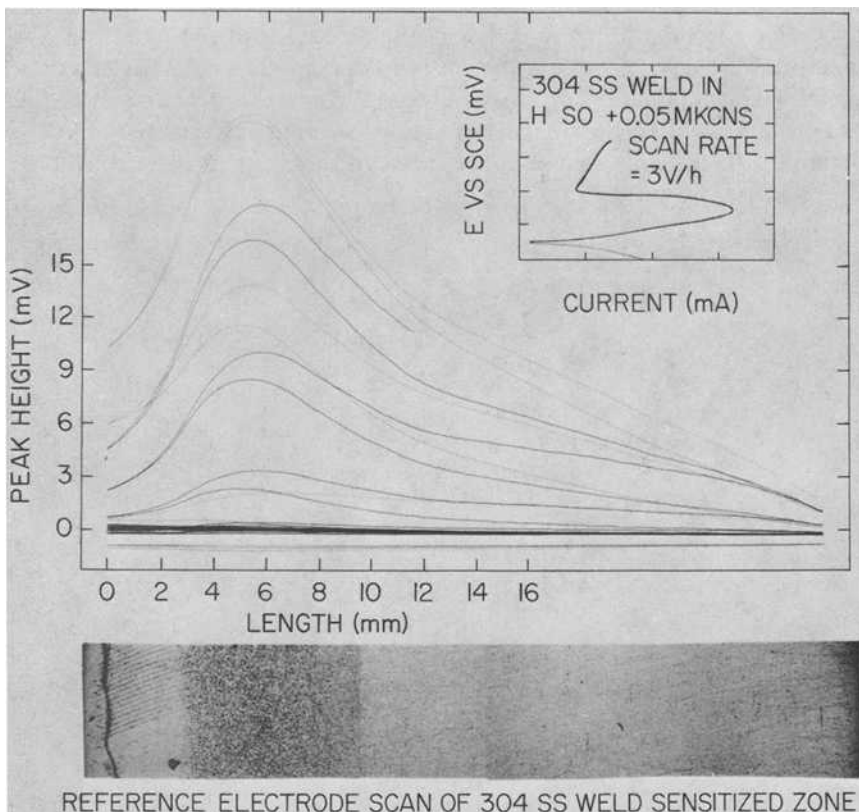


FIG. 19—Potential field produced by intergranular corrosion of the heat-affected zone adjacent to Type 304 stainless steel weldment in 1 N H_2SO_4 + 0.05 M $KCNs$. Also shown is the micrograph of the etched boundaries and the polarization curve of the sample by the back-scan technique (Ref 21).

ment. In order to understand the mechanism of cracking in any particular metal-environment system, it is necessary to determine the electrochemical reaction(s) that takes place at the crack tip. The SRET provides an ideal system for studying this reaction; in this section an example is given of SCC of Type 304 stainless steel in a chloride solution.

The electrochemical cell around the sample is shown in Fig. 20. A tensile specimen with a 90 deg notch having a radius of about $125\ \mu\text{m}$ at the tip was inserted through slits in a thin-walled fluorinated container. The specimen was sealed to the container with silicon rubber. The sample was loaded horizontally in a tensile machine to an initial stress of 8.5 ksi. The upper face of the specimen with the V-notch was metallographically polished, and all but part of this surface around the notch was coated with the silicon rubber. The

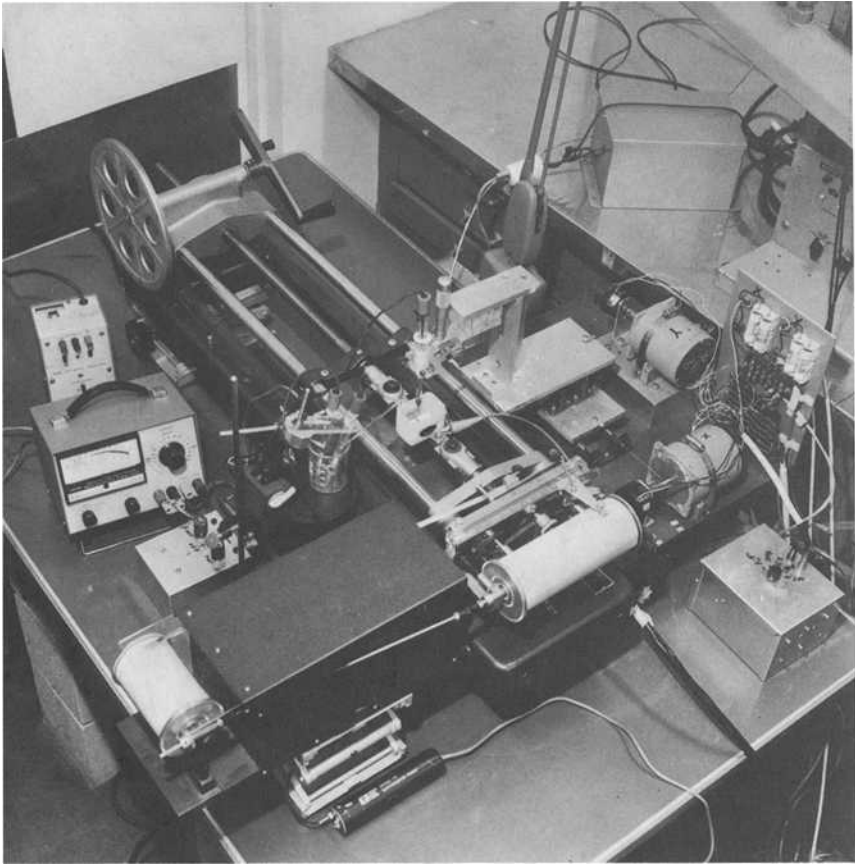


FIG. 20—Detail of the electrochemical cell and the loading system attached to the SRET for stress-corrosion cracking studies.

electrolyte used was 20 molal lithium chloride (LiCl) controlled at 90°C using an infrared lamp.

Following the initial exposure to the electrolyte, pitting was observed optically. The progress of large pits that remained active was monitored using the SRET. After some time, the intensity of the pitting decreased and the potential of the specimen rose. When the pitting stopped, potential peaks were observed at the root of the notch associated with the initial stages of cracking. Figure 21 shows the potential peaks observed after the cracking had progressed into the metal. The propagation of the potential peaks was studied. Figure 22 gives the magnitude of potential peaks along the length of the crack at various times taken from figures similar to Fig. 21. The shape of

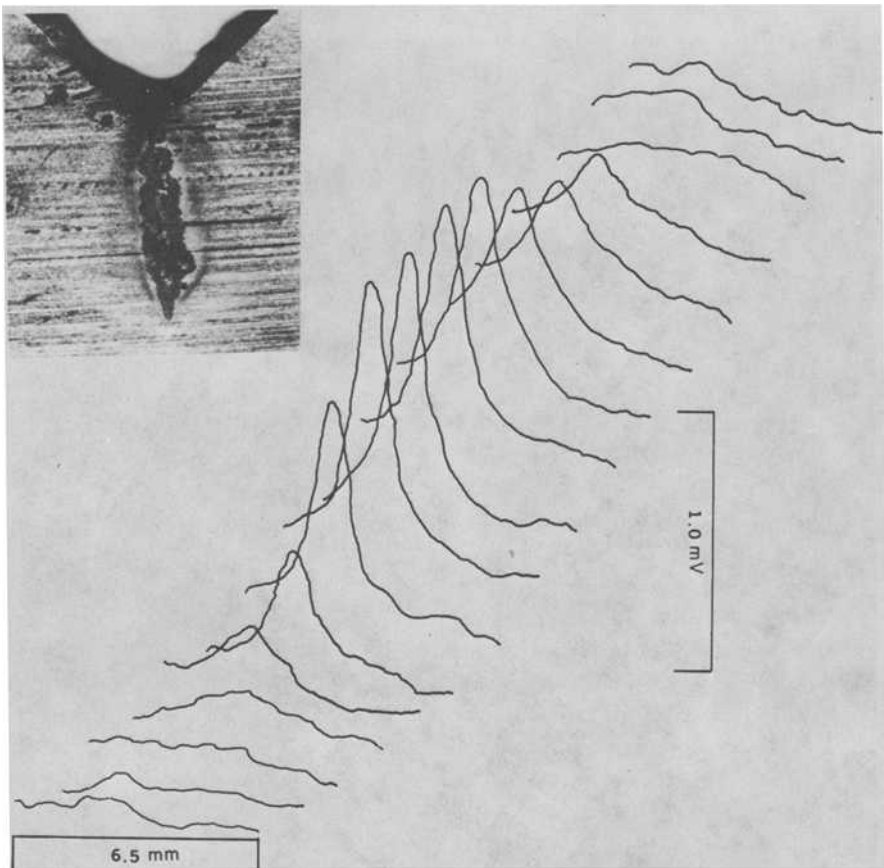


FIG. 21—Potential scan across a propagating stress-corrosion crack in Type 304 stainless steel exposed to LiCl at 90°C at a stress of 8.5 ksi. The crack is shown in the micrograph.

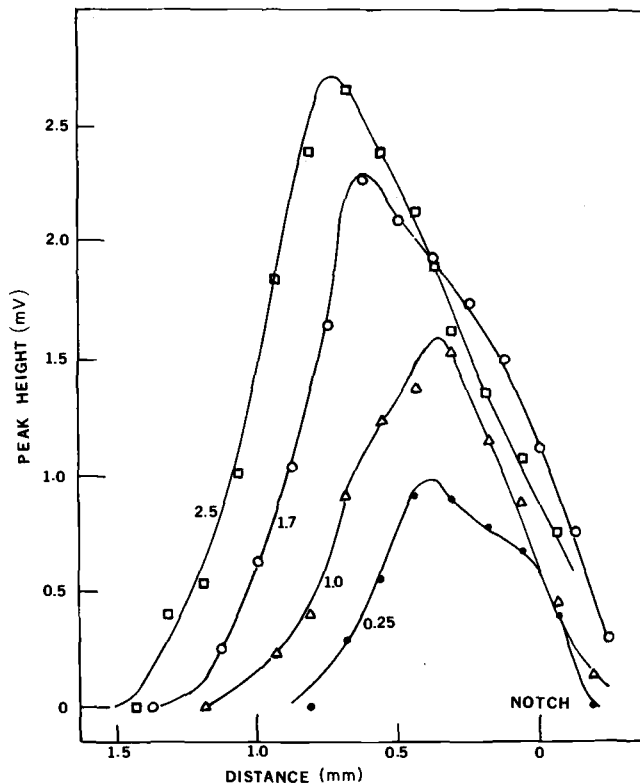


FIG. 22—Potential profiles along the stress-corrosion crack at various stages of the propagation in Type 304 stainless steel exposed to LiCl at 90°C at 8.5 ksi.

these nonsymmetrical plots indicates that, although the dissolution rate was greatest at the crack tip, the entire crack remained active. These observations are consistent with most theories of stress-corrosion cracking; that is, rapid dissolution takes place at the high-stress intensity at the crack tip where fresh metal is continuously exposed to the corrosive environment [42]. However, the persistent anodic dissolution of the crack surfaces shown using SRET, during cracking and after the specimens fail, is in conflict with models that suggest the crack surface must passivate to account for crack propagation. The SRET suggests that the exposed metal remains active but with decreased dissolution rates. The theory based on the rupture of passivating oxide layers appears to be a simplification of the process. The detailed theory would require taking into account rupture of a more complex corrosion product or other processes, such as stress-stimulated dissolution at the crack tip, to be consistent with these observations.

Summary

The SRET has been shown to offer a technique for studying localized forms of corrosion including pitting, intergranular corrosion, and stress-corrosion cracking. These processes are associated with relatively rapid dissolution rates and observable potential variation in solution. The technique is also useful in separating preferential dissolution or cathodic reactions under controlled potentials where external currents flow.

Other electrochemical measurements (for example, polarization techniques) can give detailed information about processes under study, but difficulties arise in the complete separation of the anodic and cathodic areas and duplicating the conditions operative during corrosion. The SRET overcomes these difficulties, offers an approach for *in situ* determination of the corrosion processes, and allows for clarification of the factors involved, without extraneous effects influencing the corrosion.

Acknowledgments

This research was carried out under the auspices of the United States Department of Energy. Appreciation is extended to K. Sutter for conducting the corrosion tests and to Dr. J. R. Weeks for helpful discussions during the course of this investigation.

References

- [1] *Localized Corrosion—Cause of Metal Failure*, ASTM STP 516, American Society of Testing and Materials, 1972.
- [2] Brown, B. F., Kruger, J., and Staehle, R. W., Eds., *Localized Corrosion*, National Association of Corrosion Engineers, 1974.
- [3] Evans, U. R. and Hoau, T. P., *Proceedings of the Royal Society*, Vol. 137, 1932, p. 343.
- [4] Compton, K. G. and Turley, J. A. in *Galvanic and Pitting Corrosion—Field and Laboratory Studies*, ASTM STP 576, American Society for Testing and Materials, 1976, p. 56.
- [5] Coriou, H., Monnier, A., Pinard-Legry, G., and Plante, G. in *Localized Corrosion*, National Association of Corrosion Engineers, Houston, 1974, p. 368.
- [6] Baboian, R. in *Electrochemical Techniques for Corrosion*, National Association of Corrosion Engineers, 1977, p. 73.
- [7] Lajain, H., *Zeitschrift für Werkstofftechnik*, Vol. 2, 1971, p. 19.
- [8] Lajain, H., *Werkstoffe und Korrosion*, Vol. 23, 1972, p. 537.
- [9] Evans, U. R. and Agar, J. N., see Evans, U. R., *The Corrosion and Oxidation of Metals*, Edward Arnold, 1960, p. 862; Evans, U. R., *Journal of the Iron and Steel Institute*, Vol. 141, 1940, p. 219.
- [10] Jaenicke, W., *Zeitschrift für Physikalische Chemie*, Vol. A191, 1943, p. 350.
- [11] Jaenicke, W. and Bonhoeffer, K. F., *Zeitschrift für Physikalische Chemie*, Vol. 193, 1944, p. 301.
- [12] Copson, H. R., *Journal of the Electrochemical Society*, Vol. 84, 1943, p. 71.
- [13] Rozenfeld, I. L., *Atmospheric Corrosion of Metals*, National Association of Corrosion Engineers, 1972, p. 83.
- [14] Hildebrand, H. and Schwenk, W., *Werkstoffe und Korrosion*, Vol. 23, 1972, p. 364.
- [15] McCafferty, E., *Journal of the Electrochemical Society*, Vol. 124, 1977, p. 1869.
- [16] Smyol, W. M. and Newman, J., *Journal of the Electrochemical Society*, Vol. 123, 1976, p. 1423.

- [17] Waber, J. T., *Corrosion*, Vol. 13, 1957, p. 95t.
- [18] Waber, J. T. and Rosenbloth, M., *Journal of the Electrochemical Society*, Vol. 102, 1955, p. 344.
- [19] Wagner, C., *Journal of the Electrochemical Society*, Vol. 98, 1951, p. 116.
- [20] Isaacs, H. S. in *Localized Corrosion*, National Association of Corrosion Engineers, Houston, 1974, p. 158.
- [21] Vyas, B. and Isaacs, H. S., *Intergranular Corrosion of Stainless Alloys*, ASTM STP 656, R. F. Steigerwald, Ed., American Society for Testing and Materials, 1978, p. 133.
- [22] Bhansali, J. J. and Hepworth, M. T., *Journal of Physics, E., Scientific Instruments*, Vol. 7, 1974, p. 681.
- [23] Gainer, L. J. and Wallwork, G. R., *Corrosion*, Vol. 35, 1979, p. 61.
- [24] Rosenfeld, I. L. and Danilov, I. S., *Corrosion Science*, Vol. 7, 1967, p. 129.
- [25] Eyring, H. J., *Physical Chemistry*, Vol. 9A, 1970, p. 359.
- [26] Engell, H. J. and Stolice, N. D., *Zeitschrift für Physikalische Chemie*, Vol. 20, 1959, p. 113.
- [27] Sato, N., Nakagawa, T., Kudo, K., and Sakashita, M. S. in *Localized Corrosion*, National Association of Corrosion Engineers, Houston, 1974, p. 447.
- [28] Isaacs, H. S. and Kissel, G., *Journal of the Electrochemical Society*, Vol. 119, 1972, p. 1628.
- [29] Wilde, B. E. and Williams, E., *Journal of the Electrochemical Society*, Vol. 117, 1970, p. 775.
- [30] Galvele, J. R. in *Passivity of Metals*, R. P. Frankenthal and J. Kruger, Eds., The Electrochemical Society, 1978, p. 285.
- [31] Wilde, B. E. and Williams, E., *Electrochimica Acta*, Vol. 16, 1971, p. 1971.
- [32] Cowan, R. L. and Tedmon, Jr., C. S., *Advances in Corrosion Science and Technology*, Vol. 3, 1973, p. 293.
- [33] Henthorne, M. in *Localized Corrosion—Cause of Metal Failure*, ASTM STP 516, American Society for Testing and Materials, 1972, p. 66.
- [34] Tedmon, Jr., C. S., Vermilyea, D. A., and Rosolowski, J. H., *Journal of the Electrochemical Society*, Vol. 118, 1971, p. 192.
- [35] Pande, C. S., Suenaga, M., Vyas, B., Isaacs, H. S., and Haring, D. F., *Scripta Metallurgica*, Vol. 11, 1977, p. 601.
- [36] Novak, P., Steppe, R., and Franz, F., *Corrosion*, Vol. 31, 1975, p. 344.
- [37] Clarke, W. L., Cowan, R. L., and Walker, W. L. in *Intergranular Corrosion of Stainless Alloys*, ASTM STP 656, R. F. Steigerwald, Ed., American Society for Testing and Materials, 1978, p. 99.
- [38] Grubitsch, H. and Zirkl, A., *Werkstoffe und Korrosion*, Vol. 23, 1972, p. 565.
- [39] Brautigam, F. C., *Corrosion*, Vol. 31, 1975, p. 101.
- [40] Gooch, T. C., Honeycombe, J., and Walker, P., *British Corrosion Journal*, Vol. 6, 1971, p. 148.
- [41] Cihal, V. and Prazak, M. J., *Iron and Steel Institute*, Vol. 193, 1959, p. 360.
- [42] Latanision, R. M. and Staehle, R. W. in *Fundamental Aspects of Stress Corrosion Cracking*, R. W. Staehle, A. J. Forty, and D. van Rooyen, Eds., National Association of Corrosion Engineers, 1969, p. 278.

Potential Dependence of Localized Corrosion in Iron

REFERENCE: Toušek, Jaromír, "Potential Dependence of Localized Corrosion in Iron," *Electrochemical Corrosion Testing, ASTM STP 727*. Florian Mansfeld and Ugo Bertocci, Eds., American Society for Testing and Materials, 1981, pp. 34-42.

ABSTRACT: Two passivating potentials, E_{F1} and E_{F2} , can be observed for iron in chloride containing media. From the existence of these two passivating potentials the existence of two breakdown potentials follows: the first breakdown potential, E_{b1} , and the second breakdown potential E_{b2} . In the regions immediately positive to these potentials, the rate of localized corrosion (that is, the total current density and the number of pits) rises exponentially with the potential. According to the solution composition, the current density in the pits is potential independent or obeys the exponential dependence.

KEY WORDS: corrosion, localized corrosion, polarization, iron

The total current density j , the number of pits z , and the current density in the pits j_L , are of importance in the localized corrosion kinetics. Until now only a few attempts have been made to determine the current density in the pits [1-4].² The reason may lie in the widespread opinion that the dissolution of metals in the pits is controlled by diffusion, and thus offers little information about the metal dissolution mechanism. Furthermore, the kinetics of localized corrosion are often very complicated [5], and it is difficult and in some cases impossible to derive equations that would enable one to evaluate the rate of metal dissolution in the pits.

In this paper the potential and time dependence of localized corrosion in iron—especially of the dissolution rate in the pits—is given with the aim of gaining some information concerning the localized corrosion mechanism.

Experimental Procedure

The localized corrosion of iron (99.999 percent) was measured by the potentiostatic and potentiodynamic methods. Under potentiostatic conditions the electrode was passivated for 10 min, then the potential was raised

¹Czechoslovak Academy of Sciences, Institute of Physical Metallurgy, Brno, Czechoslovakia.

²The italic numbers in brackets refer to the list of references appended to this paper.

above the breakdown potential, and the time dependence of current density and of the number of pits was followed. From these data the corrosion current density in the pits was calculated. The potentiodynamic polarization curves were recorded at a fast scanning rate of $dE/dt = 10 \text{ mVs}^{-1}$. All chemicals used were of *pro analysi* purity. The temperature was controlled at 21°C . The potentials are quoted against the saturated calomel electrode (SCE).

Results and Discussion

The potential dependence of localized corrosion of iron is illustrated by the potentiodynamic polarization curve 1 (Fig. 1). On this curve there are these characteristic potentials: the first passivating potential E_{F1} , the first breakdown potential E_{b1} , the second passivating potential E_{F2} , and the second breakdown potential E_{b2} . There are Regions A and C where the localized corrosion current rises, and Region B where it decreases with the potential. The corrosion rate in Regions A, B, and C depends on the composition of corrosion medium; therefore, usually only a part of this polarization curve is recorded. In this paper we shall be interested in the potential dependence of localized corrosion in Regions A and C.

The polarization curve involving Region A, for example, is obtained in the solutions containing strongly adsorbed anions (chlorides) alone or together with ClO_4^- , (Curve 2), OH^- , NO_3^- , SO_4^{2-} , etc. The analysis of the potential dependence of localized corrosion in Region A in the sodium chloride +

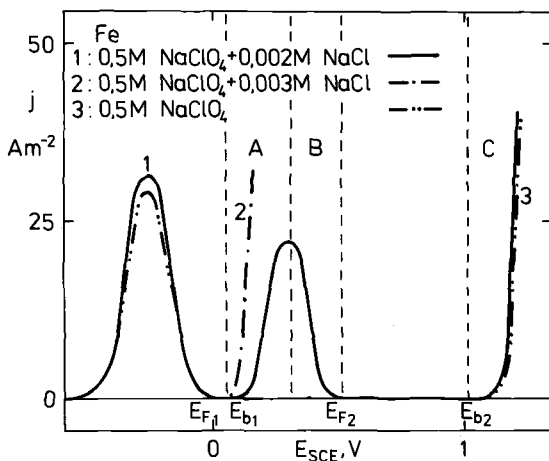


FIG. 1.—Potentiodynamic polarization curves of iron in solution containing ClO_4^- and $\text{ClO}_4^- + \text{Cl}^-$ ions.

sodium sulfate ($\text{NaCl} + \text{Na}_2\text{SO}_4$) and in the potassium chloride + potassium hydroxide ($\text{KCl} + \text{KOH}$) solutions will now be given.

The time dependences of total current density, j , and number of pits, z , in the $\text{KCl} + \text{NaSO}_4$ solution have been determined experimentally (Fig. 2). They satisfy the equations

$$j = A_1 t^2 \quad (1)$$

and

$$z = Kt \quad (2)$$

where A_1 and K are constants, and t is the time. At the potential $E = 0.035$ V, the constant $A_1 = 1.5 \cdot 10^{-4} \text{ Am}^{-2}\text{s}^{-2}$ and $K = 10^4 \text{ m}^{-2}\text{s}^{-1}$. The calculation of the pit radius, r , and of the current density in the pits, j_L , may be presented as follows [6]: The shape of a pit is hemispherical and for its growth it holds that

$$(2/3)\pi r^3 = (V_M/2F) \int_0^{t-t_i} Idt \quad (3)$$

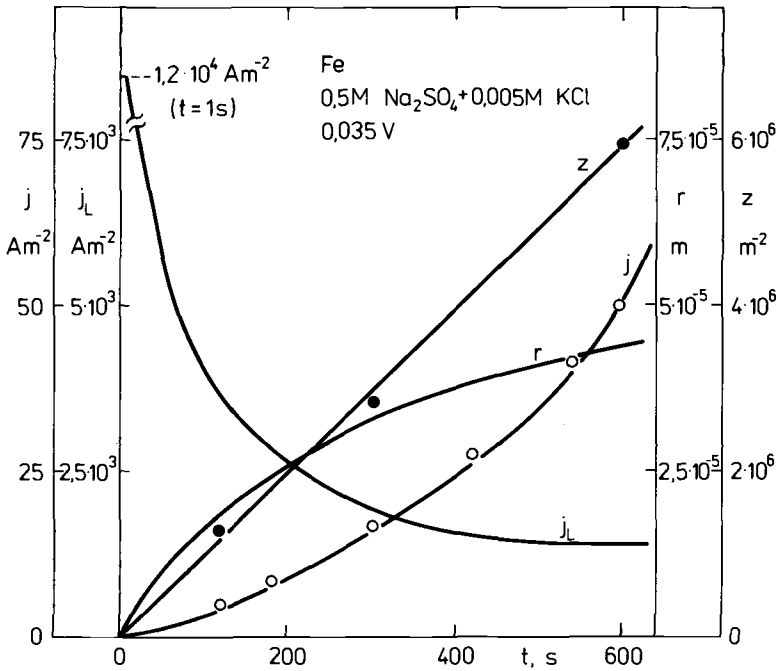


FIG. 2—Time dependence of the total current density j , the number of pits z , the current density in the pits j_L , and the radius of the pit r , in a solution containing $\text{SO}_4^{2-} + \text{Cl}^-$ ions.

where

- V_M = molar volume of iron,
- F = Faraday constant,
- I = current from one pit,
- $(t - t_i)$ = age of the pit, and
- t_i = time at which the pit was initiated.

The current, I , at the time t , for a pit that initiated at the time t_i , can be found from

$$I = c_1(t - t_i) \quad (4)$$

where c_1 is a constant. The number of pits, z , at the time t_i , is $z = Kt_i$.

For the time interval from t_i to $t_i + dt$ the increment of the number of pits is

$$dz = Kdt \quad (5)$$

and the increment of the total current density is

$$dj = jdz = c_1(t - t_i)Kdt \quad (6)$$

Integrating Eq 6 leads to

$$j = c_1K \int_0^t (t - t_i)dt = c_1Kt^2/2 \quad (7)$$

From Eqs 7, 4, and 1 it follows that $c_1 = 2A_1/K$ and $I = 2A_1(t - t_i)/K$.

By substituting the equation for I in Eq 3, the pit radius, r , at $t_i \rightarrow 0$ can be calculated as

$$r = C_1^3 \sqrt{(jt/z)} = C_1^3 \sqrt{(A_1 t^2/K)} \quad (8)$$

where $C_1 = \sqrt[3]{(3V_M/4\pi F)}$.

The current density, j_L , for the active pit surface can be calculated from the equation $j_L = I/P$, where P is the pit surface

$$P = 2\pi r^2 \quad (9)$$

On inserting the dimensions of the pit (Eq 8) into Eq 9, it can be determined that

$$j_L = B_1^3 \sqrt{(A_1/Kt)} = B_1^3 \sqrt{(j/zt^2)} \quad (10)$$

where $B_1 = \sqrt[3]{(16F^2/9\pi V_M^2)}$. It follows from Eq 10 that the current density in active pits decreases during the localized corrosion. The time dependence of r and j_L calculated from Eqs 8 and 10 is given in Fig. 2.

In the KCl + KOH solution the time dependence of the total current density j follows the equation

$$j = A_2 t^3 \quad (11)$$

and the number of pits is given by Eq 2 as has been found by the analysis of the experimental determined time dependencies of j and z presented in Fig. 3. In this case $A_2 = 1.8 \cdot 10^{-5} \text{ Am}^{-2} \text{ s}^{-3}$ and $K = 2.9 \cdot 10^4 \text{ m}^{-2} \text{ s}^{-1}$ at $E = 0V$. By a similar way, as in the foregoing case, we obtain for the pit radius

$$r = C_2^3 \sqrt{(jt/z)} = C_2^3 \sqrt{(A_2/K)} \cdot t \quad (12)$$

where $C_2 = \sqrt[3]{(3V_M/4\pi F)}$, and for the current density in the pits [6]

$$j_L = B_2^3 \sqrt{(A_2/K)} = B_2^3 \sqrt{(j/zt^2)} \quad (13)$$

where $B_2 = \sqrt[3]{(6F^2/\pi V_M^2)}$. In contrast to the localized corrosion in the KCl + Na_2SO_4 solution, the pit radius rises linearly with time and the current density in the pits remains constant. The calculated time dependencies of r and j_L are given in Fig. 3.

The potential dependencies of j , j_L , and z are illustrated by the lines in

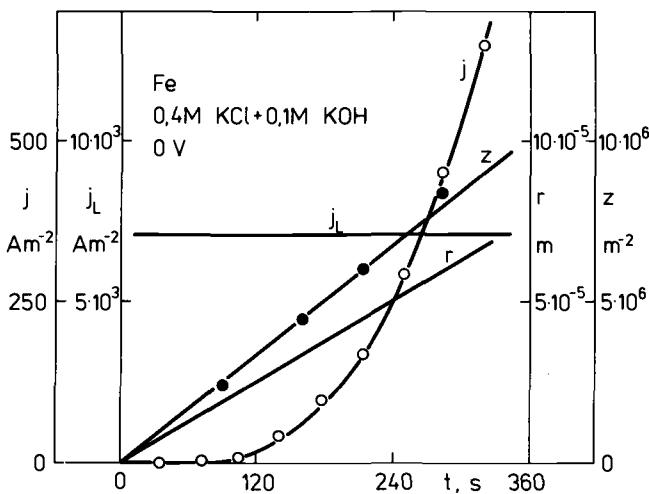


FIG. 3—Time dependence of the total current density j , the number of pits z , the current density in the pits j_L , and the radius of the pit r , in a solution containing $\text{OH}^- + \text{Cl}^-$ ions.

Figs. 4 and 5. The potential dependencies for j and z were found experimentally; the dependence for j_L was calculated by means of Eqs 10 and 13.

For a constant time, temperature, and concentration it holds that

$$j = j_D \exp(2.303 \Delta E/b) \quad (14)$$

$$z = z_D \exp(2.303 a \Delta E) \quad (15)$$

$$j_L = j_{L,D} \exp(2.303 \Delta E/b_0) \quad (16)$$

where

$j_D, z_D, j_{L,D}$ = current density, the number of pits, and the current density in the pits, respectively, at the breakdown potential E_{b1} ,

$\Delta E = E - E_{b1}$, and

a, b, b_0 = constants that are connected by the equation $1/b = a + 3/b_0$ [7].

If $a = 1/b$, the current density j_L is potential independent as observed in $\text{Na}_2\text{SO}_4 + \text{KCl}$ (Fig. 4). If $a < 1/b$, the current density j_L depends on the potential, and the metal dissolution in the pits is of an electrochemical character (Fig. 5, $\text{KCl} + \text{KOH}$). The value 0.45 V has been found for the constant b_0 .

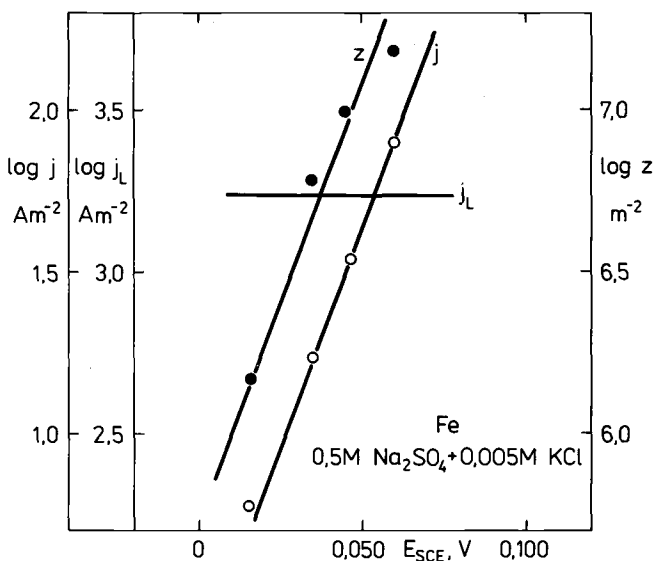


FIG. 4—Potential dependence of the total current density j , the current density in the pits j_L , and the number of pits z , in a solution containing $\text{SO}_4^{2-} + \text{Cl}^-$ -ions.

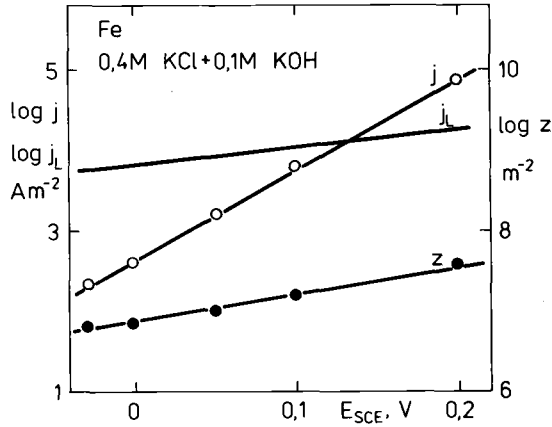


FIG. 5—Potential dependence of the total current density j , the current density in the pits j_L , and the number of pits z , in a solution containing $OH^- + Cl^-$ -ions.

The localized corrosion in Region C takes place when polarizing iron, for example, in the solutions containing ClO_4^- -ions (Curve 3) (Fig. 1). The alcoholic solution of $NaClO_4$ was used for the time and potential analysis because in this medium the pits are distinct and have a hemispherical form, whereas those in aqueous solutions are irregular and the calculation of j_L is impossible.

The time dependence of the total current density and of the number of pits have been found to be (curves for j and z in Fig. 6)

$$j = A_3 t \quad (17)$$

$$z = \text{const} \quad (18)$$

where $A_3 = 0.16 A m^{-2} \cdot s^{-1}$ and $z = 7.9 \cdot 10^6 m^{-2}$. For the pit radius and the current density in the pits the following equations are valid [8]:

$$r = C_3^3 \sqrt{(jt/z)} = C_3^3 \sqrt{(A_3 t^2/z)} \quad (19)$$

where $C_3 = \sqrt[3]{(3V_M/8\pi F)}$; and

$$j_L = B_3^3 \sqrt{(A_3/zt)} = B_3^3 \sqrt{(j/zt^2)} \quad (20)$$

where $B_3 = \sqrt[3]{(8F^2/9\pi V_M^2)}$. The current density in the pits decreases with time during the corrosion process as observed in methyl alcohol + sodium perchlorate ($CH_3OH + NaClO_4$). The time dependences of the calculated values of r and j_L are also in Fig. 6.

The potential dependences of j , z , and j_L are given in Fig. 7. As in case A they are expressed by Eqs 14 to 16, in which $\Delta E = E - E_{b2}$.

The complicated form of the polarization curves is connected with the mechanism of localized corrosion in iron. Two main theories concerning the localized corrosion mechanism are often discussed: (1) the potential in the pits is so low that the metal dissolution in them takes place in the active dissolution region [1,2,9-11], and (2) the metal dissolves at the potentials that are high enough for an oxide to form [12,13]. In our previous measurements [7,8,14] some evidence for the second theory was given. Also, the value of $b_0 = 0.45$ V found in this paper for the metal dissolution in pits in an alkaline KCl solution is substantially higher than that which corresponds to the active metal dissolution. The decrease of current density j_L can be caused by changes in the properties of the oxide-film in the pits during localized corrosion. Also, the decrease of the dissolution rate at the second passivating potential, E_{F2} , and the rise of the corrosion at the second breakdown potential, E_{b2} , are very probably caused by changes in the composition of this oxide film.

Conclusions

The time and potential dependence of the localized corrosion of iron were measured, and the equations for the evaluation of the current density in the

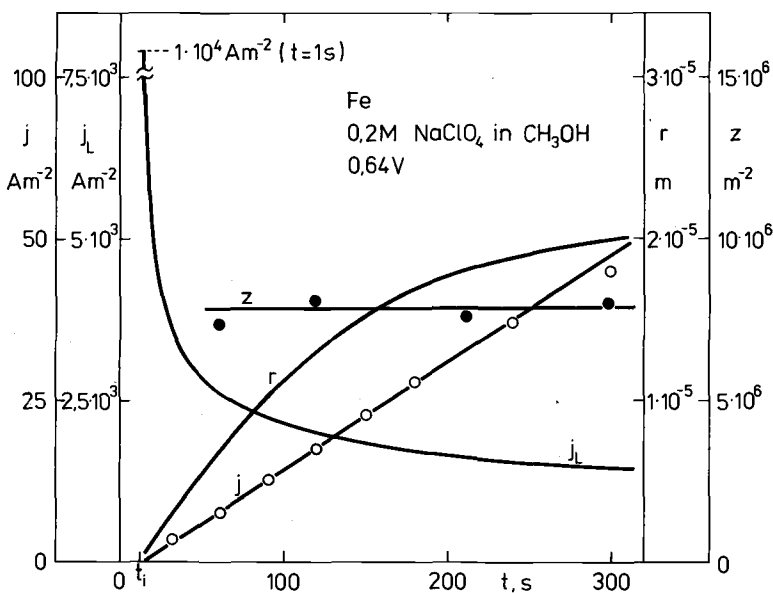


FIG. 6—Time dependence of the total current density j , the number of pits z , the current density in the pits j_L , and the radius of the pit r , in a solution containing ClO_4^- -ions.

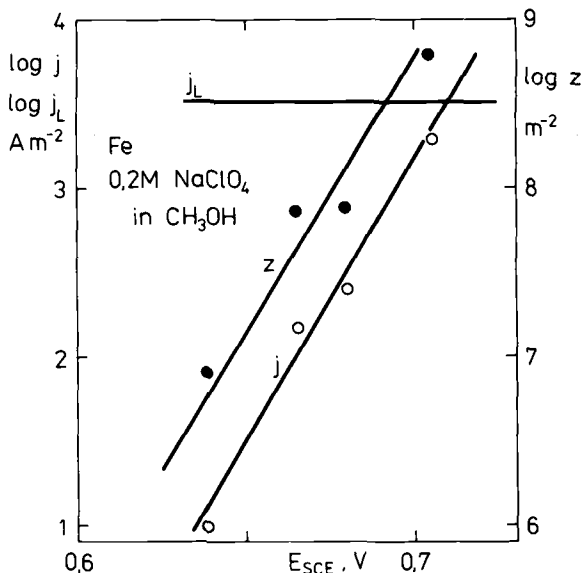


FIG. 7—Potential dependence of the total current density j , the current density in the pits j_L , and the number of pits z , in a solution containing ClO_4^- ions.

pits at different corrosive environments were derived. The results give some evidence for the existence of an oxide film in the pits. It may be supposed that a more detailed study of the potential dependence of the localized corrosion will give useful information about the localized corrosion mechanism.

References

- [1] Engell, H. J. and Stolica, N. D., *Zeitschrift für Physikalische Chemie (Neue Folge)*, Vol. 20, 1959, p. 113.
- [2] Herbsleb, G. and Engell, H. J., *Zeitschrift für Physikalische Chemie*, Vol. 215, 1960, p. 167.
- [3] Strehblow, H.-H. and Weners, J., *Zeitschrift für Physikalische Chemie (Neue Folge)*, Vol. 98, 1975, p. 199.
- [4] Strehblow, H.-H. and Ives, M. B., *Corrosion Science*, Vol. 16, 1976, p. 317.
- [5] Szklarska-Smialowska, Z. and Janik-Czachor, M., *British Corrosion Journal*, Vol. 4, 1969, p. 188.
- [6] Toušek, J., *Corrosion Science*, Vol. 12, 1972, p. 1.
- [7] Toušek, J., *Corrosion Science*, Vol. 18, 1978, p. 53.
- [8] Toušek, J., *Corrosion Science*, Vol. 14, 1974, p. 251.
- [9] Herbsleb, G. and Engell, H.-J., *Werkstoffe und Korrosion*, Vol. 17, 1966, p. 365.
- [10] Pourbaix, M., *Corrosion*, Vol. 26, 1970, p. 431.
- [11] Pickering, H. W. and Frankenthal, R. P., *Journal of the Electrochemical Society*, Vol. 119, 1972, p. 1297.
- [12] Hoar, T. P., Mears, D. C., and Rothwell, G. P., *Corrosion Science*, Vol. 5, 1965, p. 279.
- [13] Hoar, T. P., *Corrosion Science*, Vol. 7, 1967, p. 341.
- [14] Toušek, J., *Corrosion*, Vol. 33, 1977, p. 193.

T. S. Lee¹

A Method for Quantifying the Initiation and Propagation Stages of Crevice Corrosion

REFERENCE: Lee, T. S., "A Method for Quantifying the Initiation and Propagation Stages of Crevice Corrosion," *Electrochemical Corrosion Testing, ASTM STP 727*, Florian Mansfeld and Ugo Bertocci, Eds., American Society for Testing and Materials, 1981, pp. 43-68.

ABSTRACT: An electrochemical approach for investigating crevice-corrosion initiation and propagation phenomena is discussed. The method varies from previous ones in that it is applicable in natural environments and requires no artificial stimulation. Quantitative measurement of electrochemical parameters provides a basis for further understanding the nature of crevice corrosion.

The test technique allows measurement of time to initiation and rate of propagation of crevices. This is achieved by electrically coupling a small test specimen (anode) through a zero-impedance ammeter to a larger specimen (cathode). Both specimens are immersed in an electrolyte and the anode is "sandwiched" between two nonmetallic plates. This creates a crevice. The current between the cathode and the anode is monitored as a function of time.

Data are reported for Types 304 and 316 stainless steel exposed in natural seawater. Times to initiation and propagation rates as determined from current measurements are compared with visual observations of times to initiation and gravimetrically determined propagation rates.

The ability to determine a "protection" potential to prevent crevice corrosion is reviewed, and the utility of the technique in evaluating the effects of alloy and environmental variables on crevice corrosion is discussed.

KEY WORDS: crevice corrosion, localized corrosion, stainless steel, seawater, protection potential, electrochemical techniques, temperature effects

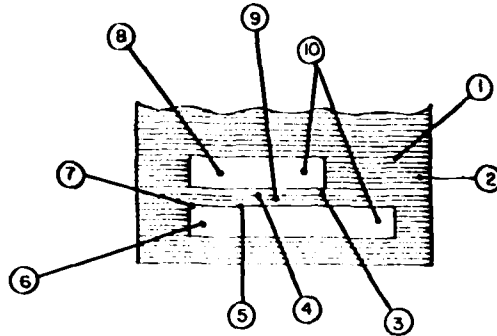
Numerous localized-corrosion theories have been advanced [1-6],² and a variety of experimental techniques have been utilized to investigate crevice-corrosion behavior of materials [6-13]. This array of experimental tools and interpretive methods has often led to conflicting conclusions on the localized-corrosion behavior of a given material. In addition many investigations are

¹Marine Corrosion Section Manager, LaQue Center for Corrosion Technology, Inc., Wrightsville Beach, N.C. 28480.

²The italic numbers in brackets refer to the list of references appended to this paper.

conducted in laboratories under simulated environmental conditions and extrapolated to the operating environment. In the case of a natural, complex environment such as seawater, data generated in artificial environments can sometimes be misleading [14]. Given the number of factors that can influence crevice corrosion, it is not surprising that correlation of laboratory and operating data often is not achieved. These factors are summarized in a schematic representation of a crevice (Fig. 1) [15].

Recent advances in quantifying crevice-corrosion processes through



- | | |
|-----------------------------------------|-------------------------------------------|
| 1) BULK SOLUTION COMPOSITION | 6) ALLOY COMPOSITION |
| - Cl ⁻ content | - major constituents |
| - O ₂ content | - minor additions |
| - pH | - impurities |
| 2) BULK SOLUTION ENVIRONMENT | 7) PASSIVE FILM CHARACTERISTICS |
| - temperature | - passive current |
| - agitation | - film stability |
| 3) MASS TRANSPORT IN AND OUT OF CREVICE | 8) CREVICE TYPE |
| - migration | - metal/metal |
| - diffusion | - metal/non-metal |
| - convection | - metal/marine growth |
| 4) CREVICE SOLUTION | 9) CREVICE GEOMETRY |
| - hydrolysis equilibria | - gap |
| 5) ELECTROCHEMICAL REACTIONS | - depth |
| - metal dissolution | 10) TOTAL GEOMETRY |
| - O ₂ reduction | - exterior to interior crevice area ratio |
| - H ₂ evolution | - number of crevices |

FIG. 1—Factors affecting crevice corrosion.

mathematical modelling [15, 16] have assumed a four-stage mechanism [17]. These stages include (1) deoxygenation of the environment within the crevice, (2) increase in acidity and chloride content of solution in the crevice, (3) breakdown of the passive film within the crevice, and (4) propagation.

The object of the present investigation was to develop quantitative data that would accurately assess the crevice-corrosion susceptibility of stainless steels in seawater. Development of an appropriate evaluation technique that would allow a distinction between initiation and propagation stages was deemed necessary. The concept of a galvanic couple consisting of a creviced anode and a boldly exposed cathode with provisions for measurement of a current between the two was chosen. Other investigations [18-22] have utilized a similar concept with varying degrees of success. Many have required artificial activation of the crevice specimen via polarization or solution acidification to achieve initiation. This could be often attributed either to an insufficient "driving force" (that is, cathodic surface area) or to the presence of localized corrosion on the cathode specimen. The technique described in this paper was utilized to provide naturally occurring initiation and propagation stages for measurement.

Experimental Procedure

Specimen Configuration

The test apparatus is schematically depicted in Fig. 2. Two specimens, immersed in a common seawater container, were electrically coupled through a zero-impedance ammeter (ZIAM). The ZIAM allowed for the measurement of current between the specimens at magnitudes of less than 10^{-7} A. Current measurements were recorded several times daily during the initial stages of each test and with decreasing frequency as current stabilized. Electrical connections at the specimens remained above the seawater level and were coated with silicone for protection. The use of machined tabs or "flags" on the specimens provided the site for connections, but necessarily created an air/water interface area on each specimen.

The larger of the specimens (250 by 300 mm) was boldly exposed and supported at two points with nonmetallic insulators. Efforts were made to minimize contact area on this specimen to avoid potential crevice sites. A smaller specimen (10 by 20 mm) was exposed between two acrylic plastic blocks (Fig. 3). The acrylic blocks were tightly held against the metal specimen surfaces to create an area of restricted seawater access. To avoid conditions of inconsistent "wetting" of the stainless-steel surfaces by seawater beneath these acrylic blocks, specimens were immersed in seawater prior to tightening the blocks. The crevice specimens or anodes were then immediately exposed in seawater and coupled through the ZIAM to the bold specimen that served as the cathode.

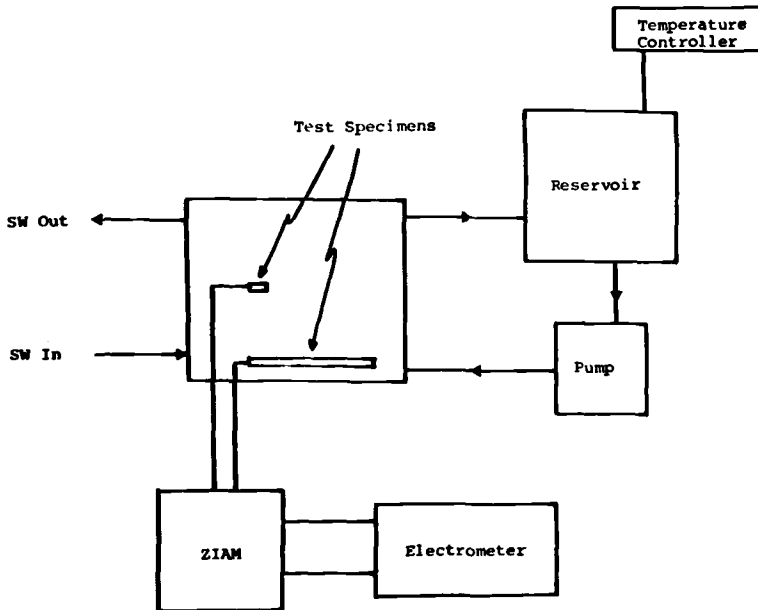


FIG. 2—Schematic of test loop utilized for remote crevice evaluations.

Physical Measurements

The crevice specimens were weighed (± 1.0 mg) before and after exposure to allow determination of weight loss and calculation of corrosion rate. Depths of attack were measured with a needle-point micrometer (± 0.01 mm). During the course of the experiments, visual observations of the crevice specimens provided an assessment of the times at which crevice corrosion initiated. This was evidenced by the presence of dark staining on the specimen surface beneath the acrylic block. The corroded surface area was measured after exposure and subsequently used in corrosion-rate calculations.

Corrosion-Rate Calculations

Current measurements provided an indication of the time to initiation and the rate of propagation of active corrosion. The time to initiation was taken as the point at which a rapid change in the magnitude of current occurred. The magnitude of current after initiation provided the propagation rate. Corrosion rates were calculated from these currents in accordance with Faraday's Law.

Area Ratio Experiments

For the majority of the results reported, five crevice specimens were coupled to a single bulk cathode specimen. The crevice specimens were coupled through the ZIAM to allow measurement of current to each specimen. A cathode (bulk) to anode (crevice) area ratio of 75:1 was established with these conditions. One series of exposures was conducted, with only one crevice specimen, creating a cathode:anode area ratio of 375:1. A third area ratio of 50:1 was achieved with a modified crevice assembly containing 15 crevices. In this case one surface (10 by 20 mm) of each crevice specimen was "creviced" beneath an acrylic plastic block, while the remaining surfaces and electrical connections were embedded in an epoxy resin. No weight-loss determinations were made on these specimens.

Polarization Experiments

A series of potentiostatic and potentiodynamic experiments were conducted to define the ability to inhibit crevice corrosion via potential control of the specimens. These tests utilized an Aardvark Model MEC-1B and Potentiodyne Analyzer potentiostat, respectively. Current for polarization was applied via a platinum auxiliary electrode and a silver/silver chloride reference electrode ($E = -0.240 V_{SHE}$) was used for potential monitoring.

Potentiodynamic tests were conducted at several polarization rates ranging from 1 to 100 V/h; current was recorded automatically. Specimens were polarized from active potentials ($-1.2 V$) to noble potentials and then

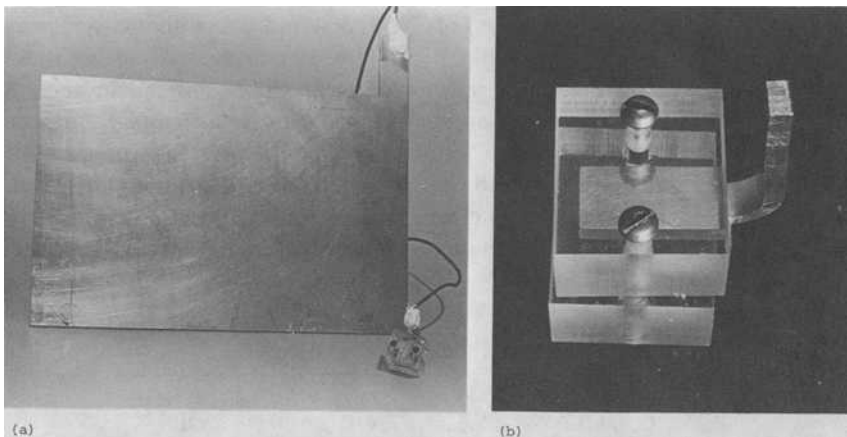


FIG. 3—(a) Relative size of boldly exposed and crevice specimens; (b) Close-up of crevice specimen showing stainless steel creviced between acrylic blocks. Protruding tab utilized for electrical connections.

polarized in the reverse direction. These tests were conducted in natural, aerated seawater on stainless-steel electrodes in a typical electrochemical corrosion test cell [23]. Electrodes were surface ground with 600 grit SiC paper, and retained in a sample holder that exposed 1 cm² surface area with an O-ring gasket acting as a crevice site.

Potentiostatic tests were conducted on a complete remote crevice assembly consisting of the boldly exposed cathode and 15 individual crevice specimens. While polarized, the current from the cathode to the crevices was measured as before. Separate specimen assemblies were utilized for each increment of polarization. These tests were controlled to within ± 5 mV of the desired potential (using the reference electrode in close proximity to the cathode specimen), and measurements were performed with a high ($> 10^{11} \Omega$) input impedance electrometer.

Environment

All evaluations were conducted in refreshed, recirculated natural seawater test loops. The test loops contained a seawater volume of 60 L with a refreshment rate of 0.6 L/min. A nominal velocity of 0.1 m/s was maintained by the use of a recirculating pump. Seawater temperature was controlled at the desired levels of 10, 25, and 50°C ($\pm 2^\circ\text{C}$) with heating/cooling immersion units. Typical seawater chemistry and nominal dissolved oxygen levels for each seawater temperature are shown in Table 1.

Materials

Sheet material (3 mm thickness) of Types 304 and 316 stainless steel was utilized for test specimens. Table 2 lists the chemical analysis of these materials. The bold or cathode specimens were cleaned in nitric acid to remove mill scale and received no surface grinding treatments, while the crevice specimens were surface ground with 600 grit SiC paper. All specimens were acetone degreased and pumice scrubbed prior to exposure. After exposure, specimens were cleaned in cold 30 percent nitric acid to remove corrosion products {as recommended in ASTM Recommended Prac-

TABLE 1—Nominal seawater chemistry.

pH	Cl ⁻ , g/L	HCO ₃ ⁻ , g/L	SO ₄ ⁻ , g/L	Dissolved Oxygen, mg/L
8.0	18.8	0.15	2.5	8.0 at 10°C
...	6.0 at 25°C
...	4.0 at 50°C

TABLE 2—*Stainless steel alloy compositions.*

	Weight Percent								
	Ni	Cr	Mo	Mn	C	Si	S	P	Fe
T-304	8.4	19.0	0.14	1.41	0.051	0.66	0.013	0.034	balance
T-316	13.8	17.1	2.16	1.73	0.050	0.45	0.012	0.043	balance

tice for Preparing, Cleaning, and Evaluating Corrosion Test Specimens [G 1-72 (1979)]}.

Results and Discussion

While Kain [14] has defined some factors influencing the reproducibility of seawater crevice-corrosion data, Anderson [11] has proposed that the phenomenon is statistical in nature. For this reason, a series of tests was conducted with five crevice specimens coupled to each cathode specimen to provide a broad baseline from which further evaluations could be made.

The tests were conducted for 28 days to evaluate the crevice-corrosion behavior of Types 304 and 316 stainless steel as a function of seawater temperature. The resultant data are shown in Tables 3 and 4, and contain physical measurements of weight loss, maximum attack depth, and corrosion rates derived from current measurements.

Crevice Initiation

The current to each of the crevice specimens is shown as a function of exposure time in Figs. 4 and 5. These graphs illustrate the magnitude of current at each seawater temperature and the relative degree of reproducibility between each of the five specimens in a given test. The time at which visual detection of crevice corrosion was evident is depicted by arrows.

The data at 10 and 50°C indicate that the rapid current changes generally observed at 25°C were not typical at these seawater temperatures. Most of the specimens at 10 and 50°C displayed either a relatively constant current or a gradually changing current over the test duration. Mathematical modelling of crevice-corrosion initiation by Oldfield and Sutton [15] indicates that the rapid increase in current at 25°C would coincide with the attainment of a crevice-solution chemistry sufficiently aggressive to cause the rapid breakdown of passivity within the crevice (Stage III) and a concurrent increase in corrosion rate. The modelled process does not presently define the observed behavior at 10 and 50°C, but further research may clarify these observations.

TABLE 3—Remote crevice assembly corrosion data for Type 304 stainless steel in seawater at 10, 25, and 50°C.

		Corroded							
		Weight Loss, g	Surface Area, cm^2	Time to Initiation, b h	Maximum Attack Depth, c mm	Gravimetric Corrosion Rate, d mm/year	Mean Current, e A	Amperometric Corrosion Rate, f mm/year	Propagation Rate, g mm/year
10°C									
I-1		0.044	1.6	24	0.20 (0)	0.45	1.49×10^{-4}	1.06	4.92
I-2		0.026	0.6	17	0.11 (0)	0.71	0.23×10^{-4}	0.44	1.48
I-3		0.030	0.6	17	0.29 (0)	0.82	0.22×10^{-4}	0.42	1.54
I-4		0.020	1.2	60	0.32 (0)	0.27	0.15×10^{-4}	0.14	0.42
I-5		0.016	1.0	16	0.11 (0)	0.26	0.14×10^{-4}	0.16	0.50
Mean						0.50 ± 0.25		0.44 ± 0.37	1.77 ± 1.84
25°C									
I-1		1.313	3.5	6	1.44 (1.73)	6.16	1.97×10^{-3}	6.42	5.80
I-2		1.583	4.3	1	1.68 (1.71)	6.04	2.44×10^{-3}	6.48	3.13
I-3		2.005	4.3	3	1.92 (2.54)	7.66	2.95×10^{-3}	7.83	4.78
I-4		1.903	4.8	3	2.10 (1.78)	6.51	3.04×10^{-3}	7.23	6.32
I-5		1.694	4.5	3	1.94 (0.89)	6.18	2.49×10^{-3}	6.31	4.06
Mean						6.51 ± 0.67		6.85 ± 0.66	4.82 ± 1.29
50°C									
I-1		0.285	2.1	0.25	0.05 (1.47)	2.22	4.30×10^{-4}	2.34	5.76
I-2		0.102	1.7	0.25	0.02 (1.02)	0.99	2.22×10^{-4}	1.49	1.79
I-3		0.258	1.6	18	0.03 (1.39)	2.93	2.70×10^{-4}	1.93	4.08
I-4		0.166	2.2	48	<0.01 (1.78)	1.24	2.89×10^{-4}	1.50	1.46
I-5		0.093	2.1	0.25	<0.01 (0.51)	0.73	1.43×10^{-4}	0.78	1.63
Mean						1.62 ± 0.92		1.61 ± 0.58	2.94 ± 1.90

^a Estimated at test completion.^b Based on visual observation.^c Within crevice area (outside crevice area).^d Based on weight loss.^e Average current over test duration.^f Based on average current.^g Based on current during last 5 days of 28-day exposure.

TABLE 4—Remote crevice assembly corrosion data for Type 316 stainless steel in seawater at 10, 25, and 50°C.

		Corroded										
		Weight Loss, g	Surface Area, cm ²	Time to Initiation, h	Maximum Attack Depth, mm	Gravimetric Corrosion Rate, mm/year	Mean Current, A	Amperometric Corrosion Rate, mm/year	Propagation Rate, mm/year			
10°C												
I-1		0.006	0.4	72	<0.01 (0)	0.25	0.37×10^{-5}	0.11	0.28			
I-2		0.002	0.5	72	<0.01 (0)	0.06	0.16×10^{-5}	0.04	0.08			
I-3		0.019	0.7	16	0.03 (0)	0.44	1.69×10^{-5}	0.28	0.84			
I-4		0.007	0.8	16	0.04 (0)	0.14	0.38×10^{-5}	0.05	0.08			
I-5		0.006	0.4	16	0.02 (0)	0.25	0.46×10^{-5}	0.13	0.14			
Mean						0.23 ± 0.14		0.12 ± 0.10	0.28 ± 0.32			
25°C												
I-1		1.040	4.2	72	1.78 (1.29)	4.04	1.50×10^{-3}	4.12	3.95			
I-2		0.342	2.0	72	1.37 (0.25)	2.79	0.43×10^{-3}	2.48	3.92			
I-3		1.563	4.2	72	1.67 (0.51)	6.08	2.23×10^{-3}	6.12	4.94			
I-4		0.606	2.4	72	1.50 (0.81)	4.12	0.93×10^{-3}	4.47	1.30			
I-5		0.913	4.1	72	1.34 (0.64)	3.64	1.19×10^{-3}	3.35	1.55			
Mean						4.13 ± 1.21		4.11 ± 1.36	3.13 ± 1.61			
50°C												
I-1		0.011	0.8	2	0.03 (0.02)	0.22	1.39×10^{-5}	0.20	0.26			
I-2		0.007	0.4	20	<0.01 (0.36)	0.29	0.71×10^{-5}	0.20	0.15			
I-3		0.015	0.1	66	0 (0.33)	2.45	2.55×10^{-5}	2.94	5.67			
I-4		0.017	1.0	18	0.03 (0.25)	0.28	3.06×10^{-5}	0.35	0.81			
I-5		0.012	0.5	42	<0.01 (0.32)	0.39	1.62×10^{-5}	0.37	0.26			
Mean						0.73 ± 0.97		0.81 ± 1.19	1.43 ± 2.38			

^a Estimated at test completion.^b Based on visual observation.^c Within crevice area (outside crevice area).^d Based on weight loss.^e Average current over test duration.^f Based on average current.^g Based on current during last 5 days of 28-day exposure.

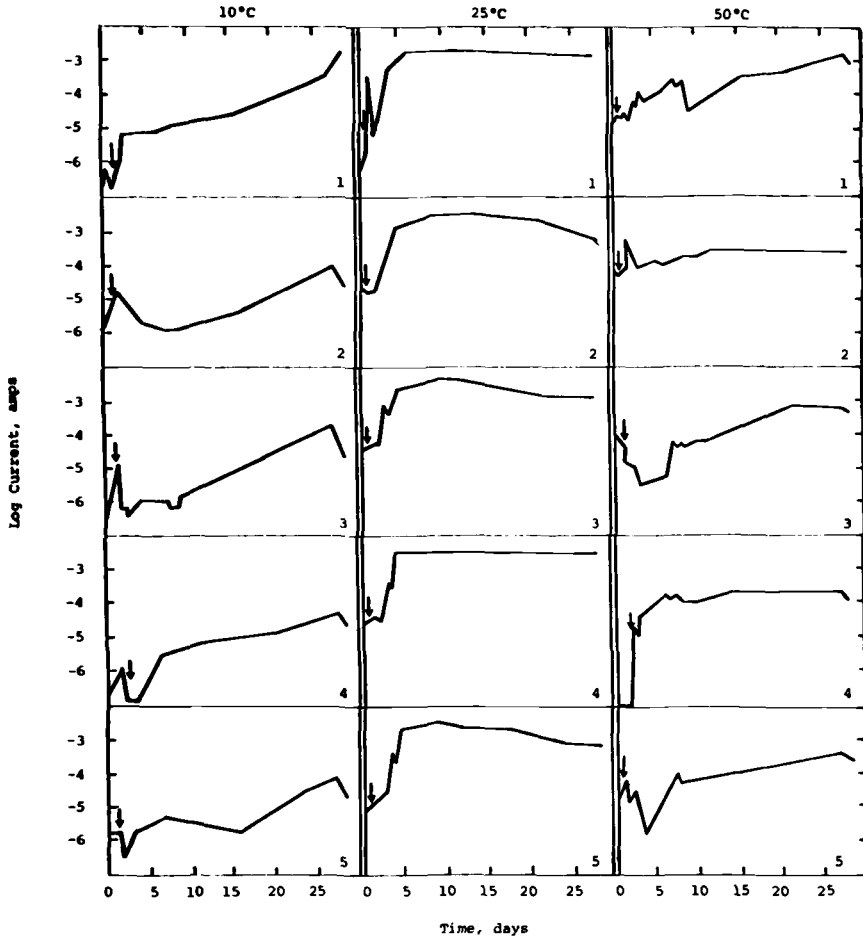


FIG. 4—Current (logarithmic) to remote crevices as a function of time for Type 304 stainless steel during a 28-day exposure in seawater at 10, 25, and 50°C. Arrows denote crevice initiation as determined visually.

Assessment of the area of the individual crevice specimens that exhibited corrosive attack after the 28-day exposure resulted in a calculation of the percent of specimen area where crevice corrosion was initiated (Fig. 6). Two facts are evident:

1. More extensive initiation of crevice corrosion occurred at 25°C than at either 10 or 50°C. While this observation has been documented [14] for these alloys with other types of artificial crevice devices in seawater, the causative nature of the phenomenon has not been fully explained. Kain [14] has

postulated several factors which may contribute, including changes in corrosion resistance of the cathodic areas and alterations in cathodic surface films.

It is likely that two mechanisms may be operative to explain a maximum rate of crevice incidence at 25°C. Reduced reaction-rate kinetics may account for less attack at 10°C as compared to that observed at 25°C. Upon increasing the temperature to 50°C, cathodic surface reactions seem a likely causative agent for the reduced attack. An increase in the general corrosion rate of the cathodic surface or the presence of a surface film acting as a diffu-

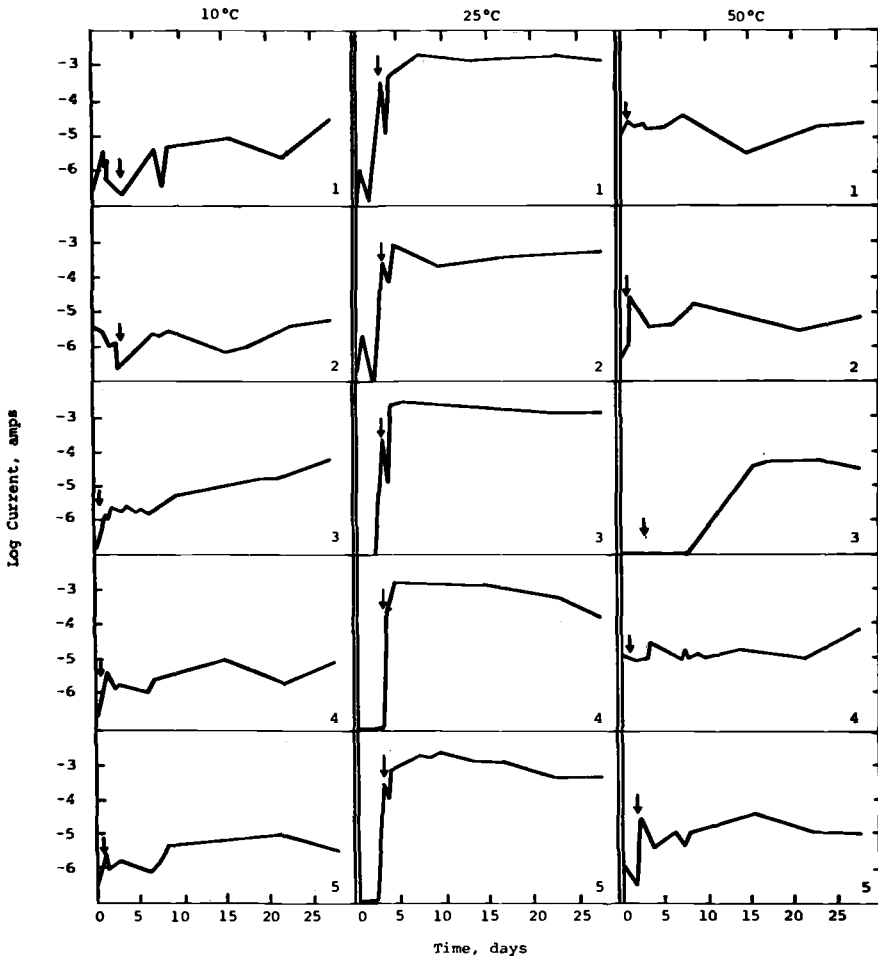


FIG. 5—Current (logarithmic) to remote crevices as a function of time for Type 316 stainless steel during a 28-day exposure in seawater at 10, 25, and 50°C. Arrows denote crevice initiation as determined visually.

sion barrier would serve to reduce the rate-controlling cathodic oxygen reduction reactions. This would reduce the "driving force" necessary to sustain crevice corrosion.

2. Type 304 exhibited somewhat more extensive initiation than did Type 316 at each temperature.

Figure 7 shows the typical appearance of two crevice specimens that exhibit a varying degree of crevice initiation in the 28-day exposure duration. While it may be argued that this type of variance denotes the statistical nature of crevice corrosion [11], it seems more likely that it may represent a variance in crevice geometry. This has been mathematically shown to affect initiation times [15] and, experimentally, closer control of the use of a nonmetallic multiple-crevice assembly has reduced the crevice-initiation variability observed [14].

Crevice Propagation

Utilizing the corroded surface area of each crevice specimen, corrosion rates were calculated using weight-loss data and average current measurements over the entire 28-day exposure period. These data are shown in Figs. 8 and 9 for Types 304 and 316 stainless steel, respectively. These data indicate, as do the initiation data, a maximum susceptibility to crevice corrosion at 25°C, and only a slight improvement in performance with Type 316 over Type 304.

Excellent agreement between the two methods of determining corrosion rates was obtained. This indicates that the net current to the crevice specimens was primarily anodic with minimal contributing cathodic current. If the anodic metal dissolution reactions were sustained by cathodic hydrogen evolution at noncorroding sites on the crevice specimen, then the net current should indicate a lesser extent of corrosion than would be indicated by weight-loss measurements. It would appear that the controlling cathodic reactions, in this case, would then be oxygen reduction at the bold cathode surface. This is not unexpected, given the large cathode-to-anode area ratio and the ready availability of oxygen at the bold surfaces.

In addition to the corrosive attack sustained in the crevice area, varying degrees of localized attack were evidenced at the air/water interface on the tab portion of the crevice specimens. One of the more severe instances of this attack is shown in Fig. 10. Since both weight-loss and current measurements include a contribution from this attack, maximum depths of attack measurements were obtained to quantify the severity of the attack relative to that observed on the intentionally creviced areas. Figures 11 and 12 summarize these measurements for both alloys as a function of seawater temperature. It can be seen that minimal interface attack occurred at 10°C, while an equal depth of attack was measured both within the crevice and at

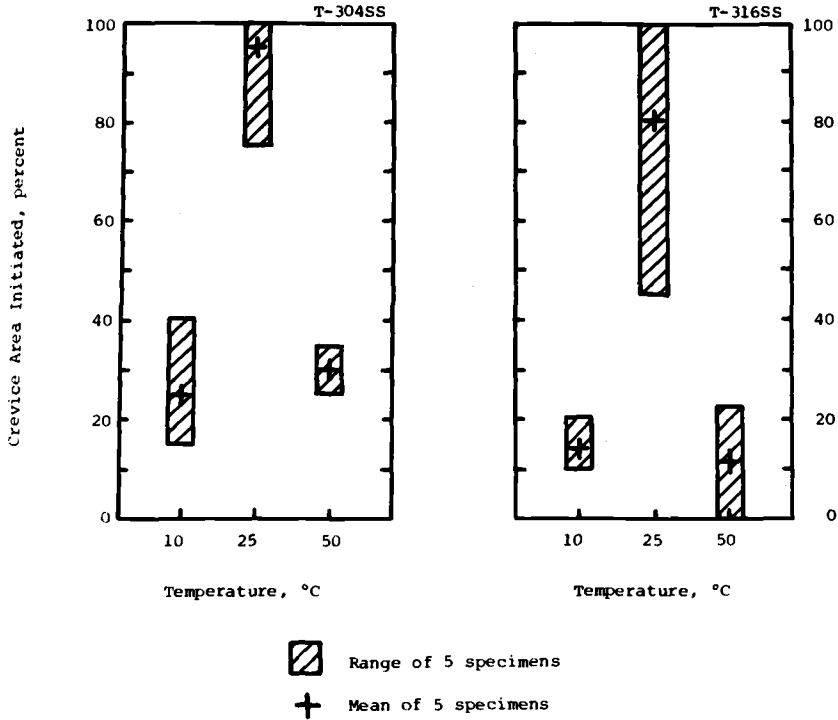


FIG. 6—Percent of crevice area exhibiting visible corrosive attack for Types 304 and 316 stainless steel after 28 days in seawater at 10, 25, and 50°C.

the interface in 25°C seawater. At 50°C, more penetration was evident at the interface than at the crevice areas.

Whether this attack occurred as a result of a differential aeration cell created by condensate, a crevice area created by suspended particulate matter in the seawater, or a variation in test temperature at the interface (ambient air temperature was ~20°C) is presently a matter of conjecture. Previous research [14] indicates that the phenomenon does not represent an inherent susceptibility to pitting in 50°C seawater. Kain has shown that edge-pitting sensitivity was reduced when conducting crevice evaluations in seawater at 50°C as compared to 25°C exposures. Based on Kain's results, it would appear likely that the attack at the interface represents behavior under environmental conditions more closely simulating those at 25°C.

The interface attack on specimens exposed in 25°C seawater could be a result of edge-pitting sensitivity or, more likely, represents the typical crevice-corrosion performance apparent at that temperature (assuming possible crevice sites as discussed previously).

Further refinement of the exposure method of the crevice specimens

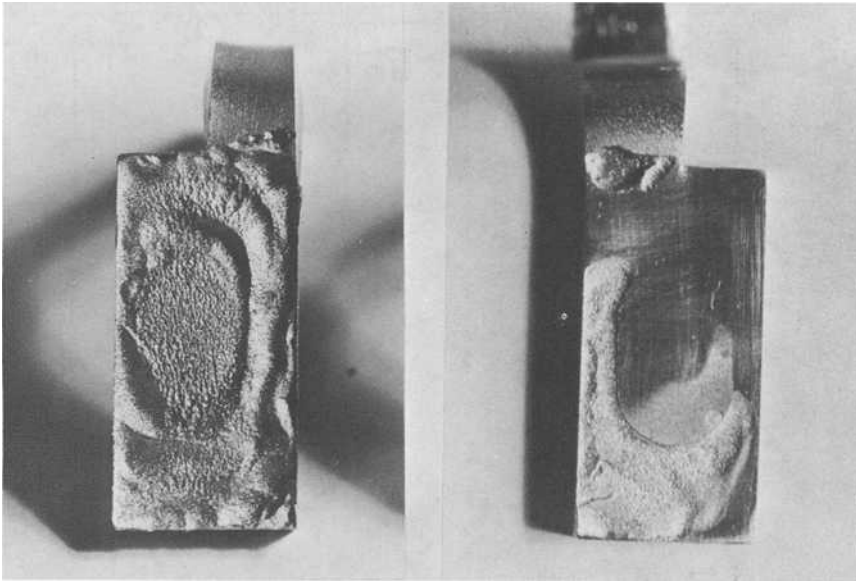


FIG. 7—Typical crevice specimens depicting nature of corrosive attack beneath acrylic blocks.

should eliminate this complicating factor of interface corrosion. If appropriately protected electrical connections are immersed in seawater to eliminate an air/water interface, a crevice site will exist at the sealant. If this can be minimized, however, it may be preferred to the present situation.

While the methods of data analysis discussed thus far represent a cumulative behavior over the entire test duration, an analysis of current at any time represents the measure of the propagation at that time. Figure 13 shows corrosion rates calculated from the average current during the final five days of the seawater exposures. These were determined using the nominal corroded surface area of the crevice specimens. It should be noted that, based on visual observations, the relative area of corroded surface did not change appreciably during the final five days of test. The calculated corrosion rates can only represent an approximate value, however, since a determination of the exact area of a roughened corroded surface is not easily made.

These data represent the relative rate of propagation of localized corrosion occurring at the end of the test duration. A comparison with the data in Figs. 8 and 9 shows this rate of propagation at 10 and 50°C to be greater than the average rate for the 28-day period. At 10°C the rates represent propagation within the crevice area, while at 50°C the data include a contribution from the previously discussed interface attack. Assuming this contribution would

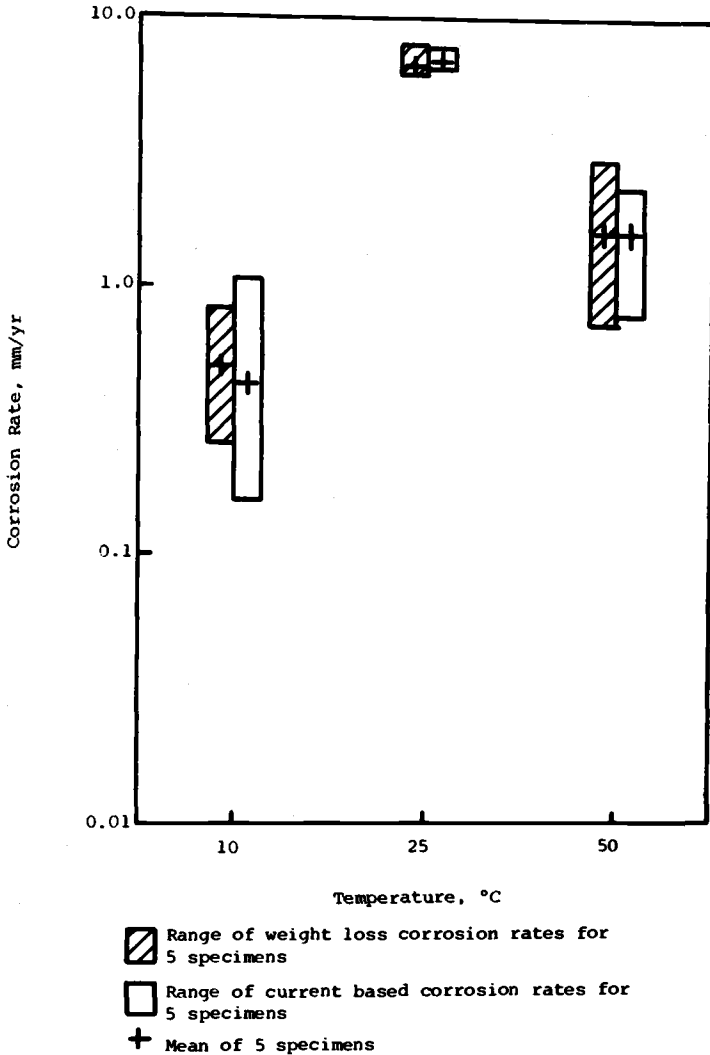


FIG. 8—Corrosion rates for remote crevices of Type 304 stainless steel in seawater for 28 days at 10, 25, and 50°C.

be eliminated with experimental modification, a somewhat lower propagation rate at 50°C would be expected. In contrast to the behavior at 10 and 50°C, the propagation rates at 25°C for both alloys are less than the average for the entire duration.

When comparing the data for all three temperatures and reviewing the trends of the current-time curves in Figs. 4 and 5, it is evident that at 10 and

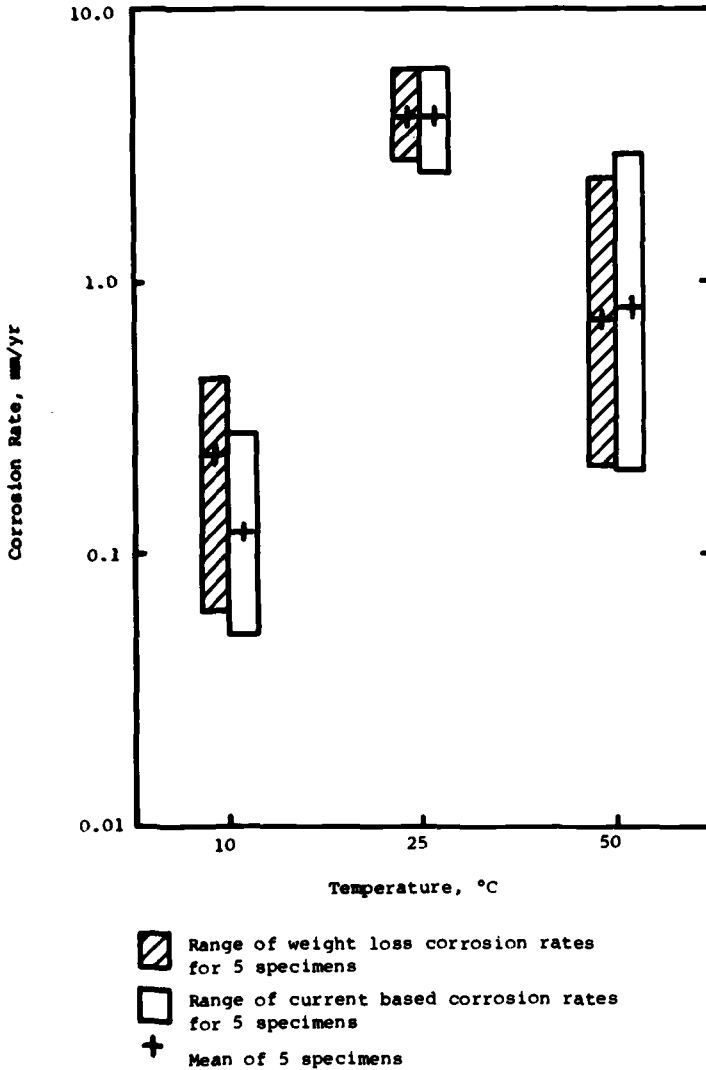


FIG. 9—Corrosion rates for remote crevices of Type 316 stainless steel in seawater for 28 days at 10, 25, and 50°C.

50°C a continued increase in the rate of propagation may occur beyond the 28-day duration of the present exposures. At 25°C, however, the rate of propagation appears to have peaked between days 5 and 10. At the end of the test duration, the rate of propagation has generally declined to a lower stable level or is continuing to decline. This trend may either reflect the limiting propagation nature of these alloys under the given environmental conditions

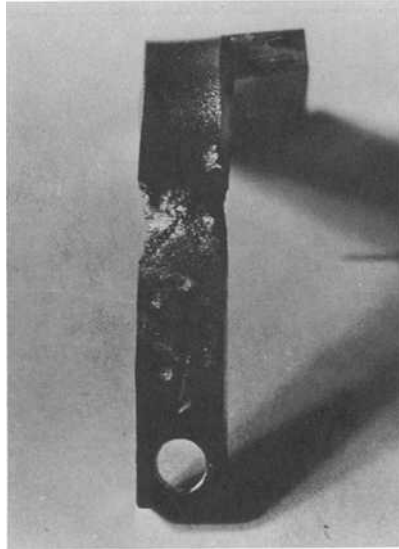


FIG. 10—Typical attack at air/water interface on tab for electrical connection to crevice specimen.

or may be a limitation imposed by geometrical factors of the crevice assemblies [15]. Further research, utilizing other alloys and crevice geometries, will be required to determine the causative factors for this phenomenon.

Effect of Area Ratio

To determine the influence of bold-to-crevice area ratio on the extent of crevice attack, a series of exposures with a varying number of crevice specimens was conducted. These tests involved Type 304 stainless steel in seawater at 25°C; the resultant data are tabulated in Table 5. The current measurements were recorded at 10 days, since the prior results indicated a maximum after approximately this duration. Figure 14 summarizes the range of measurements, average current, and the total current for each of the three area ratios. The total current represents the sum of current measurements to each individual crevice, while the average represents the mean of those values. With only one crevice utilized for the 375:1 area ratio tests, these two values are equivalent.

In the present tests, corrosion potentials of the assemblies were monitored with respect to a reference electrode in close proximity to the boldly exposed specimens. No correlations were obtained between these measurements and either current measurements or visual observations. Some specimens ex-

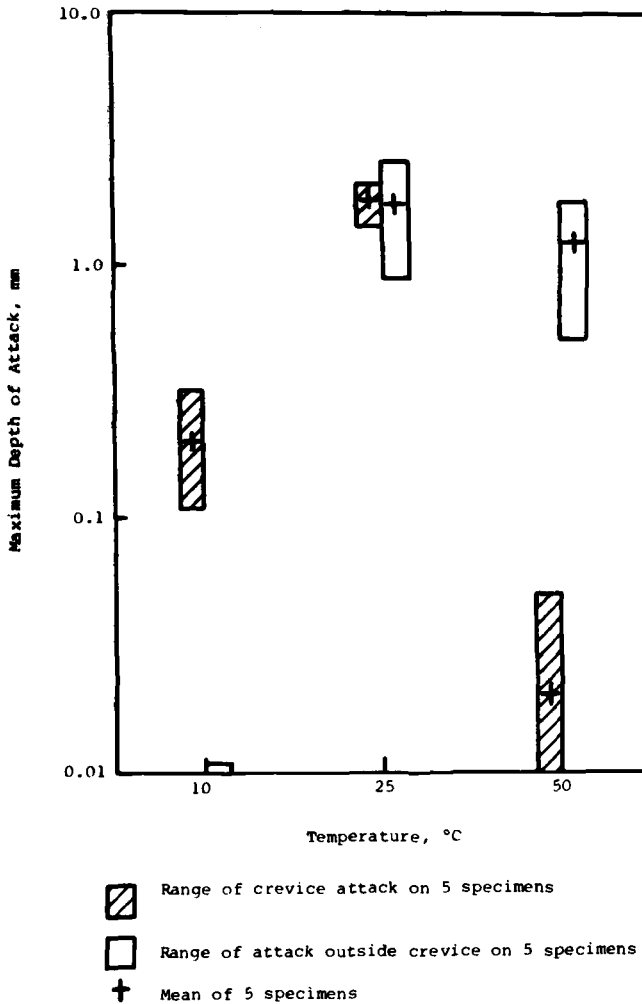


FIG. 11—Maximum depth of attack for Type 304 stainless steel after 28 days in seawater at 10, 25, and 50°C.

hibited potentials in the range of $-0.2 - -0.1 V_{Ag/AgCl}$ while others remained relatively noble at $0 - +0.05 V_{Ag/AgCl}$. Other assemblies exhibited random shifts of potential between these nominal values. The presence of crevice corrosion was not always concurrent with an observed active potential.

The current data demonstrate the fact that crevice corrosion of stainless steel in seawater is under cathodic control; that is, the capacity for oxygen reduction to occur at the cathode dictates the extent of crevice corrosion at anodic sites. It also demonstrates the need to carefully select the area ratios

for crevice test specimens to assure that either correlation with service conditions is achieved or, in the case of screening evaluations, a maximum degree of susceptibility is measured.

Effect of Polarization

As previously discussed, a variety of electrochemical approaches are utilized to quantify the susceptibility of materials to localized corrosion. Among these are potentiodynamic and potentiostatic polarization tests. Figure 15

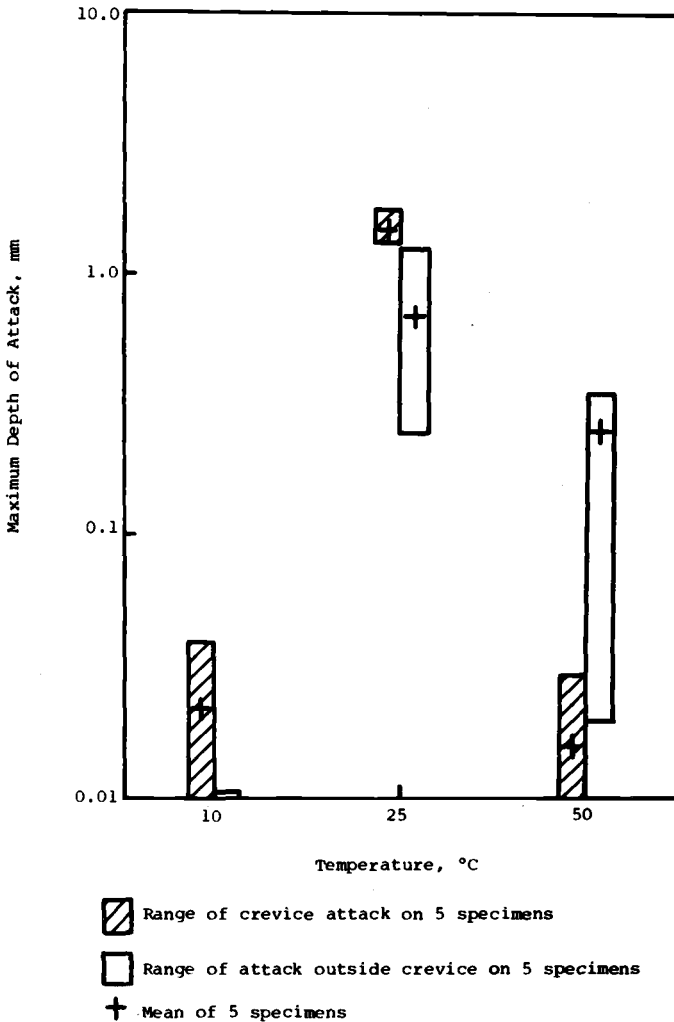


FIG. 12—Maximum depth of attack for Type 316 stainless steel after 28 days in seawater at 10, 25, and 50°C.

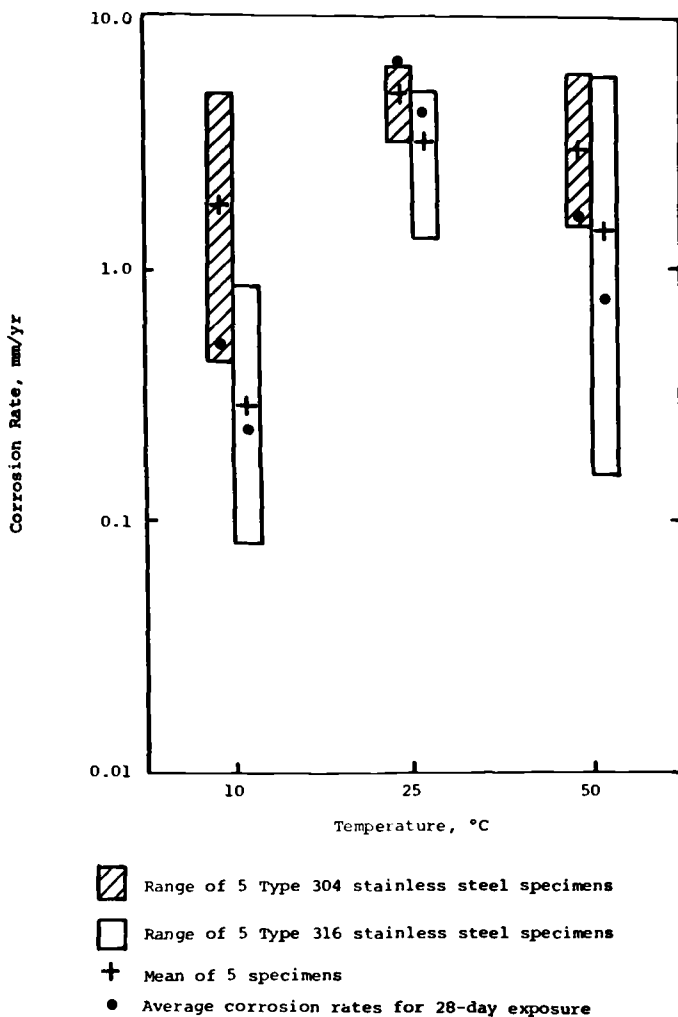


FIG. 13—Propagation corrosion rates for remote crevices in seawater at 10, 25, and 50°C. Rates are calculated from average current during the final five days of a 28-day exposure. Also depicted are average corrosion rates for the 28-day period from Figs. 9 and 10.

shows a series of potentiodynamic polarization curves for Type 304 stainless steel in seawater at 25°C. The curves were generated utilizing a range of polarization scan rates (1, 50, and 100 V/h) and, as expected, yielded a range of zero-current potentials, passivation current densities, and pitting potentials.³ Of interest, however, is the relative reproducibility of the zero-

³ See ASTM Recommended Practice for Conventions Applicable to Electrochemical Measurements in Corrosion Testing (G 3-74).

TABLE 5—Effect of cathode/anode area ratio on crevice corrosion of Type 304 stainless steel in seawater at 25°C.

Cathode/ Anode Area Ratio	Crevice Speci- men No.	Current Magnitude at 10 Days, A	Total Current, A	Mean Current, A
50:1	1	10×10^{-4}
	2	4.0×10^{-4}
	3	5.0×10^{-4}
	4	3.0×10^{-4}
	5	4.4×10^{-4}
	6	4.4×10^{-4}
	7	5.6×10^{-4}
	8	$< 10^{-6}$
	9	2.0×10^{-4}
	10	$< 10^{-6}$
	11	4.8×10^{-4}
	12	1.6×10^{-4}
	13	5.0×10^{-4}
	14	$< 10^{-6}$
	15	10.2×10^{-4}	6.0×10^{-3}	4.0×10^{-4}
75:1	1	3.0×10^{-3}
	2	3.5×10^{-3}
	3	5.4×10^{-3}
	4	4.4×10^{-3}
	5	4.0×10^{-3}	2.0×10^{-2}	4.1×10^{-3}
375:1	1	4.5×10^{-2}	4.5×10^{-2}	4.5×10^{-2}

current potential on the reverse polarization scan at approximately $-0.2 V_{Ag/AgCl}$. This has been defined by others [24] as the "protection" potential and is therefore designated as E_{prot} . By definition, a specimen potential more active than this will result in cessation of localized corrosion, and a specimen potential more noble than this will result in propagation of previously activated localized corrosion.

To determine the applicability of this potential in defining the crevice-corrosion behavior of Type 304 stainless steel in seawater, a limited series of potentiostatic tests was conducted at 25°C on assemblies consisting of the bold cathode coupled to 15 individual crevice specimens. The data are summarized in Table 6; included are the average current to the crevice specimens during the final five days of exposure and the calculated corrosion rate based on the measurements. At potentials equal to and more active than $-0.2 V$, no corrosion of the crevice specimens was evident. However, at a potential of $-0.1 V$ (more noble than the measured "protection" potential), a slight increase in average corrosion rate was measured and visual evidence of corrosion of the crevice specimens was observed. While the magnitude of propagation was slight compared to the earlier freely corroding specimens, it does indicate the ability for crevice corrosion to initiate at controlled potentials more noble than the "protection" potential, but more active than typically measured pitting potentials (Fig. 15).

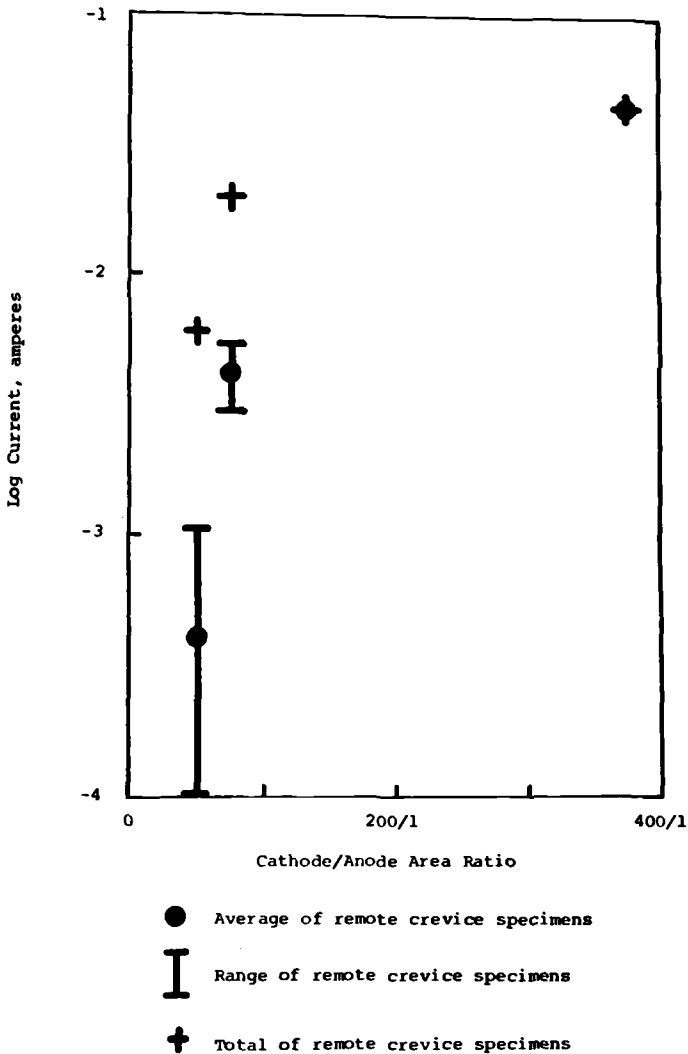


FIG. 14—Effect of cathode-to-anode area ratio on current to remote crevices of Type 304 stainless steel at 25°C after 10 days' exposure.

Figure 16 demonstrates an additional use of this specimen assembly in characterizing crevice-corrosion behavior. The graphs depict the potential and current for a remote crevice assembly with 15 crevices that was polarized at $E = -0.2 \text{ V} (\pm 5 \text{ mV})$ for 30 days, followed by a 5-day period under freely corroding conditions, and finally for 5 days again polarized to $E = -0.2 \text{ V}$. As previously indicated, no corrosion was evident during polarization. Upon disconnection of the potentiostat, however, an immediate increase in current

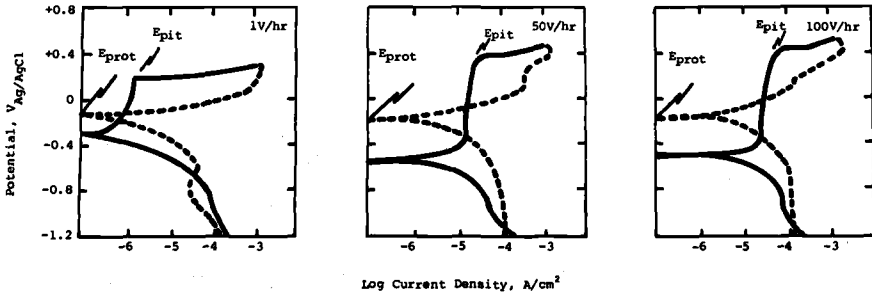


FIG. 15—Potentiodynamic polarization curves for Type 304 stainless steel in seawater at 25°C. Polarization scan rates of 1, 50, and 100 V/h were utilized.

TABLE 6—Effect of controlled potential on crevice corrosion of Type 304 stainless steel in seawater at 25°C.

Controlled Potential, V versus Ag/AgCl	Exposure Duration, days	Average Current, ^a A	Corrosion Rate, ^b $\mu\text{m}/\text{year}$	Visual Evidence of Corrosion
-0.400	30	3.7×10^{-7}	0.5	no
-0.300	31	6.5×10^{-7}	0.9	no
-0.250	33	1.8×10^{-6}	2.5	no
-0.200	30	2.6×10^{-6}	3.7	no
-0.100	21	9.8×10^{-6}	13.9	yes ^c

^a Average of 15 crevices during final 5 days of exposure.

^b Based on average current.

^c Based on staining and etched surface.

to the crevice specimens was measured along with a shift in potential to more noble values. Visual evidence of corrosion was apparent within one hour, and the extent of the corrosion increased over the five days while freely corroding conditions existed.

Considering this observation in the context of the various stages of crevice corrosion, it is obvious that Stage III (the onset of crevice corrosion via the breakdown of the passive film) occurred very rapidly. This implies that oxygen depletion (Stage I) and an increase in acidity and chloride content within the crevice (Stage II) had occurred to some extent while the specimen was polarized. At this level of polarization, an anodic current exists at a very low level ($< 1 \mu\text{A}/\text{cm}^2$). Over the 30-day period of polarization, the degree of corrosion which this current represents apparently was sufficient to result in oxygen depletion and a partial acidification of the crevice environment. Upon allowing the specimen to freely corrode, the time to achieve the acidification that resulted in the breakdown of the passive film was brief.

When the specimen was repolarized to $E = -0.2 \text{ V}$ there was an immediate return to a current magnitude comparable to that prior to crevice ac-

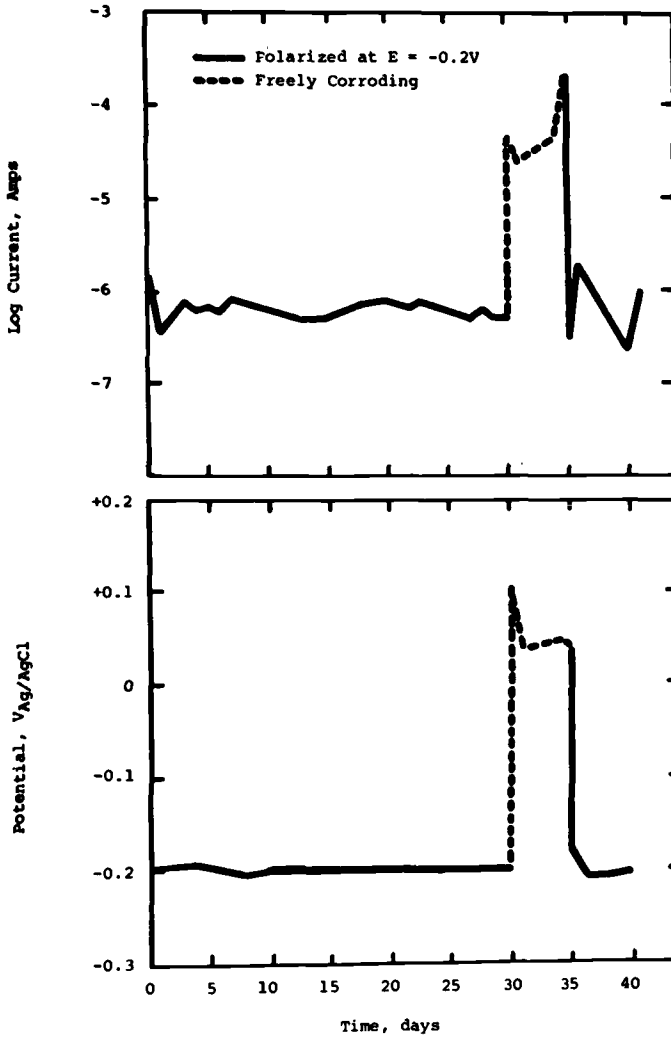


FIG. 16—Typical current (logarithmic) and potential values versus time for Type 304 stainless steel in seawater at 25°C. Specimen was polarized at -0.2 V (Ag/AgCl) between days 0 and 30 and between days 35 and 40. Specimen was freely corroding between days 30 and 35.

tivation. While the current appeared to be somewhat less stable in this latter state of polarization, it nonetheless indicates an arrest of the crevice corrosion.

Further experimentation will delineate the effects of elapsed time during both the initial polarization period and the freely corroding period. This might be expected to influence the time to achieve initiation and the ability to deactivate propagating crevices, respectively.

Conclusions

1. A test technique has been described that allows assessment of the crevice-corrosion resistance of stainless steels in seawater. This technique provides a quantitative measure of the initiation times and propagation rates.

2. Excellent correlation exists between corrosion rates determined from conventional weight loss and current measurements between creviced anodes and a bold cathode.

3. Crevice corrosion of Types 304 and 316 stainless steel is shown to be at a maximum at 25°C, with less attack observed at 10 and 50°C.

4. The test technique allows for determining the effect of external polarization on crevice-corrosion initiation and propagation. For Type 304 stainless steel in seawater at 25°C, the significance of a conventionally measured "protection" potential has been identified as related to the crevice-corrosion initiation and deactivation processes.

Acknowledgments

The author acknowledges F. W. Hammond for his valuable assistance in the experimental aspects of this work, J. H. Waldorf for assistance in the preparation of this manuscript, R. M. Kain for helpful discussions, and Inco Ltd. for permission to publish.

References

- [1] Rosenfeld, I. T. and Marshakov, I. K., *Corrosion*, Vol. 20, April 1964, p. 115.
- [2] Karlberg, G. and Wranglen, G., *Corrosion Science*, Vol. 11, July 1971, p. 499.
- [3] Galvele, J. R., *Journal of the Electrochemical Society*, Vol. 123, April 1976, p. 464.
- [4] Rosenfeld, I. L. et al, *Journal of the Electrochemical Society*, Vol. 125, November 1978, p. 1729.
- [5] Bombara, G. et al, *Electrochimica Metallorum*, Vol. III, 1968, p. 81.
- [6] France, W. D. in *Localized Corrosion—Cause of Metal Failure*, ASTM STP 516, American Society for Testing and Materials, 1972, p. 164.
- [7] Jones, D. A. and Greene, N. D., "Electrochemical Detection of Localized Corrosion," *Corrosion*, Vol. 25, September 1969, p. 367.
- [8] Pessal, N. and Liu, C., *Electrochimica Acta*, Vol. 16, 1971, p. 1987.
- [9] Wilde, B. E., *Corrosion*, Vol. 28, August 1972, p. 283.
- [10] Bates, J. F., *Corrosion*, Vol. 29, January 1973, p. 28.
- [11] Anderson, D. B. in *Galvanic and Pitting Corrosion*, ASTM STP 576, American Society for Testing and Materials, February 1976, p. 231.
- [12] Morris, P. E. in *Galvanic and Pitting Corrosion*, ASTM STP 576, American Society for Testing and Materials, February 1976, p. 261.
- [13] Garner, A., *Corrosion*, Vol. 34, August 1978, p. 285.
- [14] Kain, R. M., "Crevice Corrosion Resistance of Austenitic Stainless Steels in Ambient and Elevated Temperature Seawater," *CORROSION/79*, Paper No. 230, March 1979.
- [15] Oldfield, J. W. and Sutton, W. H., *British Corrosion Journal*, Vol. 13, January 1978, p. 13.
- [16] Oldfield, J. W. and Sutton, W. H., *British Corrosion Journal*, Vol. 13, March 1978, p. 104.

- [17] Fontana, M. G. and Greene, N. D., *Corrosion Engineering*, McGraw-Hill, New York, 1967.
- [18] France, W. D. and Greene, N. D., *Corrosion*, Vol. 24, August 1968, p. 247.
- [19] Eford, K. D., "Crevice Corrosion of a Copper Nickel Alloy and Its Relationship to the Experimental Pourbaix Diagram," Masters thesis, University of Florida, 1970.
- [20] Verink, E. D. et al, "Chemistry of Crevice Corrosion," *CORROSION/74*, Paper No. 141, March 1974.
- [21] Peterson, M. H. and Lennox, T. J., *Corrosion*, Vol. 29, October 1973, p. 406.
- [22] Drugli, J. M. and Bardal, E., *Corrosion*, Vol. 34, December 1978, p. 419.
- [23] Verink, E. D. and Pourbaix, M., *Corrosion*, Vol. 27, December 1971, p. 497.
- [24] Pourbaix, M., *Corrosion*, Vol. 26, October 1970, p. 431.

C. Amzallag,¹ B. Mayonobe,¹ and P. Rabbe¹

A Strain-Control Technique for Assessing the Corrosion-Fatigue Sensitivity of Stainless Steels

REFERENCE: Amzallag, C., Mayonobe, B., and Rabbe, P., "A Strain-Control Technique for Assessing the Corrosion-Fatigue Sensitivity of Stainless Steels," *Electrochemical Corrosion Testing, ASTM STP 727*, Florian Mansfeld and Ugo Bertocci, Eds., American Society for Testing and Materials, 1981, pp. 69-83.

ABSTRACT: Recent studies have clearly shown the effect of mechanical depassivation on the behavior of stainless steels subject to stress corrosion. When these steels are cyclically deformed, the passive film can be locally perturbed by cyclic modifications of the topography of the underlying metal. Under these conditions the sensitivity of a stainless steel to fatigue in a corrosive medium depends, to a large extent, on the respective kinetics of mechanical depassivation and electrochemical repassivation.

From a study conducted on different stainless steels, a method is proposed for evaluating the sensitivity of stainless steels to corrosion fatigue. Low-cycle fatigue tests under strain control have been carried out in a chloride solution. Evaluation of transient electrochemical parameters recorded during the tests enables us to give a coherent explanation of the behavior of these materials during long-life fatigue tests and of the fatigue crack growth rates. The experimental apparatus and methods used to interpret the mechanical and electrochemical results are discussed.

KEY WORDS: corrosion fatigue, strain rate, crack growth rate, cyclic depassivation, experimental technique

Stainless steels in corrosive solutions are protected by a thin passive layer through which the diffusion of ions is markedly reduced [1,2].² This protective layer can be represented as a dynamic equilibrium state that results from a permanent competition between passivation and depassivation phenomena. These phenomena can be accelerated by various chemical effects (introduction of halogen ions in the passive layer and pollution of the solution by corrosion products) or by mechanical effects (plastic deformation of the metal and superficial abrasion).

The simultaneous action of mechanical and chemical effects that depassivate the metal is encountered in stress-corrosion and corrosion-fatigue

¹Engineer, Department of Mechanics, Creusot-Loire, Centre de Recherches, Firminy, France.

²The italic numbers in brackets refer to the list of references appended to this paper.

phenomena. In both cases the damage mechanisms, during the initiation and propagation stages, can be related to localized corrosion phenomena [3,4]. In order to interpret the materials behavior during these two stages, and to evaluate, in a global manner, their sensitivity to stress corrosion, Parkins et al [5] have used for several years a constant strain-rate tension test. In this context, Rollins et al [6,7] have studied, in the case of corrosion fatigue, the cyclic mechanical perturbations of the metal-solution interface by means of high-strain fatigue tests in corrosive media.

Using an experimental approach close to that of Rollins et al, we have developed a test method for evaluating corrosion-fatigue sensitivity. In this paper we describe the experimental techniques and the behavior of two stainless steels, and we discuss, from the results obtained, the application of the method to other passive materials.

Presentation of the Study

Corrosion-fatigue phenomena are generally studied either by rupture tests on smooth specimens in the high-cycle region or by crack propagation tests on precracked specimens. The first type of test gives better control of the electrochemical characteristics during the test. However, this test does not allow a detailed interpretation of the fatigue behavior because it englobes both the initiation and propagation stages. The second type of test gives the fatigue crack growth rate as a function of the stress-intensity factor range ΔK (related to the defect size and the applied stress). The results obtained can be quantified in mechanical terms, but not in electrochemical terms, because of the confinement of the solution at the crack tip [8-10]. The results obtained with both these tests are essentially phenomenological. In addition, the classification obtained with one type of test can differ from that obtained with the other type, and can also depend upon the metal-electrolyte system.

This problem can be illustrated by the results obtained on an AISI 316 austenitic stainless steel and a ferritic steel containing 26Cr-1Mo [11].

Figures 1 to 4 show the rotating-bending $S-N$ (stress versus number of cycles to failure) curves and the fatigue crack growth rate curves obtained on the two materials in air and in a 3 percent sodium chloride (NaCl) solution. It is observed that the corrosive solution has a weak effect on the crack growth rate and a large effect on the endurance characteristics of the AISI 316 steel; an opposite behavior is observed for the 26Cr-1Mo steel.

In a first analysis, these results can be explained by the competition between the phenomena of depassivation and dissolution, which occur differently in the two types of tests. We shall subsequently examine the validity of this hypothesis.

Since corrosion-fatigue failures are initiated by a process of localized cyclic-mechanical depassivation, we have attempted to simulate this process on a macroscopic scale. We have therefore carried out high-strain fatigue tests on the preceding materials in corrosive media. This experimental ap-

proach is summarized in Fig. 5. The tests have been conducted on smooth specimens under imposed total strain in order to study the cyclic breakdown of the passive film. The evolution of the electrochemical characteristics of the metal-solution interface was recorded during the tests.

Two types of experiments have been carried out: (1) low-cycle fatigue tests to rupture in order to determine the correlation between total strain and fatigue life, and (2) cyclic-mechanical depassivation (CMD) tests to assess the damage mechanism of the passive layer and to try to quantify the sensitivity to corrosion fatigue.

Test Conditions

Experimental Apparatus

The tests were carried out under alternating strain on a servo-hydraulic machine. Figure 6 shows the overall apparatus used for the tests in the corrosive medium.

The specimen gage length was immersed in a plexiglass cell and was partially coated by a layer of silicone grease. A cylindrical area of 1 cm^2 was left directly in contact with the corrosive solution. This solution was constantly refreshed by a regular circulation between the cell and a large capacity reservoir. The recirculated 3 percent NaCl solution was not deaerated, and its pH fluctuated only slightly about the initial value.

The corrosion potential of the specimen was measured with reference to a saturated calomel electrode (SCE), with a capillary probe placed between the reference electrode and the metal-solution system at a constant distance of 1 mm from the specimen.

The electrochemical potentials were measured with a high-impedance electronic voltmeter. A potentiostat was used to impose a constant potential difference between the specimen (SPEC) and the reference electrode (REF). In these conditions, an electrochemical current was measured in the counter-electrode circuit (CE) by the potential drop at the terminals of a calibrated resistance ($R = 1000 \Omega$). The response time of the potentiostat was sufficiently short ($5 \mu\text{s}$) to correctly control the potential. We could then consider that the variations of the current $I(t)$ accurately reflect the behavior of the metal-solution interface. The cyclic strains were imposed with a protected axial extensometer, using quartz knife-edges directly attached to the specimen. The time variations of the mechanical parameters [load $P(t)$ or strain $\epsilon(t)$] and electrochemical parameters $I(t)$ were displayed simultaneously on a two-track recorder.

Experimental Procedures

The specimens were carefully degreased in acetone before testing. After mounting in the cell, they were left in contact with the corrosive solution for

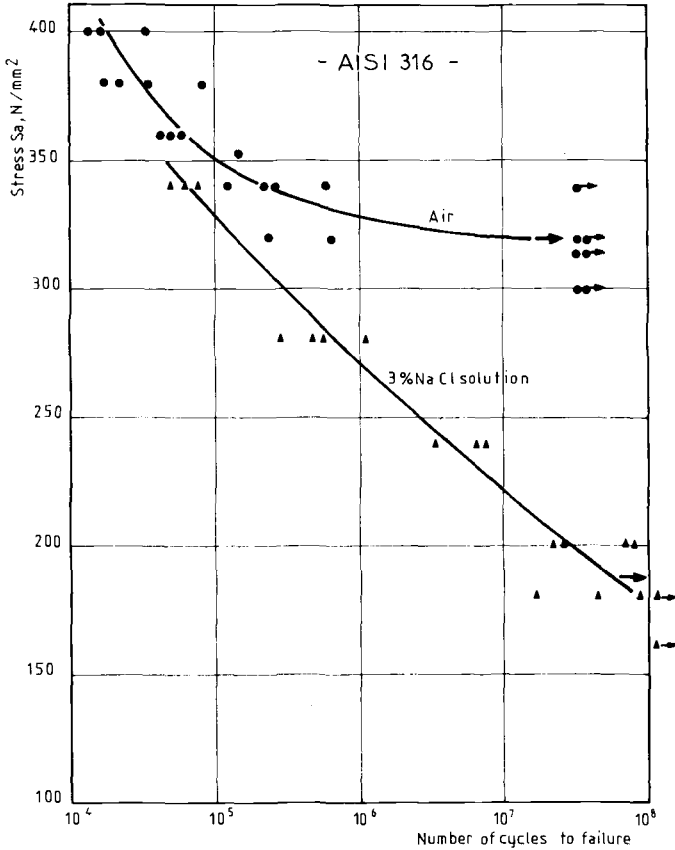


FIG. 1—Rotating-bending fatigue results of the AISI 316 steel.

about 30 min in order to allow the free corrosion potential to stabilize. The potential was then imposed for 10 min before applying the strain.

Low-Cycle Fatigue Tests—During the tests the strain was applied with a triangular waveform at a constant strain rate $\dot{\epsilon}_t$, usually $\dot{\epsilon}_t = 4 \cdot 10^{-3}/s$. Some tests were also carried out with $\dot{\epsilon}_t = 4 \cdot 10^{-4}/s$ and $4 \times 10^{-2}/s$. For given experimental conditions, tests conducted at different strain ranges to failure give an endurance curve of strain ($\Delta \epsilon_t/2$)-life (N_r) (Figs. 7 and 8).

The type of mechanical and electrochemical behavior observed during a test is presented in Fig. 9. The change in the strain range shows the usual cyclic strain-hardening behavior (Fig. 9a). Initially, the metal hardens at each cycle, and the plastic strain amplitude in the imposed total strain decreases. The stress then reaches a "plateau", during which the plastic strain amplitude remains constant. Eventually the development of macroscopic cracks leads to a rapid drop in $\Delta \sigma/2$ and, finally, specimen failure

after a number of cycles (N_r). The behavior shown in Fig. 9a demonstrates cyclic variations of the electrochemical activity of the metal-solution interface.

The perturbations of the metal-solution interface are demonstrated by the variations of the overall anodic current density, J , which changes in phase with the applied strain (Fig. 9b). During the first part of a cycle in tension, J increases (essentially during the plastic deformation) up to a value J_T corresponding to the maximum strain. Similarly, at the maximum compressive strain a small peak (J_c) can be detected, but this peak is substantially smaller than the peak observed in tension (J_T). During the elastic strain, the current density decreases rapidly and becomes virtually null in compression (J_M).

These observations can be explained by the successive cyclic ruptures of the passive film due to the emergence of reversible slip bands at the surface of the deformed metal [6, 7], and the initiation and propagation of cracks at the end of the test.

The damaging role of the corrosive medium probably intervenes during crack initiation by a cumulative process of cyclic transient phases of metal dissolution [12]. This environmental effect may be quantified by measuring the quantity of electricity, ΔQ , generated per cycle, that is, the area under the

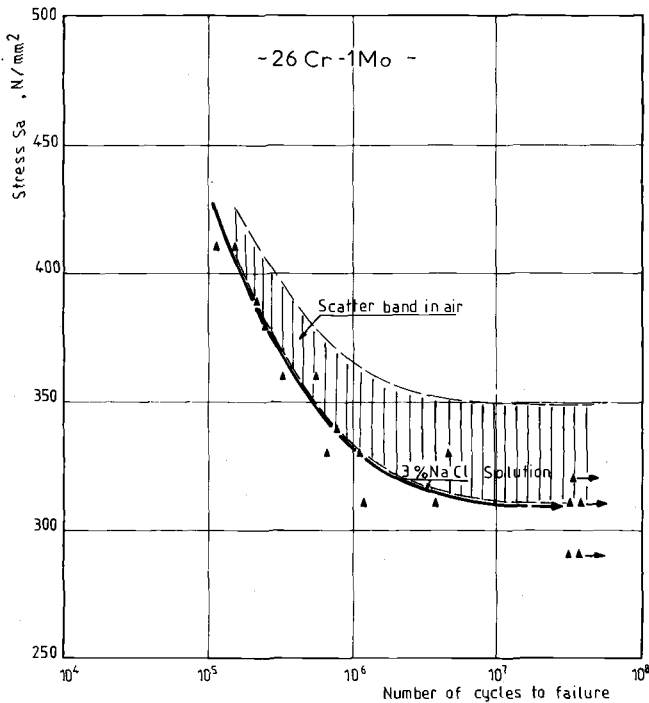


FIG. 2—Rotating-bending fatigue results of the 26Cr-1Mo steel.

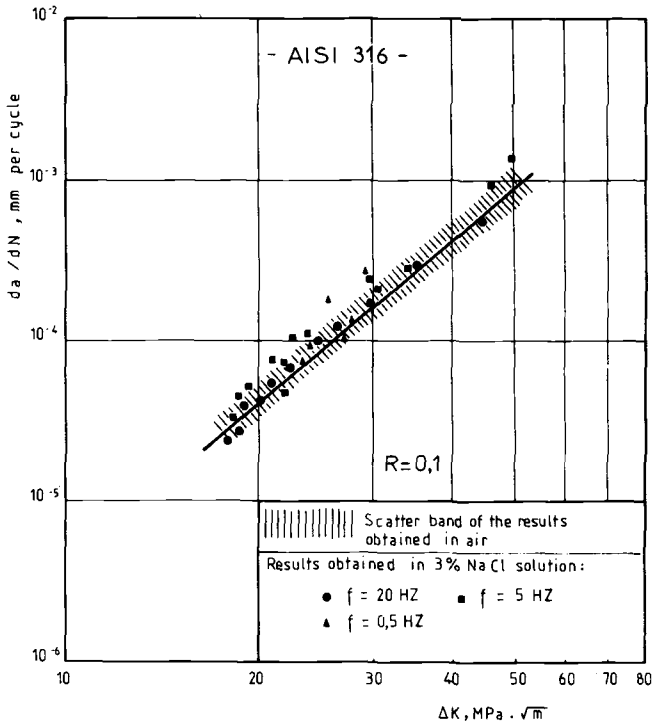


FIG. 3—Fatigue crack growth rates of the AISI 316 steel in air and in a 3 percent NaCl solution.

curve $J(t)$ per cycle. Faraday's law may then be used to relate this parameter to the mass of metal dissolved during a cycle.

Cyclic-Mechanical Depassivation Tests—The electrochemical measurements made with a triangular waveform do not allow us to quantify precisely the electrochemical effects of the tensile and compressive parts of the cycle, and do not separate the depassivation and repassivation phases. We have therefore carried out tests with a symmetrical trapezoidal waveform (Fig. 10).

The strain-rates were varied from $4 \cdot 10^{-5}$ to $4 \cdot 10^{-1}$ /s; the hold time in tension and in compression was 10 s. This time is considered to be much greater than the time necessary for the metal to repassivate. The tests were carried out for 30 cycles.

The low-cycle fatigue tests to failure, performed with a triangular waveform, have shown (Fig. 9) that (1) both the transient dissolutions and the stress levels stabilize simultaneously in about 20 cycles, and (2) the parameter ΔQ_T can be used to quantify the environmental effect.

In the cyclic-mechanical depassivation tests we have measured the quantity ΔQ_T at the 20th cycle (ΔQ_{T-20}) in order to evaluate the stability of the passive layer.

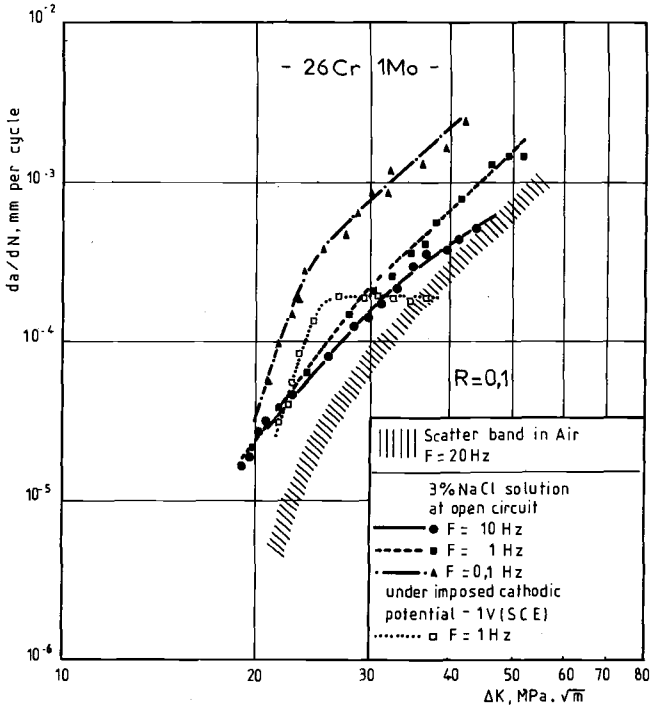


FIG. 4—Fatigue crack growth rates of the 26Cr-1Mo steel in air and in a 3 percent NaCl solution.

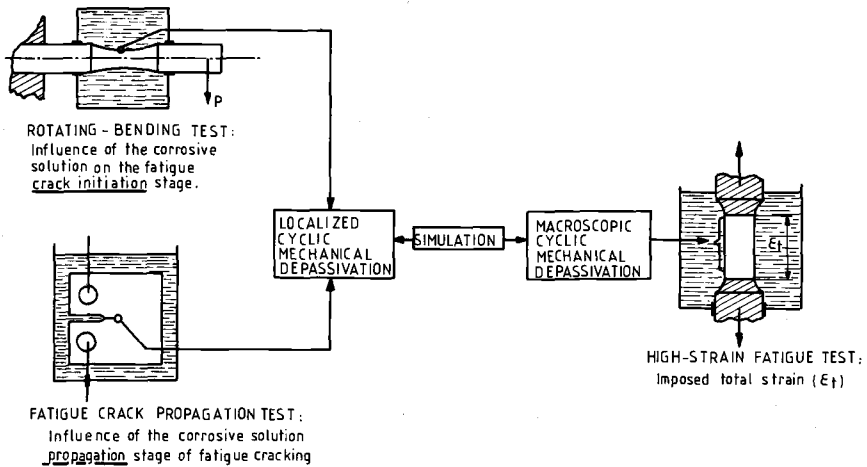


FIG. 5—Experimental approach used to study the mechanisms of corrosion-fatigue of stainless steels.

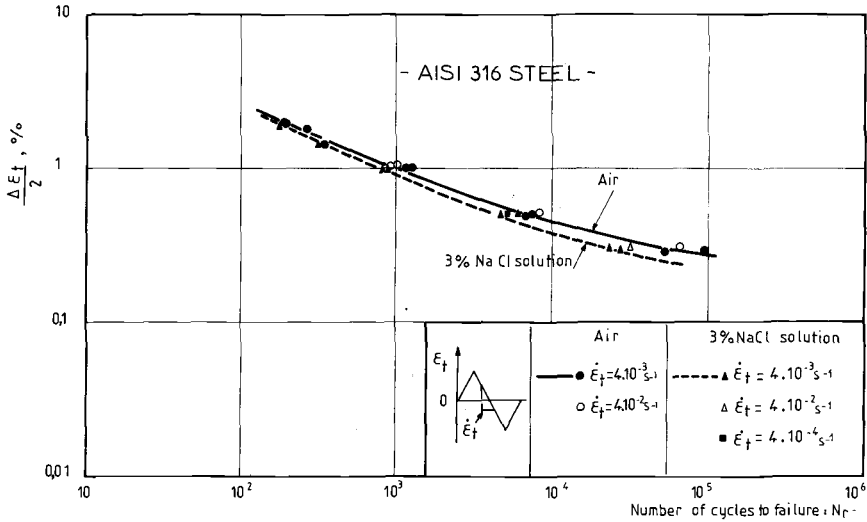


FIG. 7—Low-cycle fatigue curves of the AISI 316 steel—effect of the environment.

Figure 10 illustrates the type of mechanical and electrochemical behavior observed.

Results

Low-Cycle Fatigue Tests

Figures 7 and 8 show that the corrosive solution leads to relatively small reductions of fatigue life that are almost identical on the two materials.

For the austenitic steel, the sensitivity to the environment seems to be independent of the strain-rate ($4 \times 10^{-4}/s \leq \dot{\epsilon}_f \leq 4 \times 10^{-2}/s$) (Fig. 7).

For the two materials, the fatigue life tends to decrease slightly at low-strain ranges. We can therefore propose the following interpretation: (1) in high-strain ranges, mechanical damage is predominant, and (2) in low-strain ranges, the accumulated loss of metal at the emerging reversible slip bands accelerates the crack initiation process.

For the ferritic steel, tests carried out with a cathodic potential lead to a decrease in fatigue life (Fig. 8). This behavior may be the consequence of a phenomenon of hydrogen embrittlement, the origin of which would be the preferential adsorption of cathodic hydrogen atoms at the slip bands [13, 14].

Cyclic-Mechanical Depassivation Tests

Figure 11 illustrates the variation of the quantity of electricity ΔQ_{T-20} (measured at the 20th cycle) as a function of the strain rate $\dot{\epsilon}_f$.

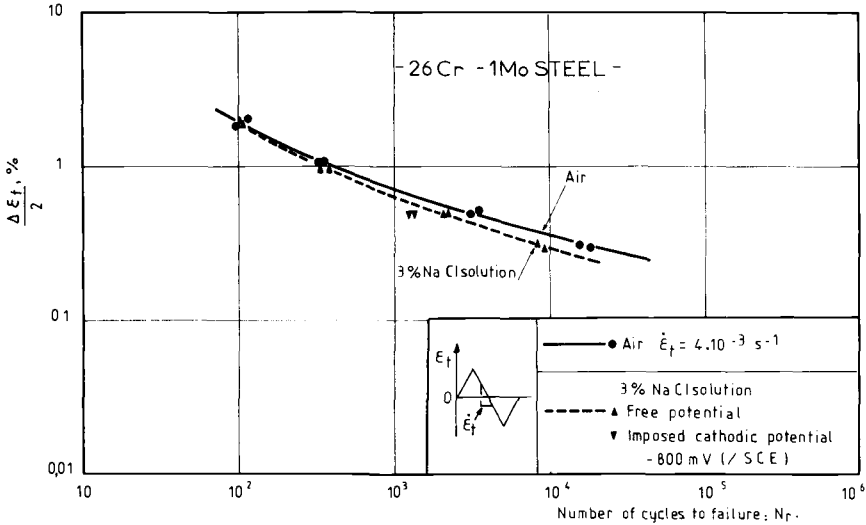


FIG. 8—Low-cycle fatigue curves of the 26Cr-1Mo steel—effect of the environment.

For all metal-solution couples examined: (1) the transient dissolutions fall to zero for $\dot{\epsilon}_{t0} = 4 \cdot 10^{-5}/s$, and (2) the transient dissolutions are maximum for a given value ($\dot{\epsilon}_{tM}$ of $\dot{\epsilon}_t$). In the experimental conditions used, this value of $\dot{\epsilon}_{tM}$ seems to be independent of the pH of the corrosive solution.

For the austenitic steel: $\dot{\epsilon}_{tM} \approx 2 \cdot 10^{-4}/s$
 For the ferritic steel: $\dot{\epsilon}_{tM} = 2 \cdot 10^{-3}/s$

At high strain rates, the transient dissolutions decrease and seem to reach an asymptotic value, independent of the strain rate. The transient electrochemical activity is more pronounced for the austenitic steel than for the ferritic steel. This difference is particularly marked at low strain rates in an acid solution.

The respective positions of the $\Delta Q_t - \dot{\epsilon}_t$ curves demonstrate a better mechanical stability of the passive film of the ferritic steel. For a given metal-solution system the transient quantity of electricity (ΔQ_T) depends mainly upon two parameters related to the strain-rate ($\dot{\epsilon}_t$): (1) the rate of development of slip bands; this rate has to be sufficient to give rise to dissolution ($\dot{\epsilon}_t > \dot{\epsilon}_{t0}$), and (2) the slip band geometry. When the strain rate increases, the slip bands become narrower and more numerous [15]; the area of depassivated metal decreases, thus leading to a general decrease of the amount of dissolved metal [3].

$\dot{\epsilon}_{tM}$ is then the strain rate for which the conjunction of these two parameters leads to a maximum transient dissolution.

Evaluation of the Sensitivity of Stainless Steels to Corrosion Fatigue

Interpretation of the Behavior Observed in Rotating-Bending (High-Cycle) and Crack-Propagation Tests on the Basis of the Results of the High-Strain (Low-Cycle) Tests

During the high-cycle fatigue tests on smooth specimens, the mechanical degradations of the passive layer are similar to those which occur during low-cycle fatigue. In the high-cycle tests, however, though the plastic deformation per cycle is very much smaller, the process of accumulation of transient dissolutions is much more important. This process results in a localized attack of the metal that can lead to a significant reduction of the fatigue life.

In this case the highest values of ΔQ_T are recorded for the austenitic steel. These values express a poorer mechanical stability of the passive layer, and thus explain the effect of the environment on the rotating-bending tests results.

During the crack-growth tests, the mechanical depassivation is localized at the crack tip. The solution, which is confined at the crack tip, is deaerated and acidified [8,9], particularly at the low frequencies for which the duration of the tests are very long and the pumping effect negligible [10].

The results of the cyclic-mechanical depassivation tests conducted in acid solution (pH = 2) may be used for a rough estimate of the transient dissolutions at the crack tip.

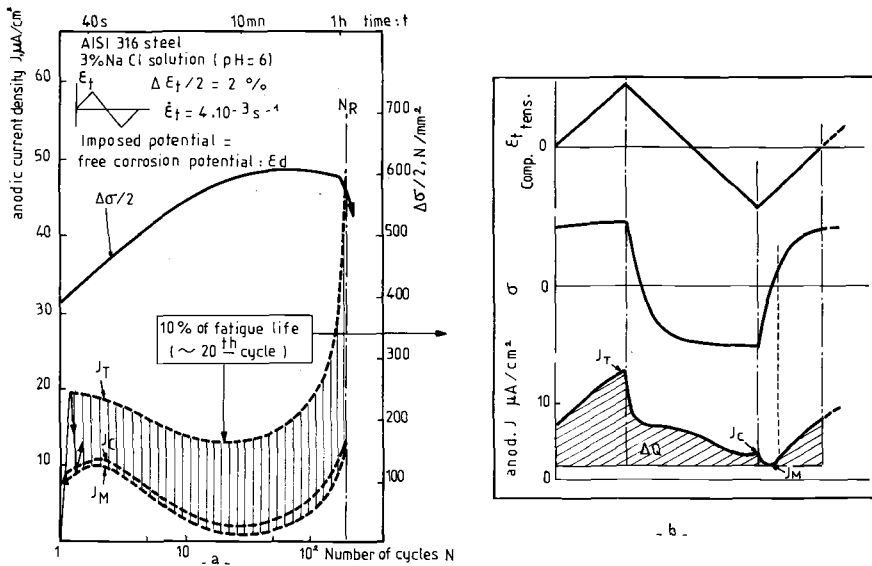


FIG. 9—High-strain fatigue test in a corrosive solution—Evolution of the stress range ($\Delta\sigma/2$) and of the current density (J) as a function of the number of cycles.

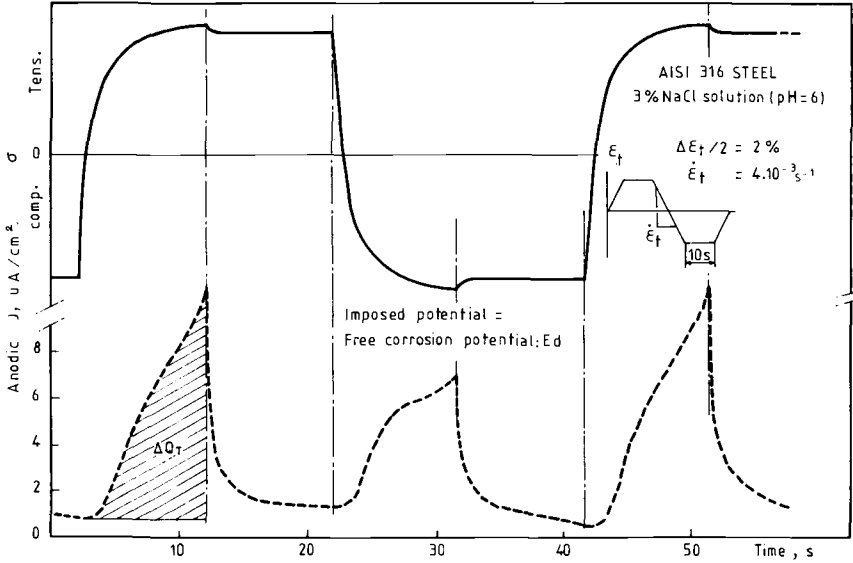


FIG. 10—Cyclic-mechanical depassivation test—Evolution of the stress (σ) and of the current (J) as a function of time.

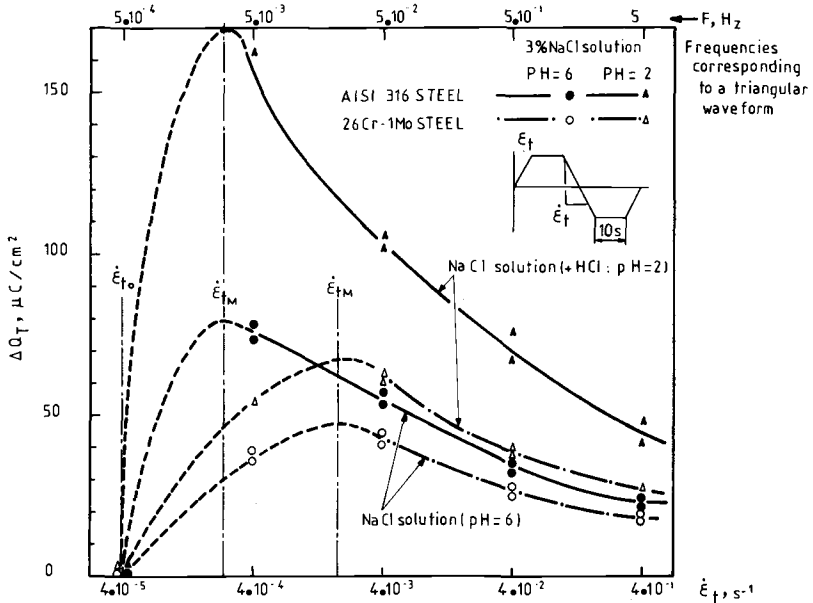


FIG. 11—Variation of the quantity of electricity (ΔQ_T) at the 20th cycle as a function of the total strain rate ($\dot{\epsilon}_t$).

From the values of ΔQ_T obtained on the austenitic steel, the crack growth should be sensitive to salt water. The results of crack growth tests (Fig. 3), however, are inconsistent with this prediction. To explain this discrepancy, one should note that the notion of accumulated metallic dissolutions cannot be applied to the cracking process, since during crack propagation the depassivated sites follow the plastic zone in the region of the advancing crack tip. In this case the electrochemical contribution to propagation can be considered negligible.

Moreover, the lowest frequency used during the crack-growth tests was 0.5 Hz, which corresponds to a relatively low value of ΔQ_T (Fig. 11). At a lower frequency (for example, $5 \cdot 10^{-3}$ Hz; see Fig. 11) the transient dissolutions are more intense, and it is then probable that for very low frequencies the environment would increase the crack-growth rate.

The low-cycle fatigue tests carried out under an imposed cathodic potential have shown a sensitivity of the ferritic steel to hydrogen embrittlement. During crack propagation, the transient dissolutions at the crack tip are accompanied by the evolution of cathodic hydrogen. These hydrogen atoms, cyclically adsorbed on the depassivated metal, would diffuse in the deformed zones and thereby favor crack propagation by cleavage [16, 17]. We must recognize that in this case the measurement of ΔQ_T did not provide much valuable information.

The Possibility of Evaluating Corrosion-Fatigue Sensitivity by High-Strain Fatigue Tests in Corrosive Media

The previous results and analyses allow us to examine the possibility of a more general use of high-strain fatigue tests in corrosive media.

It would appear that in a given solution the low-cycle fatigue tests do not accurately reflect the influence of accumulated metallic dissolutions on crack initiation process in high-cycle fatigue tests. On the other hand, the measurements of ΔQ_T during the cyclic-mechanical depassivation tests can classify the materials with regard to the cyclic-mechanical stability of their passive layers. This parameter characterizes each alloy as a function of the local behavior of the metal-solution interface. We can, in fact, consider that the measurement of ΔQ_T takes into account local parameters such as the thickness of the passive layer, the geometry of the reversible slip steps, the reactivity of the atoms at the surface of the bare metal, etc.

From the point of view of the environmental influence on fatigue crack growth, the experimental approach must necessarily be different.

From the results obtained on the ferritic steel in salt water, it seems that hydrogen embrittlement is chiefly responsible for a higher crack growth. In this case the values of ΔQ_T are not representative of the environmental effects and the cyclic-mechanical depassivation tests are unjustified. The lines

in high-strain fatigue, however, seem sensitive to the effect of an imposed cathodic potential (Fig. 8).

Low-cycle fatigue tests under cathodic conditions would enable one to classify the materials with respect to their hydrogen sensitivity. A possible advantage of this type of test is to simulate, in a simple way, the cyclic introduction of hydrogen as it occurs at the crack tip. This last application of high-strain fatigue in corrosive media should be confirmed on other metal-solution systems at room temperature. In particular, it would be convenient to study the behavior of instable austenitic stainless steels and martensitic stainless steels. Several authors suggest, in fact, that hydrogen embrittlement is responsible for the stress-corrosion and corrosion-fatigue phenomena observed in martensitic structures [18,19].

Conclusions

We have presented a strain-control technique for assessing the corrosion-fatigue sensitivity of stainless steels. Two types of tests have been carried out: (1) low-cycle fatigue tests to failure, and (2) cyclic-mechanical depassivation (CMD) tests. On the basis of the results obtained, we have attempted to interpret the rotating-bending and crack-propagation results of an austenitic and a ferritic steel in a chloride solution.

The electrochemical measurements performed during the CMD tests enabled us to quantify the tendency to depassivation and dissolution of these steels by specifying the quantity of electricity, ΔQ_T , generated per cycle.

For the rotating-bending results, measurements of ΔQ_T can be used to correctly interpret the observed behavior.

For the crack-propagation results, the measurement of ΔQ_T on the ferritic steel does not take into account the environmental effect associated with hydrogen embrittlement.

The validity of the experimental approach used in this study should be verified on other metal-electrolyte systems.

References

- [1] Uhlig, H. H., *Corrosion and Corrosion control*, Wiley, New York, 1967.
- [2] Okamoto, G., *Corrosion Science*, Vol. 13, 1973, p. 471.
- [3] Staehle, R. W., *International Corrosion Conference Series*, National Association of Corrosion Engineers, Vol. NACE-5, 1973, p. 180.
- [4] Duquette, D. J., *International Corrosion Conference Series*, National Association of Corrosion Engineers, Vol. NACE-2, 1972, p. 12.
- [5] Humphries, M. J. and Parkins, R. N., *Corrosion Science*, Vol. 7, 1967, p. 747.
- [6] Pyle, T., Rollins, V., and Howard, T., *Journal of the Electrochemical Society*, Vol. 122, 1975, p. 1445.
- [7] Rollins, V., Patel, C., and Pyle, T. in *Proceedings*, International Conference on Environment Sensitive Cracking of Materials, The Metals Society, London, 1977, p. 367.
- [8] Fontana, M. G. and Greene, N. D., *Corrosion Engineering*, McGraw-Hill, New York, 1967, p. 39.

- [9] Barsom, J. M., *International Journal of Fracture Mechanics*, Vol. 7, 1971, p. 163.
- [10] Hartt, W. A., Stennant, J. S., and Hooper, W. C. in *Corrosion-Fatigue Technology, ASTM STP 642*, American Society for Testing and Materials, 1978, p. 5.
- [11] Amzallag, C., Rabbe, P., and Desestret, A. in *Corrosion-Fatigue Technology, ASTM STP 642*, American Society for Testing and Materials, 1978, p. 117.
- [12] Pelloux, R. M., Stoltz, R. E., and Moskowitz, J. A., *Materials Science and Engineering*, Vol. 25, 1976, p. 193.
- [13] McGright, R. D., *International Corrosion Conference Series*, National Association of Corrosion Engineers, Vol. NACE-5, 1973, p. 306.
- [14] Bernstein, J. M. and Thomson, A. W. in *Proceedings*, International Conference on Environment Sensitive Cracking of Materials, The Metals Society, London, 1977, p. 412.
- [15] Jaoul, B. in *Etude de la plasticité et application aux Métaux*, Dunod, Ed., Paris, 1965, p. 220.
- [16] Vosikovsky, O., *Journal of Engineering Materials and Technology*, Transactions of the American Society of Mechanical Engineers, Vol. 97, 1975, p. 298.
- [17] Austen, I. M. and Walker, E. F. in *Proceedings*, International Conference on the Influence of Environment on Fatigue, Institution of Mechanical Engineers, London, 1977, p. 1.
- [18] Atkinson, J. D. and Lindley, T. C. in *Proceedings*, International Conference on the Influence of Environment on Fatigue, Institution of Mechanical Engineers, London, 1977, p. 65.
- [19] Wilde, B. E., *International Corrosion Conference Series*, National Association of Corrosion Engineers, Vol. 27, 1971, p. 326.

K. J. Kessler¹ and H. Kaesche¹

Potential and Strain-Rate Effects in Slow Strain-Rate Stress Corrosion Cracking of Type 304 Stainless Steel in 35 Percent Magnesium Chloride at 120°C

REFERENCE: Kessler, K. J. and Kaesche, H., "Potential and Strain-Rate Effects in Slow Strain-Rate Stress Corrosion Cracking of Type 304 Stainless Steel in 35 Percent Magnesium Chloride at 120°C," *Electrochemical Corrosion Testing, ASTM STP 727*, Florian Mansfeld and Ugo Bertocci, Eds., American Society for Testing and Materials, 1981, pp. 84-95.

ABSTRACT: Constant extension rate experiments have been performed on Type 304 stainless steel round tension-test specimens in 35 percent magnesium chloride at 120°C as a function of electrode potential and extension rate. When potentiostatic measurement was applied, an extension rate of $4.4 \times 10^{-6} \text{ s}^{-1}$ was found to be acceptable as an accelerated test. These tests are compared with constant load measurements by variation of the electrode potential. Both methods indicate that stress-corrosion cracking decreases by lowering electrode potential and disappears below -380 mV (saturated calomel electrode). Current density-time plots made during constant straining and fractographic observations show different types of crack formation. The number of cracks increases with increasing potential, and the crack depth decreases with accelerated straining. Transgranular stress-corrosion cracking is observed accompanied by pitting. The selective corrosion in the early stage of cracking was revealed by scanning electron microscope (SEM) micrographs and SEM analysis. Iron and nickel are dissolved and a chromium-rich phase is formed along the crack walls. Although the first attack appears to be intercrystalline, the fracture shows only transgranular features.

KEY WORDS: stress corrosion cracking, slow straining, austenitic stainless steels, fracture properties, electrochemistry, crack initiation, magnesium chloride

Conventionally, time-to-failure tests such as static constant loading and U-bend techniques are used to reveal stress-corrosion cracking (SCC) susceptibility. The application of constant strain-rate testing technique in stress-corrosion cracking was investigated for different systems by Parkins et al

¹Institut für Werkstoffwissenschaften, Lehrstuhl Korrosion und Oberflächentechnik, Universität Erlangen-Nürnberg, West Germany.

[1,2]² and others [3-7]. The relationship between stress-elongation behavior of tension tests in air and in aqueous solutions allows us to describe SCC susceptibility by mechanical properties. However, locally different strain conditions caused by crack formation, crack propagation, and crack branching show that constant extension is not equivalent to constant straining of specimens. Consequently, some authors propose slow straining or slow strain rate, which indicates that SCC is only found by slow tensile tests.

SCC susceptibility is a function of extension rate; its influence on metallic materials is schematically depicted in Fig. 1, which shows that the corrosive environment may be without any influence (curve 1). The shape of curve 2 is assumed for the classical types of stress corrosion occurring even during static constant loading (a deterioration of mechanical properties by pitting or general corrosion could also take place). The nonclassical type of SCC shown in curve 3 with its highest sensitivity at intermediate strain rates points up the disappearance of SCC below a certain lower critical strain rate.

The aim of this paper is to compare constant extension-rate tests with the work of our own and other measurements with respect to static constant loading and potentiostatic measurements in a chloride environment. A scanning electron microscope (SEM) was employed to reveal SCC susceptibility and the early stage of crack formation and crack propagation.

Experimental Information

The slow strain-rate assembly is shown in Fig. 2. The electrochemical cell consisted of a glass tube enclosed with machined poly tetrafluoroethylene (PTFE) plates. The PTFE-covered ends of the pull rods guaranteed that only the stressed working electrode was in contact with the solution. The potential was controlled by a potentiostat and using a Pt counter electrode and a satu-

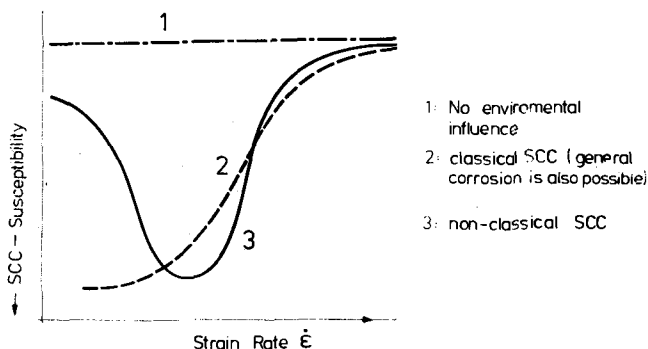


FIG. 1—SCC susceptibility as a function of strain rate (schematic).

²The italic numbers in brackets refer to the list of references appended to this paper.

rated calomel reference electrode (SCE). This testing assembly was installed in a load frame, the pull rod of which was connected to a gear exchange mechanism for crosshead speeds ranging from 10^{-7} to 10^{-2} mm/s. During tension tests, stress was measured continuously by a load cell, and elongation was obtained by multiplying the test period with the crosshead speed.

The test solution used in all tests was 35 percent magnesium chloride (MgCl_2) with a pH of 3.5 at room temperature. Since MgCl_2 disassociates and becomes more acidic with temperature, however, a pH of 1.5 [8] at 120°C is assumed.

Specimens

Specimens were machined from commercial 18Cr-9Ni stainless-steel material rounds (their chemical composition is listed in Table 1). The gage length and cross section of the specimens were 30 mm and 4 mm, respectively. Prior to use they were solution annealed at 1050°C for 20 min in a vacuum and subsequently water quenched.

Procedure

The unstressed round tension specimens were held at constant potential during heat-up. In about an hour 120°C was reached, and after 30 min at this temperature the current density became stationary. Tension tests were then initiated at various strain rates and with cathodic and anodic polarization. All specimens were pulled to failure, and their fracture surfaces were examined subsequently by SEM. In addition, photomicrographs were obtained to reveal the SCC susceptibility.

Results and Discussion

Polarization Behavior

Although the well-known polarization curve of Type 304 stainless steel [8] in MgCl_2 (Fig. 3) does not directly show a passive region, previous workers found that the true active-passive behavior of stainless steels in MgCl_2 is simply suppressed by the hydrogen reduction kinetics at elevated temperatures. Well-known studies [9] distinguish three regions: cathodic protection, stress-corrosion cracking, and the latter accompanied by pitting when specimens were anodically polarized.

SCC Susceptibility as a Function of Extension Rate

The dynamic testing method (slow straining) is an accelerated test in comparison with static constant loading (which takes a particularly long time to

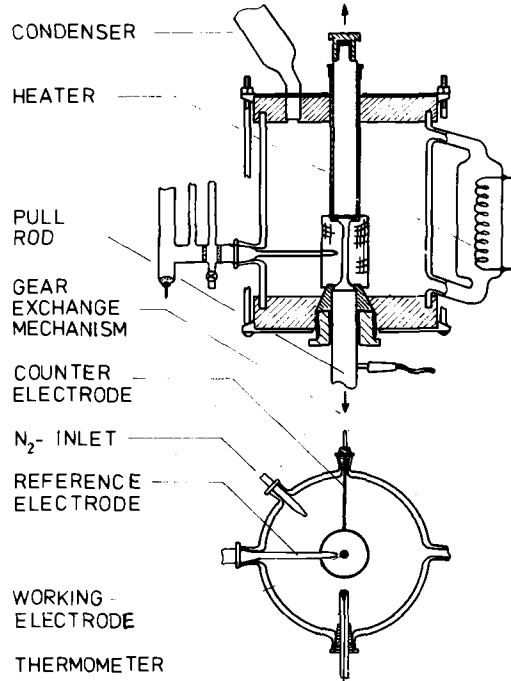


FIG. 2—SCC testing cell.

TABLE 1—Properties of specimens.

Chemical Properties, weight percent								
	C	Si	Mn	P	S	Cr	Ni	
	0.041	0.60	1.19	0.026	0.015	18.89	11.23	
Mechanical Properties, N/mm ²								
	25°C		100°C		120°C		200°C	
Yield strength	180		155		140		125	
Ultimate tensile strength	570		520		500		460	
Percent ϵ_F	77		65		55		45	

show evidence of failure). Figure 4 shows the important dependence of the mechanical properties on strain rate. In this case, SCC susceptibility is represented by the strength properties that decrease with lowered applied extension rate and reach an almost constant value for crosshead speeds below 10^{-7} s^{-1} . It is obvious that the decrease of mechanical properties at -370 mV is ob-

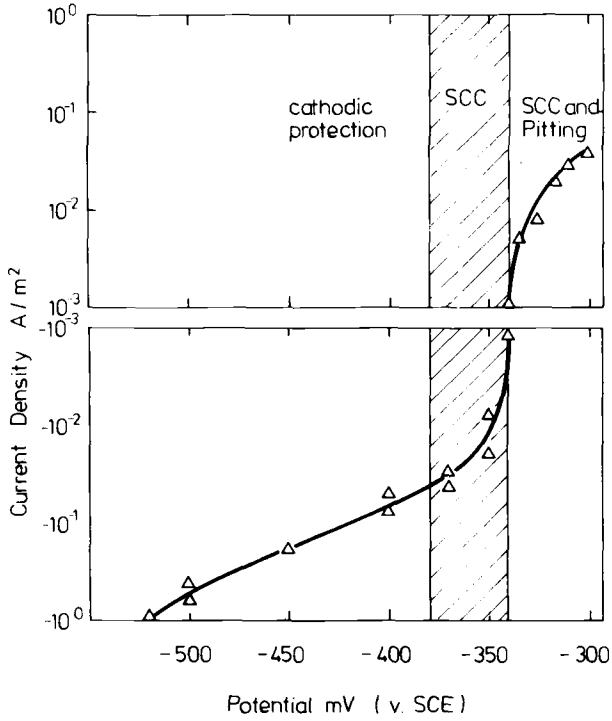


FIG. 3—Current-potential curve for X5CrNi-18-9 in $MgCl_2$ at $120^\circ C$.

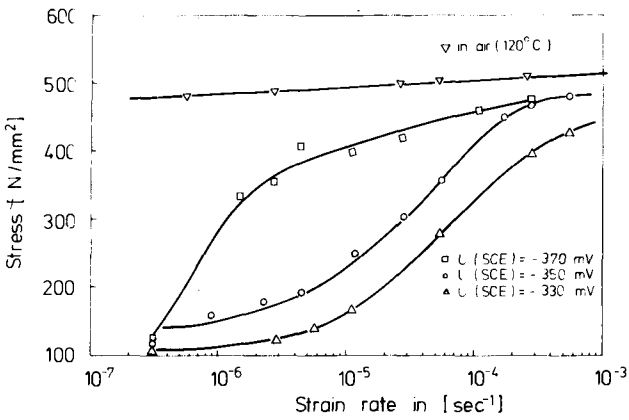


FIG. 4—Maximum strength as a function of strain rate.

served only when slow straining is applied because surface cracks in the upper part of the curve show little effect on tensile strength. At this point the question arises whether an acceptable extension-rate test in the whole SCC region exists that would qualify as an accelerated test. As will be shown later (Fig. 8), metallographic observations are necessary to define an acceptable crosshead speed for SCC measurements. It is found that dynamic tension tests below 10^{-5} s^{-1} are almost similar to static constant load tests whereas in the rising part of the curves straining becomes faster than crack propagation. This causes notch-like transgranular penetrations instead of those typical transgranular and branched fissures.

Stress-elongation curves (Fig. 5) show the dependence of physical properties on extension rate. As the crack propagation rate is proposed to stay constant [10] the lowering of crosshead speed severely decreases strain to failure as well as ultimate tensile strength. Sometimes not even the yield strength is reached and the typical characteristics of austenitic stainless steels (for example, toughness) are completely lost.

Effect of Electrode Potential

Knowledge of all these limiting quantities now allows us to compare constant extension-rate tests with constant load tests (Fig. 6). The negative gradient of the time-to-failure curves and the decrease of ultimate tensile strength by means of strain-rate tests are almost similar, which indicates a lower critical potential below which stress-corrosion cracking is prevented [9, 11-13]. It is noteworthy that corrosion stops exactly at this well-defined potential

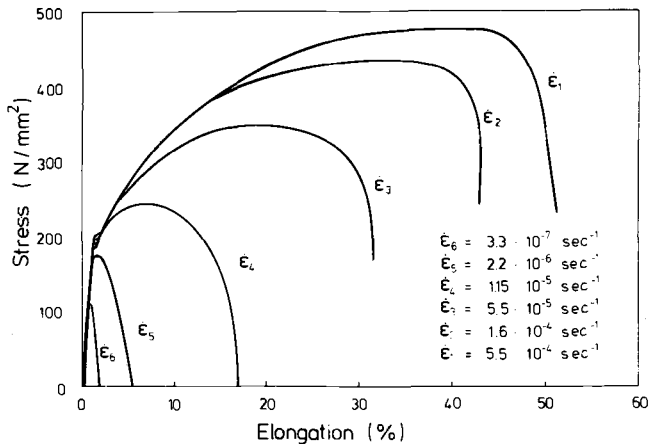


FIG. 5—Stress elongation curves in 35 percent MgCl_2 at 120°C and various strain rates; $U(\text{SCE}) = -350 \text{ mV}$.

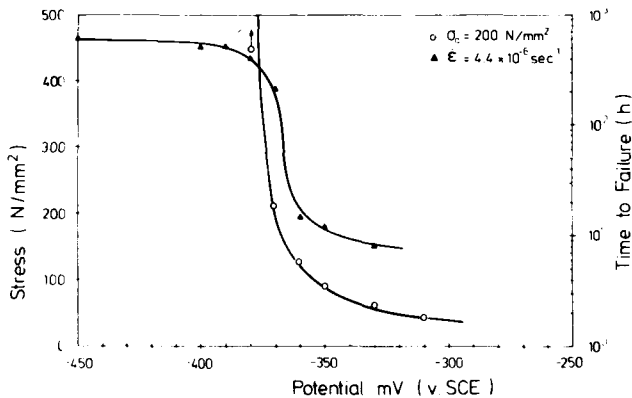


FIG. 6—Effect of applied potential on SCC: (a) constant load tests; (b) slow strain-rate tests.

even when specimens are pulled to failure. Cathodic protection reveals ductile fracture comparable to tension tests in air.

The current density-time plot recorded during straining shows the effect of the potential on the stability of a passivating surface film (Fig. 7). At -350 mV (SCE) activation starts with straining. This corresponds to constant load tests with a supposed limiting stress below yield strength [9,11]. The activation peak at -360 mV occurs near yield strength whereas at -370 mV current density does not increase before reaching ultimate tensile strength. These examples correspond to static constant loading which detects SCC in the range of plastic strain [13].

SCC mechanisms, such as the slip dissolution model, must fail if we regard only the elastic range, since dislocation movement and active slip cannot take place. Two different and independent crack nucleation mechanisms are instead proposed. In the region of Hooke's law, the development of crystallographic pits and the later coalescence initiate crack formation. In the case of plastic straining, the slip dissolution model is relevant because a network of corroded slip plains covers the surfaces of the specimen, which leads finally to transgranular cracks. Evidently, in most of the experiments pitting is masked by severe dissolution of countless slip plains.

Fractographic observations of specimens tested by slow straining at -350 mV confirm this assumption (Fig. 8). Very low straining caused a maximum strength far below general yield. The specimens show brittle fracture mode with initial cracks forming in enlarged pits. In the following transition region, active slip steps are finally predominant until the strain rate becomes too fast and ductile fracture with slightly corroded slip plains is observed. Mechanical properties are almost equal to those found in air.

The disastrous influence of chloride in a narrow range of potential on SCC of stainless steels has been known for a long time, but until now only a

few papers have reported detailed facts of SCC initiation. The role of chloride ions in SCC under anodic polarization is described by Jones [15]. In addition, SEM studies of stressed and cathodically polarized specimens are compared with unstressed specimens held in the pitting region in the present experiments.

It becomes apparent from micrographs that pitting is the result of a type of localized corrosion cell developed under the surface film (Fig. 9). The corroded regions were found by SEM analysis to be highly enriched in chromium and almost depleted of iron and nickel. The chromium-rich phase left on the cell floor is chromium based and most likely chromium oxide. Most probably, stressed specimens under anodic polarization fail by cracks running down one of the oxide cracks in the chromium-enriched phase.

SCC initiation under cathodic polarization may be described by the same phenomena because SEM studies show the same type of localized and selective corrosion (Fig. 10). It is supposed that the chloride ions penetrate the original oxide layer and produce "filiform" corrosion cells [15]. Corrosion products expand and burst the solid phase. SCC starts within this phase by the coalescing of some oxide cracks with the same orientation. It is not clear

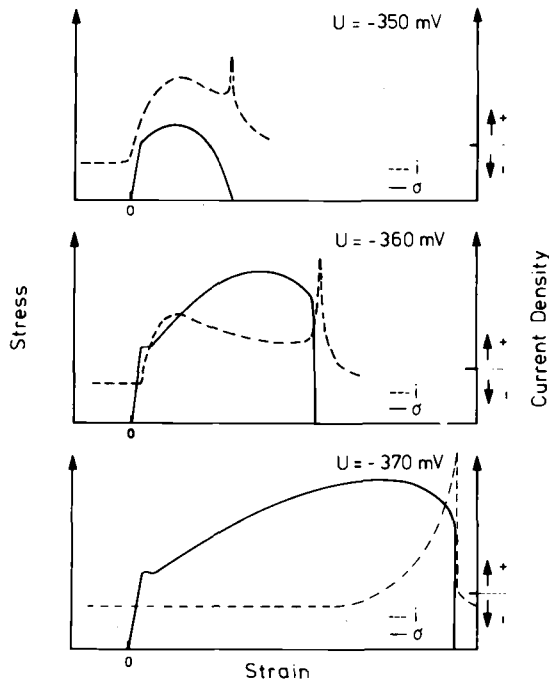


FIG. 7—Effect of applied potential on σ - ϵ - and i - t -behavior.

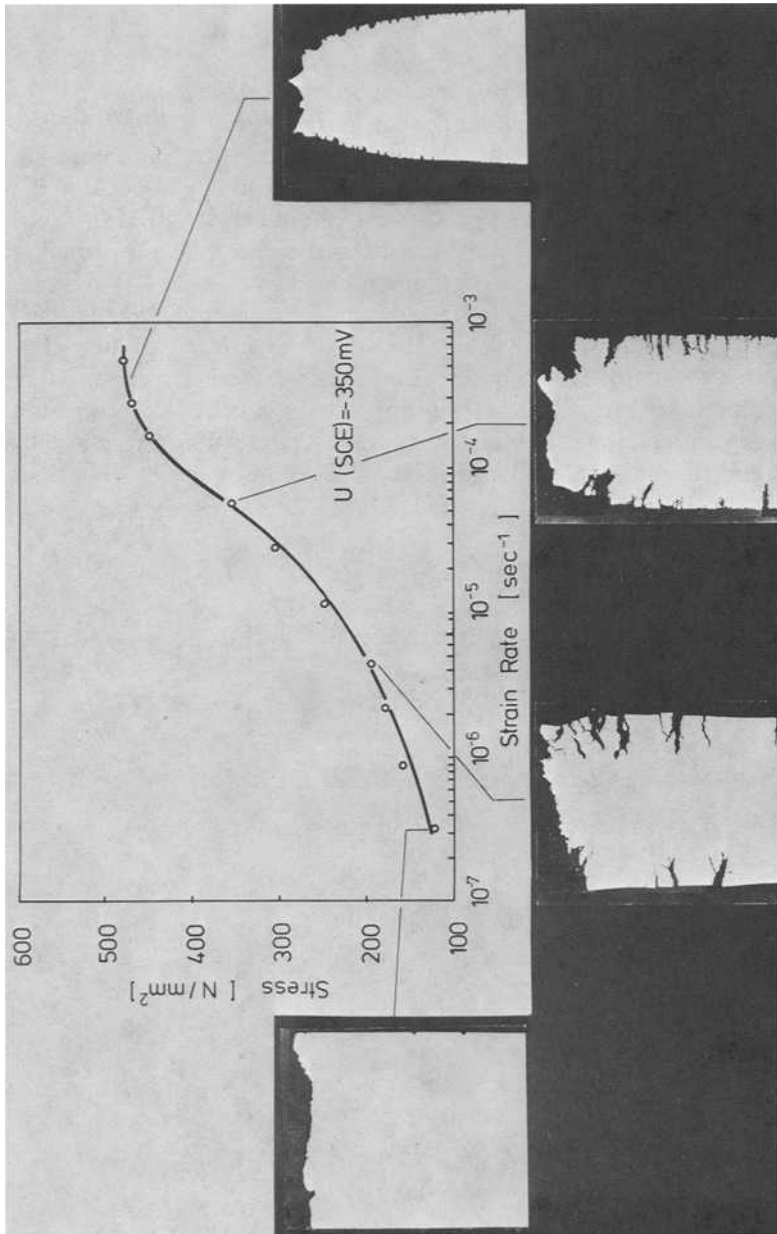


FIG. 8—Stress-corrosion morphology as a function of strain rate and electrode potential.

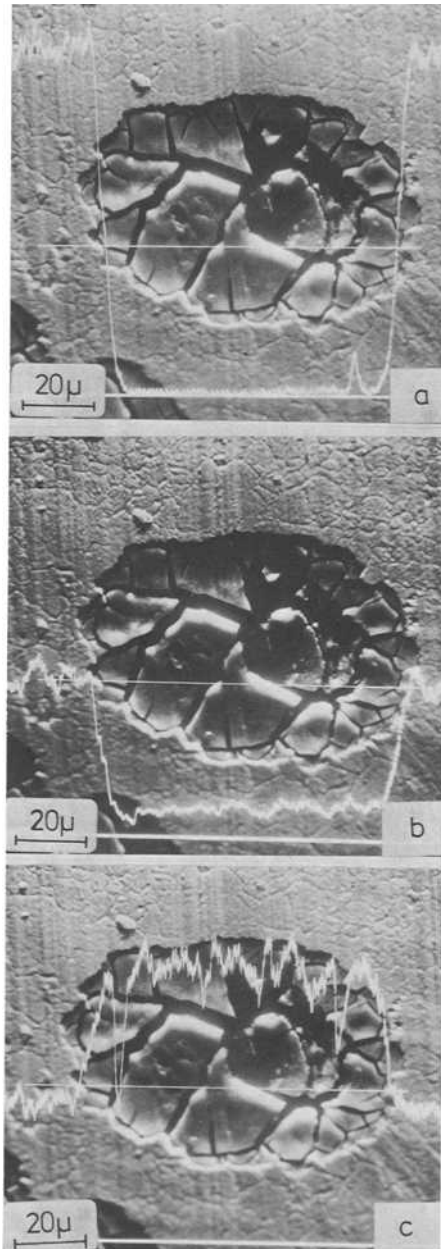


FIG. 9—X-ray scanning pictures showing element distributions in a corrosion pit: (a) iron; (b) nickel; (c) chromium.

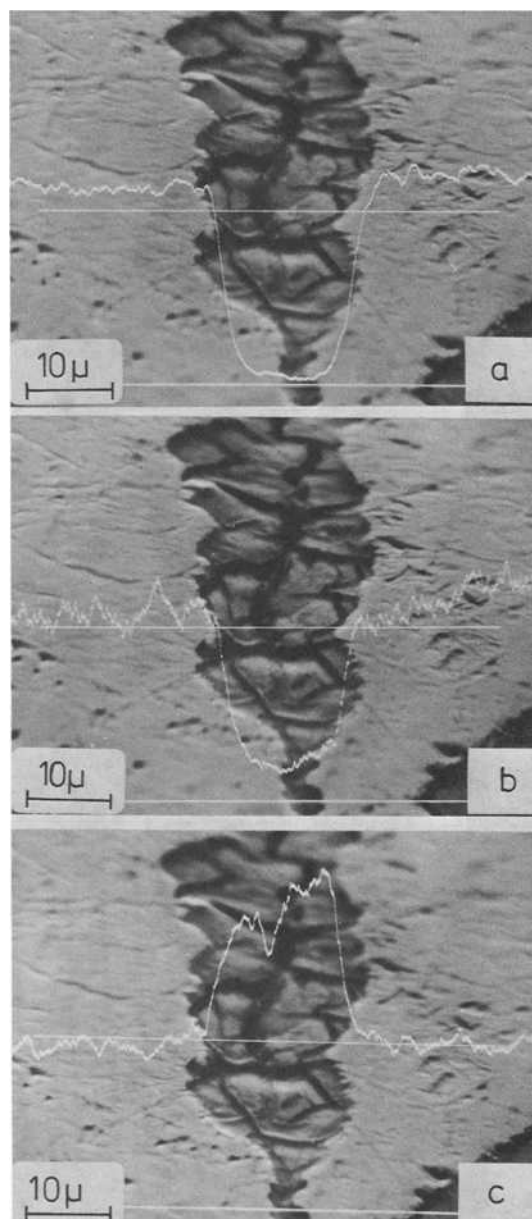


FIG. 10—X-ray scanning pictures showing element distributions of a crack nucleus: (a) iron; (b) nickel; (c) chromium.

whether chromium-enrichment is confined only to crack nucleation or whether it is also part of the crack propagation.

Conclusions

1. Potential-controlled extension-rate experiments demonstrate that SCC susceptibility is a function of strain rate. Slow straining below 10^{-5} s^{-1} reveals typical transgranular SCC. Nevertheless, it is fast enough to be acceptable as an accelerated test. The severe decrease of elongation to fracture and the reduction in area and tensile strength show the disastrous influence of SCC on mechanical properties.

2. Accelerated tests at $3.4 \cdot 10^{-6} \text{ s}^{-1}$ indicate that the sensitivity to SCC as determined by means of dynamic testing decreases with lowered electrode potential. In spite of the severe testing method, the limiting potential of SCC is found at -380 mV to be in agreement with constant load conditions.

3. Cracking is preceded by localized and selective corrosion. The corroded regions were found to be depleted of iron and nickel and highly enriched in chromium. The chromium-rich phase is most likely chromium oxide. Stressed specimens most probably fail because of cracks initiated within this phase.

References

- [1] Humphries, M. J. and Parkins, R. N., *Corrosion Science*, Vol. 7, 1967, p. 747.
- [2] Sutcliffe, J. M., Fessler, R. R., Boyd, W. K., and Parkins, R. N., *Corrosion*, Vol. 28, 1972, p. 313.
- [3] Hishida, M. and Nakada, H., *Corrosion*, Vol. 33, 1977, p. 332.
- [4] Buhl, H., *Werkstoffe und Korrosion*, Vol. 29, 1978, p. 725.
- [5] Kessler, K. J. and Wendler-Kalsch, E., *Werkstoffe und Korrosion*, Vol. 28, 1977, p. 78.
- [6] Povich, M. J., *Corrosion*, Vol. 34, 1978, p. 162.
- [7] Kraub, H., Hirth, F. W., and Speckhardt, H., *Zeitschrift fuer Werkstofftechnik*, Vol. 9, 1978, p. 273.
- [8] Wiegand, H., Naumann, R., and Speckhardt, H., *Werkstoffe und Korrosion*, Vol. 22, 1971, p. 612.
- [9] Brauns, E. and Ternes, H., *Werkstoffe und Korrosion*, Vol. 19, 1968, p. 1.
- [10] Hoar, T. P. and Hines, J. P. in *Stress Corrosion Cracking and Embrittlement*, W. D. Robertson and R. Bakisch, Eds., New York, 1956, p. 107.
- [11] Herbsleb, G. and Westerfeld, K.-J., *Werkstoffe und Korrosion*, Vol. 27, 1976, p. 479.
- [12] Herbsleb, G. and Schwenk, W., *Werkstoffe und Korrosion*, Vol. 21, 1970, p. 1.
- [13] Hoar, T. P. and Hines, J. P., *Journal of the Iron and Steel Institute*, Vol. 182, 1956, p. 124.
- [14] Spähn, H. and Steinhoff, U., *Werkstoffe und Korrosion*, Vol. 20, 1969, p. 733.
- [15] Jones, R. J., *Corrosion*, Vol. 31, 1975, p. 424.

H. S. Tong¹

Corrosion and Electrochemical Behavior of Iron-Chromium-Nickel Alloys in Concentrated Sulfuric Acid Solutions

REFERENCE: Tong, H. S., "Corrosion and Electrochemical Behavior of Iron-Chromium-Nickel Alloys in Concentrated Sulfuric Acid Solutions," *Electrochemical Corrosion Testing, ASTM STP 727*, Florian Mansfeld and Ugo Bertocci, Eds., American Society for Testing and Materials, 1981, pp. 96-109.

ABSTRACT: The electrochemical and corrosion behavior of Types 304 and 316 stainless steels and Carpenter 20 Cb-3 alloy in 99 percent sulfuric acid solutions have been investigated at temperatures up to 127°C. The open-circuit potentials (OCP) have been monitored against immersion time. Oscillations of the OCP at high temperature were observed in some cases. Correlation between OCP-time behavior and corrosion resistance has been established. Metallurgical studies have been carried out for alloys after each test. Changes in the corrosion behavior on the alloy surfaces as a function of temperature and solution concentration were observed.

The corrosion rate of each alloy/medium system has been determined by the conventional weight-loss measurement. Comparison of the corrosion resistance among three alloys has also been made. Corrosion rate was found to increase with increasing temperature, stirring rate, and iron content in the solution.

KEY WORDS: corrosion, electrochemistry, anodic polarization, stainless steels

Sulfuric acid (H_2SO_4) is the most widely used inorganic acid for industrial use. Consequently, sulfuric acid corrosion is the most frequently encountered corrosion in chemical processing. In high concentrations (above about 85 percent) it becomes strongly oxidizing and is best handled by materials resistant to oxidizing conditions.

Control of corrosion and improvement of acid purity are important to the chemical industry. In view of the technical importance of sulfuric acid, its corrosive properties are of considerable interest [1-5].² Many electrochemical measurements have been reported for stainless steel alloys in dilute sulfuric acid (less than 10 percent by weight) [6-7]. These studies have

¹Staff metallurgist, Corporate Development Center, Allied Chemical Corporation, Morristown, N.J. 07960.

²The italic numbers in brackets refer to the list of references appended to this paper.

been essentially concerned with the anodic reaction involving iron and water at various hydrogen ion concentrations. Sulfuric acid acted as the solute in the water-solvent systems. In concentrated sulfuric acid, however, the cathodic reactions are different. In the absence of iron in the acid, the cathodic process may be the reduction of SO_4^{2-} into S, SO_2 , HS^- , etc. With the addition of iron, the main process is the reduction of ferric (Fe^{3+}) ion to the ferrous (Fe^{2+}) state. Although it has been reported that steel can be passivated in 67 percent sulfuric acid and in oleum [1, 8], very few reports [9] have been released discussing the electrochemical characteristics of stainless steel alloys in very concentrated solutions of sulfuric acid.

The electrochemical behavior of most metals falls into three categories (see Fig. 1). As was discussed elsewhere [10], Case 3 behavior is the most desirable, since the corrosion occurs in the passive state and usually at a low rate. A significantly higher corrosion rate is possible when the metal exhibits

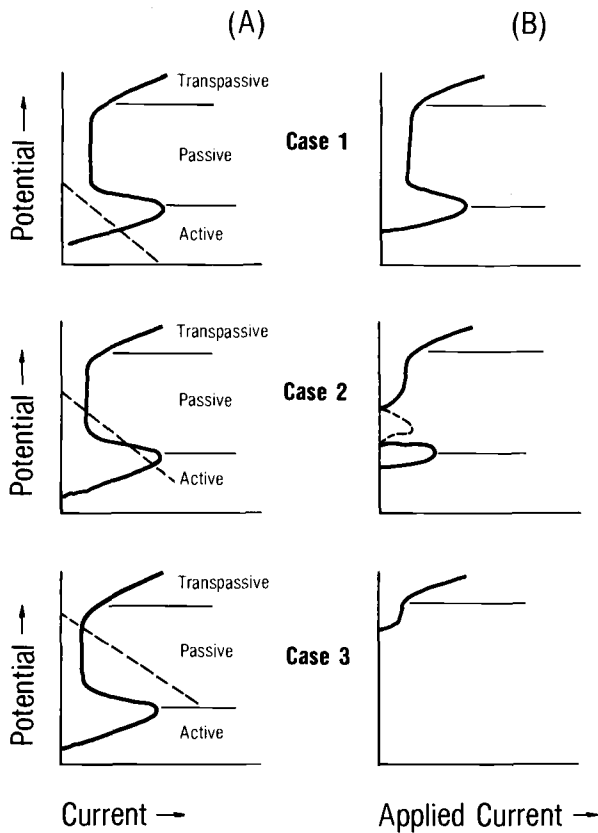


FIG. 1—Theoretical Case 1, 2, and 3 behavior. Curves (A) are potential-versus-current diagrams. Curves (B) are anodic potential-versus-applied current diagrams.

Case 1 behavior. A specimen exhibiting Case 2 behavior may also exhibit either Case 1 or Case 3 behavior, depending on many factors, such as immersion condition, surface condition, etc. When poor duplication is observed in conventional corrosion tests, Case 2 behavior is often responsible.

The main object of the present study is to investigate the anodic polarization behavior of Type 304, Type 316, and Carpenter 20 Cb-3 stainless steels in 99 percent H_2SO_4 solution. Corrosion rates were determined by the conventional weight-loss measurement per ASTM Recommended Practice for Preparing, Cleaning, and Evaluating Corrosion Test Specimens [G 1-72 (1979)]. The effect of iron content in the solution and the effect of temperature on the corrosion behavior were also studied.

Experimental Procedure

The test electrodes were prepared from commercial-grade Type 304, Type 316, and Carpenter 20 Cb-3 alloys in the "as-received" condition (mill annealed). The chemical compositions of the test alloys are given in Table 1. The specimens were machined to a shape per ASTM G 1. Just prior to immersion, the specimens were abraded with 120 grit SiC paper, rinsed in water, degreased with acetone, and dried. Industrial grade 99 percent sulfuric acid solutions containing 9 ppm iron were used to simulate industrial process liquids. For the solutions with higher iron concentration, iron was added as ferric sulfate. A white product, which was found to be a mixture of ferrous and ferric compounds [11], was always observed to precipitate in the solutions. Therefore the iron content of the solutions referred to in this text represents only the dissolved iron concentration (as analyzed spectrophotometrically using 1,10-phenanthroline according to the procedures of Harvey et al [12]). The test solutions were purged with a stream of pre-purified nitrogen for 1 h. A Princeton Applied Research (PAR) Model 173 potentiostat in combination with a universal programmer (PAR-175) and X-Y recorder were used to record potential-current density curves. Potentiodynamic polarization curves were determined at 6 mV/min.

Open-circuit potential (OCP)/time curves were recorded in separate tests for various temperature/concentration combinations. The specimen was immersed in the electrolyte, and its OCP was monitored as a function of time.

TABLE 1—Chemical composition of alloys studied.

Material	Composition, %					
	Ni	Cr	Fe	Mo	Cu	C
304 SS	8.9	18.3	68.6	0.2	0.3	0.05
316 SS	10.1	15.9	71.1	3.4	0.4	0.05
Carpenter 20 Cb-3	33.3	20.8	43.1	2.5	3.4	0.06

The polarization measurement was not initiated until the corrosion potential exhibited a stable constant value. Corrosion rates were also determined by conventional weight-loss tests per ASTM G 1. The surface of the specimens was examined after the corrosion test using optical microscopy to determine its corrosion morphology.

Results and Discussion

Effect of Temperature

Anodic Polarization Behavior—The potentiodynamic anodic polarization curves for three alloys in 99 percent sulfuric acid with 9 ppm iron at 30°C are given in Fig. 2. A complete passive range was obtained for all materials in this acid solution at this temperature. The electrochemical characteristic appears to be different from that in 93 percent H_2SO_4 solution. For example, an anodic current maximum, which was not observed in 93 percent H_2SO_4 [13], was present between +650 mV and +1.0 V for all three alloys. Similar observations have been noted by Fisher and Brady [11] for ASTM Tentative Specification for Low and Intermediate Tensile Strength Carbon-Steel Plates of Flange and Firebox Qualities (A 285-57T) Grade C steel in 100 percent H_2SO_4 containing 33 ppm iron; they attributed these observations to the oxidation of Fe^{2+} to Fe^{3+} . In addition, the transpassivity range is not evident even upon reaching a potential of 1.5 V. Attempts to produce transpassivity by using polarization potentials up to 4 V produced no increase in polariza-

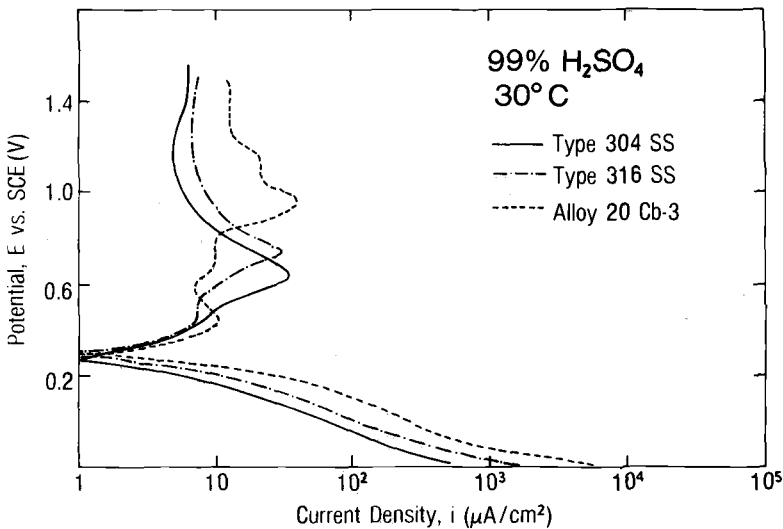


FIG. 2—Polarization curves in 99 percent H_2SO_4 at 30°C.

tion current nor any visible evolution of oxygen. It should be noted that, in more dilute H_2SO_4 solutions, oxygen evolution is generally observed in the potential range between +800 mV and +1.0 V saturated calomel electrode (SCE). Simultaneously with oxygen evolution, applied current will increase very rapidly with increasing positive potential. The absence of transpassivity of the specimens in this acid solution indicates that no intermediate species, such as water, is present on the anodic surface. The reason is that the intermediate species would readily decompose to form molecular oxygen at high noble potentials. Therefore, above the potential where the maximum current density peak exists, corrosion current densities remained on the order of $10 \mu A/cm^2$ and were independent of potential.

With an increase in the temperature from 30 to $74^\circ C$, it was found that the polarization behavior changed significantly, as is shown in Fig. 3. An apparent passive-to-active transition was observed for Type 304 alloy at ~ -100 mV, and a significant increase of the corrosion rate was expected accordingly, as will be discussed later. The location of this transition correlates well with the OCP-time studies discussed in the next section. It should be noted that this apparent passive-to-active transition could be also due to precipitation of ferrous sulfate ($FeSO_4$) or ferrous bisulfate [$Fe(HSO_4)_2$] or both [1]. The reason for this is two-fold. Firstly, the currents in the passive region are relatively high. Secondly, the potential appears to be too noble to represent active behavior; consequently, the peak can not represent an active-passive transition. The curves also suggest that Type 316 and Carpenter 20 alloys remain in their passive corrosion states at $74^\circ C$.

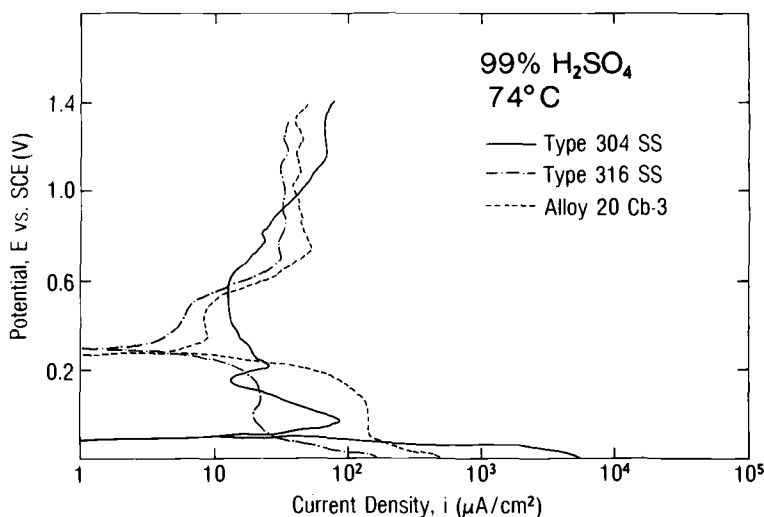


FIG. 3—Polarization curves in 99 percent H_2SO_4 at $74^\circ C$.

However, an increase in the passive current density was observed for both alloys.

Further increasing the temperature to 127°C resulted in an apparent active-passive transition for all three alloys (see Fig. 4). In addition, comparing the polarization curves of Type 304 alloy in Figs. 3 and 4, one finds that increasing the temperature shifts the anodic dissolution curves to a more noble direction. A significant increase in the i_{\max} was also observed for Type 304 alloy. Table 2 lists the i_{\max} data for the three alloys at the three temperatures.

Open-Circuit Behavior—The open-circuit potential (OCP) of each alloy has been monitored as a function of immersion time. The value of OCP of Type 316 lies in a steady noble region at 30°C, but indicates an active-to-noble oscillation at 74°C (Fig. 5). It is believed that the change on this OCP behavior is due to the changes of its corrosion status. The relatively noble OCP and the low corrosion rate (which will be discussed later) strongly suggest that Type 316 alloy shows Case 3 behavior at 30°C. Increasing the temperature shifts the anodic reaction curves to a higher current density region, and may result in a multiple intersection with cathodic reaction curves, that is, Case 2 condition.

Increasing temperature greatly increased the number of fluctuations per unit time. However, a stable active shift of OCP may be obtained eventually in this case. At 127°C, for example, a stable OCP was obtained for Type 316 after 7 h of OCP fluctuation. Comparison of the OCP-time curves and the anodic polarization results indicates that the extremities of these potential

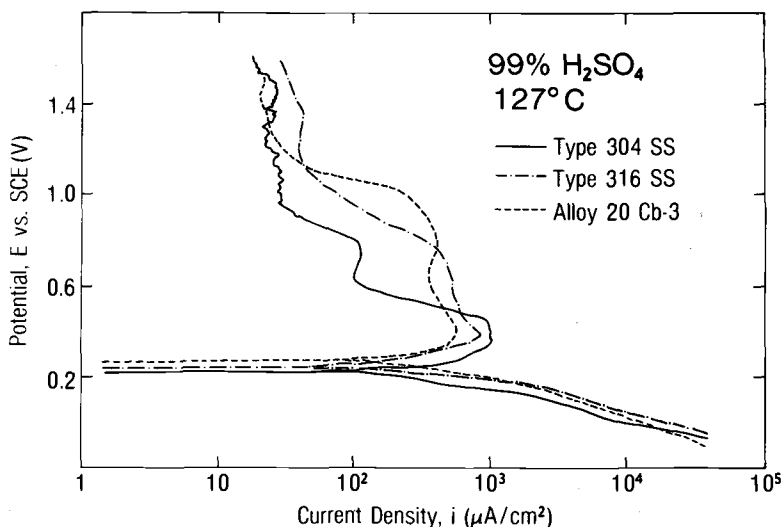


FIG. 4—Polarization curves in 99 percent H_2SO_4 at 127°C.

TABLE 2—Maximum current densities and corrosion behavior for Type 304, Type 316, and Carpenter 20 Cb-3 alloys in concentrated sulfuric acid solutions.

Alloy	Temperature, °C	99 % H ₂ SO ₄ + 9 ppm Fe	99 % H ₂ SO ₄ + 23 ppm Fe	99 % H ₂ SO ₄ + 53 ppm Fe
		i_{\max}^a , $\mu\text{A}/\text{cm}^2$	i_{\max} , $\mu\text{A}/\text{cm}^2$	i_{\max} , $\mu\text{A}/\text{cm}^2$
Type 304	30	<i>P</i> ^b	<i>P</i>	<i>P</i>
	74	85	84	91
	127	950	910	900
Type 316	30	<i>P</i>	<i>P</i>	<i>P</i>
	74	<i>P</i>	21	18
	127	850	860	880
Carpenter 20 Cb-3	30	<i>P</i>	<i>P</i>	<i>P</i>
	74	<i>P</i>	<i>P</i>	<i>P</i>
	127	700	850	1000

^a i_{\max} = Maximum current density, $\mu\text{A}/\text{cm}^2$.

^b*P* = Passive state.

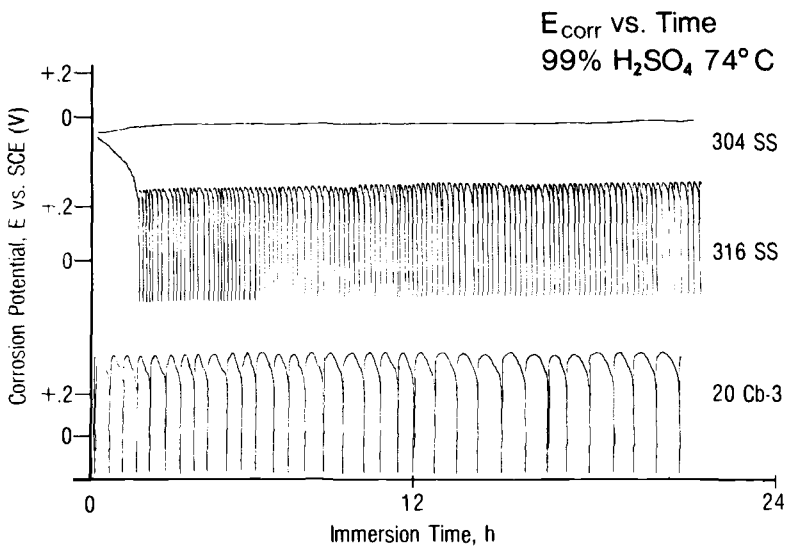


FIG. 5—Open-circuit potential of the three alloys in 99 percent H₂SO₄ at 74°C.

fluctuations lie at potentials near the active-passive transition and within the passive region, respectively. A similar behavior has been reported by Morris et al [10] on Type 316 and Alloy 825 in sulfuric acid. It was suggested that this unstable behavior is due to the existence of multiple intersections between the anodic and cathodic polarization curves (Fig. 1, Case 2). In addi-

tion to the fundamental behavior, large critical current density and high corrosion current in the active state tend to contribute to unstable conditions. In cathodic reductions the existence of several sulfur-bearing compounds complicated the situation. This complexity results from the difficulty in determining which reaction is rate controlling at any given time.

Stirring the solution resulted in an increase in oscillation frequency that depended directly on stirring velocity. This phenomenon can be explained as follows. The concentration of cathodic reaction product, which is high at the electrode surface, will be decreased. On the other hand, the concentration of Fe^{3+} ions, which would be the lowest at the electrode's surface, will then be increased upon stirring. Since the Fe^{3+} reduction reaction should provide higher cathodic reduction current, it would then follow that the intersections between anodic and cathodic polarization curves should shift to the higher current density region upon increasing iron concentration. Corrosion current would be increased at the new location of the intersections, which would begin to approach the value of the critical current density. This will contribute more to the instability of the corroding system, and hence the frequency of the oscillations should increase.

An apparent passive-to-active transition of the OCP was also observed for Type 304 alloy. However, no OCP-time fluctuation was observed in this alloy at 74°C. Instead, a stable and relatively active OCP was obtained. It is believed that the fluctuation may occur at lower temperatures in this case. The absence of the OCP oscillation is believed due to the fact that Type 304 alloy has a much greater i_{max} than either Type 316 or Carpenter 20 Cb-3 alloy. Thus Type 304 alloy is much more likely to corrode actively than either Type 316 or Carpenter 20 Cb-3. The large i_{max} makes it more difficult for oscillation to occur, since higher diffusion limited cathodic currents are required to clear the anodic "nose". OCP-time fluctuations were observed for Carpenter 20 Cb-3 alloys at both 74 and 127°C.

Corrosion Rate. The corrosion rates of the alloy/medium systems were determined by conventional weight-loss measurement; the results are illustrated in Table 3. These results show that the corrosion rate increased significantly with increasing temperature. All three alloys exhibit negligibly low corrosion rates at room temperature. As temperature increased to 74°C, Type 316 and Carpenter 20 Cb-3 alloys show better corrosion resistance than Type 304 alloy. Referring to the OCP-time behavior, it was obvious that the apparent passive-to-active shift of the OCP of Type 304 alloy at 74°C results in a much higher corrosion rate compared with that of the Type 316 and 20 Cb-3 alloys, for which the OCP fluctuates at this temperature. It is interesting to note, however, that a much more rapid increase in corrosion rate was obtained for Type 316 and 20 Cb-3 alloys at even higher temperatures (for example, 127°C) compared with that of Type 304 alloy. This may be owing to the fact that corrosion product surface scales form faster and thicker

TABLE 3—Corrosion rates^a of Type 304, Type 316, and Carpenter 20 Cb-3 in 99 percent H₂SO₄.

Alloy	Temperature, °C	Corrosion Rate, mpy			
		99 % H ₂ SO ₄ + 9 ppm Fe		99 % H ₂ SO ₄ + 23 ppm Fe	99 % H ₂ SO ₄ + 53 ppm Fe
		Stagnant	Stirring	Stagnant	Stagnant
Type 304	30	~0	0.01	0.08	0.08
	74	4.5	3.1	2.0	1.9
	127	12.1	23.5	14.7	16.5
Type 316	30	~0	0.01	~0	~0
	74	0.5	0.8	0.9	1.1
	127	13.1	16.0	12.8	12.8
Carpenter 20 Cb-3	30	~0	0.006	~0	~0
	74	1.1	2.6	1.1	1.2
	127	13.7	23.0	6.7	7.1

^aCorrosion rates were determined by conventional weight-loss measurements.

layers on Type 304 (due to higher dissolution rates), and that these thicker scales impede the subsequent dissolution of Type 304 compared with Type 316 and Alloy 20 Cb-3.

Effect of Iron Additions

Anodic Polarization Behavior—The effect of iron contaminants in the acid on the anodic polarization of the three alloys in 99 percent H₂SO₄ at 30°C has also been studied. In general, the shape of the polarization curves and the corrosion potential behavior were not appreciably changed by the addition of iron. However, the anodic polarization curve was found to shift to a slightly higher current density region with increasing iron content. The effects of iron additions were also studied at higher temperatures. It was found that the addition of iron shifted the potential where maximum current density occurred toward more noble values. The OCP was also shifted to a more noble region; however, the maximum current densities were not significantly affected.

It is believed that the dissolution process in this alloy/medium system is under concentration polarization. The theoretical anodic/cathodic reaction curves with iron addition are illustrated in Fig. 6. In general, increasing the iron concentration will shift the limiting diffusion current of the cathodic reaction curves to a higher current region. Therefore the anodic polarization curves tend to shift toward higher current densities with increasing iron concentration. Furthermore, at lower temperatures (for example, 30°C) the corrosion behavior exhibits Case 3 condition. The intersection of the anodic and cathodic reaction curves (that is, the OCP) will not be affected significantly by increasing iron concentration (see Fig. 6a). By increasing the temperature

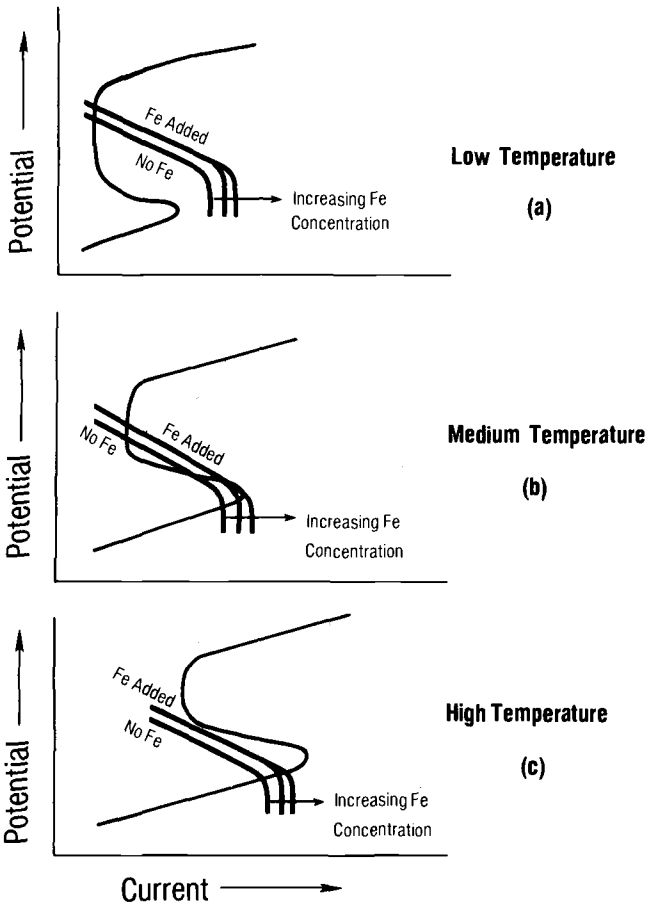


FIG. 6—Effect of temperature and iron concentration on the potential-versus-current diagrams.

to 74 and 127°C, however, the corrosion behavior of the alloy/medium system may shift to Case 2 or even Case 1 condition, as was described previously. If this occurs, the intersection of the anodic and cathodic reaction curves will tend to shift to a more noble region with increasing iron concentration (see Figs. 6a and 6b). The results described previously are consistent with this hypothesis.

In summary, the addition of iron may slightly decrease the corrosion resistance of the alloys. This observation has been also confirmed by the corrosion rate determination and will be discussed later.

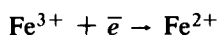
Open-Circuit Potential Behavior—No noticeable difference was observed on the OCP-time curves with increasing iron content at 30 and 74°C for the three alloys. Nevertheless, it is noteworthy that at 127°C the time required

for Type 316 alloy to shift its OCP from the "fluctuation" situation into a stable and relatively active region decreases with increasing iron content. For example, the OCP of Type 316 alloy fluctuates about 7 h before reaching its stable corrosion potential in 99 percent H₂SO₄ solution with 9 ppm iron. With increasing iron content of the solution, much less fluctuation was observed before reaching this stable active corrosion potential, namely, 3 h and less than 1 h for the solutions with 23 and 53 ppm iron, respectively. A comparison of the cycling at 127°C by 20 Cb-3 alloy in 99 percent H₂SO₄ solution with different iron content further shows that the frequency of the OCP of 20 Cb-3 alloy increases with increasing iron content.

Corrosion Rate—The corrosion rates of three alloys in 99 percent H₂SO₄ with various iron contents are shown in Table 3. It was found that the corrosion rate increased slightly with increasing iron content in the solution, which is consistent with the results reported earlier. This effect can be attributed to an increase in cathodic current, as was described previously. In the absence of iron in the solution, the main cathodic reactions are the reduction of SO₄²⁻ to S, SO₂, HS⁻, H₂S, etc. With the addition of iron to the solution, the cathodic process is the sum of the sulfur reaction and the reduction of ferric ion (Fe³⁺) to ferrous ion (Fe²⁺). When a sufficient amount of dissolved iron is present in the acid solution, the cathodic polarization rate becomes independent of further increase in iron concentration. However, by comparing the results for the solution with different amounts of iron additions, it appears that the iron effect in 99 percent H₂SO₄ is not as significant as that observed in 93 percent H₂SO₄ [13]. The most plausible explanation for this result is that the solution being used was industrial grade reagent, which contained approximately 9 ppm iron before the additions were made.

Effect of Stirring

As was mentioned earlier, the dissolution process in this alloy/medium system is believed to be under concentration polarization. In this study the effect of stirring was carried out to verify this hypothesis, and the results are illustrated in Table 3. It was found that in 99 percent H₂SO₄ the open-circuit dissolution rate of all three alloys increases slightly when stirring the solution. To interpret this result, it should be noted that an important cathodic reaction in the alloy/medium system is primarily the reduction of ferric ions, that is,



Depletion of trivalent iron from both the solutions at the electrode surface during extended polarization results in a concentration polarization effect at the cathode. Thus, in the presence of iron, the dissolution rate would be affected by the transport of ferric ion to the metal surface. Stirring the solution

speeds up the transport of the ferric ion during the dissolution process, and therefore increases the dissolution rate.

Metallurgical Studies

The specimen surface after 48-h immersion was examined using optical microscopy. It was found that all three alloys exhibited general corrosion in 99 percent H_2SO_4 at 30°C . However, with an increase of the temperature from 30 to 74°C , Type 316 and Carpenter 20 alloys reveal intergranular attack in addition to general corrosion, while Type 304 alloy still exhibits uniform corrosion (Fig. 7a). Figures 7b and 7c show the presence of intergranular corrosion on the surface of Type 316 and Carpenter 20 alloys. Intergranular attack at approximately the same temperature has also been reported for both Type 316 alloy [9, 13] and Carpenter 20 alloy [13] in 93 percent H_2SO_4 . The cause of this intergranular attack is not understood. A possible explanation is that the rate of repassivation of grain boundaries may be slower than that of the grain interior. In addition, an active-passive oscillation of the corrosion potential of these alloys results in a repeated film dissolution-repassivation process and subsequently causes intergranular attack [14]. Further increasing the temperature to 127°C results in pitting corrosion for all three alloys. Much more severe corrosion is evident at this temperature. The pitting damage is believed to be caused by the existence of insoluble, thick porous corrosion product scales on the test electrode surfaces which act as crevices. During extended artificial polarization periods, dissolution is forced to occur preferentially through the pores in these scales, which results in nonuniform damage on the electrode.

Summary

From the results obtained earlier, one may conclude the following:

1. A shift of OCP with increase in temperature from a stable passive region to an active-passive oscillation and finally to a stable and relatively active region indicates that a transition of the corrosion status from Case 3 to Case 2 condition occurs. Apparent active-to-passive current peaks were observed for the alloy exhibiting stable active OCP. However, because of the high passive current densities and abnormally noble OCP (if considering Case 1 condition) obtained in the anodic polarization curves, it is not clear whether these anodic current peaks represent true critical current density or occur because of precipitation of FeSO_4 or $\text{Fe}(\text{HSO}_4)_2$ or both.

2. In general, corrosion rates increase with increasing temperature and iron content in the acid solution and with stirring the acid solution. The order of decreasing corrosion resistance can be arranged as Type 304, Type 316, and Carpenter 20 at low temperatures. However, at high temperatures

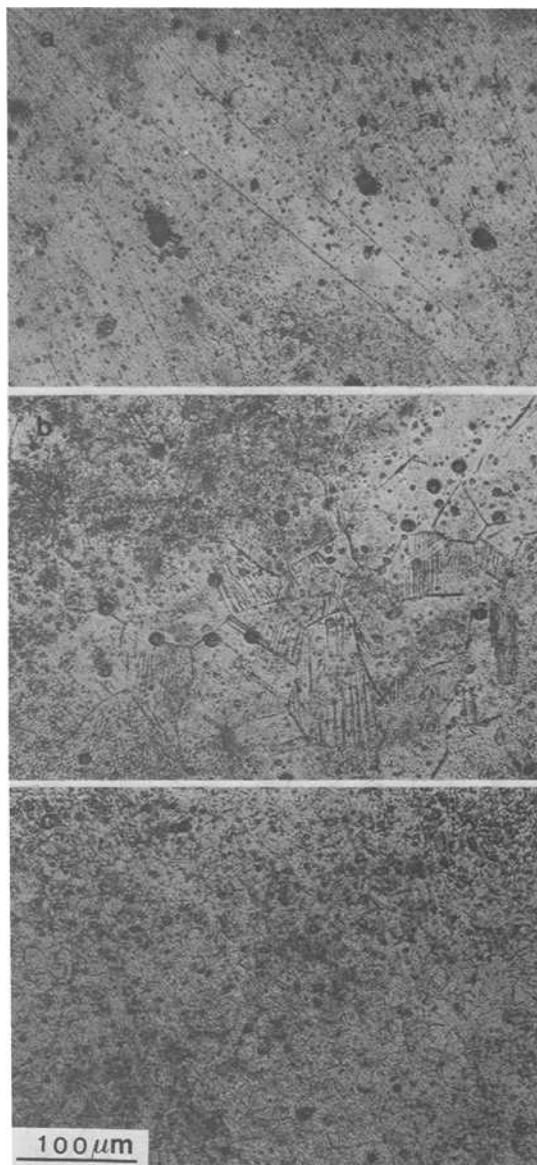


FIG. 7—Corrosion morphology after exposed to 99 percent H_2SO_4 at $74^\circ C$.

(for example, $127^\circ C$) all three alloys exhibited unacceptable corrosion resistance.

3. The three alloys exhibit general corrosion at room temperature. Upon increasing the temperature to $74^\circ C$, Type 316 and Carpenter 20 Cb-3 alloys

reveal intergranular attack in addition to general corrosion, while Type 304 alloy exhibits only general corrosion morphology. Further increasing the temperature to 127°C results in pitting corrosion for all three alloys. In addition to the occurrence of localized corrosion damage, these specimens also exhibited high corrosion rates.

Acknowledgments

It is a great pleasure to thank my colleagues, D. J. Swartz, Dr. A. Damjanovic, and Dr. R. Yeh, for useful discussions during the preparation of this manuscript. The author also wishes to thank P. E. Morris for reviewing this manuscript.

References

- [1] Brady, J. F., *Corrosion*, Vol. 19, 1963, p. 238t.
- [2] Finley, T. C. and Myers, J. R., *Corrosion*, Vol. 26, 1970, p. 544.
- [3] Steigerwald, R. F. and Greene, N. D., *Journal of the Electrochemical Society*, Vol. 109, 1962, p. 1026.
- [4] Bonhoeffer, F., *Corrosion*, Vol. 11, 1955, p. 32.
- [5] Barlett, J. H. and Stephenson, S., *Journal of the Electrochemical Society*, Vol. 99, 1952, p. 504.
- [6] Uhlig, H. H., *Journal of the Electrochemical Society*, Vol. 108, 1961, p. 4.
- [7] Myers, J. R., Beck, F. H., and Fontana, M. G., *Corrosion*, Vol. 21, 1965, p. 177.
- [8] Sidbury, J. D., Riggs, O. L., Jr., and Shock, D. A., *Corrosion*, Vol. 16, 1960, p. 47t.
- [9] For example, Morris, P. E. and Kain, R. M., *Chemical Engineering Progress*, Vol. 73, 1977, p. 103.
- [10] Morris, P. E. and Scarberry, R. C., *Corrosion*, Vol. 26, 1970, p. 169.
- [11] Fisher, A. O. and Brady, J. F., *Corrosion*, Vol. 19, 1963, p. 37t.
- [12] Harvey, A. E., Jr., Smart, J. A., and Amis, E. S., *Analytical Chemistry*, Vol. 27, 1955, p. 1.
- [13] Tong, H. S., unpublished results, 1978.
- [14] Morris, P. E., private communication, 1978.

Electrochemical Impedance Techniques in Corrosion Science

REFERENCE: Macdonald, D. D. and McKubre, M. C. H., "Electrochemical Impedance Techniques in Corrosion Science," *Electrochemical Corrosion Testing, ASTM STP 727*, Florian Mansfeld and Ugo Bertocci, Eds., American Society for Testing and Materials, 1981, pp. 110-149.

ABSTRACT: A review is presented of the use of impedance techniques in corrosion science. Emphasis is placed on defining the type of data that is required in corrosion studies, and then comparing different methods for generating the required information by electrochemical impedance methods. The performance characteristics of the various techniques, including cost, are critically compared to assist readers in selecting the most appropriate system for their needs.

KEY WORDS: corrosion, electrochemistry, polarization resistance, impedance, experimental methods

Electrochemical techniques are now widely used for monitoring the rates of corrosion processes in ionically conducting media. The principal use of these electrochemical techniques is for estimating the polarization resistance, R_p , in order to calculate the corrosion current using the Stern-Geary relationship

$$i_{\text{corr}} = \beta_a \beta_c / 2.303 R_p (\beta_a + \beta_c) \quad (1)$$

where β_a and β_c are the Tafel coefficients for the anodic and cathodic partial reactions, respectively [1, 2].³ The weight loss of the corroding specimen may then be estimated from [3]

$$\Delta W = \overline{M} Q_{\text{corr}} / \overline{n} F \quad (2)$$

¹Professor and director, Fontana Corrosion Center, Department of Metallurgical Engineering, The Ohio State University, Columbus, Ohio 43210; formerly, senior physical chemist, SRI International, Menlo Park, Calif. 94025.

²Electrochemist, SRI International, Menlo Park, Calif. 94025.

³The italic numbers in brackets refer to the list of references appended to this paper.

where

$$Q_{\text{corr}} = \int_0^t i_{\text{corr}} dt = [\beta_a \beta_c / 2.303(\beta_a + \beta_c)] \int_0^t (1/R_p) dt \quad (3)$$

and \bar{M} and \bar{n} are the composition-averaged molecular weight and change in oxidation number, respectively.

The success of the electrochemical methods for monitoring corrosion rate depends critically on our ability to measure the polarization resistance at all times of exposure and on our knowledge of values for the Tafel coefficients [3]. In principle, the Tafel coefficients can be estimated from the same data that are used to obtain the polarization resistance, provided the excitation is sufficiently large that nonlinear effects are apparent in the current-voltage response [2]. In practice, this technique appears to work well for "clean systems" exhibiting relatively low polarization resistances, but it often gives spurious results for more complex systems.

In this paper we examine the reliable determination of the polarization resistance. We focus our attention in particular on the methods used to measure the interfacial impedance of a corroding interface, and discuss how the polarization resistance can be extracted from this quantity.

Polarization Impedance and Resistance

If the impedance of a corroding interface can be represented by an ensemble of linear components, then the response to any arbitrary electrical excitation can be described by the generalized Ohm's law [4]

$$E(t) = Z(p) \cdot I(t) \quad (4)$$

$$I(t) = Y(p) \cdot E(t) \quad (5)$$

where $Z(p)$ and $Y(p)$ are the impedance and admittance functions, respectively, and p is the impedance operator defined as $p = d/dt$ and $1/p = \int dt$. The impedance function $Z(p)$ [or admittance function $Y(p)$] is so chosen that the operation of $Z(p)$ on the current or $Y(p)$ on the voltage yields the observed voltage and current, respectively. For example, the voltage drops across resistive, capacitive, and inductive elements in response to an applied current, $I(t)$, are given by

$$E(t) = RI(t), \quad Z(p) = R \quad (\text{resistive}) \quad (6)$$

$$E(t) = (1/C) \int Idt, \quad Z(p) = 1/pC \quad (\text{capacitive}) \quad (7)$$

$$E(t) = L(dI/dt), \quad Z(p) = Lp \quad (\text{inductive}) \quad (8)$$

Furthermore, the total voltage drop across a series combination of components is given by

$$E(t) = \sum_i E_i(t) \quad (9)$$

whereas the total current through a parallel network is

$$I(t) = \sum_i I_i(t) \quad (10)$$

Accordingly, the impedance and admittance functions for series and parallel combinations of components, respectively, are given by

$$Z(p) = \sum_i Z_i(p) \quad (11)$$

$$Y(p) = \sum [1/Z(p)] = \sum Y_i(p) \quad (12)$$

Heaviside in Ref 4 showed that upon transformation of Eqs 4 and 5

$$\bar{E}(s) = Z(s) \cdot \bar{I}(s) \quad (13)$$

$$I(s) = Y(s) \cdot \bar{E}(s) \quad (14)$$

with

$$\mathcal{L}[f(t)] = \bar{f}(s) = \int_0^{\infty} f(t)e^{-st} dt \quad (15)$$

the impedance, $Z(s)$, and admittance, $Y(s)$, functions have the same analytical forms as $Z(p)$ and $Y(p)$, respectively, with the impedance operator, p , replaced by the Laplace variable s . This convenient property permits the straight-forward derivation of an expression for the Laplace transform of the response to any arbitrary excitation in terms of the variable s . Inverse transformation therefore yields the response in the time domain.

If we assume that the excitation is sufficiently small [typically <5 mV for $E(t)$, <5 μ A for $I(t)$], the electrical properties of a metal-solution interface can be represented by a linear electrical equivalent circuit. The simplest circuit of general interest is shown in Fig. 1a, and consists of a parallel RC combination in series with a resistance R_s . R_s is frequently associated with the "solution" resistance; in reality it contains all purely resistive components

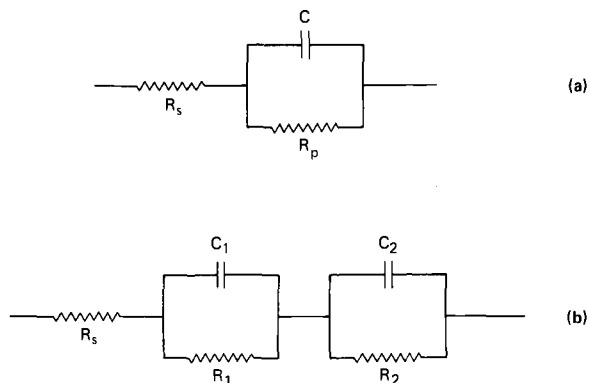


FIG. 1—Simple equivalent circuits for a corroding interface.

(solution, electrical leads, films, etc.), and those impedance elements that mimic pure resistances under the conditions of the measurement. This point is best illustrated by considering the equivalent circuit shown in Fig. 1*b*. The impedance of this network is given by Eq 16

$$\begin{aligned} \bar{Z}(j\omega) = R_s + R_2 / (1 + \omega^2 R_2^2 C_2^2) + R_1 / (1 + \omega^2 R_1^2 C_1^2) \\ - j\omega [R_2^2 C_2 / (1 + \omega^2 R_2^2 C_2^2) + R_1^2 C_1 / (1 + \omega^2 R_1^2 C_1^2)] \end{aligned} \quad (16)$$

where ω is the frequency of the sinusoidal excitation. If the highest frequency chosen for the measurement of $\bar{Z}(j\omega)$ is such that $R_2 \ll 1/\omega C_2$, and if $1/R_2 C_2 \gg 1/R_1 C_1$, then Eq 16 reduces to

$$\begin{aligned} \bar{Z}(j\omega) = R_s + R_2 + R_1 / (1 + \omega^2 R_1^2 C_1^2) \\ - j\omega C_1 R_1^2 / (1 + \omega^2 R_1^2 C_1^2) \end{aligned} \quad (17)$$

which is, of course, the impedance expression for an equivalent circuit consisting of resistors R_s and R' in series with a parallel RC combination. Clearly, within the frequency range considered, the $R_2 C_2$ combination, which gives rise to a relaxation at high frequencies, appears purely resistive in character.

The d-c resistance (that is, polarization resistance) of an interface is obtained from the low-frequency limit of the impedance $\bar{Z}(j\omega)$. Thus, with reference to Fig. 1*b* and Eq 16, it is clear that as $\omega \rightarrow 0$

$$\bar{Z}(j\omega) \rightarrow R_s + R_1 + R_2 \quad (18)$$

Subtraction of the solution resistance, R_s , therefore, yields a quantity that

for corroding systems is termed the "polarization" resistance. In practice it is frequently not possible to sample a system at zero frequency. Accordingly, the extraction of the polarization resistance from the measured impedance requires extrapolation of the observed value for $\bar{Z}(j\omega)$ to $\omega = 0$. Such an extrapolation relies upon a knowledge of the functional form of $\bar{Z}(j\omega)$; for example, the equivalent circuit shown in Fig. 1b gives rise to a complex-plane plot of the form shown in Fig. 2. Clearly, if the lowest frequency employed is ω_2 , and if two and only two relaxations are present in the system, extrapolation to the real-axis intercept of $R_1 + R_2 + R_s$ at $\omega = 0$ is relatively straightforward. If the lowest frequency employed is ω_1 , however, extrapolation to zero frequency yields a resistance $R_s + R_2$, which is considerably lower than the true d-c resistance $R_1 + R_2 + R_s$. In this case the low-frequency relaxation is not detected, and the R_1C_1 network makes a negligible contribution to the observed impedance.

Although the aforementioned equivalent circuits are in general unrealistically simple (see the following section), they serve to illustrate a very important requirement for impedance measurements; namely, a sufficiently wide frequency range must be investigated to ensure detection of all relaxation phenomena that are present at the interface. This requirement also applies to other relaxation techniques including linear polarization, potential step, current step, etc. In the latter two cases this requirement is defined in terms of time by time-to-frequency transformation (an operation illustrated later in this paper).

The frequency range normally required for impedance studies in corrosion science is 0.1 mHz to 10 kHz. The lower limit is determined by relaxations involving mass transfer and very large interfacial resistances and capacitances, particularly those associated with film growth and pseudo-capacitive electrochemical adsorption phenomena. The upper limit is sufficiently high that the impedance of most systems of interest is dominated by the solution resistance R_s .

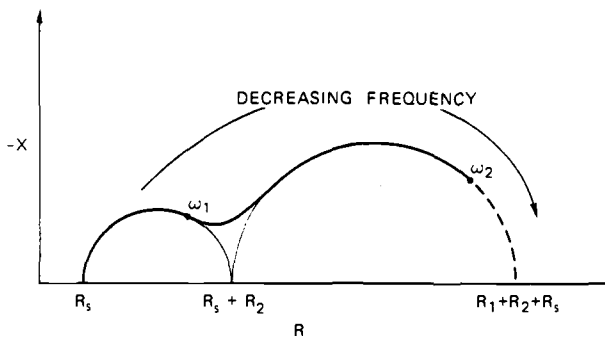


FIG. 2.—Schematic complex-plane diagram for the equivalent circuit shown in Fig. 1b.

Equivalent Circuits

An extensive discussion of the concept of equivalent circuits in corrosion science and electrochemistry is beyond the scope of this paper. It is useful, however, to briefly review the topic, since it provides the link between the electrical observable (impedance) and the chemical/electrochemical processes responsible for the behavior of the system.

The first step in the elucidation of an electrochemical (corrosion) mechanism from a measured frequency dispersion of an impedance is generally to postulate an electrical circuit that has the same impedance spectrum as the system under investigation. All circuit representations, even those from which prediction of measurable results is possible, only fulfill the role of an equivalent circuit, and are not descriptions of the physical mechanisms involved. For any electrical circuit it is possible to describe the impedance as a function of frequency and thus determine circuits having equivalent electrical properties, but it is not possible to uniquely define the combination of electrical circuit elements that constitutes the circuit under test. The situation is further complicated by the fact that charge carriers may be ions or electrons or both. Ions may carry a positive or negative charge and may be multivalent, and ionic transport is influenced by chemical as well as electric field gradients. Furthermore, electrochemical charge-transfer processes are generally non-ohmic in character, since the current varies exponentially with the applied overvoltage and the capacitance of the double layer (for example) is a function of voltage. Equivalent circuits are therefore valid only under those conditions where the responses can be linearized.

Consider a simple charge-transfer reaction that exhibits Butler-Volmer kinetics:

$$i = i_0[\exp(\eta/\beta_a) - \exp(\eta/\beta_c)] \quad (19)$$

where i_0 is the exchange current for the reaction, and β_a and β_c are the Tafel constants for the anodic and cathodic processes, respectively. Expansion of Eq 19 as a series in overpotential (η) yields

$$i = i_0 \left\{ \sum_{n=1}^{\infty} \eta^n [1/\beta_a^n - 1/(-\beta_c)^n]/n! \right\} \quad (20)$$

Linearization is achieved only when the second and subsequent terms are negligible compared with the first. This condition can be mathematically expressed as

$$\eta_{\max} \approx 0.1 \beta_a \beta_c / (\beta_a + \beta_c) \quad (21)$$

Using typical values for β_a and β_c (for example, 0.06 V and 0.12 V, respec-

tively) indicates that the maximum perturbation should be no greater than 0.004 V.

The simple equivalent circuits shown in Fig. 1 are not particularly realistic for most charge-transfer processes, since they do not recognize the existence of mass-transfer processes. A more appropriate equivalent circuit is shown in Fig. 3, in which W represents the Warburg impedance⁴

$$\bar{Z}_d = [RT/nF(i_L - i)][\tanh(\sqrt{j}u)/\sqrt{j}u] \quad (22)$$

where i_L is the limiting current for pure diffusion, i is the steady-state current at overpotential η , and u is defined as

$$u = \omega\delta^2/D \quad (23)$$

The parameters ω , δ , and D are the sinusoidal excitation frequency, hydrodynamic diffusion-layer thickness, and diffusion coefficient, respectively. The d-c diffusion-layer thickness is a function of the hydrodynamic properties of the system; for example, in the case of a rotating disk under laminar flow conditions

$$\delta = 1.61 \nu^{1/6} D^{1/3} \Omega^{-1/2} \quad (24)$$

where ν is the kinematic viscosity of the medium, and Ω is the rotational velocity of the disk. For sufficiently high values of frequency, ω , or low values of the rotational velocity Ω ,

$$\bar{Z}_d(j\omega) = (RTD^{1/2}/nF\delta i_L)/(j\omega)^{1/2} \quad (25)$$

which is the well-known Warburg impedance for semi-infinite diffusion. This particular function is valid for a-c diffusion-layers much smaller in dimension than the d-c diffusion layer, and describes the linear region on the high-frequency side of the second semicircle. At still higher frequencies the War-

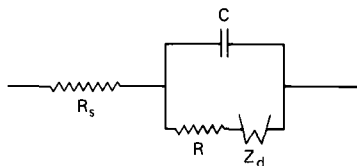


FIG. 3—Equivalent circuit for metal-solution interface recognizing mass transfer control at $\omega \rightarrow 0$.

⁴Equation 22 is a simplified form of a more general expression given by Sluyters-Rehbach and Sluyters [5].

burg impedance is negligible, and the equivalent circuit reduces to that shown in Fig. 1a. In this case the complex-plane diagram assumes the form of a semicircle centered on the real axis, and which contains kinetic information on the interfacial reaction. At the limit of low frequencies, however, the complex plane intersects the real axis at a value containing the diffusional resistance R_d (Fig. 4). This is the only quantity that can be determined using the traditional steady-state methods for systems under mass-transfer control; clearly, the frequency dispersion of the impedance permits a great deal of additional kinetic information to be obtained.

It is frequently observed that the semicircles displayed in the complex plane are centered below the real axis (see, for example, the data plotted in Fig. 20 for the corrosion of 90:10 copper:nickel (Cu:Ni) alloy in flowing oxygenated seawater [6]). Although this behavior is frequently attributed to a distribution in relaxation times, this terminology is strictly incorrect, since the transients no longer are exponential in character. A more satisfactory electrical model for the interface is a transmission line that is generally associated with the presence of porous films on the surface or excessive surface roughness. The reader is referred to the excellent review by de Levie [7] for a discussion of this topic.

Irrespective of the exact form of the equivalent circuit, diffusional processes (if important) generally begin to dominate the interfacial impedance at frequencies below 1 Hz for most systems. Accordingly, a detailed analysis of the interface in this regime requires experimental methods for accurately measuring impedance at frequencies as low as 1 mHz.

Instrumental Methods

We have previously stated that the electrical response of a system to any small signal excitation can be expressed in terms of an operational impedance in the frequency domain. When describing the instrumental

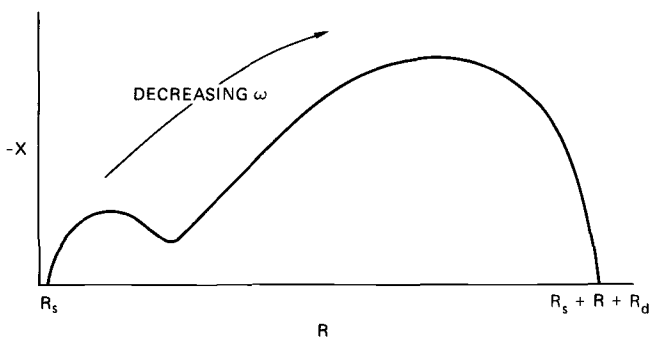


FIG. 4—Schematic complex-plane diagram for a system subject to mass transfer control.

methods, however, it is convenient to divide techniques according to the type of excitation function employed, particularly with respect to the independent variable. Thus frequency-domain measurements are carried out using a small-amplitude sinusoidal excitation with frequency as the independent variable. On the other hand, the perturbation and response may be recorded in the time domain with time as the independent variable, and the impedance as a function of frequency can then be extracted by time-to-frequency transformation techniques.

Frequency-Domain Measurements—Small-Amplitude Sinusoidal Perturbation

This group can be further subdivided into bridge or null techniques where impedance parameters are measured by the fixed mathematical relation between the unknown resistance and reactance, the setting of variable resistive and reactive standards at a condition of balance, and methods involving the direct measurement of magnitude and phase relationships between the current through, and voltage drop across, the unknown element.

Audio-Frequency Bridges

In the past, impedance measurements using reactively substituted Wheatstone bridges at audio frequencies have been the easiest to accomplish. Consequently, a great deal of emphasis has been historically placed on electrochemical processes having characteristic impedance spectra in the range of 20 to 20 000 Hz—namely, double-layer capacitive and moderately fast reaction kinetic effects at plane parallel electrodes.

As the mathematics and methodology of such measurements are well understood [8, 9], we will restrict our discussion to the limitations imposed by the use of this type of bridge, since these will influence the point at which an experimentalist will select a more complex measuring device.

High-Frequency Limitations—The upper operating limit is primarily imposed by reactivity and nonlinearity of available resistive standards (chiefly inductive effects) and by the effects of stray capacitive shunts. By employing a Wagner earth [9, 10] the latter effect can be often reduced sufficiently to allow sensible measurements at frequencies up to 10^5 Hz. However, the importance of Wagner earthing varies greatly depending on the magnitude of the impedances being measured [8]. In general, elimination of stray capacitance is most important at high frequencies when measuring small capacitances or large resistances (that is, for small-area electrodes).

Low-Frequency Limitations—The null detection system traditionally employed with an audio-frequency bridge consists of an amplifier, filter, and a-c voltmeter. This combination imposes three limitations at low frequencies:

1. Null detection employing a magnitude voltmeter or oscilloscope is most sensitive when the resistive and reactive components of the unknown impedance are of the same magnitude, since the total bridge out of balance signal contains terms proportional to each. For an impedance bridge used to measure the electrical properties of electrochemical cells this imposes a limit on accuracy at low frequencies, since the reactive terms, which are primarily capacitive, dominate the cell impedance with decreasing frequency. Increasing the gain in order to observe more precisely the resistive component results in saturation of the detection system with the reactive out-of-balance signal. An admittance bridge similarly suffers low-frequency insensitivity to the reactive component.

2. A significant source of noise at the detector may result from harmonic distortion originating in the oscillator or caused by nonlinearity in the system under test or in subsequent amplifiers. In such cases the signal at balance consists mainly of second harmonic. At high frequencies this signal can be effectively removed by the use of suitably sharp low-pass or band-pass filters, but at low frequencies analog filters of band-width less than 10 Hz are less easy to construct and control.

3. The second major source of noise at low frequencies is mains pickup. This may be on the order of hundreds of millivolts superimposed on the test signal unless major efforts are made at shielding and ground-loop suppression. Usually, unless an adequate notch filter is also used, the experimentalist must be satisfied with reduced precision at frequencies below about 100 Hz.

These three effects can be reduced to a large extent by using a phase-sensitive detector (PSD) to measure separately the real and imaginary components of the bridge out-of-balance signal. By separate amplification of the in-phase and quadrature components, differential sensitivities in excess of 100:1 can be accomplished.

In normal operation a PSD is completely insensitive to the second harmonic, but most commercial instruments have the additional facility of being able to select a reference signal at twice the fundamental frequency. By this means the extent of second harmonic distortion, which often reflects not an error signal (that is, noise) but an expected response of the system under test, can be measured.

In addition, and unlike traditional band-pass filters, a PSD has a band-pass characteristic with band width decreasing with decreasing frequency, and can frequently be used within ± 5 Hz of 60 db of mains pickup.

By employing phase-sensitive null detection the practical low-frequency limit becomes a function of the particular form of bridge chosen. For the most commonly used Wein form [8], however, this limit is imposed by the selection of suitably large adjustable capacitance standards at frequencies below about 20 Hz.

Limitations of Imposed Potential—A considerable limitation on the use of this form of bridge is that it necessitates the use of a two-terminal cell. While it is often possible to construct a cell in which the working electrode impedance greatly exceeds that of the counter electrode, potentiostated conditions cannot be adequately established with this type of bridge.

Closely associated with this is the fact that in normal usage, the cell current and voltage are not explicit functions of the measured out-of-balance voltage, and vary with the settings of the resistive and reactive standards.

Transformer Ratio Arm Bridges

The operation of a transformer ratio arm bridge is shown schematically in Fig. 5. Briefly, voltages 180 deg out of phase are fed from the secondary winding of the input "voltage" transformer to the cell or unknown impedance, and to resistance and capacitance standards. The "arms" of the bridge consist of a series of ratio taps of the primary windings of an output "current" transformer. The standard and unknown impedances are connected to the output transformer in such a way that a detector null is achieved when the sum of the flux induced by the unknown and standard currents in the output transformer is zero. In this condition

$$\frac{r_1}{Z_x} = \frac{r_2}{R} + j\omega Cr_3$$

independent of V_{in} , where r_1 , r_2 , and r_3 are ratios (usually decade) selected separately.

Several advantages accrue from the use of this type of bridge:

1. Error resulting from the impurity of standard variables can be virtually eliminated. Because ratios are selectable over a wide range (usually 1000:1), standards can be small. Also, with decade-spaced transformer ratios, standards need be variable only over a range of about 11:1. Consequently, standards can be employed that closely approximate to ideality (for example, the use of air-gap capacitors), and one standard can be used to measure a wide impedance range.

2. By the use of precision transformers as ratio arms, highly accurate ratio values can be obtained that are extremely frequency independent well into the megahertz range.

3. A suitable range of impedance measurement can be selected for the in-phase and quadrature components of the unknown impedance by separately selecting r_2 and r_3 .

4. Impedances may be measured in all four quadrants by selecting positive or negative ratios. Of particular importance is the use of pure

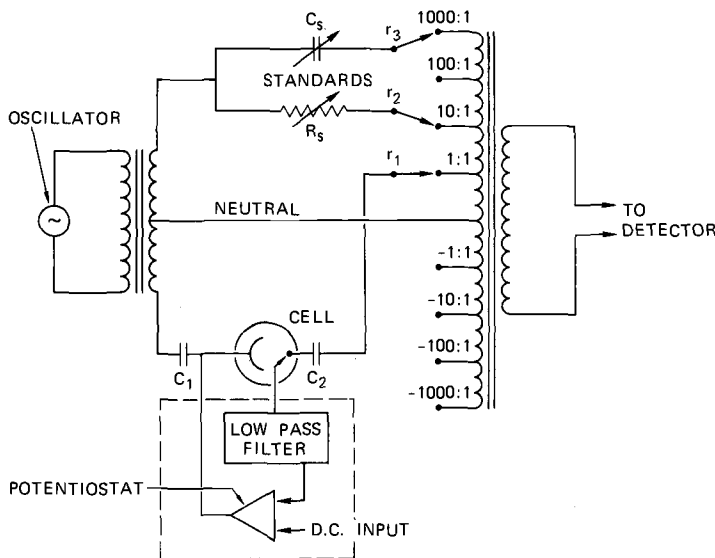


FIG. 5—Transformer ratio arm bridge with d-c potentiostatic control.

capacitive standards to measure unknowns with a positive (inductive) reactance.

We will discuss the limitations on the use of transformer ratio arm bridges under the same headings used under Audio-Frequency Bridges.

High-Frequency Limitations—In normal use for electrochemical cells the effective upper operating limit is imposed by effects external to the bridge. These have been described in detail by Armstrong et al [8] and consist primarily of transmission-line effects in connecting cables, the effect of residual series inductance in leads and cells, and normally undesired impedance dispersion effects of solid electrodes. In the latter group, edge effects [11] and transmission-line effects due to surface roughness [12,13] become dominant with increasing frequency.

Low-Frequency Limitations—The use of input and output transformers results in cell current and voltage, and detector signals, that are dependent on frequency. This effect becomes apparent only at low frequencies, and imposes a practical lower limit on the order of 100 to 200 Hz with commercial bridges [14].

Limitations of Potential Control—It is not possible to apply the a-c potential via a reference electrode only to the interface of interest, and the measured impedance necessarily includes series terms associated with electrolyte resistance and counter-electrode impedance.

Direct-current potentials can be applied to the interface of interest by us-

ing a circuit of the form shown within the dashed lines in Fig. 5. However, direct current must be excluded from the bridge windings by the use of blocking capacitors C_1 and C_2 . The impedance of these two will be included in the measured "cell" impedance.

Berberian-Cole Bridge

An active null admittance measuring instrument that incorporates many of the advantages of the transformer ratio arm technique while obviating many of the disadvantages of passive bridges has been reported by Berberian and Cole [15]. Fig. 6 shows a form of this bridge modified to measure impedance and to remove some of the limitations of the earlier instrument [16].

The basic operation is as follows. The external variable decade standards are R_1 and C . R' and R'' are internal and fixed. With reference to Fig. 6:

At all times

$$i_1 + i_2 + i_3 = 0 \quad (26)$$

At balance

$$V_s = 0$$

and

$$i_1 = AV_A/R_1 \quad (V_A = IZ) \quad (27)$$

$$i_2 = AV_A(j\omega C) \quad (V_A = IZ) \quad (28)$$

$$i_3 = BV_B/R'' \quad (V_B = -IR') \quad (29)$$

where \bar{Z} is the impedance between the working electrode and the reference electrode, and I is the current flowing through the cell. Therefore, for the condition of balance at the summing point

$$BIR'/R'' = AI\bar{Z}/R_1 + AI\bar{Z}(j\omega C) \quad (30)$$

Removing I and solving for the unknown impedance yields

$$\bar{Z} = \frac{BR'R_1}{AR''} \cdot \left(\frac{1}{1 + \omega^2 R_1^2 C^2} \right) (1 - j\omega R_1 C) \quad (31)$$

There are many advantages to this system:

1. Measurements can be made on two-, three-, or four-terminal cells,

which allow the isolation of the impedance component of interest from the total cell impedance. This is not possible with a passive bridge, and it is frequently unfeasible to construct a cell for which the impedance of interest is much greater than all series terms. This is particularly true when measuring the impedance of an electrode of large area or in a highly resistive electrolyte, or when the impedance of interest is that of a highly conductive electrolyte.

2. Measurements can be effectively made down to 0 Hz. The bridge shown in Fig. 6 is direct coupled; thus the low-frequency limits are those of the null detection system and the patience of the experimentalist.

3. Measurements can be made in the presence of a d-c bias under potentiostatic control without the use of blocking capacitors.

4. Impedances can be measured over an extremely wide range from below $10^{-3} \Omega$ to greater than $10^9 \Omega$.

5. Error resulting from the impurity of standards can be virtually eliminated.

6. A suitable range of impedance measurements can be selected for each component.

7. Impedances may be measured in all four quadrants with resistance and capacitance standards.

Because the gains of Amplifiers *A* and *B* perform the same function as the ratios in a transformer ratio arm bridge, the aforementioned advantages 5, 6, and 7 apply for the same reasons as advantages 1, 3, and 4 under Transformer Ratio Arm Bridges.

The modified Berberian-Cole bridge has several limitations:

High-Frequency Limitations—Inaccuracies at high frequencies can occur

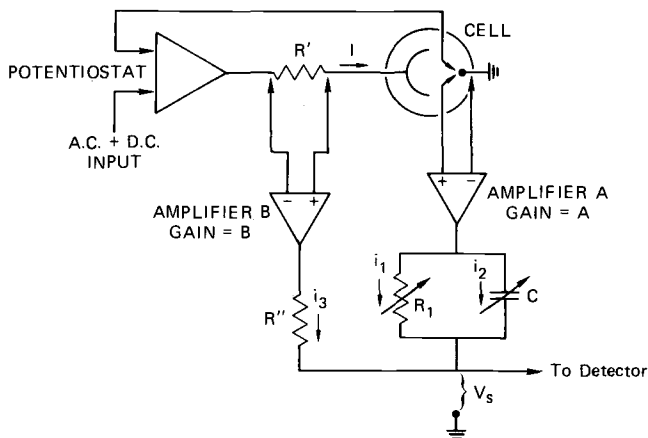


FIG. 6—Modified Berberian-Cole bridge shown as a three-terminal interfacial impedance measuring system with potentiostatic control of the working electrode.

due to errors in the gain functions A and B with decreasing amplifier open-loop gain. Fig. 7 shows schematically a practical bridge of this type. Gain errors in the voltage followers are negligible and, since Amplifiers A and B are identical devices and their gains appear as a ratio in Eq 31, inaccuracies in this term are partially compensated for. Nevertheless, the upper operating frequency limit for the bridge shown in Fig. 7 is about 10 kHz, depending somewhat on the magnitude of the unknown impedance.

Low-Frequency Limitations—As stated previously, the low-frequency operating limit is imposed by the detection system. At frequencies down to 0.5 Hz, a two-component PSD performs an ideal null detection function [16]. At frequencies below 10^{-3} Hz, a low-pass filter and oscilloscope or picoammeter can be used [15].

Direct Measurement

An essential element of electrode kinetics is the characteristic dependence of electrode reaction rates on the electrode potential. Thus, for many electrode studies, the use of potentiostatic control is the most convenient method of obtaining relevant kinetic and mechanistic parameters. A general limitation of passive bridge methods is their inflexibility with regard to potential control; in many cases, the experimentalist must forego the advantages of simplicity and sensitivity associated with these in order to control the alternating or direct current potentiostatically at a single interface.

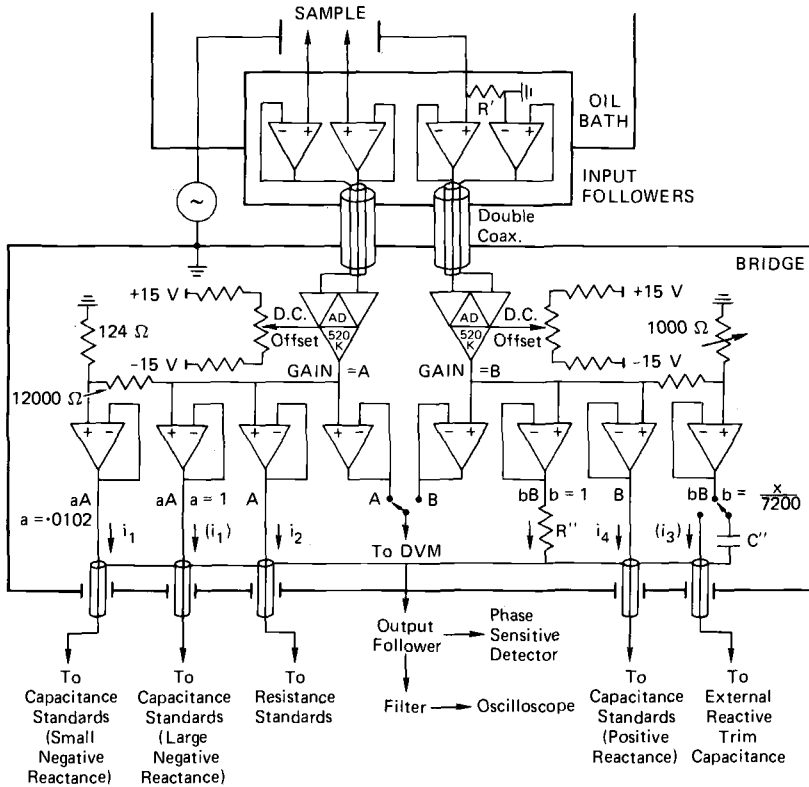
The operational impedance can be expressed in the frequency domain by the vectorial form of Ohm's law

$$\vec{Z}(j\omega) = \vec{V}(j\omega)/\vec{I}(j\omega) \quad (32)$$

where the bars denote vector quantities. Thus, if cell current and voltage are measured with regard to the magnitude and phase relations, the impedance can be directly determined from Eq 32. Figure 8 shows in simplified form a circuit that allows the direct measurement of impedance under potentiostatic control.

It is necessary at the outset to separate phase shifts associated with \vec{Z} from those attributable to the potentiostat control loop. Commercial potentiostats are normally optimized for fast step response, and their potentiostating function becomes substantially in error for sinusoidal inputs with increasing frequency as the amplifier open-loop gain approaches the ratio $\vec{Z}_T:\vec{Z}$. The upper frequency limit for which V_2 can be considered equal to V_{AC} is a function of the cell impedance as well as the electrical parameters of the potentiostat. These parameters have been analyzed by Pilla et al [17] and Macdonald [18]. For electrochemical cells this frequency limit may occur as low as 200 Hz.

If accurate impedance measurements are to be made over a wide frequency range, it is imperative that measurements are made of the cell current (V_1)



TA-350522-298

FIG. 7—Schematic diagram of a working (modified) Berberian-Cole bridge shown as a four-terminal impedance measuring system.

and cell voltage (V_2), preferably simultaneously and with identical measuring instruments, in order to eliminate systematic instrumental error.

Two-Channel Oscilloscope Measurement—By recording V_1 and V_2 on a twin-beam oscilloscope, the magnitude of the impedance can be calculated for the ratio of the two peak-to-peak voltages, and the phase angle observed directly. By using storage techniques, impedance can be measured from effectively 0 to greater than 10^6 Hz.

The primary limitation of this technique is precision. Oscilloscope linearity is seldom better than 1 percent, and it is difficult to measure phase angles with a precision of better than 2 deg. Measurements can be usually accomplished with an uncertainty for R and $X(\bar{Z} = R - jX)$ of ± 3 percent.

Lissajous Figures—Elimination of t between expressions for I and V of the form (see Analytical Transformation)

$$I = I_0 \sin(\omega t) \tag{33}$$

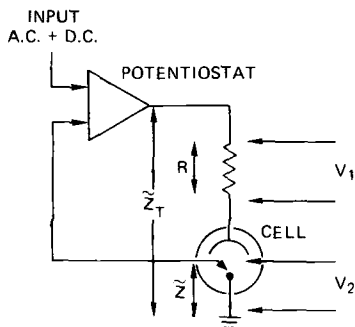


FIG. 8—Direct measurement of an interfacial impedance under a-c and d-c potentiostatic control.

$$V = V_0 \sin(\omega t + \phi) \quad (34)$$

leads to an equation of the form of an ellipse. When I and V are plotted orthogonally using an oscilloscope or X - Y recorder, this ellipse is traced out and the components of the impedance can be calculated from its dimensions (see Fig. 9)

$$|\tilde{Z}| = \Delta E / \Delta I \quad (35)$$

$$\sin \phi = \Delta I' / \Delta I = \alpha \beta / \Delta I \cdot \Delta E \quad (36)$$

$$R = |\tilde{Z}| \cos \phi \quad (37)$$

$$-X = |\tilde{Z}| \sin \phi \quad (38)$$

where R and X are the real and imaginary components of the impedance.

Limitations of oscilloscopic recording are essentially those of precision described in Two-Channel Oscilloscope Measurement. For X - Y recording, a precision of better than 1 percent of $|\tilde{Z}|$ can be obtained at frequencies below 1 Hz.

Phase-Sensitive Detection—The real and imaginary components of a voltage can be directly measured with respect to a reference signal using a phase-sensitive detector. Because of the requirements for linearity (Equivalent Circuits) small input signals must be used to measure electrochemical impedances, and noise problems often make it unpractical to use either V_1 or V_2 as a reference signal. Accordingly, V_1 and V_2 must be alternately measured in terms of a coherent reference signal of arbitrary phase, and the impedance determined from the complex quotient

$$\tilde{Z} = \frac{V_1 R}{V_2} \frac{(V_1' + jV_1'')}{(V_2' + jV_2'')} \tag{39}$$

where primed and double-primed variables refer to in-phase and quadrature voltages, respectively.

With commercial instruments employing analog-output filtering, impedance can be measured with 0.1 percent precision in both components at frequencies between 0.5 and 100 kHz [19]. At frequencies from below 10^{-3} to 10^4 Hz, a recently developed phase-sensitive detection system can be used that employs synchronous digital demodulation over an integral number of cycles with the same order of precision [20].

The advantages of phase-sensitive detection over other direct measurement techniques at low frequencies are generally those described in Audio-Frequency Bridges.

Time-Domain Methods

According to Eq 3 the impedance of a system may be determined from time-domain perturbation and response data as

$$Z(s) = \bar{E}(s)/\bar{I}(s) \tag{40}$$

where $\bar{E}(s)$ and $\bar{I}(s)$ are the Laplace transforms of potential and current, and s is the Laplace variable. The variable s is a complex quantity

$$s = \sigma + j\omega \tag{41}$$

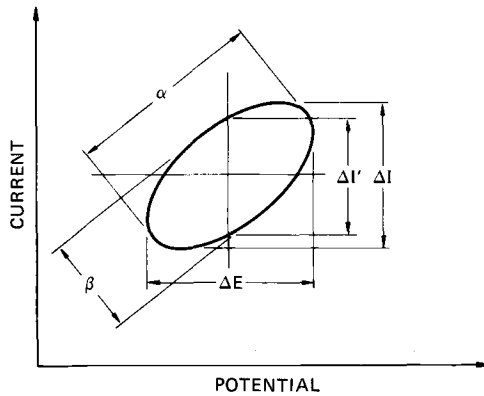


FIG. 9—Lissajous figure for the evaluation of impedance.

where σ is the real part having units of reciprocal time, and ω is the frequency. The Laplace transform of a real-valued function $f(t)$ is

$$\bar{f}(s) = \int_0^{\infty} e^{-\sigma t} e^{-j\omega t} f(t) dt \quad (42)$$

$$= \bar{f}(\sigma) + \bar{f}(j\omega) \quad (43)$$

where

$$\bar{f}(\sigma) = \int_0^{\infty} e^{-\sigma t} f(t) dt \quad (44)$$

$$\bar{f}(j\omega) = \int_0^{\infty} e^{-j\omega t} F(t) dt \quad (45)$$

Equation 44 is frequently referred to as the “real-axis transformation” (see Pilla [21]) and is operationally identical with Macdonald’s “analysis in Laplace space” [18] for systems that involve diffusion. On the other hand, Eq 45 is commonly termed the “imaginary-axis transformation” and the reader will recognize the form as being identical to that for the single-sided Fourier transformation. Although both transformations have been employed in fundamental electrochemical studies, few applications in corrosion science have been reported.

A good illustration of the analytical simplifications afforded by real-axis transformation is the case of a quasi-reversible reaction at a plane electrode under potentiostatic control [18]



Solution of Ficks’ second law for this case yields the current transient as

$$i = nFA(k_f C_O^b - k_b C_R^b) \exp(Q^2 t) \operatorname{erfc}(Qt^{1/2}) \quad (47)$$

where

$$Q = k_f/D_O^{1/2} + k_b/D_R^{1/2} \quad (48)$$

The direct manipulation of Eq 47 for the evaluation of the rate constants k_f and k_b is extremely difficult unless certain simplifying assumptions are

made. The real-axis Laplace transform of Eq 47, however, is much less complicated algebraically

$$1/\bar{i}(\sigma)\sigma^{1/2} = [Q/nFA(k_f C_O^b - k_b C_R^b)] + [1/nFA(k_f C_O^b - k_b C_R^b)]\sigma^{1/2} \quad (49)$$

where $\bar{i}(\sigma)$ is numerically evaluated using Eq 44. Thus a plot of the left-hand side against $\sigma^{1/2}$ for different bulk concentrations of O and R permits complete evaluation of the rate constants. Although the aforementioned analysis is not couched strictly in terms of impedance functions, it nevertheless illustrates the usefulness of transformation techniques in electrochemistry and corrosion science.

The transformation method just outlined may be employed in two ways. An equivalent circuit for the interface may be assumed, and an analytical expression then generated for the expected response. The response function, which is obtained in the time domain, may be used to estimate values for the components of the impedance. Alternatively, numerical transformation of the perturbation and response functions may be performed for different values of σ and ω , and the impedance function evaluated over a wide frequency range. This second technique has been extensively developed by Pilla [21] and others [22].

Analytical Transformation

As an illustration of this method, consider the simple equivalent circuit shown in Fig. 10 and assume that the *time*-dependent perturbation is given as

$$E(t) = E_m \sin \omega t \quad (50)$$

Transformation therefore yields

$$\bar{E}(s) = \omega/(s^2 + \omega^2) \quad (51)$$

The impedance function for the assumed equivalent circuit is

$$Z(s) = R + 1/sC \quad (52)$$

Application of Eq 40 therefore yields the transform of the current as

$$\bar{I}(s) = E_m \omega s / R(s + 1/RC)(s^2 + \omega^2) \quad (53)$$



FIG. 10—Series RC equivalent circuit used to illustrate analytical transformation (see *Analytical Transformation*).

Inverse transformation is relatively straightforward to yield

$$I(t) = [E_m \omega C / (1 + \omega^2 R^2 C^2)] [\cos \omega t + \omega CR \sin \omega t - e^{-t/RC}] \quad (54)$$

That is,

$$I(t) = [E_m \omega C / (1 + \omega^2 R^2 C^2)] [\sin(\omega t + \phi) - e^{-t/RC}] \quad (55)$$

where

$$\tan \phi = 1/\omega CR \quad (56)$$

Equation 55 shows that the observed current consists of two components: a sinusoidal component shifted by a phase angle ϕ relative to the perturbation, and a transient whose magnitude decreases exponentially with time. Impedance measurements are usually made under steady-state (or pseudo-steady-state) conditions so that the current reduces to

$$I(t)_{ss} = [E_m \omega C / (1 + \omega^2 R^2 C^2)] [\sin(\omega t + \phi)] \quad (57)$$

This example is important for two reasons. Firstly, it illustrates the essential features of the analytical transformation technique. Secondly, it forms the mathematical basis for the direct measurement of impedance by analysis of Lissajous figures generated by the simultaneous orthogonal recording of the perturbation and response functions. This method is discussed in detail in *Direct Measurement—Lissajous Figures*.

Elsewhere in this paper we have emphasized the fact that any time-dependent signal can be used to determine the impedance of a system, provided transformation of both the perturbation and response into Laplace space can be accomplished. Similarly, in principle, the components of a given equivalent circuit can be evaluated from the response, provided an analytical expression in real time can be obtained. An example of this type of analysis for small-amplitude cyclic voltammetry (SACV) has been discussed by Macdonald [23]. In his analysis, the equivalent circuit shown in Fig. 1a was assumed and the equations were solved for a small-amplitude triangular perturbation (Fig. 11). This case is particularly important in corrosion science, since it corresponds to one form of the "linear polarization" tech-

nique used for the *in situ* measurement of polarization resistance and hence corrosion rate (see Eqs 1 to 3).

The response functions obtained for the forward and reverse sweeps are given as

$$I^f(t') = (E_m/a\lambda)\{t' - e^{-at'/b}(R_p C - b/a)[2(e^{-2na/b} + e^{a\lambda/b})/(1 + e^{a\lambda/b}) - e^{-2na\lambda/b}] + (R_p C - b/a)\} \quad (58)$$

$$I^r(t'') = (E_m/a\lambda)\{\lambda - t'' + e^{-at''/b}(R_p C - b/a)[2(e^{-2na\lambda/b} + e^{a\lambda/b})/(1 + e^{a\lambda/b}) - e^{-(2n+1)a\lambda/b}] - (R_p C - b/a)\} \quad (59)$$

where t' and t'' are the times from the start of the forward and reverse sweeps, respectively, and λ is the time of reversal of the voltage scan. The parameters a and b are defined as

$$a = R_s + R_p \quad (60)$$

$$b = R_s R_p C \quad (61)$$

Again, the response consists of a periodic component and a transient. Under steady-state conditions ($n \rightarrow \infty$) the response functions reduce to

$$I_{ss}^f(t') = (v/a)\{t' - (R_p C - b/a)[(2e^{a(E_m - vt')/vb}/[1 + e^{aE_m/vb}]) - 1]\} \quad (62)$$

$$I_{ss}^r(t'') = (v/a)\{E_m/v - t'' + (R_p C - b/a)[(2e^{a(E_m - vt'')/vb}/[1 + e^{aE_m/vb}]) - 1]\} \quad (63)$$

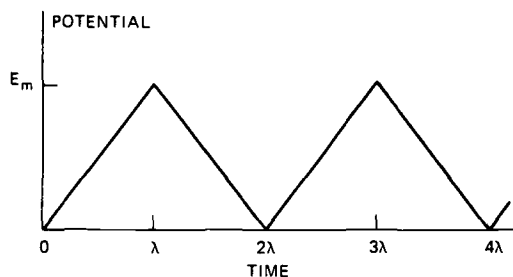


FIG. 11—Excitation function used for small-amplitude cyclic voltammetry (SACV).

Typical current-voltage curves computed using Eqs 62 and 63 are plotted in Fig. 12.

The small-amplitude cyclic voltammograms plotted in Fig. 12 are characterized by three useful quantities

$$\Delta I = I_{ss}^f(t' = \lambda/2) - I_{ss}^r(t'' = \lambda/2) \tag{64}$$

$$1/R_{app} = (\delta I_{ss}^f / \delta E)_{t' = \lambda} \tag{65}$$

$$1/R_d = [I_{ss}^f(t' = \lambda) - I_{ss}^r(t'' = \lambda)] / E_m \tag{66}$$

each of which are depicted graphically in Fig. 12. The hysteresis current, ΔI , is related to the components of the equivalent circuit by

$$\Delta I = 2R_p^2 C [1 - 23aE_m/2vb / (1 + e^{aE_m/vb})] v / (R_s + R_p)^2 \tag{67}$$

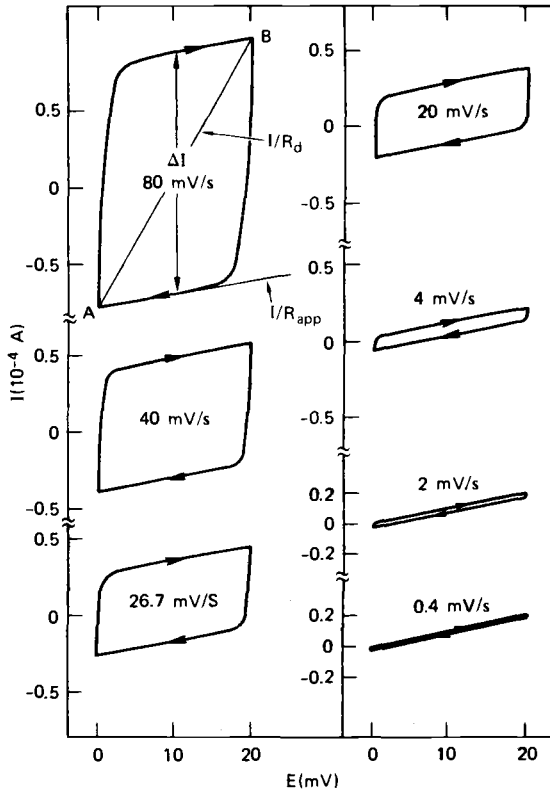


FIG. 12—Small-amplitude cyclic voltammograms for the electrical equivalent circuit shown in Fig. 1a as a function of voltage sweep-rate. $R_s = 10 \Omega$, $R_p = 1000 \Omega$, $C = 1000 \mu F$, $E_m = 20 mV$.

and the apparent and diagonal conductances are given by

$$1/R_{app} = 1/(R_s + R_p) + 2R_p/R_s(R_s + R_p)(1 + e^{aE_m/vb}) \quad (68)$$

$$1/R_d = 1/(R_s + R_p) + [2R_p^2C(e^{aE_m/vb} - 1)/E_m(R_p + R_s)^2(e^{aE_m/vb} + 1)]v \quad (69)$$

Clearly, all three quantities are dependent on the voltage sweep-rate (v) as expected, because the polarization resistance is shunted by the capacitor C . Calculated values for $1/R_{app}$, $1/R_d$, and ΔI as a function of voltage sweep-rate for assumed values for R_s , R_p , and C are shown in Figs. 13 and 14. At both very low and very high sweep rates the two resistances approach $R_s + R_p$ and R_s , respectively. These limits are identical to the limiting low and high frequency values for $\tilde{Z}(j\omega)$ as determined in the frequency domain. At intermediate voltage sweep-rates, however, the two conductances are neither equal to one another nor do they correspond to any simple algebraic combination of R_s and R_p alone.

Values for ΔI plotted in Fig. 14 show that the hysteresis current passes through a maximum as a function of voltage sweep-rate. The derivative at limiting low sweep-rates

$$(d\Delta I/dv)_{v \rightarrow 0} = 2R_p^2C/(R_p + R_s)^2 \quad (70)$$

can be used to estimate the capacitance C , provided values for R_s and R_p are available from the conductance versus sweep-rate correlations (Eqs 68 and 69).

The impedance analysis of small-amplitude cyclic voltammetry given

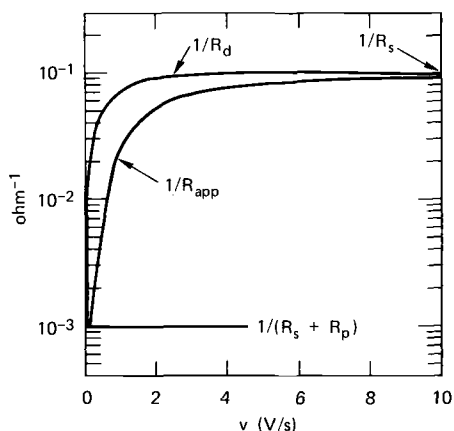


FIG. 13—Variation of $1/R_{app}$ and $1/R_d$ with voltage sweep-rate for SACV. Note the two limits given by $1/R_s$ and $1/(R_s + R_p)$. $R_s = 10 \Omega$, $R_p = 1000 \Omega$, $C = 1000 \mu F$, $E_m = 0.020 V$.

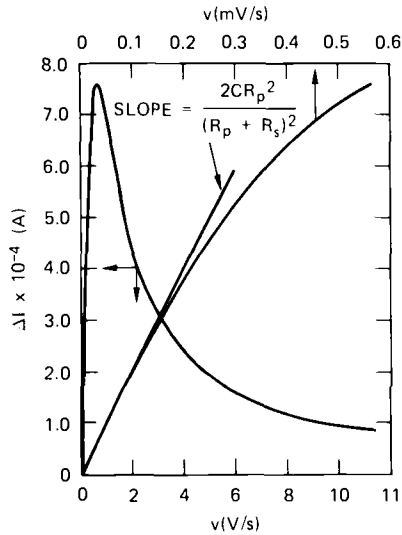


FIG. 14—Dependence of the hysteresis current (ΔI) on voltage sweep-rate (v) for SACV. The arrows indicate the appropriate sweep-rate axes. $R_s = 10 \Omega$, $R_p = 1000 \Omega$, $C = 1000 \mu F$, $E_m = 0.020 V$.

previously has a number of very important implications for the linear polarization method of estimating polarization resistance. Firstly, reliable values for R_p can only be obtained at sufficiently low sweep-rates that the second terms in Eqs 68 and 69 are small compared with the first. Experimentally, this condition can be recognized as that which yields no apparent hysteresis ($\Delta I = 0$) in the current-voltage response. For many systems, hysteresis is still apparent even at the lowest sweep-rate that is practical to employ. A good example of such a system is corroding 90:10 Cu:Ni alloy in flowing seawater [23], voltammograms for which are plotted in Fig. 15. Data for $1/R_{app}$ and $1/R_d$ versus sweep-rate for this system are plotted in Fig. 16. Only at the lowest sweep-rate employed is the measured resistance close to the d-c value of $v = 0$. A second problem with the linear-polarization technique is that the measured resistance at $v = 0$ depends upon both R_p and the solution resistance (R_s) between the reference electrode probe and the corroding surface. Clearly, for very low conducting media such as "pure" water, the measured polarization resistance could be greatly in error.

The analysis for SACV has been extended to other equivalent circuits. For example, many corroding systems (such as iron in inhibited sulfuric acid [24]) exhibit pseudo-inductive behavior at low frequencies; a behavior that can be explained by the equivalent circuit shown in Fig. 17. Analytical transformation [25] of the appropriate impedance expressions yields voltammograms of the type plotted in Fig. 18 for various values of the inductance L .

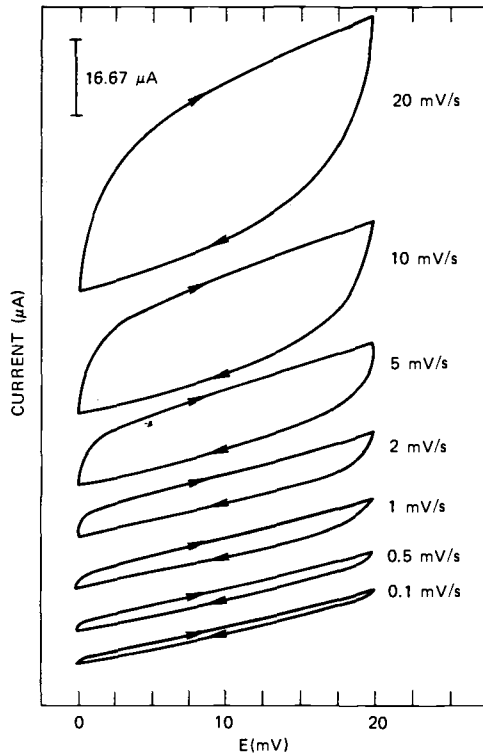


FIG. 15—Small-amplitude cyclic voltammograms for 90:10 Cu:Ni alloy in flowing seawater. Flow velocity = 1.62 m/s, $[O_2] = 0.045$ mg/L, specimen area = 11.05 cm², temperature = 26°C, exposure time = 50 h.

Also plotted in this figure are complex-plane impedance diagrams for the equivalent circuit with the appropriate values for the parameters C , L , ρ , and R_t . For the case where $C < L/\rho^2$, the contribution from the inductance dominates the reactive component of the impedance at low frequencies, as shown by the fourth-quadrant semicircle in the complex plane. At higher frequencies the imaginary component of the impedance changes sign, and the system exhibits normal, noninductive behavior. This change in behavior is reflected in the SACV response of the circuit as a reversal in the direction of rotation of the current-voltage response from counterclockwise for low-voltage sweep-rates to clockwise for high sweep-rates. To our knowledge no systems that exhibit pseudo-inductance have been analyzed using the SACV technique. However, the appropriate equations for the analysis have been derived [25]. They are

$$1/R_{app}(t=0) = (1/R_t + 1/\rho) - 2/\rho(1 + e^{-\rho\lambda/L}) \quad (71)$$

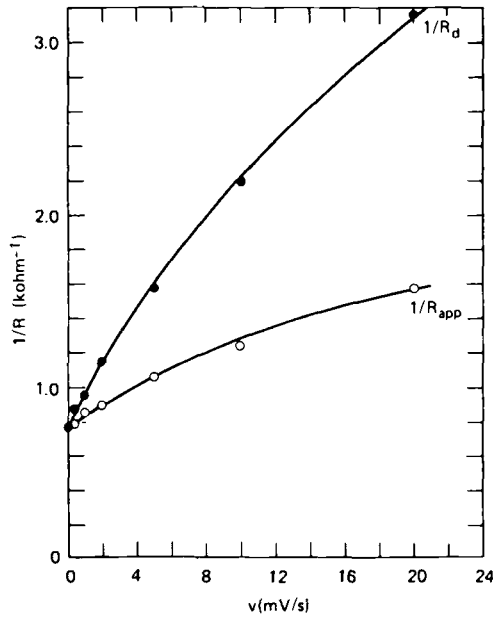


FIG. 16—Plots of Eqs 68 and 69 for 90:10 Cu:Ni alloy in flowing seawater. Experimental conditions are as listed in Fig. 15.

$$1/R_{app}(t = \lambda) = (1/R_t + 1/\rho) - 2e^{-\rho\lambda/L}/\rho(1 + e^{-\rho\lambda/L}) \quad (72)$$

$$1/R_d = (1/R_t + 1/\rho) + (2/E_m) \times \{C - E/\rho^2 + 2Le^{-\rho\lambda/L}/\rho^2(1 + e^{-\rho\lambda/L})\}v \quad (73)$$

$$\Delta I = \{2(C - L/\rho^2) + 4Le^{-\rho\lambda/2L}/\rho^2(1 + e^{-\rho\lambda/L})\}v \quad (74)$$

These parameters are depicted graphically in the top left-hand diagram of Fig. 18. These equations show clearly that the overall SACV response of the system depends critically on the relative values for C and L/ρ^2 . If $C < L/\rho^2$, for example, the ΔI may be negative owing to the counterclockwise rotation of the Lissajous figure (as indicated earlier in this discussion). From the corrosion scientist's point of view, probably the feature of greatest significance is that reliable estimates for R_t and ρ can be obtained only at sweep-rates where hysteresis is effectively nonexistent. This conclusion parallels that drawn earlier for the more common resistive-capacitive system.

Numerical Transformation

The analytical transformation technique described previously suffers from the major disadvantage of requiring an *a priori* assumption of an equivalent

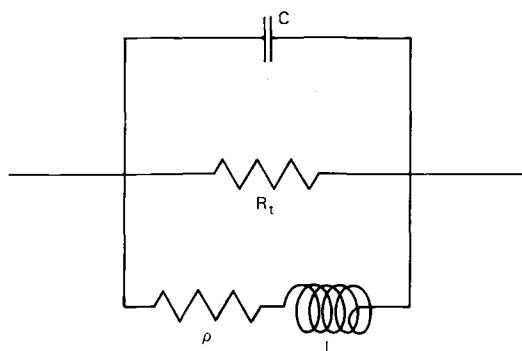


FIG. 17—Equivalent circuit for systems that exhibit pseudo-inductance.

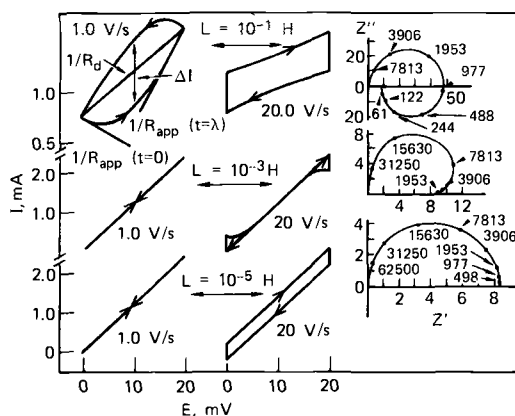


FIG. 18—Current-voltage curves for the SACV response and complex impedance plane diagrams for the equivalent circuit shown in Fig. 17. $C = 10^{-5}$ F, $\rho = 10$ Ω , $R_t = 50$ Ω , $E_m = 0.020$ V. Upper three curves: $L = 10^{-1}$ H; middle three curves: $L = 10^{-3}$ H; lower three curves: $L = 10^{-5}$ H. The numbers next to the data points in the complex-plane diagrams refer to frequencies in rad/s. Z' and Z'' have units of ohms.

circuit for the system in order to carry out the analysis. Indeed, it is well recognized in fundamental electrochemical studies that the power of the impedance technique lies in the fact that the frequency dispersion of $\tilde{Z}(j\omega)$ permits the equivalent circuit to be determined in addition to the evaluation of the purely resistive components from the high- and low-frequency limits. In other words, the frequency dispersion of $\tilde{Z}(j\omega)$ not only permits the series resistances to be evaluated, but it also allows mechanistic information to be obtained.

The basis of numerical transformation is to evaluate Eqs 44 and 45 directly from the perturbation and response versus time functions using numerical integration techniques. This method is extremely versatile since, in principle,

any functional forms for $E(t)$ and $I(t)$ may be handled, provided the integrals converge. Furthermore, the analysis is conveniently carried out in both the "real" and "imaginary" frames as noted earlier. In this paper we will restrict ourselves to a discussion of numerical "imaginary-axis transformation"; the reader is referred to the extensive work by Pilla [21] for a description of numerical "real-axis transformation".

Because the impedance $\bar{Z}(j\omega)$ is a complex number, it is convenient to first expand the integrals using the identity

$$e^{-j\omega t} = \cos \omega t - j \sin \omega t \quad (75)$$

Accordingly,

$$\bar{E}(j\omega) = \int_0^{\infty} E(t) \cos \omega t - j \int_0^{\infty} E(t) \sin \omega t dt \quad (76)$$

and

$$\bar{I}(j\omega) = \int_0^{\infty} I(t) \cos \omega t - j \int_0^{\infty} I(t) \sin \omega t dt \quad (77)$$

The impedance

$$\bar{Z}(j\omega) = \bar{E}(j\omega)/\bar{I}(j\omega) \quad (78)$$

therefore becomes

$$\bar{Z}(j\omega) = Z'(\omega) - jZ''(\omega) \quad (79)$$

with the real and imaginary parts given as

$$Z'(\omega) =$$

$$\frac{\int_0^{\infty} E(t) \cos \omega t dt \int_0^{\infty} I(t) \cos \omega t dt + \int_0^{\infty} E(t) \sin \omega t dt \int_0^{\infty} I(t) \sin \omega t dt}{\left[\int_0^{\infty} I(t) \cos \omega t dt \right]^2 + \left[\int_0^{\infty} I(t) \sin \omega t dt \right]^2} \quad (80)$$

$$Z''(\omega) =$$

$$\frac{\int_0^{\infty} E(t) \sin \omega t dt \int_0^{\infty} I(t) \cos \omega t dt - \int_0^{\infty} E(t) \cos \omega t dt \int_0^{\infty} I(t) \sin \omega t dt}{\left[\int_0^{\infty} I(t) \cos \omega t dt \right]^2 + \left[\int_0^{\infty} I(t) \sin \omega t dt \right]^2} \quad (81)$$

Two problems must be considered in the numerical evaluation of these functions. Firstly, the integrals must converge or at least must be made to converge. Secondly, it is necessary to assume some analytical relationship between neighboring points in order to perform the integration. Since a transient is expected to tend towards some constant value at very long times, the easiest way of ensuring convergence for the numerical integral is to write $f(t)$ as

$$f(t) = f(t) - f(t = \infty) + f(t = \infty) \quad (82)$$

$$= f_{\text{var}}(t) + f(t = \infty) \quad (83)$$

Because $f(t = \infty)$ is a constant, Laplace transformation of Eq 83 yields

$$\tilde{f}(j\omega) = \int_0^{\infty} f_{\text{var}}(t) e^{-j\omega t} dt + f(t = \infty)/j\omega \quad (84)$$

where $f(t)$ is identified as $E(t)$ or $I(t)$ or both, as the case requires. For example, for a potential step (ΔE) of infinitely fast rise-time

$$\tilde{E}(j\omega) = \Delta E/j\omega \quad (85)$$

Because of mathematical simplicity, relaxation analyses are frequently made using "ideal" step functions. It is important to note however, that numerical evaluation of the transformation integral may be performed even though the perturbation is not "ideal" over the time of interest. This is a very important advantage of numerical transformation over analytical transformation, since it is generally not possible to perform the latter over the period of instability of the control device. Thus the very short time, and hence high-frequency domain, is accessible using numerical transformation, whereas it is generally not in the case of analytical transformation.

The second problem of choosing a suitable analytical function to describe the variation of $f(t)$ between neighboring points has been considered in depth by Pilla [21] and Sierra-Alcazar [22]. The appropriate functions for the real and imaginary components of $f(j\omega)f(t) \equiv E(t)$, Eq 76 or $I(t)$, Eq 77 for

linear, quadratic, and exponential functions are summarized in Table 1. These expressions are derived [22] by discretizing the integral contained in Eq 84.

No extensive comparative study of the approximate functions listed in Table 1 for the numerical evaluation of the impedance from time-domain data appears to have been reported. The forms of these functions deserve comment, however, if for no other reason than to indicate the conditions under which they can be expected to be valid. Thus, both the quadratic and exponential functions reduce to the linear approximation for sufficiently closely spaced data points. Experimental conditions may be chosen so that the linear approximation is satisfactory; these conditions may be inconveniently restrictive, however, particularly for rapidly changing functions of time. It is well known that equivalent circuits of the type shown in Fig. 1a give rise to exponential-type transients on imposition of step perturbations. Accordingly, the exponential approximation is expected to provide a reasonably precise representation of the variation of $f(t)$ between neighboring points, particularly over the range frequency where the impedance is characterized by a single relaxation. In the case of multiple relaxations, the situation is more complex, but nevertheless the exponential approximation intuitively appears superior to the linear form. The quadratic approximation clearly attempts to recognize the generally expected nonlinear behavior of $f(t)$, but its form does not appear to have any sound theoretical basis.

Algorithms based on the approximations summarized in Table 1 are available in the literature [21,22]. As noted earlier, numerical transformation of both the perturbation and response functions can be performed from times much shorter than that required to establish control by an external control device. The technique is thus capable of yielding impedance data at very high frequencies (> 100 MHz). Also, the lowest accessible frequency is determined by the time of data acquisition, and hence ultimately by the stability of the system. For every stable system, reliable impedance data at frequencies down to 0.1 mHz can be obtained. An additional feature of this technique is that the impedance versus frequency data are computed from a single transient that requires considerably smaller acquisition time than the more traditional point-by-point techniques.

Correlation Techniques

In recent years the advent of hard-wired real-time Fourier transform units and low-cost high-powered digital computers have allowed hitherto unattainable methods of impedance measurement to be accomplished. A particularly powerful example that has come into recent prominence employs correlation techniques to determine a system transfer function.

Transfer-Function Analysis—General—The transfer function is the mathematical description of the relationship between any two signals. In the

TABLE 1—Discretized functions for the evaluation of $f(\omega)$ (Eq 84)—Functions taken from Ref 22.

Function, $F_{\text{var}}(t)$	Re, $f(j\omega)$	Im, $f(j\omega)$
Linear, $A + Bt$	$\sum_i (1/\omega) \{ f_{\text{var}}(t_{i+1}) \sin \omega t_{i+1} - f_{\text{var}}(t_i) \sin \omega t_i$ $+ (B/\omega) (\cos \omega t_{i+1} - \cos \omega t_i) \}$	$\sum_i (1/\omega) \{ f_{\text{var}}(t_{i+1}) \cos \omega t_{i+1} - f_{\text{var}}(t_i) \cos \omega t_i$ $- (B/\omega) (\sin \omega t_{i+1} - \sin \omega t_i) \} - [f(t = \infty)/\omega]$
Quadratic, $A + Bt + Ct^2$	$\sum_i (1/\omega) \{ f_{\text{var}}(t_{i+2}) \sin \omega t_{i+2} + (B + 2Ct_{i+2}) \times$ $\cos \omega t_{i+2} - (2C \sin \omega t_{i+2}/\omega^2) - f_{\text{var}}(t_i) \sin \omega t_i$ $- [(B + 2Ct_i) \cos \omega t_i/\omega] + (2C \sin \omega t_i/\omega^2) \}$	$\sum_i (1/\omega) \{ -f_{\text{var}}(t_{i+2}) \cos (\omega t_{i+2}) + (B + 2Ct_{i+2}) \times$ $\sin \omega t_{i+2} + (2C \cos \omega t_{i+2}/\omega^2) + f_{\text{var}}(t_i) \cos \omega t_i$ $- [B + 2Ct_i] \sin \omega t_i/\omega] - (2C \cos \omega t_i/\omega^2) \} -$ $[f(t = \infty)/\omega]$
Exponential, Ae^{-at}	$\sum_i 1/(a^2 + \omega^2) \{ f(t_{i+1}) [-a \cos \omega t_{i+1} + \omega \sin \omega t_{i+1}]$ $+ f(t_i) [a \cos \omega t_i - \omega \sin \omega t_i] \}$	$\sum_i 1/(a^2 + \omega^2) \{ -f(t_{i+1}) [\omega \cos \omega t_{i+1} + a \sin \omega t_i]$ $+ f(t_i) [\omega \cos \omega t_i + a \sin \omega t_i] \}$

special case where the signals of interest are the input (current excitation) and output (voltage response) of a linear electrical system, then the transfer function is equivalent to the system impedance.

Mathematically,

$$H(\omega) = \frac{V(j\omega)}{I(j\omega)} = \frac{FV(t)}{FI(t)} = \bar{Z}(j\omega) \text{ (compare Eqs 13 and 14)} \quad (86)$$

$$H(\omega) = \frac{G_{yx}(\omega)}{G_{xx}(\omega)} \quad (87)$$

where

$H(\omega)$ = transfer function (ω indicates that this is a frequency domain parameter),

F = a Fourier transform,

V and I = system voltage and current, respectively,

$G_{yx}(\omega)$ = average cross-power spectrum of input and output, and

$G_{xx}(\omega)$ = average power spectrum of input.

Up to this point we have described methods in which impedance is measured in terms of a transfer function of the form given by Eq 86. For frequency-domain methods, the transfer function is determined as the ratio of frequency-domain voltage and current, and for time-domain methods as the ratio of the Fourier or Laplace transforms of the time-dependent variables. We will now briefly describe methods by which the transfer function can be determined from the power spectra of the excitation and response using Eq 87.

Transfer-Function Analysis Employing White-Noise Excitation—By invoking the equivalence of Eqs 86 and 87, and noting that the power spectrum of a noise current is the Fourier transform of its correlation function [26], $H(\omega)$ can be obtained in a manner that offers a number of advantages. In the most general method, low-amplitude Gaussian white noise is superimposed on the input, and the transfer function is determined from the average power spectra calculated using correlation techniques [27].

This method has several advantages:

1. It is an averaging method and thus affords the same type of insensitivity to asynchronous system noise as phase-sensitive detection.

2. $H(\omega)$ is determined for all frequencies simultaneously and in the time required for the lowest frequency alone by conventional methods. Thus, impedance can be measured to relatively low frequencies in time-varying systems, and impedance parameters can be measured as a function of time in, for example, a rapidly corroding environment.

3. Correlation analysis can be performed on internally generated noise in the complete absence of an external excitation function. Because the ionic events that produce this noise are not synchronized to an external trigger, the correlation function in this case contains no phase information, but may be considered as analogous to the magnitude of the impedance. This technique (potentially an extremely powerful one) allows equilibrium and steady-state conditions to be approached very closely.

4. The coherence function provides an internal check on the validity of the measurement.

Methods that determine impedance as the ratio of the imposed input to the observed output do so without regard to the degree of causality between the two signals. For example, in a system exposed to mains noise or containing electrolyte pumped in an oscillatory or peristaltic fashion, a component of the output signal power results from frequencies characteristic of the environment or system, but not of the input. Another frequent cause of error in a measured electrochemical impedance is due to nonlinearity of the interfacial reaction impedance at large perturbations. Excitation at frequency ω_0 thus results in harmonic distortion and a component of output power at frequencies $2\omega_0$, $3\omega_0$, etc. that may invalidate the "impedance" measured at these frequencies.

The coherence function, $C(\omega)$, can be calculated to determine the validity of a transfer-function measurement, if the extent of extraneous input and nonlinearity is not known.

$$C(\omega) = \frac{\overline{G_{xy}(\omega)^2}}{\overline{G_{xx}(\omega)} \overline{G_{yy}(\omega)}} \quad (88)$$

where bars denote average quantities, and G_{yy} is the auto power spectrum of the output signal $y(t)$ [27]. Coherence function values range between 0 and 1. A coherence value of 1 means there is complete coherence between input and output, which indicates there is only one input and the system is linear.

The primary limitation of this method of impedance measurement is cost.

Discussion

Performance Characteristics

Although in principle many of the techniques described previously are capable of yielding impedance data over a wide range of frequency, in practice some techniques are found to be more applicable than others over the frequency range of interest in corrosion science (0.1 mHz to 10 kHz). The limitations of any given technique generally fall into two classes: (1) signal-to-noise ratio and (2) system stability. The first limitation is a direct result of

the necessity for using small-amplitude excitations; thus pickup from nearby electrical circuits and "intrinsic" system noise generally impose a lower limit of 0.1 to 1 mV on the size of the exciting impulse. The solution to this problem is frequently instrumental; the use of shielded cables and the careful elimination of "ground-loops" can often improve the signal-to-noise ratio substantially. Also, signal averaging and lock-in amplification techniques have been used to further improve the precision of impedance data.

The second limitation is far more insidious, since it is generally independent of the measuring technique employed. Many corroding systems require considerable time to achieve a "steady state"; defined here as a state in which the *electrical* parameters for the system are invariant with time. From a practical viewpoint, sufficient stability may be claimed if the spontaneous corrosion potential does not change by more than 10 percent of the magnitude of the excitation voltage over the time of acquisition of the impedance data. This condition should be regarded as a rough guide only, since it also depends on the technique used and on the properties of the system. The current for a system corroding in the "passive" state, for example, is relatively insensitive to changes in potential, so that the impedance is generally less time-dependent than for a system undergoing a spontaneous transition from an active to a passive state.

A third, and frequently the most insurmountable barrier, is cost. In principle, impedance measurements can be made using very simple equipment capable of measuring the relative amplitudes and phase differences between the excitation and response functions. The trend in recent years, however, has been towards more sophisticated techniques that require more complex equipment both for excitation and detection. Impedance measuring equipment can now range in cost from less than \$1000 to over \$30 000; it is important to note that frequently no direct relationship exists between cost and the quality of the results or the frequency range that is accessible.

Although a direct comparison of the various methods for measuring interfacial impedance is difficult, it is nevertheless useful to list some of the characteristics of each technique on a comparative basis. Such a listing for many of the more familiar techniques is given in Table 2. As we have stated frequently in this review, the most important and demanding characteristic of corrosion studies is the ability to sample low-frequency relaxations. This characteristic demands both a minimum in acquisition time and a maximum in signal-to-noise ratio. The time-domain techniques (particularly those involving a step-function excitation) and the correlation methods clearly have advantages in this regard, since a single experiment is capable of yielding impedance data for a very wide range of frequencies. For example, an ideal potential step excitation imposed for 1000 s is capable of yielding reasonably precise impedance data at all frequencies down to 1 mHz. Unfortunately, signal averaging cannot be accomplished using the single-impulse methods, so that the precision of the experiment is limited by signal-to-noise

TABLE 2—Comparison of impedance-measurement techniques.

	Frequency Range, Hz	Optimum Precision for $ Z $, % ^a	Approximate Cost, \$ ^b	Comments
Frequency-Domain Techniques				
Audio-frequency bridges	20 to 20k	±0.1	<5000	Two-terminal technique—requires $ Z $ (working electrode) $\gg Z $ (counterelectrode). Phase-sensitive null detection greatly improves low-frequency performance. Frequency-by-frequency measurements only.
Transformer ratio arm bridges	200 to >10M	±0.1	<10 000	Two-terminal technique—requires $ Z $ (working electrode) $\gg Z $ counterelectrode. Particularly suited for high-frequency studies.
Berbertian-Cole bridge ^c	1m to 10k	±0.1	<10 000	Frequency-by-frequency measurements only. Multiple-terminal technique—only bridge technique that strictly allows potentiostatic control. High precision over an extremely wide frequency range. Frequency-by-frequency measurements only.
Direct measurement				
Two-channel oscilloscope measurements	<1m to >1M	±5	<7000	Three-terminal technique—hence, "potentiostatic" control of the working electrode is possible. Care must be taken to ensure that extraneous phase shifts due to the control amplifier are absent. Frequency-by-frequency measurements only possible—data treatment tends to be laborious except for phase-sensitive detection methods.
Lissajous figures	<1m >	±1	<7000	
Phase-sensitive detection	0.5 to 100k	±0.1	<5000	
Analog demodulation	0.1m to 1M	±0.1	<20 000	
Digital demodulation				
Time-Domain Techniques				
Analytical transformation	...	±1	<5000	Three-terminal technique. Limited by the assumption of an equivalent circuit for the interface. Experimental independent variable is time (for example, potential step) or related parameter (voltage sweep rate—SACV). Yields values for the components of the equivalent circuit only.
Numerical transformation	<1m to 1000M	±1	10 000 to 20 000	Three-terminal technique. Minimum acquisition time required, since all frequencies are sampled in a given transient. Data storage/computer interfacing required for extraction of impedance parameter. Data may be analyzed by both "real axis" and "imaginary axis" transformations. Any time-dependent excitation may be used.
Correlation Techniques	<1m to >10M	±0.1	<20 000	Hard-wired Fourier transform units—similar in principle to Numerical Transformation. Signal averaging possible. Data for all frequencies determined simultaneously—hence, short data acquisition time. Coherence function provides internal check on the validity of the measurement. Can use self-generated noise—no external perturbation necessary.

^a Stated precision may not be available over entire frequency range.

^b Approximate cost range for commercially available instruments. Devices may be fabricated for greatly reduced materials cost.

^c Apparently not available on a commercial basis, versatile bridge for high-precision low-frequency measurements can be constructed for a materials cost of about \$500 [16].

characteristics. Repetitive impulse techniques overcome this limitation, provided the system is sufficiently stable. On the other hand, while signal averaging is possible using many of the point-by-point (frequency-by-frequency) methods, excessively long data acquisition times are involved, and ultimately the validity of the technique is limited by system stability.

Comparison of Techniques

Few in-depth studies have been made of the various techniques that are available for measuring interfacial impedance, particularly for spontaneously corroding systems. The lack of such a comparison is surprising, since traditionally impedance measurements are frequently found to be "technique dependent"; that is, small but nevertheless significant differences are commonly found in the impedance parameters measured using different

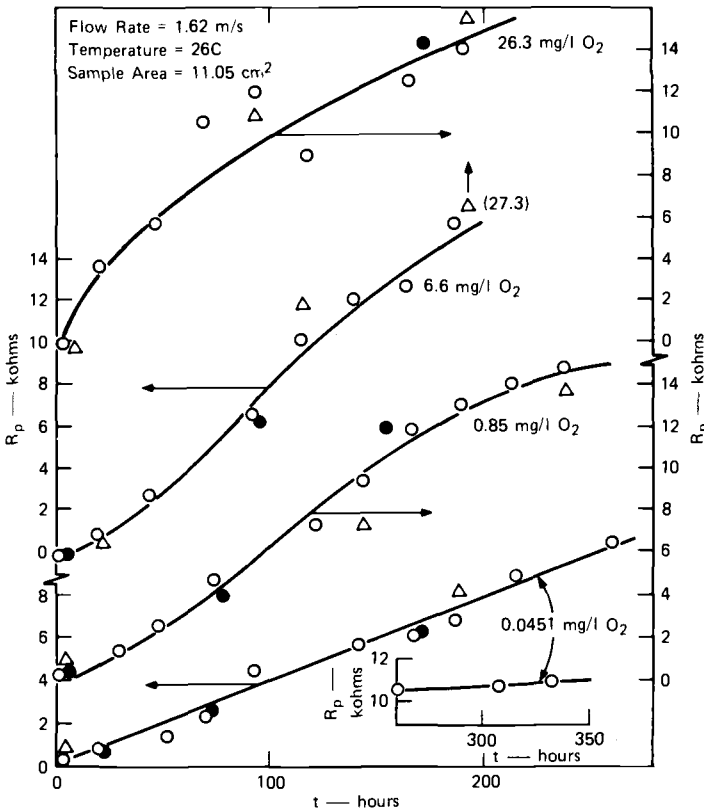


FIG. 19—Polarization resistance (R_p) as a function of time and oxygen concentration for 90:10 Cu:Ni alloy in flowing seawater.

methods on supposedly identical systems. These differences almost always arise from uncompensated resistances and stray capacitances in external circuits, and from unexpected phase-shifts due to active elements in control devices (for example, potentiostats). The elimination of these extraneous effects is frequently a major problem in accurate impedance work.

One of the most important uses of impedance techniques in corrosion science is the estimation of the polarization resistance of the interface as a function of exposure time. An example of such measurements is shown in Fig. 19 [6]. The low-frequency (infinite time) impedance ($\equiv R_p - R_s$) for 90:10 Cu:Ni alloy in flowing oxygenated seawater was measured by using the Lissajous figures methods in the frequency domain over the range 1500 Hz to 5 mHz, and by employing the SACV and potential step techniques in the time domain. All three techniques yield polarization resistances that generally agree within the level of precision of the experiments. It is important to note that the scatter in the experimental data does not reflect the precision of the impedance measuring techniques alone; intrinsic fluctuations in the corrosion rate as a function of time are most likely the principal contributors to the uncertainty that is apparent in the data.

A typical frequency-dispersion plot of the impedance for the corrosion of 90:10 Cu:Ni in flowing oxygenated seawater is shown in Fig. 20. These data

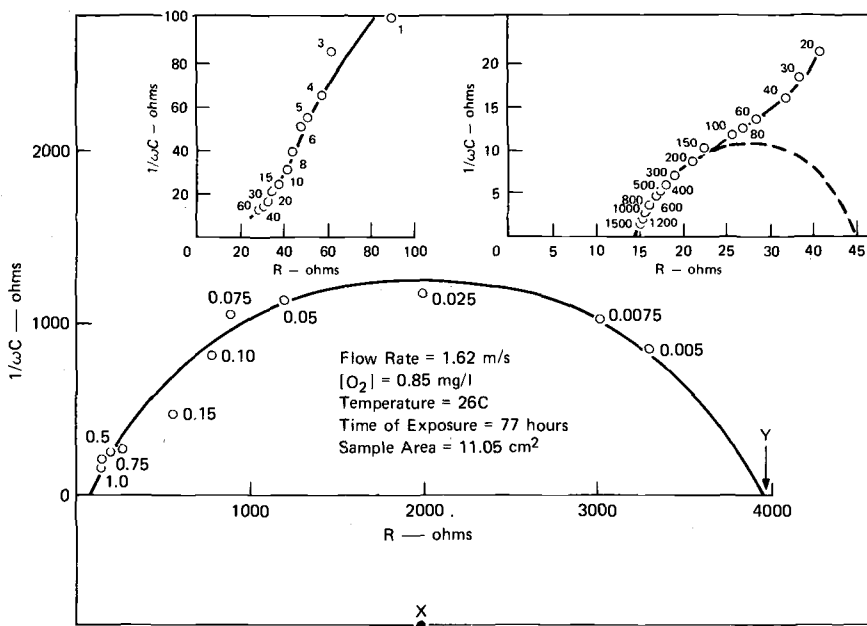


FIG. 20—Complex impedance plane plot for 90:10 Cu:Ni alloy in flowing seawater. (The number next to each point designates frequency in hertz.)

show that even at the lowest frequency employed (5 mHz) the impedance still contains a significant reactive component. Extrapolation of $\bar{Z}(j\omega)$ to $R_s + R_p$ (Point Y, Fig. 20) is made on the basis that the low-frequency data may be represented satisfactorily by a semicircle centered below the real axis.

The frequency dispersion data shown in Fig. 20 demonstrate that at least two relaxations are observed in the electrical properties of the interface. The high-frequency semicircle was found to be centered on or near the real axis and to be invariant with time. On the other hand, the low-frequency semicircle is centered well below the real axis (Point X, Fig. 20), and the zero-frequency intercept is found to extend to higher resistance values with time. The fact that the center of this semicircle lies below the real axis demonstrates that a simple equivalent circuit of the type shown in Fig. 1a is incapable of representing the electrical properties of the interface. Instead, the data indicate that a transmission-line model for the low-frequency behavior would be more appropriate [7].

References

- [1] Stern, M. and Geary, A. L., *Journal of the Electrochemical Society*, Vol. 104, 1957, p. 56.
- [2] Mansfeld, F., *Advances in Corrosion Science Technology*, Vol. 6, 1976, p. 163.
- [3] Syrett, B. C. and Macdonald, D. D., *Corrosion*, Vol. 35, 1979, p. 505.
- [4] Goldman, S., *Transformation Calculus and Electrical Transients*, Prentice-Hall Inc., New York, 1950.
- [5] Sluyters-Rehbach, M. and Sluyters, J. H. in *Electroanalytical Chemistry*, Vol. 4, A. J. Bard, Ed., Marcel Dekker, New York, 1966, pp. 1-128.
- [6] Macdonald, D. D., Syrett, B. C., and Wing, S. S., *Corrosion*, Vol. 34, 1978, p. 289.
- [7] de Levie, R. in *Advances in Electrochemistry and Electrochemical Engineering*, Vol. 6, P. Delahay, Ed., Wiley-Interscience, New York, 1969, pp. 329-368.
- [8] Armstrong, R. D., Race, W. P., and Thirsk, H. R., *Electrochimica Acta*, Vol. 13, 1968, pp. 215-239.
- [9] Hague, B., *Alternating Current Bridge Methods*, Pitman, London, 1957.
- [10] Delahay, P. and Trachtenberg, I., *Journal of the American Chemical Society*, Vol. 79, 1957, p. 2355.
- [11] de Levie, R., *Electrochimica Acta*, Vol. 10, 1965, pp. 113-130.
- [12] de Levie, R., *Electrochimica Acta*, Vol. 8, 1963, p. 751.
- [13] de Levie, R., *Electrochimica Acta*, Vol. 9, 1964, pp. 1231-1245.
- [14] McKubre, M. C. H., "Membrane Polarization," Master's thesis, Victoria University, Wellington, New Zealand, 1972.
- [15] Berberian, J. G. and Cole, R. H., *Review of Scientific Instruments*, Vol. 40, 1969, p. 811.
- [16] McKubre, M. C. H., "Membrane Impedance in Simulated Rocks," Ph.D. thesis, Victoria University, Wellington, New Zealand, 1976.
- [17] Pilla, A. A., Roe, R. B., and Herrmann, C. C., *Journal of the Electrochemical Society*, Vol. 116, 1969, p. 110.
- [18] Macdonald, D. D., *Transient Techniques in Electrochemistry*, Plenum Press, New York, 1977.
- [19] Princeton Applied Research, "Lock-In Amplifier; Model 129A," instruction manual, 1975.
- [20] Hills, G. J., and McKubre, M. C. H., "Low-Frequency Phase Sensitive Detection Employing Gated Digital Demodulation," to be published.
- [21] Pilla, A. A. in *Informational Chemistry: Computer-Assisted Chemical Research Designs* (Papers and Discussions at the Joint Japan—United States Seminar), 1973, pp. 181-193.
- [22] Sierra-Alcazar, H., Ph.D. thesis, University of Newcastle-upon-Tyne, U.K., 1976.

- [23] Macdonald, D. D., *Journal of the Electrochemical Society*, Vol. 125, 1978, p. 1443.
- [24] Epelboin, I., Keddam, M. and Takenouti, H., *Journal of Applied Electrochemistry*, Vol. 2, 1972, p. 71.
- [25] Macdonald, D. D., *Journal of the Electrochemical Society*, Vol. 125, 1978, p. 1977.
- [26] Rice, S. O. in *Noise and Stochastic Processes*, N. Wax, Ed., Dover, New York, 1954, p. 133.
- [27] Hewlett Packard Applications Note 140-0.

I. Epelboin,¹ C. Gabrielli,¹ M. Keddam,¹ and H. Takenouti¹

Alternating-Current Impedance Measurements Applied to Corrosion Studies and Corrosion-Rate Determination

REFERENCE: Epelboin, I., Gabrielli, C., Keddam, M., and Takenouti, H., "Alternating-Current Impedance Measurements Applied to Corrosion Studies and Corrosion-Rate Determination," *Electrochemical Corrosion Testing, ASTM STP 727*, Florian Mansfeld and Ugo Bertocci, Eds., American Society for Testing and Materials, 1981, pp. 150-166.

ABSTRACT: The general features of the a-c impedance at a metal-electrolyte interface as a function of frequency are depicted, and recently developed measurement techniques are described. It is established that at low and very low frequencies, down to the millihertz domain, relaxation phenomena are found in those cases where the assumptions used in Stern's derivation are not met. Under such conditions polarization resistance techniques can hardly be used owing to experimental and theoretical reasons. Charge transfer resistance, when used instead of polarization resistance in a Stern's type equation, is proved to overcome these difficulties on the basis of a theoretical derivation. Correlation between charge transfer resistance and corrosion rate is illustrated by practical examples of pure iron and anodized aluminum alloys.

KEY WORDS: corrosion rate, corrosion mechanism, test, alternating current impedance, frequency response, transfer function analyzer, Faradaic impedance, charge transfer resistance, polarization resistance, iron, sulfuric media, inhibition, aluminum alloys, anodic oxide films, salt spray test

The use of a-c techniques for studying metal-electrolyte interfaces at which corrosion takes place can be traced to the end of the past century. For a long time, however, these studies were carried out only at acoustic frequencies. About 15 years ago, they started developing in two quite different directions. On the one hand, the subacoustic frequencies, down to very low frequencies in the millihertz range, became accessible to electrode impedance measure-

¹Director of the Laboratory, Chargé de Recherche, Maître de Recherche, and Chargé de Recherche, respectively, Groupe de Recherche n° 4 du CNRS, Physique des Liquides et Electrochimie, Paris, France. Professor Epelboin died on Feb. 10, 1980.

ments [1].² When applied to various interfaces such as iron, nickel, chromium, and titanium in acidic media, very low frequency impedance measurements allow relaxation phenomena to be analyzed. The latter are mainly concerned with the elementary processes involved in corrosion reactions (active dissolution, passivation, inhibition, cathodic reactions, mass transfer, etc.) [2,3]. On the other hand, the estimation of corrosion rate based on polarization resistance measurements has been used more and more extensively [4]. In order to achieve more accurate and reproducible values of the polarization resistance, several authors apply periodic voltage or current waves to the specimen. Under such conditions, in most cases, the response of the metal-electrolyte system is far more complicated than that expected for the single equivalent circuit: polarization resistance—double layer capacitance in parallel.

Nowadays, the study of corrosion mechanisms and the estimation of the corrosion rate by means of electrochemical techniques tend to be increasingly connected to each other. The present paper encompasses both approaches of corrosion using a-c techniques. The usefulness of impedance techniques will be emphasized in those cases where kinetic effects not considered in the Stern's derivation are proved to take part in the corrosion process. Applications of a-c techniques to corrosion-rate estimation are illustrated by a number of examples dealing with inhibited and noninhibited iron corrosion and with the protection against corrosion by organic and inorganic coatings.

A-C Impedance: Definition, Experimental, and Theoretical Aspects

Definition

The impedance can be defined for any physicochemical system that is characterized by a steady-state current-voltage relationship. Hence for most of the electrode-electrolyte interfaces (Fig. 1a), V denotes the voltage actually measured between the working electrode and an arbitrary reference electrode, including the ohmic drop. At every point $P(I_0, V_0)$, a small amplitude sine wave perturbation $\Delta V(t)$ can be superimposed to the voltage [or $\Delta I(t)$ to the current]. Provided the amplitude of ΔV or ΔI remains small enough to fulfill the so-called linearization, both ΔV and ΔI obey a sinusoidal time-dependence. At any frequency f , the amplitude ratio $|\Delta V|/|\Delta I| = |Z|$, and the phase shift ϕ between $\Delta V(t)$ and $\Delta I(t)$ is as defined in Fig. 1b. $|Z|$ and ϕ represent the modulus and the argument of the complex impedance $Z(f)$ respectively.

$$Z(f) = \frac{\Delta V}{\Delta I} = |Z|e^{j\phi} = \frac{|\Delta V|e^{2\pi jft}}{|\Delta I|e^{j(2\pi ft - \phi)}} \quad \text{where } j = \sqrt{-1} \quad (1)$$

²The italic numbers in brackets refer to the list of references appended to this paper.

or in terms of its real part Re , and imaginary part, Im ,

$$Z(f) = \text{Re}(f) + j \text{Im}(f) \quad (2)$$

Except in the case of a purely resistive behavior, Z is frequency dependent. The variations of Z as a function of f can be plotted in the complex plane (Re , $j\text{Im}$) under the form of an impedance diagram (Fig. 1c). In the field of electrochemistry, negative Im values are usually plotted as positive ordinates; they correspond to the capacitive behaviors commonly encountered in the early a-c studies performed at acoustic frequencies [5]. In contrast, a-c impedances in the very low frequency range can involve inductances ($\text{Im} > 0$) or negative resistances ($\text{Re} < 0$) [1-3].

Experimental

The impedance is a function of both frequency and steady-state polarization point (I_o , V_o) (Fig. 1a). As a rule, the steady-state is controlled by means of a potentiostat, a galvanostat, or any other regulating device [6]. The frequency is varied. In the early apparatus the circuits used for controlling the d-c polarization and the a-c signal were isolated by means of electric filters. During the last 15 years wide band-pass, d-c coupled electronic regulators have been devised that allow both the d-c and a-c components of the polarization to be controlled at the same time in a frequency range extending from zero to some tens of kilohertz [7].

The impedance measurement can be performed by using signals of different profile. Provided their amplitude is small enough, the use of spectral analysis (Laplace and Fourier transformations) yields the impedance. In practice such a procedure is used mainly for semiquantitative purposes [8-11]. Most often the interface impedance is accurately measured frequency-by-frequency with a sinusoidal polarizing signal. At each frequency either a phase-sensitive detector (lock-in amplifier) or a digital transfer function analyser (TFA) is used. Both of these devices ensure a very high noise rejection, and therefore allow low-amplitude measuring signals to be used even in presence of spurious noises. The frequency range extending far below one hertz, however, can be covered only by means of TFA, which was introduced in corrosion studies by our group and has been increasingly used in the last ten years [7]. The experimental set-up for impedance measurement based on a digital TFA is shown in Fig. 2.

General Features of the A-C Impedance at the Metal-Electrolyte Interface

A large number of experimental data have shown that the impedance of a metal-electrolyte interface at each d-c polarization point is frequency depen-

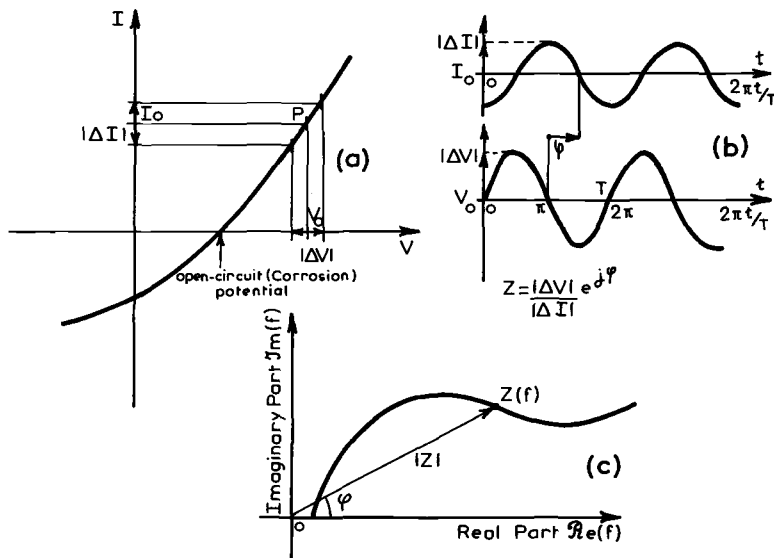


FIG. 1—(a) Steady-state current-voltage curve with superimposed voltage $|\Delta V|$ and current $|\Delta I|$ small-amplitude perturbations involved in the impedance measurement at the polarization point P ; (b) Current and voltage sine waves given in time-scale with phase shift ϕ ; and (c) Impedance Z plotted in a complex plane (impedance diagram) by its modulus $|Z|$ and phase shift ϕ , or real, Re , and imaginary part, Im . The parameter is the frequency of measuring sine wave f .

dent. The ohmic electrolyte resistance, R_e , is reached as the high-frequency limit (some tens of kilohertz). The low-frequency limit is $(R_e + R_p)$, R_p being the polarization resistance, that is, the slope dE/dI of the steady-state current-voltage curve $I(E)$ corrected for ohmic drop. Between these two limits the frequency dependence of Z , that is, its nonresistive behavior, stems from the same origin as the change of the current-voltage curve with the direction and rate of potential sweep under potentiodynamic conditions. There are two causes: (1) a capacitive contribution due to the electrochemical double layer, and (2) a so-called faradaic contribution due to the noninstantaneous change of some surface-state determining parameters (for example, surface concentrations of reactants, layer thickness and conductance, surface roughness, etc.) when they are driven by the measuring signal. For the practical purpose of concern in this paper, one can consider that capacitive and faradaic effects are additive, so that the general electrical circuit shown in Fig. 3a is valid.

In some cases of outstanding theoretical relevance the faradaic impedance, Z_F , is frequency independent and is represented by a purely resistive compo-

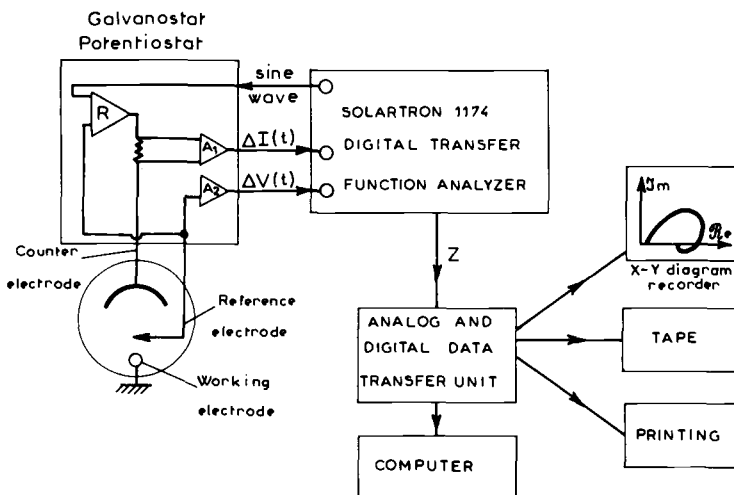


FIG. 2—Experimental setup of impedance measurement. Home-made regulation device, R , shown in a potentiostatic configuration. A_1 and A_2 are respectively current and voltage signal amplifiers, which allow us to subtract d-c components. Transfer function analyzer: Solartron Schlumberger 1174.

nent; the charge transfer resistance R_t is therefore equal to R_p . The corresponding complex impedance diagram is given in Fig. 3b. As will be established, such a situation is encountered in those cases where the conditions of applicability of the polarization resistance technique [7] are met: one-step, Tafelian, charge-transfer-controlled anodic and cathodic currents. In fact, the use of periodic polarizing signals for either evaluating R_p or measuring the impedance has shown that Z_F is hardly ever identical to a single resistance. In most cases, capacitances or selfinductances or both are reported in a frequency range between some tens of hertz and some millihertz.

Figure 4a gives as an example an impedance diagram measured for an iron sample at its free corrosion potential in a sulfuric acid solution. Z_F exhibits two inductances at low frequencies and can be correctly approximated by the equivalent circuit shown in Fig. 4b. Provided that the time constants $R_i C_{dl}$, L_1/ρ_1 and L_2/ρ_2 are not too close, the impedance diagram will consist of three well-resolved semicircles. A number of experiments performed on corroding electrodes have shown the existence of several faradaic time constants [1,2,9] except during the hydrogen evolution reaction [9,12]. It is worth noting that faradaic impedance may also arise from the relaxation of space distributed parameters, in which case no equivalent circuit can be found by using frequency-independent (R, C, L) components. This can be best illustrated by the well-known diffusion impedance [5].

Data available from impedance measurement include (in addition to R_p):

1. Electrolyte Resistance, R_e , of which contribution to the overall impedance, R_p included, must be corrected for in every poorly conducting medium (diluted solutions, natural waters, organic media, etc.).

2. Double-Layer Capacitance, C_{dl} , in the kilohertz range, tentatively correlated by some authors to the surface coverage by organic species and to their inhibiting efficiency [13,14].

3. Charge Transfer Resistance, R_t , and the frequency dependence of the faradaic impedance related to the reaction path, mass transfer, and elementary processes involved in the overall corrosion phenomenon. Among the most extensively studied processes are the inhibiting or passivating effects of neutral or ionic species originating from either the electrolyte or a preceding reaction step [2,3,15].

A-C Impedance and the Estimation of Corrosion Rate

Experimental and theoretical studies based on the faradaic impedance method can be regarded as pertaining predominantly to electrochemical kinetics problems. However, the matter is also of some relevance to the electrochemical techniques for estimating the corrosion rate.

If Z_F is significantly different from $R_t = R_p$ two questions arise:

1. From the experimental viewpoint, does the evaluation of R_p by means of periodic or time-dependent signals remain possible? Which quantity is actually measured?

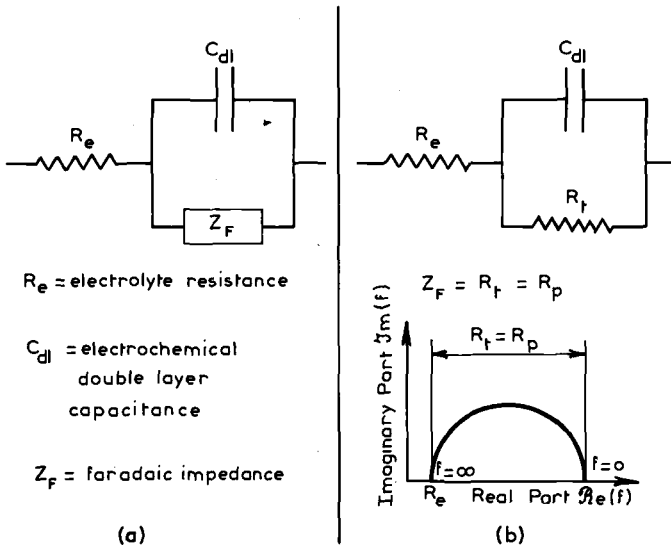


FIG. 3—(a) Schematic representation of interface impedance; and (b) The simplest case of (a) where Z_F is identical to the charge transfer resistance, R_t , and its impedance diagram.

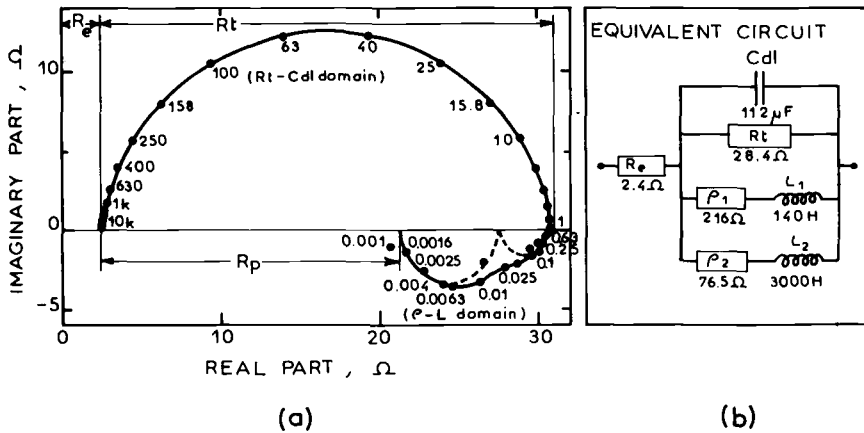


FIG. 4—(a) Impedance diagram of a corroding electrode: Holzer-type Fe in deoxygenated 1 M H_2SO_4 (rotating disk electrode: 0.2 cm^2 , rotation speed 1600 rpm); and (b) Equivalent circuit describing the impedance of the diagram (a).

2. From the theoretical viewpoint, does R_p remain correctly correlated to the rate of corrosion? Does the impedance give any quantity more relevant than R_p to corrosion rate estimation?

The former point can be fully answered in terms of circuit theory provided the impedance is known under the form of either equivalent circuit or tabulated values. The latter one can be dealt with to some extent by considering a general model for the faradaic impedance along with some practical applications.

A-C Impedance and Polarization Resistance Measurements by Means of Periodic Signals

By definition R_p must be measured at steady state, in fact, at vanishingly small frequencies. In practice, sinusoidal [16], triangular [10, 11], or square [17, 18] waves are used in a frequency domain between a fraction of hertz and some tens of hertz. At frequencies above some hertz the impedance lies in the $R_t - C_{dl}$ semicircle of the diagram. The impedance modulus increases as the frequency decreases, so that a relationship of the Stern type between corrosion rate and impedance should be itself frequency dependent [16, 19]. Obviously, extrapolating the $R_t - C_{dl}$ semicircle to zero frequency gives R_t . Experiments at frequencies far below 1 Hz are most often performed owing to commercially available "corrosion-rate meters" using triangular waves. In this frequency domain the faradaic contribution is determining and usually results in a distorted response with respect to that expected from a parallel $R_p - C_{dl}$ circuit. In spite of that, extrapolating to zero sweep rate allows an

estimation of R_p in those cases where Z_F obeys a simple circuit [10,11]. Unfortunately, the derivation of the response to a triangular wave in terms of impedance can no longer be handled if Z_F is represented by distributed time constants. This case is commonly encountered for passive surfaces; even though the impedance diagram is close to a semicircle, a parallel R - C description of the impedance may provide strongly frequency-dependent components (Fig. 5). Therefore a numerical procedure must be used to deduce the response to a triangular wave from the a-c impedance [20]. For the case shown in Fig. 5, the response to any signal takes so long that R_p can hardly be determined in practice. Estimating R_p when Z_F undergoes large changes in the low-frequency domain is a very difficult task, but in any case once Z is known every technique used for estimating R_p can be rigorously assessed. From a number of experimental data [16,19] it can be inferred that a-c impedance measurements in a medium range of frequency (for example, between 1 and 100 Hz) are likely to provide a resistance value as relevant as R_p to corrosion-rate studies and even easier to be measured.

Theoretical Background

As mentioned previously the assumptions on which the polarization resistance technique is based are not met when Z_F is frequency dependent. Particularly, concentration polarization or secondary electrochemical reactions or both must be occurring. With the usual notations, the overall current, I_S , can be considered as the sum of an anodic current, I_a , and a cathodic current, I_c , corresponding respectively to irreversible reactions of metal oxidation and electrolyte reduction.

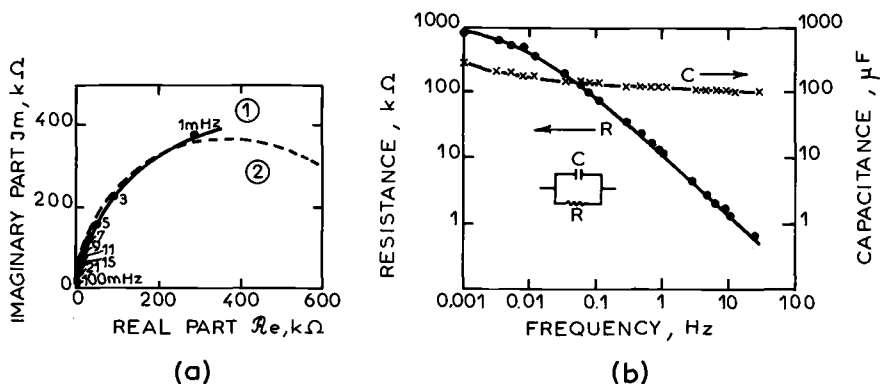


FIG. 5—(a) Impedance diagram of a corroding electrode in the passivity: Fe-17Cr-16Ni, 5.5Mo-2.7Cu-0.03C in air opened 1.8 M H_2SO_4 (stationary square electrode: 4.2 cm^2) (1) Experimental (2) Best-fitted half circle; and (b) R-C charge with respect to f when the measured impedance is assimilated to a parallel R-C circuit. Electrolyte resistance (ca 1 Ω) is negligibly small.

$$I_S = I_a + I_c \quad (3)$$

If I_a and I_c are assumed to be potential dependent and able to follow with no delay any variation of this potential, by differentiating Eq 3 we obtain

$$\frac{\Delta I_S}{\Delta E} = \frac{1}{Z_F} = \frac{\Delta I_a}{\Delta E} + \frac{\Delta I_c}{\Delta E} = \frac{1}{R_p} \quad (4)$$

where E is the electrode potential corrected for ohmic drop.

Moreover, if I_a and I_c obey Tafel laws of slopes b_a and b_c

$$I_a = I_a^\circ \exp \frac{2.303}{b_a} E \quad (5)$$

$$I_c = I_c^\circ \exp \frac{2.303}{-b_c} E$$

much as for a true equilibrium potential. The impedance is

$$\frac{1}{Z_F} = \frac{1}{R_p} = 2.303 \left[\frac{I_a}{b_a} - \frac{I_c}{b_c} \right] \quad (6)$$

and at a zero overall current, $I_a = -I_c = I_{\text{corr}}$, the relationship between impedance and corrosion current is

$$\frac{1}{R_p} = 2.303 I_{\text{corr}} \left(\frac{b_a + b_c}{b_a b_c} \right) \quad (7)$$

In this case polarization resistance is identical to the charge transfer resistance (Fig. 3), and the faradaic impedance is frequency independent. Basically, the frequency dependence of Z_F can be expressed by assuming that I_a or I_c or both are dependent not only on E , but also on one (or several) parameter which does not instantaneously follow E . For example, if only one parameter p_a is involved in the anodic component

$$\frac{\Delta I_S}{\Delta E} = \frac{1}{Z_F} = \left(\frac{\Delta I_a}{\Delta E} \right)_{p_a} + \left(\frac{\Delta I_c}{\Delta E} \right)_{p_a} + \left(\frac{\Delta I_a}{\Delta p_a} \right) \frac{\Delta p_a}{\Delta E} \quad (8)$$

In contrast with Eq 4, only the first two terms of the right hand side of Eq 8 give a frequency-independent contribution to Z_F . The third term is a function of the dynamic behavior of p_a versus E that is time dependent and controlled by an equation of the general form

$$\frac{d\Delta p_a}{dt} = \lambda_a \Delta p_a + \mu_a \Delta E \quad (9)$$

if ΔE and consequently Δp_a are subjected to sinusoidal time variation of small amplitude. Equation 9 gives the frequency behavior of Δp_a

$$2\pi j f \Delta p_a = \lambda_a \Delta p_a + \mu_a \Delta E \quad (10)$$

or

$$\frac{\Delta p_a(f)}{\Delta E} = \frac{\mu_a}{2\pi j f - \lambda_a} \quad (11)$$

At high frequencies p_a is frozen; that is, it can no longer follow electrode potential in the way it does at sufficiently low frequencies when the steady-state is achieved:

$$f \rightarrow 0 \quad \frac{\Delta p_a(f)}{\Delta E} \rightarrow \left(\frac{\Delta p_a}{\Delta E} \right)_{st.} = \frac{-\mu_a}{\lambda_a} \quad (12)$$

Thus Eq 8 can be split into two terms:

$$\frac{1}{Z_F} = \frac{1}{R_t} + \frac{\Delta I_a}{\Delta p_a} \frac{\mu_a}{2\pi j f - \lambda_a} \quad (13)$$

Equation 13 accounts for the general features of the frequency dependence of Z_F just stated, namely

$$f \rightarrow \infty \quad Z_F = R_t \quad (14)$$

$$f \rightarrow 0 \quad \frac{1}{Z_F} = \frac{1}{R_t} + \frac{\Delta I_a}{\Delta p_a} \left(\frac{\Delta p_a}{\Delta E} \right)_{st.} = \frac{1}{R_p}$$

According to Eq 11, Z_F is frequency dependent at finite-frequency values. Consequently, exploring a narrow-potential domain around the corrosion potential does not eliminate, as is sometimes believed, the complications arising from surface changes with potential. From the viewpoint of the estimation of the corrosion rate, it is worth considering the derivation given previously in a number of particular cases. It can be shown that Eq 8 is able to provide a relationship similar to the Stern's formula, in which R_t is concerned instead of R_p [21]. Obviously, both formulas tend to become identical

in those cases where the Stern's derivation is fully valid, so that $R_t \rightarrow R_p$. Table 1 gives under different assumptions for the anodic and cathodic reactions the relationships between R_p and I_{corr} on the one side, R_t and I_{corr} on the other side. It is seen that I_{corr} can be related to R_t through a Stern-type relation in two cases of interest (partial diffusion control and multistep electron transfer) where the usual polarization resistance technique will fail. The only case where R_p should be preferably used is for passive electrodes.

Much as for R_p the value of the technique is primarily to indicate changes of corrosion rate with respect to variables in the corrosive environment. Values of the Tafel slopes were successfully used for the corrosion of iron in acid media [21] where both anodic and cathodic reactions took place through a two-consecutive-step reaction [22]. But most often the Tafel slopes of the steps that are not rate determining cannot be obtained easily, and a calibration procedure (based, for instance, on weight loss data) must be used. The experimental data presented next illustrate the relevance of a-c impedance measurement to corrosion-rate estimation under various conditions.

Experimental Data

Active Corrosion of Iron in an Aerated 0.5 M Sulfuric Acid (H_2SO_4) Solution—Anodic and cathodic reactions both occur in two consecutive irreversible steps. Faradaic impedance measurements provided the values of $\sum 1/b_a^i$ and $\sum 1/b_c^i$ which are involved in the relation between R_t and I_{corr} (right-hand column of Table 1). A good agreement was found between weight-loss experiments and the absolute value of the corrosion rate deduced from R_t for either a high purity (Johnson-Matthey) iron ($0.8 \text{ mg cm}^{-2} \text{ h}^{-1}$) or a pure iron of industrial origin (Holzer type) ($2 \text{ mg cm}^{-2} \text{ h}^{-1}$) [21].

A correct estimation of the relative changes of corrosion rate is also of practical interest. Corrosion-rate estimations based on R_t , R_p , and C_d measurements were compared to weight-loss data for a Holzer-type iron in $0.5 \text{ M } H_2SO_4$ as a function of an inhibitor (propargylic alcohol) concentration. Figure 6a shows the complex impedance diagram at the corrosion potential for an inhibitor concentration of 2 mM . Much as in the case of uninhibited iron corrosion (Fig. 4a) two inductances are found at low frequencies. They were proved to originate from the potential dependence of the surface coverages by the inhibiting species (hydrogen or hydrogen bonded organic compound) at lower frequencies and by the anodic intermediate species $FeOH$ at higher frequencies [13,23]. Relative corrosion rates with respect to the uninhibited conditions are expressed in terms of the dimensionless inhibiting efficiency

$$H = \frac{100 (x_0 - x)}{x_0} \quad (15)$$

TABLE 1—Theoretical relationships under various anodic and cathodic kinetics between corrosion current and polarization and charge transfer resistances.

Kinetics Control of		Relation to Corrosion Current I_{corr}	
Anodic Reaction	Cathodic Reaction	Polarization Resistance, R_p	Charge Transfer Resistance, R_t
one step, Tafelian, electron transfer	one step, Tafelian, electron transfer	$\frac{b_a b_c}{2.303(b_a + b_c)I_{corr}}$	$\frac{b_a b_c}{2.303(b_a + b_c)I_{corr}}$
one step, Tafelian, electron transfer	purely diffusional	$\frac{b_a}{2.303 I_{corr}}$	$\frac{b_a b_c}{2.303(b_a + b_c)I_{corr}}$
one step, Tafelian, electron transfer	mixed control, partially diffusional	complicated equation (depends upon the degree of control by diffusion)	$\frac{b_a b_c}{2.303(b_a + b_c)I_{corr}}$
n_a irreversible, Tafelian, consecutive steps (b_a^i)	n_c irreversible, Tafelian, consecutive steps (b_c^j)	complicated equation (depends upon the whole set of rate constants)	$\frac{1}{2.303 \left\{ \frac{1}{n_a} \sum_{i=1}^{n_a} \frac{1}{b_a^i} + \frac{1}{n_c} \sum_{j=1}^{n_c} \frac{1}{b_c^j} \right\} I_{corr}}$
passive dissolution	one irreversible, Tafelian transfer on the passive area	$\frac{b_c}{2.303 I_{corr}}$	complicated equation (depends upon the kinetics of dissolution and passivation)

where x_0 is the corrosion rate in the absence of inhibitor, and x is the corrosion rate in the presence of inhibitor. x is either measured directly by weight loss (H_{dir}) or calculated from R_i or R_p , which are assumed inversely proportional to x . According to Ref 13, H_{Cdl} depends on a standardization coefficient K_1

$$HC_{dl} = 100 K_1 \left(\frac{C_{dlo} - C_{dl}}{C_{dlo}} \right) \quad (16)$$

K_1 is chosen so that $H_{Cdl} = H_{dir}$ at 0.5 mM of propargylic alcohol.

As shown in Fig. 6b, the values of R_i are in agreement with those of H_{dir} , except at very high concentrations when indications become pessimistic. The values of H_{R_p} can be considered as acceptable, but beyond an inhibitor concentration of 2 mM, they predict a negative inhibition, that is, an acceleration of the corrosion, in complete disagreement with direct measurements. According to the theoretical derivation given previously, this discrepancy is related to the increasing size of the low-frequency inductive arc as the inhibitor concentration is increased, which results in a corresponding difference between R_p and R_i .

The values of H_{Cdl} show the same type of error as R_p at high inhibitor concentrations.

Corrosion of Iron Coated with Epoxy Paint—Faradaic impedance measurements on painted iron (Fig. 7a) show that the metal is corroded in

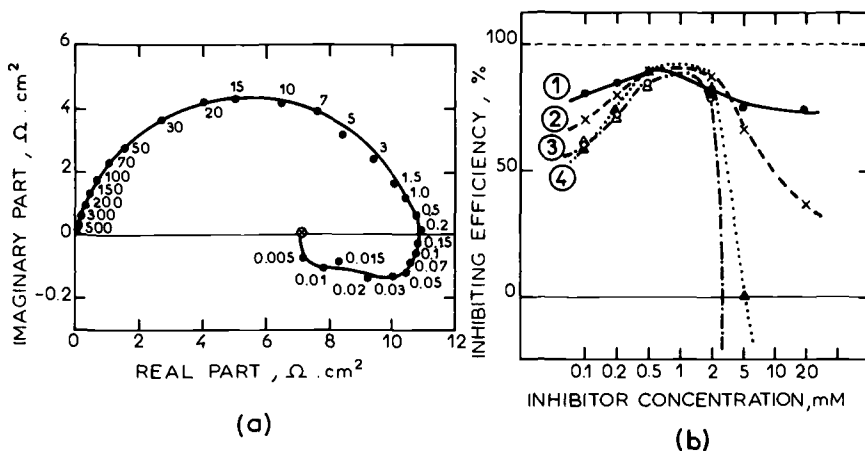


FIG. 6—(a) Impedance diagram of corroding electrode: Holzer-type Fe electrode in air opened 0.5 M H_2SO_4 + 2 mM propargylic alcohol; and (b) Inhibiting efficiency (see text), with respect to the inhibitor (propargylic alcohol) concentration, determined by (1) weight loss, (2) R_i measurements, (3) R_p measurements and (4) C_{dl} measurements. Negative inhibiting efficiency indicates the acceleration of corrosion.

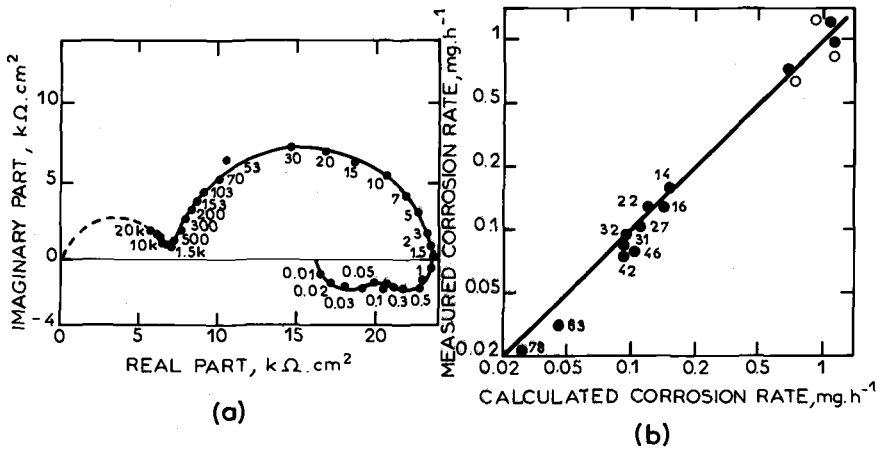


FIG. 7—(a) Impedance diagram of a corroding electrode. Armco iron ($S = 60 \text{ cm}^2$) covered by $40\text{-}\mu\text{m}$ epoxy paint (ICI 5802022). Impedance given for unit surface area. High-frequency arc ($f > 1.5 \text{ kHz}$) is due to the presence of paint film itself and the impedance at $f < 1.5 \text{ kHz}$ is similar to the corrosion of the naked iron (see Fig. 4); and (b) Estimated corrosion rate by R_t measurement compared to the results of the weight-loss measurement. Iron sheet (Goodfellow) covered by various thickness of epoxy paint film; parameter is film thickness in μm . 0 corresponds to the naked specimen.

the same way as when unprotected, but on a much reduced area, at the place where the paint layer presents pore-like flaws [24], whereas the isolating part of the paint layer gives rise to a characteristic capacitive behavior at high frequencies (Fig. 7a).

Consequently, R_t is expected to be successfully applied to corrosion-rate estimation of painted iron. Corrosion rates calculated from R_t data were compared to weight loss for a number of specimens protected with epoxy paint layers from 0 to $80 \mu\text{m}$ in thickness. Coated thin foils of high-purity Goodfellow iron were exposed to attack in a $0.5 \text{ M H}_2\text{SO}_4$ solution for two to four days. The rate of corrosion increased continuously during the exposure, and R_t was measured as a function of time. The average calculated corrosion rate was compared to weight loss at different layer thicknesses. A very good correlation was found (the thicker the layer, the better the protection) (Fig. 7b).

Anodized Aluminium Alloys—The resistance against corrosion of aluminum base alloys protected by an anodic oxide layer is usually evaluated by a salt-spray test that needs a long time exposure. Alternating-current impedance can constitute a rapid technique with the same degree of reliability [25]. The anodized sample to be tested is immersed in a 3 percent sodium chloride (NaCl) solution buffered at pH 4 by a hydrogen chloride (HCl) + 0.02 M sodium acetate solution deoxygenated by nitrogen bubbling. The impedance is measured at its free corrosion potential. Figure 8a shows the im-

pedance diagram. Two capacitive contributions can be resolved when the high-frequency behavior is enlarged (Fig. 8b). This shorter time constant very likely arises from the dielectric property of the oxide layer; a correlation between corrosion susceptibility and impedance behavior must be reasonably expected in the low-frequency domain. In fact, a good correlation was found between the low-frequency resistance R_{LF} (Fig. 8a) and the exposure time after which the first pit opened. The impedance technique being nondestructive, a-c impedance and salt-spray tests can be applied successively to the same sample so that a highly significant comparison can be performed. No faradaic model of corrosion is available in the case of aluminum, and R_{LF} can be hardly dealt with in terms of either R_i or R_p . Therefore, the value of the test must be founded on a large number of experiments. Figure 8c gives as an example the selection made among 83 samples from the same batch on the basis of a-c measurement or salt-spray test. A "yes" to "no" transition at a threshold value of $R_{LF} = 5.5 \text{ M}\Omega$ can be considered as correctly equivalent to the occurrence of at least one pit after a 300-h exposure to the spray. A similar correlation was found between both techniques for different compositions of aluminum alloys and oxidizing baths.

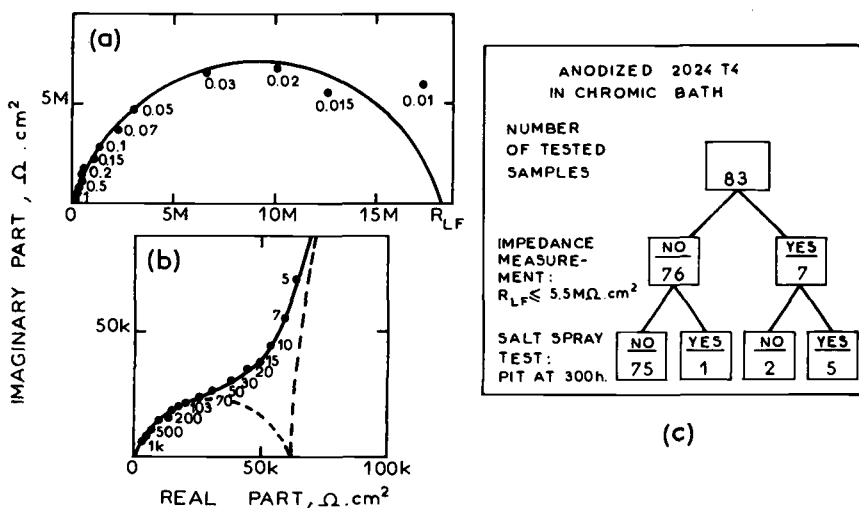


FIG. 8—(a) Impedance diagram of a corroding electrode: 2024-T4 alloy anodized in chromic bath ($S = 50 \text{ cm}^2$) in $0.18 \text{ M NaCl} + 0.0115 \text{ M CH}_3\text{COOH} + 0.02 \text{ M CH}_3\text{COONH}_4$. Impedance given for a unit surface area; (b) Enlarged diagram in the high-frequency range of the diagram (a); and (c) Comparison of impedance measurement and salt-spray test. "NO" corresponds to the samples correctly protected. The threshold value $5.5 \text{ M}\Omega \cdot \text{cm}^2$ is empirically determined.

Conclusion

The degree of complexity of a corroding process can be evaluated from the frequency dependence of the impedance over a large frequency domain. In those cases where the impedance is significantly different from a parallel resistance-capacitance circuit, the applicability of the resistance polarization technique is doubtful, and the charge transfer resistance, R_t , can be advantageously used instead of R_p in a Stern-type equation. This is illustrated by comparing the corrosion rate deduced from R_t measurement to the weight loss for uninhibited, inhibited, and painted iron. In the case of anodized aluminum alloys the susceptibility to localized pitting corrosion under a long exposure to salt-spray can also be evaluated by a rapid test lying on a-c impedance measurements. The technique should deserve a growing interest with future development of low-cost impedance-based corrosion-rate meters.³

References

- [1] Epelboin, I. and Keddam, M., *Electrochimica Acta*, Vol. 17, 1972, p. 177.
- [2] Armstrong, R. D., Firman, R. E., and Thirsk, H. R., *Faraday Discussions of the Chemical Society* n°56, 1973, pp. 244-263.
- [3] Epelboin, I., Keddam, M., and Lestrade, J. C., *Faraday Discussions of the Chemical Society* n°56, 1973, pp. 264-275.
- [4] Mansfeld, F. in *Advances in Corrosion Science and Technology*, Plenum Press, New York, Vol. 6, 1976, pp. 163-262.
- [5] Grahame, D. C., *Journal of the Electrochemical Society*, Vol. 99, 1962, p. 370C.
- [6] Epelboin, I., Gabrielli, C., Keddam, M., Lestrade, J. C., and Takenouti, H., *Journal of the Electrochemical Society*, Vol. 119, 1972, p. 1632.
- [7] Gabrielli, C. and Keddam, M., *Electrochimica Acta*, Vol. 19, 1974, pp. 355-362.
- [8] Boyer, M. L., Epelboin, I., and Keddam, M., *Electrochimica Acta*, Vol. 11, 1966, p. 221.
- [9] Epelboin, I., Keddam, M., and Morel, P., *Third International Meeting on Metallic Corrosion*, Moscow, 1960, English edition, Svets-Zeitlinger, Amsterdam, 1963, Vol. 1, p. 110.
- [10] Macdonald, D. D., *Journal of the Electrochemical Society*, Vol. 125, 1978, pp. 1443-1449.
- [11] Macdonald, D. D., *Journal of the Electrochemical Society*, Vol. 125, 1978, pp. 1977-1981.
- [12] Epelboin, I., Morel, P., and Takenouti, H., *Journal of the Electrochemical Society*, Vol. 118, 1971, p. 1282.
- [13] Murakawa, T., Nagaura, S., and Hackerman, N., *Corrosion Science*, Vol. 7, 1967, p. 79.
- [14] Dus, B. and Szklarska-Smialowska, Z., *Corrosion*, National Association of Corrosion Engineers, Vol. 25, 1969, p. 69.
- [15] Conway, B. E., *Journal of the Electrochemical Society*, Vol. 124, 1977, pp. 410C-421C.
- [16] Schwenk, W. and Buhler, H. E., *Corrosion Science*, Vol. 3, 1963, pp. 261-272.
- [17] Rowlands, J. C. and Bentley, M. N., *British Corrosion Journal*, Vol. 2, 1967, pp. 92-34.
- [18] Neufeld, P. and Queenan, E. D., *British Corrosion Journal*, Vol. 5, 1970, pp. 72.
- [19] Pražák, M. and Bartoň, K., *Corrosion Science*, Vol. 7, 1967, pp. 159-163.
- [20] Gabrielli, C., Keddam, M., Takenouti, H., Vu Quang Kinh, and Bourelrier, F., *Electrochimica Acta*, Vol. 24, 1979, pp. 61-65.
- [21] Epelboin, I., Keddam, M., and Takenouti, H., *Journal of Applied Electrochemistry*, Vol. 2, 1972, pp. 71-79.

³French Patent No. 78-20166.

- [22] Epelboin, I. and Keddam, M., *Journal of the Electrochemical Society*, Vol. 117, 1970, p. 1052.
- [23] Epelboin, I., Keddam, M., and Takenouti, H., *Third European Symposium on Corrosion Inhibitors*, Ferrara, Italy, 1970, Vol. 5, No. 5, p. 237.
- [24] Beaunier, L., Epelboin, I., Lestrade, J. C., and Takenouti, H., *Surface Technology*, Vol. 4, 1976, pp. 237-254.
- [25] Bodu, J. J., Brunin, M., Epelboin, I., Keddam, M., Sertour, G., and Takenouti, H., *Alluminio*, Vol. 46, 1977, pp. 277-280.

S. Haruyama¹ and T. Tsuru¹

A Corrosion Monitor Based on Impedance Method

REFERENCE: Haruyama, S. and Tsuru, T., "A Corrosion Monitor Based on Impedance Method," *Electrochemical Corrosion Testing, ASTM STP 727*, Florian Mansfeld and Ugo Bertocci, Eds., American Society for Testing and Materials, 1981, pp. 167-186.

ABSTRACT: Theoretical and experimental studies were performed on the impedance characteristics of corroding metal with the aid of a new a-c corrosion monitor. According to the theory of impedance of a mixed potential electrode, the subtraction of the impedance at a high frequency from that at a low frequency yields, in most cases, transfer resistance that is readily reduced to the corrosion rate of the electrode (if an appropriate selection of the two frequencies has been made). By using a superimposed signal of two a-c voltages of 10 kHz and 0.01 Hz, the a-c corrosion monitor was designed to yield either transfer resistance or corrosion current on a recorder in logarithmic scale. The monitor permitted the measurement of the corrosion rate in less-conductive environments, such as tap water, distilled water, and soil. Initiation of localized corrosion was also detected in most cases by a sharp increase in corrosion current. The corrosion currents obtained with the a-c corrosion monitor and by the weight-loss measurement gave a good correlation on various metals under various environments, which cover corrosion rates of 15 to 0.0007 mm/year.

KEY WORDS: electrochemistry, corrosion, corrosion monitor, interfacial impedance, impedance diagram, local corrosion, pitting

Mixed potential theory introduced by Wagner and Traud [1]² forms the basis for electrochemical methods used to determine corrosion rate. These are the Tafel extrapolation, the polarization resistance method [2,3], and the various nonstationary methods developed recently. Although the measurement can be performed with high accuracy, there are numerous restrictions that must be removed before the Tafel extrapolation method can be successfully used. The disadvantages of the Tafel extrapolation method can be largely overcome by using the polarization resistance method, and numerous works have been devoted to the application of this method to corrosion monitoring. However, the refinement of the polarization resistance method by Oldham and Mansfeld [4,5], Callow et al [6], and Nagayama [7] has not produced any dramatic improvements on the reliability and feasibility of the

¹Tokyo Institute of Technology, Faculty of Engineering, Tokyo, Japan.

²The italic numbers in brackets refer to the list of references appended to this paper.

method as a corrosion monitor. The method encountered great difficulty in measuring the corrosion rate in less-conductive environments, although the problem can be avoided to some extent by using the two-electrodes probe [8] instead of the three-electrodes probe. An ambiguous concept of stationary measurement and the resultant poor reproducibility necessarily limit the reliability of the polarization resistance method. Recently, in order to solve these problems, various nonstationary electrochemical methods have been applied to the monitoring of corrosion rate. These are the potential pulse [9], current pulse [7,10], differential pulse [11], coulometric pulse [12], and impedance [13] methods. The impedance method seems to be the most promising from the viewpoint of automatic corrosion monitoring.

Application of the impedance method to the measurement of corrosion rate was first made by Epelboin et al [13], and the mathematical analysis of the impedance of mixed potential electrodes was presented by Haruyama [14].

The purpose of this paper is to establish the impedance characteristics of corroding metal and to study the performance of the automatic a-c corrosion monitor designed and constructed based on the impedance method.

Impedance of Metal at Corrosion Potential

Impedance characteristics of metal/solution interface can be represented by the equivalent circuit shown in Fig. 1, where R_{sol} , C_{dl} , and $G_f(j\omega)$ indicate solution resistance, interfacial capacitance, and faradaic impedance, respectively, ω is the angular frequency ($\omega = 2\pi f$, f is frequency), and $j = \sqrt{-1}$. The total impedance, $Z(j\omega)$, of the equivalent circuit can be written as a complex function

$$Z(j\omega) = R_{sol} + \frac{G_f(j\omega)}{1 + j\omega C_{dl} G_f(j\omega)} \quad (1)$$

The faradaic impedance, $G_f(j\omega)$, in Eq 1 was already solved for various types of mixed potential systems [14,15].

When both the anodic and cathodic reaction concerned with a mixed potential are controlled by charge transfer, $G_f(j\omega)$ is simply written as

$$G_f(j\omega) = RT / F[(1 - \alpha_c)n_c + \alpha_a n_a] \cdot i_{corr} = K / i_{corr} = R_{corr} \quad (2)$$

where

- F = Faraday constant,
- α = transfer coefficient,
- n = number of charge,
- K = a constant,
- i_{corr} = corrosion current,

R_{corr} = charge transfer component of polarization resistance, and a and c = the partial anodic and cathodic reaction, respectively.

Hence, the cell impedance is given by

$$Z(j\omega) = R_{\text{sol}} + \frac{R_{\text{corr}}}{1 + j\omega C_{\text{dl}} R_{\text{corr}}} \tag{3}$$

The frequency dependency of Eq 3 is schematically shown as Curve 1 in Fig. 1. Although the complex plane plot of interfacial impedance may be rather popular among electrochemists, it is less convenient for discussing the impedance as a function of frequency. The impedance diagram of Fig. 1 is made by plotting the phase shift between a-c potential and current, and the logarithm of the absolute value of impedance against the logarithm of frequency. This plot is similar to the Bode diagram that is commonly used in the field of automatic control and electronics. The diagram of the absolute value consists of two impedance arrests on either side of the frequency axis, and a diagonal straight line with the slope of -1 at intermediate frequencies.

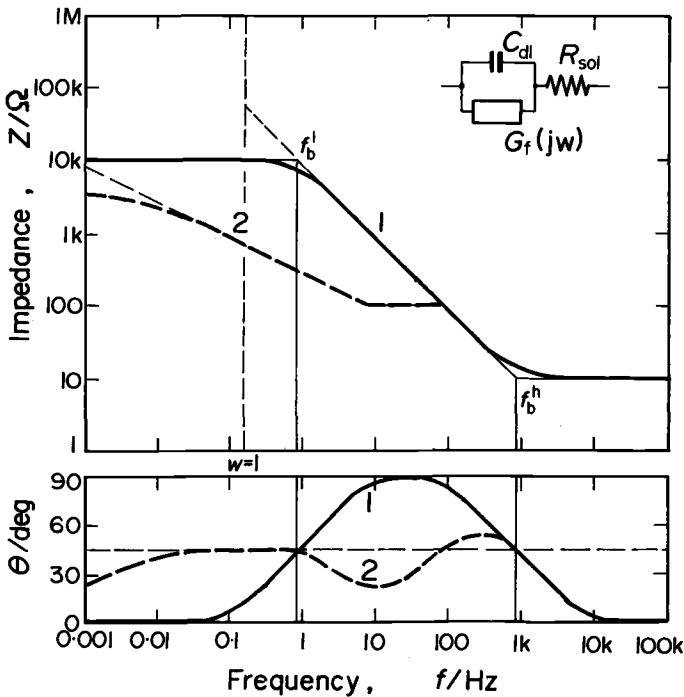


FIG. 1—Equivalent circuit and impedance diagrams of metal/electrolyte interface; (1) transfer control, and (2) Warburg impedance.

The impedance arrests of high frequencies, R_∞ , and of low frequencies, R_0 , correspond to R_{sol} and $(R_{\text{sol}} + R_{\text{corr}})$ respectively. Hence R_{corr} is given by

$$R_{\text{corr}} = R_0 - R_\infty \quad (4)$$

Corresponding to the behavior of the absolute value of impedance, the phase shift between potential and current is reduced to zero on either side of the frequency axis and may increase up to 90 deg at intermediate frequencies. The frequencies at the two break points on the absolute value diagram, where the phase shifts are 45 deg, are written in terms of R_{corr} , R_{sol} , and C_{dl} . Thus

$$2\pi f_b^h = 1/R_{\text{sol}}C_{dl}, \quad 2\pi f_b^l = 1/(R_{\text{sol}} + R_{\text{corr}})C_{dl} \quad (5)$$

where f_b^h and f_b^l indicate the break point frequencies with higher and lower frequency, respectively. It is readily seen by simple calculation of the a-c circuit that the absolute value of impedance at f_b^h is 42 percent larger than R_∞ , and that at f_b^l is 29 percent less than R_0 . Since the change in phase shift is sensitive to the frequencies, especially in the vicinity of the break point, it is sometimes easier to determine f_b^h and f_b^l from the phase shift of 45 deg. The value of C_{dl} can be obtained either from the break point frequency by using Eq 5 or from the absolute value of impedance at $\omega = 1$, which is extrapolated from the diagonal line of the diagram. It is well known that a complex plane representation of Eq 3, the Cole-Cole plot, yields a semicircle. In this plot the corrosion rate is estimated from the diameter of the semicircle, as has been pointed out by Epelboin et al [13] and Haruyama [14].

When the cathodic reaction is controlled by a diffusion-limiting current at corrosion potential, the cell impedance is also written as Eq 3, whereas $G_f(j\omega)$ is given by

$$G_f(j\omega) = RT / F\alpha_a n_a i_{\text{corr}} = K' / i_{\text{corr}} = R_{\text{corr}} \quad (6)$$

In the derivation of Eq 6 it was assumed that the impedance of a process controlled by diffusion-limiting current was infinitely large [15]. Since this assumption may not be true in the case of a-c polarization, however, it seems likely that the value of K' in Eq 6 approaches that of K in Eq 2.

The corrosion rate of metal in passive state is supposed to be controlled by the rate of dissolution of passive film, without depending on potential. Therefore the stationary polarization curve of passive metal seems to be similar to that found under diffusion control. As has been reported elsewhere, however, the impedance measurements of iron [16,17] and iron oxides [18,19] in the passive state exhibited an impedance diagram similar to Curve 1 of Fig. 1, although the break point appeared at very low frequency because of low corrosion rate. The dissolution rate, namely the stationary current in

passive state, was well estimated from $(R_0 - R_\infty)$ by assuming charge transfer control.

When a-c signal participates to the thickening and thinning of the diffusion layer, then the cell impedance is written as [14]

$$Z(j\omega) = R_{\text{sol}} + \frac{R_{\text{corr}} + A/\sqrt{\omega} - jA/\sqrt{\omega}}{1 + j\omega C_{\text{dl}}(R_{\text{corr}} + A/\sqrt{\omega}) + C_{\text{dl}}A/\sqrt{\omega}} \quad (7)$$

$$A = i_{\text{corr}}/\sqrt{2D_o n_c [\bar{O}]F} \quad (7')$$

where $[\bar{O}]$ and D_o indicate the stationary surface concentration and the diffusion coefficient of oxidant, respectively. The impedance diagram of Eq 7 is schematically shown as Curve 2 in Fig. 1. The impedance arrest at high frequencies, where the phase shift is zero, corresponds to R_{sol} . At low frequencies, however, the impedance diagram exhibits a straight line with the slope of -0.5 , where the phase shift maintains 45 deg. This behavior is characteristic of the Warburg impedance. In this case R_{corr} corresponds to the impedance arrest appearing at the intermediate frequencies where the phase shift is below 45 deg. The Cole-Cole plot of Eq 7 yields a semicircle at high frequencies and a straight line with the slope of 1 at low frequencies. In this plot the corrosion rate can be estimated from the diameter of the semicircle [14]. It was also pointed out by Haruyama [14], however, that the Warburg impedance of this type occurs only when both the anodic and cathodic reactions are controlled by diffusion. Therefore, as will be stated later, the Warburg impedance was rarely observed in corrosion systems.

Impedance Diagram of Corroding Iron

Experimental Method

Specimens were cut from a pure iron sheet 0.2 mm thick. After soldering a copper lead wire, specimens were molded in an epoxy resin, except for a flat plane of 0.1 cm² which served as electrode. The electrodes were then polished by an emery paper (#1500) until the surface showed a mirror brightness. Two similar electrodes were placed facing each other with a gap of 0.2 cm in an electrolytic cell using an electrode holder. The impedance measurements were made on the two-electrode system.

Sinusoidal voltage of ± 5 mV was supplied across the two electrodes by a function generator. The circuit was arranged so that the sinusoidal components of both the voltage and current were recorded on a two-channel storage oscilloscope. The absolute value of impedance was calculated from the ratio of the stationary amplitudes of voltage and current. The phase shift was read

directly from the traces of the sinusoidal waves. Measurements were performed in the frequency range between 10 kHz and 0.001 Hz. The error involved in the impedance measurement was ± 5 percent for phase shift and ± 2 percent for absolute value. A similar impedance measurement can be made on a three-electrode system using a potentiostat [17].

Experimental Results

Examples of the impedance diagrams of iron in acidic solutions are shown as curve 1, 2 and 3 in Fig. 2. The shapes of all the curves are quite similar to that of Curve 1 in Fig. 1. Most corroding specimens exhibited this type of impedance diagram. As is shown in Fig. 2, the impedance diagram of iron in sulfuric acid changes greatly with time. According to Eqs 3 and 4, the decrease of R_0 with time indicates that the corrosion rate becomes progressively greater. On the other hand, the decrease in the impedance on the diagonal line implies that the interfacial capacitance of iron increases with time; namely, the capacitance of corroding iron increased from 85.5 to 2490 $\mu\text{F}/\text{cm}^2$ in 70 h. Such an extraordinary large capacitance of iron was also observed by the coulostatic method [12] under a similar condition. The capacitance of iron in hydrochloric acid (HCl) solution was 75.8 $\mu\text{F}/\text{cm}^2$ regardless of time. The diagram of iron in aerated 0.1 *N* potassium chloride

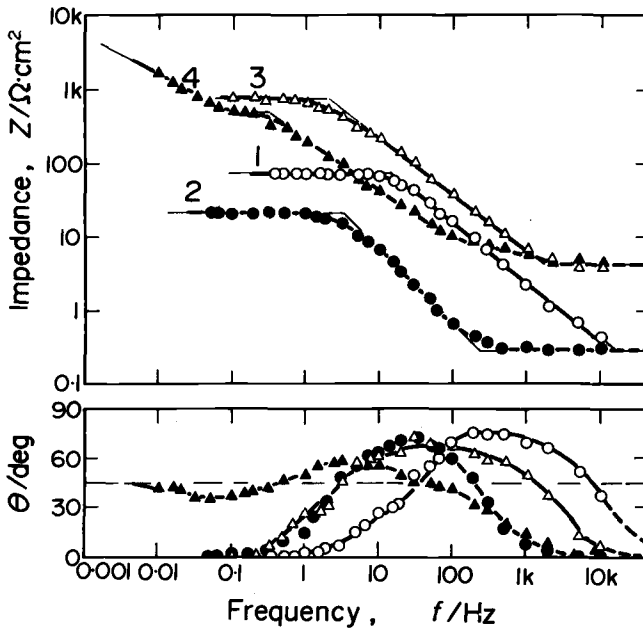


FIG. 2—Impedance diagrams of iron in various solutions: (1) 2 *N* H_2SO_4 (2 h after immersion), (2) 2 *N* H_2SO_4 (70 h after immersion), (3) 0.1 *N* HCl, and (4) 0.1 *N* KCl.

(KCl) is shown as Curve 4 in Fig. 2. The diagram exhibits a straight line with a slope of -0.5 at low frequencies where the phase shift maintains 45 deg. The behavior is characteristic of the Warburg impedance, as indicated in Fig. 1. The corrosion rate of iron in neutral solution is usually controlled by a diffusion-limited cathodic reduction of oxygen, which yields the impedance diagram similar to Curve 1 in Fig. 1. When the cathodic reduction was poorly controlled by the diffusion of oxygen, however, the Warburg impedance appeared at low frequencies. Curve 4 in Fig. 2 is one of the few examples in this study that exhibited the Warburg impedance. In this case the corrosion rate can be estimated from the impedance arrest at the intermediate frequencies where the phase shift is below 45 deg.

Figure 3 shows the impedance diagrams of iron in acidic solutions in the presence of propargyl alcohol. By comparing Fig. 2 to Fig. 3, it can be noted that the diagram in HCl solution is not substantially affected by the addition of propargyl alcohol. On the other hand, the diagram in sulfuric acid is greatly affected by the presence of the inhibitor, especially at low frequencies; namely, the absolute value of impedance decreases with decreasing frequency at the low-frequency region where the phase shift maintains negative

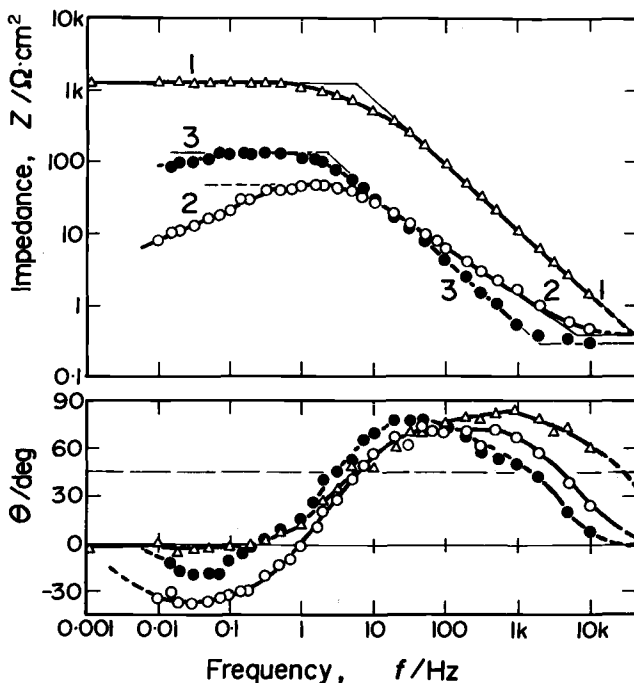


FIG. 3—Impedance diagrams of iron in acidic solutions containing propargyl alcohol 5 mM/L; (1) 12 percent HCl, (2) 2 N H_2SO_4 (0.5 after immersion), and (3) 2 N H_2SO_4 (18 h after immersion).

value. This behavior is characteristic of an inductance that exhibits a negative loop on the complex plane diagram. This inductive behavior was first found by Epelboin et al [13] in similar conditions. Although the mechanism of the inductive behavior is still not elucidated completely, the corrosion rate seems to correspond to the impedance maximum where the phase shift intersects the horizontal axis. As can be seen in Fig. 3, however, the inductive behavior diminished with time and finally faded away, accompanied by the increase in impedance. It should be noted that, among the inhibitors that were tested, only propargyl alcohol exhibited a distinct inductive behavior [20].

Summary of Impedance Measurements on Corroding Iron

As stated in the preceding section, the general features of the impedance diagram of corroding iron were well consistent with those expected from theory. Similar impedance measurements have been made on various metals under various environments; results showed that most of the corroding systems exhibited the impedance diagram corresponding to Curve 1 in Fig. 1. The Warburg impedance and inductive impedance were rarely observed (as two exceptional cases throughout the experiments). Although the corrosion rates were estimated from both the impedance diagram and the weight-loss measurement, the agreement between the two corrosion rates was sometimes equivocal depending on the conditions. Since impedance measurement over a wide range of frequencies takes a long time, it is somewhat difficult to identify when the corrosion rate has been measured. Since the corrosion rate usually changes with time, it is not reasonable to evaluate the applicability of the impedance method simply in comparison with the weight-loss measurement. While the impedance method has the advantage of separating R_{corr} from the total resistance, the measurement is too time consuming to be suited for corrosion monitoring in practice. In order to overcome this disadvantage, an automatic corrosion monitor has been designed and constructed based on the impedance method.

Automatic A-C Corrosion Monitor

Design and Function

It has been stated in the preceding sections that the corrosion rate can be estimated, in most cases, from the difference between R_0 and R_∞ . Therefore it should be possible to monitor the corrosion rate of metal only by two frequencies, if the frequencies of two a-c signals were favorably chosen. The automatic a-c corrosion monitor has been devised on this principle [21].

The following items were considered in designing the monitor:

1. Direct reading and recording of corrosion resistance or corrosion rate.
2. Facility in operation by eliminating any adjustment or calibration.

3. Toughness against external noise and the possibility of extending a long lead wire to samples.
4. Feasibility of monitoring the corrosion rates of a number of samples at a regular time interval.
5. Coverage of a wide range of corrosion rates.
6. Feasibility of monitoring the corrosion rate in less-conductive environments.

The selection of the frequencies of the two a-c signals is closely related to the range of corrosion rate, interfacial capacitance, and electric resistance of environment that should be covered by the monitor. The relation between these variables and the impedance diagram is shown in Fig. 4. Since the absolute values of impedance at f_b^l and f_b^h are only 29 percent less and 42 percent larger than R_0 and R_∞ , respectively, the following discussion on the selection of the signal frequencies will be made for simplicity on the basis of the frequencies at break points. The solid diagonal line in Fig. 4 indicates the impedance diagram of the capacitance of $20 \mu\text{F}$. When R_{sol} and $(R_{sol} + R_{corr})$ of a corroding metal are 10Ω and $10 \text{ k}\Omega$, respectively, the break points appear at 0.796 and 796 Hz , respectively (see Eq 5). This means that the high and low frequency of the two a-c signals should be higher than 796 Hz and less than 0.796 Hz , respectively, in order to measure the corrosion rate of this system. As can be noted from Fig. 4, f_b^l decreases with increasing capacitance or corrosion resistance. On the other hand, f_b^h increases with de

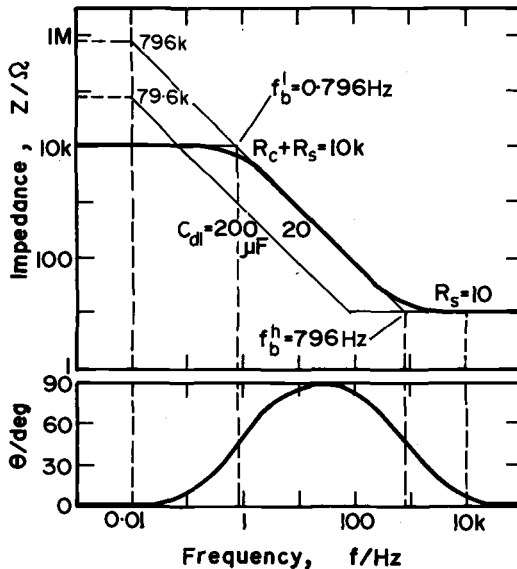


FIG. 4—Impedance diagrams of equivalent circuits with various time constants.

ing capacitance or solution resistance. Compromising these conditions, we chose a-c signals of 10 kHz and 0.01 Hz for the present general-purpose a-c corrosion monitor. Consequently, the monitor covers the corrosion resistance up to 796 k Ω at the capacitance of 20 μ F and 79.6 k Ω at 200 μ F. It is also noted that the frequency of the high-frequency signal can be reduced in usual applications, since the electric resistance of the environment is usually higher than that considered in the previous discussion. When a reasonable selection has been made on the frequencies, there must be no phase shift between voltage and current on either of the two signals.

In order to eliminate a circuit with high impedance, the two-electrode method was adopted in this monitor. Two similar specimens with the same surface area were placed facing each other, across which a-c signal was applied. Therefore the monitor measures the series combination of two identical interfacial impedance in fact. In the case of the d-c polarization resistance method, the two-electrode probe has difficulties when an appreciable potential difference and net current flow exists between the electrodes. Even in such circumstances, the a-c method yields an average corrosion rate of the two electrodes.

The block diagrams of the a-c corrosion monitor and the calculation unit are shown in Fig. 5. The amplitudes of the two a-c signals were 1.5 mV for 10 kHz and 8.2 mV for 0.01 Hz. The two signals may be applied alternatively to the electrodes. Since it is desirable to measure the peaks of two a-c currents at the same time, however, in this monitor the two a-c signals are mixed by using an adder, and the resultant modulated a-c signal is fed across the two electrodes. The output impedance of the monitor is on the order of 10^{-2} Ω . The modulated a-c current through the cell is then separated by filter circuits into the two a-c currents with the original frequencies. The peak values of the two a-c currents, i_h and i_l , are written as

$$i_h = v_h / R_{\text{sol}} = (V_h) \quad (8)$$

$$i_l = v_l / (R_{\text{sol}} + 2R_{\text{corr}}) = (V_l) \quad (9)$$

where v_h and v_l are the peak voltage of the a-c signals of 10 kHz and 0.01 Hz, respectively. Since i_h and i_l are converted into voltage signals, they are written as V_h and V_l . Equations 8 and 9 give

$$v_l / V_l - v_h / V_h = \frac{k}{V_l} \cdot \frac{k' V_h - V_l}{V_h} = 2R_{\text{corr}} \quad (10)$$

where k and k' are the constants given by $k = v_h$ and $k' = v_l / v_h$. The calculation unit shown in Fig. 5b is designed to yield voltage V_{out} equivalent to the logarithm of Eq 10. Thus

$$-V_{\text{out}} = \log[(k' V_h - V_l) / V_h] - \log(V_l / k) = \log(2R_{\text{corr}}) \quad (11)$$

Referring to Eqs 2 and 6, we readily see that V_{out} is proportional to $\log i_{corr}$. Thus

$$V_{out} = \log i_{corr} - \log(2K) \tag{12}$$

Therefore the monitor permits us to indicate i_{corr} directly on the recorder if reasonable K -value is given. The monitor is equipped with a switching unit, so that it yields the corrosion rates of several specimens consecutively at regular time intervals.

Two types of corrosion monitors, each with a different calculation unit, were designed and constructed. In the analog calculation type (shown in Fig. 5b), the calculation of Eq 11 is made by analog signal throughout. In the digital type, the performance and feasibility of the monitor were extended by using a microprocessor. Since the digital calculation unit is synchronized to the switching unit, the time sequence of the corrosion rate of each specimen is memorized and printed out separately. Moreover, it is possible to set a

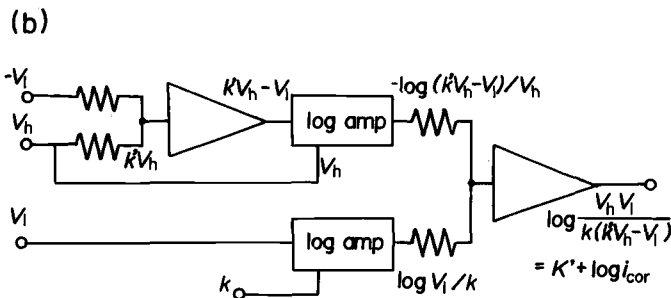
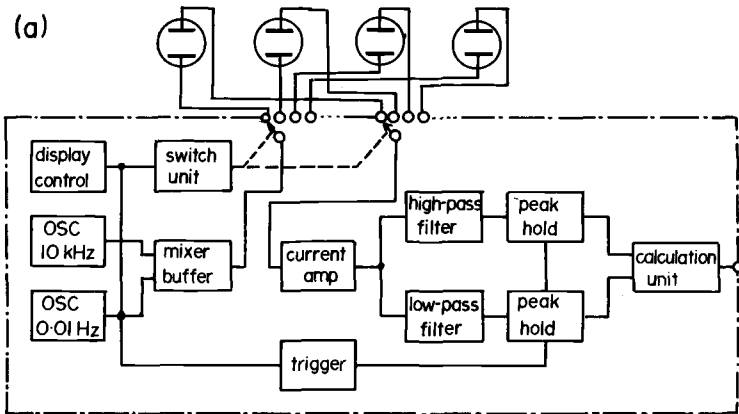


FIG. 5—Block diagram of a-c corrosion monitor; (a) overall diagram, and (b) calculation unit.

program that yields the time integration of corrosion rate, namely, the total amount of corrosion.

The output voltage of the corrosion monitor was calibrated using a dummy circuit (Fig. 6). We see that V_{out} is inversely proportional to the logarithm of R_c over four decades. With increasing R_{sol} , however, the error of subtraction in the calculation unit increased and the linear region of Fig. 6 was depressed. Generally speaking, the a-c corrosion monitor should be used under the condition $R_{corr}/R_{sol} \geq 0.1$. For corrosion monitoring in a less-conductive environment, the digital-type monitor is programmed to increase the voltages of the a-c signals automatically by ten times in order to compensate the ohmic loss in the environment. The restriction on the R_{corr}/R_{sol} ratio can be also overcome in practice by decreasing both the surface area and the gap of two electrodes. Since the corrosion rate in a less-conductive environment is usually low, however, the restriction may not be so serious a problem in application.

The value of K in Eq 12 was determined by comparing the time average of R_{corr} with the average corrosion current obtained from the weight-loss measurement by using the least-squares method over 93 data under various conditions to be stated later. The following data on corrosion-current density will be given by using the K -value of 0.0209 V thus determined.

This two-frequency method can be also applied to a three-electrode system (the working, the counter, and the reference electrode) by using a potentiostat, although many difficulties may arise in instrumentation (mainly from the frequency-response, stability, and noise of the potentiostat).

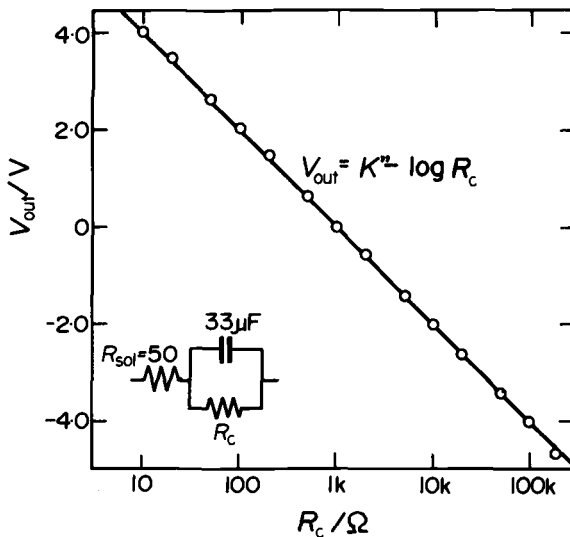


FIG. 6—Performance diagram of a-c corrosion monitor on dummy circuit.

Experimental Method

The surface area of specimen was 2 cm² in most cases. The experiments were made on the various combinations of metals and environments summarized in Table 1. The corrosion rate of a pair of specimens was monitored in a cylinder-type cell of 200 mL at 25 ± 0.2°C. The total weight of the pair of specimens was measured before and after the experiment, and the average corrosion rate was calculated. The present monitor can connect ten sets of samples and be reset at any point. Since the sampling time of corrosion monitoring on each set of specimen was chosen as 12 min, one cycle of measurement over 10 sets of specimens took 2 h; the cycle was repeated continuously until the monitor was reset.

Experimental Results

The traces of data on the recording chart of the a-c corrosion monitor on the corrosion of iron and 304 stainless steel in aerated various solutions are shown in Fig. 7. The vertical axis represents the output voltage of the monitor V_{out} , which corresponds to either $-\log R_{corr}$ or $\log i_{corr}$, as is noted in Eq 11 or 12. The diagram covers a wide range of corrosion current from 1 mA/cm² to 0.05 μ A/cm² in logarithmic scale. Since stainless steel was passive in aerated 1 *N* sulfuric acid (H₂SO₄), the corrosion current was on the order of 0.01 μ A/cm², which was close to the lower limit of application of the monitor. Since the specific resistivity of aerated distilled water (> 660 k Ω) exceeded the limit of application of the monitor, the measurement was made on the specimens with gap of 0.1 cm where the net solution resistance was below 60 k Ω . The corrosion rate of iron in aerated tap water or distilled water exhibited an irregular fluctuation due to the fall of a brown corrosion product from the metal surface. A more vigorous vibration in corrosion current was observed on iron in aerated sodium chloride (NaCl) solution [15]. When the solution was bubbled by nitrogen gas, however, the vibration stopped, accompanied by the decrease in corrosion current.

The corrosion rate of iron in 1 *N* H₂SO₄ with the presence of propargyl alcohol exhibited a maximum rate at initial periods and then decreased with time. The final corrosion rate was about 1/100 of that in the absence of the inhibitor. This behavior is consistent with that of the impedance measurements shown in Fig. 3.

The monitor also permits us to detect the initiation of localized corrosion by a sharp increase in corrosion current [22]. It was established that, even when localized corrosion occurred, the net corrosion rate was well estimated by the monitor. Examples of pitting corrosion of 304 stainless steel are shown in Fig. 8. Specimens were passivated in advance in 30 percent hydrogen nitrate (HNO₃) solution at 50°C for 30 min, and then the experiments were made in NaCl solution containing potassium ferricyanide [K₃Fe(CN)₆]. The initiation of pits is easily recognized by the sharp increase in corrosion cur-

TABLE 1—Average corrosion rate of metals in various environments.

No.	Specimen	Environment	Corrosion Current by Monitor, $\mu\text{A}/\text{cm}^2$	Corrosion Current by Weight Loss, $\mu\text{A}/\text{cm}^2$	Duration, h	Remarks
1	Fe	1 N H ₂ SO ₄	1950	1850	66	
2	Fe	1 N H ₂ SO ₄	1790	1100	64	
3	Fe	1 N H ₂ SO ₄	1070	1100	44	
4	Fe	1 N H ₂ SO ₄	1040	950	46	
5	Fe	0.3 N H ₂ SO ₄	780	620	67	
6	Fe	1 N H ₂ SO ₄	634	660	87	
7	Fe	1 N HCl	699	400	64	
8	Fe	1 N HCl	520	500	44	
9	Fe	1 N H ₂ SO ₄	439	380	67	
10	Fe	1 N H ₂ SO ₄	382	390	39	
11	Fe	0.3 N HCl	374	280	67	
12	Fe	0.1 N HCl	293	220	44	
13	Fe	1 N HCl	228	180	87	
14	Fe	0.03 N H ₂ SO ₄	205	185	72	
15	Fe	1 N H ₂ SO ₄	122	135	72	
16	SUS 304 ^b	1 N HCl	122	100	44	
17	Fe	1 N H ₂ SO ₄	65.0	110	45	
18	Fe	1 N H ₂ SO ₄	65.0	105	111	
19	SUS 304	1 N HCl	39.0	75	114	
20	Fe	0.5 N NaCl	43.9	63	66	
21	Fe	1 N H ₂ SO ₄	47.2	58	46	
22	Fe	0.03 N HCl	40.7	58	72	
23	Fe	0.01 N HCl	36.6	54	67	
24	Fe	1 N H ₂ SO ₄	18.7	56	96	
25	Fe	1 N HCl	18.4	44	72	
26	Ni	1 N HCl	26.8	35	96	
27	Inconel 600 ^c	1 N HCl	28.5	29	96	
28	Inconel 600	1 N H ₂ SO ₄	33.3	25.5	138	
29	Cu	1 N H ₂ SO ₄	35.8	17	89	

0.2 mM PA^a

3 % thiourea

1 mM PA

5 mM PA

partially immersed
20 mM PA

5 mM PA

5 mM PA

30	Fe	0.5 N NaCl	22.8	24	100	
31	Fe	0.5 N NaCl	18.7	19	64	
32	Fe	sea water	14.6	19	138	
33	Fe	tap water	12.7	18.5	111	
34	Fe	0.5 N NaCl	12.2	14	87	
35	Fe	sea water	10.1	14	75	partially in air and sands
36	Fe	sea water	8.46	12	75	partially buried in sands
37	Fe	tap water	6.83	9.3	87	
38	Fe	distilled water	5.69	13.5	111	
39	Fe	sea water	2.61	2.2	164	
40	Fe	0.5 N NaCl	1.43	3.0	284	
41	SUS 304	1 N H ₂ SO ₄	0.0407	0.032	403	fully buried in sands
42	SUS 304	0.3 N NaCl	564	630	30	decearated
43	SUS 304	0.25 N NaCl	528	571	18	0.1 N PFC, d pit ^e
44	SUS 304	0.25 N NaCl	654	520	18	0.1 N PFC, pit
45	SUS 304	0.25 N NaCl	593	487	18	0.1 N PFC, pit
46	SUS 304	0.4 N NaCl	351	456	27	0.01 N PFC, pit
47	SUS 304	0.25 N NaCl	358	450	30	0.1 N PFC, pit
48	SUS 304	0.2 N NaCl	593	432	18	0.1 N PFC, pit
49	SUS 304	0.4 N NaCl	363	412	30	0.1 N PFC, pit
50	SUS 304	1 N NaCl	278	344	26	0.05 N PFC, pit
51	SUS 304	0.4 N NaCl	341	302	28	0.1 N PFC, pit
52	SUS 304	0.1 N NaCl	418	285	245	0.1 N PFC, pit
53	SUS 304	0.5 N NaCl	229	278	18	0.05 N PFC, pit
54	SUS 304	0.1 N NaCl	291	272	245	0.1 N PFC, pit
55	SUS 304	0.1 N NaCl	280	202	245	0.1 N PFC, pit
56	SUS 304	0.1 N NaCl	259	181	245	0.1 N PFC, pit
57	SUS 304	0.1 N NaCl	260	167	245	0.1 N PFC, pit
58	SUS 304	0.1 N NaCl	218	166	245	0.1 N PFC, pit
59	SUS 304	0.1 N NaCl	341	154	245	0.1 N PFC, pit
60	SUS 304	0.05 N NaCl	179	128	160	0.1 N PFC, pit
61	SUS 304	0.5 N NaCl	53.2	110	66	0.05 N PFC, pit
62	SUS 304	0.5 N NaCl	42.9	92.9	64	0.05 N PFC, pit
63	Fe	tap water	15.6	48.6	145	running water
64	Fe	tap water	19.4	46.9	145	running water
65	Fe	tap water	21.6	45.9	145	running water

TABLE 1—Continued.

No.	Specimen	Environment	Corrosion Current by Monitor, $\mu\text{A}/\text{cm}^2$	Corrosion Weight Loss, $\mu\text{A}/\text{cm}^2$	Duration, h	Remarks
66	SUS 304	0.5 N NaCl	69.3	45.4	66	shallow pit
67	SUS 304	0.5 N NaCl	48.9	45.3	66	shallow pit
68	SUS 304	0.5 N NaCl	49.4	40.4	70	shallow pit
69	SUS 304	0.5 N NaCl	46.0	38.4	70	shallow pit
70	Fe	tap water	16.9	35.5	145	running water
71	SUS 304	5 % NaCl	48.2	50.3	22	0.67 % H_2O_2 , crevice/
72	SUS 304	5 % NaCl	84.8	42.0	192	0.67 % H_2O_2 , crevice
73	SUS 304	5 % NaCl	60.8	32.2	192	0.33 % H_2O_2 , crevice
74	SUS 304	5 % NaCl	56.9	57.3	192	0.33 % H_2O_2 , crevice
75	SUS 304	5 % NaCl	60.2	29.6	192	0.33 % H_2O_2 , crevice
76	SUS 304	5 % NaCl	49.8	29.4	192	0.33 % H_2O_2 , crevice
77	SUS 304	5 % NaCl	52.0	24.6	192	0.33 % H_2O_2 , crevice
78	SUS 304	5 % NaCl	27.6	24.6	22	0.67 % H_2O_2 , crevice
79	SUS 304	5 % NaCl	32.8	23.8	22	0.67 % H_2O_2 , crevice
80	SUS 304	5 % NaCl	42.0	20.4	22	0.67 % H_2O_2 , crevice
81	SUS 304	5 % NaCl	31.6	18.6	192	0.17 % H_2O_2 , crevice
82	SUS 304	5 % NaCl	49.2	18.2	192	0.17 % H_2O_2 , crevice
83	SUS 304	5 % NaCl	42.0	17.6	22	0.67 % H_2O_2 , crevice
84	SUS 304	0.1 N NaCl	8.62	15.6	51	0.05 N PFC, no pit ^g
85	SUS 304	0.1 N NaCl	6.18	3.80	245	0.1 N PFC, no pit
86	SUS 304	0.01 N NaCl	2.93	2.50	170	0.05 N PFC, no pit
87	SUS 304	0.05 N NaCl	3.74	2.30	170	0.05 N PFC, no pit
88	SUS 304	5 % NaCl	1.27	2.52	160	no crevice corr. ^h
89	SUS 304	5 % NaCl	1.07	1.98	160	no crevice corr.
90	SUS 304	5 % NaCl	1.01	1.76	160	no crevice corr.
91	SUS 304	5 % NaCl	1.38	1.54	160	no crevice corr.
92	SUS 304	5 % NaCl	0.732	1.50	160	no crevice corr.
93	SUS 304	5 % NaCl	0.814	1.26	160	no crevice corr.

^a Propargyl alcohol ($\text{CH} \equiv \text{CCH}_2\text{OH}$).^b SUS 304 stainless steel.^c Inconel 600 alloy.^d Potassium ferricyanide [$\text{K}_3\text{Fe}(\text{CN})_6$].^e Visible pit was found on the specimen.^f Crevice corrosion occurred.^g No visible pit was found.^h Crevice corrosion did not occur within the duration.

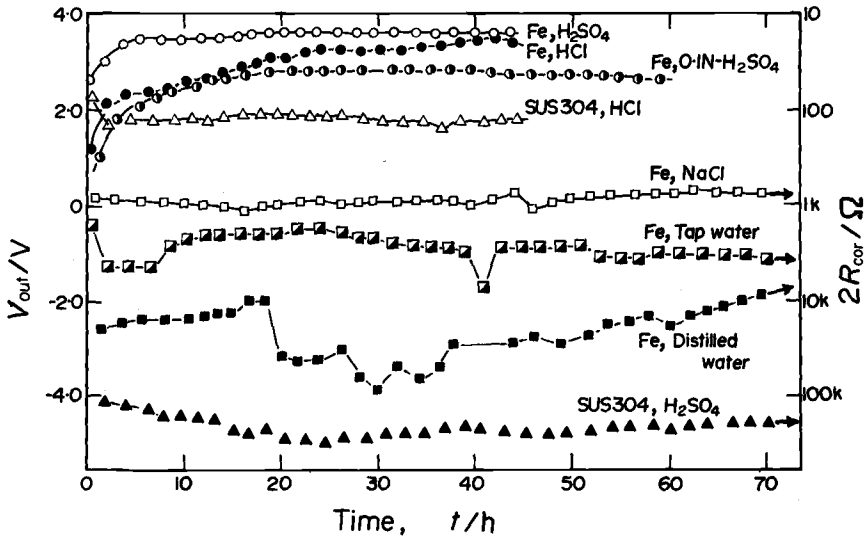


FIG. 7—Traces of data obtained with a-c corrosion monitor on iron and SUS 304 stainless steel in various solutions.

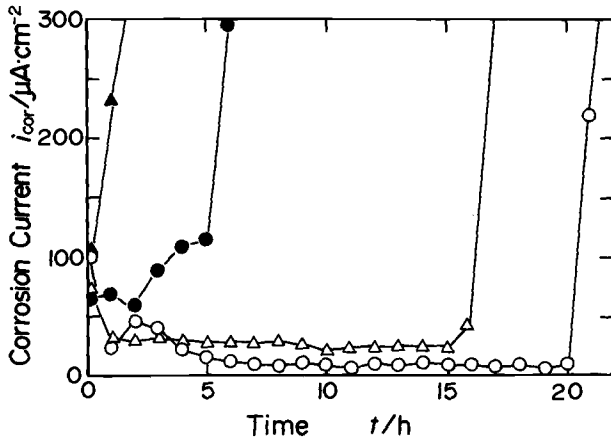


FIG. 8—Change in corrosion current of SUS 304 stainless steel by pitting. Solution, 0.25 N NaCl + 0.1 N $K_3Fe(CN)_6$.

rent in Fig. 8, although the induction period for pitting scatters evenly on the same material under the same condition. It must be noted in Fig. 8 that the larger the corrosion rate before the pit initiation, the shorter the induction periods. This fact seems to indicate that the induction period is related to the probability of the breakdown of passivity followed by repassivation.

Experiments were also made on the crevice corrosion of stainless steel [22]. In these experiments a pair of sample sheets was fixed by bolts and nuts of acryl resin together with a filter paper of 4 by 2 cm² as a spacer that functioned as an artificial crevice. The experiments were conducted in NaCl solution containing hydrogen peroxide (H₂O₂). The occurrence of crevice corrosion was recognized by gradual increases in the corrosion current of the specimen, which were otherwise passive.

In addition to the aforementioned experiments, the monitoring of corrosion rate was made on various metals under various environments, such as sea water, running water, wet sand, partial immersion, etc. All the experimental conditions hitherto tested and the average corrosion current densities obtained by the a-c corrosion monitor and the weight-loss measurement are summarized in Table 1. The data in Table 1 are listed in decreasing order of corrosion rate under the categories of uniform and localized corrosion.

Conclusion

The average corrosion current densities obtained with the a-c monitor are plotted against those with the weight-loss measurement on a logarithmic scale in Fig. 9. (Although the points are not specified in Fig. 9, their data can be easily found in Table 1.) It is readily seen that the data are in fair agreement

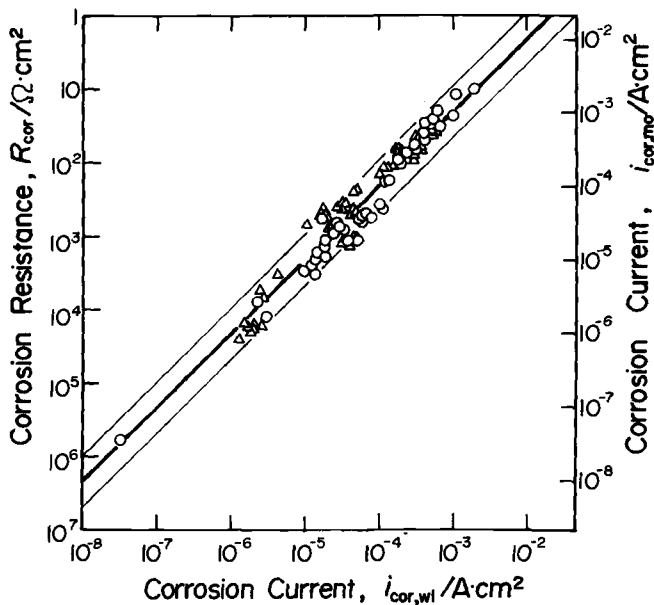


FIG. 9—Correlation between corrosion currents obtained with a-c corrosion monitor and with weight-loss measurement; ○ uniform corrosion, and △ local corrosion.

with either Eq 2 or 12 over five decades of corrosion current. The K value of 0.0209 V used in the previous section has been determined by the least-squares method from the regression line of $-\log R_{\text{corr}} \sim \log i_{\text{corr}}^*$ diagram of all the data in Table 1 (i_{corr}^* is the corrosion current estimated from weight-loss measurement). Thus

$$-\log R_{\text{corr}} = 1.68_0 + \log i_{\text{corr}}^* \quad (13)$$

where the standard deviation σ was 0.211₆. Since the data covered a wide range of corrosion rates on various metals in various environments, the standard deviation is a little large. It must be also noted that the weight-loss measurement may contain a fairly large margin of error, especially in case of localized corrosion. When the data on localized corrosion were excluded from the plot, the standard deviation decreased up to 0.191₄. This situation will be further improved with the accumulation of data. Under a fixed condition of metal and environment, the error can be reduced below 30 percent by adopting a suitable K -value. At present the K -value of the monitor is adjusted to 0.0209, so that the corrosion current can be read directly on the recorder with practically permissible error. The K -value is also consistent with those relating to the d-c polarization resistance method.

When the Warburg impedance participates, the corrosion rate can be measured by adjusting the low-frequency signal to the frequency where the impedance arrest appears and lowering the phase shift below 45 deg (see Fig. 1). This adjustment is easily made by the observation of phase shift using a two-pen recorder or a two-channel oscilloscope.

Thus the a-c corrosion monitor permits us to measure the corrosion rate in the range of 200 k Ω to 10 Ω , which corresponds to the corrosion rate of iron between 0.0007 and 15 mm/year. It must be noted that the monitor gives the net corrosion rate of specimen regardless of either uniform or localized corrosion. The initiation of localized corrosion was detected in most cases by a sharp increase in corrosion current. Since the electric resistance of environment is subtracted from the indication automatically, the a-c corrosion monitor is able to measure the corrosion rate in a less-conductive environment, such as distilled water or soil.

References

- [1] Wagner, C. and Traud, W., *Zeitschrift für Elektrochemie*, Vol. 44, 1938, pp. 7, 391.
- [2] Stern, M. and Geary, A. L., *Journal of the Electrochemical Society*, Vol. 104, 1957, p. 56.
- [3] Stern, M., *Corrosion*, Vol. 14, 1958, p. 440.
- [4] Oldham, K. B. and Mansfeld, M., *Corrosion Science*, Vol. 13, 1973, p. 813.
- [5] Oldham, K. B. and Mansfeld, M., *Corrosion*, Vol. 27, 1971, p. 434.
- [6] Callow, L. M., Richardson, J. A., and Dawson, J. L., *British Corrosion Journal*, Vol. 11, 1976, pp. 123, 132.
- [7] Nagayama, M., *Denki Kagaku* [Journal of the Electrochemical Society of Japan], Vol. 42, 1974, p. 382.

- [8] Marsh, G. A. in *Proceedings*, 2nd International Congress on Metallic Corrosion, National Association of Corrosion Engineers, 1963, p. 936.
- [9] Rowlands, J. C. and Bentley, M. N., *British Corrosion Journal*, Vol. 2, 1967, p. 92.
- [10] Okamoto, G., Sato, N., and Nagayama, M., *Denki Kagaku* [Journal of the Electrochemical Society of Japan, Vol. 25, 1957, p. 166.
- [11] Boto, K. G. and Williams, L. F. G., *Corrosion Science*, Vol. 17, 1977, pp. 11, 917.
- [12] Kanno, K., Suzuki, M., and Sato, Y., *Boshoku Gijutsu* [Journal of the Japan Society of Corrosion Engineering], Vol. 26, 1977, p. 697.
- [13] Epelboin, I., Keddam, M., and Takenouchi, H., *Journal of Applied Electrochemistry*, Vol. 2, 1972, p. 71; in *Proceedings*, 5th International Congress on Metallic Corrosion, National Association of Corrosion Engineers, 1972, p. 90.
- [14] Haruyama, S. in *Proceedings*, 5th International Congress on Metallic Corrosion, National Association of Corrosion Engineers, p. 82.
- [15] Haruyama, S., Tsuru, T., and Anan, M., *Boshoku Gijutsu* [Journal of the Japan Society of Corrosion Engineering], Vol. 27, 1978, p. 449.
- [16] Tsuru, T. and Haruyama, S., *Journal of the Japan Society of Metals*, Vol. 41, 1977, p. 306.
- [17] Haruyama, S. and Tsuru, T. in *Passivity of Metals*, R. P. Frankenthal and J. Kruger, Eds., The Electrochemical Society, Princeton, N.J., 1978, p. 564.
- [18] Haruyama, S. and Masamura, K., *Corrosion Science*, Vol. 18, 1978, p. 263.
- [19] Tsuru, T., Zaitse, T., Masamura, K., and Haruyama, S., *Journal of the Japan Society of Metals*, Vol. 42, 1978, p. 197.
- [20] Krithivasan, N., Tsuru, T., and Haruyama, S., *Boshoku Gijutsu* [Journal of the Japan Society of Corrosion Engineering], Vol. 29, 1980, p. 275.
- [21] Tsuru, T. and Haruyama, S., *Boshoku Gijutsu* [Journal of the Japan Society of Corrosion Engineering], Vol. 27, 1978, p. 573.
- [22] Tsuru, T., Maeda, R., and Haruyama, S., *Boshoku Gijutsu* [Journal of the Japan Society of Corrosion Engineering], Vol. 28, 1979, p. 638.

J. D. Scantlebury,¹ K. N. Ho,¹ and D. A. Eden¹

Impedance Measurements on Organic Coatings on Mild Steel in Sodium Chloride Solutions

REFERENCE: Scantlebury, J. D., Ho, K. N., and Eden, D. A., "Impedance Measurements on Organic Coatings on Mild Steel in Sodium Chloride Solutions," *Electrochemical Corrosion Testing, ASTM STP 727*, Florian Mansfeld and Ugo Bertocci, Eds., American Society for Testing and Materials, 1981, pp. 187-197.

ABSTRACT: Alternating-current impedance techniques were applied to organic coatings on mild steel in dilute sodium chloride solutions. The coatings used and the thicknesses employed were chosen to be typical of those systems frequently used for total immersion in marine conditions. A transfer function analyzer was used with high-impedance interfaces, and information was obtained concerning the impedance behavior of these coatings at frequencies that had previously been impossible. Equivalent circuit models analyzed the data obtained, and an assessment of the behavior of these coatings was made in the light of the analysis.

KEY WORDS: organic coatings, immersion test (corrosion), electrical impedance

The electrochemical nature of corrosion processes of uncoated metals in aqueous environments was first demonstrated graphically by Evans [1]². Mayne pursued this line of investigation and demonstrated that corrosion processes occurring under organic coatings were also electrochemical in nature [2,3]. It follows that an assessment of the anticorrosive ability of an organic coating might be made on the basis of electrochemical measurements, and a body of data has accumulated whereby various electrical parameters have been highlighted as being important when considering an anticorrosive paint coating. The subject has been summarized in a review by Wolstenholme [4] and more recently by Leidheiser [5].

The important parameter has been thought by many to be the coating ionic resistance measured under direct-current conditions [6,7]. However, Mikhailovskii pointed up [8] that in many instances the d-c resistance may not necessarily be a true measure of the anticorrosive ability of a paint, and

¹Corrosion and Protection Centre, University of Manchester Institute of Science and Technology, Manchester, England.

²The italic numbers in brackets refer to the list of references appended to this paper.

that many coatings are found whose d-c resistance is low but which have a good anticorrosive ability. He suggested that a more meaningful term was that of a resistance related to a retardation of the electrochemical processes occurring at the coating metal interface. This concept is analogous to the term "polarization resistance" as used by Stern and Geary [9].

The application of polarization resistance techniques to coated metal substrates was attempted by many workers [10-12] with variable success. The major deficiencies of their approaches have been recently considered [13], and this paper is an attempt to extend this work by taking into account these deficiencies. The systems under investigation have been chosen to be typical of paint coatings used under immersed conditions, namely chlorinated rubber and coal tar epoxy. The solution is not untypical of marine environments, and the coating thicknesses used are frequently specified for single-coat systems.

Experimental

Materials

Mild steel plate was prepared as electrodes of 20 by 30 mm and were pickled prior to coating. The precise steel composition and the pickling techniques have been given elsewhere [13].

The coal tar epoxy was supplied by W. and J. Leigh and Co. (Epigrip L.611), and was mixed in accordance with the manufacturer's instructions. The second coating material studied was a plasticized chlorinated rubber lacquer; the precise details of this coating have been given elsewhere [13].

The test solution was 3 percent weight/weight sodium chloride in distilled water that was fully aerated both before and during the course of each experiment. A platinum electrode of 3200 mm² was used as the counter electrode in a two-electrode system; the other electrode was the coated mild steel.

Preparation

Specimens were painted by a dip process in a dust-free atmosphere at ambient temperatures. The evenness of coating was controlled by withdrawing the samples from the paint at a constant rate. Specimens were allowed to dry in a ventilated dust-free atmosphere for 48 h and for a further two days in an air-circulating oven at 323 K. Further chemical changes in the film due to solvent evaporation or chemical curing were therefore deemed insignificant during the test period. Specimen thickness (measured by using a Minitector 150 thickness gage by Elcometer) was $60 \pm 5 \mu\text{m}$.

Short pieces of glass tube were used as insulating sleeves for the mild steel rods connected to the specimens. The sleeves were secured using epoxy resin. The specimens were then masked with either paraffin wax or epoxy resin to

exclude edge effects and to expose an area of 1 cm² for testing. Preliminary experiments had established an inverse relationship between impedance and specimen area.

Test Method

In order to provide a signal to the test electrode a transfer function analyzer (TFA) by Schlumberger (Solartron 1172) was utilized. This apparatus provides a rapid and accurate means of monitoring the frequency response of the system to various signals, and consists of a programmable generator that provides the stimulating signal, a correlator that analyzes the system response, and a display that presents the results in a digital format. The generator supplies an output signal of known amplitude and frequency, which for the purpose of this work was in the form of a sine wave $A \sin \omega t$. Automatic frequency scanning was employed in the frequency range of 10⁴ to 10⁻⁴ Hz at a signal amplitude of 20-mV root mean square (rms). The response of the system was in the form $B \sin (\omega t + \phi)$. Previous experiments at 10, 20, and 100 mV rms showed no significant differences in response. In addition to the fundamental term, harmonics due to the nonlinearities of the system random noise would also be present in the output. The response of the system was analyzed by a correlation process, and B and ϕ were determined. This technique has the advantage of rejecting all harmonics and minimizing the effects of random noise. In the simplest case, monitoring of the response of a cell to a low-amplitude sinusoidal perturbation may be achieved by utilizing a cell configuration (Fig. 1). The TFA measures the ratio of V_y/V_x and the phase shift ϕ . The cell impedance is calculated as

$$Z = \frac{V_y}{V_x} R$$

provided R is chosen so that $10^2 > V_y/V_x > 10^{-2}$; otherwise errors become more pronounced.

When the cell impedance is high, the TFA input impedance becomes important and the simple circuit shown in Fig. 1 becomes unreliable. It then becomes necessary to provide an interface between the TFA; those chosen for the purposes of this study were based on operational amplifiers either constructed from field effect transistor (FET) input operational amplifiers or in the form of commercially available potentiostats.

As has been stated previously, a two-electrode system was used (the interfacial circuitry is given in Fig. 2). The two-electrode cell should ideally consist of two identical electrodes, but when dealing with organic coatings this is a practical impossibility because of their inherent variability. Consequently, a platinum counter electrode was used that did not contribute an appreciable impedance to the total impedance. When there was no measurable galvanic

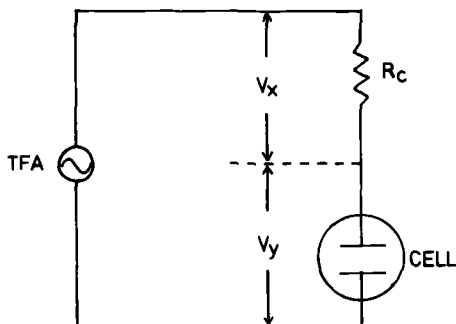


FIG. 1—Basic circuit.

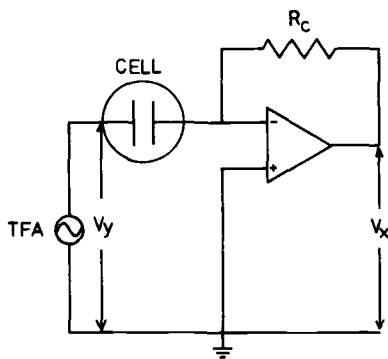


FIG. 2—Modified circuit.

action between the working and counter electrode, a J. Fet operational amplifier was used. Where galvanic action did occur, a potentiostat (Thompson 251 ministat) was used because of its capacity for d-c offset and its absence of phase shift at the frequencies investigated.

The data obtained from the TFA (namely, V_y/V_x , phase angle, and frequency) were transferred via a data transfer unit (Schlumberger Solartron DTU3217) to a teletypewriter and stored on paper tape. A computer (PDP 11/10 by Digital Equipment Corporation) together with an AR-11 interface was used to analyze the experimental data from which variables could be chosen and subsequently plotted in an X - Y plane in a 700×1000 point matrix. This was fed into an oscilloscope and an X - Y recorder. This whole unit facility, including the computer program, has been described elsewhere [14].

The coated samples described previously were immersed in the aerated test solution; the frequency response of the system was monitored over periods of up to 200 days. The derived information was obtained in the form of complex

impedance plots (Z' versus Z''), typical examples of which are presented later. Data extracted from these and other plots are also presented in tabular form.

It was considered necessary and interesting to investigate the effect of a small discontinuity in the coating to simulate a typical paint holiday. A coal tar epoxy coating was deliberately damaged with a sharp point to introduce a defect of 1 mm diameter. These data will also be given later.

Results and Discussion

Figure 3 shows the complex impedance data for the chlorinated rubber system after four days immersion in the aerated solution. The behavior indicates that the response of the system is purely capacitive with the equivalent circuit consisting of a capacitor and resistor in series. The values for the resistor and capacitor that can be determined from the data are given by $1.4 \times 10^6 \Omega \cdot \text{mm}^2$ and $1.95 \text{ pF} \cdot \text{mm}^{-2}$, respectively. This result is what would be expected if the coating were acting purely as a dielectric barrier. Figure 3 also shows the impedance behavior of the same specimen at seven, eight, and sixteen days immersion. Here the response of the coating is significantly altered from that at four days. The intercept of the curves with the Z' -axis is unaltered, $1.4 \times 10^6 \Omega \cdot \text{mm}^2$, but instead of continuing verti-

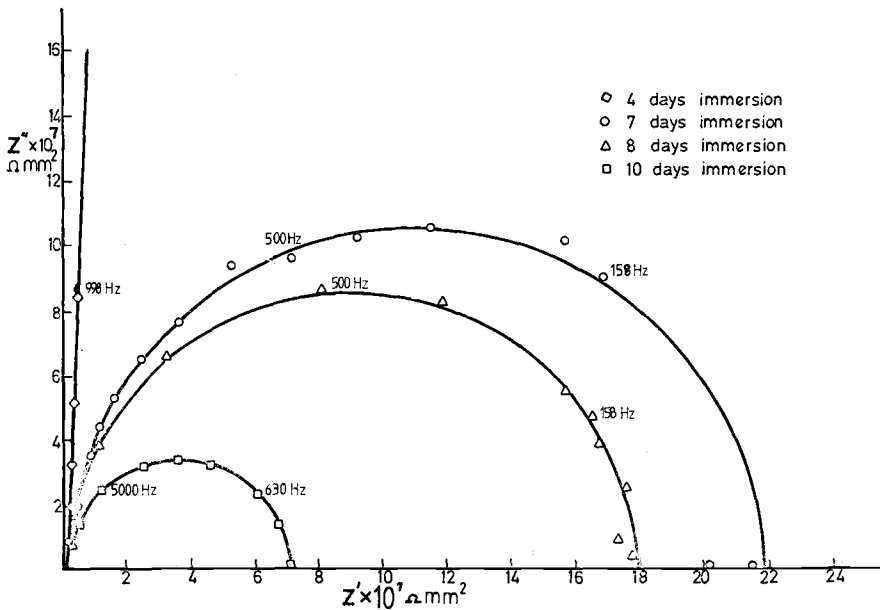


FIG. 3—Impedance data for chlorinated rubber on mild steel.

cally upwards in a purely capacitive manner the response curves are semicircles with the centers of the semicircles lying along the Z' -axis. Similar behavior has been noted before in corrosion studies, initially by Randles [15] and subsequently by many other workers, and has been discussed in terms of the equivalent circuit given in Fig. 4. For a freely corroding metal under activation control, R has been shown to be the solution resistance, R_θ is the charge transfer resistance, and c is the double-layer capacity. Furthermore, R_θ has been shown to be related to the corrosion current via the Stern-Geary equation [16].

With an organic coating the equivalent circuit mentioned previously appears to fit the results perfectly, but in view of the values presented Table 1 a different interpretation must now be placed on the three terms in the circuit.

The values presented in Table 1 have been calculated from Fig. 3 and similar plots. Clearly the values for R now no longer represent a solution resistance of less than $10^4 \text{ ohm } \Omega \cdot \text{mm}^2$, and $R \Omega$ now has values in excess of $10^6 \text{ } \Omega \cdot \text{mm}^2$. C , the double-layer capacitance, has changed from $0.3 \text{ } \mu\text{F mm}^{-2}$ to approximately $2.00 \text{ pF} \cdot \text{mm}^{-2}$. The value for $R \Omega$ implies that there is an ohmic drop occurring in the film as well as in the solution. If we assume the capacitance of the film to be related to its water absorption [17], then the aforementioned data would suggest that the water absorption of the film did not change during the time of immersion. This is in accordance with the con-

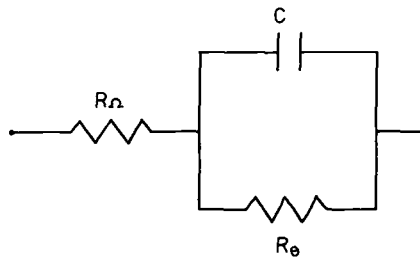


FIG. 4—Simple equivalent circuit.

TABLE 1—Chlorinated rubber.

Immersion Time, days	$R\Omega, \Omega \cdot \text{mm}^2$	$R\theta, \Omega \cdot \text{mm}^2$	$C, \text{pF} \cdot \text{mm}^{-2}$
2	1.4×10^6	...	1.98
4	1.4×10^6	...	2.01
7	1.4×10^6	2.1×10^8	2.16
8	1.4×10^6	1.8×10^8	2.00
9	1.4×10^6	6.8×10^7	2.33
10	1.4×10^6	5.5×10^7	2.22

cept of the "fast change" as proposed by Mayne [7] whereby changes in water absorption of a coating took place within the first hour of immersion.

The magnitude of R_θ and its change with time is an interesting phenomenon and is worthy of some comment. As has been already stated, R_θ in a corroding, film-free situation represents the resistance at the metal interface to charge transfer. It is interesting at this stage to speculate whether a similar meaning can be given to R_θ as measured under an organic coating. In this case the relatively high values of R_θ , at least initially ($2.1 \times 10^8 \Omega \cdot \text{mm}^2$), imply a very slow charge transfer process occurring across the film. Indeed, during the first few days no corrosion was observed through the transparent chlorinated rubber film. After ten days immersion the values for R_θ had fallen an order of magnitude, and at the same time small areas of corrosion could be observed as black spots under the film. It is our contention that the value of R_θ on a coated substrate is related to corrosion processes under the film, and a knowledge of the former could be a useful indication of the latter. In our investigation the onset of observable corrosion and the decrease in R_θ occurred at the same time. This final value, although obtained by a different method, lends credence to the criteria suggested by Bacon et al for bad coatings [6]. Figure 5, which is totally different from Fig. 3 is the impedance behavior of the same chlorinated rubber coating after three months immersion. The corrosion of the specimen was well established, and its nature consisted of orange-yellow material loosely bound to the outer surface of the coating surface and black material underneath. Furthermore, the solution was contaminated with an orange gel suspension. The intercept of the impedance curve with the real axis is now $2.4 \times 10^3 \Omega \cdot \text{mm}^2$. This would imply a smaller ohmic drop in the film, which would hardly be surprising since the

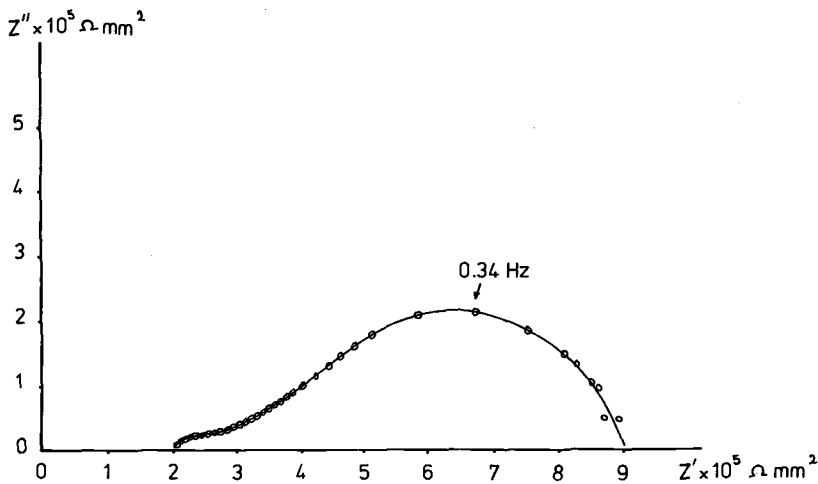


FIG. 5—Impedance data for chlorinated rubber on mild steel (coating failed).

film is on the point of rupture and may well be penetrated by pores. The overall shape of the impedance curve is also totally different, being more akin to the diffusion layer model first proposed by Sluyters and developed by Armstrong, where the infinite diffusion layer was replaced by a finite one [18].

Figure 6 is a series of impedance plots for a coal tar epoxy coating varying from a 20-minute immersion to a 194-days immersion. Table 2 shows the data extracted from these and similar plots for $R\Omega$, $R\theta$, and C . The behavior up to 60 days is similar to the chlorinated rubber system where the behavior can be explained simply by using the original Randles circuit. The values for $R\Omega$ are of the same order of magnitude. The values for $R\theta$ are now varying between 5×10^8 and $10 \times 10^8 \Omega \cdot \text{mm}^2$. Within the first 60 days no corrosion of the substrate and no clouding of the solution were noted, which added

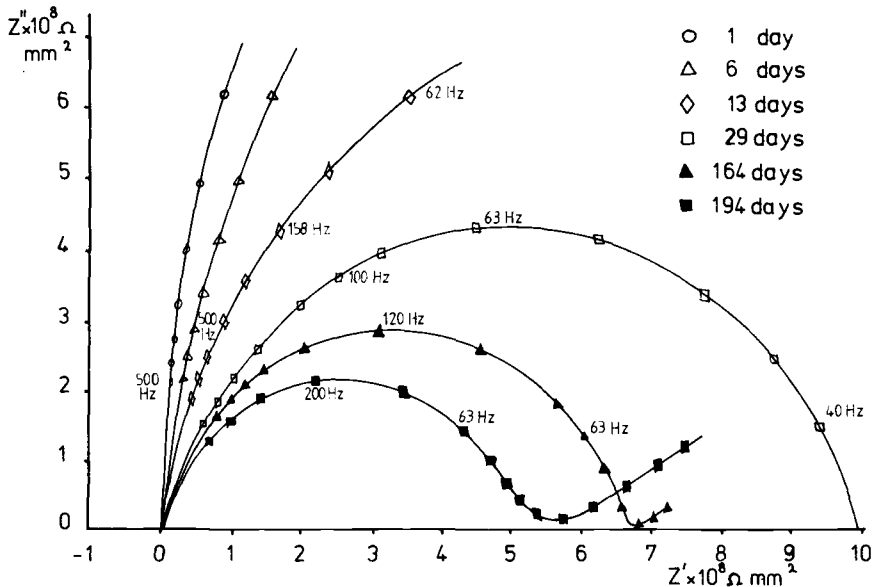


FIG. 6—Impedance data for coal tar epoxy on mild steel.

TABLE 2—Coal tar epoxy.

Immersion Time, days	$R\Omega$, $\Omega \cdot \text{mm}^2$	$R\theta$, $\Omega \cdot \text{mm}^2$	C , $\mu\text{F} \cdot \text{mm}^{-2}$
1	1×10^6	10^9	1.20
6	1×10^6	10^9	1.25
13	1×10^6	1.8×10^9	1.30
29	1×10^6	8.6×10^8	1.50
164	1×10^6	7.0×10^8	1.87
194	1×10^6	5.1×10^8	2.02

credence to the suggestion that R_{θ} is a measure of the electrochemical processes taking place at the interface.

After 60 days and especially at 194 days the impedance begin to show certain changes from those observed previously. At low frequencies there is a linear region of positive slope. This behavior has been analyzed by other workers and has been explained by postulating an extra impedance term in the Randles equivalent circuit entitled the Warburg impedance [17]. Figure 7 illustrates the equivalent circuit. This behavior has been suggested by some to be associated with diffusion processes, but the direct relationship between the low-frequency data presented in Fig. 6 and the physical processes taking place through the coating still requires further clarification. It is interesting to note that even after 194 days of immersion the coal tar epoxy coating was still not showing any visible signs of corrosion and breakdown.

Figures 8 and 9 demonstrate the effect of rapidly exposing a small area of bare steel on the impedance behavior. The purpose of this experiment was to simulate a coating in service that received damage in the form of a scratch. Figure 8 shows the impedance data after 20 min of inflicting the damage; Fig. 9 is some 18 h later. The electrode response is clearly completely different from that of the intact coating in two respects. Firstly, the high-frequency intercept on the real axis, the R_{Ω} term, is now much lower, and probably represents the solution resistance in the pore. Secondly, the impedance plots are no longer of a simple shape, and they change within the 18 h between Figs. 8 and 9. The full analysis of these data has not yet been attempted, but a possible explanation of both the shapes and changes in Figs. 8 and 9 is that two distinct processes are apparently occurring. One is a time-dependent process given by the high-frequency arc due to corrosion processes at the base of the pinhole, and the other is given by a low-frequency arc most probably associated with a mass transfer process down the pore.

In summary, this paper has attempted to demonstrate the following:

1. Using sinusoidal low-voltage frequency scanning techniques with suitable interfacing, data may be obtained from typical organic coatings on mild steel applied at typical thicknesses.
2. The data in the chlorinated rubber system may be analyzed in terms of

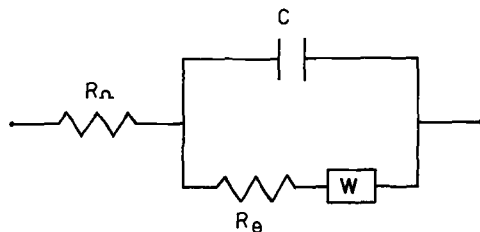


FIG. 7.—Equivalent circuit showing Warburg impedance.

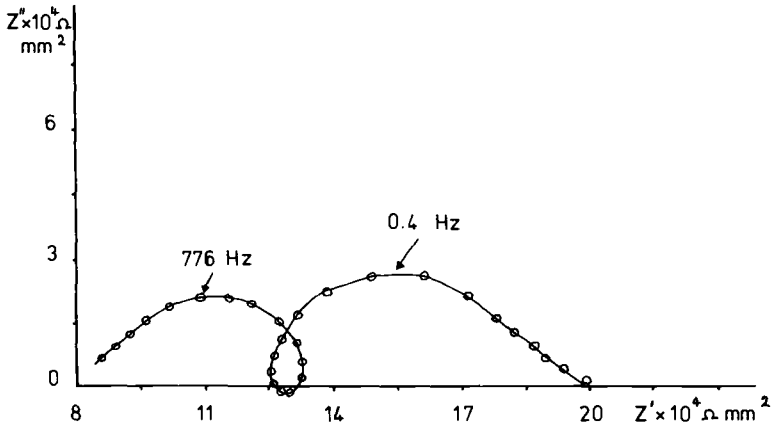


FIG. 8—Pin-holed coal tar epoxy (20 min).

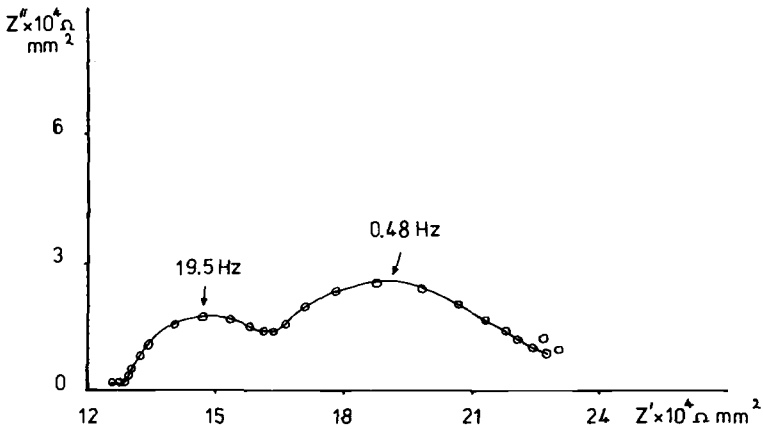


FIG. 9—Pin-holed coal tar epoxy (3 h).

a Randles equivalent circuit where R_θ seems to provide an estimate of the film integrity and protective capacity.

3. The coal tar epoxy shows similar behavior to the chlorinated rubber, with the exception that after a long time of immersion diffusion parameters are present.

4. Pin-holing processes have been considered, and impedance data have been produced from such a system.

Acknowledgments

The authors wish to thank the Procurement Executive, Ministry of Defence, for financial support and encouragement, without which this work could not have been carried out.

References

- [1] Evans, U. R., *The Corrosion and Oxidation of Metals*, Edward Arnold, London, 1960.
- [2] Mayne, J. E. O., *Chemistry and Industry*, Vol. 23, 1951, pp. 293-294.
- [3] Mayne, J. E. O., *Journal of the Oil and Colour Chemists Association*, Vol. 40, 1957, pp. 183-191.
- [4] Wolstenholme, J., *Corrosion Science*, Vol. 13, 1973, pp. 521-528.
- [5] Leidheiser, H., Jr. in *Proceedings*, Conference on Corrosion Control by Coatings, Lehigh University, 1978, pp. IIE1-39.
- [6] Bacon, R. C., Smith, J. J. and Rugg, F. M., *Industrial and Engineering Chemistry*, Vol. 40, 1948, pp. 161-167.
- [7] Mayne, J. E. O., *Transactions of the Institute of Metal Finishing*, Vol. 41, 1964, pp. 121-126.
- [8] Mikhailovskii, Y. N., Leonov, V. V., and Tomashov, N. D. in *Corrosion of Metals and Alloys*, N. D. Tomashov and E. N. Mirolyubov, Eds., Israel Programme for Scientific Translation, Jerusalem, 1966, pp. 202-209.
- [9] Stern, M. and Geary, A., *Journal of the Electrochemical Society*, Vol. 104, 1957, pp. 56-62.
- [10] Bureau, M., *Corrosion Treatment Protection Finition*, Vol. 16, 1968, pp. 235-241.
- [11] Kleniewski, A., *British Corrosion Journal*, Vol. 10, 1975, pp. 19-28.
- [12] Beaunier, L., Epelboin, I., Lestrade, J. C., and Takenouti, H., *Surface Technology*, Vol. 4, 1976, pp. 237-254.
- [13] Scantlebury, J. D. and Ho., K. N., *Journal of the Oil and Colour Chemists Association*, Vol. 62, 1979, pp. 89-92.
- [14] Hladky, K., "AC Impedance Measurements on Copper and Copper Base Alloys in Sea Water Environments," Ph.D. thesis, The Victoria University of Manchester, 1978.
- [15] Randles, J. E. B., *Discussions of the Faraday Society*, Vol. 1., 1947, pp. 11-16.
- [16] Epelboin, I., Kedda, M., and Takenouti, H., *Journal of Applied Electrochemistry*, Vol. 2, 1972, pp. 71-79.
- [17] Brasher, D. M. and Kingsbury, A. H., *Journal of Applied Chemistry*, Vol. 4, 1954, pp. 62-69.
- [18] Armstrong, R. D., Bell, M. F., and Metcalfe, A. A. in *Electrochemistry* The Chemical Society, London, 1978, pp. 98-127.

W. H. Smyrl¹

Digital Faradaic Impedance Measurements on Corroding Copper in Acid Solutions

REFERENCE: Smyrl, W. H., "Digital Faradaic Impedance Measurements on Corroding Copper in Acid Solutions," *Electrochemical Corrosion Testing, ASTM STP 727*, Florian Mansfeld and Ugo Bertocci, Eds., American Society for Testing and Materials, 1981, pp. 198-214.

ABSTRACT: The faradaic impedance of a rotating copper disk has been investigated in oxygenated acid solutions. The impedance measurement system is based on a digital acquisition and analysis of multiple frequency signals. The frequency range investigated was 0.1 to 500 Hz. In sulfuric acid the corrosion involves the peroxide intermediate whose transport behavior strongly influences the impedance results. Peroxide is not important in hydrochloric acid, but the transport of cuprous ions determines the impedance behavior. Measurements at frequencies higher than about 400 Hz in sulfuric acid show a strong frequency dispersion of the capacitance due to a nonuniform current distribution.

KEY WORDS: impedance, copper corrosion, sulfuric acid, hydrochloric acid, digital signal analysis

Digital signal analysis has become widely used in a routine way in many different fields in recent years. Seismology, electrical circuitry analysis, vibration analysis of machinery, spectroscopy, and impedance measurements for electroanalytical applications are a few of these applications. Part of the interest has been caused by the increasing availability and reliability of digital equipment, both for performing analog-to-digital data conversion and for data reduction, analysis, and digital filtering. The most important single contribution to this field was the development of an efficient algorithm for performing a Fourier transform on the discrete, digitized data. This algorithm is usually called the Fast Fourier Transform (FFT), and has been widely adapted and used with minicomputers and, more recently, microcomputers. This paper will discuss the application of these techniques in performing digital faradaic impedance measurements (DFIM) on copper corrosion in acidic environments. The purpose is to describe the details of the

¹Technical staff member, Sandia Laboratories, Albuquerque, N.M. 87185.

measurement technique and to illustrate some of the advantages that make it particularly appropriate for corrosion applications.

The measurement techniques described here are closely related to those of Smith and co-workers [1-7]², who have developed a very elegant system for electroanalytical measurements. Many of the ideas are very similar to those developed for corrosion measurements by the Epelboin group [8-10].

The elements of digital signal analysis are well established, and one may consult such excellent references as the book by Stearns [11] for details. As a summary, time-domain data is converted to frequency-domain data by a discrete Fourier transform (for example, by the FFT algorithm). A close analogy exists between a Fourier series analysis of an arbitrary time-domain signal and a discrete Fourier transform of such a signal. One approximates a complex spectrum as the superposition of a number of sinusoidal signals of known frequency and amplitude. This is mathematically expressed by a finite Fourier series

$$f(t) = \sum_{k=-K}^K C_k e^{ik\omega_0 t} \quad (1)$$

where the components of the computed series occur only at multiples or harmonics of the fundamental frequency ω_0 . If one has N -samples $f_n(t)$ of the periodic function $f(t)$ at time t_n , the coefficients of the discrete Fourier series are

$$C_k = \frac{1}{N} \sum_{n=0}^{N-1} f_n(t) e^{-ik\omega_0 t_n} \quad (2)$$

The Discrete Fourier Transform (DFT) of the sampled periodic function is, in similar notation, for a component of the frequency spectrum

$$\bar{F}_m = \sum_{n=0}^{N-1} f_n(t) e^{-i(2\pi mn/N)} \quad (3)$$

where the frequency is

$$\omega = \frac{2\pi m}{NT} \quad m = 0, 1 \dots N - 1 \quad (4)$$

and N and T are the number of samples and the time between samples, respectively. The fundamental frequency of the computed spectrum is

$$\omega_0 = \frac{2\pi}{NT}$$

²The italic numbers in brackets refer to the list of references appended to this paper.

and the other frequency components are harmonics of this basic or fundamental frequency.

The DFT is an accurate representation of the wave form, given the number of samples, with two important restrictions. The most important is that the sampling rate of the measurement system must be greater than twice as fast as the highest frequency component of the signal. This prevents "aliasing" (compare Ref 11). The other restriction relates to periodicity; that is, the DFT assumes that the sampled waveform is periodic in the sampling period. If it is not, "leakage" occurs (compare Ref 11). One may conclude that the information on all the higher frequencies in the spectrum is obtained at the same time that the lowest frequency is sampled.

The analysis can be performed on both input and output of a system (for example, electrical circuit), and the transfer function may be determined as the ratio, input/output, at each frequency of the spectrum. The impedance transfer function

$$\frac{\text{voltage } (\omega)}{\text{current } (\omega)} = Z(\omega)$$

is a function of frequency and is determined at each frequency by the aforementioned relationship. This very general relationship for linear systems is the basis for the measurement technique to be described here.

Multiple simultaneous frequencies may be used as the excitation signal. Smith and co-workers have investigated several useful waveforms [1,2,7], among which is the "white noise" spectrum used in the present investigation. Gabrielli et al [9,10] have also used several multiple frequency spectra for impedance measurements on corrosion systems. The "white" spectra should be used whenever possible because they have a flat power spectrum that ensures a constant signal/noise ratio at all the frequencies used. (Here noise is used to denote unwanted stray signals.) The signal used in this investigation was a Gaussian white spectrum, such as is shown in Fig. 1. The measured power spectrum is shown in Fig. 2; it indicates that the signal/noise ratio is maintained out to some frequency ω_c , the cutoff frequency. This represents the maximum frequency that may be utilized for the best performance. The units are arbitrary in Figs. 1 and 2, since the *relative* magnitude is the important quantity. The voltage spectra applied in these tests were 5 to 7 mV peak to peak, and had much the same form in the three bandwidths used (0.1 to 5 Hz, 1 to 50 Hz, and 10 to 500 Hz; see Results and Discussion). The power at the cutoff frequency (Fig. 2) is lower than the flat power by about 50 percent; this has obvious implications for the signal-to-noise ratio at the higher frequencies. Another spectrum, advocated by Smith [7] and also used by de Levie et al [12], is the odd anharmonic white spectrum that covers a wide and arbitrary frequency range. This prevents measurement error due to nonlinear behavior of the electrochemical system, which may be observed with large ex-

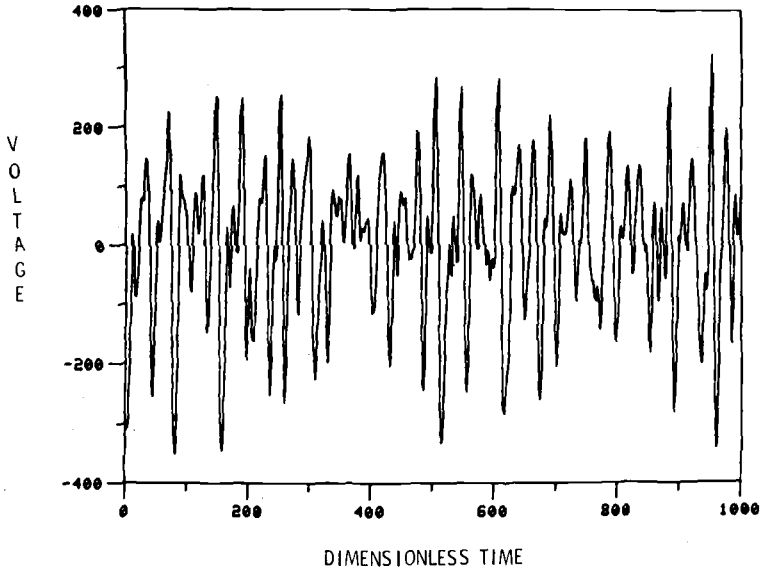


FIG. 1—Representative voltage spectrum from noise generator (similar at all three bandwidths when made dimensionless).

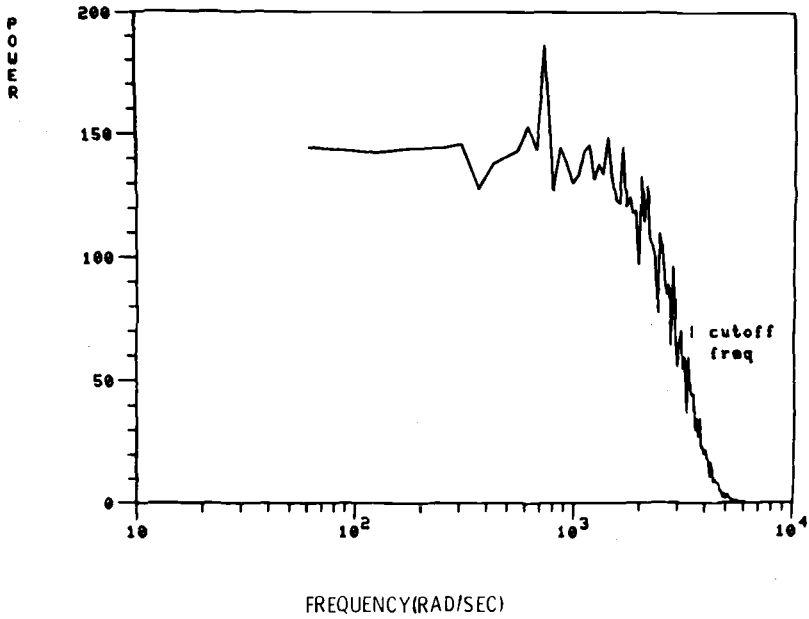


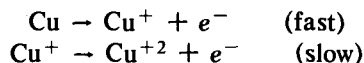
FIG. 2—Power spectrum of voltage input (500-hz band).

citation signals, at even harmonics of the spectrum. Other spectra may be used, but this illustrates that multiple frequencies are of particular interest here. It also suggests that this approach is both powerful and very flexible in the range of measurements that may be pursued.

At this point a brief aside is in order. The digital technique to be described gives the impedance of an electrochemical system as a function of excitation frequency. In this regard the technique is in all respects similar to older a-c impedance bridge methods that have been used with success in electrochemistry and less frequently in corrosion. One measures the frequency dependence in a bridge technique at each separate frequency in succession. This provides very accurate and reproducible results, provided there is no drift of the system behavior with time. The same information is provided by the Digital Faradaic Impedance Technique (DFIM), but with an important improvement. The digital technique may measure the frequency dependence at a large number of frequencies in the same time that only the lowest frequency would be measured with single-frequency excitation. In addition, successive multiple runs may be made with DFIM to improve accuracy and reliability. Any drift of the system behavior may be followed and studied with the digital technique to provide details of transient phenomena. This can be extremely important in corrosion systems where multiple simultaneous reactions cause complex, time dependent behavior of the metal-electrolyte interface.

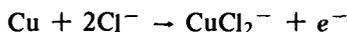
For the present paper, measurements were made on copper corroding in oxygenated acidic solutions. This system was chosen because there would be no hydrogen evolution interference, no films (either oxide or acid anion), and no hydroxide adsorption. Sulfuric acid (H_2SO_4) and hydrochloric acid (HCl) were chosen for the study. Dilute 0.1 *N* solutions were selected for the initial study.

Lu and Graydon [13] studied the free corrosion of copper in sulfuric acid and found the corrosion rate to be independent of rotation rate of the rotating copper cylinder; the oxygen dependence was half power. Gregory and Riddiford [14] studied the corrosion of a copper rotating in sulfuric acid with dichromate added as an oxidant. Cornet et al [15] found the corrosion rate of copper in sulfuric to be controlled by the rate of oxygen supplied to the surface in laminar flow, but referenced earlier work giving conflicting data on stirring rate dependence. Demedts and van Peteghem [16] have recently studied this system with added copper sulfate (CuSO_4) and have given special attention to the presence of Cu^+ ions in the solution. Their high-frequency impedance data are suspect, however, because of the frequency dispersion of the capacitance on a disk electrode at high frequencies caused by the nonuniform current distribution (see Ref 17). Most workers agree that copper dissolution in H_2SO_4 proceeds through two steps (see also Ref 18):



The cathodic reaction is more controversial. Anderson et al [19,20] found that peroxide was produced in solution with Cu^{+2} in equimolar amounts. This suggests that peroxide was not reduced further to water in their experiments. However, a recent study by Balakrishnan and Venkatesan [21] with a ring-disk electrode showed no peroxide formation in acidic chloride or sulfate media, though some was formed at higher pH. It is not clear how this discrepancy is to be resolved, but the chemical tests of Anderson et al [19,20] seem to be definitive proof that peroxide is formed at low potentials near the corrosion potential.

Corrosion in chloride media has been less studied, but Turner and Brook [22] give recent results and a survey of earlier literature. Their flow results indicated that increasing the flow rate increased the corrosion rate. They also reported impedance measurements, but did not give details of their experimental electrode design. Bertocci [23] has given a recent review of much of the literature on copper and copper alloy corrosion, including his own very important earlier work [24]. In chloride media the cuprous (+1) state is stabilized, and the dissolution under corrosion conditions is supposed to proceed principally as



with other chloride complexes being much lower in concentration.

The results of impedance measurements of copper rotating disks will be described. The effect of rotation rate and oxygen concentration on corrosion in H_2SO_4 and HCl will be reported, although the complete details will be published elsewhere.

Experimental

The measurement system has been described in some detail elsewhere [25]. It consists of a Hewlett Packard 9830 Calculator with 16 000 words of memory that controls data acquisition, data averaging, data storage, and data transmission to the time-share CDC 6600 large-scale computer. The analog data are digitized on a Biomation Transient Recorder, with each channel of 1024 words memory and each word of 10 bits. The voltage signal is provided by a Hewlett Packard Noise Generator, and is paralleled to the Wenking Potentiostat and to a low-pass amplifier and then to one channel of the transient recorder. The current signal is measured across a precision resistor in series with the electrochemical cell, and is also transmitted through a duplicate low-pass filter and then to the other channel of the tran-

sient recorder. The low-pass filter prevents frequencies higher than twice the cutoff frequency from the noise generator from reaching the input to the digitizer. The sampling rate of the Biomation Transient Recorder is operated at five times the cutoff frequency. Both the low-pass amplifier and the sampling rate prevent any aliasing effects.

The digitized data is strobed from the buffer memory of the transient recorder into the calculator memory and then stored on a floppy disk. It is subsequently averaged with other passes if there are multiple runs. The averaged data are transmitted to the large computer via a phone line, and the FFT is performed to obtain the frequency-domain data in dimensionless form. At this point the dimensionless impedance transfer function is calculated and stored. A correction procedure described by Schwall et al [7] is used to obtain the final data. This consists of making measurements on a dummy cell of precision resistors and capacitors that approximates the experimental system. These measurements are made at the same frequencies with the same amplifier settings as used in the experimental system. A correction file is calculated at each frequency, and applied to the experimental data from the electrochemical cell. This corrects for nonideal behavior of the potentiostat and other electronic components at each frequency. The calculated impedance is then output for either printout, plotting, or data storage. Using the term "correction file" is somewhat of a misnomer, and the term "calibration file" might be better. This procedure essentially incorporates all the amplifier gains, and accomplishes both correction and calibration for the impedance measurement. The data is dimensionless until the correction (calibration) file is applied. The calibration determines the magnitude of the real and imaginary parts of the applied file; correction for nonideal behavior of system components usually amounts to less than 2 percent of the magnitude. Schwall et al have discussed the procedure in more detail [7].

The acids were analytical reagent grade ampoules diluted with deionized water to 0.1 *N* solutions. The copper was polycrystalline oxygen-free, high-conductivity (OFHC) rod of 99.99 percent purity. An electrode was fashioned by tapping one end of a 1.2-cm-high by 0.94-cm-diameter rod. This was screwed onto a brass shaft that fit onto the rotating shaft-assembly. The copper and brass assembly was press-fitted into a Teflon body, so that only the bottom copper disk was exposed. The Teflon-copper interface was found to have a good liquid-tight seal when examined under a microscope. The rotation rate could be continuously varied up to 3600 rpm. The same disk electrode was used for all tests. Various dissolved oxygen concentrations were produced by bubbling air and ultrahigh purity (UHP) gas mixtures of oxygen and nitrogen through the solutions. The concentration was measured with a specific oxygen electrode. The gas delivery system had only stainless steel and Teflon come in contact with the gas.

The surface of the copper was prepared by mechanical polishing with

0.05- μm alumina on a metallography wheel on which only deionized water was used. Identical results were obtained when the freshly polished surface was etched with 1 *M* nitric acid (HNO_3) before use, except for surface roughness effects as described later.

Results and Discussion

The operating characteristics of the noise generator dictated that the frequency range investigated be split into different bands, that is, 0.1 to 5 Hz, 1 to 50 Hz, and 10 to 500 Hz. These three bands were used exclusively for the data described here, except as noted. (Much lower and much higher frequencies could be generated if desired.) Each band consisted of a fundamental frequency and 50 higher harmonics, both even and odd, with a power spectrum as shown in Fig. 2. The system was manually set for a particular frequency band, data were taken, then the system was manually set for another band, and so on. The data collection time is controlled by the period of the lowest frequency in the spectrum. A complete set of data of 153 frequencies could be collected in less than 45 s, not including the manual setup between bands. Multiple runs were made at each band for some of the data; this required a multiple of the collection time quoted earlier.

0.1 N Sulfuric Acid

Data Analysis—Impedance measurements were made at several rotation rates on a copper electrode corroding at the corrosion potential in oxygenated H_2SO_4 . An example of the results is shown in Fig. 3; the results will be discussed in greater detail elsewhere. The measurements were made after the freshly polished electrode had rotated in the solution at 700 rpm for 5 min, and the rotation rate was adjusted to that noted for the impedance measurements. The preconditioning gave a reproducible and fairly constant surface morphology for the measurements. Surface roughness effects were to cause scatter of the data, primarily through area changes as noted later.

The data in Fig. 3 were analyzed to show a charge-transfer semicircle at high frequencies and convective Warburg diffusion behavior at low frequencies. The data analysis procedures of Sluyters [26] and de Levie et al [27-29] were used to determine the parameters of the respective processes. Sluyters' procedure was used predominantly at high oxygen concentration and low rotation rates where the best separation of the two processes occurred. The technique proposed by de Levie was used where the diffusional impedance was dominant. Figure 4 shows the 1000-rpm data taken from Fig. 3, plotted now as suggested by Sluyters [26]. The data followed linear behavior at intermediate frequencies, as expected for charge-transfer behavior. The parameters in this region are R_s , R_p and CA , and were found to be 20 Ω , 155 Ω , and 38.9×10^{-6} F, respectively (A is the area of the electrode, 0.694

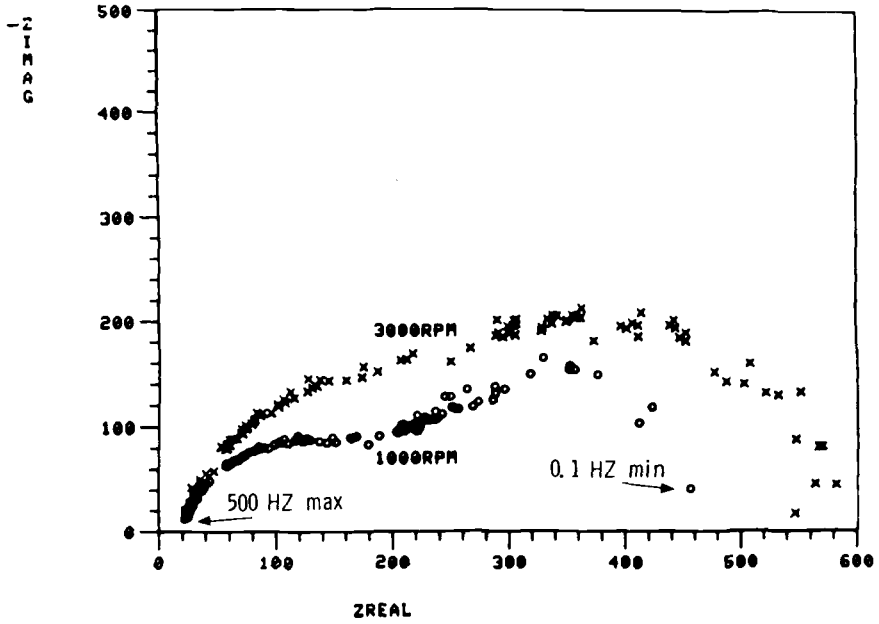


FIG. 3—Impedance of copper in 0.1 N sulfuric acid (rotating disk, 32.5 ppm oxygen).

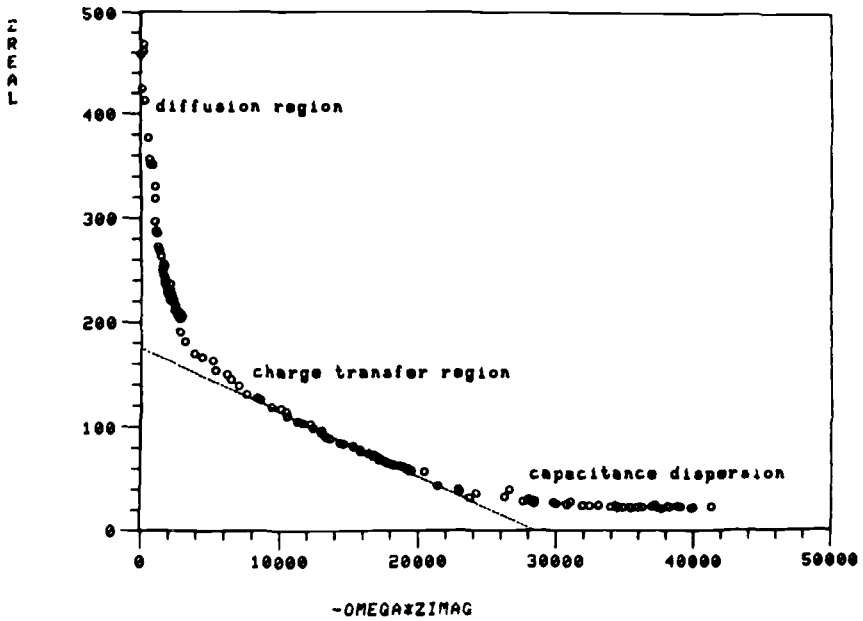


FIG. 4—Impedance of copper in 0.1 N sulfuric acid (rotating disk, 32.5 ppm oxygen).

cm^2). These are the parameters for the equivalent circuit in Fig. 5. R_s characterizes the solution resistance, and the experimental value compares favorably with the $18\ \Omega$ calculated for the experimental arrangement. R_p and C are the charge-transfer "polarization resistance" and double-layer capacitance, respectively.

The deviation from this linear behavior at low frequencies was caused by diffusion. This was confirmed by deconvoluting the semicircle from the experimental data for 1000 rpm and plotting the result as the real versus imaginary parts of Z_w , without assuming any particular behavior for Z_w . The results are shown in Fig. 6. The data may be extrapolated through the origin with a 45 deg slope, and bends over into a circular arc at low frequencies, as expected for a convective Warburg diffusion curve on a rotating disk [30]. The significant parameter for this curve is the zero-frequency intercept. The extrapolation to zero frequency is facilitated by referring again to Fig. 4 and noting that the low-frequency behavior of the convective Warburg diffusion curve is linear in these coordinates. The low-frequency intercept for Z_w (corrected for R_s and R_p) was found to be $285\ \Omega$. The shape of the curve in Fig. 6 is exactly that expected, at all frequencies, for a convective Warburg curve [30].

Dependence on Rotation Rate—It was found that the values of R_p and Z_w ($\omega \rightarrow 0$) were increased with increasing rotation rate at all oxygen concentrations used. All the data were taken at the corrosion potential (that is, zero net d-c current flowing). It was also observed that as the rotation rate increased the corrosion potential decreased (that is, became more negative) and the anodic current increased (at a constant potential). This behavior of the corrosion potential has been noted by others [16,22], and the anodic-current observation has been also made under deoxygenated conditions [31]. Under these deoxygenated conditions, the anodic current effect has been shown to be caused by the transport of both Cu^+ and Cu^{+2} ions away from the elec-

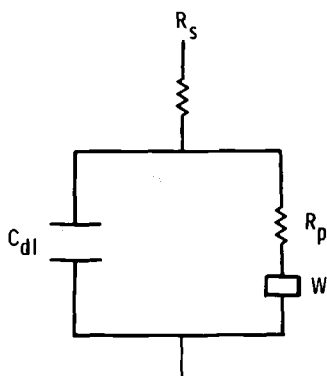


FIG. 5—Equivalent circuit of the impedance of an electrode.

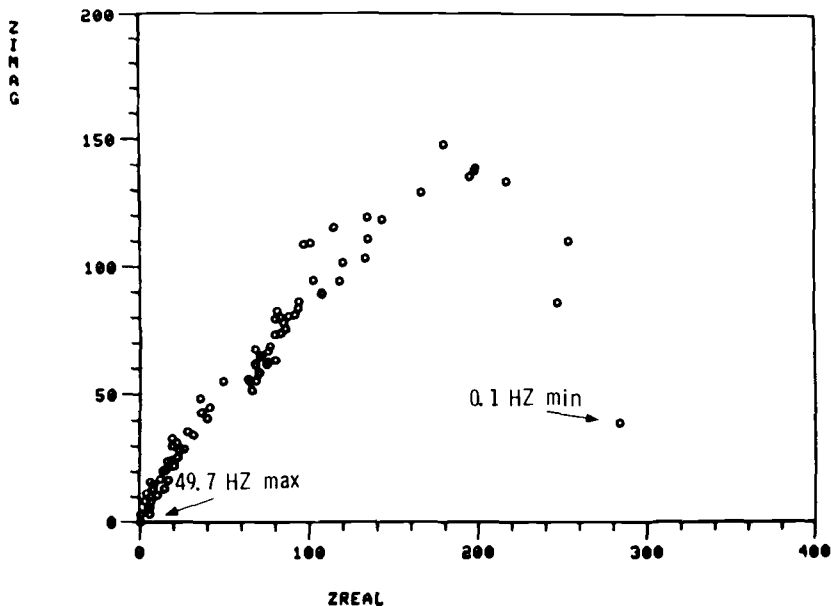
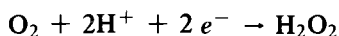


FIG. 6—Impedance of copper in 0.1 N sulfuric acid after deconvolution of the charge-transfer contribution.

trode. The net effect would be an increase in the anodic current at a constant potential. Under corrosion conditions, the corrosion potential must then be displaced in a negative direction until a new balance between the anodic copper reactions and the cathodic oxygen reactions is achieved. The corrosion current should then be increased by an increase in rotation rate.

Our observations on the corrosion potential and anodic current are consistent with these predictions, but the behavior of R_p and Z_w ($\omega \rightarrow 0$) are not. An alternative explanation is consistent with all observations, and involves not the copper reactions but the cathodic oxygen system. Oxygen is reduced in acid solutions through the two-step process

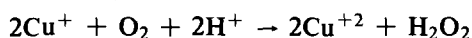


and

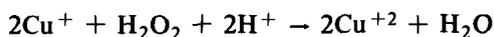


Both reactions are highly irreversible, and the back reactions (anodic) should be negligible. At low currents where the mass transfer of oxygen is not limited, the transport of hydrogen peroxide (H_2O_2) from the electrode surface will decrease the net cathodic reaction at a constant potential because of

the decrease of current from the second reaction. The total current will then become more anodic at a constant potential without having to involve any change of the copper reactions. The corrosion potential will then be more negative with increased rotation rate and, more importantly, the corrosion current will decrease with increased stirring. There could be transport effects on the copper reaction as well, but they must be of smaller magnitude. A quantitative treatment of the system is being conducted that will include transport effects on both copper and oxygen reactions, as well as the influence of the homogenous reactions



and



Anderson et al [19,20] found that the reaction of dissolved oxygen with the intermediate Cu^+ ion had a profound influence on the corrosion rate. This reaction effectively "short-circuits" the cuprous to cupric electrode reaction. They found the corrosion rate to be ten times faster than expected from simple superposition at the corrosion potential. The effect of oxygen on the intermediate cuprous ions was also found earlier in ammonia solutions by Bertocci [32]. A complete analysis of this system of processes is being conducted and progress will be reported elsewhere.

Dependence on Oxygen Concentration—The corrosion rate has been found to increase with an increase of oxygen concentration. In Table 1 the quantity $1/R_p$, which is proportional to the corrosion rate, given versus the dissolved oxygen concentration for two rotation rates. The dependence is lower than first power, and seems to be smaller at higher rotation rates and higher oxygen concentrations. This presumably reflects the influence of transport effects on the oxygen cathodic reactions.

Dispersion of Capacitance at High Frequencies—The marked deviation from linearity shown in Fig. 4 at high frequency occurs where

$$-\frac{1}{\omega CA} \rightarrow Z(\text{IMAG})$$

and

$$Z(\text{REAL}) \rightarrow R_s$$

This is the region where a nonuniform current distribution will cause a capacitance dispersion, as discussed by Newman [17] for a disk electrode. The current distribution will vary from that characteristic of d-c polarization, which can be quite uniform, to the primary distribution. It approaches the nonuniform current distribution at high frequencies, that is, high compared

TABLE 1—Dependence of $1/R_p$
on oxygen concentration in 0.1 N H_2SO_4 .

1000 rpm		3000 rpm	
$1/R_p, \Omega^{-1}$	C_{O_2}, ppmw^a	$1/R_p, \Omega^{-1}$	C_{O_2}, ppmw
0.00222	3.25	0.00154	3.25
0.00435	6.8	0.00263	6.8
0.00667	15	0.00408	15
0.0100	33.5	0.00476	33.5

^appmw = parts per million by weight.

to the fundamental frequency of the (R_pCA) circuit. We adopt this model for the frequency dispersion, but it is the subject of continued study. It should be noted that this effect obviates any measurements at very high frequency on the disk electrode, and may invalidate the high-frequency impedance measurements of Demedts and van Peteghem [16] mentioned earlier.

0.1 N HCl Solutions

Data Analysis—The procedure of de Levie [27] was followed for this system because the Warburg diffusion impedance was dominant. The high-frequency value of R_s was found to be about 13 Ω . The plot of $Y(\text{REAL})/\omega$ versus $Y(\text{IMAG})/\omega$ yielded the value of CA (in the range of 20 to 22 $\times 10^{-6}$ F) for the system. Deconvolution of these values from the experimental impedance data yielded the Warburg curve. The high-frequency intercept on the real axis gave a value for R_p . The low-frequency intercept was Z_w ($\omega \rightarrow 0$). This analysis procedure gave results quite sensitive to R_s . The values for R_p were on the order of 400 to 800 Ω for all tests, but are the subject of continued study to obtain more precise results.

Dependence on Rotation Rate—The impedance behavior as a function of rotation rate is shown in Fig. 7. All the curves coincide at high frequency, as expected for a diffusional impedance in parallel with the double-layer capacitance. The influence of rotation rate on the impedance is the inverse of that for sulfuric acid, that is, increasing the rotation rate decreases the (diffusion) impedance Z_w . The corrosion potential becomes more negative with an increase of rotation rate, as in sulfuric acid, and the net anodic current increases with rotation rate as well. The transport of Cu^+ will cause the observed corrosion potential and anodic current dependence as well as the behavior of Z_w , as was shown by arguments given earlier for the sulfuric acid system. The transport dependent behavior of the oxygen reduction involving the peroxide intermediate is then not as important as for the sulfuric acid system. (A quantitative treatment of this system will be presented elsewhere.)

Dependence on Oxygen Concentration—The value of Z_w ($\omega \rightarrow 0$) for the copper electrode is listed in Table 2 as a function of oxygen concentration at

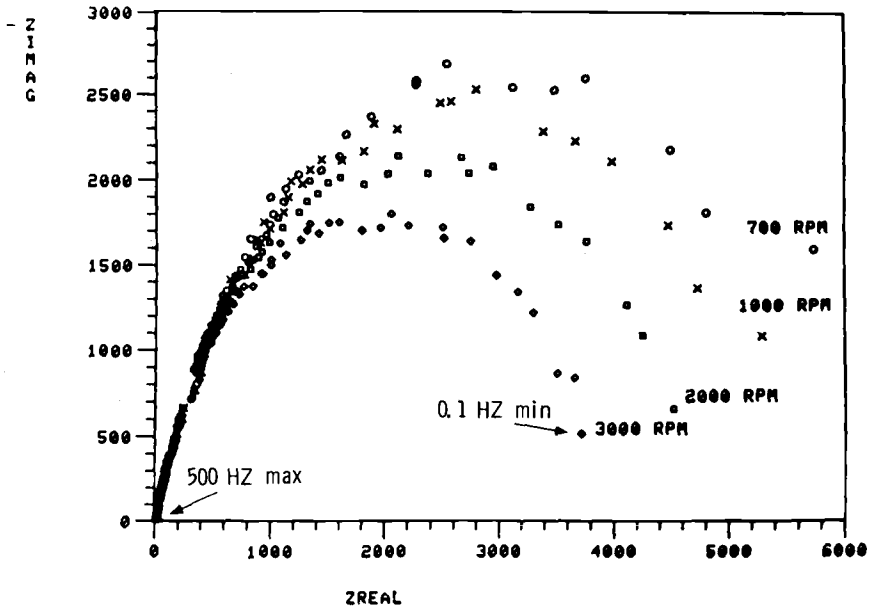


FIG. 7—Impedance of copper in 0.1 N HCl (rotating disk, 7.05 ppm oxygen).

TABLE 2—Dependence of $Z_w(\omega \rightarrow 0)$ on oxygen concentration at 1000 rpm.

$Z_w(\omega \rightarrow 0), \Omega$	C_{O_2}, ppmw^a
13500	3.25
5200	6.8
2800	15
2000	33.5

^appmw = parts per million by weight.

1000 rpm. The behavior is an inverse first-order dependence on oxygen. This is consistent with the previous discussion, where it was concluded that the peroxide intermediate is less important for this system.

Surface Morphology

There seems to be a correlation between the surface roughness and the value of CA for the system. In HCl, where the polarization resistance R_p was high (even at high oxygen concentration), the surface retained its polish even after 8 min in the solution. A slight etch of the surface to reveal the polycrystalline grain structure could be observed under a microscope. CA had values of 20 to 22×10^{-6} F for these solutions. In sulfuric acid, the sur-

face was etched more heavily even at the lowest oxygen concentration (3.25 ppmw). CA was 20 to 25×10^{-6} F in this solution, but was 25 to 30×10^{-6} F in 6.8 parts per million by weight (ppmw), 30 to 35×10^{-6} in 15 ppmw and 40 to 45×10^{-6} in 33.5 ppmw oxygen. Both the corrosion rate and the surface roughness increased in the same order. Multiple etch pits were characteristic of the surface appearance at the highest corrosion rates. It is proposed that the original highly polished surface had a double-layer capacitance of 28 to 32×10^{-6} F/cm², and that the deviation from this value for the other systems was due primarily to a surface roughness effect. The most highly etched surface would only have to be given a roughness factor of 2 for this to be valid, and this seems a reasonable value for these surfaces.

Conclusions

This study has demonstrated some of the advantages of digital faradaic impedance measurements in corrosion studies:

1. Multifrequency impedance measurements are rapid and provide a rather complete description of the corrosion behavior in a very short time.
2. The measurements are accurate, and with averaging the accuracy is increased even further.
3. Data are acquired in a form that facilitates analysis, reduction, and data manipulation.
4. The technique provides a clear indication of the processes that occur in a corrosion system, and guides one in determining valid corrosion rates where ordinary d-c techniques would fail.

These and other advantages suggest that the technique may become more widely used as familiarity and equipment are acquired. Microcomputer systems appear to be the key to more widespread utilization.

Further development of the instrumentation will be required before the technique is used in other than research laboratory investigations. Some of the applications in the field of corrosion that seem quite feasible, given the instrumentation, are in the areas of control and monitoring, inhibitor development, and optimization. A promising research field is that of investigating time-dependent (that is, transient) phenomena in corrosion systems.

Control and monitoring applications can be imagined where a spectral "signature" is acquired that determines some automatic response by the digital controller. Digital and adaptive filtering to remove annoying stray "noise" are almost trivial exercises that are widely used and show great promise.

Inhibitor development has always been a rather tedious and difficult activity. Digital Faradaic Impedance Measurement systems have the poten-

tial of assessing the detailed role of the inhibitor and aiding the optimization of the system. A large-scale inhibitor program can be envisioned in which multiple corrosion-inhibitor systems would be scanned in a routine and programmed investigation to determine system performance as a function of time. The corrosion engineer would be enabled to recommend the best inhibitor, at the best concentration level, and the system would be tailored for the material-environment combination of interest.

The application of the DFIM technique to copper corrosion has revealed the relative importance of charge transfer and transport phenomena in sulfuric and hydrochloric acids. In addition, the measurements have revealed differences in oxygen-reduction behavior in the two systems, with peroxide playing an important role in the sulfuric acid system but not in hydrochloric acid. The investigation has also revealed several fruitful areas for further research, and these will be reported on at a later date.

Acknowledgments

The author wishes to acknowledge the significant assistance of L. L. Stephenson in all the experimental phases of this work. Dr. J. W. Braithwaite was quite helpful in preparation of the manuscript.

This work was supported by the United States Department of Energy under Contract No. DE-AC04-76DP00789.

References

- [1] Creason, S. C. and Smith, D. E., *Electroanalytical Chemistry—Interfacial Electrochemistry*, Vol. 36, 1972, Appendix 1.
- [2] Creason, S. C. and Smith, D. E., *Electroanalytical Chemistry—Interfacial Electrochemistry*, Vol. 40, 1972, p. 1.
- [3] Smith, D. E., *Analytical Chemistry*, Vol. 48, 1976, p. 221A.
- [4] Smith, D. E., *Analytical Chemistry*, Vol. 48, 1976, p. 517A.
- [5] Schwall, R. J. Bond, A. M., and Smith, D. E., *Journal of Electroanalytical Chemistry*, Vol. 85, 1977, p. 217.
- [6] Bond, A. M., Schwall, R. J., and Smith, D. E., *Journal of Electroanalytical Chemistry*, Vol. 85, 1977, p. 231.
- [7] Schwall, R. J., Bond, A. M., and Smith, D. E., *Analytical Chemistry*, Vol. 49, 1977, p. 1805.
- [8] Epelboin, I., Keddam, M., and Takenouti, H., *Journal of Applied Electrochemistry*, Vol. 2, 1972, p. 71.
- [9] Gabrielli, C. and Keddam, M., *Electrochimica Acta*, Vol. 19, 1974, p. 355.
- [10] Blanc, G., Epelboin, I., Gabrielli, C., and Keddam, M., *Electrochimica Acta*, Vol. 20, 1975, p. 599.
- [11] Stearns, S. D., *Digital Signal Analysis*, Hayden Book Company, Rochelle Park, N. J., 1975.
- [12] de Levie, R., Thomas, J. W., and Abbey, K. M., *Journal of Electroanalytical Chemistry*, Vol. 62, 1975, p. 111.
- [13] Lu, B. C. Y. and Graydon, W. F., *Canadian Journal of Chemistry*, Vol. 32, 1954, p. 153.
- [14] Gregory, D. P. and Riddiford, A. C., *Journal of the Electrochemical Society*, Vol. 107, 1960, p. 950.
- [15] Cornet, I., Barrington, E. A., and Behrsing, G. U., *Journal of the Electrochemical Society*, Vol. 108, 1961, p. 947.

- [16] Demedts, G. and van Peteghem, A. P., *Corrosion Science*, Vol. 18, 1978, p. 1041.
- [17] Newman, J., *Journal of the Electrochemical Society*, Vol. 117, 1970, p. 198.
- [18] Mattsson, E. and Bockris, J. O'M., *Transactions of the Faraday Society*, Vol. 55, 1959, p. 1586.
- [19] Anderson, T. N., Ghandehari, M. H., and Eyring, H. *Journal of the Electrochemical Society*, Vol. 122, 1975, p. 1580.
- [20] Ghandehari, M. H., Anderson, T. N., and Eyring, H., *Corrosion Science*, Vol. 16, 1976, p. 123.
- [21] Balakrishnan, K. and Venkatesan, V. K., *Electrochimica Acta*, Vol. 24, 1979, p. 131.
- [22] Turner, M. and Brook, P. A., *Corrosion Science*, Vol. 13, 1973, p. 973.
- [23] Bertocci, U. in *Encyclopedia of Electrochemistry of the Elements*, Vol. II, A. J. Bard, Ed., Marcel Dekker, New York, 1974.
- [24] Bertocci, U., *Electrochimica Acta*, Vol. 11, 1966, p. 1261.
- [25] Smyrl, W. H. and Pohlman, S. L. in *Corrosion/78*, Paper 166, Houston, Tex., March 1978.
- [26] Sluyters, J. H., *Recueil*, Vol. 79, 1960, p. 1092.
- [27] de Levie, R., *Electrochimica Acta*, Vol. 10, 1965, p. 395.
- [28] de Levie, R. and Pospisil, L., *Journal of Electroanalytical Chemistry*, Vol. 22, 1969, p. 277.
- [29] Moreira, H. and de Levie, R., *Journal of Electroanalytical Chemistry*, Vol. 29, 1971, p. 353.
- [30] Homsy, R. V. and Newman, J., *Journal of the Electrochemical Society*, Vol. 121, 1974, p. 521.
- [31] Brown, O. R. and Thirsk, H. R., *Electrochimica Acta*, Vol. 10, 1965, p. 383.
- [32] Bertocci, U., *Electrochimica Metallorum*, Vol. 3, 1968, p. 275.

Florian Mansfeld¹

Evaluation of Electrochemical Techniques for Monitoring of Atmospheric Corrosion Phenomena

REFERENCE: Mansfeld, Florian, "Evaluation of Electrochemical Techniques for Monitoring of Atmospheric Corrosion Phenomena," *Electrochemical Corrosion Testing, ASTM STP 727*, Florian Mansfeld and Ugo Bertocci, Eds., American Society for Testing and Materials, 1981, pp. 215-237.

ABSTRACT: A review is presented of past and present efforts to use electrochemical techniques to evaluate basic phenomena of atmospheric corrosion, measure time of wetness, and perform corrosion-rate measurements in outdoor exposure. This is followed by a summary of recent work carried out in the author's laboratory. Time-of-wetness measurements have been carried out continuously over a three-year period at the same location using copper/steel and copper/zinc sensors. An analysis of the monthly distribution of relative humidity and corrosion rates determined with the same sensors has resulted in correlations between them. Weight-loss measurements under thin layers of electrolytes that are drying out at RH < 100 percent have shown that, in most cases, corrosion rates are much higher under these conditions than in bulk solutions. Electrochemical measurements carried out under identical conditions show the continuous increase of corrosion rates during the drying period. A comparison of corrosion rates determined by weight loss and electrochemical techniques under thin layers of electrolytes indicates that the electrochemical data underestimate the true corrosion rates. The determination of cell factors based on weight-loss data is one approach for using the electrochemical technique in a more quantitative manner.

KEY WORDS: time of wetness, corrosion monitors, thin layer studies, outdoor exposure, weight loss data, cell factor

Electrochemical techniques are now commonly used for corrosion monitoring and control in aqueous bulk environments, and commercial devices are available for such purposes. It seems to be widely accepted that atmospheric corrosion is of an electrochemical nature (as discussed by Kaesche [1],² Evans [2], and Rozenfeld [3], among others), but only very few attempts have been made to use electrochemical techniques routinely. This is so probably because of the experimental problems owing to corrosion occurring

¹Group manager, Rockwell International Science Center, Thousand Oaks, Calif. 91360.

²The italic numbers in brackets refer to the list of references appended to this paper.

under very thin electrolyte layers that are present only for a fraction of the total exposure time (the so-called time of wetness, t_w).

Most of the efforts to use electrochemical techniques have been in the area of time-of-wetness (t_w) measurements, which do not produce information concerning corrosion rates, but at least show under which atmospheric conditions (temperature, relative humidity, nature of the metal, etc.) corrosion reactions can occur. Sereda [4,5] has described a method for measuring t_w that uses a cell of platinum-foil electrodes on steel or zinc panels. When moisture is present on these cells, a galvanic couple exists. In Sereda's arrangement, the current flow through a shunt resistor is recorded continuously as the potential drop across this resistor. Since the shunt resistor is very large, the measured current is smaller than the galvanic current measured with a zero-resistance ammeter (ZRA) [6]. Time of wetness was arbitrarily defined as the interval during which the potential exceeds 0.2 V. Large variations in t_w values have been found by Sereda [7], the significance of which are not entirely understood. Guttman [8], using Sereda's device, has reported for a location in Canada that t_w corresponded to the time during which relative humidity exceeded 86.5 percent based on four-year averages.

A different approach for t_w measurement is based on early work by Tomashov [9] who used a "galvanic corrosion battery" that consisted of alternate copper and iron plates, and measured the galvanic current using a sensitive galvanometer or a recording microammeter. Kucera et al [10,11] developed this technique further in an attempt to measure the instantaneous rate of atmospheric corrosion of metals. In addition to galvanic cells (copper/steel), electrolytic cells were used with electrodes of only one metal (steel, zinc, or copper) to which an external electromotive force was applied. An instrument containing an electronic integrator was described [10]. The relation between corrosion rates determined from weight-loss data and from electrochemical data obtained with electrolytic cells was found to be relatively constant, but it varied between different exposure sites. It was concluded that after calibration using weight-loss data, the electrochemical technique is suitable for determination of short-term variations of corrosion rates [11]. Haagenrud [12] has performed similar studies with zinc and iron cells in Norway. Jirovsky et al [13] have described an instrument for digital and analog recording of time of wetness using electrolytic sensors of a design determined by the application of the device.

Mansfeld and co-workers have been using copper/steel and copper/zinc sensors, and have determined the galvanic current flow using a ZRA and a logarithmic converter; the effects of salt particles and pollutants have been studied in this manner in the laboratory [14-16]. The changes in cell current with time in outdoor exposure have been recorded, time-of-wetness data have been determined, and attempts have been made to correlate these data with relative humidity.

Friehe and Schwenk [17] have evaluated the use of copper/iron cells, and

have concluded in a limited number of laboratory experiments and outdoor exposures that these electrochemical data cannot be used for determining properties of steels in short-term experiments. They consider the technique more useful for long-term studies and determination of the corrosivity of the environment at a given test site. Kucera and Gullman, however, have found that cells of steel and weathering steel showed different behavior, and concluded that their electrochemical measurements should help to explain the reasons for the protective properties of the corrosion products on weathering steel.³ Gonzales [18], on the other hand, has claimed good agreement between electrochemically obtained information on the influence of various corrosion factors and their real effect on the attack of metals exposed to the atmosphere. In this case, polarization-resistance measurements were performed on a two-electrode system using steel plates in a configuration similar to that of Kucera and Mansfeld. Polarization-resistance measurements have also been performed by Kuznetsov et al [19] for copper and steel. The changes with time of the polarization resistance and ohmic resistance under bulk electrolytes and under thin layers of electrolyte were determined in laboratory experiments. The authors concluded that this measuring technique yields qualitative information about the corrosion kinetics under various atmospheric conditions. Mansfeld and Tsai [20] have used a two-electrode system (steel or zinc) with periodic reversal of the applied electromotive force ($\Delta E = 30$ mV) to determine corrosion rates during drying out of thin electrolyte layers at different relative humidity with or without 1 ppm sulfur dioxide (SO_2). Weight-loss data have been also obtained under thin layers under identical conditions. As will be discussed later, the electrochemical data underestimate the true corrosion loss, and it is necessary to determine correction factors as found by Kucera in outdoor exposure in Sweden [11].

Mazza et al [21] have used a galvanic cell bronze/artificial corrosion products/porous gold plate to study atmospheric corrosion phenomena in laboratory and outdoor exposure with the aim of measuring corrosion rates under various exposure conditions and evaluating the effectiveness of various methods of corrosion protection of gold-plated bronze works of art.

Mikhailovskii and co-workers have employed, in a series of papers, electrochemical techniques for the study of basic phenomena in atmospheric corrosion. Thin films of metals were deposited on glass substrates, and the corrosion rates of the metals were calculated from the changes of the resistance of the current-carrying layer [22]. In this manner, the electrochemical kinetics of the corrosion of zinc and iron under thin layers of electrolytes (30 to 500 μm thickness) have been studied [22,23]. In further work [24], a method for continuous monitoring of atmospheric corrosion rates has been discussed, which uses "differential" and "integral" sensing elements. Good

³This publication, pp. 238-255.

agreement between these data and weight-loss data were reported for a six-month period. Time-of-wetness data were recorded using a copper wire tightly wound around a rod made from the metal under investigation. The processing of experimental data is described. It is concluded that the atmospheric corrosion sensing elements produce information that can be used to estimate atmospheric corrosion rates in different climatic regions from their meteorological characteristics. This technique was also used in developing a general method for calculating atmospheric corrosion rates, which takes into account that corrosion is due to adsorption and phase films of moisture [25]. Data were obtained for cadmium and zinc in natural environments [25] and in artificial climate chambers [26] where the corrosion constants, which have to be known in order to calculate the expected corrosion effects under natural exposure conditions, were obtained. The effects of meteorological factors such as relative humidity, air temperature, wetting time by phase layers of moisture, and chemical composition of the atmosphere on the corrosion rates of aluminum and its alloys have been studied in a similar manner [27].

By means of continuous resistance measurements on steel wire specimens, time-of-wetness measurements, SO_2 concentrations, and solar radiation data over a three-year period, a model of atmospheric corrosion of steel in rural districts has been developed using a statistical treatment of experimental data [28]. Foil sensors [24], the resistance of which changed owing to corrosion, were used in a study of simulated atmospheric corrosion phenomena in artificial climate chambers [29]. An atmospheric test rig has been described that uses sectioned electrolytic cells made of brass as sensors for the phase films of moisture [30]. SO_2 concentration, relative humidity, temperature, and weight loss of a number of different materials were also monitored. The resulting information was used in calculating the corrosion accelerating factors in the presence of SO_2 , which have to be known in order to estimate the atmospheric corrosion rates in industrial atmospheres in various climatic zones based on the approach developed by Mikhailovskii and his colleagues [25,27].

Strekalov, Mikhailovskii, and co-workers have also used a quartz resonator to study corrosion processes of metals under adsorbed films of electrolytes. Initial studies showed that in a pure moist atmosphere (relative humidity = 93 percent) the oxide film on magnesium grew by about 5 to 7 Å in the first hour and less during further exposure [31]. The effect of temperature on the adsorption of moisture and the corrosion rate of zinc under atmospheric conditions has been studied with the same technique [32]. A number of further studies with this technique, which is not of an electrochemical nature and will therefore not be discussed further in this review, has been published by this group [33-39]. Lee et al [40] have used *in situ* quartz crystal oscillator microbalance and electrical resistance change measurements to study atmospheric corrosion phenomena.

This summary of recent work with electrochemical techniques applied

under the special conditions of atmospheric corrosion shows that progress has been made, especially in the determination of time-of-wetness data (t_w) and, to some extent, atmospheric corrosion rates. The dependence of t_w on atmospheric and materials parameters is not yet clear, and more research under a variety of experimental conditions is necessary. The determination of instantaneous corrosion rates with electrochemical techniques has to be evaluated critically in the light of Friehe and Schwenk's comments [17] and Kucera's findings [11] that a cell factor that is site dependent has to be determined from weight-loss data in order to make the electrochemical technique useful. It has to be considered, at this point, that Kucera's approach (electrolytic cell with external electromotive force) produces data from which it is not possible to quantitatively calculate corrosion rates. The polarization-resistance measurements of Gonzales [18] and Kuznetsov et al [19] lend themselves easier to a calculation of corrosion rates. Mansfeld and Tsai [20] have used this technique in the laboratory (discussed later). The approach of the Russian workers is very interesting. Models for atmospheric corrosion processes under various climatic conditions have been prepared, and a broad experimental program aimed at determining the data needed to apply the model to real situations is being carried out.

Some of the questions that remain to be answered concerning the application of electrochemical techniques to the investigation of atmospheric corrosion phenomena have been evaluated in the author's laboratory. Recent results concerning the correlation between t_w and relative-humidity data, the importance of the corrosion occurring in the time period during which thin electrolyte layers dry out, and a comparison of weight-loss and electrochemical data obtained under identical conditions in the laboratory will be discussed next.

Experimental Results and Discussion

Time-of-Wetness Data and Correlation with Relative Humidity

Atmospheric corrosion monitors (ACM) consisting of copper/steel or copper/zinc galvanic cells have been exposed since 1975 on the Science Center roof [14-16]. The electrochemical data in the form of the logarithm of the galvanic current I_g have been recorded continuously as have the relative humidity, air temperature, and temperature of a galvanized steel panel exposed in the same manner as the ACM (30 deg angle to the south). Figure 1 shows typical examples of the output of a copper/zinc ACM ($\log I_g$), relative humidity and temperature of the air (T_{air}) and the galvanized steel panel (T_{me}) for a 36-h period in February 1979. Also included in Fig. 1 is a linear plot of I_g and the integrated charge, Q_g , which was obtained by graphical integration of the I_g time plot over 1-h periods. During the time period covered in Fig. 1, rainfall occurred on February 21, and relative humidity exceeded

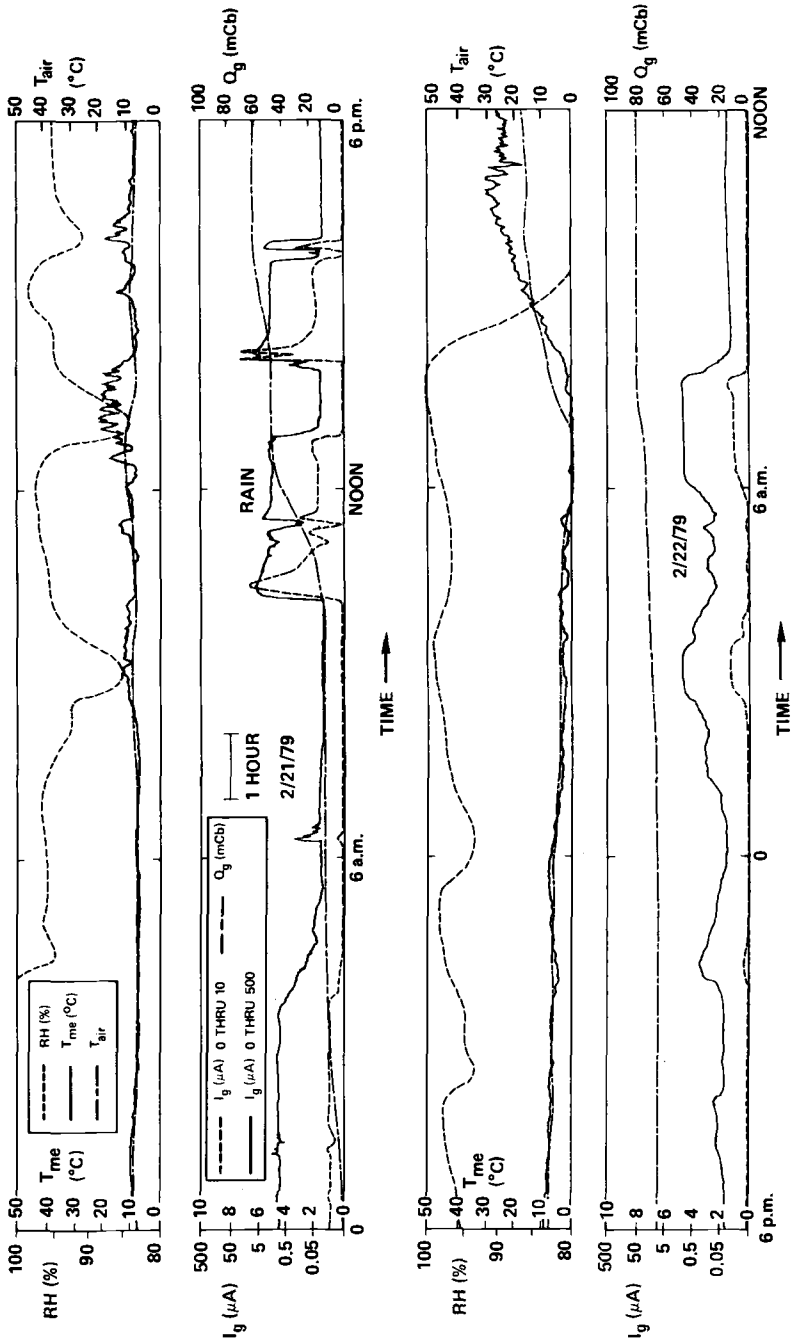


FIG. 1—Current flow of copper/zinc ACM, relative humidity, air (T_{air}) and galvanized steel panel (T_{me}) temperature for a 36-h period.

80 percent for the entire time except for the last 3 h. The air temperature fluctuated between 0 and 15°C; the panel temperature was between 0 and 30°C. The current flow was fairly high during the night hours, and then dropped sharply to $I_g < 0.05 \mu\text{A}$ until rainfall occurred at about 10:00 a.m. for 3 h. Large fluctuations of the current were observed, as can be seen more clearly on the linear current plot. Current flow exceeding $1 \mu\text{A}$ occurred again during the night and the early morning hours of February 22. The plot of the total charge as a function of time indicates the importance of the rain period to the overall corrosion loss; an increase of Q_g by a factor of three is observed. For the rest of the time period shown in Fig. 1, Q_g increased by another 30 percent to a final value of 87 mC ($19 \text{ mC}/\text{cm}^2$). The current flow corresponds to a corrosion rate of $0.65 \text{ mg}/\text{dm}^2 \cdot \text{day}$ or $3.3 \mu\text{m}/\text{year}$, which is a reasonable value for galvanized steel. From data such as shown in Fig. 1, monthly t_w averages have been calculated, which are shown in Fig. 2 for a three-year period (1976–1978). For most of the time, t_w was taken as the time for which the galvanic current exceeded the background current of the ZRA amplifier ($0.02 \mu\text{A}$). Starting in June 1978, t_w was redefined as the time for which $I_g > 0.05 \mu\text{A}$ (about $0.01 \mu\text{A}/\text{cm}^2$) (t_w' in Fig. 2). As shown in Fig. 1, for most of the wetness period the corrosion current was rather low; significant corrosion occurred only during the drying-out periods or during rain. It might be necessary to define t_w as the time for which a certain corrosion rate (for example, $1 \mu\text{m}/\text{year}$) is exceeded, which would correspond to about $0.1 \mu\text{A}/\text{cm}^2$ for steel and $0.07 \mu\text{A}/\text{cm}^2$ for zinc. This approach would reduce the t_w data in Fig. 2 considerably.

The spread in t_w is quite large; average values as high as 22.8 h/day (95

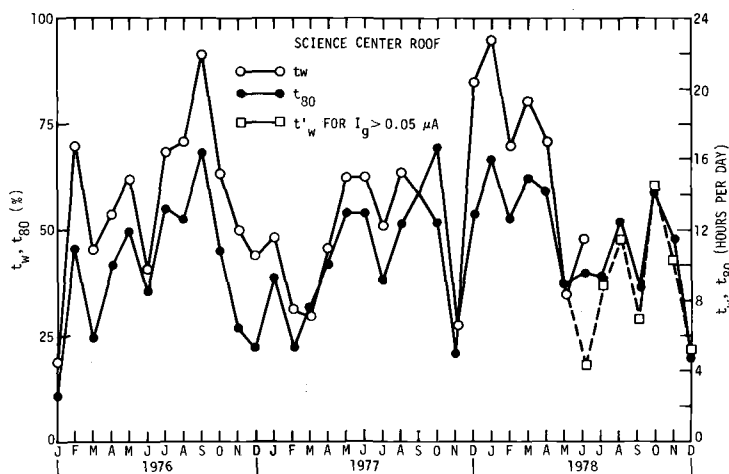


FIG. 2—Time-of-wetness (t_w) and time for relative humidity ≥ 80 percent (t_{80}) for a three-year period on the Science Center roof (copper/steel and copper/zinc ACMs).

percent) and as low as 4.5 h/day (19 percent) can occur. For the rather dry year of 1977, t_w did not exceed 17 h/day (71 percent), while for the rain period between December 1977 and April 1978, t_w exceeded 16 h/day (67 percent) for five consecutive months. Also shown in Fig. 2 is the time t_{80} for which relative humidity > 80 percent. In most cases $t_w > t_{80}$, which suggest that t_w , in the present definition, is related to a relative-humidity value lower than 80 percent. The agreement between t_{80} and t_w' is very close except for June 1978.

In order to obtain correlations between corrosion rates as measured by the galvanic current I_g and relative humidity, the distribution of different levels of I_g and relative humidity has been determined for the time between June 1978 and March 1979. Figure 3 shows as an example the distribution of relative humidity between June and September 1978. These relative humidity versus percent-of-time curves have a characteristic shape, with almost identical data for June and July, a small shift to lower values for September, and a larger shift to higher relative humidity values for August. The corresponding $\log I_g$ versus percent-of-time plot is shown in Fig. 4. The dependence of I_g on relative humidity has been obtained by combining the data in Figs. 3 and 4. An exponential relationship between $\log I_g$ and relative humidity seems to be indicated (Figs. 5 and 6) in the form

$$\log I_g = a \cdot e^{b \cdot \text{relative humidity}} \quad (1)$$

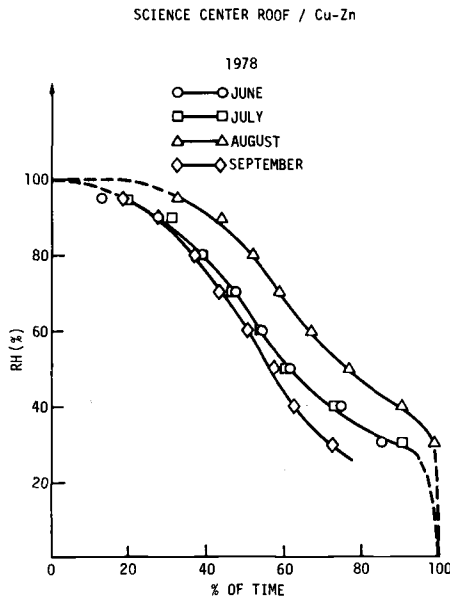


FIG. 3—Distribution of relative humidity as a function of time for June to September 1978.

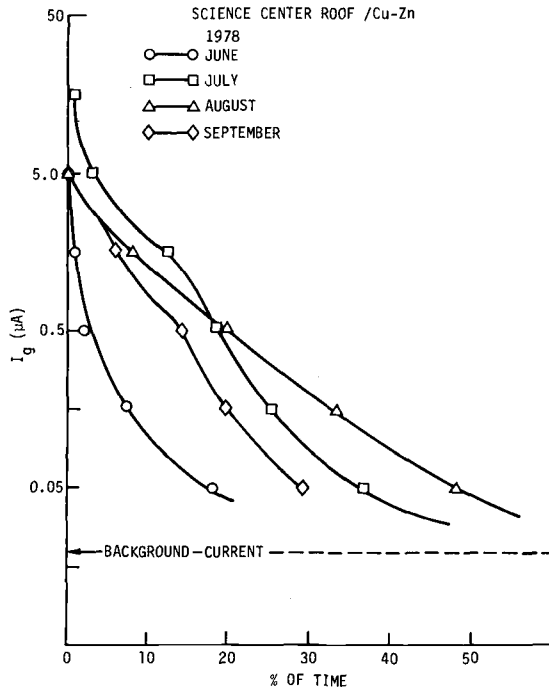


FIG. 4—Distribution of $\log I_g$ as a function of time for June to September 1978 (copper/zinc ACM).

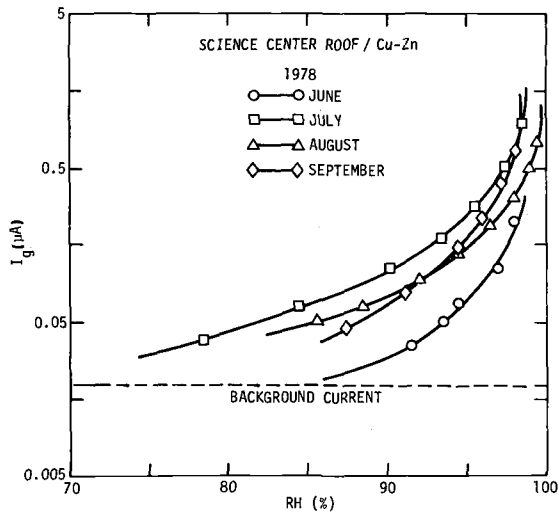


FIG. 5—Dependence of $\log I_g$ on relative humidity for June to September 1978.

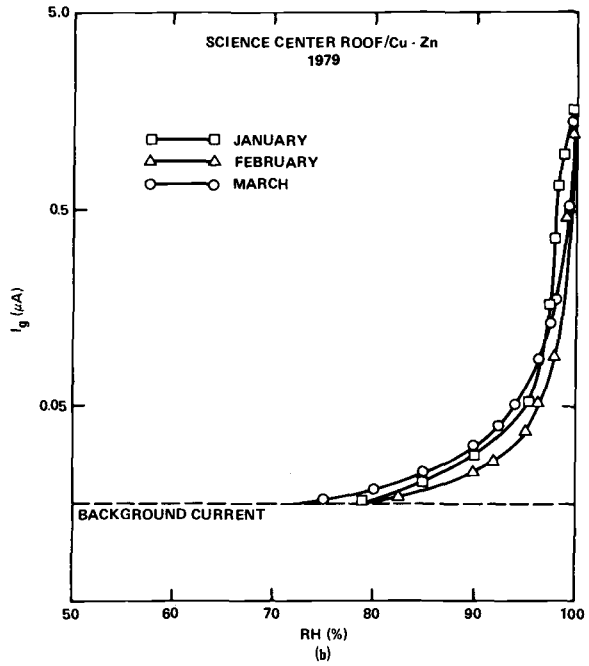
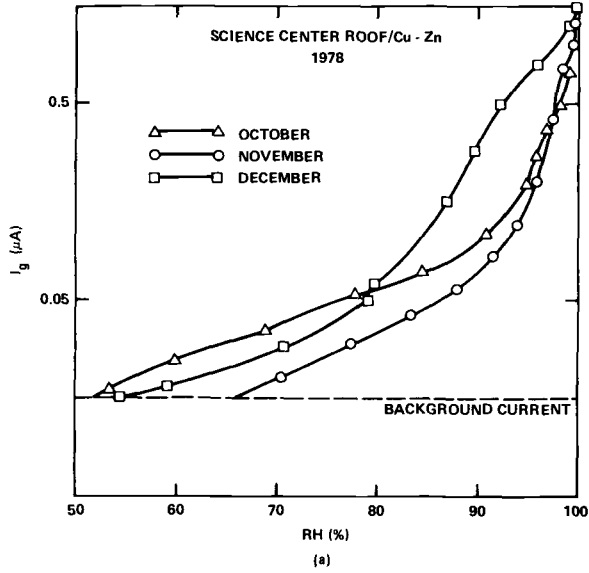


FIG. 6—Dependence of $\log I_g$ on relative humidity for (a) fourth quarter of 1978 and (b) first quarter of 1979.

Significant corrosion occurs only for relative humidity ≥ 70 to 90 percent, where based on weight-loss data the "critical humidity" for atmospheric corrosion of steel occurs [41]. The results for different months fall on different curves.

It is interesting to note that while the relative humidity values were similar for June and July in Fig. 3, the $\log I_g$ -relative humidity curves in Fig. 5 show the largest spread between June, which has the lowest corrosion rate at a given relative humidity, and July, which has the highest I_g values. These results suggest that the corrosion rate–relative humidity relationship is determined by additional factors, such as pollutant concentrations etc. Therefore it does not seem to be sufficient to rely solely on relative humidity data to predict atmospheric corrosion rates, as is sometimes suggested. The spread of data in Fig. 5 is about a factor of three. Further examples of $\log I_g$ -relative humidity relationships are given in Fig. 6 for the fourth quarter of 1978 and the first quarter of 1979. There is a marked difference between these two time periods with much smaller current flow for the first quarter of 1979.

Corrosion Behavior Under Thin Layers of Electrolytes

The work carried out by Rozenfeld and his co-workers [3] has shown that corrosion rates are greatly accelerated under thin layers of electrolytes due to a decrease of the diffusion layer, which results in a higher rate of oxygen reduction (the rate-controlling reaction in a diffusion-controlled process). The results concerning the kinetics of corrosion reactions under thin electrolyte layers obtained in this laboratory have been reported elsewhere [42]. Further experiments have been carried out in which corrosion rates have been determined under thin layers drying out at relative humidity < 100 percent using a unique weight-loss technique and a polarization-resistance technique under identical environmental conditions [20]. Some of the more important results are summarized in the next three sections.

Weight-Loss Experiments—For the thin-layer electrolyte studies, flat plates (2 by 2 in.) of 4130 steel and zinc (99.9 percent) were exposed horizontally in glass containers through which air at constant relative humidity with or without 1 ppm SO_2 was flowing at a rate of 2 L/min. A 0.5-mm-thick layer of electrolyte [0.01 *N* sodium chloride (NaCl), sodium sulfate (Na_2SO_4), hydrochloric acid (HCl), sulfuric acid (H_2SO_4), or deionized water] was placed on the samples, the unexposed side of which was coated with an organic coating. Experiments were carried out at relative humidity = 30, 45, 60 and 75 percent. For comparison, weight-loss data were also obtained by total immersion in bulk electrolyte for 4 h, which is the time for drying-out at relative humidity = 60 percent for steel. The weight loss was determined after removal of the corrosion products and taking into account a correction factor for blank samples. Figures 7 to 9 show the results in air and air + SO_2 for steel and zinc in four different electrolytes and in deionized water.

Increasing relative humidity increases the weight loss for steel in air and in air + SO₂ (Fig. 7), most likely owing to the longer time period during which corrosion can occur. An accelerating effect of SO₂ becomes evident at the higher relative humidity values. A comparison of the thin layer and bulk data shows that, particularly in neutral solutions, corrosion is much more severe under thin-layer conditions. The results obtained with additions of sodium nitrite (NaNO₂) and the vapor phase inhibitor dichan (dicyclohexylamine nitrate) and the weight-loss data collected in argon and argon + SO₂ have been discussed elsewhere [20].

For zinc (Fig. 8), no effect of SO₂ was observed for NaCl and Na₂SO₄. For H₂SO₄, surprisingly, the weight loss Δm was lower than in the neutral solutions and independent of relative humidity. In HCl, a strong effect of relative humidity was found in air; in air + SO₂, Δm was much lower than in air and similar to that obtained in H₂SO₄. In NaCl and Na₂SO₄, corrosion rates

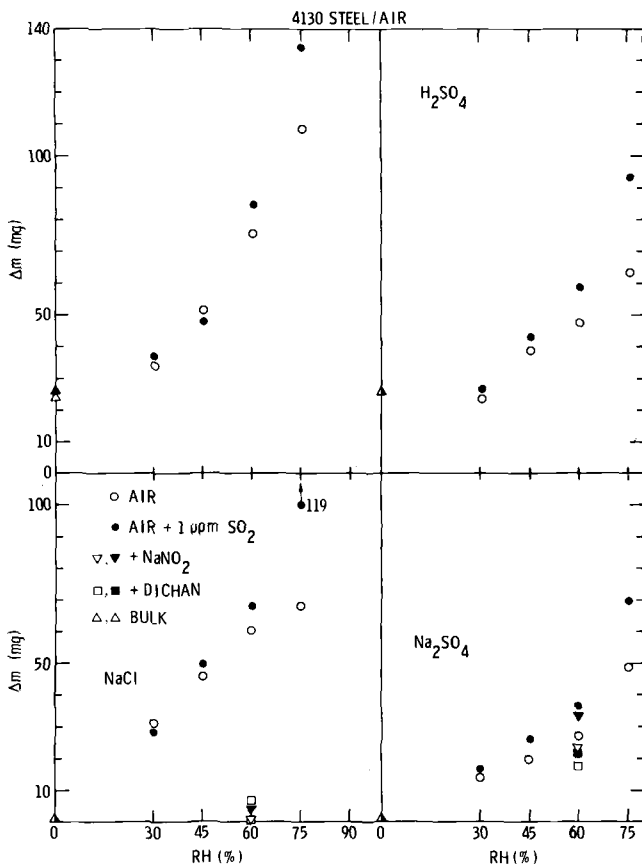


FIG. 7.—Weight-loss data for 4130 steel in bulk and under thin electrolyte layers.

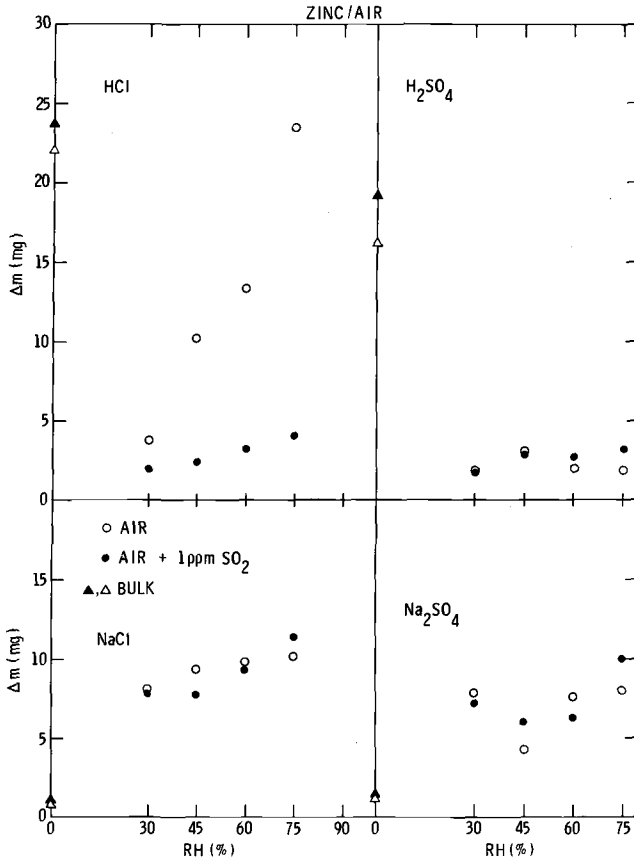


FIG. 8—Weight-loss data for zinc in bulk and under thin electrolyte layers.

were much higher under thin layers than in bulk solutions; for HCl and H₂SO₄, on the other hand, corrosion rates were much higher in the bulk electrolyte.

Experiments were also carried out in deionized water to eliminate the effect of anions on the action of SO₂. The effects of SO₂ were different for steel and zinc (Fig. 9): for steel, Δm increased with increasing relative humidity and SO₂ accelerated corrosion; for zinc, relative humidity also accelerated corrosion, but SO₂ had an inhibiting effect.

The effect of electrolyte concentration, c , on corrosion rates under thin layers of electrolytes was investigated in Na₂SO₄ (Fig. 10). For both 4130 steel and zinc, an approximately linear increase of Δm with $\log c$ was observed.

The corrosion rates calculated from the weight-loss data are very high: $\Delta m = 50$ mg for steel corresponds to 1160 mg/dm²·day or 5.4 mm/year,

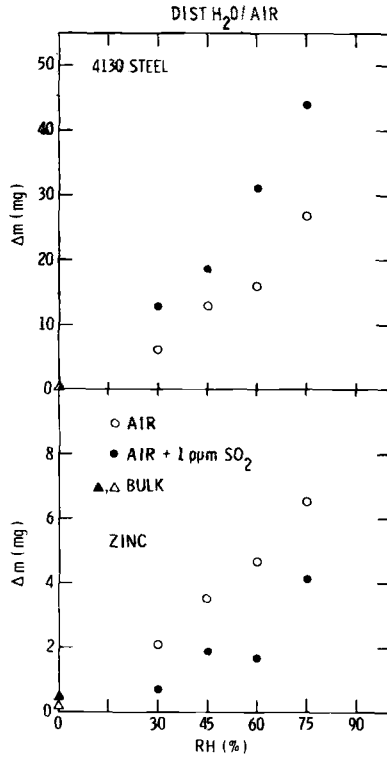


FIG. 9—Weight-loss data for 4130 steel and zinc under thin layers of deionized water.

while $\Delta m = 10$ mg for zinc corresponds to $230 \text{ mg/dm}^2 \cdot \text{day}$ or 1.2 mm/year assuming a corrosion period of 4 h. With respect to atmospheric corrosion conditions, one has to consider that the surfaces are completely wetted only for a fraction of the total exposure time, and that periods of high corrosion activity occur only for very short time periods (as shown in Fig. 1). The electrolyte is most likely also less concentrated than $10^{-2} N$, which would lead to lower corrosion rates according to the results of Fig. 10.

Electrochemical Experiments—The electrochemical experiments were conducted in the same manner as the weight-loss data. Two types of ACMs were used: the galvanic type, which is also being used for outdoor exposure (copper/steel, copper/zinc), and a type consisting of plates of one metal (steel or zinc) arranged so that a two-electrode system is established [20]. A potential difference $\Delta E = 30 \text{ mV}$ is applied to these cells with polarity reversal occurring every 50 s to avoid irreversible changes of the two electrodes. The measured current, I_{30} , is related to the corrosion current, I_{corr} , by

$$I_{\text{corr}} = \frac{2BI_{30}}{\Delta E} = \frac{B}{R_p} = kI_{30} \quad (2)$$

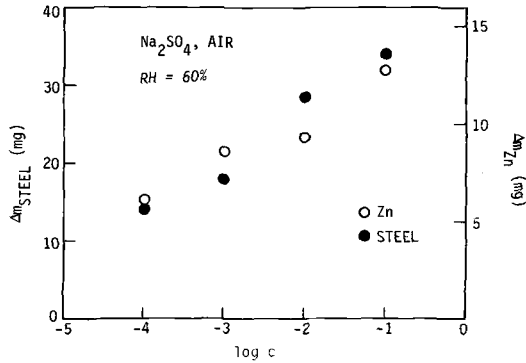


FIG. 10—Weight-loss data for 4130 steel and zinc under thin layers as a function of Na_2SO_4 concentration.

where R_p is the polarization resistance, and B is a function of Tafel slopes, which can have values between $B = 6.5$ and 52 mV for theoretical Tafel slopes, leading to an average of $k = 0.43$ to 3.47 for $\Delta E = 30$ mV [43]. The ACMs were polished with 600 SiC paper and placed in the glass cells; a 0.5-mm layer of electrolyte was applied. The current was recorded continuously until the surface layer had dried out (indicated by a sharp drop of the current). The results obtained for copper/steel and steel ACMs under a layer of 0.01 N Na_2SO_4 as a function of relative humidity are shown in Figs. 11 and 12. The current-time curves are characterized by a continuous increase of the current, which becomes more pronounced when the visible electrolyte layer starts to disappear. This phenomenon is similar to the results obtained in outdoor exposure [15, 16, 20]. For both types of ACMs, the time at which the current maximum occurs and the time at which the current decreases to values less than $1 \mu\text{A}$ both increase with increasing relative humidity except at relative humidity = 30 and 45 percent, where the main effect of increasing relative humidity is an increase of the current maximum and the total current flow.

In contrast with copper/steel, a sharp current maximum is not observed for copper/zinc during the drying-out period (Fig. 13). On the other hand, sharp maxima occur for the zinc ACM (Fig. 14) except at relative humidity = 90 percent, where significant current flow is observed up to 6 h. For relative humidity ≤ 75 percent, the time at which the surface dries out is less than 3 h.

In Figs. 11 to 14, the charge Q obtained by graphical integration of the current-time curves is listed. Higher values of Q are observed for galvanic couples than for one-metal ACMs. It should be noted that the charge data for steel and zinc have to be multiplied by the factor k (Eq 2) to obtain the total charge corresponding to the corrosion loss during the drying-out process.

The charge data plotted in a semilog plot in Fig. 15 as a function of relative humidity suggests a relationship in the form

$$Q = c \cdot e^{d \cdot \text{relative humidity}} \quad (3)$$

which is similar to that found for the relative-humidity dependence of $\log I_g$ in outdoor exposure (Eq 1).

Comparison of Weight Loss and Electrochemical Results—Since the weight loss and the electrochemical data were obtained under identical conditions in the laboratory, it is possible to determine the degree to which ACM data provide accurate information concerning corrosion rates. This question becomes even more important when one considers Kucera's finding [11] that the current flow from steel sensors polarized at constant $\Delta E = 100$ mV accounted for only about 15 percent of the weight loss observed in outdoor exposure. According to Faraday's law, a weight loss $\Delta m = 1$ mg/cm² corresponds to

$$3.45 \text{ C/cm}^2 \text{ for iron } (z = 2)$$

and

$$2.94 \text{ C/cm}^2 \text{ for zinc } (z = 2)$$

A comparison of weight loss (Δm) and electrochemical data (Q) per unit area is given in Fig. 16 for copper/steel and copper/zinc, and in Fig. 17 for steel

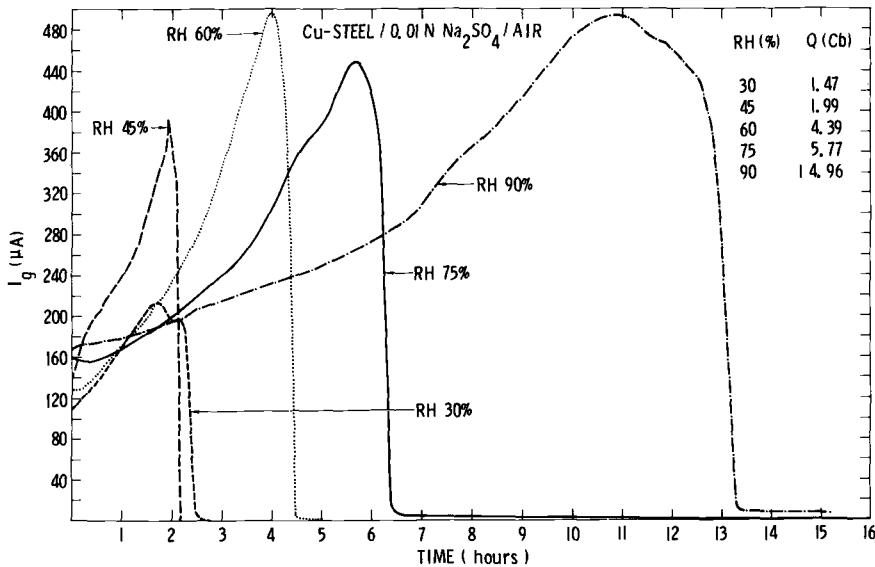


FIG. 11—Galvanic current flow for copper/steel during drying out of a thin 0.01 N Na_2SO_4 layer at different relative humidity values.

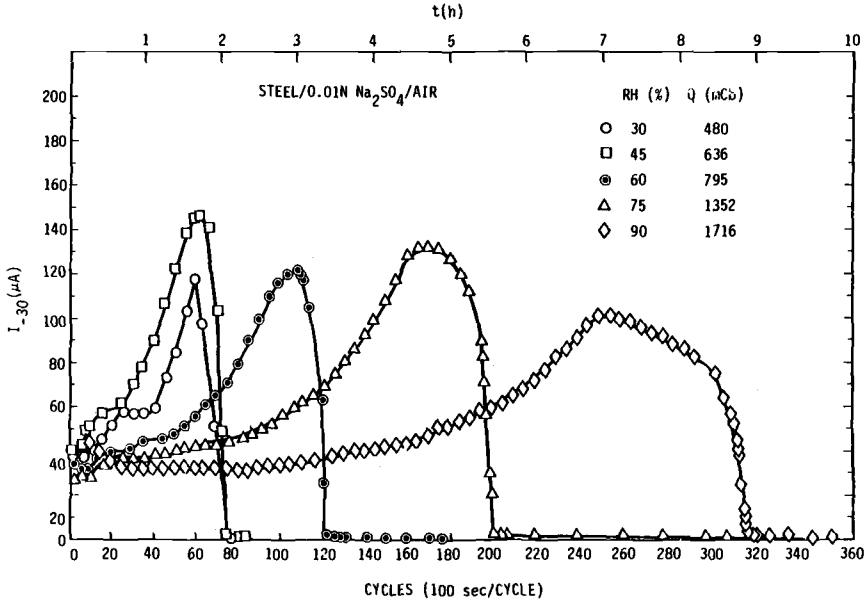


FIG. 12—Current flow at $\Delta E = \pm 30$ mV for 4130 steel during drying out of a thin 0.01 N Na₂SO₄ layer at different relative humidity values.

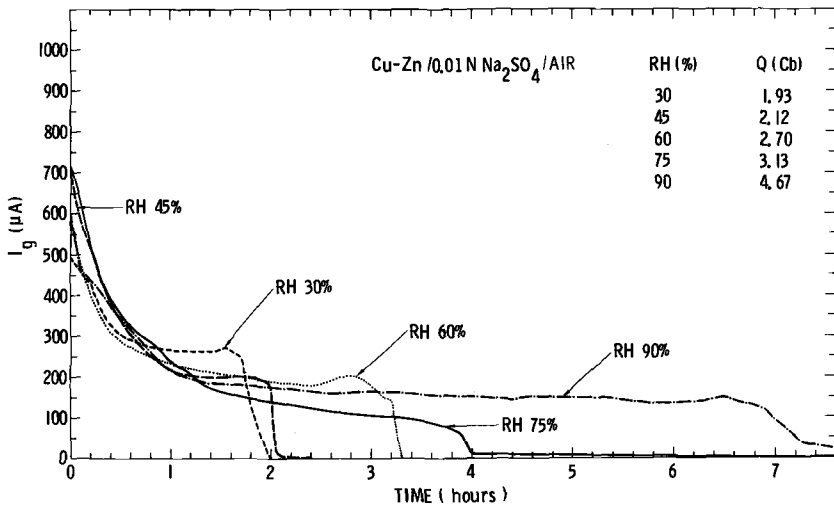


FIG. 13—Galvanic current flow for copper/zinc during drying out of a thin 0.01 N Na₂SO₄ layer at different relative humidity values.

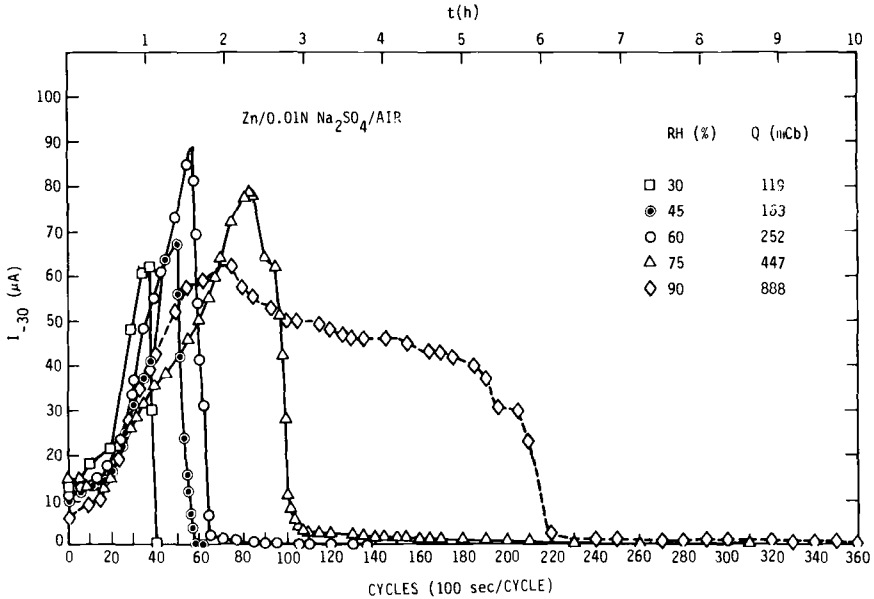


FIG. 14—Current flow at $\Delta E \pm 30$ mV for zinc during drying out of a thin 0.01 N Na₂SO₄ layer at different relative humidity values.

and zinc. A linear relationship is observed for copper/steel and steel; for copper/zinc and zinc, Δm seems to be independent of Q . The latter result is owing to the lack of change of the weight loss with relative humidity (shown in Fig. 8). For copper/steel, a slope of 0.75 C/mg and for steel a slope of 0.28 C/mg are observed, both slopes being too low. In Table I the ratio of the charge obtained by the electrochemical (Q_g) and weight-loss (Q_{wl}) measurement is given for steel and zinc as a function of relative humidity. For steel an average of 0.20 is found, which is close to Kucera's result. For zinc the average is 0.72, with larger scatter.

The data obtained with 30-mV pulses have not been converted into corrosion currents because of the uncertainty of the correct values of the conversion factors B, k . However, since for diffusion control [15]

$$I_g = I_{\text{corr}},$$

the ratio

$$\frac{I_g}{I_{30}} = \frac{I_{\text{corr}}}{I_{30}} = k' = \frac{Q_g}{Q_{30}} \quad (4)$$

can be determined from the experimental data for steel and zinc ACMs. As

Table I shows, the experimental k' values fall between 1.5 and 4.4 for steel and between 3.0 and 8.1 for zinc. This indicates that, at least for steel, the kinetics of the corrosion process show the expected behavior.

Another factor that can affect the electrochemical measurements is the IR-drop due to low solution conductivity, which would lead to an effective $\Delta E_{\text{eff}} < \Delta E = 30$ mV and correspondingly smaller I_{30} values. It was found, however, using a-c impedance measurements for steel and zinc ACMs under 0.01 N Na_2SO_4 , that the solution resistance during the first 3 h of the experiment during which the surface was wet was about 12Ω ($28 \Omega \cdot \text{cm}^2$), which does not seem high enough to cause a significant change of ΔE . The plot in Fig. 18 of the imaginary part Z'' versus the real part Z' was obtained with a Solartron 1174 frequency analyzer and a zero-resistance ammeter over a frequency range of 100 kHz to 10 mHz. The intercept at high frequencies at the Z' -axis is the solution resistance. The diameter of the semicircles in Fig. 18 decrease with time owing to the decrease of the polarization resistance.

The most likely reason for a low cell factor is probably corrosion occurring on a single plate without electrolytic connection to a neighboring plate. In this case, no current flow would be registered despite the occurrence of corro-

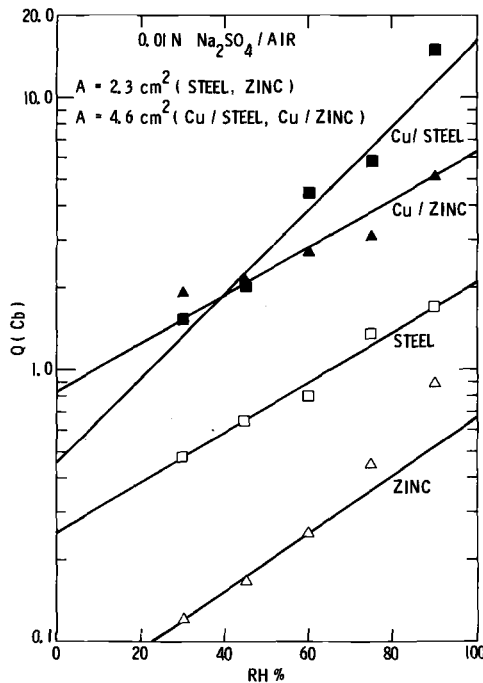


FIG. 15—Integrated current values (Q) as a function of relative humidity for the four different ACMs (Figs. 11 to 14).

TABLE 1—Comparison of charge data obtained in 0.01 N Na₂SO₄/air (Q in C/cm²).

Test Condition	Q _{w1}	Q _g	Q _g /Q _{w1}	Q ₃₀	Q _g /Q ₃₀ = k'
Steel					
RH, % ^a					
30	1.90	0.320	0.17	0.209	1.53
45	2.75	0.433	0.16	0.276	1.57
60	3.62	0.954	0.26	0.345	2.77
75	6.49	1.254	0.19	0.587	2.13
90	not determined	3.252		0.746	4.36
Zinc					
RH, %					
30	0.89	0.42	0.47	0.05	8.11
45	0.48	0.46	0.96	0.07	6.50
60	0.87	0.59	0.68	0.11	5.36
75	0.90	0.68	0.76	0.19	3.50
90	not determined	1.14	...	0.39	2.95

^a RH = relative humidity.

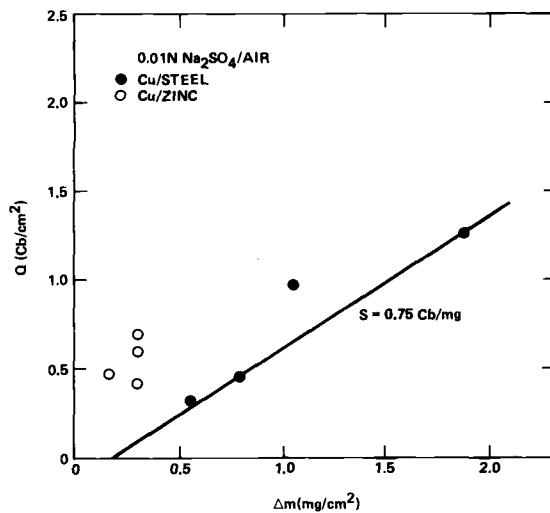


FIG. 16—Correlations between weight loss (Δm) and electrochemical (Q) data for copper/steel and copper/zinc ACMS.

sion. An example of this possibility was found when carbon particles were spread over a freshly polished copper/steel ACM which was then exposed at relative humidity \approx 95 percent. No current flow was measured for several hours. When the particles were removed, however, pronounced corrosion on the steel plates was observed by using a low-magnification microscope, with some discoloration on the copper plates where the carbon particles had been situated.

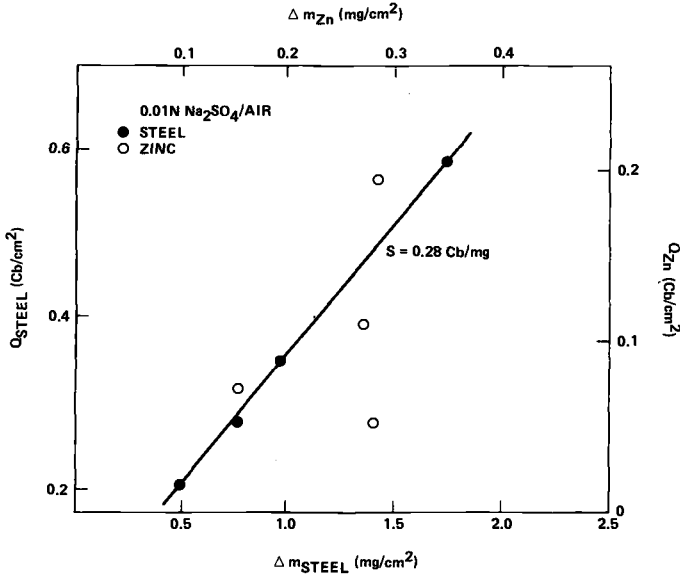


FIG. 17—Correlations between weight loss (Δm) and electrochemical (Q) data for steel and zinc ACMs.

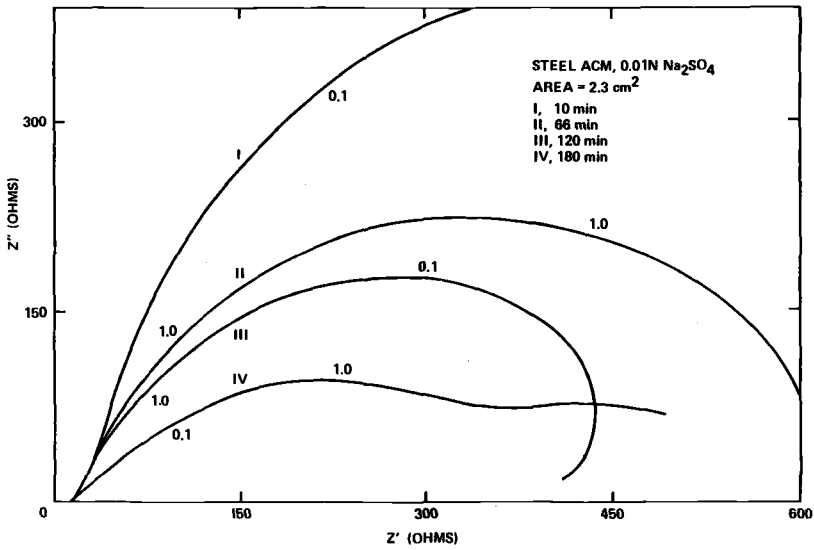


FIG. 18—Alternating-current impedance plot for steel ACM under 0.01 N Na₂SO₄ over a 3-h time period (frequency in hertz).

Summary and Conclusions

1. A review of past and present efforts to use electrochemical techniques to evaluate basic phenomena of atmospheric corrosion, measure time of wetness, and perform corrosion-rate measurements in outdoor exposure has been given.

2. Time-of-wetness (t_w) measurements have been recorded continuously over a three-year period at the same location. Wide fluctuations of t_w are observed. For a better definition of t_w , it is probably necessary to define t_w as the time during which a certain corrosion rate is exceeded.

3. An analysis of the monthly distribution of relative humidity and electrochemical data (I_g) recorded at the same location suggests an exponential dependence of $\log I_g$ on relative humidity.

4. Weight-loss measurements under thin layers of electrolytes drying out at relative humidity < 100 percent have shown that, in most cases, corrosion rates are much higher under these conditions than in exposure to bulk solutions. Electrochemical measurements show the continuous increase of corrosion rates during the drying-out period.

5. The results of laboratory and exposure tests indicate that the electrochemical data obtained with ACMs underestimate the true corrosion rates. This is most likely owing to problems in quantitatively analyzing these data, corrosion on single-cell plates without electrolytic contact to neighboring plots, and to IR-drop effects. The determination of cell factors based on weight-loss data is one approach to using electrochemical techniques in a more quantitative manner.

Acknowledgments

This work was sponsored, in part, by the Office of Naval Research under Contract N00014-75-C-0788, NR 036-108. S. Tsai and S. L. Jeanjaquet assisted in collecting the experimental data.

References

- [1] Kaesche, H., *Werkstoffe und Korrosion*, Vol. 15, 1964, p. 379.
- [2] Evans, U. R., *Nature*, Vol. 206, 1965, p. 980; *Corrosion Science*, Vol. 9, 1969, p. 813; *Corrosion Science*, Vol. 12, 1972, p. 227.
- [3] Rozenfeld, I. L., *Atmospheric Corrosion of Metals*, National Association of Corrosion Engineers, 1972.
- [4] Sereda, P. J., "Measurement of Surface Moisture and Sulfur Dioxide Activity at Corrosion Sites," ASTM Bulletin No. 246, American Society for Testing and Materials, 1960, p. 47.
- [5] Sereda, P. J., *Industrial and Engineering Chemistry*, Vol. 52(2), 1965, p. 157.
- [6] Lauer, G. and Mansfeld, F., *Corrosion*, Vol. 26, 1970, p. 504.
- [7] Sereda, P. J. in *Corrosion in Natural Environments*, ASTM STP 558, American Society for Testing and Materials, 1974, p. 7.
- [8] Guttman, H. in *Metal Corrosion in the Atmosphere*, ASTM STP 435, American Society for Testing and Materials, 1968, p. 223.
- [9] Tomashov, N. D., *Theory of Corrosion and Protection of Metals*, Macmillan, New York, 1966, Chapter 14.

- [10] Kucera, V. and Mattson, E. in *Corrosion in Natural Environments*, ASTM STP 558, 1974, p. 239.
- [11] Kucera, V. and Collin, M. in *Proceedings*, 6th European Congress on Metallic Corrosion, Society of Chemical Industry, London, 1977, p. 189.
- [12] Haagenrud, S. E., "Investigation of the Atmospheric Corrosivity by Means of an Electrochemical Technique," paper presented at the 154th Electrochemical Society Meeting, Pittsburgh, Pa., 15-20 Oct. 1978.
- [13] Jirovsky, I., Kokoska, I., and Prusek, J., *Werkstoffe und Korrosion*, Vol. 27, 1976, p. 16.
- [14] Mansfeld, F. and Kenkel, J. V., *Corrosion Science*, Vol. 16, 1976, p. 111.
- [15] Mansfeld, F. and Kenkel, J. V., *Corrosion*, Vol. 33, 1977, p. 13.
- [16] Mansfeld, F., *Werkstoffe und Korrosion*, Vol. 30, 1979, p. 38.
- [17] Friehe, W. and Schwenk, W., *Stahl und Eisen*, Vol. 97, 1977, p. 686.
- [18] Gonzales, J. A., *Werkstoffe und Korrosion*, Vol. 29, 1978, p. 556.
- [19] Kuznetsov, V. A., Polyakov, S. G., Gerasimenko, Yu. S., and Kotlov, Yu. G., *Protection of Metals*, Vol. 12, 1976, p. 578.
- [20] Mansfeld, F. and Tsai, S., *Corrosion Science*, Vol. 20, 1980, p. 853.
- [21] Mazza, B., Pedferri, P., Re, G., and Sinigaglia, D., *Corrosion Science*, Vol. 17, 1977, p. 535.
- [22] Zinevich, A. M., Sergeeva, E. I., Mikhailovskii, Yu. N., and Serofimovich, V. B., *Protection of Metals*, Vol. 6, 1970, p. 310.
- [23] Gladkikh, Yu. P., Mikhailovskii, Yu. N., Shuvakhina, L. A., and Nazarova, R. I., *Protection of Metals*, Vol. 6, 1970, p. 456.
- [24] Mikhailovskii, Yu. N., Shuvakhina, L. A., Klark, H. B., and Agafonov, V. V., *Protection of Metals*, Vol. 7, 1971, p. 125.
- [25] Mikhailovskii, Yu. N., Klark, G. B., Shuvakhina, L. A., Sanko, A. P., Gladkikh, Yu. P., and Agafonov, V. V., *Protection of Metals*, Vol. 7, 1971, p. 466.
- [26] Mikhailovskii, Yu. N., Shuvakhina, L. A., and Wang, C. H., *Protection of Metals*, Vol. 9, 1973, p. 135.
- [27] Mikhailovskii, Yu. N., Klark, G. B., Shuvakhina, L. A., Agafonov, V. V., and Zhuravleva, N. I., *Protection of Metals*, Vol. 9, 1973, p. 240.
- [28] Mikhailovskii, Yu. N., Agafonov, V. V., and Sanko, V. A., *Protection of Metals*, Vol. 13, 1977, p. 429.
- [29] Shuvakhina, L. A., Mikhailovskii, Yu. N., Sharonova, N. F., and Sedova, V. S., *Protection of Metals*, Vol. 13, 1977, p. 130.
- [30] Mikhailovskii, Yu. N., Sanko, V. A., Sokolov, N. A., and Kudryatsev, P. N., *Protection of Metals*, Vol. 14, 1978, p. 426.
- [31] Strekolov, P. V. and Mikailovskii, Yu. N., *Protection of Metals*, Vol. 7, 1971, p. 120.
- [32] Strekolov, P. V., Agafonov, V. V., and Mikhailovskii, Yu. N., *Protection of Metals*, Vol. 8, 1972, p. 521.
- [33] Mikhailovskii, Yu. N. and Strekalov, P. V., *Protection of Metals*, Vol. 8, 1972, p. 128.
- [34] Strekalov, P. V. and Mikhailovskii, Yu. N., *Protection of Metals*, Vol. 8, 1972, p. 517.
- [35] Strekalov, P. V., Mikhailovskii, Yu. N., and Balandina, T. S., *Protection of Metals*, Vol. 10, 1974, p. 264.
- [36] Mikhailovskii, Yu. N., Strekalov, P. V., and Balandina, T. S., *Protection of Metals*, Vol. 12, 1976, p. 451.
- [37] Strekalov, P. V., Danilova, M. V., and Mikhailovskii, Yu. N., *Protection of Metals*, Vol. 13, 1976, p. 226.
- [38] Strekalov, P. V., Mikhailovskii, Yu. N., and Danilova, M. V., *Protection of Metals*, Vol. 14, 1978, p. 195.
- [39] Mikhailovskii, Yu. N., Strekalov, P. V., and Balandina, T. S., *Protection of Metals*, Vol. 14, 1978, p. 199.
- [40] Lee, W. Y., Siegmann, H. C., and Eldridge, J. M., *Journal of the Electrochemical Society*, Vol. 124, 1977, p. 1744.
- [41] Barton, K., *Schutz Gegen Atmospharische Korrosion*, Verlag Chemie, Weinheim, West Germany, 1973.
- [42] Mansfeld, F., "Laboratory Studies of Atmospheric Corrosion—II. Corrosion Kinetics Under Thin Layer Electrodes," paper submitted to *Corrosion Science*.
- [43] Mansfeld, F. in *Advances in Corrosion Science and Technology*, Vol. 6, Plenum Press, New York, 1976, p. 163.

Vladimir Kucera¹ and Jan Gullman¹

Practical Experience with an Electrochemical Technique for Atmospheric Corrosion Monitoring

REFERENCE: Kucera, Vladimir and Gullman, Jan, "Practical Experience with an Electrochemical Technique for Atmospheric Corrosion Monitoring," *Electrochemical Corrosion Testing, ASTM STP 727*, Florian Mansfeld and Ugo Bertocci, Eds., American Society for Testing and Materials, 1981, pp. 238-255.

ABSTRACT: An electrochemical technique based on integration of the current in electrolytic cells with an external impressed voltage has been used in various investigations. Cells that permit measurements extending over several years without risk of short-circuiting by corrosion products have been developed. The electronic integrator has been proved to function reliably during all measurements. Even if the electrochemical background of the technique is not well defined, a relation has been found to exist between the cell current and the corrosion rate. The relation is fairly constant in measurements at one site, but depends to some extent on the degree of pollution, which is a serious limitation. The technique appears, however, to be well suited for comparative studies of different alloys and the protective effect of corrosion products, and for studies of copper and zinc in runoff from building structures. The time of wetness measured by the technique may be of interest in the study of the influence of climatic factors.

KEY WORDS: atmospheric corrosion testing, electrochemical measurements, corrosivity of atmosphere, time of wetness, urban storm water, carbon steel, weathering steel, copper, zinc, aluminum

Atmospheric corrosion is a complicated process; the rate is dependent, among other factors, on certain climatic parameters and on the properties of the corrosion products. A technique that makes it possible to establish the instantaneous value of the corrosion rate would be of great significance in clarifying how different parameters affect atmospheric corrosion. Such a technique would, however, be usable particularly for accelerated corrosion tests and short-time tests without corrosion-accelerating conditions.

In the early seventies, therefore, the Swedish Corrosion Institute instituted a project for the development of an electrochemical technique for the study of atmospheric corrosion. It was a further development of methods known at

¹Head of R & D Department and senior research scientist, respectively, Swedish Corrosion Institute, Stockholm, Sweden.

the time which are based on galvanic cells [1,2]² and has earlier been described in detail [3]. The technique has since been further developed and used for different purposes both in field and laboratory tests. These results have hitherto been published only to a small extent [4,5]. The object of this paper is to review the possibilities of using the electrochemical technique for different purposes in both field and laboratory tests. The following topics have been studied:

1. The influence of the cell construction and of the impressed voltage on the integrated cell current and time of wetness.
2. The relation between the integrated current in carbon steel cells and weight loss of simultaneously exposed steel plates at three sites in the Gothenburg region, and the relation between the integrated current in copper and zinc cells and the amount of copper and zinc ions in the runoff from test specimens.
3. The utility of the technique for fast comparative investigations of the corrosion resistance of two aluminum alloys in different polluted atmospheres.
4. The possibility of examining the protective properties of corrosion products by comparative measurements with electrochemical cells made of carbon steel and weathering steel.

Experimental Procedure

The electrochemical equipment has been described by Kucera and Mattsson in greater detail [3]. Here the technique will be only briefly described. The principle of the electrochemical equipment is shown in Fig. 1. The equipment consists of an electrolytic cell, a zero resistance ammeter, and a built-in d-c voltage source with which the impressed voltage can be varied

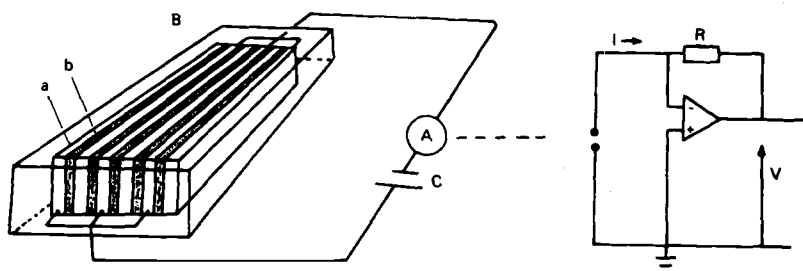


FIG. 1—General arrangement of electrochemical device for measurement of atmospheric corrosion: (A) is a zero resistance ammeter, the circuit of which is shown to the right; (B) is an electrolytic cell [(a) electrodes, (b) insulators]; (C) is a constant d-c voltage source.

²The italic numbers in brackets refer to the list of references appended to this paper.

within the range of 0 to 2 V. The current flowing in the cells when they are exposed to the atmosphere can be continuously measured in a resistanceless way and, if desired, recorded on a recorder. The cell current on exposure to outdoor atmosphere varies over a wide range depending on the precipitation, humidity, and pollution conditions. To be able to use the cell current for quantitative purposes it proved desirable to integrate the current over lengthy periods. An electronic integrator was therefore developed that integrates the current, and also gives the so-called time of wetness, which has been defined as the time when the cell current in steel, zinc, and copper cells is greater than 10^{-6} A. The reason for the choice of this current threshold is that the time during long-term exposures outdoors may be in principle divided between "wet periods" when the cell current is high (usually $>10^{-6}$ A) and "dry periods" when the cell current is low (usually $<10^{-7}$ A) [3]. The rate of the current change between these two levels has been found to be rapid, and the amount of integrated current during "wet periods" more than 90 percent of the total. The cells consisted of ten 1.0-mm-thick or twenty 0.5-mm-thick plates (65 by 20 mm) insulated from one another with polycarbonate foil. The details concerning plate and insulation thickness and impressed voltage will be given in connection with the description of the different investigations.

Results

Influence of Cell Construction and Impressed Voltage

For practical use of the technique it is of great importance to investigate how the cell construction and the impressed voltage affect the cell current and thereby the relation between cell current and corrosion rate.

In the initial tests an attempt was made to keep the plate thickness and particularly the insulation thickness as small as possible so as to increase the "sensitivity" of the cells. Insulation thicknesses of 50 and 100 μm were therefore used. In such cells, however, especially after lengthy use, short-circuits usually arise due to electrically conductive solid corrosion products. This applies to carbon steel and zinc cells and, to some extent, copper cells.

Later the problem was studied more systematically. Carbon steel cells of 0.5 mm plate thickness were exposed, the insulation thickness being varied between 100 and 400 μm . The voltage impressed on cells with 100- μm insulation was varied between 100 and 300 mV, and the effect of an increase of the plate thickness from 0.5 to 0.9 mm was also studied. All exposures were made during one-month periods out-of-doors in Stockholm. The results obtained with cells of 0.5 mm plate thickness during one period have been compiled in Table 1 and may be briefly summarized as follows:

Effect of Insulation Thickness—The cell current diminishes linearly as the insulation thickness increases. As a result the so-called cell factor (the ratio between current converted to weight loss and weight loss of simultaneously

TABLE 1—*Influence of cell construction and impressed voltage on current from C steel cells during a one-month exposure in Stockholm.*

Insulation Thickness, μm	Impressed Voltage, mV	Time of Wetness, h	I Weight Loss Cell, g/m^2	II Weight Loss Panel, g/m^2	Cell Factor, I/II
100	100	79.1	2.8	19.8	0.14
200	100	75.0	2.1	19.8	0.10
400	100	63.8	1.4	19.8	0.07
100	100	79.1	2.8	19.8	0.14
100	200	78.4	4.4	19.8	0.22
100	300	81.6	5.6	19.8	0.28

exposed panels) diminishes correspondingly. For steel cells the cell factor was 0.14, 0.10, and 0.07 for, respectively, 100, 200, and 400 μm insulation. The time of wetness, on the other hand, diminishes only slightly with an increase of the insulation thickness.

Effect of Impressed Voltage—Increasing the impressed voltage from 100 to 200 to 300 mV causes the cell current of steel cells with insulation thicknesses of 100 and 400 μm to increase linearly by about 50 percent and 100 percent, respectively. An increase of the impressed voltage causes only a very slight change of the time of wetness.

Effect of Plate Thickness—In addition to the tabulated values of insulation thickness and impressed voltage, the effect of an increase of the plate thickness has been also studied. Increasing the plate thickness of steel cells with 100- μm insulator from 0.5 to 0.9 mm causes the current per unit area to diminish by about 30 percent. The time of wetness also diminishes very slightly.

Examination of Protective Properties of Corrosion Products

To examine whether the electrochemical technique can be used for the study of the protective effect of corrosion products two carbon steel cells |SIS (Swedish Standard) 14 11 45| and two cells of weathering steel (CORTEN A) were exposed. The plate thickness was 1 mm, the insulation thickness was 400 μm , and the impressed voltage was 200 mV. The test is being conducted in an outdoor atmosphere in Stockholm, and at the same time test panels of both materials are being exposed for determination of weight loss. Both cells and test panels are exposed at 45 deg; the rear sides of the panels are protected by paint. The investigation has been proceeding for nearly four years.

The results hitherto show that the curves for weight loss and for integrated cell current have a similar course (Fig. 2). The results will be analysed in detail only after the end of the exposure, which is planned to last for 5 years. But it may be mentioned that the differences in current between carbon steel

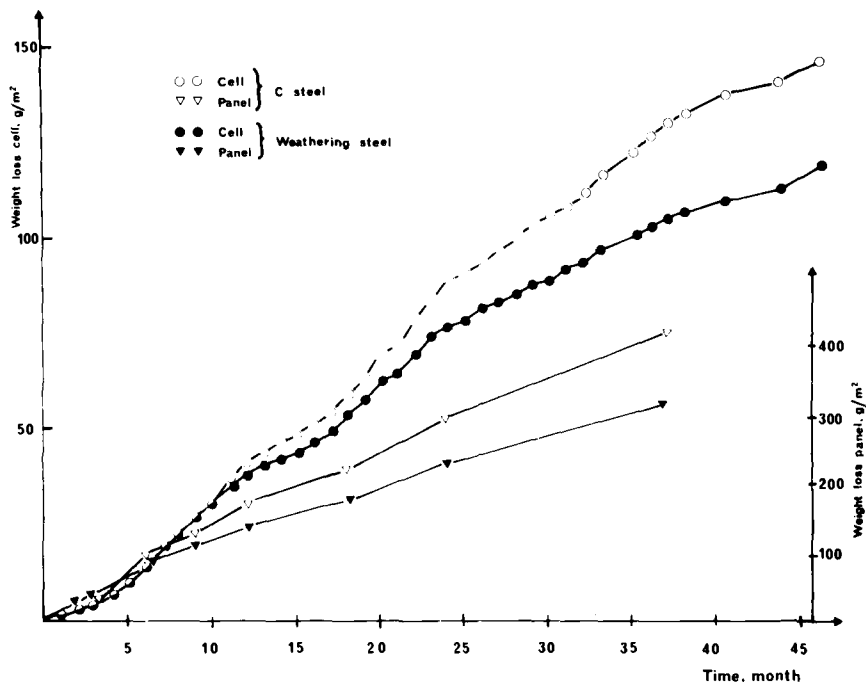


FIG. 2—Integrated current from carbon steel and weathering steel cells converted to weight loss and weight loss of panels during outdoor exposure in Stockholm from June 1975 to April 1979.

and weathering steel cells have been small during long wet periods, but increase substantially during the warmer period of the year. This indicates that measurements with the electrochemical cells should be usable for studying the protective effect of the corrosion products, and should also help to explain the action of the protective coating of rust on weathering steels.

Comparative Investigation of Corrosion Properties of Aluminum Alloys

One can study whether the electrochemical technique can be used for comparative tests of the corrosion resistance of different alloys. This would be of great practical significance, particularly for the development of alloys.

For this study two different aluminum alloys of type Al-Zn-Mg, denoted Alloys A and B, were used. Empirically it is known that the higher-alloyed metal (B) has a considerably inferior corrosion resistance relative to that with the lower content of alloying elements (A). The tests were performed with electrolytic cells made of 1-mm plate with 100- μ m insulation and 100-mV impressed voltage. Test panels of both alloys were exposed at the same time for determination of weight loss. Two accelerated test methods were used:

1. A test in a climatic chamber with 0.5-ppm sulfur dioxide (SO_2) with the cyclic variation of the temperature between 20 and 40°C at 90 percent relative humidity during four 4-h intervals, followed by one 8-h dry period at 40°C and 40 percent relative humidity.

2. The salt-spray test with discontinuous injection of 0.1 percent sodium chloride (NaCl) solution. The salt spray was injected for 10 min each hour at a temperature of 35°C.

The results are presented in Fig. 3 and Table 2, showing mean values for parallel tests. The electrochemical measurements show that the cell current for Alloy B in both test procedures was about twice as great as for Alloy A. This was consistent with a determination of weight loss of panels of the two alloys in the SO_2 -bearing atmosphere. In measurements in a chloride-bearing atmosphere the different inclines of the exposed surface of cells (45 deg to horizontal) and of panels (90 deg to horizontal) have probably had some effect in degrading the correlation.

A detailed examination of the current-time curves shows that the cells vary quite sensitively with variations of the climatic parameters. It may be mentioned that a difference in cell current between Alloys A and B was noticeable after only a few hours' exposure, that is, much earlier than any difference

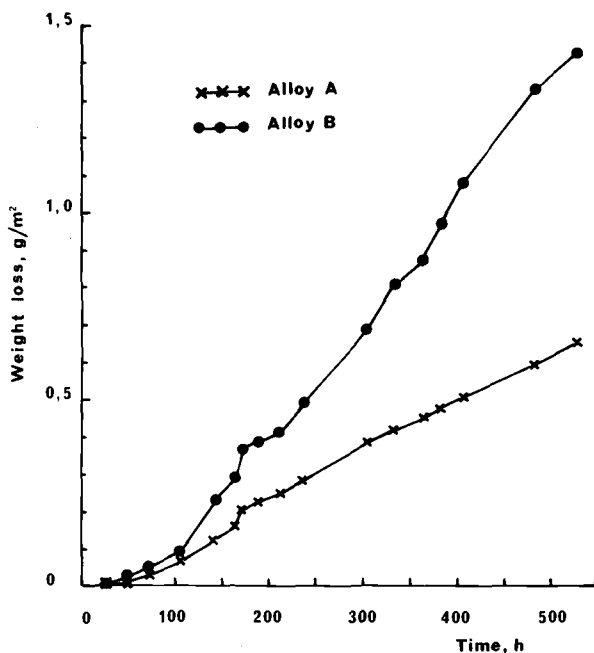


FIG. 3—Integrated current from two different Al-Zn-Mg alloy cells converted to weight loss at exposure in a climate chamber with 0.5-ppm SO_2 .

TABLE 2—Accelerated tests of two Al-Zn-Mg alloys with electrolytic cells and test panels.

Exposure Conditions	Material	I Weight Loss Cell, g/m ²	II Weight Loss Panel, g/m ²	Ratio, I/II	Ratio, Alloy A/Alloy B	
					Cell	Panel
0.5 ppm SO ₂ 21 days	Alloy A	0.65	7.70	0.08	2.20	1.97
	Alloy B	1.43	15.16	0.09		
0.1% NaCl spray 52 days	Alloy A	0.23	1.41	0.16	1.65	1.19
	Alloy B	0.38	1.68	0.23		

could be observed visually or determined, for example, by weight-loss measurements.

Relation Between Cell Current and Corrosion Rate

A key question in the use of the electrochemical technique is whether a relation exists between the cell current and the corrosion rate. As the initial tests indicated that the ratio between cell current and weight loss, the so-called cell factor, was fairly constant, the technique was used in an extensive investigation in the Gothenburg area [5]. The objective was to determine, on the one hand, the relation between the atmospheric corrosion of carbon steel, zinc, copper, and different climatic parameters, and, on the other, the relation between the atmospheric corrosion of building structures and the contents of zinc and copper in urban storm water. One of the objectives of using the electrochemical technique was the desire to study the variations of the corrosion rate during short periods in response to, for example, high content of atmospheric pollution. This may be of significance in determining the contents of copper and zinc ions in urban storm water that may cause disturbances in the biological step in sewage-treatment plants.

Test Sites—The investigation was made at three test sites in the Gothenburg area—at Vegagatan in the central part, at Mellbyleden on the outskirts, and in Floda about 35 km outside the city in an area of detached houses.

Methods for Determination of Corrosion Rate—The corrosion has been studied in the following ways:

1. The weight loss was determined on test panels of carbon steel, copper, and zinc with painted rear sides. Some of the panels were exposed simultaneously at the start of the test period and removed successively after one to twelve months. Others were exposed on a monthly basis using both fresh panels and panels precorroded in a defined manner.
2. The current was determined using zinc and copper cells of 0.5-mm-thick plate with 200- μ m-thick insulation using an impressed voltage of 100

mV. The carbon steel cells consisted of 0.9-mm-thick plates with 400- μ m-thick insulation using an impressed voltage of 200 mV.

3. The amount of metal ions in the runoff from plane and funnel-shaped specimens of zinc and copper was analysed on a monthly basis during about 25 rain periods.

Because the results are very voluminous only some which illustrate the relation between current, weight loss, and runoff are presented in this report.

The weight loss, integrated current, and runoff after one year of exposure are shown in Table 3. It will be seen that the corrosion behavior, determined by the three methods, differs, but it has earlier been shown that its variation with time is similar [5]. The relations between the three values are shown in Table 4.

Relation Between Cell Current and Weight Loss—The cell factor has in earlier investigations proved to be relatively constant on exposure of both steel and zinc cells at a single site [4]. In the present investigation, after an initial period of about three months, the cell factors were fairly constant for all metals at each site. On the other hand, the cell factors varied between sites and, for all metals, were highest at the most polluted site, Vegagatan, and lowest at the least polluted site, Floda. One explanation of this may be that the conductivity is greater in the electrolyte film on the cell surface in the more polluted atmosphere at Vegagatan. This is confirmed by the fact that

TABLE 3—Weight loss, total amount of current converted to weight loss, and runoff from funnel-shaped specimens after one year of exposure.

Site	Weight Loss, g/m ² ·year			Total Amount of Current as Weight Loss, g/m ² ·year				
	Cu	Zn	C Steel	Cu	Zn	C Steel	Cu	Zn
Vegagatan	10	15	300	7.4	7.3	39	4.8	14
Mellbyleden	11	16	270	4.2	4.0	19	3.2	11
Floda	12	12	230	3.2	3.0	13	2.1	6

TABLE 4—Cell factors (integrated current/weight loss), the relation between total amount of current and runoff, and the relation between runoff and weight loss, after one year of exposure.

Site	Total Current/Weight Loss			Total Current/Runoff		Runoff/Weight Loss	
	Cu	Zn	C Steel	Cu	Zn	Cu	Zn
Vegagatan	0.71	0.48	0.13	1.5	0.52	0.46	0.91
Mellbyleden	0.39	0.24	0.07	1.3	0.36	0.29	0.67
Floda	0.26	0.24	0.06	1.5	0.52	0.17	0.46

the best correlation between the cell factor for carbon steel and the climatic parameters studied appears to exist with the SO_2 content in the atmosphere [5]. This may provide a means for correction of the cell factor if the SO_2 content at the exposure site is known.

A more general way of expressing the relation between cell current and weight loss will be seen in Fig. 4 where all monthly values measured for carbon steel at the three sites have been plotted. The relation between cell current and weight loss has been assumed to be linear. The following empirical equation was obtained by least-squares refinement of the data:

$$W = 2.96 Q + 14.6 \quad r = 0.77$$

where

- W = weight loss of panels, $\text{g}/\text{m}^2 \cdot \text{month}$,
- Q = integrated current converted to weight loss using Faraday's law, $\text{g}/\text{m}^2 \cdot \text{month}$, and
- r = correlation coefficient.

It should be stressed, however, that extrapolation outside the investigated interval of integrated current and weight loss can not be generally recommended.

The integrated currents for carbon steel and zinc for all sites are shown in Figs. 5 and 6. For both metals the Vegagatan site shows very high values during the winter months. The weight losses at Vegagatan are also higher during this period but, as appears from Fig. 4, the integrated currents deviate from the linear relation. This indicates that during the period of heavy pollution the cells may deliver an "unproportionately" high current. Nor, in the case of zinc, can it be ruled out that during that period there may have been short-circuiting phenomena owing to formation of electron-conducting corrosion products on the cell surface.

For zinc one sees a relation between corrosion rate and cell current only for values from single sites as indicated in Fig. 7, which shows weight loss and integrated current at the Mellbyleden site on a monthly basis. The relation between weight loss and integrated cell current, however, cannot be satisfactorily represented by a single equation for all three sites.

Relation Between Cell Current and Runoff—The ratio between integrated current and the amount of metal ions in the runoff was roughly equal at all sites (see Table 4). From Figs. 8 and 9 it is seen that, both for copper and zinc, there is a close correlation between integrated current and the amount of metal ions in runoff if January to March at Vegagatan is disregarded. During this period there is admittedly high cell current but little runoff, as in the cold period the precipitation is usually not in the form of rain, which washes the corrosion products off the metal surface. The results obtained with the electrochemical technique thus appear to be suited for estimating the quanti-

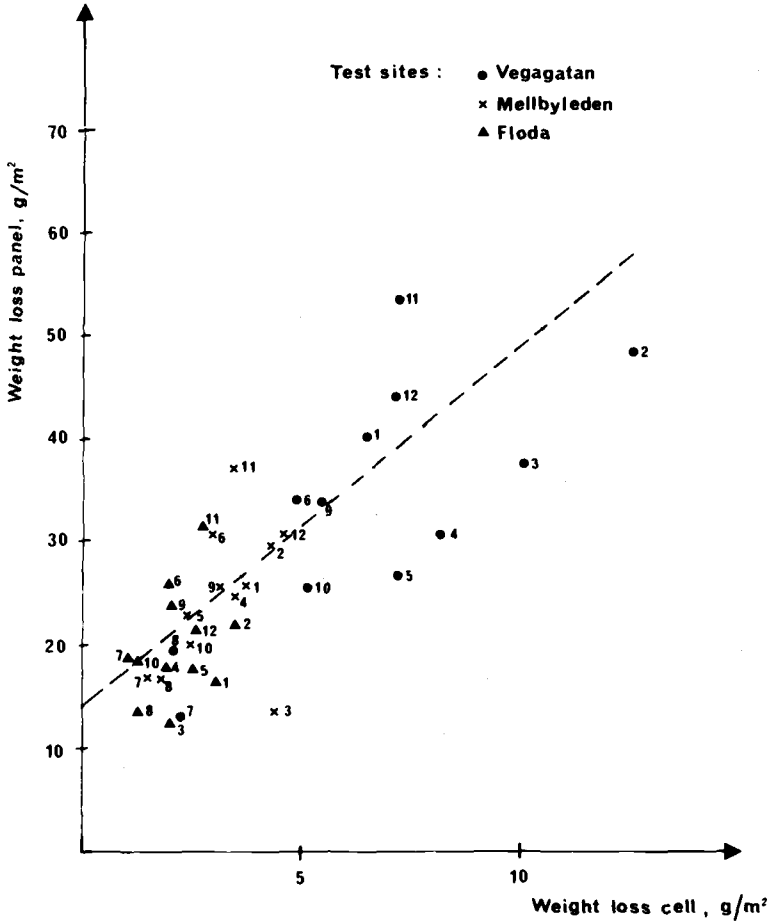


FIG. 4—Weight loss of carbon steel after one-month exposure versus integrated cell current converted to weight loss. The numbers in the figure give the ordinal numbers of the month during the exposure period from November 1975 to October 1976.

ties of copper and zinc in the runoff from corroding metal surfaces except when freezing temperatures prevail. This may also make it possible to use the cells for study of the contents of metal ions in the runoff during short periods, for example, single rainfalls.

Time of Wetness—The measured time of wetness during different months is shown in Fig. 10. The times of wetness during one year were 1116, 1190, and 1138 h for the Vegagatan, Mellbyleden, and Floda sites respectively. This constitutes about 13 percent of the total time. As appears from Figs. 5 and 10, the integrated current is not directly proportional to the time of wetness. The results show that the time of wetness measured with electrochemi-

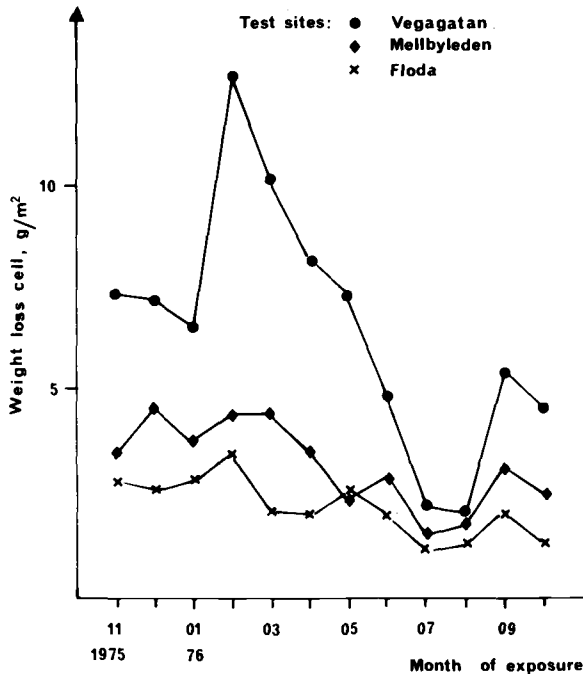


FIG. 5—Integrated current from carbon steel cells converted to weight loss during different months.

cal cells was about 0.45 of the time during which the relative humidity exceeded 90 percent or 2.1 to 2.6 times the precipitation period for the three sites.

Discussion

The electrochemical technique for the investigation of atmospheric corrosion with electrolytic cells with an impressed d-c voltage has been used for a number of years both at the Swedish Corrosion Institute and by, among others, Haagenrud [6] and Mansfeld [7]. A summary of the Swedish findings appears to be appropriate in order to demonstrate both the practical use of the technique and its limitations.

Cell Structure

The parameters in the cell structure that principally affect the cell current and thus the cell factor are the thicknesses of the insulation and plates. On grounds of principle one would prefer the least possible insulation thickness

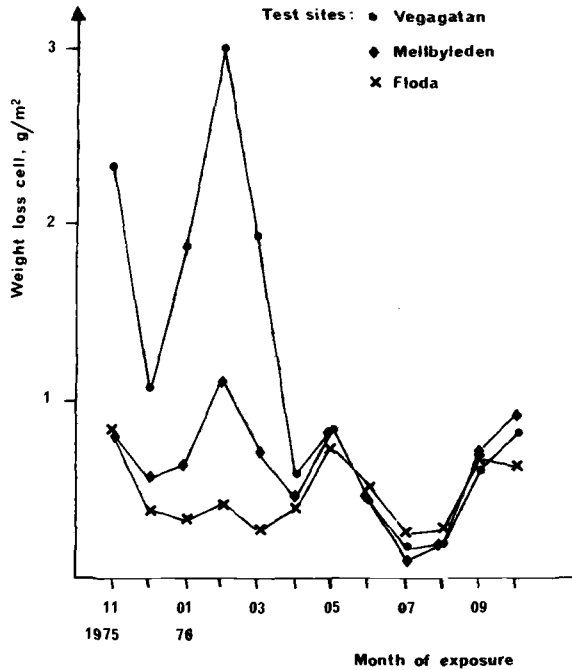


FIG. 6—Integrated current from zinc cells converted to weight loss during different months.

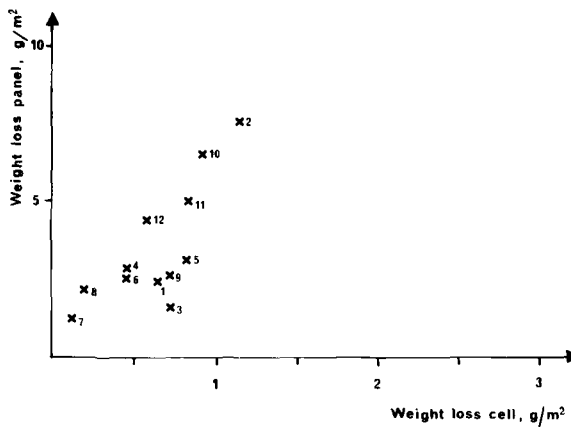


FIG. 7—Weight loss of zinc after one-month exposure versus integrated cell current converted to weight loss. The numbers in the figure give the ordinal numbers of the month during the exposure period from November 1975 to October 1976 on the Mellbyleden site.

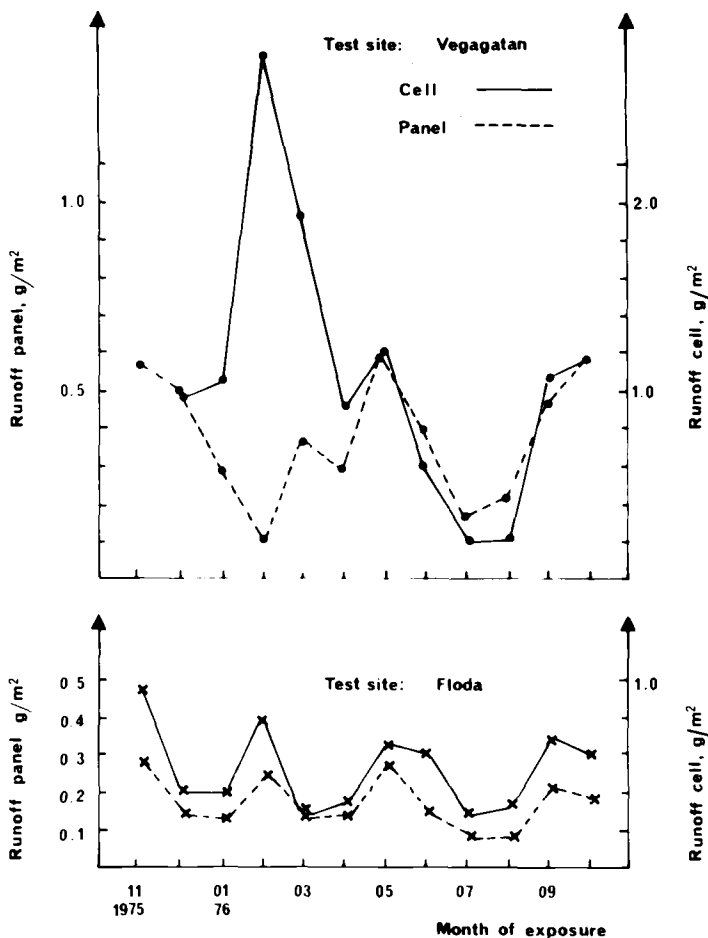


FIG. 8—Integrated current from copper cells converted to runoff and copper runoff from panels during different months.

in order that the cell, which constitutes a model of the electrochemical cells occurring on corroded surfaces, should not deviate too much from reality.

In cells of steel, zinc, and, to some extent, copper, with thin insulators, short-circuits may occur with electron-conducting corrosion products. An increased insulation thickness results in a linear reduction of the cell current. For carbon steel cells an increase of insulation thickness from 100 to 400 μm results in halving the cell current, which does not indicate any fundamental change in the behavior of the cells. Since the time of wetness is only a little affected by an increase of the insulation thickness, this measure appears appropriate for increasing the life of the cells.

An increase of the plate thickness may be desirable if one wishes, for ex-

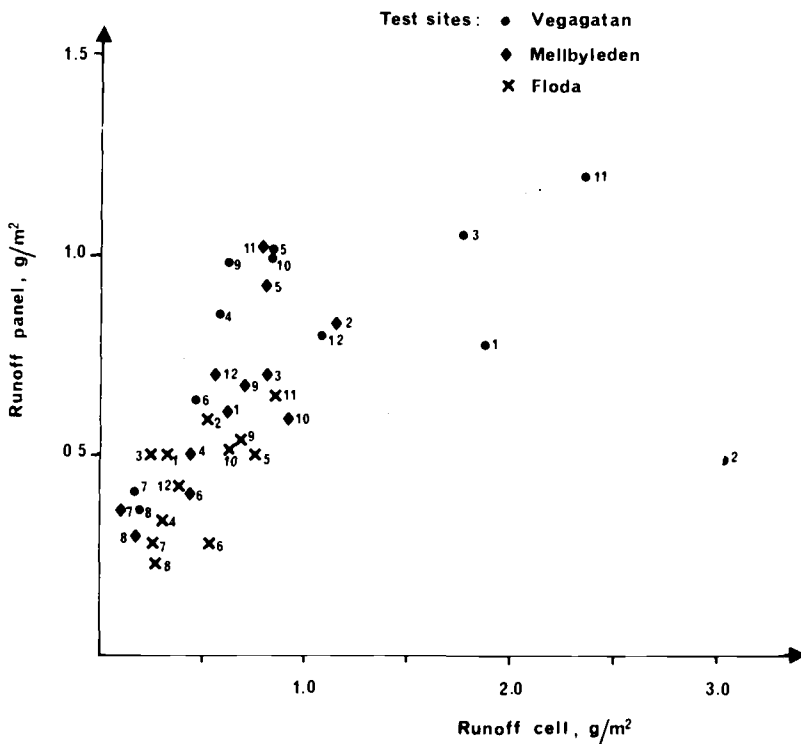


FIG. 9—Zinc runoff from panels during different months versus integrated zinc cell current converted to runoff. The numbers in the figure give the ordinal numbers of the month during the exposure period from November 1975 to October 1976.

ample, to study the protective effect of the corrosion products. An increase of thickness from 0.5 to 0.9 mm resulted in a reduction of the cell current per unit area by about 30 percent. This measure does not indicate any fundamental alteration of the function of the cells. It should also be noted that with cells of the aforementioned forms the visible corrosion attacks on the plates were never found to be concentrated at the edges. They were uniformly distributed over the entire anode surface and the entire cathode surface, the anode surface being apparently somewhat more corroded.

On an increase of the impressed voltage the cell current increases linearly. For an increase from 100 to 300 mV it is about 100 percent. Neither this measure nor a change of the plate thickness appreciably alters the time of wetness. The reason for this is apparently that the difference in cell current between "dry" and "wet" periods is usually one or several orders of magnitude while the influence of changes in cell construction and imposed voltage is much smaller. Moreover, the current normally shifts rapidly between the two current levels on wetting or drying the surface.

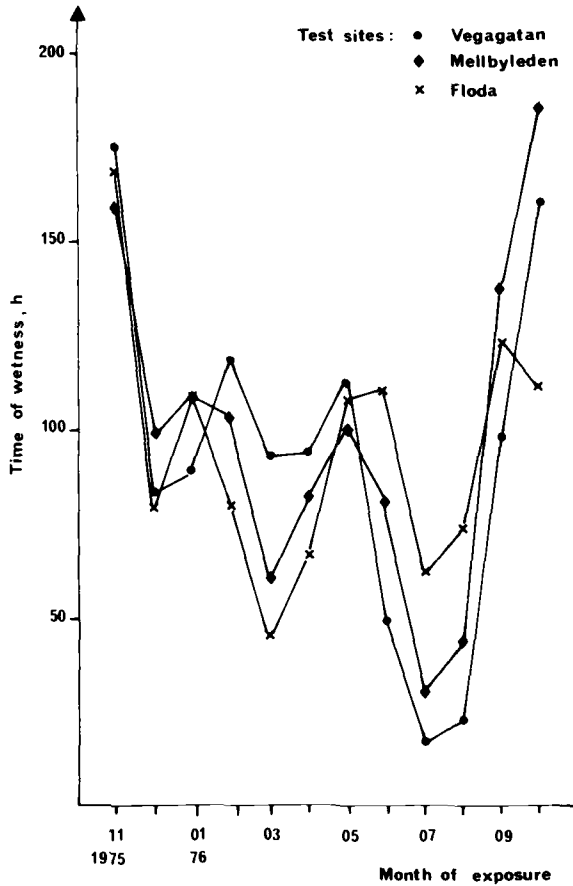


FIG. 10—Time of wetness measured with carbon steel cells during different months.

On the basis of this study, and of experience of its use in practice, the electrolytic cells of Table 5 with 0.5 to 1 mm plate thickness may be recommended for long-time tests comprising measurement of current and time of wetness without significant risk of short-circuiting through corrosion products.

Significance of Cell Current

Although the electrochemical technique for measuring the cell current is simple, it is not so easy to interpret the measured current in electrochemical terms and its connection with the corrosion rate. The voltage impressed on the cell is distributed between an ohmic voltage drop and polarization of the electrodes. The ohmic voltage drop is caused by the resistance in the electro-

TABLE 5—*Recommended insulation thickness and impressed voltage for electrolytic cells.*

Material	Insulation Thickness, μm	Impressed Voltage, mV
Carbon steel, weathering steel	400	200
Zinc	300	100
Copper	200 to 300	100
Aluminum	100	100

lyte film and in possible protective layers, such as the oxide film on aluminum. The polarization phenomena occur both at the anode and the cathode. The distribution of the voltage between IR drop and polarization has not yet been studied, but may be presumed to vary with exposure conditions. Also the polarization of the electrodes may, at least theoretically, vary between the linear and the Tafel region. To get a more reliable relation between the cell current and the corrosion rate a better understanding of the electrochemical background is necessary. Efforts in this way are presently in progress. In this investigation a practical approach in the use of the cell current as a predictor of the atmospheric corrosion rate has been adopted, and a relation has been found to exist between the cell current and the corrosion rate at atmospheric corrosion. In initial experiments this relation has been expressed as the ratio of cell current expressed as weight loss using Faraday's law and weight loss obtained from simultaneous weight-loss determinations of test panels. It has been shown that this so-called cell factor is fairly constant after a brief initial period, except in extreme climatic conditions such as cold and humid periods with high contents of pollution and with low precipitation in the form of rain. One example may be periods when the surface of zinc cells is covered with snow. On the other hand, for all metals the cell factor exhibits variations between the different sites. This, of course, is a serious limitation. In order to use the electrochemical technique for quantitative purposes a calibration is required, with determination of weight loss, to obtain the cell factor. Thereafter the method should provide interesting information concerning, for example, short-time variations of the corrosion rate that cannot be detected by conventional methods such as weight loss determination since the latter are not sufficiently sensitive.

Efforts have been also made to find alternative ways to express the relation between the cell current and the corrosion rate that avoids the aforementioned drawbacks of the cell factor variation in atmospheres with different pollution levels. As there seems to be a correlation between the cell factor and the SO_2 level a correction of the cell factor may be possible if the SO_2 -content of the site is known. Another alternative that has been tried is to assume a linear relationship between the integrated cell current and weight loss ob-

tained at different sites. By least-squares refinement of data a pure empirical linear equation has been obtained that shows a reasonable correlation for monthly exposure of carbon steel.

As the relation between current and quantities of copper and zinc in runoff is roughly similar at all sites, an interesting possibility appears to exist for estimating their contents in runoff from corroding metal surfaces.

The proportion of the time during which the cell current exceeds 10^{-6} A has been previously denoted as the time of wetness. The time of wetness appears to be a factor of great significance for atmospheric corrosion. Investigations are at present being made in international research projects to compare different ways of measuring the time of wetness and to correlate the resulting values with the weight loss of panels. An evaluation of the significance of time of wetness measured by the present electrochemical technique should await the results of the comparative investigations.

Possible Applications and Further Development of the Technique

The experience gained hitherto with the electrolytic cells shows that the technique in its present form can be used for various purposes. Among the most interesting applications are comparative studies of different metals both in field exposure and in accelerated tests. This applies, for example, to alloy development. It can be used also for following the buildup of protective layers of corrosion products. It appears possible in this connection to study how different climatic factors, for example, long wet periods or cyclical drying and wetting, affect the process. This should be of interest in studying weathering steels, for example.

Attempts have been also made to use the electrochemical technique in its present form for studying the protective effect of films of paint on steel. The possibility of studying, with modified cells, the corrosion resistance of metallic coatings is at present being investigated. Finally, it may be mentioned that the Swedish Cement and Concrete Research Institute uses the technique for studying the corrosion of steel embedded in concrete [8].

The possibilities and limitations of the technique for study of the effect of climatic factors have been discussed in the preceding section. An advantage of the technique is its comparative simplicity and cheapness and that it has proved to function completely without trouble over such long measurement periods as four years.

It is nevertheless desirable to continue the development of the electrochemical technique for study of atmospheric corrosion. Work to this end is already in progress in several countries, and the possibilities are also being studied at the Swedish Corrosion Institute. Methods based on the polarization resistance or impedance techniques would appear to be of great interest in this connection.

Conclusions

The electrochemical technique based on integration of the current in electrolytic cells with an external impressed voltage has been used in various investigations. The practical experience gained from these has led, *inter alia*, to a development of cells that permit measurements extending over several years without risk of short-circuit with electron-conducting corrosion products. The electronic integrator has also proved to function reliably during all measurements. Even if the electrochemical background of the technique is not well defined, a relation has been found to exist between the cell current and the corrosion rate. This relation is, however, not as simple as the initial tests indicated. The cell factor is admittedly fairly constant in measurements at one site, but it depends to some extent on the degree of pollution of the atmosphere, which is a serious limitation. The technique appears to be well suited, however, for comparative studies of different alloys, of the protective effect of the corrosion products, and for studies of the contents of copper and zinc in runoff from metallic surfaces in building structures. The time of wetness measured by this technique may prove to be of interest in the study of the influence of climatic factors on the corrosion rate.

References

- [1] Tomashov, N. D., Berukshtis, G. K., and Lokotilov, A. A., *Zavodskaiia Laboratoriia*, Vol. 22, 1956, pp. 345-349.
- [2] Sereda, P. J., "Measurement of Surface Moisture—A Progress Report," ASTM Bulletin, No. 228, American Society for Testing and Materials, February 1958, pp. 53-55.
- [3] Kucera, V. and Mattsson, E. in *Corrosion in Natural Environments*, ASTM STP 558, American Society for Testing and Materials, 1974, pp. 239-260.
- [4] Kucera, V. and Mattsson, E. in *Proceedings*, 7th Scandinavian Congress on Metallic Corrosion, Royal Norwegian Council for Scientific and Industrial Research, Trondheim, Norway, 1975, pp. 202-217.
- [5] Kucera, V. and Collin, M. in *Proceedings*, 6th European Congress on Metallic Corrosion, Society of Chemical Industry, London, 1977, pp. 189-196.
- [6] Haagenrud, S. E., *Extended Abstracts of the 154th Electrochemical Society Meeting*, Vol. 78-2, The Electrochemical Society, Princeton, N.J., 1978, pp. 327-328.
- [7] Mansfeld, F. and Tsai, S., *Corrosion Science*, Vol. 20, 1980, pp. 853-872.
- [8] Tuutti, K. in *Proceedings*, 6th European Congress on Metallic Corrosion, Society of Chemical Industry, London, 1977, pp. 655-661.

An Electrochemical Technique to Measure Diffusible Hydrogen in Metals (Barnacle Electrode)

REFERENCE: DeLuccia, J. J. and Berman, D. A., "An Electrochemical Technique to Measure Diffusible Hydrogen in Metals (Barnacle Electrode)," *Electrochemical Corrosion Testing, ASTM STP 727*, Florian Mansfeld and Ugo Bertocci, Eds., American Society for Testing and Materials, 1981, pp. 256-273.

ABSTRACT: The electrochemical measurement of mobile hydrogen, utilized in hydrogen-through-iron permeation studies, is adapted to yield an extremely sensitive, yet simple, practical device to assess embrittlement in high-strength steel parts. The electrochemical permeation of hydrogen through metal foils is achieved by causing an electrochemical source and sink for hydrogen to co-exist on either side of a foil. The hydrogen is cathodically introduced at the input side and anodically extracted (oxidized to water) at the exit side. The extraction side of the permeation cell provides the basis for the barnacle electrode hydrogen measurement device. The hydrogen oxidation current is measured and related to the mobile hydrogen concentration by the solution to the diffusion equation using the appropriate boundary conditions. The device can accurately detect and measure diffusible hydrogen contents in the range of 100 parts per billion by weight. Its effectiveness has been demonstrated in (1) indexing embrittlement of high-strength AISI 4340 steel as a function of hydrogen content, (2) the loss of hydrogen in an HY-130 steel weldment, and (3) changes in hydrogen content of cadmium plated steel which were measured, leading to a better understanding of bakeout and delayed failure mechanisms.

KEY WORDS: hydrogen embrittlement, embrittlement indexing, mobile hydrogen, hydrogen permeation, hydrogen measurement, environmental embrittlement, electrochemical technique, barnacle electrode, high strength steels, sustained load testing, electroplating

It is well known that hydrogen can enter high-strength steels in many ways (for example, during plating, cathodic protection, welding, or corrosion) causing a loss in ductility which may result in catastrophic failure of structures in service [1].² As higher strength materials come to be more in demand, the problem of hydrogen embrittlement becomes more acute. According to Troiano, hydrogen, even in very low concentrations in the bulk lattice, can migrate to areas of high triaxial stress, thereby magnifying its effect and

¹Division superintendent and research chemist, respectively, Aeronautical Materials Division, Aircraft and Crew Systems Technology Directorate, Naval Air Development Center, Warminster, Pa. 18974.

²The italic numbers in brackets refer to the list of references appended to this paper.

causing delayed failure [2]. Troiano argues that it is this mobile (rather than the total) hydrogen with which we should be concerned [3]. Most methods for determining hydrogen in metals are destructive and cumbersome [1,4], but their greatest drawback is that they measure total hydrogen. It is therefore important to have a method of determining mobile, or damaging, hydrogen which can then be related to actual service conditions [3].

The barnacle electrode has been developed to measure this mobile hydrogen [5], and is being used to correlate hydrogen concentrations with delayed failure in high-strength steels. The principle of the barnacle electrode is based on the electrochemical method of hydrogen permeation developed by Devanathan et al [6,7]. This method requires that a diffusion gradient exist within the metal foil by producing hydrogen on one side, such as by cathodic charging, and removing it on the other side by anodic polarization with a potentiostat. By keeping the exit surface at zero hydrogen concentration in this manner, the oxidizing current is therefore a direct measure of the rate of permeation of hydrogen. Analysis of the buildup and decay transients can then be used to give diffusivity or concentration information [8,9]. The barnacle electrode technique makes use of only the extraction side of the permeation cell, since the hydrogen is assumed to be already uniformly distributed throughout the specimen. A major simplification of the barnacle electrode over the electrochemical permeation technique is the use of the nickel/nickel oxide electrode to replace the potentiostat and act as a stable, nonpolarizing power electrode (cathode) that maintains zero hydrogen concentration at the exit surface of the steel (anode) by oxidizing the emerging hydrogen atoms to water.

The boundary conditions (Fig. 1) are thus established for solution of Fick's second law

$$\frac{\partial^2 C}{\partial x^2} - \frac{1}{D} \frac{\partial C}{\partial t} = 0 \quad (1)$$

where

C = concentration of hydrogen in the steel, mol/cm³,

D = diffusivity of hydrogen through the steel, cm²/s,

x = distance into the specimen, cm, and

t = time, s.

Using a Laplace transform method, Fullenwider et al [10,11] arrived at a solution

$$\begin{aligned} C(x,t) = & C_0 - C_0 \sum_{n=0}^{\infty} (-1)^n \operatorname{erfc} \frac{(2n+1)L-x}{2(Dt)^{1/2}} \\ & - C_0 \sum_{n=0}^{\infty} (-1)^n \operatorname{erfc} \frac{(2n+1)L+x}{2(Dt)^{1/2}} \end{aligned} \quad (2)$$

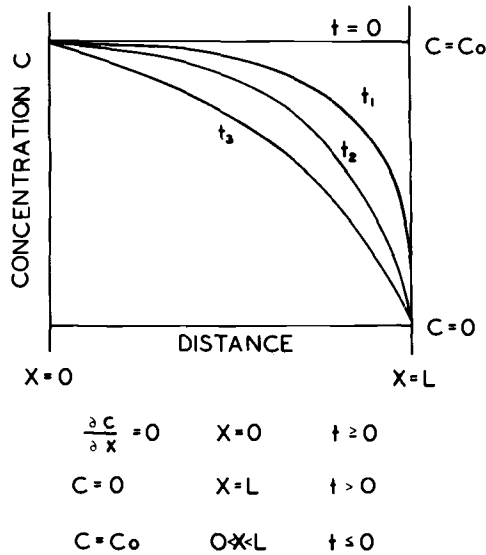


FIG. 1—Boundary conditions for barnacle electrode hydrogen extraction.

Since

$$\frac{J_t}{zF} = -D \left(\frac{\partial C}{\partial x} \right)_{x=L}, \quad \text{Fick's first law,} \quad (3)$$

we have

$$\frac{J_t}{zF} = C_0 \left(\frac{D}{\pi t} \right)^{1/2} [1 - e^{-L^2/Dt} + e^{-4L^2/Dt} \dots] \quad (4)$$

where

- J_t = oxidation current density at time t , A/cm²,
- L = thickness of the part, cm,
- C_0 = uniform hydrogen concentration in the part,
- z = number of electrons involved in the oxidation (one), and
- F = Faraday, 96 500 C per mole hydrogen.

It is possible to drop all exponential terms and use a first-term solution to Eq 4 if $L^2/Dt \geq 4$; that is,

$$t_{\max} = \frac{L^2}{4D} \quad (5)$$

The first-term solution is

$$\frac{J_t}{zF} = C_o \left(\frac{D}{\pi t} \right)^{1/2} \quad (6)$$

The value t_{\max} of Eq 5 is the time up to which C_o may be calculated from the experimental value of J using the first-term solution (Eq 6). Thus, for a 1-mm-thick specimen of 4340 steel having a diffusivity of 2.5×10^{-7} cm²/s, t_{\max} is 10^4 s, or approximately 3 h; for Armco iron, $D = 2 \times 10^{-5}$, it is only 2 min. For practical applications where thicknesses are usually in excess of 1 mm and diffusivities are on the order of 10^{-7} , the approximation of Eq 6 should hold true for the actual times for measurement, usually on the order of one-half hour.

If the experimental extraction current density-time transient fits the theoretical curves plotted from Eq 6, and if the diffusivity of hydrogen through the given steel is known, a measurement of J at any given extraction time will give the hydrogen content C_o . If D is unknown, the value $D^{1/2}C_o$ can be determined; that is, the current (or current density) at a given time is proportional to the hydrogen concentration.

The degree of embrittlement is a function, not only of the hydrogen concentration, but also of the material, including its heat treatment and its geometry, which determines the stress concentration at notches and sharp corners. It is therefore necessary to do mechanical testing and correlate failure data with the electrochemical measurements for the material of interest.

This paper describes the applicability of the barnacle electrode system to a wide variety of situations: (1) the indexing of the degree of embrittlement by determining threshold hydrogen values, (2) the study of delayed failure and hydrogen migration in plated steels, and (3) the loss of hydrogen in a weldment with time.

Experimental

Apparatus

The barnacle electrode cell is shown in Fig. 2. It consists of a steel specimen (anode), a nickel/nickel oxide electrode (cathode), and a Teflon block that has a circular opening and a silicone rubber gasket which, when clamped to the specimen, defines an exact area. The cell is filled with a 0.2 M sodium hydroxide (NaOH) solution for measurements. The potential dif-

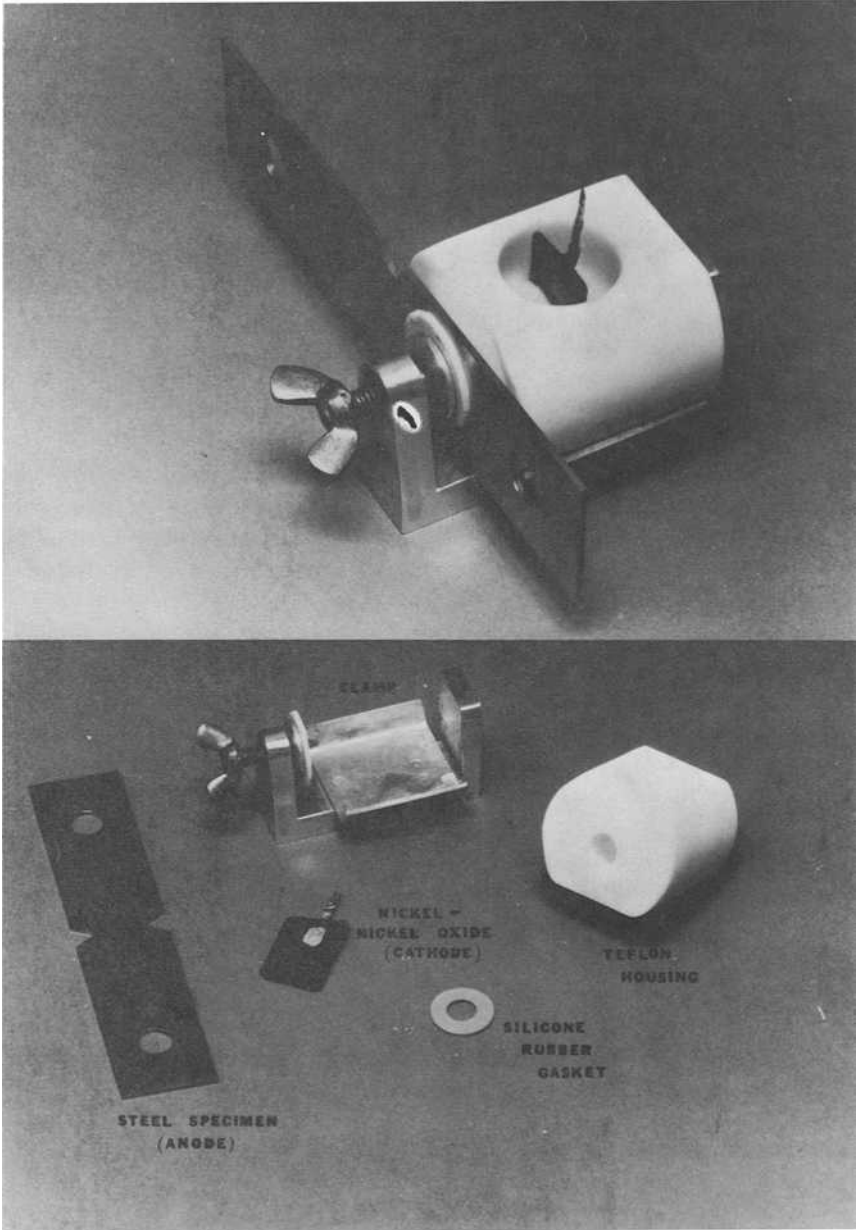


FIG. 2—Barnacle electrode cell.

ference developed between the steel and the nickel/nickel oxide is on the order of 750 to 850 mV, depending on the hydrogen content (the fully charged nickel/nickel oxide is 310 mV noble to the saturated calomel electrode in this solution). Future versions of the cell will have a magnetic clamping system for use on structural parts, hence the name "barnacle." A prototype has been built under contract by Rockwell International Science Center and is being evaluated under laboratory and field conditions.

The measuring system is shown schematically in Fig. 3. The current is determined from the IR drop. The results have been compared with those obtained using more sophisticated methods, such as zero-resistance ammeter circuits, and have been found to be almost identical.

Specimens

The specimens used in the embrittlement and plating studies were 1.60-mm (0.063-in.)-thick, flat, long transverse, double-notched tensile bars of AISI 4340 steel, finished by surface grinding. The properties are given in Table 1.

The weldment was a multi-pass, continuously welded, shielded metal-arc weldment of 25-mm (1-in.)-thick HY-130 steel plate measuring 300 mm (12 in.) long by 225 mm (9 in.) wide. It was cut on a band saw so that measurements could be made on internal surfaces. Irregular surfaces were flattened on a belt sander.

Procedures

Indexing the Degree of Embrittlement—The tensile bars were prepared by swabbing with two percent aqueous hydrochloric acid in methanol, rinsing with methanol, and wiping with a tissue. They were then cathodically charged for 3 h in a solution containing one weight percent each of sodium hydroxide and sodium cyanide, the latter acting as a poison to promote hydrogen uptake [12]. The charging rate was varied from 25 to 750 $\mu\text{A}/\text{cm}^2$ in order to prepare specimens with different hydrogen concentrations. The anode was a cylindrical platinum gauze surrounding the specimen to provide a uniform current density.

After charging, the specimen was rinsed with water, then with methanol, and dried with a tissue. The barnacle electrode was then assembled, and the current measurement started within 15 min after charging.

After the 30-min current measurement, the specimen was rinsed with water and dried, then immediately assembled in a constant-load stress rupture machine at the predetermined load. Failure usually occurred within one-half hour for these bare specimens. Those still intact after one week were considered unembrittled. (The one-week limit was set after it had been deter-

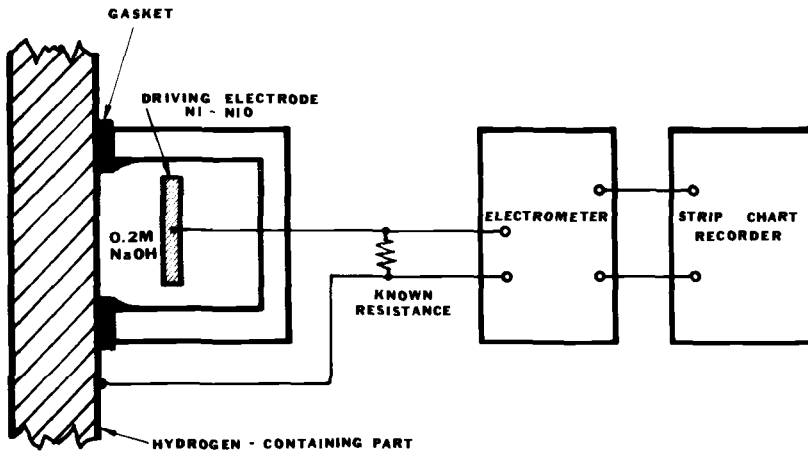


FIG. 3—Schematic of barnacle electrode measuring apparatus.

TABLE 1—Properties of AISI 4340 steel.

Composition, %	Physical Properties
Mn—0.84	strength level—1790 to 1930 MPa (260 to 280 ksi)
Si—0.25	notched tensile strength—1650 MPa (240 ksi)
Ni—1.92	geometrical stress concentration factor, K_t —5.6
Cr—0.86	
Mo—0.21	

mined that unplated specimens would either fail rapidly upon loading or not at all.) Thus a fail/no-fail criterion was established.

Determining Residual Hydrogen in Cadmium-Plated Steel—The specimens were cleaned and plated from a conventional cadmium cyanide bath. They were then baked at 190°C (375°F). Both the plating thickness and baking time were varied. The plate was removed by swabbing with ammonium nitrate solution (120 g/L; 1 lb/gal) and abrading with extra fine (grade A) Scotchbrite abrasive immediately before assembling in the barnacle cell. The current was then measured for 30 min.

The sustained-load failure experiments were performed on the plated specimens. They were loaded at 75 percent of the notched tensile strength and allowed to go until failure. They were then measured for hydrogen as above.

Hydrogen in Weldments—The weld and heat affected zones were prepared for measurement by abrading with 320-mesh silicon carbide paper and wiping with benzene. The barnacle cell was attached to the weldment with a C-clamp.

Results and Discussion

Indexing the Degree of Embrittlement

It was shown in earlier work with the barnacle electrode [5] that a threshold hydrogen concentration probably exists below which failure will not occur at a given sustained load. This is in agreement with the work of others [2,13]. The results presented here are an expansion of this preliminary work.

Flat, double-notched tensile bars of 4340 steel were charged at different current densities in order to introduce varying levels of hydrogen. The hydrogen extraction transients were then determined with the barnacle electrode, and the specimens loaded at various percentages of the notched tensile strength (NTS) in order to develop the embrittlement threshold curve.

Typical barnacle extraction curves are shown in Fig. 4. Barnacle readings at any selected time can be correlated with the sustained-load failure results. It was shown, for example, that for 30-min barnacle measurements of 0.37, 0.69, and 0.76 $\mu\text{A}/\text{cm}^2$, specimens loaded at 25 percent NTS did not fail,

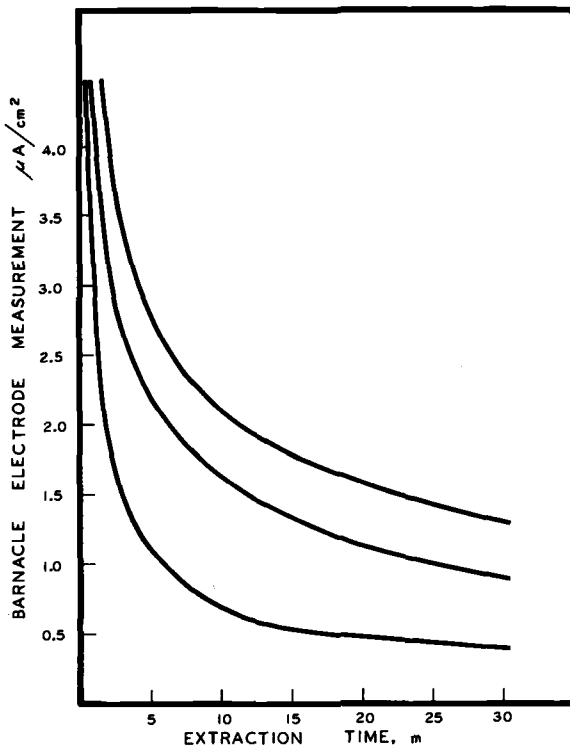


FIG. 4—Typical barnacle electrode extraction transients for different hydrogen concentrations.

whereas those giving readings of 0.93 and 0.99 did. In this way, "fail/no-fail" data were generated for loads of 15 to 40 percent NTS. Figure 5 shows a straight line drawn through the highest "no-fail" 30-min barnacle current densities (left-hand axis) versus sustained loads. The curve is shown with a 10 percent safety factor. This threshold curve is the line giving the hydrogen extraction current density above which failure will be expected at the given sustained load for bare (unplated) AISI 4340 steel heat treated to the 1790 to 1930 MPa (260 to 280 ksi) strength level. This straight line plot is valid for loads between 15 to 40 percent of the notched tensile strength.

The foregoing illustrates an empirical method of correlating the electrochemical (barnacle) and mechanical data without using the diffusivity or considering the actual hydrogen concentrations. If the diffusivity is unknown, Eq 6 can still be used to calculate the combined value $D^{1/2}C_0$.

If hydrogen concentrations are desired, it is necessary to know the diffusivity and to know that the extraction curves follow Eq 6. The diffusivity of the material used here was determined by the electrochemical permeation method [8,9] and found to be 2.5×10^{-7} cm²/s. Adherence to the equation is best determined graphically by comparing slopes of an experimentally determined log J versus log t plot (Fig. 6) against those drawn using Eq 6.

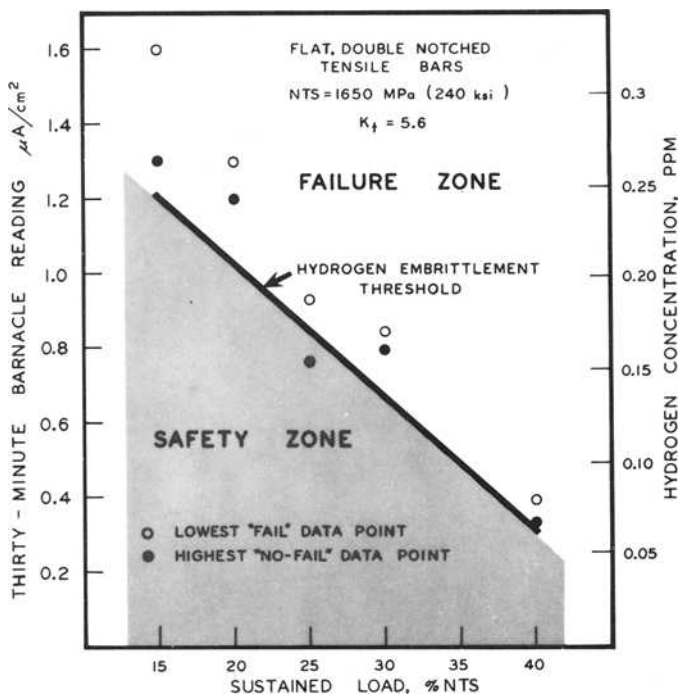


FIG. 5—Indexing the degree of embrittlement of AISI 4340 steel using 30-min barnacle electrode measurements.

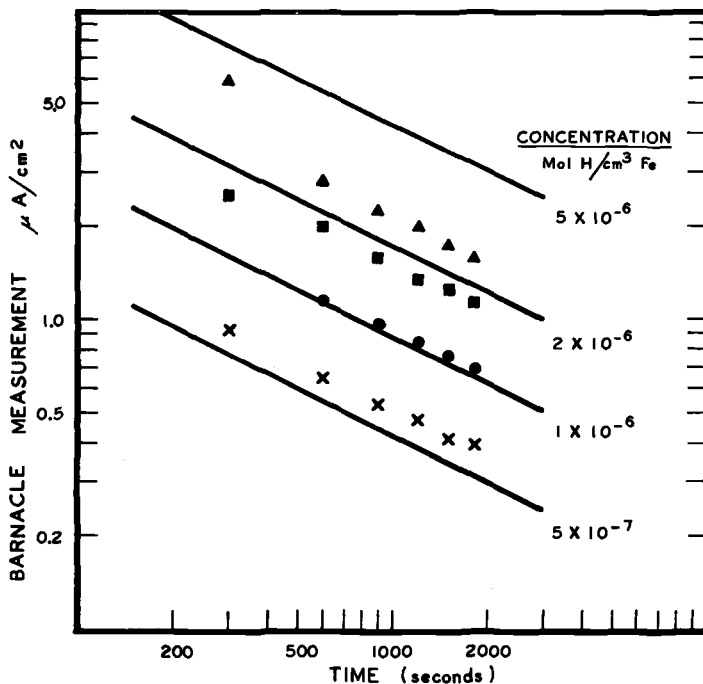


FIG. 6—Typical barnacle electrode hydrogen extraction data versus theoretical curves calculated from Eq 6 for AISI 4340 steel, $D = 2.5 \times 10^{-7} \text{ cm}^2/\text{s}$.

The slope of the line for a hydrogen-containing specimen obeying Eq 6 is -0.5 . It would be expected that a hydrogen-containing steel would act accordingly, so long as the hydrogen concentration is high enough to give values significantly higher than background (blank) measurements, and that no oxidation currents are present other than that for hydrogen and the very low steel passivating current. The slopes of typical barnacle extraction curves are given in Table 2. Calculations can also be made from Eq 6 by using current densities at different times. If the extraction transient follows the equation, the calculated concentration will be the same for all times; that is, it is constant in the specimen being measured. The obedience of Eq 6 and the constancy of concentration were found in the current study, as can be seen from Table 2. Once it has been established that the system conforms to theory, it is necessary to use the current density (in the region where the data best matches the theoretical slope) at one time only, such as at 20 or 30 min, to calculate the concentration. The validity of the calculations has been confirmed by independent³ determinations for mobile hydrogen using a hot-extraction method [14]. The comparative results for replicate specimens are

³K. B. Das, The Boeing Company, Seattle, Wash.

TABLE 2—*Calculated hydrogen concentrations, ppm, at selected times, and slopes of typical barnacle electrode extraction curves.*

Specimen	Calculated Hydrogen Concentration, ppm, from Current Density at Selected Times, min						Slope of Curve (Fig. 6)
	5	10	15	20	25	30	
A	0.077	0.076	0.076	0.078	0.076	0.079	-0.48
B	0.13	0.14	0.14	0.14	0.14	0.14	-0.48
C	0.21	0.23	0.23	0.22	0.23	0.23	-0.58
D	0.50	0.33	0.33	0.33	0.32	0.32	-0.53

shown in Table 3. The specimens were 4340 steel, plated with cadmium to retain the hydrogen until the determinations were made.

It is often desirable to use weight parts per million (ppm) rather than moles per cubic centimetre as the unit of concentration. These values are shown on the right-hand axis of Fig. 5 ($1 \text{ mol H/cm}^3 \text{ Fe} = 1.3 \times 10^5 \text{ ppm}$). Table 4 gives the critical hydrogen concentrations as obtained from the threshold curve (Fig. 5).

In earlier work [5, 15] a Teflon gasket was used rather than a silicone rubber one. This may have caused a crevice, similar to that reported in an aluminum-Teflon system [16], resulting in a larger wetted surface area. This results in a much larger measured current than that obtained with the silicone gasket, which necessitates the use of an area factor to adjust the data to a truer current density caused by hydrogen oxidation. The results reported in this section were adjusted in this manner using an area factor of 7.5 arrived at by comparing current measurements using the two gaskets on replicate specimens (Table 5).

It should be emphasized that these results are for bare specimens that lose hydrogen relatively rapidly and will therefore not undergo long-time delayed failure. In practice, this steel is not used without plating, but this study clearly demonstrates the relationship that can exist between stress and hydrogen content even with very low mobile hydrogen concentrations. Plated specimens may provide a more dangerous situation, since common plating materials such as cadmium constitute a barrier preventing the easy loss of hydrogen. This barrier effect of the plating can promote the migration of hydrogen to areas of high triaxial stress, which results in possible delayed failure at even lower bulk hydrogen concentrations, as is discussed in the following section.

Hydrogen in Cadmium-Plated Steels

It has been well established that high-strength steels plated with cadmium from a cyanide bath become highly embrittled with hydrogen [1]. Though low-embrittlement baths are constantly being developed, the bright cad-

TABLE 3—Comparison of mobile hydrogen concentrations in replicate 4340 steel specimens by two methods.

Method	Hydrogen, ppm	
	Set 1	Set 2
Barnacle electrode (three specimens each set)	0.41	0.16
Hot-extraction ^a (four specimens each set)	0.34	0.19

^aK. B. Das, The Boeing Company, Seattle, Wash.

TABLE 4—Critical hydrogen concentrations for failure of bare AISI 4340 steel in sustained load testing.
 $K_1 = 5.6$, NTS = 1650 MPa (240 ksi).

Load, % NTS	Critical Hydrogen Concentration, ppm
15	0.25
20	0.21
25	0.17
30	0.13
35	0.10
40	0.06

TABLE 5—Comparison of 30-min barnacle electrode current measurements on replicate specimens of 4340 steel using Teflon and silicone rubber sealing gaskets.

	n	Average Current, μ A		
		Teflon	Silicone	Ratio
Blank	5	1.6	0.22	7.3
H-containing	7	4.4	0.59	7.5

mium plate produced from the cyanide bath is still preferred for many applications owing to its excellent coverage and superior corrosion resistance. Brown [17] showed by mechanical means, however, that even prolonged baking did not always relieve high-strength steel of this embrittlement.

This study was therefore undertaken to determine whether the presumably very low levels of residual hydrogen could be detected with the barnacle electrode, thus affording a nondestructive method of monitoring plated and baked parts. It was further decided to follow changes in the hydrogen concentration during room temperature aging, thus providing a better understanding of the delayed failure mechanism.

The specimens used were half tensile bars (the broken specimens from the indexing work described previously). It was established that specimens could be used repeatedly. It was also shown that two measurements could be made on opposite sides of the same specimen, provided the plate was not removed from the second side until after the first measurement was made, and that the two measurements followed each other within a few minutes.

As can be seen in Table 6, slight variations in plating conditions from batch to batch can result in large differences in hydrogen uptake as well as variable hydrogen concentrations after the bakeout procedure. This work demonstrates that a bright cadmium plate may offer an impenetrable barrier toward the exit of hydrogen. The data in Table 6 indicate that even after baking, the residual hydrogen would be sufficient to cause failure in stressed parts in many situations (see Fig. 5).

It has been theorized that a duplex-plating procedure (thin plate, bake, overplate) would eliminate hydrogen embrittlement. It was thought that the thin plate of cadmium would allow sufficient outgassing of hydrogen while baking, yet provide a barrier to additional hydrogen entry during overplating. The results given in Table 6, however, do not show any improvement in the duplex-plating procedure over the single-plating procedure. These results are in agreement with the work of others using mechanical tests [18].

The study of the changes in hydrogen concentration (barnacle measurements) with ambient aging is being done to shed light on the mechanism of

TABLE 6—Thirty-minute barnacle electrode measurements on cadmium-plated AISI 4340 steel using single and duplex plating methods and variable baking times at 190°C (background measurement = 0.22 $\mu\text{A}/\text{cm}^2$).

Typical barnacle measurements, $\mu\text{A}/\text{cm}^2$, from different batches plated to 0.015 mm thickness.			
	Set 1	Set 2	Set 3
Unbaked	0.40	0.67	0.72
Baked 24 h	0.60	0.51	...
Baked 24 + 48 h	0.44	0.39	...
Baked 48 h	0.36
Baked 48 + 72 h	0.26
Typical barnacle measurements, $\mu\text{A}/\text{cm}^2$, from different batches plated to 0.005 mm thickness, then overplated to 0.015 mm thickness.			
	Set 1	Set 2	Set 3
0.005 mm, unbaked	0.83	0.69	0.57
Baked 10 h	0.26	0.25	0.51
0.015 mm, unbaked	0.31	0.46	0.39
Baked 24 h	0.23	0.35	0.50

delayed failure: redistribution of hydrogen within the steel or movement into the steel from the plate [17]. A duplex plate and a single 0.015-mm (0.0005-in.)-thick plate were used. It was found in the former that even with the thin plate the hydrogen concentration in the steel increased with aging. The duplex plate gave essentially the same end result as a single plate. In all cases, a source of hydrogen and a barrier toward hydrogen egress seemed to be set up, which caused an increase in the hydrogen content in the steel with aging time. This phase of the work is still in progress; however, there appears to be a pattern in all of the data that indicates a rise in hydrogen concentration after aging for a few weeks at room temperature. This change reaches a maximum which may shift in time depending on the barrier effectiveness and thickness of the plate.

A limited number of tensile specimens have been tested for delayed failure under sustained load. Although the results are not totally conclusive, two failures occurred in three to four weeks with plated specimens loaded to 75 percent NTS, which lends support to the theory that hydrogen may enter the steel from the plate. Further work is needed to answer the question as to whether the bulk mobile hydrogen concentration increases with time or whether delayed failure is due only to migration of hydrogen to the region of high stress.

It is expected that with the barnacle electrode system as now perfected, very small changes in hydrogen concentration upon aging can be detected, and the times to reach maximum hydrogen concentration determined. These measurements in turn can be correlated with results of sustained-load tests to determine the concentration of hydrogen that can cause failure. Table 7 shows the precision of the measurements. It should be noted that as the

TABLE 7—*Reproducibility of barnacle electrode measurements using replicate specimens of cadmium-plated AISI 4340 steel.*

Specimen Preparation	No. of Specimens	Average 30-Min Barnacle Reading	Standard Deviation, s
Background (blank)			
Plated, plate removed, H measured, stored in desiccator, abraded, degreased	5	0.22 $\mu\text{A}/\text{cm}^2$ (zero ppm H)	0.019
Plated	4	0.51 $\mu\text{A}/\text{cm}^2$ (0.10 ppm) ^a	0.022
Plated to 0.015 mm thickness, aged 6 days (ambient), plate removed, abraded, degreased	4	1.5 $\mu\text{A}/\text{cm}^2$ (0.30 ppm) ^a	0.096
Charged/Plated			
Cathodically charged at 1 mA/cm ² for 2 h, plated (0.015 mm), aged 6 days (ambient), plate removed, abraded, degreased	4	1.5 $\mu\text{A}/\text{cm}^2$ (0.30 ppm) ^a	0.096

^a Calculated from Eq 6.

hydrogen concentration decreases so that the current density approaches the background measurement, deviation from the theoretical slope of -0.5 is to be expected. Therefore, for these cases, it is not possible to make calculations for the hydrogen concentration using Eq 6, which is based on the slope of -0.5 . Differences in the barnacle readings, however, even very near to the background value shown in Table 7, can still provide a valid method to indicate changes in hydrogen concentrations.

Hydrogen in a Weldment

The last phase of this work demonstrates the use of the barnacle electrode on a more massive, structural component rather than on a small, laboratory specimen. It also illustrates an example of hydrogen originating from a source other than an electrolytic reaction.

The weldment of HY-130 steel was prepared by the shielded metal-arc process 8 h before the first measurement was made. It was sectioned to give a large and small section in order to observe the difference in the hydrogen egress, and also later to obtain internal measurements. The 30-min barnacle measurements versus aging time are given in Figure 7. The base metal showed essentially a steady barnacle value throughout. The weld metal, on the other hand, showed a high hydrogen concentration at the start, which

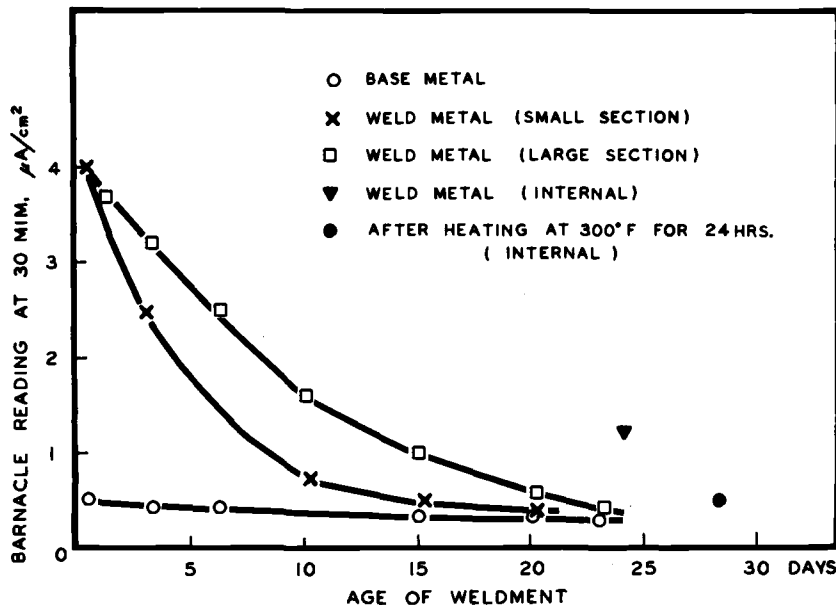


FIG. 7—Loss of hydrogen in an HY-130 steel weldment as shown by barnacle electrode measurements.

steadily diminished to values comparable to background after about 25 days, the smaller section losing hydrogen faster than the larger one. A sectioning at 24 days showed that there was still some hydrogen remaining in the weld metal of the large section even though the surface measurement showed none. This hydrogen was removed by baking for 24 hours at 150°C (300°F), as shown by the internal measurement after a final cut (Fig. 7).

The concentration of hydrogen in the weld metal was calculated using Eq 6 and the determined diffusivity of 4×10^{-7} cm²/s for the weld metal, and was found to be 0.6 ppm eight hours after fabrication. It should be noted that the lower strength level of the HY-130 steel versus the 4340 steel (900 MPa versus 1790 MPa) makes it less susceptible to hydrogen embrittlement. It can therefore tolerate more hydrogen prior to breaking than can the 4340 steel of this study.

Summary and Conclusions

The barnacle electrode system has been shown to be a very useful and versatile hydrogen measuring tool. In this study it has been applied to three hydrogen-containing systems—plated and unplated 4340, and an HY-130 weldment. It has been shown to be potentially useful as a field tool to detect hydrogen in massive weldments, as a quality assurance instrument to determine the efficiency of the post cadmium plating bakeout procedure, and as a research tool to determine very small hydrogen concentrations and embrittlement limits, and to study delayed failure mechanisms.

The system has been improved by using a silicone rubber sealing gasket that ensures the reproducibility of a well-defined cell contact area. This has resulted in, not only a better precision of measurement, but the ability to detect less than 0.1 ppm of mobile hydrogen.

It has been shown that the barnacle hydrogen extraction transients (current density versus time plots) obey the equation resulting from the solution of the diffusion equations so long as the thickness is sufficient to ensure the proper boundary conditions. This also means that no oxidation reactions other than that for hydrogen are significant unless the hydrogen concentration is considerably lower than 0.1 ppm, that is, as the 30-min current density approaches the background value of 0.22 $\mu\text{A}/\text{cm}^2$ for this system.

A threshold hydrogen embrittlement curve was developed for cathodically charged, flat, double-notched tensile bars of AISI 4340 steel of 1790 to 1930 MPa strength level and a stress concentration factor (K_t) of 5.6 by correlating hydrogen concentrations with sustained-load testing in the range between 15 and 40 percent of the notched tensile strength. For example, critical hydrogen concentrations of 0.25, 0.17 and 0.06 ppm were found for failure at loads of 15, 25 and 40 percent NTS.

It has been shown that the bakeout process produces variable results depending on the nature of the plate (for example, porosity) and that a

bright, relatively nonporous, cyanide cadmium plate can be very impervious toward the passage of hydrogen. Thus the barnacle electrode could be a very useful tool in determining the effectiveness of the baking. It should be emphasized that though others have shown a loss in ductility, this work has shown definitively that this loss is due to the presence of hydrogen. We have also shown that a duplex cadmium plating treatment has no advantage over the single-plating procedure in reducing the ultimate hydrogen concentration.

The capability of measuring very low hydrogen levels and the high precision now attainable make it possible to investigate very minute changes in hydrogen concentrations in a set of aging, plated specimens. Though still somewhat preliminary, results to date indicate that hydrogen is stored in the cadmium plate after baking, and is gradually lost both to the atmosphere and into the underlying steel. The diffusion into the specimen causes a rise in hydrogen concentration that appears to peak at several weeks. This correlates with delayed failure data.

Finally, it was shown that the loss of hydrogen with time from a steel weldment could be tracked using the barnacle electrode, and that there was still some hydrogen inside the 25-mm (1-in.)-thick HY-130 weldment after aging for one month at ambient conditions.

Acknowledgments

The authors wish to express their thanks to the Naval Air Systems Command, Washington, D.C. for financial assistance; to L. Biggs for his able assistance; and to Dr. V. Agarwala and S. Ketcham, Naval Air Development Center, and Dr. F. Mansfeld, Rockwell International Science Center, Thousand Oaks, Ca., for stimulating and helpful discussions.

References

- [1] Beck, W., Jankowsky, E. J., and Fischer, P., "Hydrogen Stress Cracking of High Strength Steels," Report No. NADC-MA-7140, Naval Air Development Center, Warminster, Pa., December 1971.
- [2] Troiano, A. R., *Transactions*, American Society for Metals, Vol. 52, 1960, pp. 54-80.
- [3] Troiano, A. R. in *Hydrogen in Metals*, I. M. Bernstein and A. W. Thompson, Eds., American Society for Metals, Metals Park, Ohio, 1974, pp. 3-15.
- [4] Bernstein, I. M. and Thompson, A. W., Eds., *Hydrogen in Metals*, American Society for Metals, Metals Park, Ohio, 1974.
- [5] Berman, D. A., Beck, W., and DeLuccia, J. J. in *Hydrogen in Metals*, I. M. Bernstein and A. W. Thompson, Eds., American Society for Metals, Metals Park, Ohio, 1974, pp. 595-607.
- [6] Devanathan, M. A. V. and Stachurski, Z., *Procedures of the Royal Society*, Vol. A270, 1962, pp. 90-102.
- [7] Devanathan, M. A. V., Stachurski, Z., and Beck, W., *Journal of the Electrochemical Society*, Vol. 110, 1963, pp. 886-891.
- [8] McBreen, J., Nanis, L., and Beck, W., *Journal of the Electrochemical Society*, Vol. 113, 1966, pp. 1218-1222.

- [9] Nanis, L. and DeLuccia, J. J. in *Materials Performance and the Deep Sea*, ASTM STP 445, American Society for Testing and Materials, 1969, pp. 55-67.
- [10] Fullenwider, M., "The Electrochemical Permeation of Hydrogen in Metals," Ph.D. dissertation, University of Pennsylvania, Philadelphia, 1969.
- [11] Bockris, J. O'M., Genshaw, M. A., and Fullenwider, M., *Electrochimica Acta*, Vol. 15, 1970, pp. 47-60.
- [12] Beck, W., Glass, A. L., and Taylor, E., *Journal of the Electrochemical Society*, Vol. 112, 1965, pp. 53-59.
- [13] vanLeeuwen, H. P., *Sonderdruck aus Materialprufung*, Vol. 16, 1974, pp. 263-269.
- [14] Das, K. B. in *Hydrogen in Metals*, I. M. Bernstein and A. W. Thompson, Eds., American Society for Metals, Metals Park, Ohio, 1974, pp. 609-621.
- [15] Berman, D. A., "Indexing the Degree of Hydrogen Embrittlement of 4340 Steel Using the Barnacle Electrode," Report No. NADC-76359-30, Naval Air Development Center, Warminster, Pa., November 1976.
- [16] Fitzpatrick, V. F. and Ayres, J. A., *Materials Protection*, Vol. 9, 1970, pp. 27-30.
- [17] Brown, B. F., "Effect of Baking on Delayed Fracture of Electroplated Ultra High Strength Steel," NRL Report 4839, Naval Research Laboratory, Washington, October 1956.
- [18] Beck, W., Jankowsky, E. J., and Fischer, P., "Hydrogen Stress Cracking of High Strength Steels," Report No. NADC-MA-7140, Naval Air Development Center, Warminster, Pa., December 1971, p. 162.

Robert Baboian¹ and G. S. Haynes¹

Cyclic Polarization Measurements— Experimental Procedure and Evaluation of Test Data

REFERENCE: Baboian, Robert and Haynes, G. S., “Cyclic Polarization Measurements—Experimental Procedure and Evaluation of Test Data,” *Electrochemical Corrosion Testing, ASTM STP 727*. Florian Mansfeld and Ugo Bertocci, Eds., American Society for Testing and Materials, 1981, pp. 274–282.

ABSTRACT: ASTM Subcommittee G01.11 on Electrochemical Measurements in Corrosion Testing has conducted round-robin testing on the reproducibility of cyclic potentiodynamic polarization measurements for determining susceptibility to localized corrosion. This work was used in the development of a practice that provides a standard experimental procedure for conducting these tests. This paper presents the experimental procedure and results of the round-robin tests with statistical analysis of the data. The reproducibility of the measurements and sources of error are discussed.

KEY WORDS: cyclic polarization, pitting potential, protection potential, localized corrosion, stainless steels, potentiodynamic polarization, polarization curves, pitting corrosion, passivation, crevice corrosion

Polarization techniques have been widely used in assessing resistance to localized corrosion of stainless steels and other iron, nickel, or cobalt-based alloys [1–5].² More recently, metals have been polarized from active to more noble potentials until some critical value has been reached, and subsequently polarization has been reversed towards more active potentials (cyclic polarization) to evaluate resistance to localized corrosion. Little agreement exists on the mechanisms involved or interpretation of data; however, the technique has been applied to the study of initiation of pitting and crevice corrosion, propagation of existing pits and crevices, and galvanically induced localized corrosion [4, 6–8].

Since this technique has been widely used, ASTM Subcommittee G01.11 on Electrochemical Measurements in Corrosion Testing established a task group on the reproducibility of cyclic potentiodynamic polarization measurements for determining susceptibility to localized corrosion. The work of this

¹Laboratory head and project head, respectively, Electrochemical and Corrosion Laboratory, Texas Instruments, Inc., Attleboro, Mass. 02703.

²The italic numbers in brackets refer to the list of references appended to this paper.

group led to the development of an ASTM Practice for Conducting Cyclic Potentiodynamic Polarization Measurements for Localized Corrosion (G 61-78), which provides a standard experimental procedure for conducting these tests. This paper presents an experimental procedure and results of round-robin tests with statistical analysis of the data. The reproducibility of the measurements is discussed.

Experimental Procedure

The materials evaluated by the task group³ were Type 430 stainless steel, Type 304 stainless steel, Type 316 stainless steel, Carpenter 329, Hastelloy G, and Hastelloy C-276. All materials were in the mill annealed condition, and 1.6-cm (0.625-in.) diameter flat specimens were prepared from the sheet material. Specimens were wet-polished to a 600 grit silicon carbide (SiC) paper finish before ultrasonic cleaning for 5 min in a detergent solution, followed by a distilled water rinse.

Specimens were mounted in a specimen holder designed to expose 1 cm² of the flat strip to the test solution. This specimen holder has been described previously [9-10]. It is important that the circular Teflon gasket be drilled and machined flat in order to minimize mounting crevices. The polarization cells were similar, although not identical, to the one described in the ASTM Recommended Practice for Standard Reference Method for Making Potentiostatic and Potentiodynamic Anodic Polarization Measurements (G 5-78). The potentiodynamic circuits were similar to the one described by Greene [11] or commercially available units. A salt bridge—luggin probe combination was used to separate the saturated calomel electrode (SCE) from the solution in the test cell. The probe tip was located approximately 2 mm from the specimen. The auxiliary electrode was platinum.

Conditions for the cyclic polarization tests are listed in Table 1. The electrolyte was prepared by dissolving 34 g of reagent grade sodium chloride (NaCl) in 920 mL of distilled water. A sliding seal for the specimen holder was used to maintain the specimen above the electrolyte level in the cell while

TABLE 1—Conditions for cyclic polarization tests.

Electrolyte	3.56 weight percent sodium chloride
Temperature	25 ± 1°C
Deaeration	Argon (overnight) or hydrogen
Specimen finish	600 grit SiC paper
Starting potential	Corrosion potential
Scan rate	0.6 V/h

³H. H. Lawson and R. Smith, Armco, Inc.; L. C. Rowe and M. S. Walker, G. M. Corporation; J. B. Harrell and R. L. Martin, Petrolite Corporation; F. Mansfeld and J. V. Kenkel, Rockwell International Corporation; and R. Baboian and G. S. Haynes, Texas Instruments, Inc.

TABLE 2—Steps in cyclic polarization scan.

-
- 1 Immerse specimen 1 h before scan.
 - 2 Measure platinum potential 50 min after specimen immersion.
 - 3 Measure corrosion potential before beginning polarization.
 - 4 Begin polarization at corrosion potential and scan in noble direction at 0.6 V/h.
 - 5 When corrosion current reaches 5 mA/cm², reverse scan direction (towards more active potentials).
 - 6 Continue reverse scan until hysteresis loop is complete or corrosion potential is reached.
-

purging with argon at 150 cm³/min overnight. In one laboratory the solution was purged with hydrogen for 1.5 h before specimen immersion.

The steps in the cyclic polarization scan are shown in Table 2. The sliding seal was used to accomplish immersion of the specimen 1 h before the scan. Specimen and platinum potentials at specified time intervals were measured. The exact instructions for the scan were (1) initiating at E_{corr} , scan in the more noble potential direction, until surface film breakdown occurs (E_c) (as indicated by a rapid increase in current); (2) reverse scanning direction (towards more active potentials) when corrosion current reaches 5 mA; and (3) continue reverse scan until repassivation occurs (E_p) (hysteresis loop is complete or corrosion potential is reached).

Results and Discussion

The corrosion potentials measured just prior to initiating the scan are shown in Table 3 for the various laboratories. Factors that contributed to the wide variation in potentials between the various laboratories for each alloy include the degree of success in avoiding crevices, specimen surface preparation, and residual oxygen. Although oxygen concentrations were not measured, the more negative values observed in Laboratory A, where a hydrogen purge was used, indicate that small amounts of oxygen (when argon is used) can have a marked influence on the corrosion potential. This small amount of residual oxygen had no apparent effect on the critical values obtained for the protection potential and the breakdown potential since the results from the other laboratories were in good agreement with those from Laboratory A.

Typical polarization curves for some of the alloys are shown in Fig. 1. Two types of polarization curves were measured; one which exhibited a hysteresis effect, such as for Types 430, 304, and 316 stainless steel, and one which did not exhibit a hysteresis effect, such as for Hastelloy C-276. The presence or absence of hysteresis correlates well with the modes of corrosion observed on the specimens after the polarization tests (as shown in Table 4 and Fig. 2). Note that pitting or crevice corrosion, or both, occurred only on alloys that display a well-defined hysteresis.

More detailed data analysis was conducted on an alloy which displayed a hysteresis and one which did not for the purpose of establishing the practice. Since both pitting and crevice corrosion occurred in all but one laboratory for

TABLE 3—Corrosion potentials (instant before polarization) (volts versus SCE^a).

Alloy	Laboratory				
	A	B	C	D	E
Type 430 stainless steel	-0.430	-0.337	-0.301	+0.057	-0.600
Type 304 stainless steel	-0.480	-0.248	-0.270	-0.102	-0.450
Type 316 stainless steel	-0.479	-0.180	-0.321	+0.196	-0.350
Carpenter 329	-0.522	-0.465	-0.305	-0.183	-0.360
Hastelloy G	-0.380	-0.303	-0.315	-0.268	-0.400
Hastelloy C-276	-0.509	-0.401	-0.349	-0.475	-0.430

^aSCE = saturated calomel electrode.

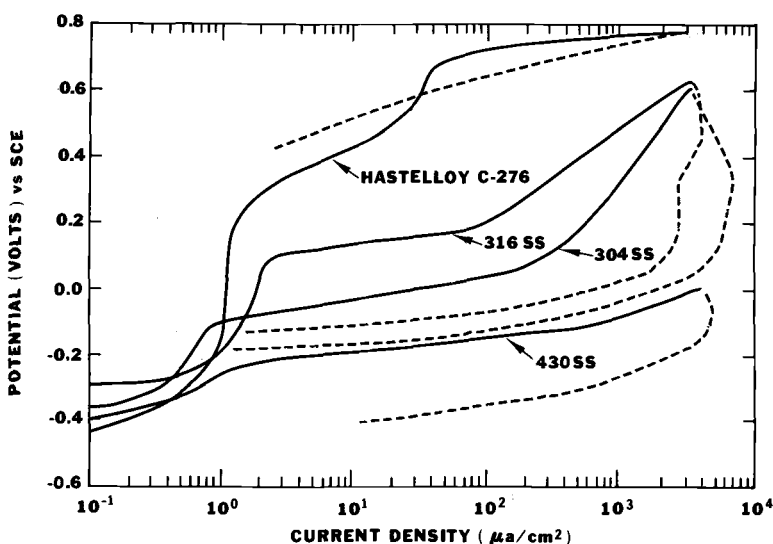


FIG. 1—Potentiodynamic polarization curves for alloys in seawater at 30°C.

Type 304 stainless steel (see Table 4), this alloy was chosen as a susceptible one, and Hastelloy C-276 was chosen as a resistant alloy. Representative polarization curves for these alloys are shown in Fig. 3. The scan direction is indicated by the arrows. Note that Type 304 stainless steel exhibits a well-defined pitting potential (E_c) and protection potential (E_p).

The values for the open circuit potential (E_{corr}), the pitting potential (E_c), and the protection potential (E_p) obtained by four of the laboratories for Type 304 stainless steel are listed in Table 5. The pitting potentials (E_c) for Type 304 stainless steel exhibited a large amount of scatter with a range of 200 mV. This result was not surprising since it is well known that pitting potentials are influenced by mounting technique, oxygen concentration, etc.

TABLE 4—Mode of localized corrosion observed.

Specimen	Laboratory				
	A	B	C	D	E
Type 430 stainless steel	CC ^a	CC,P ^b	CC,P	CC,P	CC,P
Type 304 stainless steel	CC	CC,P	CC,P	CC,P	CC,P
Type 316 stainless steel	CC	CC	CC,P	CC	CC,P
Carpenter 329	CC	CC,P	none	CC,P	CC
Hastelloy G	CC	CC,P	CC	CC	CC
Hastelloy C-276	none	none	none	none	...

^aCC = crevice corrosion.

^bP = pitting corrosion.

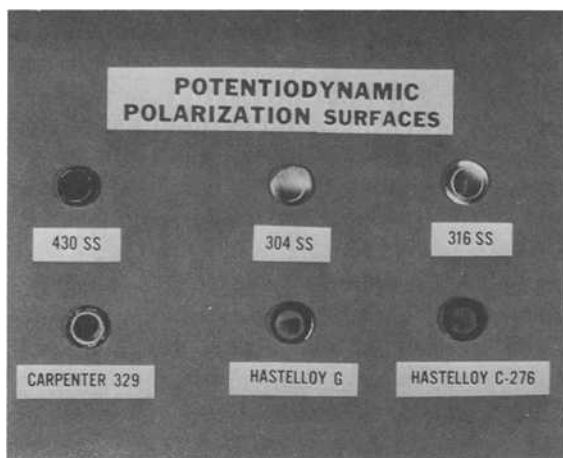


FIG. 2—Potentiodynamic polarization surfaces.

The protection potentials (E_p), however, were tightly grouped within a range of only 40 mV, which indicates that this parameter is relatively independent of these factors and is highly reproducible.

Statistical analysis was used on the data from the round-robin tests for Type 304 stainless steel and Hastelloy C-276 to construct standard reference plots for the forward (Fig. 4) and reverse (Fig. 5) scans. The mean values and a range of ± 2 standard deviations which should encompass 95 percent of all data are shown. The large amount of variation for the forward scan (Fig. 4) in the low-current range (1 to $10\mu\text{A}/\text{cm}^2$) could be due to residual oxygen or instrumental effects for both alloys. The probable causes of the large variation in the pitting potential region for Type 304 stainless steel have been already discussed. The good reproducibility for Hastelloy C-276 at the higher current values is due to the absence of localized corrosion. These currents are

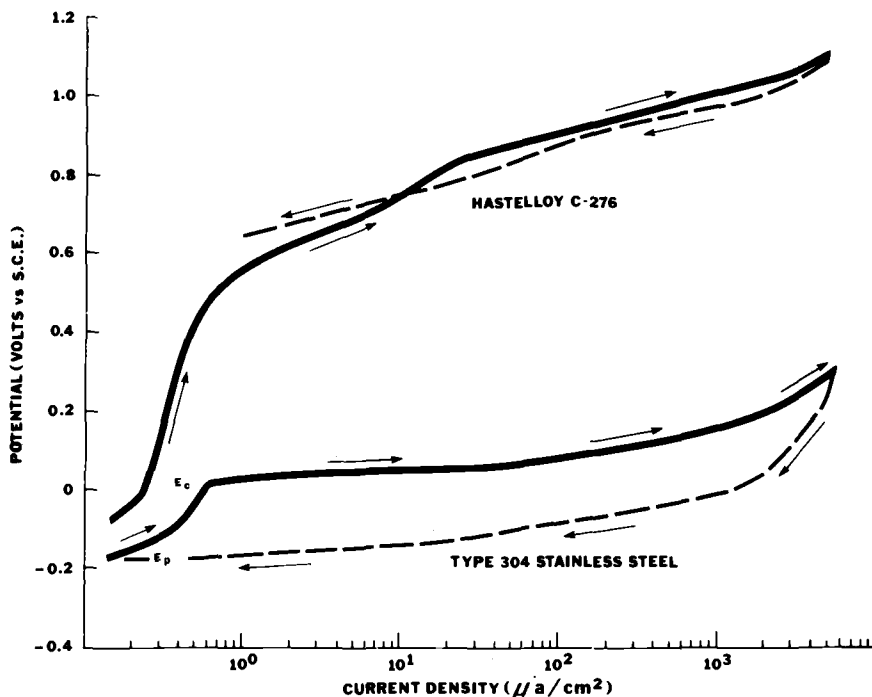


FIG. 3—Representative cyclic potentiodynamic polarization curves.

a measure of uniform corrosion in the transpassive or oxygen evolution region.

In contrast to the forward scan, the reverse scan had a high degree of reproducibility. The small variation in the data for Type 304 stainless steel and Hastelloy C-276 indicates that the protection potential is not sensitive to those factors that affected the forward scan.

Summary

The scope of ASTM G 61 summarizes the work of the task group. It states:

This practice gives a suggested procedure for conducting cyclic potentiodynamic polarization measurements to determine susceptibility to localized corrosion (pitting and crevice corrosion). If followed, this practice will provide repeatable cyclic potentiodynamic anodic polarization measurements that will reproduce data determined by others at other times in other laboratories. The procedure is preferably used for iron, nickel or cobalt-based alloys. Samples of the standard type 304 stainless steel and the Hastelloy C-276 used in obtaining the standard reference plot are available for those who wish to check their own test procedure and equipment.

TABLE 5—Results for Type 304 stainless steel.

Laboratory	Potential (volts versus SCE ^a)		
	E_{corr}	E_c	E_p
A	-0.480	+0.150	-0.160
B	-0.248	+0.040	-0.200
C	-0.270	+0.220	-0.170
D	-0.102	+0.240	-0.200

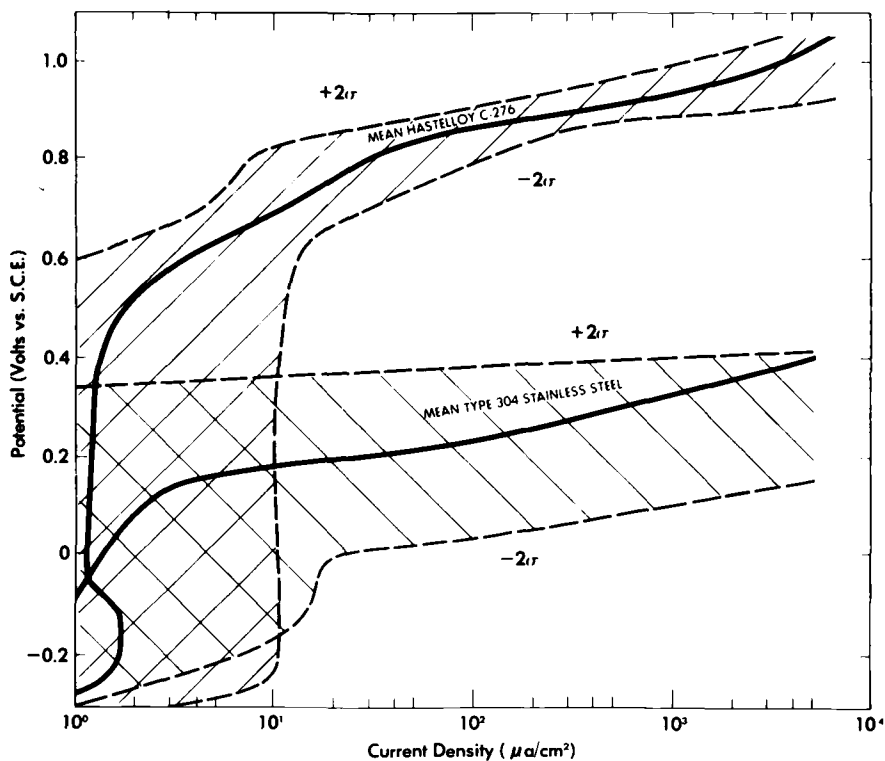
^aSCE = saturated calomel electrode.

FIG. 4—Standard potentiodynamic polarization plot (forward scan).

The reproducibility of the cyclic polarization technique has been established for the forward (Fig. 4) and reverse (Fig. 5) scans. The reproducibility of the reverse scan is significantly better than that for the forward scan for all alloys (those susceptible to localized corrosion and those which are not). This

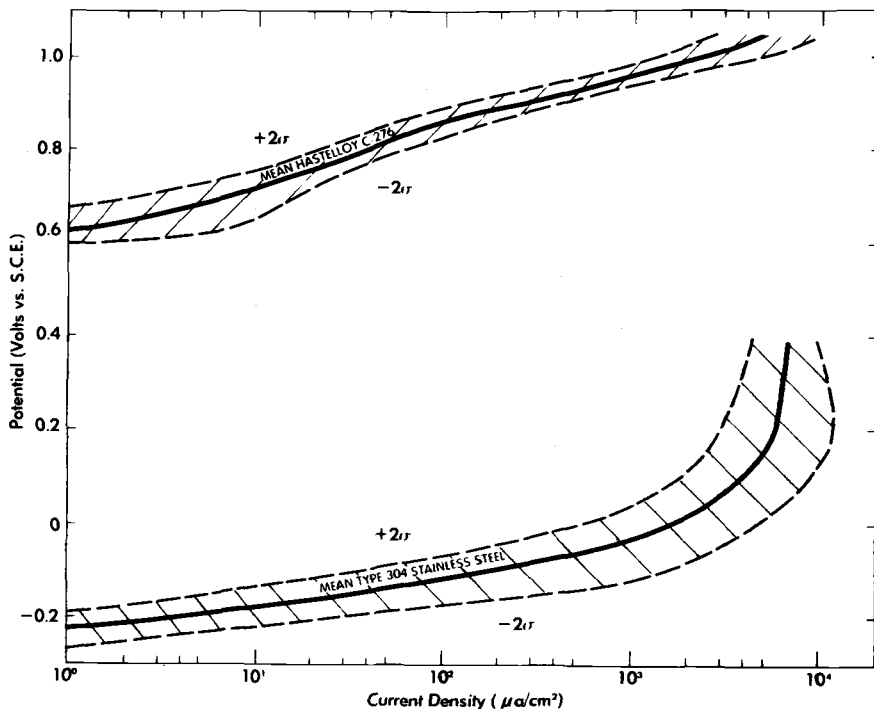


FIG. 5—Standard potentiodynamic polarization plot (reverse scan).

would indicate that the protection potential is a better criterion for resistance to localized corrosion than the critical pitting potential.

In general, localized corrosion can propagate at potentials more noble than the point where the hysteresis loop is completed (E_p). In these cases the more noble the potential E_p , the less likely E_{corr} will exceed it, and the less likely localized corrosion will occur.

An indication of the susceptibility to initiation of localized corrosion is given by the potential at which the anodic current increases rapidly. The more noble this potential, the less susceptible is the alloy to initiation of localized corrosion. The polarization curves indicate that initiation and propagation of localized corrosion occur at potentials below the oxygen-evolution potential in Type 304 stainless steel. The rapid increase in current for Hastelloy C-276 is not a result of localized corrosion but of uniform corrosion in the transpassive or oxygen-evolution region. Since the corrosion potentials for Hastelloy C-276 and Type 304 stainless steel are usually similar, these curves indicate that Hastelloy C-276 is more resistant to initiation and propagation of localized corrosion than Type 304 stainless steel.

References

- [1] Brennett, S., *Journal of the Iron and Steel Institute*, Vol. 135, 1937, p. 101.
- [2] Hospadaruk, V. and Petrocelli, J. V., *Journal of the Electrochemical Society*, Vol. 113, 1966, p. 878.
- [3] Horvath, J. and Uhlig, H. H., *Journal of the Electrochemical Society*, Vol. 115, 1968, p. 791.
- [4] Pourbaix, M., Klimzack-Mathieu, L., Mertens, C., Meunier, J. Vanleughenhaghe, C., DeNuncky, L., Laverys, J., Neelemans, L., and Warzee, M., *Corrosion Science*, Vol. 3, 1963, p. 239.
- [5] Defranoux, J. M., *Corrosion Science*, Vol. 3, 1963, p. 75.
- [6] Pourbaix, M., *Corrosion*, Vol. 26, 1970, p. 431.
- [7] Baboian, R. in *Localized Corrosion—Cause of Metal Failure. ASTM STP 516*, American Society for Testing and Materials, 1972, pp. 145-163.
- [8] Baboian, R. and Haynes, G. S., in *Corrosion in Natural Environments. ASTM STP 558*, American Society for Testing and Materials, 1974, pp. 171-184.
- [9] France, W. D., Jr., *Journal of Electrochemical Society*, Vol. 114, 1967, p. 818.
- [10] Myers, J. R., Guewlar, F. G., and Smulczynski, L. A., *Corrosion*, Vol. 24, 1968, p. 352.
- [11] Greene, N. D., *Experimental Electrode Kinetics*. Rensselaer Polytechnic Institute, Troy, N.Y., 1965.

N. K. Sarkar¹

Application of Potentiokinetic Hysteresis Technique to Characterize the Chloride Corrosion of High-Copper Dental Amalgams

REFERENCE: Sarkar, N. K., "Application of Potentiokinetic Hysteresis Technique to Characterize the Chloride Corrosion of High-Copper Dental Amalgams," *Electrochemical Corrosion Testing, ASTM STP 727*, Florian Mansfeld and Ugo Bertocci, Eds., American Society for Testing and Materials, 1981, pp. 283-289.

ABSTRACT: The potentiokinetic hysteresis technique was utilized to characterize the electrochemical reactions involved in the corrosion of six silver-tin dental amalgams containing approximately 2.0 to 15.0 weight percent copper in a 1.0 percent sodium chloride (NaCl) solution at 23°C over a potential range of -1200 to 0 mV (saturated calomel electrode). The results indicated that the corrosion of these amalgams is associated with several oxidation-reduction reactions, namely, Sn/Sn (OH)₂, Sn/Sn (OH)₄, Sn/Sn(OH)Cl, H₂O, Cu/Cu₂O, and Cu/CuCl, which are thermodynamically possible in the range of potentials scanned. The occurrence of these reactions at around their respective thermodynamic potentials was clearly indicated during the reverse scan of the potentiokinetic measurement. From the height of the peak currents associated with these various reactions, it is possible to rank these amalgams from the standpoint of electrochemical activities of copper and tin in each amalgam. These results offer an insight into the mechanism of corrosion of dental amalgams, and at the same time demonstrate the usefulness of the potentiokinetic technique in the evaluation of the corrosion resistance of dental amalgams.

KEY WORDS: electrochemical corrosion, oxidation reduction, potentiokinetic, dental amalgams, hysteresis, silver, tin, copper

Conventional dental amalgams consist of three major metallurgical phases: γ (Ag₃Sn), γ_1 (Ag₂Hg₃), and γ_2 (Sn₇Hg); the γ_2 -phase has been found to be the most susceptible to corrosion in the oral environment [1].² The electrochemical corrosion of the γ_2 -phase is believed to be responsible for the deterioration of conventional amalgam restorations [2]. Recently, in an attempt to improve the corrosion resistance of dental amalgams, copper has been added to many commercial dental amalgam alloys in concentra-

¹Associate professor, Department of Biomaterials, School of Dentistry, Louisiana State University, New Orleans, La. 70119.

²The italic numbers in brackets refer to the list of references appended to this paper.

tions higher than recommended by Specification No. 1 of the American Dental Association [3]. This addition of copper results in a reduction of the γ_2 -phase or its elimination by the formation of a copper-tin phase [3]. Microstructural studies coupled with controlled potential polarization treatments of several γ_2 -free dental amalgams have indicated that in the absence of the γ_2 -phase, the copper-tin phase undergoes selective corrosion attack [4]. However, the electrochemistry of the corrosion of the γ_2 -free dental amalgams is very little understood at this time, although the electrochemical reactions involved in the corrosion of γ_2 -containing dental amalgams have been investigated extensively [1,5,6]. The object of this investigation was to elucidate these reactions in an effort to fully appreciate the corrosion-induced problems of amalgam "fillings" encountered in clinical service.

In this investigation the potentiokinetic hysteresis technique was employed to achieve the aforementioned objective. Details of this technique have been described previously [7-9]. In essence, the technique involves electrochemical cyclic polarization of an alloy sample in a fixed potential range. In the past, the potential-current profiles generated by this technique have been utilized to characterize such corrosion-related material parameters as the breakdown potential and the protection potential. The present application of the technique is somewhat unorthodox in that emphasis is placed on the fundamental electrochemical reactions responsible for corrosion rather than such parameters. In this respect, the present approach is very similar to a "reverse" anodic stripping voltammetry technique [10] in which oxidation of selective metals from an alloy sample during forward scan has been followed by reduction of the oxidized species during reverse scan. It has been reported [4] that information on possible electrochemical reactions can be obtained from thermodynamic treatment of potentiokinetic polarization data in which the position (potential) and height (current) of oxidation-reduction peaks are characteristics of the type and concentration of the corrodible species.

Experimental Procedure

Materials

The five γ_2 -free dental amalgams studied in the present investigation are listed in Table 1 together with a γ_2 -containing dental amalgam (Micro) that was used as the control. The metallurgical nature of these amalgams has been described in detail elsewhere [4]. The amalgam specimens were prepared following the manufacturer's recommendations and Specification No. 1 of the American Dental Association. The specimens were dry-stored for eighteen months prior to testing. The sample preparation consisted of wet grinding with 600 grit SiC paper, followed by thorough rinsing in distilled water. The area of all samples was 0.125 cm².

TABLE 1—Composition of commercial dental amalgams investigated.

Amalgam	Composition of alloy, wt. %					Manufacturer
	Silver	Tin	Copper	Zinc	Indium	
Tytin	60.0	27.0	13.0	S. S. White
Sybraloy	40.0	30.0	30.0	Kerr-Sybron
Aristaloy	60.0	27.0	13.0	Baker-Engelhard
Dispersalloy	70.0	17.0	12.0	1.0	...	Johnson & Johnson
Indiloy	60.0	22.0	13.0	...	5.0	Shofu Dental
Micro	71.0	26.0	4.0	L. D. Caulk

Electrochemical Technique

The potentiokinetic hysteresis technique was employed to characterize the electrochemical reactions of the amalgams in a 1 percent sodium chloride (NaCl) solution (pH = 7) at 23°C. The choice of the electrolyte was based on past experience [5] which showed that a 1 percent NaCl solution adequately represents saliva so far as its corrosion effect on dental amalgams is concerned. A continuous ten-cycle potentiokinetic scan over a potential range of -1200 to 0 mV [versus saturated calomel electrode (SCE)] was carried out to allow appreciable oxidation of corrodible metals, and thereby enrich the electrolyte and the electrode surface with oxidized species in a reasonably short time. In each cycle the starting potential was at -1200 mV with a forward scan to 0 mV, followed by a reverse scan back to -1200 mV. The first nine cycles were scanned at a rate of 10 mV/s. Preliminary work indicated that such a high scan rate not only altered the potential at which a certain electrochemical reaction took place under equilibrium conditions, but also interfered with the development of well-defined current peaks during reverse scans. Accordingly, the scan rates for the forward and the reverse scan of the last cycle were selected at 5 and 1 mV/s, respectively.

Results and Discussion

Previous *in vivo* and *in vitro* measurements have indicated that the corrosion potential of γ_2 -containing dental amalgams is around -300mV, and that of γ_2 -free amalgams is in the range of -275 to -60 mV [4-6, 11-13]. These reported potentials are within the potential range scanned in the present investigation. A number of probable electrochemical reactions most likely to occur in this potential range on the amalgam electrodes in a neutral saline solution are listed in Table 2 [1, 4-6, 11-15]. For the sake of clarity, only results pertinent to the elucidation and clarification of these electrochemical reactions are presented and discussed here.

The potential-current profiles of Micro (conventional) and Sybraloy (γ_2 -free) obtained during the forward scan of the tenth cycle are presented in

TABLE 2—Probable electrochemical reactions and their equilibrium electrode potentials.

Reactions	Equilibrium Potential, mV versus SCE ^a
(1) $\text{Sn} + 2(\text{OH})^- \rightleftharpoons \text{Sn}(\text{OH})_2 + 2e$	-750
(2) $\text{Sn} + 2(\text{OH})^- \rightleftharpoons \text{SnO} + \text{H}_2\text{O} + 2e$	-762
(3) $\text{Sn} + 4(\text{OH})^- \rightleftharpoons \text{Sn}(\text{OH})_4 + 4e$	-675
(4) $\text{Sn} + 4(\text{OH})^- \rightleftharpoons \text{SnO}_2 + 2\text{H}_2\text{O} + 4e$	-775
(5) $\text{Sn} + (\text{OH})^- + \text{Cl}^- + \text{H}_2\text{O} \rightleftharpoons \text{Sn}(\text{OH})\text{Cl}, \text{H}_2\text{O} + 2e$	-635
(6) $2\text{Cu} + 2(\text{OH})^- \rightleftharpoons \text{Cu}_2 + \text{H}_2\text{O} + 2e$	-193
(7) $\text{Cu}_2\text{O} + 2(\text{OH})^- \rightleftharpoons 2\text{Cu} + \text{H}_2\text{O} + 2e$	-14
(8) $\text{Cu}_2\text{O} + 2(\text{OH})^- + \text{H}_2\text{O} \rightleftharpoons 2\text{Cu}(\text{OH})_2 + 2e$	-83
(9) $\text{Cu} + \text{Cl}^- \rightleftharpoons \text{CuCl} + e$	-40

^aSCE = saturated calomel electrode.

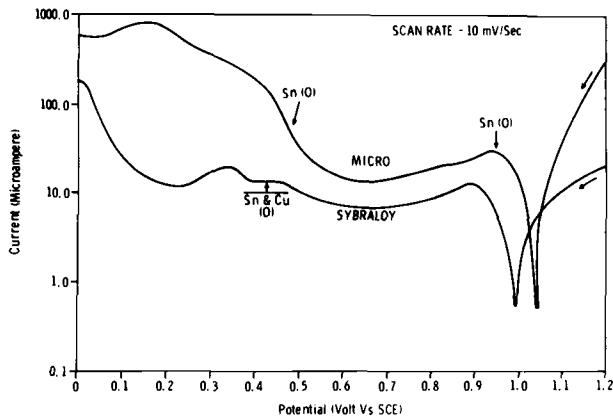


FIG. 1—Forward-scan potential-current profile of a γ_2 -free (Sybraloy) and a γ_2 -containing (Micro) dental amalgam (tenth cycle).

Fig. 1. For the conventional amalgam, the current peak at around -950 mV is associated with the oxidation of tin to form tin oxides or hydroxides as indicated by Reactions 1 to 4 in Table 2 [1]. This follows the passive zone between -950 and -500 mV, where the current remains almost steady. A significant increase in current above -500 mV is believed to be due to a breakdown of tin oxide and simultaneous formation of a tin oxychloride, as indicated by Reaction 5 in Table 2 (1,5).

The polarization curve exhibits the following characteristics for Sybraloy: (1) A current peak at around -900 mV; and (2) two closely spaced current peaks between -500 and -300 mV.

The first current peak of Sybraloy at -900 mV can be reasonably attributed to the oxidation of tin to form tin oxides or hydroxides. The last two

closely spaced peaks, on the other hand, appear to be due to the oxidation of both copper and tin. It is difficult, however, to associate copper or tin specifically with one peak or the other, since oxidation of both copper and tin is possible in this potential range, as indicated by Reactions 6 to 9 in Table 2.

It should be noted in Fig. 1 that, when compared to the conventional amalgam, Sybraloy is characterized by lower anodic current, and thereby decreases electrochemical activity or corrosion. In particular, a distinct breakdown of passivity, as indicated in the polarization curve of the conventional amalgam above -500 mV, is not observed in Sybraloy, a γ_2 -free amalgam. This is consistent with previous observations and is the only feature of the polarization curve that discriminates a non- γ_2 amalgam from a γ_2 -containing amalgam [12].

The potential-current profiles (forward scan) of the other high-copper dental amalgams were similar to that of Sybraloy in that they indicated (1) a current peak at around -900 mV, and (2) two closely spaced peaks around -400 mV (not shown). Although the anodic currents for these amalgams at various potentials were slightly different from one another, no discrimination between various non- γ_2 amalgams could be made from the standpoint of the electrochemical activities of copper and tin. The main limitation was the presence of the two current peaks around -400 mV, neither of which could be specifically attributable to the oxidation of either copper or tin.

Figure 2 presents the potential-current profile of Tytin obtained during the last cycle (forward and reverse) polarization. For the purpose of comparison, the polarization curve of the conventional amalgam is also shown in Figure 2. Whereas the forward-scan profile of Tytin is typical of a γ_2 -free amalgam and is distinguishable from that of the conventional amalgam by the absence of any breakdown of passivity at around -400 mV, the following charac-

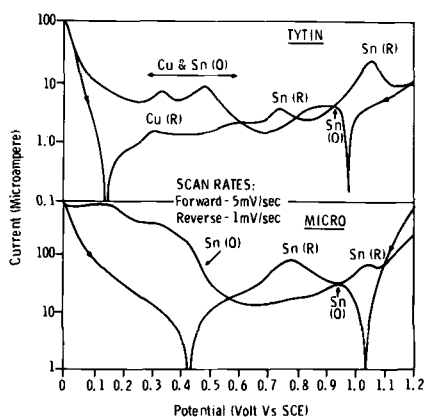


FIG. 2—Cyclic potential-current profile of a γ_2 -free (Tytin) and a γ_2 -containing (Micro) dental amalgam (tenth cycle).

teristics of the reverse-scan profile of both amalgams require special attention. For the conventional amalgam, the reverse-scan profile indicates the presence of two cathodic current peaks—one at about -750 mV and the other at around -1050 mV. Both these peaks are believed to be due to the reduction of tin [16]. More specifically, this reduction of tin involves the reverse Reactions 1 to 5 listed in Table 2. The reverse-scan profile of Tytin, on the other hand, indicates the presence of a third peak at about -300 mV, related to the reduction of copper involving reverse Reactions 6 to 9 in Table 2. It should be noted that both current peaks associated with the reduction of tin in Tytin are lower than the corresponding peaks for the conventional amalgam.

It should be noted further that the reverse-scan polarization profiles of the other γ_2 -free amalgams also indicated the presence of three distinct current peaks, although the magnitude of the current associated with each reduction reaction varied for different brands. Moreover, because of the similar electrochemical behavior of tin and indium, no separate peak related to the reduction of indium was observed in the polarization profile of Indiloy, the indium-containing amalgam.

In previous studies involving dental casting alloys [4], it was hypothesized that the appearance of these peaks is an indication of the presence of corrodible "species" in a given alloy system, since reduction suggests prior oxidation (corrosion). The higher the peak current, the greater is the concentration of the "corrodible" species and, therefore, the more corrosion-prone is the material. Based on this hypothesis and from the magnitude of the peak currents associated with the reduction of tin and copper in various amalgams, it is apparent that a relative ranking of the investigated amalgams in terms of the electrochemical activities of tin and copper is possible.

Conclusions

1. The electrochemical reactions responsible for the corrosion of high-copper dental amalgams can be characterized by the use of the potentiokinetic hysteresis technique.
2. Specifically, these reactions include several oxidation-reduction reactions involving tin, copper, $(\text{OH})^-$, and Cl^- .
3. From the height of the peak currents associated with the reduction reactions involving tin and copper at various electrode potentials, it is possible to rank these amalgams from the standpoint of tin and copper corrosion.

Acknowledgments

This research was supported by NIDR Grant DE 05126-02.

References

- [1] Sarkar, N. K. and Greener, E. H., *Journal of Oral Rehabilitation*, Vol. 2, 1975, p. 49.
- [2] Sarkar, N. K., *Journal of Oral Rehabilitation*, Vol. 5, 1978, p. 413.
- [3] Sarkar, N. K., *Journal of Oral Rehabilitation*, Vol. 6, 1979, p. 1.
- [4] Sarkar, N. K., Fuys, R. A., Jr., and Stanford, J. W. in *Corrosion and Degradation of Implant Materials, ASTM STP 684*, American Society for Testing and Materials, 1979, p. 277.
- [5] Sarkar, N. K., Marshall, G. W., Moser, J. B., and Greener, E. H., *Journal of Dental Research*, Vol. 54, 1975, p. 1031.
- [6] Sarkar, N. K. and Greener, E. H., *Journal of Oral Rehabilitation*, Vol. 4, 1977, p. 55.
- [7] Wilde, B. E. and Williams, E., *Journal of the Electrochemical Society*, Vol. 117, 1970, p. 775.
- [8] Wilde, B. E. and Williams, E., *Journal of the Electrochemical Society*, Vol. 118, 1971, p. 1058.
- [9] Wilde, B. E., *Corrosion*, Vol. 28, 1972, p. 283.
- [10] Copeland, T. R. and Skogerboe, R. K., *Analytical Chemistry*, Vol. 46, 1974, p. 1257 A.
- [11] Sarkar, N. K. and Greener, E. H., *Journal of Oral Rehabilitation*, Vol. 2, 1975, p. 139.
- [12] Sarkar, N. K. and Greener, E. H., *Journal of Oral Rehabilitation*, Vol. 2, 1975, p. 157.
- [13] Nomoto, S., Ano, M., and Onose, H., *Journal of Dental Research*, Vol. 58, 1979, p. 1688.
- [14] Latimer, W. M., *Oxidation Potentials*, Prentice Hall, New York, 1952.
- [15] Pourbaix, M., *Atlas of Electrochemical Equilibria in Aqueous Solutions*, Pergamon Press, New York, 1966.
- [16] Sarkar, N. K., "The Electrochemical Behavior of Dental Amalgams and Their Component Phases," Ph.D. dissertation, Northwestern University, Evanston, Illinois, 1973.

John Postlethwaite¹

Direct Measurement of the Corrosion Current for Oxygen-Reduction Corrosion

REFERENCE: Postlethwaite, John, "Direct Measurement of the Corrosion Current for Oxygen-Reduction Corrosion," *Electrochemical Corrosion Testing, ASTM STP 727*, Florian Mansfeld and Ugo Bertocci, Eds., American Society for Testing and Materials, 1981, pp. 290—302.

ABSTRACT: The polarization-resistance technique has received considerable attention in the past decade as a means of determining the rate of corrosion. In aerated solutions of pH greater than 4, where oxygen reduction is the major cathodic reaction, there is a much simpler and more direct method of determining the corrosion current. The method involves the deaeration of the solution while the corroding specimen is held potentiostatically at its previously determined corrosion potential (E_{corr}). The current supplied by the potentiostat when the solution is deaerated is the corrosion current (i_{corr}). This method is suitable for laboratory and pilot-plant scale testing when the solution can be deaerated. The application of the method for the measurement of corrosion rates under controlled hydrodynamic conditions in pilot-plant pipelines carrying water and aqueous slurries is discussed along with the limitations of the method.

KEY WORDS: corrosion, oxygen reduction, corrosion rate measurement

The most common corrosion problem is the corrosion of iron in aerated water. Under such conditions, where corrosion product films are formed, the classical Stern-Geary equation is of doubtful validity [1].² Tafel slopes are apparently increased due to the presence of an ohmic resistance through the corrosion product layer. Further, the assumption that the oxygen-reduction reaction is diffusion controlled may not be valid [1-3].

This paper describes a simple direct method of measuring the corrosion current when oxygen reduction is the cathodic reaction. The aforementioned problems are avoided by the use of this method.

¹ Professor, Department of Chemistry and Chemical Engineering, University of Saskatchewan, Saskatoon, Canada.

² The italic numbers in brackets refer to the list of references appended to this paper.

Direct Measurement of the Corrosion Current

Consider the kinetic corrosion diagram (Fig. 1a). At the corrosion potential, E_{CORR} , the anodic current corresponding to the anodic dissolution of iron is equal in magnitude to the cathodic current for the reduction of dissolved oxygen. If the corroding metal is made the working electrode in a three-electrode electrochemical test cell and is brought under potentiostatic control at E_{CORR} , the net current, i , flowing through the cell will be zero.

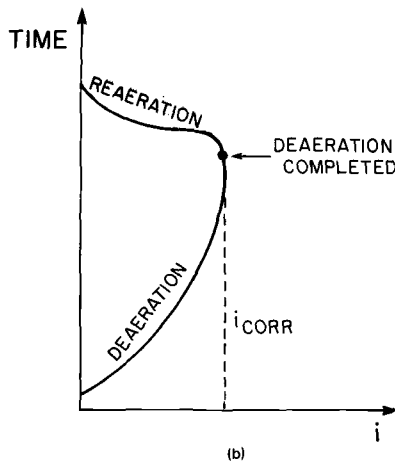
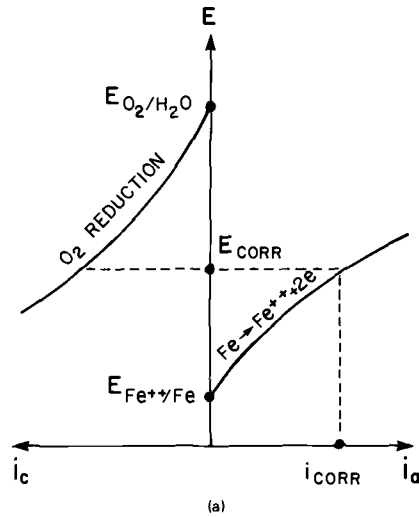


FIG. 1—Direct measurement of corrosion current when oxygen reduction is the cathodic reaction. (a) kinetic corrosion diagram; (b) deaeration and measurement of i_{CORR} with specimen held at E_{CORR} .

Subsequent deaeration of the solution with the specimen maintained under potentiostatic control at E_{corr} will give rise to a flow of current i through the cell, since $i_{\text{Fe} \rightarrow \text{Fe}^{++} + 2e} > i_{\text{O}_2 + 4\text{H}^+ + 4e \rightarrow 2\text{H}_2\text{O}}$; the value of i will rise as the oxygen is removed until $i = i_{\text{Fe} \rightarrow \text{Fe}^{++} + 2e}$ when the solution is completely deaerated (Fig. 1*b*). Of course, then $i = i_{\text{corr}}$ and the application of Faraday's laws converts this to a corrosion rate. For iron $1 \text{ mA/cm}^2 \equiv 11.6 \text{ mm/year}$.

Corrosion potentials for iron in aerated "near neutral" solutions are more positive than the Nernst potential for the $2\text{H}^+ + 2e = \text{H}_2$ reaction; hydrogen evolution need not be considered. For example, at $\text{pH} = 7$, $E_{\text{H}^+/\text{H}_2} = -0.41 \text{ V}$; the corrosion potential for iron in aerated tap water is well above this value [4]. It is likely that the hydrogen evolution reaction would make a significant contribution to the cathodic current for the corrosion of iron at pH values < 4 , where the deaeration technique would not be applicable, and the polarization-resistance technique would be required.

Following a corrosion-rate measurement and reaeration of the solution, the specimen is removed from potentiostatic control and corrodes naturally until the next measurement is required. Thus the changes in the corrosion rate with time can be observed.

The advantages of this method are:

1. Prior knowledge of the electrochemical behavior of the system is not required. It does not matter whether or not a corrosion product is present, or whether or not the oxygen reduction is diffusion controlled. The method simply measures the rate of anodic dissolution at E_{corr} .

2. The metal remains at E_{corr} and is not polarized to a region of different electrochemical behavior, which might affect its subsequent corrosion behavior.

The disadvantages of the method are:

1. It cannot be used for in-line corrosion measurements in industrial equipment, since deaeration of the solution is required. A complex by-pass or bleed system with deaeration facilities would be required.

2. iR drop compensation should be made if the metal is to remain at the true E_{corr} value when the solution is deaerated and $i = i_{\text{corr}}$ is flowing through the cell.

3. The normal corrosion chemistry will be disturbed when the oxygen-reduction reaction is eliminated during the measurement of i_{corr} .

The method is especially suitable for following the rate of corrosion in recirculating pipeline systems where deaeration to 0.05 ppm and subsequent reaeration can be accomplished in a period of about 30 min. The use of a steady-flow system gives a smooth deaeration curve and more easily identifiable plateau as the oxygen is removed. A flow system designed for use with this technique is now described.

Electrochemical Flow System

There are five requirements of this electrochemical flow system:

1. The system should be capable of being deaerated in a short time with rapid reaeration to minimize the disturbance of the normal corrosion chemistry.

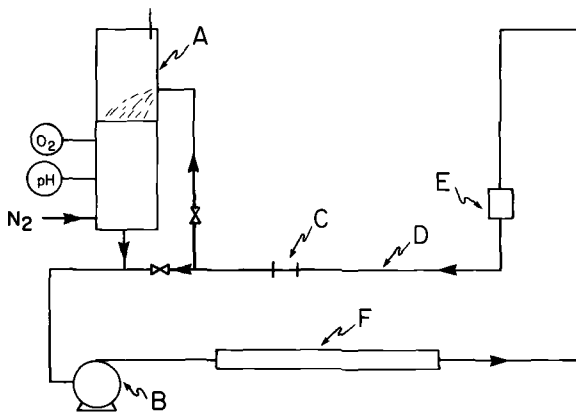
2. The flow cell should have a geometry for which the flow pattern is reproducible, and for which there are well established mass-transfer correlations to enable any possible mass-transfer effects to be quantified. Tubular- or duct-shaped systems are preferred to rotating disks and cylinders, since the flow pattern in the former is the same as that in a wide range of industrial equipment processing aqueous solutions.

3. The length of the working electrode should be large enough to enable fully developed mass-transfer conditions to be established. A substantial electrode surface will also reveal any flow effects, such as those found in erosion-corrosion [5].

4. The working electrode should be truly flush with the cell walls and not nominally flush as with some commercial probes.

5. The working electrode should be small to minimize iR drop effects [6]. (This requirement is obviously incompatible with Requirement 3.)

The flow system (Fig. 2) and the electrochemical test cell (Fig. 3) were designed with these requirements in mind.



A—Aeration/Deaeration Column
 B—Centrifugal Pump, 5 hp
 C—Electrochemical Test Cell
 D—5-cm-diameter PVC, Lucite, and Glass Pipe
 E—Magnetic Flowmeter
 F—Double-Pipe Heat Exchanger

FIG. 2—Pilot-plant flow system for direct measurement of i_{corr} .

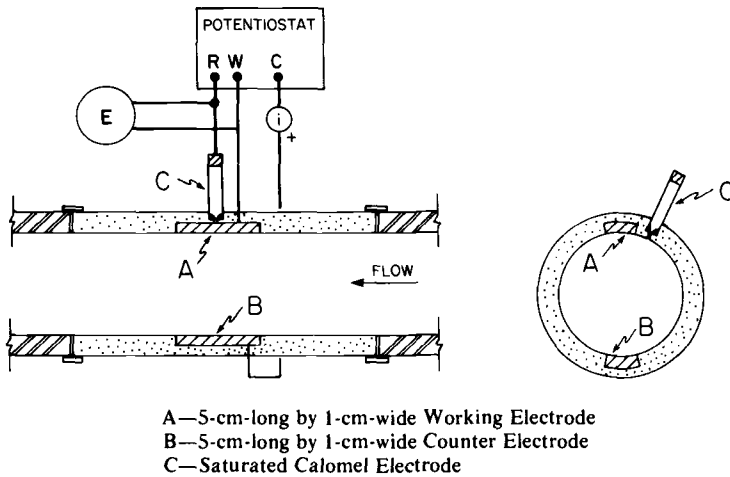


FIG. 3—Electrochemical flow cell and potentiostat.

Some of the solution is passed throughout the vertical column where there is good mixing at the solution-air interface which keeps the solution fully aerated. When deaeration is required, the column is closed except for a small vent and nitrogen is bubbled through the column. The 90-L system is deaerated in 15 to 30 min, and reaeration is accomplished quickly when the nitrogen flow is stopped and the cover removed.

In the majority of industrial applications the flow of aqueous solutions through pipes, heat exchangers, and other equipment corresponds to the turbulent-flow regime. In the present 5-cm-diameter system, laminar flow would be attained only at velocities below 4.2 cm/s corresponding to a Reynolds number of 2100. In practice, velocities of 1 to 3 m/s are used corresponding to well-developed turbulent flow. The diffusional-convective mass transfer between the pipe wall and the solution, considering the solution resistance but not that offered by any surface films, can be determined by application of the Chilton-Colburn relationship [7-12]

$$k(SC)^{2/3}/U_m = f/2 = 0.023 Re^{-0.2} \quad (1)$$

where

- k = mass-transfer coefficient, m/s,
- Sc = Schmidt number = $\mu/\rho D$, dimensionless,
- U_m = mean velocity, m/s,
- f = Fanning friction factor, dimensionless,
- Re = Reynolds number = $dU\rho/\mu$, dimensionless,
- D = diffusion coefficient, m^2/s ,

ρ = density, kg/m³,
 μ = viscosity, kg/ms, and
 d = diameter, m.

The mass-transfer boundary layer develops in a short distance in turbulent flow with the average k -value approaching the value given by Eq 1 at $L/d = 4$ at $Re = 20\ 000$ [12]. For shorter mass-transfer lengths a d/L term should be included [12].

Clearly, if it is wished to have fully developed mass-transfer conditions at the working electrode condition, Requirement 5 cannot be met. In the present system it was decided to use electrodes 5 cm in length, that is, $L/d = 1$, as a compromise between the electrochemical and mass-transfer requirements. The width (1 cm) of the electrodes is considered sufficient to overcome any edge effects [10]. Another approach to obtaining fully developed mass-transfer conditions and meeting Requirement 5 would be the use of a long freely corroding specimen immediately upstream from the working electrode.

In the laminar regime the Leveque or Graetz equations can be applied. Here the mass-transfer boundary layer develops over a much longer distance, for example, for $Sc = 2000$ and $Re = 500$, $L = 125\ 000 d$ for fully developed conditions [13].

Suitable hydrodynamic entrance and exit lengths must be also provided to the electrochemical cell to ensure fully developed hydrodynamic flow at the working electrode [14]; for laminar flow through tubes the inlet length, L_e , is given by the empirical formula $L_e/d = 0.03 Re$, and for turbulent flow the inlet length lies between 25 and 40 diameters.

The working electrodes (5 cm long by 1 cm wide) were cut from carbon steel pipe [ASTM Specification for Pipe, Steel, Black and Hot-Dipped, Zinc-Coated Welded and Seamless (A 53-79), Type F]. The mill scale was removed and the electrode set into the walls of the tubular Lucite cell (Fig. 3) with epoxy resin to give a flush fit. Final polishing with silicon carbide papers after the electrodes were positioned ensured a smooth, flush finish. This method has been found to be much cheaper and less complex than the use of the detachable decks described previously [5]. The counter electrode was nickel. The reference electrode was tapped into the cell wall alongside the working electrode as close as practical to the electrode edge.

The system has been used to measure corrosion rates of carbon steel pipe in water and various slurries [5] and to determine inhibitor efficiencies in slurries [4]. The earlier cell used in these studies [15] (where a full pipe electrode was used with a resin coating to mask all but the working area, and the counter electrode was a pipe section downstream of the working electrode) is now considered to be unsatisfactory, the subsequent results for slurries without inhibitors show lower corrosion rates [4,5].

Some of the i - t curves obtained in this work are now discussed to illustrate the utility of the technique.

Results and Discussion

The deaeration/re-aeration i - t curve in Fig. 4 is for carbon steel in Saskatoon mains water, which is a partially softened water [5] with a saturation index of +0.5, pH 9. The value of i_{corr} for the 5-cm² working electrode was 0.175 mA. Application of Faraday's laws gives a corrosion rate of 0.41 mm/year. Kerst [2], using a linear polarization technique, obtained a 1-h value of 0.24 mm/year in a synthetic cooling water with a saturation index of +1.56; the rate then fell off rapidly with time. On the other hand, the values measured by Hausler [1] in aerated Des Plaines tap water (medium hardness) rose with time to about 1 mm/year; clearly, varied behavior can be expected depending upon the water, flowrate, and probably, unfortunately, the particular electrochemical technique used to measure the corrosion rate and the details of its application.

A comparison of some weight-loss and electrochemical measurements from some other work [16] is given in Table 1. This work was done in a rectangular flow cell described elsewhere [17]. The weight losses were for 5-cm² mild steel electrodes that were also used for the electrochemical

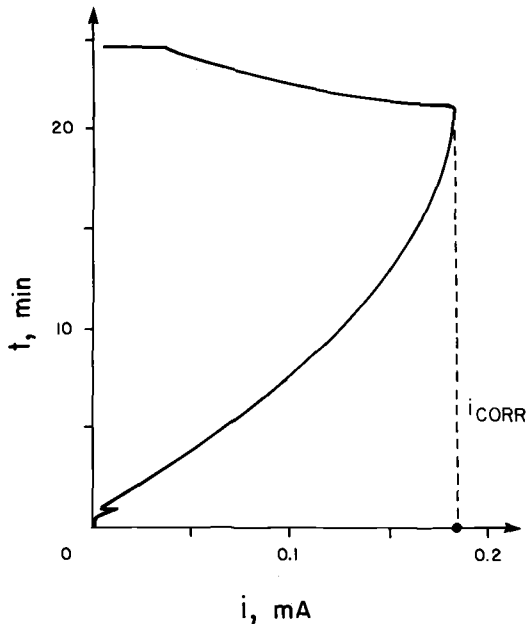


FIG. 4—Measurement of i_{corr} for carbon steel in water at 2 m/s.

TABLE 1—Comparison of actual weight losses with weight losses based on electrochemical measurements using the deaeration technique for mild steel in aerated tap water. Specimen 5 cm long by 1 cm wide.

Reynolds Number	Temp, °C	Time, h	Actual Weight Loss, mg	Weight Loss Based on Electrochemical Measurements, mg
500	30 ± 1	143.5	31.4	12.4
500	25 ± 1	148.3	11.9	12.9
28000	25 ± 1	148.3	89.5	43.3
28000	30 ± 1	147.0	84.1	37.0

measurements. The weight losses calculated from the electrochemical measurements were based on graphically integrated values of $i_{\text{corr}}t$. The ratio (weight loss actual/weight loss based on electrochemical measurement) varied from 0.92 to 2.5; the deaeration technique is clearly not a panacea for the electrochemical measurement of corrosion rates in neutral solutions. The weight loss actual/resistance polarization weight loss for aerated tap water shows values ranging from 0.62 to 1.2 when the rather unusual values of Tafel slopes, $b_a = b_c = 200$ mV, were applied (data from Hausler) [1]. Hausler did comment on the considerable doubt as to the correct values of the Tafel slopes to be used. Of course, this is not a problem with the deaeration technique which gives a direct measurement of the corrosion current. Further, Hausler found that the actual weight loss was twice that predicted by polarization-resistance measurements in aerated tap water containing 0.5 g sodium bicarbonate (NaHCO_3)/L.

Some of the results for the present system, obtained after a 1-h exposure, are compared with the maximum theoretical rates based on the diffusion of dissolved oxygen through the solution to the corroding surface (Fig. 5). The maximum theoretical corrosion rate is calculated from the limiting current for oxygen reduction

$$i_{\text{corr}} = i_{\text{lim}} = kzFc_b$$

where

$$z = 4,$$

k = mass-transfer coefficient for oxygen, m/s,

C_b = bulk concentration of dissolved O_2 , mol/m³, and

F = Faraday, C/mol.

Although the corrosion rates for iron in water are not reproducible, it is clear that they are an order of magnitude below the rates based on oxygen diffusion through the solution. These results were obtained with electrodes

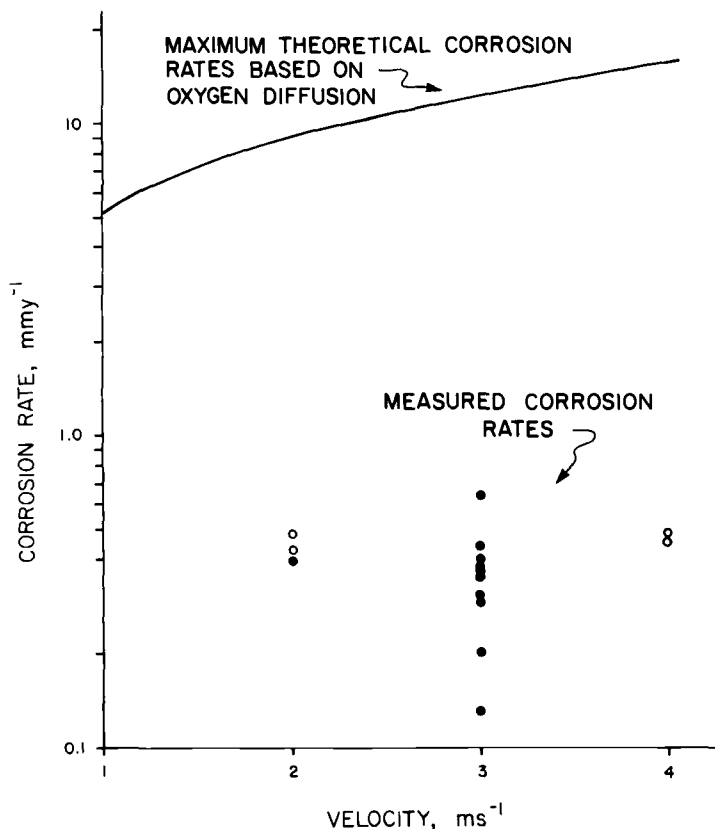


FIG. 5—Comparison of measured corrosion rates for carbon steel in water and theoretical maximum rates based on diffusion of oxygen to bare pipe wall. ●, different specimens; ○, same specimen.

having a brightly polished finish at the start of each experiment; the electrodes were presumably covered with an air-formed film when placed into solution. When the corrosion rates were measured after 1 h, the electrodes were not covered with a visible rust film. The suggestion made following previous work [15] that the presence of rust films which stifle oxygen diffusion to the iron surface is responsible for the order of magnitude difference shown in Fig. 5 may therefore be incorrect. It may well be that the cathodic reaction is under mixed charge transfer/diffusion control, and the overall corrosion reaction is under mixed cathodic/anodic control.

It appears that this is also true when substantial rust films are formed when cathodic diffusion control is not indicated by the polarization curves [1,2]. The reduction in the corrosion rate as thick rust films grow may well be due to the worsening charge-transfer situation with the thick rust film

acting as a cathode but a worse one than the air-formed ferric oxide (Fe_2O_3) film.

The i - t curve in Fig. 6 is for a 20 volume percent aqueous slurry of 30 to 50 mesh (0.55 to 0.28 mm) silica sand at 2 m/s. The corrosion rate was 2.08 mm/year with the working electrode in the 4 o'clock position. The noise on the i - t curve is the result of the macroturbulence encountered in such systems [18].

The i - t curve (Fig. 7) is for coal, 40 volume percent, -14 mesh (1.2 mm) at 2 m/s where the corrosion rate was 0.3 mm/year; with inhibitor [48 ppm potassium dichromate ($\text{K}_2\text{Cr}_2\text{O}_7$)] added this value dropped to 0.09 mm/year. With an effective inhibitor present there is much less noise on the i - t curve; the curve then has similar characteristics in this respect to those for water with no solids present. The complete results of the electro-

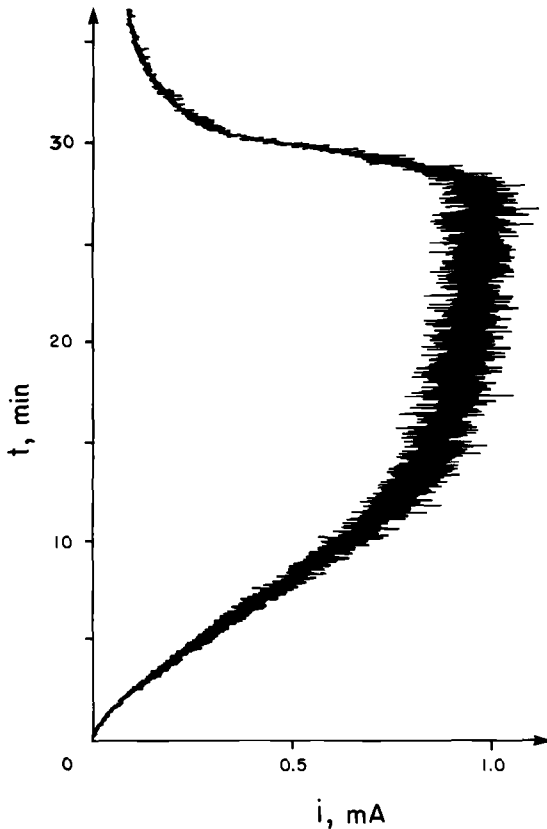


FIG. 6—Measurement of i_{corr} for carbon steel in a 20 volume percent aqueous slurry of sand at 2 m/s.

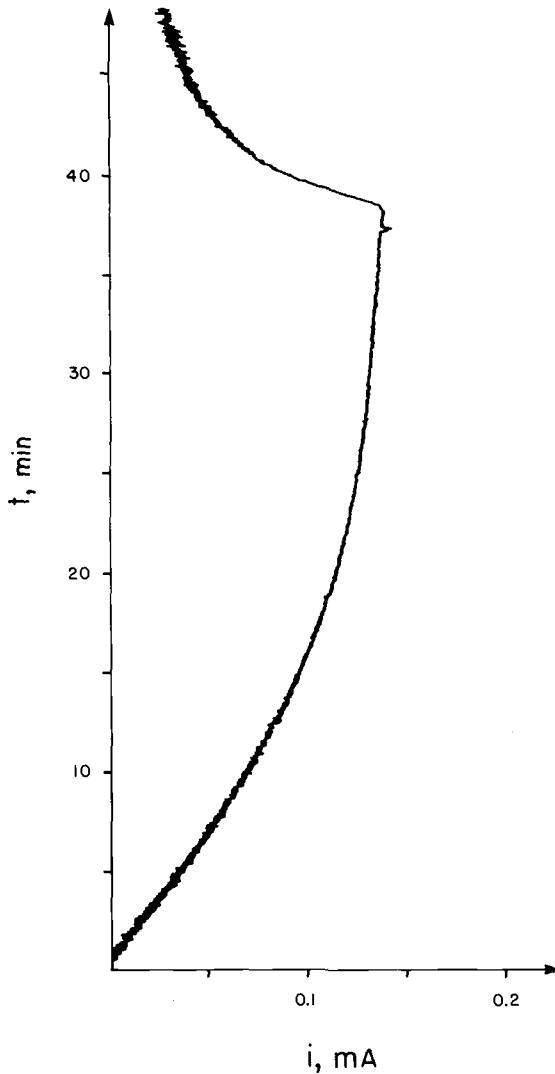


FIG. 7—Measurement of i_{corr} for carbon steel in a 40 volume percent aqueous coal slurry at 2 m/s.

chemical screening of inhibitors for sand, coal, and iron ore slurries are given elsewhere [4].

This method can only be used with inhibitor present if the inhibitor does not contribute to the cathodic current by being reduced at the test electrode. As discussed elsewhere [4] it appears that chromates do not contribute to the cathodic current during the corrosion of iron in neutral solutions.

Ohmic overpotential corrections have not yet been attempted in these studies. The iR drops have been measured in this system using a square pulse technique [19]. With a cell current of 0.1 mA the iR drop was about 15 mV. The cell current of 0.1 mA corresponds to a corrosion rate of 0.2 mm/year for the 5-cm² electrode, and is in the range of values that might be required to be measured for iron in water. With a current of 0.1 mA, corresponding to the anodic dissolution of iron at this rate, the iron would be 15 mV more negative than the true value of E_{corr} , measured at $i = 0$, resulting in an underestimate of the corrosion rate. The error would depend on the slope of the E - i curve for the anodic dissolution of iron at E_{corr} . At a cell current of 0.1 mA the change in the current with a 15 mV shift in potential was about 25 percent, which does not constitute a major error in this type of work. In systems with Tafel slopes of $b_a = 100$ mV and $b_a = 50$ mV, calculation shows that $i_{\text{true}}/i_{\text{measured}} = 1.41$ and 2.37, respectively, for a 15-mV deviation; if necessary, iR -drop compensation should be used.

One other problem with the deaeration technique is that in systems where the value of E_{corr} is changing rapidly with time the plateau on the i - t deaeration curve may not be achieved. This was the case with some coal slurry work presented elsewhere, where several hours were allowed for E_{corr} to reach a steady value [4]. In some recent work with 0.1 M potassium nitrate (KNO₃) solutions, E_{corr} did not stabilize sufficiently even after 10 h to permit a corrosion-rate measurement to be made.

This paper has been written in the hope that it will stimulate discussion of the advantages and disadvantages of this experimentally simple technique for determining corrosion rates in solutions where oxygen reduction is the cathodic reaction. The method does have some advantages over the polarization-resistance technique for laboratory and pilot-plant studies, especially in solutions where rust films are formed and polarization-resistance results are difficult to interpret.

Acknowledgments

This work was done under Research Agreement No. 153-2-78, Energy Mines and Resources, Canada. The measurements were made by D. G. Soveran.

References

- [1] Hausler, R. H., *Corrosion*, Vol. 33, No. 4, April 1977, pp. 117-128.
- [2] Kerst, H., "The Use of Electrochemical Techniques in Studies of Corrosion Inhibitors and Their Evaluation," Paper No. 121, *Corrosion/1974*, National Association of Corrosion Engineers, Houston.
- [3] Tait, W. S., *Corrosion*, Vol. 34, No. 6, June 1978, pp. 214-218.
- [4] Postlethwaite, J., *Corrosion*, Vol. 35, No. 10, October 1979, pp. 475-480.

- [5] Postlethwaite, J., Brady, B. J., Hawrylak, M. W., and Tinker, E. B., *Corrosion*, Vol. 34, No. 7, July 1978, pp. 245-250.
- [6] Mansfeld, F., *Corrosion*, Vol. 32, No. 4, April 1976, pp. 143-146.
- [7] Chilton, T. H. and Colburn, A. P., *Industrial and Engineering Chemistry*, Vol. 26, 1934, pp. 1183-1187.
- [8] Lin, C. S., Denton, E. B., Gaskell, H. S., and Pitman, G. L., *Industrial and Engineering Chemistry*, Vol. 43, 1951, pp. 2136-2143.
- [9] Newman, J. S., *Electrochemical Systems*. Prentice-Hall, Englewood Cliffs, N.J., 1973, p. 320.
- [10] Hubbard, D. W. and Lightfoot, E. N., *Industrial and Engineering Chemistry Fundamentals*. Vol. 5, 1966, pp. 370-379.
- [11] Postlethwaite, J., Fiadzigbe, E., and Aruliah, S., *Corrosion*, Vol. 34, No. 3, March 1978, pp. 85-88.
- [12] Von Shaw, P., Reiss, L. P., and Hanratty, T. J., *American Institute of Chemical Engineers Journal*, Vol. 9, 1963, pp. 362-364.
- [13] Ross, T. K. and Wragg, A. A., *Electrochimica Acta*, Vol. 10, 1965, pp. 1093-1106.
- [14] Schlichting, H., *Boundary Layer Theory*. 6th ed., McGraw-Hill, New York, 1968.
- [15] Postlethwaite, J., Tinker, E. B., and Hawrylak, M. W., *Corrosion*, Vol. 30, No. 8, August 1974, pp. 285-290.
- [16] Postlethwaite, J. and Siddiqui, H., in preparation.
- [17] Postlethwaite, J., Fiadzigbe, E., and Aruliah, S., *Corrosion*, Vol. 34, No. 3, March 1978, pp. 85-88.
- [18] Postlethwaite, J. and Holdner, D. N., *Canadian Journal of Chemical Engineering*, Vol. 54, 1976, pp. 255-258.
- [19] Postlethwaite, J. and Sharp, D. M., *Transactions of the Institute of Chemical Engineering*, Vol. 47, No. 6, September 1969, pp. T198-T203.

Electrochemical Behavior of Carbon Steel in Fused Salts

REFERENCE: Chen, C. M. and Theus, G. J., "Electrochemical Behavior of Carbon Steel in Fused Salts," *Electrochemical Corrosion Testing, ASTM STP 727*, Florian Mansfeld and Ugo Bertocci, Eds., American Society for Testing and Materials, 1981, pp. 303-326.

ABSTRACT: The polarization resistance method was used to assess the corrosion rate and to study the oxidation kinetics of carbon steel in a fused nitrate-sulfate-chloride salt mixture at 316°C (600°F) and in an alkali iron trisulfate salt at 677°C (1250°F). The same method was also applied to estimate the corrosion rate of carbon steel through the solidified frozen alkali iron trisulfate salt.

Equilibrium potential/ pO^{2-} diagrams were constructed for iron, nitrate, and nitrate-reaction products to aid in the interpretation of corrosion data for the nitrate-rich salt and to determine the various chemical reactions causing the corrosion.

KEY WORDS: polarization resistance, Tafel slope, admittance, fused salt, solidified frozen salt layer, potential/ pO^{2-} diagram

The polarization resistance method is widely used to assess the corrosion rate at the corrosion potential in aqueous solutions. We used this method to study the kinetics of iron oxidation in a fused nitrate-sulfate-chloride salt mixture and in an alkali iron trisulfate salt. The method was further applied to assess the corrosion rates of iron covered by a frozen alkali iron trisulfate layer immersed in the molten salt.

To complement experimental data, equilibrium potential/pH diagrams in aqueous solutions are often used to verify or predict corrosion reactions. We constructed potential/ pO^{2-} diagrams for the nitrate-rich salt system to predict the corrosion behavior of iron as affected by potential and pO^{2-} . The thermodynamic data used for these diagrams are from Kelley [1],² Kubaschewski et al [2], and JANAF [3]. Two particular salts were chosen for testing. The first, with a chemical composition of 84.5 percent sodium nitrate ($NaNO_3$) + 9.5 percent sodium sulfate (Na_2SO_4) + 6.0 percent sodium chloride ($NaCl$), is a promising candidate for thermal storage systems [4].

¹Senior research engineer and group supervisor, respectively, Babcock & Wilcox, Alliance, Ohio 44601.

²The italic numbers in brackets refer to the list of references appended to this paper.

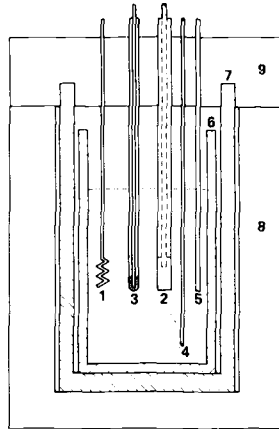
The second, with a chemical composition of 46.6 percent potassium sulfate (K_2SO_4) + 53.4 percent iron sulfate [$Fe_2(SO_4)_3$] (usually called alkali iron trisulfate), is a typical aggressive corrodant that causes hot corrosion of fossil boiler superheaters and reheaters [5,6].

Experimental Equipment

Isothermal polarization experiments were conducted in both salts, and nonisothermal experiments were conducted in the molten alkali iron trisulfate salt.

Isothermal Tests

Figure 1 shows the isothermal polarization apparatus used for the nitrate-rich salt. The alumina crucible is lined with a graphite crucible that contains the fused salt. The assembly is placed in an electric furnace where the salt was heated to $316 \pm 3^\circ C$ ($600 \pm 5^\circ F$) and nitrogen gas was bubbled through the fused salt. A cylindrical specimen was used as the working electrode (test



1. PLATINUM ELECTRODE (COUNTER ELECTRODE)
2. SPECIMEN
3. Ag/Ag^+ ELECTRODE (REFERENCE ELECTRODE)
4. NITROGEN BUBBLER
5. THERMOCOUPLE
6. GRAPHITE CRUCIBLE
7. ALUMINA CRUCIBLE
8. FURNACE
9. FURNACE LID

FIG. 1—Test cell for isothermal system.

specimen), a platinum wire as the counter electrode, and a silver/silver chloride electrode as the reference electrode.

Nonisothermal Tests

Figure 2 shows the nonisothermal test cell (isothermal tests for the alkali iron trisulfate were also conducted in this apparatus). The specimen temperature was controlled by passing cold air (ambient temperature) through a hollow test specimen. Figure 3 shows the details of the test specimen arrangement wherein a double tube allows pressurized air to flow down the center tube and out through the annular space between the two tubes. An alumina sleeve covers most of the outer tube, and the area left uncovered is considered the actual test specimen. The temperature of the inner wall of the specimen was monitored by a skin thermocouple embedded in the wall. Tests were conducted with the inner-wall temperature at 260, 316, 371, 482, 538, 593, and 677°C (500, 600, 700, 900, 1000, 1100, and 1250°F). No correction was made for minor temperature increases across the wall of the tube due to heat transfer. The temperature of the molten salt was kept at $677 \pm 6^\circ\text{C}$ ($1250 \pm 10^\circ\text{F}$); thus a frozen salt layer existed between the specimen and the molten salt. A silver/silver sulfate electrode was used as the reference electrode, and a platinum wire was used as the counter electrode. A high-purity alumina crucible was used to contain the molten salt. The purpose of this system is to measure the corrosion rate of metals through a solidified salt layer on the surface of the metals. Examples of such corrosion problems are the coal-ash corrosion of superheater and reheater tubes in fossil boilers, and corrosion problems in the lower part of the Kraft recovery furnaces.

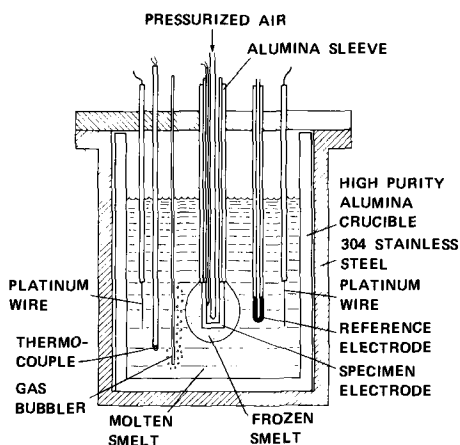


FIG. 2.—Test cell for nonisothermal system.

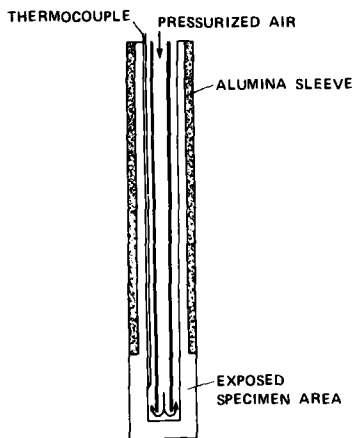


FIG. 3—Test specimen for nonisothermal system.

In order to determine the accuracy and thus the validity of results obtained using electrochemical techniques, conventional weight-loss measurements of iron at different immersion periods were also made in the nitrate-rich salt. In this case the oxide corrosion products were removed by inhibited hydrochloric acid solution (5 percent HCl + 0.2 percent Rodine 213³) at 190°F (88°C) for about 20 min. The weight-loss values are corrected for chemical cleaning losses.

Test Material

The chemical composition of the carbon steel used for these tests is shown in Table 1.

Results

Molten Nitrate-Sulfate-Chloride Salt

Polarization Curves—Figure 4 shows the polarization curves in the fused salt at 316°C (600°F) for carbon steel at immersion times of 4, 124, 244, and 360 h. As can be seen from the curves, the cathodic current for carbon steel increases smoothly in the Tafel zone (linear portion of the curves). Longer immersion times cause the cathodic curve to shift slightly in the active direction. The anodic current initially rises rapidly from the corrosion potential to about +0.1 V, and then the rate of current increase slows down. The rate of current increase again rises rapidly at +0.4 V and levels off at +0.6 V. The

³Trademark of Amchem Products, Inc., Ambler, Pa. 19002.

TABLE 1—Chemical composition of carbon steel, wt. percent.

C	Mn	P	S	Si
0.25	0.73	0.010	0.028	0.18

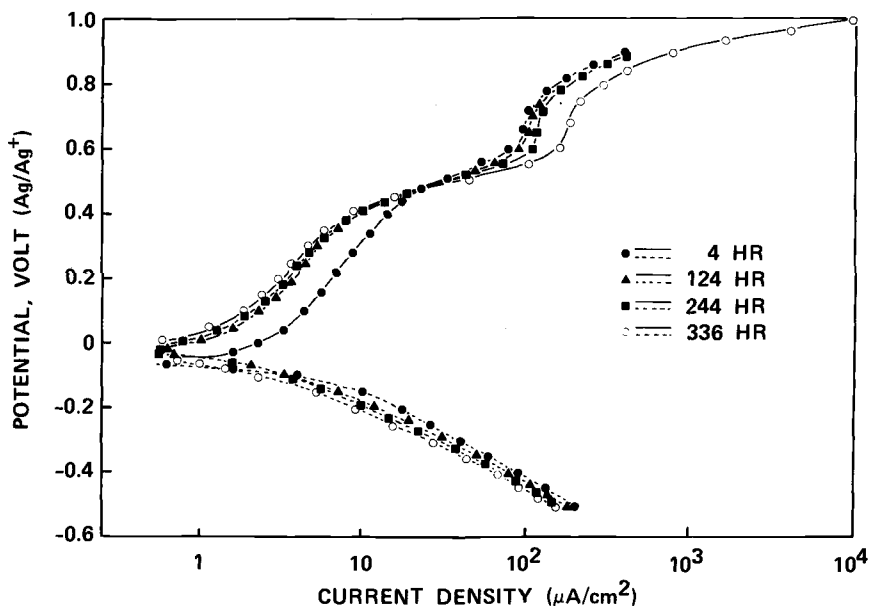


FIG. 4—Polarization curves of carbon steel affected by immersion durations in 84.5 percent NaNO_3 + 9.5 percent Na_2SO_4 + 6 percent NaCl fused salt at 316°C (600°F).

curve finally breaks away at a potential around $+0.8$ V to very high currents. Longer immersion times cause the initial portion of the anodic curve to shift in the more noble direction and the final portion of the curve to shift in the more active direction. At longer immersion times, the limiting diffusion current increased. This is between potential values of about 0.6 and 0.75 V.

Linear Polarization Curve—The Tafel constants can be obtained by using the curves from Fig. 4; that is, b_a is the anodic Tafel slope, and b_c is the cathodic Tafel slope. The Stern-Geary constant can be derived from these values:

$$\beta = \frac{b_a \times b_c}{2.3(b_a + b_c)} \quad (1)$$

The corrosion rate can be determined from the Stern-Geary equation:

$$I_{\text{corr}} = \beta \cdot \frac{\Delta I}{\Delta E} \quad (2)$$

Thus I_{corr} can be calculated by measuring the linear polarization resistance ($\Delta E/\Delta I$) or the admittance ($\Delta I/\Delta E$). Figure 5 shows the linear polarization portion of the curves of Fig. 4 at various immersion times. These data show a nearly linear relationship between current and potential in the range of ± 20 mV around the corrosion potential. The Tafel slopes are somewhat different, however, for the anodic and cathodic portions of the curve. The slope of the curve (polarization admittance) drops drastically during the initial stages of immersion, which indicates a decrease of I_{corr} , and then tends to decrease only slightly as the exposure time increases.

Electrochemical Corrosion Rate—From Eq 2 the corrosion rate at the corrosion potential can be estimated from the Tafel slope (Fig. 4) and linear polarization admittance (Fig. 5).

The corrosion rates of iron in the fused nitrate-sulfate-chloride salt, in current density ($\mu\text{A}/\text{cm}^2$) and mils per year (mpy), are shown in Table 2 at different exposure times in the fused salt at 316°C (600°F).

Conventional Corrosion Rate—Conventional weight-loss measurements were made for carbon steel after immersion periods of 500, 1000, and 2000 h. The results are shown in Table 3.

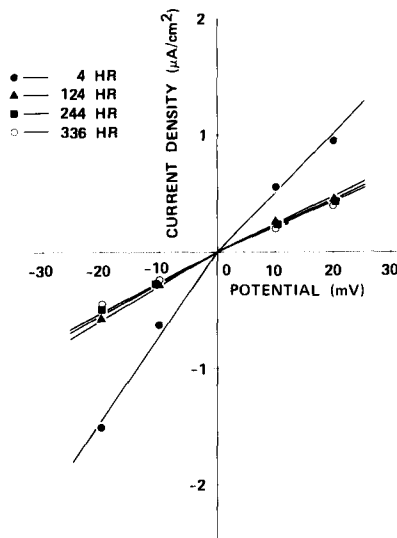


FIG. 5—Linear polarization curves of carbon steel affected by immersion durations at the potential range of ± 20 mV around the corrosion potential in 84.5 percent NaNO_3 + 9.5 percent Na_2SO_4 + 6 percent NaCl fused salt at 316°C (600°F).

TABLE 2—Tafel slopes, admittances, and corrosion rates affected by immersion duration in the fused salt at 316°C (600°F).^a

Duration, h	4	76	100	124	244	336
b_a , mV/decade	640	480	515	560	640	610
b_c , mV/decade	280	260	240	240	230	220
$\beta = \frac{b_a \times b_c}{2.3(b_a + b_c)}$, mV	84.69	73.33	71.18	73.04	73.56	70.30
$\left(\frac{\Delta I}{\Delta \phi}\right)$, $\mu\text{A}/\text{cm}^2 \text{mV}^b$	0.068	0.026	0.025	0.027	0.03	0.025
I_{corr} , $\mu\text{A}/\text{cm}^2$	5.72	1.87	1.78	1.97	2.21	1.73
Corrosion rate, mpy	2.6	0.9	0.8	0.9	1.0	0.8

^a Subscripts *a* and *c* indicate the anodic and cathodic data, respectively.

^b Average of the anodic and cathodic values.

TABLE 3—Conventional corrosion weight loss ($\mu\text{g}/\text{cm}^2$) and the overall corrosion rate (mpy) in fused nitrate-sulfate-chloride salt for carbon steel at immersion times of 500, 1000, and 2000 h at 316°C (600°F).

Immersion time, h	500	1000	2000
Weight loss, $\mu\text{g}/\text{cm}^2$	482	692	934
Corrosion rate, mpy	0.42	0.30	0.21

Molten Alkali Iron Trisulfate

Electrochemical Corrosion Rate—The polarization resistance method was also applied to determine the corrosion rates for the nonisothermal system. The Tafel slopes, polarization admittance, and corrosion rates are shown in Table 4. Included in this table are the data for iron at 677°C (1250°F), that is, the isothermal data.

Equilibrium Diagram

This section presents the development of the potential/ pO^{2-} diagrams for the nitrate-sulfate-chloride salt. However, the salt was assumed to be a 100 percent nitrate salt in order that the diagrams could be calculated. Because of this simple assumption, the actual experimental values are expected to deviate somewhat from the theoretical values.

Development of Equilibrium Diagrams

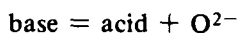
Kust and Duke [7] suggest that the nitrate ion in the fused salt dissociates to nitryl ion and oxide ion as



where the dissociation constant is

$$K = (5.7 \pm 0.1) \times 10^{-24} \text{ at } 300^\circ\text{C}$$

This is analogous to the self-dissociation of water into protons and hydroxyl ions. Lux [8] and Flood and Forland [9] assign a general form of acid-base equilibrium to all oxyanionic melts as



Therefore the concentration of O^{2-} will determine the acidity of the fused nitrates.

A thermodynamic treatment of corrosion in fused salts seems to be appropriate because of very low polarization resistances of high-temperature reactions in these media. For the electrochemical behavior of metals (such as iron) in oxyanionic melts, it is useful to construct a potential/ pO^{2-} diagram [10-12]. Although the equilibrium potential/ pO^{2-} diagram cannot accurately predict the actual corrosion behavior because of all the complications of kinetics, it does visualize the stability regions of metals, oxides, ions, and other compounds which may participate in corrosion and passivation processes.

The method and data used to construct the potential/ pO^{2-} diagrams are presented in the Appendix.

Figure 6 shows the equilibrium diagram for nitrate ions, Fig. 7 for nitrite ions, and Fig. 8 for nitril ions. The stability diagram for iron and its ions is shown in Fig. 9. In order to compare these potential/ pO^{2-} diagrams, the activity of reactants and products is assumed to be unity except for the activities of the oxide ion (O^{2-}), ferrous ion, and ferric ion.

TABLE 4—Tafel slopes, admittance, and corrosion rates through a frozen salt layer affected by

Temperature, °C (°F)	260 (500)		316 (600)		371 (700)	
Duration, h	2	50	24	48	24	50
b_a , mV/decade	470	460	475	470	500	505
b_c , mV/decade	520	520	525	505	495	470
$\frac{b_a \times b_c}{2.3(b_a + b_c)}$, mV	107	106	108	106	108	106
$(\Delta I/\Delta E)$, $\mu\text{A}/\text{cm}^2$ mV	4.8×10^{-3}	6.3×10^{-3}	1.4×10^{-2}	1.6×10^{-2}	3.0×10^{-2}	3.2×10^{-2}
I_{corr} , $\mu\text{A}/\text{cm}^2$	0.52	0.66	1.46	1.59	3.19	3.39
Corrosion rate, mpy	0.2	0.3	0.7	0.7	1.4	1.5

The stability diagram for the reaction products of nitrate ion is rather difficult because so many reactions are involved (see Figs. 6, 7, and 8). A computer program, similar to that developed in Ref 13, is being modified to determine the stability areas. Preliminary results indicate that the stability diagram is rather simple (Fig. 10).

Discussion

This section compares the dynamic polarization data in the nitrate-rich salt with the equilibrium diagrams for the fused nitrate to understand the polarization behavior and the various reactions occurring on the carbon steel electrode. Next, the corrosion rates obtained from the electrochemical data and conventional weight-loss data in the fused nitrate-rich salt are compared. Finally, the nonisothermal weight-loss data in the alkali iron trisulfate salt is discussed.

Comparison of Equilibrium Diagram with Dynamic Electrochemical Data

The electrochemical kinetic behavior of carbon steel in fused nitrate is shown in Fig. 4, and stability diagrams for iron and its ions and the nitrate ion and its reaction products are shown in Figs. 9 and 10. The neutral condition of fused nitrate at 300°C (572°F) is at $pO^{2-} = 11.5$ (from the dissociation constant $K = 5.7 \times 10^{-24}$). Here the stability diagrams predict at the corrosion potential (that is, without external polarization) the formation of iron oxides; this will consist mostly of Fe_3O_4 [14, 15] because the stability area for FeO is very narrow. From Figs. 6, 7, and 8 there are many possible reactions that could balance the oxidation reactions of iron. These can be the reduction of nitrate, nitrite, or nitryl ions. From the computerized stability diagram (Fig. 10) for the reaction products of nitrate ion, the major cathodic reaction at the corrosion potential may be the formation of nitrite ion

immersion duration in molten alkali iron trisulfate at 677°C (1250°F).

482 (900)		538 (1000)		593 (1100)		677 (1250)		
2	18	5	23	3	18	3	26	50
505	500	400	440	490	540	360	330	360
530	610	460	550	540	560	380	400	380
112	119	93	106	112	119	80.4	78.6	80.4
1.8×10^{-2}	2.1×10^{-2}	7.15	7.58	8.65	12.2	114	95	86
2.0	2.48	665	805	967	1449	9166	7467	6915
0.9	1.1	303	367	440	660	4180	3405	3153

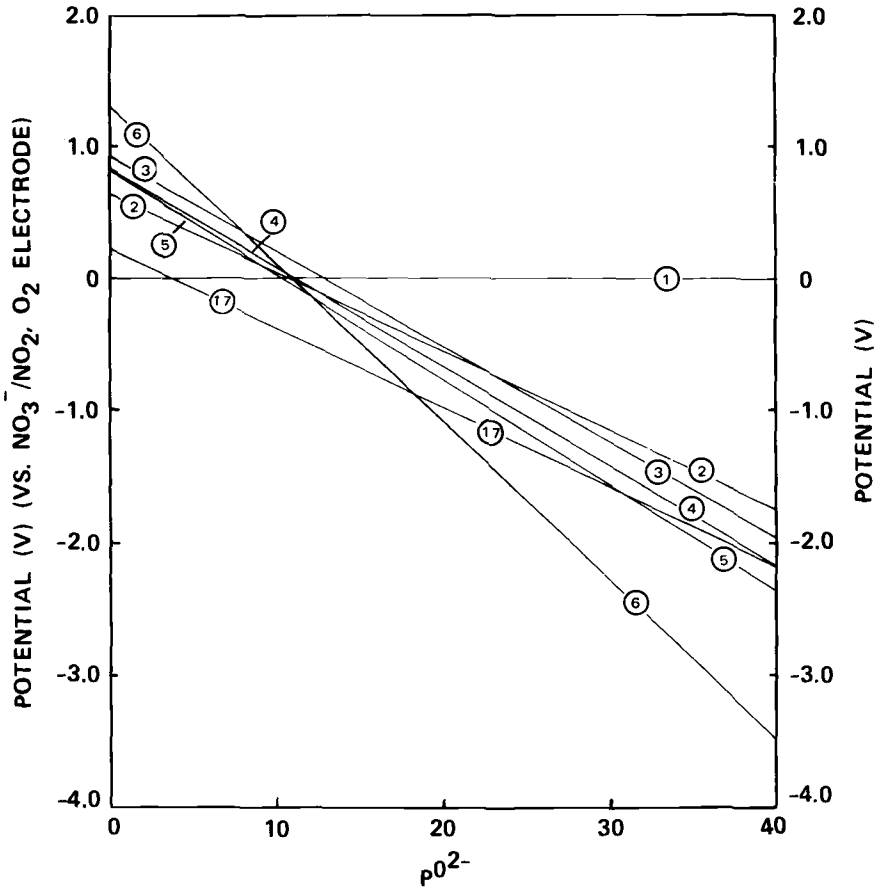
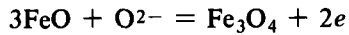
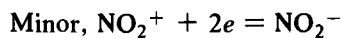
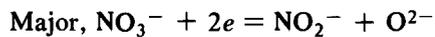


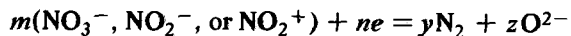
FIG. 6—Potential— pO^{2-} diagram for reactions involving nitrate ions at 600 K.

(NO_2^-). A minor cathodic reaction may be the formation of nitrogen gas (N_2). Therefore the corrosion reactions of carbon steel at the corrosion potential can be expressed as



Cathodic reactions:





Thus, it can be qualitatively stated that iron is oxidized to monoxide and subsequently to magnetite. Alternatively, nitrite ions are generated from nitrate ions and are stoichiometrically almost equivalent to the amount of magnetite.

When the potential is increased anodically from the corrosion potential, the oxidation current increases only slightly and the incipient oxides formed at the corrosion potential will be oxidized to Fe_2O_3 . When the anodic potential reaches 0.4 V [silver/silver chloride (Ag/AgCl) electrode], the anodic current increases rapidly. The longer the immersion time, the higher the limiting diffusion current in the potential region between 0.6 and 0.75 V.

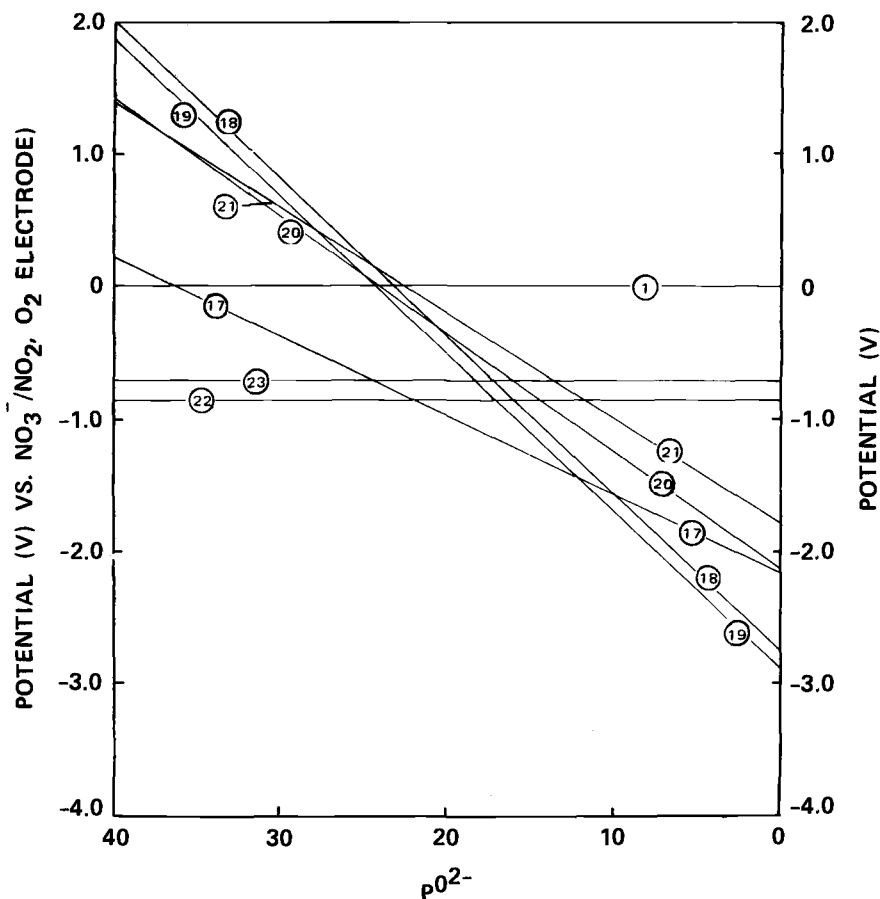


FIG. 7—Potential— $p\text{O}^{2-}$ diagram for reactions involving nitrite ions at 600 K.

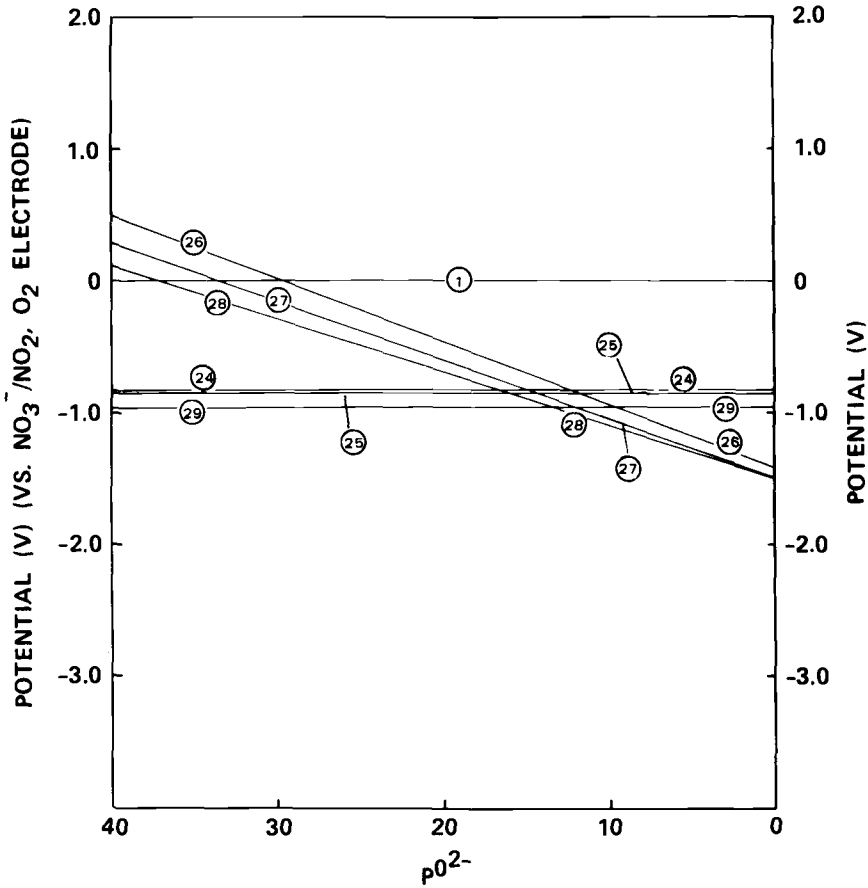


FIG. 8—Potential— pO_2^- diagram for reactions involving nitryl ions at 600 K.

The stability diagram for the reaction products of (Fig. 10) shows that this increase must be attributed to the oxidization of nitrite ions (formed by the reduction of nitrate ions at the corrosion potential) to NO_2 gas. This conclusion, derived from the equilibrium diagram, coincides with the experimental observations of Notoya and Midorikawa [16] and Lyalikov and Novik [17]. The limiting diffusion current, which is proportional to the amount of nitrite ion, is obviously a function of immersion time. When the anodic potential is raised above +0.8 V (Ag/AgCl electrode), the current increases precipitously. This could be due to oxygen evolution from the nitrate ions (line 1 in Fig. 9). Examination of the specimen after testing, however, showed it to be heavily corroded; thus, the carbon steel must also dissolve in the transpassive region (that is, the film must be ionized in this potential region).

By comparing the polarization curves (Fig. 4) and the stability diagrams (Figs. 9 and 10), it appears that the kinetic phenomena correspond qualitatively well with equilibrium thermodynamics.

As stated earlier, carbon steel is located in the passive region for the neutral nitrate salt, far away from the corrosion zone. Therefore the corrosion rate is expected to be very low. The pO^{2-} of the nitrate-sulfate-chloride salt does not deviate appreciably from the neutral condition of nitrate salt, and the corrosion rate would be expected to be low. The corrosion-rate measurements do show this to be a fact, and therefore the carbon steel can be safely used in the nitrate-rich salt for a thermal storage system.

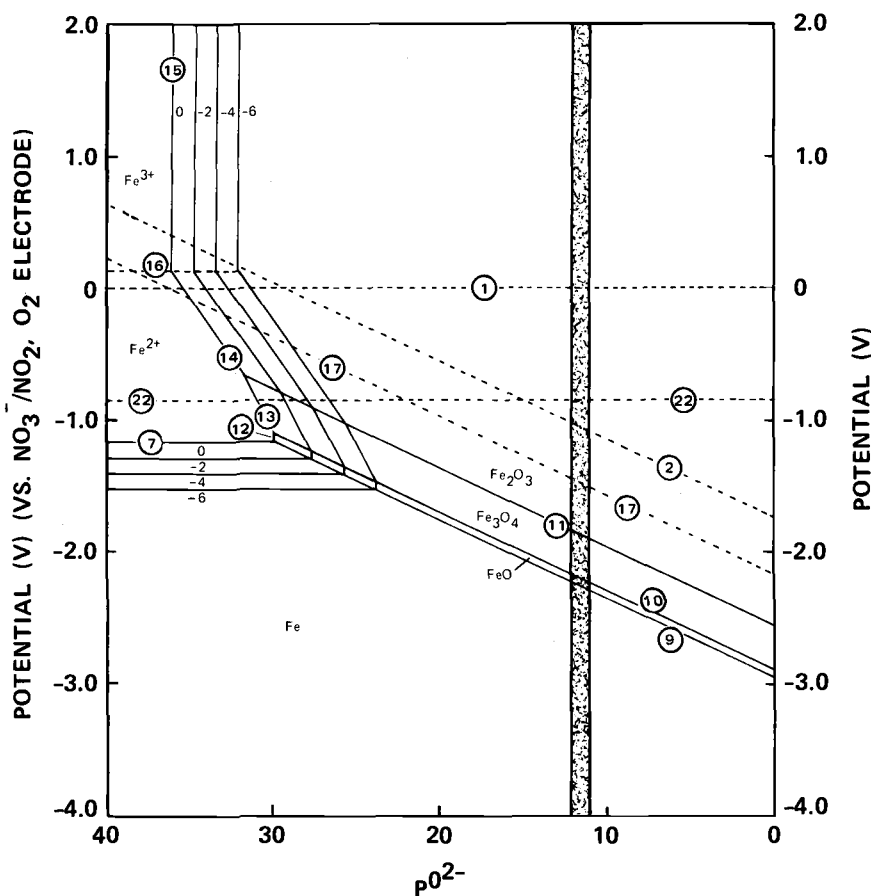


FIG. 9—Stability diagram for iron in fused nitrate at 600 K.

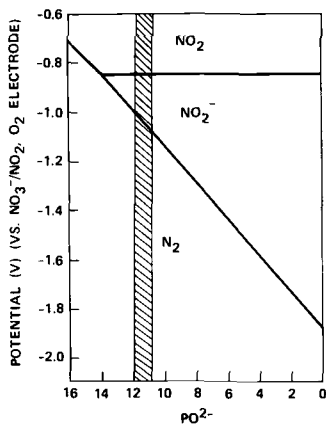


FIG. 10—Stability diagram for nitrate and its reaction products at 600 K (preliminary results).

Isothermal Corrosion Kinetics in Nitrate-Sulfate-Chloride Salt

Figure 11 shows the corrosion current at the corrosion potential as a function of immersion duration (data from Table 2). The corrosion current drops dramatically after the first few hours, and then decreases more gradually with increasing immersion time. The decrease of current can be attributed to the formation of oxide film on the surface and its thickening (or growth) with increasing exposure. After converting the corrosion currents to mass weights, the curve for weight loss versus time can be obtained. The curve roughly follows a parabolic-rate law as is shown in Fig. 12, where the logarithm of the square of weight loss is plotted as a function of the logarithm of time. The resulting curve is almost a straight line, and the slope is approximately 45 deg. Therefore the weight loss (W) due to oxidation at the corrosion potential can be expressed as

$$W^2 = k \cdot t \quad (3)$$

where

$$K = 2 \times 10^{-1} \mu\text{g}^2/\text{cm}^4 \cdot \text{s},$$

t = time, s, and

$$W = \text{weight loss, } \mu\text{g}/\text{cm}^2.$$

Iron is known to oxidize according to a parabolic-rate law in air at 250 to 500°C [18]. Thus, the oxidation mechanism of carbon steel in the fused nitrate-sulfate-chloride salt at 316°C (600°F) seems similar to that of iron in air at approximately these same temperatures. The rate constant of carbon steel by the electrochemical method in the fused nitrate-sulfate-chloride salt is about one order of magnitude higher than those of iron measured in air by

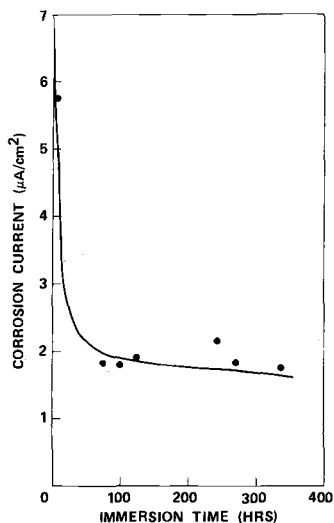


FIG. 11—Corrosion current versus immersion time for carbon steel at 316°C (600°F).

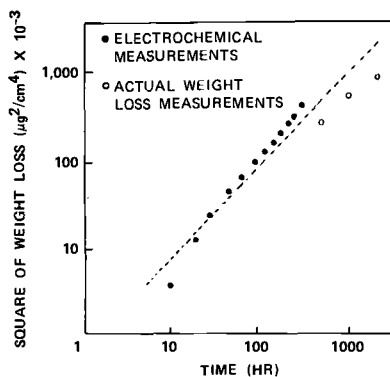


FIG. 12—Logarithmic square of weight loss versus logarithmic time to examine the parabolic-rate law of the oxidation of carbon steel in fused sodium nitrate at 316°C (600°F).

Gulbransen [19] and in fused nitrate by Notoya et al [14]. The high rate constant may be due to the low melting point of nitrate-sulfate-chloride salt, and also to the effect of chloride or sulfate ions.

To ascertain the reliability of the electrochemical technique, conventional weight-loss measurements for the carbon steel were made in the same salt. These data are plotted in Fig. 12 for both electrochemical and conventional weight-loss values. The solid circles are for the electrochemical measurements, and the open circles are for conventionally determined weight losses.

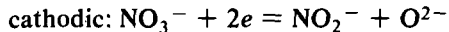
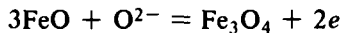
Although there is some discrepancy between the results, they are well within a tolerable range of agreement.

Nonisothermal Corrosion Kinetics in Alkali Iron Trisulfate

Figure 13 presents corrosion-rate data as a function of temperature for carbon steel in the alkali iron trisulfate salt; these data are taken from Table 4. Below 482°C (900°F) the corrosion rate is very low (less than 1.5 mpy). Above 539°C (1000°F), however, the corrosion rate increased more than two orders of magnitude to approximately 350 mpy. A further increase in temperature above the melting point [638 to 677°C (1180 to 1250°F)] increased that corrosion rate to more than 3000 mpy. Examination of Fig. 13 shows that a critical breakaway temperature occurs between 482 and 539°C (900 and 1000°F) where the corrosion rate becomes excessive. Therefore, to prevent hot corrosion in alkali iron trisulfate, the wall temperature of the carbon steel superheater or reheater tubes should not exceed the critical temperature. Incidentally, the maximum temperature for carbon steels as superheater and reheater tubes is conventionally limited to 510°C (950°F) [20]. For modern superheaters and reheaters, where temperatures exceed 510°C (950°F), the material must be improved to accommodate the more corrosive conditions. In general, ferritic Fe⁻ (1 to 9 percent) chromium alloy steels and austenitic stainless steels are used for this purpose.

Conclusions

1. Corrosion of iron in fused nitrate is due to the following electrochemical reactions:



2. The polarization resistance method is valid for estimating corrosion rates both isothermally and nonisothermally in fused salts (that is, the nitrate-sulfate-chloride and alkali iron trisulfate salts).

3. Stability diagrams were constructed to help interpret the polarization behavior of iron in fused nitrate. The kinetic phenomena could be predicted fairly accurately with the aid of the equilibrium thermodynamic data.

4. Corrosion kinetics of carbon steel followed the parabolic-rate law in the fused nitrate-sulfate-chloride salt. The rather high corrosion rate, when compared with results obtained in air and pure nitrates, may be due to the effect of chloride or sulfate ions or both.

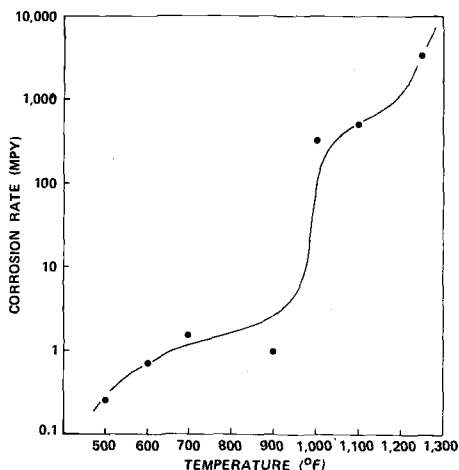


FIG. 13—Corrosion rate (mpy) versus specimen temperature for carbon steel in the molten alkali iron trisulfate at 677°C (1250°F).

5. The corrosion rate of carbon steel in the fused nitrate-sulfate-chloride salt is 1 to 2 mpy; therefore carbon steel can be satisfactorily used in this salt.

6. The nonisothermal tests in the alkali iron trisulfate salt determined that the wall temperature of the carbon steel must not exceed a critical temperature [between 482 and 539°C (900 and 1000°F)]. This coincides with the maximum temperature conventionally recommended for carbon steel superheater and reheater tubes.

Acknowledgments

The authors would like to express their appreciation to J. P. Sorenson for his skillful experiments and to J. V. Monter for his helpful suggestions in the course of this work. The authors are also grateful to T. A. McNary and Dr. J. R. Cels for their useful discussions.

APPENDIX

Potential/ pO^{2-} Diagrams in Fused Nitrates

In order to construct the potential/ pO^{2-} diagram in fused nitrates, the following methods are employed:

1. Using Pourbaix's treatment [21], the general overall electrochemical reaction is defined as a reaction in which both chemicals, M , (neutral molecules or ions or both), and electrons, e , participate as

$$\Sigma vM + ne = 0 \quad (4)$$

where v is the stoichiometric coefficient of M , and n is the number of electrons involved in the reaction.

2. At the equilibrium condition at $T^\circ K$, the electrode potential, E_T , is established as

$$\Sigma v\mu - nFE_T = 0 \quad (5)$$

Here μ represents the chemical potential of M .

$$E_T = E_T^\circ + \frac{2.303 RT}{nF} \Sigma v \log a_M \quad (6)$$

where E_T° is the standard electrode potential, and a_M indicates the activity of M .

3. The standard electrode potential is calculated from

$$\Sigma v\mu^\circ - nFE_T^\circ = 0 \quad \text{or} \quad E_T^\circ = \frac{\Sigma v\mu^\circ}{nF} \quad (7)$$

where μ° is the standard chemical potential of M .

Thermodynamic data that are required to evaluate the free energies at unit activity at 600 K for the following possible equilibria are obtained from standard sources [1-3, 22]. The standard free energies in each equilibrium are referred to the standard nitrate electrode, and the melt is assumed to be completely ionic [11].

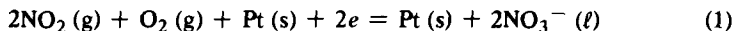
NOTE—The number assigned to the following reactions from 1 to 29 corresponds to its code number in Figs. 6, 7, 8, and 9.

The following paragraphs include (1) ionic reactions that thermodynamically describe the molten sodium nitrate salt and iron in the molten salt, (2) free energy for these reactions, (3) equilibrium equations used to describe Figs. 6 to 10, and (4) combinations of chemical reactions used to determine the free energy of the ionic reactions.

Table 5 contains all the data needed to calculate the various free energies and electrode potentials.

Nitrate Electrode

The nitrate electrode at 1 atm total pressure behaves as a reversible electrode and a very reproducible electrode [23]. The nitrate electrode at unit NO_2 and O_2 fugacity and unit nitrate-ion activity can be described by the following overall equilibrium:



Therefore, under the unit conditions described previously, the reference value is designated as

$$\Sigma v\mu^\circ = 0$$

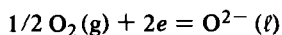
$$E = 0 - 0.119 \log a_{\text{NO}_3^-} + 0.0595 \log P_{\text{O}_2} + 0.119 \log P_{\text{NO}_2}$$

TABLE 5—Standard chemical potentials used for calculations for the potential/ pO^{2-} diagrams at 600 K.

Substance	μ° , kcal
NaNO ₃	-63.50
Na ₂ O	-80.41
Fe(NO ₃) ₂	-20.26
Fe(NO ₃) ₃	-0.32
FeO	-55.38
Fe ₃ O ₄	-218.93
Fe ₂ O ₃	-158.41
NaNO ₂	-43.88
Fe	0.0
O ₂	0.0
N ₂	0.0
NO ₂	+16.78
N ₂ O	+30.31
NO	+19.80
NO ₃ ⁻	+16.78
NO ₂ ⁻	+36.40
O ²⁻	+80.15
Fe ²⁺	-53.82
Fe ³⁺	-50.66
NO ₂ ⁺	-2.44

Oxygen/Oxide Ion Electrode

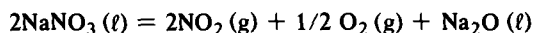
This reaction corresponds to the reversible oxygen/oxide ion electrode in the melt.



$$\Sigma \nu \mu^\circ = -80.15 \text{ kcal} \quad (2)$$

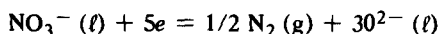
$$E_T = -1.74 + 0.0298 \log P_{O_2} + 0.0595 pO^{2-}$$

The standard chemical potentials of Eq 2 are obtained from



and Eq 1, again assuming that both sodium nitrate and sodium oxide are ionic compounds. Here the free energy of formation for NaNO₃(ℓ) is estimated as $\Delta G_f^\circ = -63.50$ kcal at 600 K [1,23].

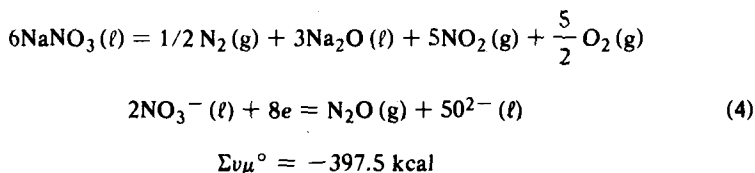
Reactions Involving Nitrate Ions



$$\Sigma \nu \mu^\circ = -223.67 \text{ kcal} \quad (3)$$

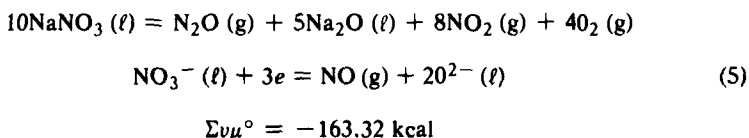
$$E_T = -1.940 + 0.0238 \log a_{NO_3^-} - 0.0119 \log P_{N_2} + 0.0714 pO^{2-}$$

This equation is calculated from Eq 1 and



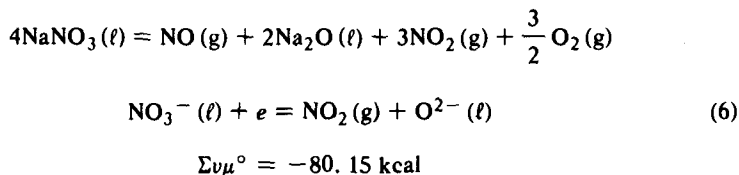
$$E_T = -2.155 + 0.0298 \log a_{\text{NO}_3^-} - 0.0149 \log P_{\text{N}_2\text{O}} + 0.0744 \text{pO}^{2-}$$

This equation is calculated from Eq 1 and



$$E_T = -2.361 + 0.0397 \log a_{\text{NO}_3^-} - 0.0397 \log P_{\text{NO}} + 0.0793 \text{pO}^{2-}$$

This equation is calculated from Eq 1 and



$$E_T = -3.476 + 0.119 \log a_{\text{NO}_3^-} - 0.119 \log P_{\text{NO}_2} + 0.119 \text{pO}^{2-}$$

This equation is calculated from Eqs 1 and 2.

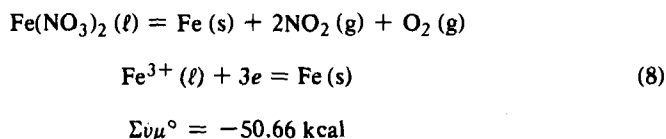
Reactions Involving Iron

The possible phases in the diagram for iron are Fe, Fe²⁺, Fe³⁺, FeO, Fe₃O₄, and Fe₂O₃. For the iron/ferrous ion electrode:



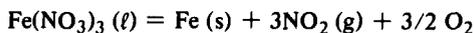
$$E_T = -1.167 + 0.0595 \log a_{\text{Fe}^{2+}}$$

This equation is calculated from Eq 1 and

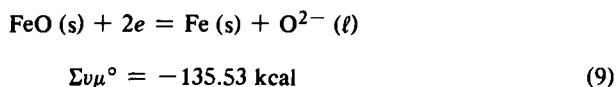


$$E_T = -0.733 + 0.0400 \log a_{\text{Fe}^{3+}}$$

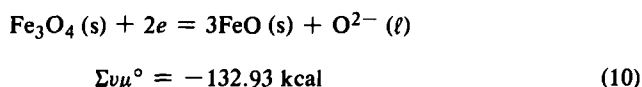
This equation is calculated from Eq 1 and



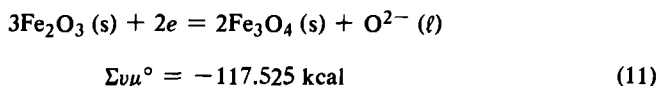
For iron/iron oxide reactions, Eq 2 offers the calculations of the chemical potential for O^{2-} ion as $\mu^\circ_{\text{O}^{2-}} = +80.15$ kcal. The following equilibria can be calculated:



$$E_T = -2.939 + 0.0595 \text{ pO}^{2-}$$

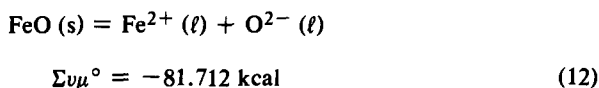


$$E_T = -2.882 + 0.0595 \text{ pO}^{2-}$$

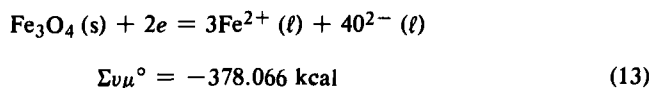


$$E_T = -2.548 + 0.0595 \text{ pO}^{2-}$$

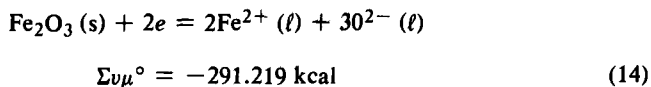
For reactions that involve ferrous or ferric ions, Eqs 7 and 8 can be used to calculate the chemical potentials for Fe^{2+} and Fe^{3+} as $\mu^\circ_{\text{Fe}^{2+}} = -53.82$ kcal, and $\mu^\circ_{\text{Fe}^{3+}} = -50.66$ kcal. The following equilibria can be calculated:



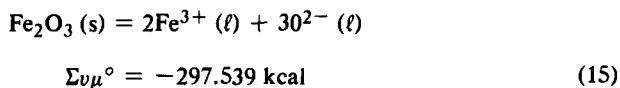
$$\log a_{\text{Fe}^{2+}} = -29.768 + \text{pO}^{2-}$$



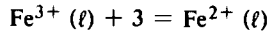
$$E_T = -8.197 - 0.1785 \log a_{\text{Fe}^{2+}} + 0.238 \text{ pO}^{2-}$$



$$E_T = -6.314 - 0.119 \log a_{\text{Fe}^{2+}} + 0.1785 \text{ pO}^{2-}$$



$$\log a_{\text{Fe}^{3+}} = -54.197 + \frac{3}{2} p\text{O}^{2-}$$



$$\Sigma \nu \mu^\circ = 3.16 \text{ kcal} \quad (16)$$

$$E_T = 0.137 + 0.119 \log a_{\text{Fe}^{3+}} - 0.119 \log a_{\text{Fe}^{2+}}$$

Reactions Involving Nitrate Ions

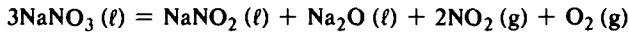
Fuse nitrate can be reduced electrolytically to nitrite [16], and the nitrate/nitrite reactions can be calculated as



$$\Sigma \nu \mu^\circ = -99.77 \text{ kcal} \quad (17)$$

$$E_T = -2.163 + 0.0595 \log a_{\text{NO}_3^-} - 0.0595 \log a_{\text{NO}_2^-} + 0.0595 p\text{O}^{2-}$$

This equation is calculated from Eq 1 and



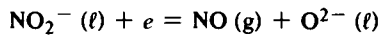
The chemical potential of nitrate ion in the melt is calculated from Eq 1 as

$$\mu^\circ_{\text{NO}_3^-} = +16.78 \text{ kcal}$$

The value of nitrite ion can be obtained from Eq 17 as

$$\mu^\circ_{\text{NO}_2^-} = +36.40 \text{ kcal}$$

Therefore the following reactions which involve nitrite ion can be calculated as



$$\Sigma \nu \mu^\circ = -63.55 \text{ kcal} \quad (18)$$

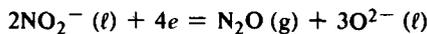
$$E_T = -2.756 + 0.119 \log a_{\text{NO}_2^-} - 0.119 \log P_{\text{NO}} + 0.119 p\text{O}^{2-}$$



$$\Sigma \nu \mu^\circ = -66.57 \text{ kcal} \quad (19)$$

$$E_T = -2.887 + 0.119 \log a_{\text{NO}_2^-} + 0.119 \log P_{\text{NO}_2}$$

$$- 0.238 \log P_{\text{NO}} - 0.0595 \log P_{\text{O}_2} + 0.119 p\text{O}^{2-}$$



$$\Sigma \nu \mu^\circ = -197.96 \text{ kcal} \quad (20)$$

$$E_T = -2.146 + 0.0595 \log a_{\text{NO}_2^-} - 0.0298 \log P_{\text{N}_2\text{O}} + 0.0893 \text{pO}^{2-}$$

$$2\text{NO}_2^- (\ell) + 6e = \text{N}_2 (\text{g}) + 4\text{O}^{2-} (\ell)$$

$$\Sigma \nu \mu^\circ = -247.8 \text{ kcal} \quad (21)$$

$$E_T = -1.791 + 0.0397 \log a_{\text{NO}_2^-} - 0.0198 \log P_{\text{N}_2} + 0.0793 \text{pO}^{2-}$$

$$\text{NO}_2 (\text{g}) + e = \text{NO}_2^- (\ell)$$

$$\Sigma \nu \mu^\circ = -19.62 \text{ kcal} \quad (22)$$

$$E_T = -0.851 + 0.119 \log P_{\text{NO}_2} - 0.119 \log a_{\text{NO}_2^-}$$

$$\text{NO} (\text{g}) + 1/2 \text{O}_2 (\text{g}) + e = \text{NO}_2^- (\ell)$$

$$\Sigma \nu \mu^\circ = -16.60 \text{ kcal} \quad (23)$$

$$E_T = -0.720 + 0.119 \log P_{\text{NO}} + 0.0595 \log P_{\text{O}_2} - 0.119 \log a_{\text{NO}_2^-}$$

Reactions Involving Nitryl Ions

The dissociation constant of the nitrate ion [7] can be used to calculate the chemical potential

$$\mu^\circ_{\text{NO}_2^+} = -2.44$$

and the reactions involving nitryl ions are

$$\text{NO}_2^+ (\ell) + e = \text{NO}_2 (\text{g})$$

$$\Sigma \nu \mu^\circ = -19.22 \text{ kcal} \quad (24)$$

$$E_T = -0.833 + 0.119 \log a_{\text{NO}_2^+} - 0.119 \log P_{\text{NO}_2}$$

$$\text{NO}_2^+ (\ell) + 2e = \text{NO}_2^- (\ell)$$

$$\Sigma \nu \mu^\circ = -38.84 \text{ kcal} \quad (25)$$

$$E_T = -0.842 + 0.0595 \log a_{\text{NO}_2^+} - 0.0595 \log a_{\text{NO}_2^-}$$

$$2\text{NO}_2^+ (\ell) + 10e = \text{N}_2 (\text{g}) + 4\text{O}^{2-} (\ell)$$

$$\Sigma \nu \mu^\circ = -325.48 \text{ kcal} \quad (26)$$

$$E_T = -1.412 + 0.0238 \log a_{\text{NO}_2^+} - 0.0119 \log P_{\text{N}_2} + 0.0476 \text{pO}^{2-}$$

$$2\text{NO}_2^+ (\ell) + 8e = \text{N}_2\text{O} (\text{g}) + 3\text{O}^{2-} (\ell)$$

$$\Sigma \nu \mu^\circ = -275.64 \text{ kcal} \quad (27)$$

$$E_T = -1.494 + 0.0298 \log a_{\text{NO}_2^+} - 0.0149 \log P_{\text{N}_2\text{O}} + 0.0446 \text{pO}^{2-}$$

$$\text{NO}_2^+ (\ell) + 3e = \text{NO} (\text{g}) + \text{O}^{2-} (\ell)$$

$$\Sigma \nu \mu^\circ = -102.39 \text{ kcal} \quad (28)$$

$$E_T = -1.480 + 0.0400 \log a_{\text{NO}_2^+} - 0.0400 \log P_{\text{NO}_2} + 0.0400 \text{pO}^{2-}$$

$$\text{NO}_2^+ (\ell) + e = \text{NO} (\text{g}) + 1/2 \text{O}_2 (\text{g})$$

$$\Sigma \nu \mu^\circ = -22.24 \text{ kcal} \quad (29)$$

$$E_T = -0.964 + 0.119 \log a_{\text{NO}_2^+} - 0.119 \log P_{\text{NO}} - 0.0595 \log P_{\text{O}_2}$$

References

- [1] Kelley, K. K., "Contribution to the Data on Theoretical Metallurgy, XIII; High Temperature Heat Content, Heat Capacity, and Entropy Data for the Elements and Inorganic Compounds," Bulletin No. 584, U.S. Bureau of Mines, 1960.
- [2] Kubaschewski, O., Evans, E. L., and Alcock, C. B., *Metallurgical Thermochemistry*, Pergamon Press, London, 1967.
- [3] *JANAF Thermodynamical Tables*, 2nd ed., National Bureau of Standards, 1971.
- [4] Solar pilot plant; conceptual design report by Honeywell, ERDA Contract No. E(04-3)-1109, May 1976.
- [5] Anderson, C. H. and Diehl, E. K., Publication No. 55-A-200, American Society of Mechanical Engineers, 1955.
- [6] Rahmel, A. in *The Mechanism of Corrosion by Fuel Impurities*, H. R. Johnson and D. J. Littler, Eds., Butterworth, London, 1963, p. 556.
- [7] Kust, R. N. and Duke, F. R., *Journal of the American Society of Mechanical Engineers*, Vol. 85, 1963, p. 3338.
- [8] Lux, H., *Elektrochemische Zeitschrift*, Vol. 45, 1939, p. 303.
- [9] Flood, H. and Forland, T., *Acta Chemica Scandinavica*, Vol. 1, 1947, p. 592.
- [10] Bando, G. and Tampa, A., *British Corrosion Journal*, Vol. 4, 1969, p. 129.
- [11] Marchiano, S. L. and Arvia, A. J., *Electrochimica Acta*, Vol. 17, 1972, p. 25.
- [12] Theus, G. J., "Electrochemical Studies of Metals in Fused Sodium Hydroxide," Ph.D. thesis, Ohio State University, 1972.
- [13] Chen, C. M. and Theus, G. J., "Chemistry of Corrosion Producing Salts in Light Water Reactors," EPRI Research Project No. 967-1, final report, October 1978.
- [14] Notoya, T. and Midorikawa, R., *Denki Kagaku*, Vol. 39, 1971, p. 931.
- [15] Arvia, A. J., Podesta, J. J., and Piatti, R. C. V., *Electrochimica Acta*, Vol. 17, 1972, p. 33.
- [16] Notoya, T. and Midorikawa, R., *Denki Kagaku*, Vol. 40, 1972, p. 104.
- [17] Lyalikov, Y. S. and Novik, R. M., *Uchenye Zapiski, Kishinevskii Gosudarstvennyi Universitet*, Vol. 27, 1957, p. 61.
- [18] Kubaschewski, O. and Hopkins, B. E., *Oxidation of Metals and Alloys*, 2nd ed., Butterworth, London, 1962, p. 37.
- [19] Gulbransen, E. A., *Journal of the Electrochemical Society*, Vol. 20, 1942, p. 187.
- [20] *Steam, Its Generation and Use*, 37th ed., Babcock & Wilcox Co., 1972, Chapter 12, p. 12-10.
- [21] Pourbaix, M., *Lectures on Electrochemical Corrosion*, Prentice-Hall, New York, 1973, p. 83.
- [22] "Selected Values of Chemical Thermodynamic Properties," Circular No. 500, National Bureau of Standards, 1961.
- [23] Triaca, W. E. and Arvia, A. J., *Electrochimica Acta*, Vol. 9, 1964, p. 919.

Yuichi Ishikawa,¹ Nobuyoshi Hosaka,¹ and Susumu Hioki¹

Galvanic Corrosion of Copper Alloys

REFERENCE: Ishikawa, Yuichi, Hosaka, Nobuyoshi, and Hioki, Susumu, "Galvanic Corrosion of Copper Alloys," *Electrochemical Corrosion Testing, ASTM STP 727*, Florian Mansfeld and Ugo Bertocci, Eds., American Society for Testing and Materials, 1981, pp. 327-338.

ABSTRACT: Quantitative galvanic corrosion data have been obtained for brass and bronze couples in flowing fresh water. Laboratory measurements of galvanic current flow between brass and bronze were made employing an automatic balancing zero impedance ammeter. The galvanic current data have been discussed with the polarization behavior of uncoupled brass and bronze determined by a separate experiment. Good agreement has been found between the dissolution current density and the rate of penetration of the brass in the couple determined by the weight-loss measurement. Furthermore, a correction has been made for the anodic current density of the brass with respect to the amount of beta brass phase, which has yielded a fair agreement between the anodic current density and the average depth of dezincification. The effect of flow rate on the galvanic current density is discussed with reference to the mass transfer treatment.

KEY WORDS: corrosion, copper alloys, galvanic corrosion

It is not always possible to avoid intimate electrical contact between dissimilar metals in certain pumping equipment applications. In order to manufacture an economical small pump for fresh water use, for example, stainless steels and bronzes cannot be used for all parts. The general effect of coupling dissimilar metals in a corrosive environment is that one metal will corrode more, and the other less, than would be expected from a consideration of the individual corrosion rates.

For prediction of the risk of galvanic corrosion through contact between dissimilar metals, a popular practice has been to use a galvanic series in which the metals are arranged according to their potentials measured in a particular environment. While these can be useful as a guide, it should be noted that there are several factors, such as the formation of films on the surface, potential variation with time, and variation of polarizability of metals with environment, which lead to drawbacks in the use of potential measure-

¹Senior research engineer, corrosion research engineer, and section head, respectively, Materials Strength and Reliability Division, Mechanical Engineering Research Laboratory, Hitachi, Ltd., Tsuchiura, Ibaraki, Japan 300.

ments and the galvanic series, as pointed up by Baboian [1].² In some case the separation between the two metals in the galvanic series gives an indication of the magnitude of galvanic corrosion. This is not always the case, as demonstrated by Mansfeld and Kenkel for galvanic corrosion of aluminum alloys [2].

Thus, as an aid to the selection of compatible materials, quantitative data should be obtained on the basis of galvanic corrosion current measurements between coupled metals at a given area ratio and in a given corrosion environment. The aim of this present study was to provide quantitative data on corrosion characteristics of brass when coupled to bronze in a fresh water that is known to cause early failure of a small household pump due to dezincification of the brass casing cover. This paper presents results of galvanic corrosion between 60-40 forged brass and bronze casting (BC 6) investigated electrochemically in flowing fresh water. The electrochemical results were compared with the direct corrosion damage measurement performed after an exposure of 180 days.

Experimental

Materials and Test Method

Table 1 lists the chemical composition of the materials studied. The structure of brass consists of 50 percent alpha and 50 percent beta. The electrode configuration selected was a tubular flow-through electrode. It was constructed from a 20-mm length of 14.6 inside-diameter tubing. The inner surfaces of the specimens were wet-polished with silicon carbide papers down to 600 grit, ultrasonically cleaned in acetone, dried, and weighed to 0.1 mg. The brass and bronze specimens to be coupled were placed in an acrylic pipe holder with a 2-mm-thick Teflon ring spacer between the specimens. A copper lead wire was inserted through a hole in the holder and made contact with the specimen. A Luggin capillary was tapped into the cell wall approximately 2 mm from the edge of the anode. These holders were connected by an acrylic cement in a series of twelve. Galvanic current for twelve different couples were measured by a zero impedance ammeter, and the galvanic corrosion potentials were monitored against a saturated calomel electrode (SCE) with a high-impedance voltmeter. Connection of the twelve different couples with the ammeter and voltmeter was made through a high-speed scanner.

Experiments were carried out under controlled flow conditions (0.1, 1.5, and 3.0 m/s). The galvanic cell and recirculating flow system are shown in Fig. 1. The connected galvanic cell were preceded by an entrance length of 160 mm and followed by an exit length of 50 mm of acrylic pipe, which were sufficient to give fully developed flow at the entrance to the galvanic cells and

²The italic numbers in brackets refer to the list of references appended to this paper.

TABLE 1—Chemical composition of the alloys by weight percent.

	Cu	Sn	Zn	Pb	Ni	Fe
60-40 forged brass	59.57	0.64	36.23	2.75	0.34	0.47
BC 6 bronze casting	82.48	5.08	5.53	6.14	0.20	0.19

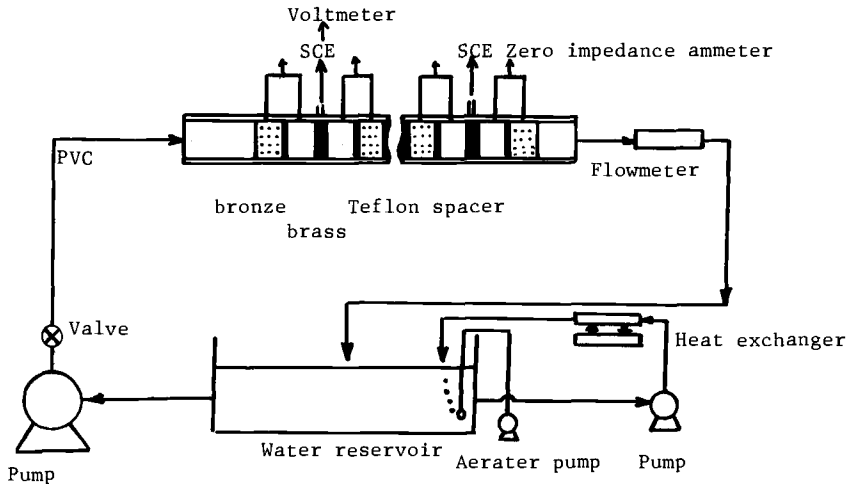


FIG. 1—Flow loop and galvanic cells.

to avoid disturbances at the outlet. Fresh water was pumped through PVC tubing, traveled through the galvanic cell section and a rotameter flow tube, and returned to the reservoir. Temperature was kept constant at 25°C. Mixing in this reservoir was facilitated both by the solution return and a gas bubbler that was connected to an aerater pump.

The water was changed once a week and was of the following nominal composition:

pH: 6.0–6.5 Ca hardness 118–126 ppm Cl^- : 116–137 ppm

SO_4^{2-} : 94–100 ppm Total dissolved solids (TDS): 495–508 ppm

Conductivity: 545–560 $\mu\text{S}/\text{cm}$

After the six month test, the specimens were washed, dried, and weighed again. Because of the difficulty encountered in removing the specimens from the holder, the weight-loss measurement was slightly unreliable, especially less than about 1 mg. Brass specimens were sectioned into five, polished, and examined metallographically. The maximum and average depth of dezincification were determined for each cross section.

Results

The corrosion rates of uncoupled brass and bronze were determined both by potentiodynamic polarization and by weight loss and dezincification depth measurements [3]. Table 2 lists the average polarization resistance (R_p^{av}) determined by graphical intergration of R_p versus time plots, the corrosion potential (E_{corr}) after exposure for 24 h, the average corrosion current density (i_{corr}), and the rate of penetration (\bar{r}), and the average dezincification depth (\bar{r}_d) determined after an exposure of 180 days.

As Ishikawa et al³ have noted, the observed changes in brass in the electrochemical parameters with flow rate are probably caused by enhanced transport of oxygen to the surface or by electrochemical reduction, while in bronze the changes are due to the more rapid removal of anodically produced metal ions.

As an example, the galvanic current density (i_g) and corrosion potential (E_g) for a couple are plotted as a function of exposure time and flow rate in Fig. 2. Since the galvanic current appeared to approach a constant value after an exposure of 8 h and to vary little thereafter, the galvanic current was measured every 30 days during the 180-day exposure period for all coupled specimens. For all twelve couples, i_g increased and E_g became more positive with increasing flow rate.

All the coupled specimens showed little tendency for random fluctuation in the galvanic corrosion potential during the 180-day exposure period and high reproducibility between the couples. From plots of i_g versus t , the average galvanic current density (i_g^{av}) was calculated by graphical integration, the values of i_g^{av} for twelve couples are plotted on normal distribution probability paper in Fig. 3. The median value was taken as \bar{i}_g , and σ represents its standard deviation.

Weight-loss measurement and metallographic examination of the speci-

³This publication, pp. 339-351.

TABLE 2—Corrosion parameters obtained for the uncoupled alloys from polarization, weight loss, and dezincification measurements [3].

	Flow Rate, m/s	E_{corr} , mV versus SCE ^a	R_p^{av} , $10^3 \Omega\text{cm}^2$	i_{corr} , $\mu\text{A}/\text{cm}^2$	\bar{r} , mm/year	\bar{r}_d , mm/year
Brass	0.1	-149	14.0	2.2	0.039	0.086
	1.5	-132	3.96	8.4	0.130	0.315
	3.0	-111	1.97	17.6	0.296	0.640
Bronze	0.1	+29	12.5	1.98	0.038	...
	1.5	+3	4.32	5.07	0.080	...
	3.0	-2	1.73	12.4	0.210	...

^aSCE = saturated calomel electrode.

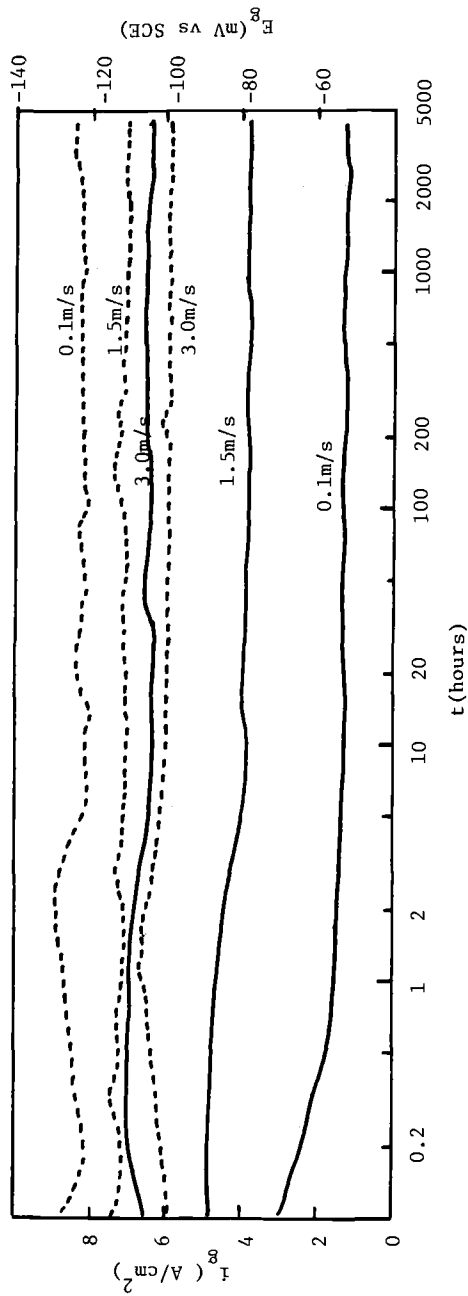


FIG. 2—Time behavior of galvanic current density (i_g) and galvanic potential (E_g).

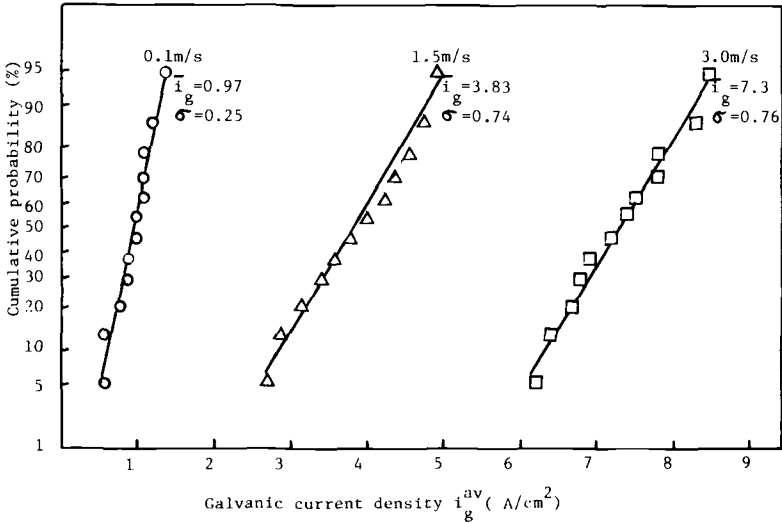


FIG. 3—Cumulative frequency distribution of galvanic current density (i_g^{av}).

mens used for the galvanic current measurement were made after an exposure of 180 days. The rate of penetration (r_g) and the depth of dezincification of brass (r_{gd}^{av}) are plotted on normal distribution paper in Figs. 4 and 5, respectively. \bar{r}_g and \bar{r}_{gd} were determined as medians of the plots. The plots of i_g give a straight line with a relatively smaller slope compared with the plots of r_g and r_{gd}^{av} , which indicates relatively larger scatter among these data.

Discussion

A general discussion of the factors determining the rate of galvanic corrosion has been given by Mansfeld et al [2,4-6]. They have classified most practical situations in galvanic corrosion in one of three cases, which can be treated theoretically using the concept of mixed potential theory. The total anodic dissolution current density (i_a) is given by

$$i_a = \Delta i_a + i_{corr} = i_g + i_{corr} \tag{1}$$

$$\Delta i_a = i_a - i_{corr} \tag{2}$$

as shown by Refs 4-6. The substitution of the measured values of i_{corr} and i_g gives the ratio $i_g/i_a = 1 - i_{corr}/i_a$, 0.29 ~ 0.31, which agrees well with the calculated values of 0.26 ~ 0.31 based on Eq [5].

$$\frac{i_g}{i_a} = 1 - \exp \left\{ - \frac{(E_g - E_{corr})}{0.434 b_a} \right\} \tag{3}$$

Fig. 6 shows plots of Δi_a against the rate of stimulation, and the difference in the rate of penetration ($r_g - \bar{r}$) and in the depth of dezincification ($r_{gd} - \bar{r}_d$) between coupled and uncoupled brass, determined by weight loss and by dezincification measurement. Circles represent the values obtained at a flow rate of 0.1 m/s, triangles at 1.5 m/s, and squares at 3.0 m/s. Open symbols

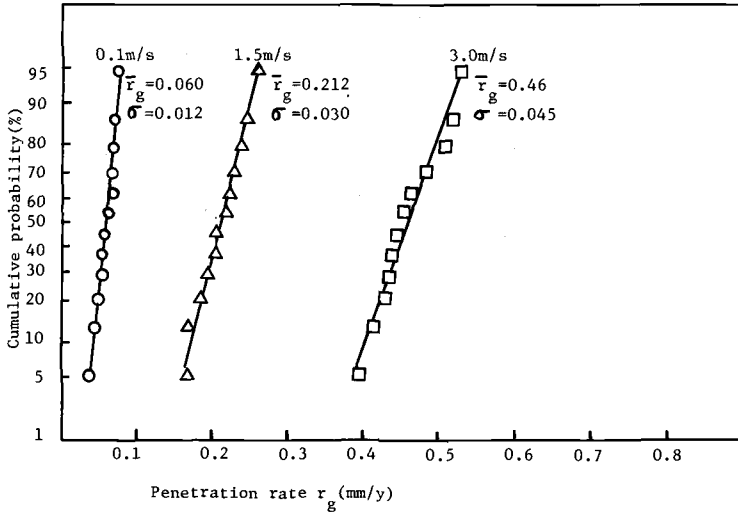


FIG. 4—Cumulative frequency distribution of penetration rate (r_g).

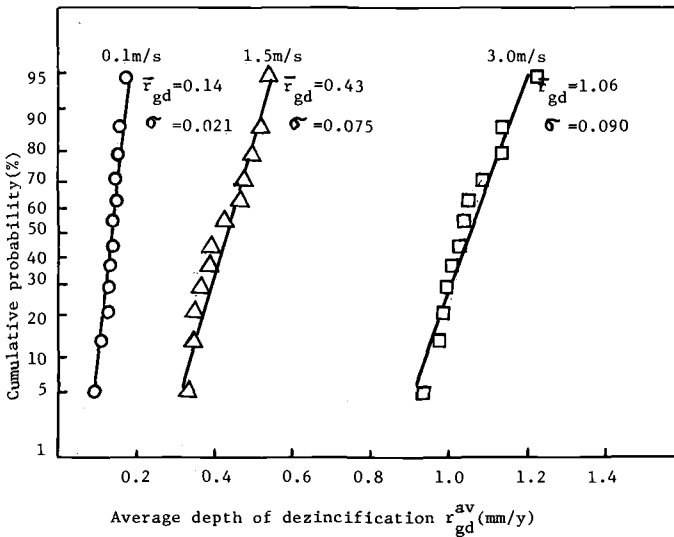


FIG. 5—Cumulative frequency distribution of average depth of dezincification (r_{gd}^{av}).

represent a relationship between Δi_a and $(r_g - \bar{r})$, and solid symbols between Δi_a and $(r_{gd} - \bar{r}_d)$.

Each data point represents a different coupled specimen. Most data points fall close to a straight line. The calculation of the rate of penetration from the current density using Faraday's law should yield the theoretical slope of 48.9 ($\mu\text{A}/\text{cm}^2$)/(mm/year) based on the nominal composition of the brass.

The calculation of the straight line ($\Delta i_a = mr + b$) of best fit to the plotted values was made using the method of least squares in ASTM Recommended Practice for Applying Statistics to Analysis of Corrosion Data [G 16-71 (1977)]. The calculated straight lines in Fig. 6 were drawn together with a plot of the 95 percent (2σ) limits of data. Since the values m and b thus determined contain errors of estimation, scatter of the expected values m and b should be evaluated. The confidence limits of m and b are given as

$$m - \frac{t(n-2, \alpha) \sqrt{V_{\Delta i_a \cdot r}}}{\sqrt{\Sigma(r_i - r)^2}} < \bar{m} < m + \frac{t(n-2, \alpha) \sqrt{V_{\Delta i_a \cdot r}}}{\sqrt{\Sigma(r_i - r)^2}} \quad (4)$$

$$b - [t(n-2, \alpha) \sqrt{V_{\Delta i_a \cdot r}}] \sqrt{\frac{1}{n} + \frac{\bar{r}^2}{\Sigma(r_i - r)^2}} < \bar{b} < b + [t(n-2, \alpha) \cdot \sqrt{V_{\Delta i_a \cdot r}}] \sqrt{\frac{1}{n} + \frac{\bar{r}^2}{\Sigma(r_i - r)^2}} \quad (5)$$

For the weight loss data calculation using these equations yields the 95 percent confidence limit of m as $35.5 < m < 49.5$ ($\mu\text{A}/\text{cm}^2$)/(mm/year) and b as $-0.8 < b < 1.8$ $\mu\text{A}/\text{cm}^2$, in which the theoretical values of $m = 48.9$ and $b = 0$ are contained. This indicates that the observed difference between the theoretical and the experimental values (average: $m = 40.4$ and $b = 0.36$) is associated with experimental error rather than the experimental and calculative methods employed.

For the dezincification depth, however, the average values of $m = 19$ ($12.5 < m < 25.5$) are too low to be attributed to experimental error. Dezincification occurred over the entire surfaces of the brass specimens, which would be expected from the potential-pH diagram for 70-30 brass in 0.1 m sodium chloride solution [7], because the galvanic potentials observed in the present work (-76 to -140 mV_{vs} SCE) lie within the dissolution region of copper and zinc.

When the dezincification is assumed to progress with the preferential dissolution of beta brass (the only process that contributes to the measured anodic current density [3]), the anodic current density (i_A) and cathodic current density (i_c) are related to the corrosion current density as

$$i_A S_A = i_c S_c = i_{\text{corr}} S \quad (6)$$

where S_A and S_c are the total surface area of the anodic sites and the cathodic sites, respectively, and S is the total surface area of the electrode. In the case of duplex alpha plus beta brass, it may be considered that beta brass becomes the anodic sites while alpha brass becomes the cathodic sites. The brass contains 50 percent alpha and 50 percent beta phase and the surface area of alpha may be considered to equal to that of beta. Then

$$S_A = S_c = \frac{1}{2}S \quad \text{and} \quad i_A \text{ is given as } i_A = 2i_{\text{corr}} \quad (7)$$

In analogy to the preceding, the dissolution current density of beta brass in the galvanic couple is given by

$$i_a^B = 2i_a^B = 2(\Delta i_a + i_{\text{corr}}^B) \quad (8)$$

This equation suggests that measured current density corresponds to half of the measured dezincification depth. The calculation of the dezincification depth from the current density should then yield the slope of $24.5 (\mu\text{A}/\text{cm}^2)/(\text{mm}/\text{year})$. This is the range of the experimental value of m ($12.5 < m < 25.5$), which suggests that the dissolution current density thus determined could be used to predict the average depth of dezincification.

It is often assumed that the rate of galvanic corrosion can be judged based

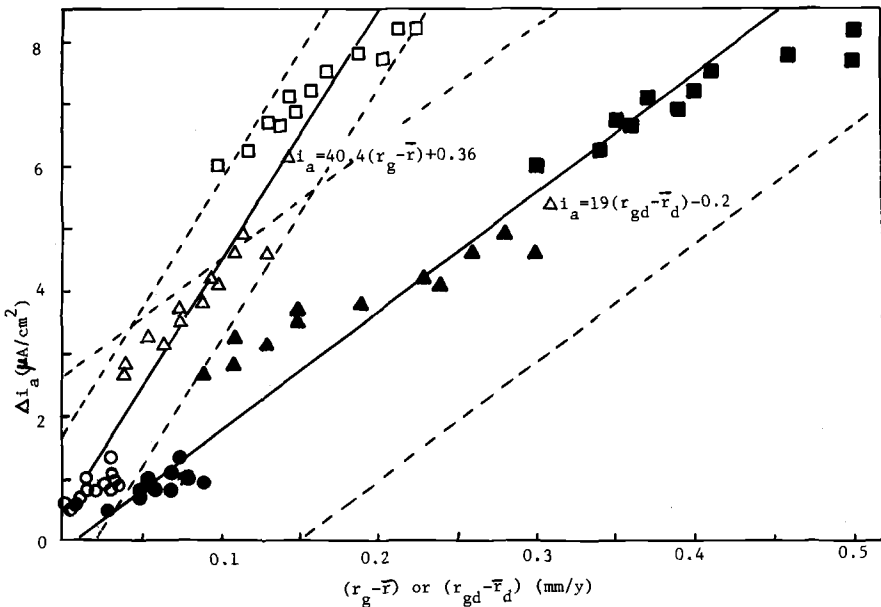


FIG. 6—Correlation between average rate of stimulation (Δi_a) and $(r_g - \bar{r})$ or $(r_{gd} - \bar{r}_d)$.

on the difference of the corrosion potentials of uncoupled dissimilar metals. Corrosion reactions are, however, determined by the kinetics of the oxidation and reduction reactions. As shown by Mansfeld and Kenkel [2], the magnitude of the galvanic current density is determined by the corrosion rates of the uncoupled metals, Tafel slopes, difference of corrosion potentials, and the area ratio.

The experimental data of this study are plotted in Fig. 7 as Δi_a versus the initial corrosion potential difference $\Delta E_{\text{corr}} = E_{\text{corr}}(\text{bronze}) - E_{\text{corr}}(\text{brass})$ of each twelve couple. Most of the data points fall close to a straight line, and a good correlation was observed. The values of Δi_a increased with increasing flow rate, and the effect of ΔE_{corr} on Δi_a also increased with flow rate.

The effect of relative velocity metal/electrolyte on galvanic corrosion has been studied for aluminum alloys coupled to copper, steel, stainless steel, titanium alloy, and zinc in 3.5 percent sodium chloride and substituted ocean water by Mansfeld and Kenkel [8]. They found a square-root dependence of i_g on angular velocity and described the velocity dependence being due to oxygen diffusion control.

As Ishikawa et al have noted [3], diffusional-convective and ionic transport between the bulk solution and the metal/solution interface control the rate of corrosion for the uncoupled brass and bronze. The velocity dependence of i_{corr} is related to that of mass transfer rate as

$$i_{\text{corr}} = \frac{k_a \bar{n} F}{(1 - t_{M\bar{n}^+})} (a_b - a_s) \quad (9)$$

where:

- k_a = mass transfer coefficient based on activities, cm/s,
- $t_{M\bar{n}^+}$ = metal-ion transport number, and
- a_b and a_s = bulk solution and metal/solution interfacial metal-ion activities, g-ion/cm³, respectively.

In the case of a tubular flow system, the k_a values can be calculated by the Leveque solution for the laminar flow, $\text{Re} < 2100$,

$$k_a = 1.614 \frac{D}{d} \left(\text{Re} \cdot \text{Sc} \frac{d}{L} \right)^{1/3} \quad (10)$$

and by the Chilton-Colburn equation for the turbulent flow, $\text{Re} > 5000$,

$$k_a = 0.023 \nu \text{Re}^{-0.2} \cdot \text{Sc}^{-2/3} \quad (11)$$

where

- d = tube diameter, cm,
- D = diffusion coefficient, cm²/s,

L = electrode length, cm,
 v = flow rate, cm/s,
 Re = Reynolds number given by $Re = dv\rho/\mu$,
 Sc = Schmidt number given by $Sc = \mu/\rho D$,
 μ = viscosity, g/cm·s, and
 ρ = density, g/cm³.

The calculated values of k_a are given in Table 3. The ratio of k_a at 1.5 and 3.0 m/s to k_a at 0.1 m/s shows a good correspondence with the ratio of \bar{i}_g at 1.5 and 3.0 m/s to \bar{i}_g at 0.1 m/s. This may suggest that the velocity dependence of \bar{i}_g may be described with the mass transfer treatment, similar to that of i_{corr} for uncoupled brass.

If the cathodic current were determined by the diffusion limited reaction of oxygen, no effect of the nature of the cathode should be observed. The observed dependence of Δi_a on ΔE_{corr} may result from different corrosion rates of uncoupled brass, different diffusion rates of oxygen through the surface film of the brass, and different rates of oxygen reduction on the bronze surface, as suggested by Mansfeld et al [6].

The flow rate undoubtedly amplifies the effect of ΔE_{corr} on Δi_a , because

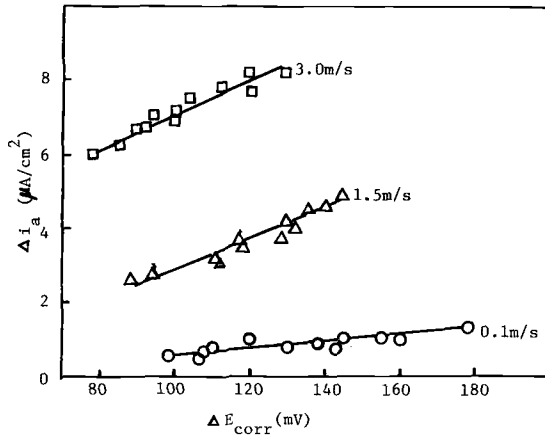


FIG. 7—Correlation between average rate of stimulation (Δi_a) and initial difference of corrosion potentials (ΔE_{corr}).

TABLE 3—Calculated mass transfer coefficient, k_a , and the effect of flow rate.

Flow Rate, m/s	k_a , cm/s	Ratio, to 0.1 m/s	\bar{i}_g , $\mu A/cm^2$	Ratio, to 0.1 m/s
0.1	2.02	1	0.97	1
1.5	7.92	3.92	3.83	3.94
3.0	13.7	6.78	7.30	7.53

increasing flow rate decreases the thickness of the surface films of brass and bronze, which would bring the thickness and nature of the films more sensitive to the potential. A quantitative evaluation of this effect appears to be necessary.

Conclusion

The rate of stimulation of the brass due to galvanic coupling with the bronze can be expressed as $\Delta i_a = i_g$. The anodic dissolution current density of the brass is given by

$$i_a = \Delta i_a + i_{\text{corr}} = i_g + i_{\text{corr}}$$

Relatively good agreement is obtained between penetration rates calculated from weight-loss data and those calculated from galvanic current data, provided that dezincification progresses with preferential dissolution of beta brass as the only contribution to the experimental anodic current.

The effect of flow rate on galvanic current density can be discussed with the mass transfer treatment.

Acknowledgments

We wish to thank Kenzo Mikada of Taga Works of Hitachi, Ltd. for his cooperation.

References

- [1] Baboian, R. in *Galvanic and Pitting Corrosion—Field and Laboratory Studies*, ASTM STP 576, American Society for Testing and Materials, 1976, pp. 5-19.
- [2] Mansfeld, F. and Kenkel, J. V. in *Galvanic and Pitting Corrosion—Field and Laboratory Studies*, ASTM STP 576, American Society for Testing and Materials, 1976, pp. 30-47.
- [3] Ishikawa, Y., Ozaki, T., and Mikada, K., to be published in *Corrosion*.
- [4] Mansfeld, F., *Corrosion*, Vol. 27, 1971, p. 436.
- [5] Mansfeld, F., *Corrosion*, Vol. 29, 1973, p. 403.
- [6] Mansfeld, F. and Parry, E. P., *Corrosion Science*, Vol. 13, 1973, p. 605.
- [7] Verink, E. D., Jr. and Heidersbach, R. H., Jr., in *Localized Corrosion—Cause of Metal Failure*, ASTM STP 516, American Society for Testing and Materials, 1972, pp. 303-322.
- [8] Mansfeld, F. and Kenkel, J. V., *Corrosion*, Vol. 33, 1977, p. 376.

Yuichi Ishikawa,¹ Toshinori Ozaki,¹ Sumio Sudo,² and
Susumu Hioki¹

Electrochemical Investigation of Cavitation-Corrosion Damages of a Pump Casing

REFERENCE: Ishikawa, Yuichi, Ozaki, Toshinori, Sudo, Sumio, and Hioki, Susumu, "Electrochemical Investigation of Cavitation-Corrosion Damages of a Pump Casing," *Electrochemical Corrosion Testing, ASTM STP 727*, Florian Mansfeld and Ugo Bertocci, Eds., American Society for Testing and Materials, 1981, pp. 339-351.

ABSTRACT: In order to clarify the roles of cavitation and erosion in the cavitation-corrosion damage of a pump casing used for pumping a corrosive chlorinated fresh water, an electrochemical study has been performed using a one-third scale prototype double-suction volute pump.

Three electrochemical corrosion monitoring electrodes consisting of a medium carbon cast steel test electrode, a stainless-steel counter electrode, and a 0.5 mm diameter stainless-steel capillary, each being separated by epoxy resin, were mounted at different locations of the casing wall. The polarization resistance was determined from the potentiodynamic polarization curves, and the corrosion current density was calculated.

Determination of the corrosion current density as a function of flow quantity revealed that at 10 percent of the normal flow capacity the corrosion current density increased to 50 mA/cm² for the eye area of the casing throat, compared with 0.03-0.08 mA/cm² measured at above 20 percent of the normal flow capacity and for the other locations at any flow range.

It may be suggested that this high corrosion current density results from the synergistic effect of cavitation induced from the reversed flow and corrosion enhancement by chlorine in the water.

KEY WORDS: electrochemical measurement, cavitation, chlorinated water pump, cast carbon steel

The specific delivery rates of pumps have been raised substantially in the past few decades. A design engineer must cope with the combined problems of cavitation erosion and corrosion of materials. The flow velocity often has significant effects on the mechanism of corrosion reactions. Various parameters affecting the corrosion process are altered by the fluid velocity, which

¹Senior research engineer, research engineer, and section head, respectively, Materials Strength and Reliability Section, Mechanical Engineering Research Laboratory, Hitachi, Ltd., Tsuchiura, Japan.

²Senior engineer, Pump Division, Tsuchiura Works, Hitachi, Ltd., Tsuchiura, Japan.

may increase attack by increasing the supply of aggressive substances, or diffusion or transfer of aggressive ions by reducing the thickness of the stagnant film at the surface. Fluid turbulences or imploding cavitation bubbles can destroy protective films formed on the surface of the metal and activate the metal surface. The newly exposed metal surface corrodes and the film is reformed. With the repetitive destruction of the film, corrosion results in severe localized damage on the metal surface.

We recently experienced a severe cavitation-corrosion damage on a pump casing used for pumping a corrosive chlorinated water. In order to clarify the roles of corrosion and cavitation, we performed electrochemical measurements using a double-suction volute pump. It will be shown that the cavitation-corrosion behavior can be predicted by an electrochemical method.

Experimental Apparatus and Procedures

The cavitation-corrosion tests were performed with a double-suction volute pump using a flow loop shown in Fig. 1. Corrosion monitoring electrodes consisted of a medium carbon cast steel test electrode, a stainless-steel counter electrode, and a 0.5 mm diameter stainless-steel capillary tube with cotton thread inside, each being separated by epoxy resin. The electrodes were placed in the holes drilled through the casing wall of the pump. Two electrodes were placed at the suction casing, one at the throat and another at the throat-eye area. One electrode was placed at the discharge casing. The surfaces of the test electrodes were polished with 400 grit silicon carbide paper, then cleaned with acetone and dried. Surface areas of the test electrodes were in the range of 0.3 to 0.7 cm².

Observation of cavitation was made through an acrylic plate window at-

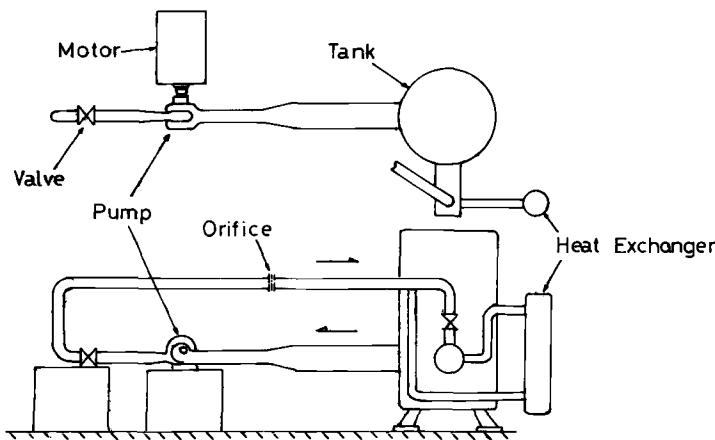


FIG. 1—Experimental flow loop.

tached to the pump casing. The cross section of the pump and locations of the electrodes are shown in Figs. 2 and 3, respectively. Pump specifications are quantity = 9.45 m³/min and head = 108.2 m.

Fresh water was recirculated from a tank (30 m³ capacity) through carbon steel pipe via a flow-adjustment valve and flow-measurement orifice. Temperature was kept constant at 25°C. The water was of the following nominal composition: pH = 8.3, total hardness = 97 ppm, calcium hardness = 41 ppm, Cl⁻ = 83 ppm, SO₄²⁻ = 244 ppm, total dissolved solids = 478 ppm, and conductivity = 782 μS/cm. Chlorination, 1.3 ppm as chlorine residual, was made by injecting sodium hypochlorite solution through a microplunger pump.

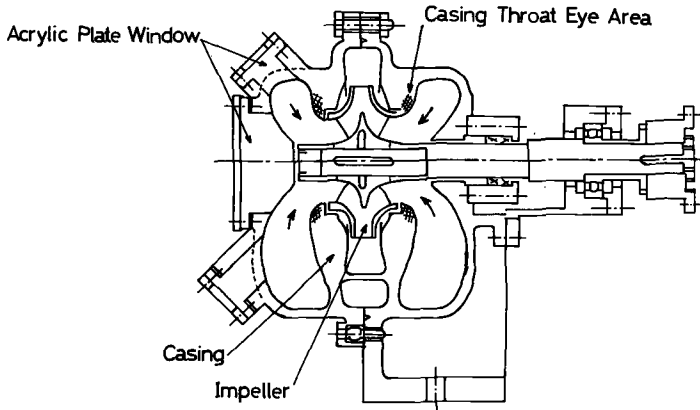


FIG. 2—Cross section of the one-third scale prototype pump.

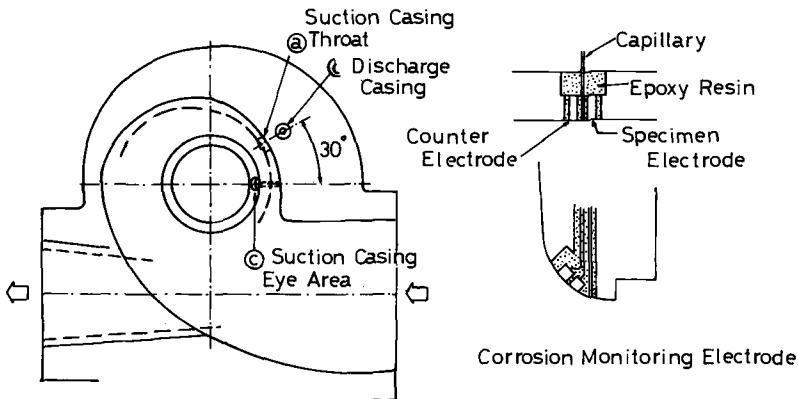


FIG. 3—Locations of the corrosion monitoring electrodes.

A potentiodynamic sweep at 0.5 mV/s was started at a potential 30 mV active to the corrosion potential (E_{corr}) and ended at 30 mV noble to E_{corr} . The polarization resistance was determined as the slope of the polarization curve at E_{corr} . The full anodic and cathodic polarization curves were obtained by separate experiments, from which the anodic and cathodic Tafel slopes were determined.

Results

Observation of Cavitation

No cavitation was observed at the throat-eye area of the suction casing during normal operating conditions (100 percent Q , where Q is the specified flow capacity). When the flow quantity was reduced to below 50 percent of the normal flow, generation of reversed flow, originating from the impeller inlet and reaching to the suction throat-eye area, was observed to induce cavitation (Fig. 4).

From the measurement of velocity distribution at the impeller inlet, it was found that between 60 and 50 percent Q , the flow direction near the casing wall changed significantly and reversed flow occurred. The velocity of the reversed flow was found to increase with reducing flow quantity. Velocity was 10 m/s at 50 percent Q and 15.5 m/s at 10 percent Q , which was considerably higher than the average velocity for normal flow (5 to 6 m/s at the throat-eye area, 4 m/s at the throat of the suction casing, and 6 m/s at the discharge casing).

The generation of this type of reversed flow is restricted under the partial flow conditions, that is, at starting and stopping transient conditions [1,2].³ The duration of this particular condition is usually very short and is not considered to result in severe cavitation damage. In fact, as shown in Fig. 5, only numerous pits were observed over the throat-eye area after 910-min exposure to the partial flow condition.

The maximum size of these pits was 0.5 mm deep and 0.5 mm diameter. 910-min would be considered an expected total duration of the partial flow conditions per year for a pump with frequent on-offs.

Electrochemical Measurements

The corrosion rates were determined as a function of flow quantity and time. Table 1 lists the anodic and cathodic Tafel slope, b_a , b_c , determined from the full anodic and cathodic polarization curves at each flow quantity.

³The italic numbers in brackets refer to the list of references appended to this paper.

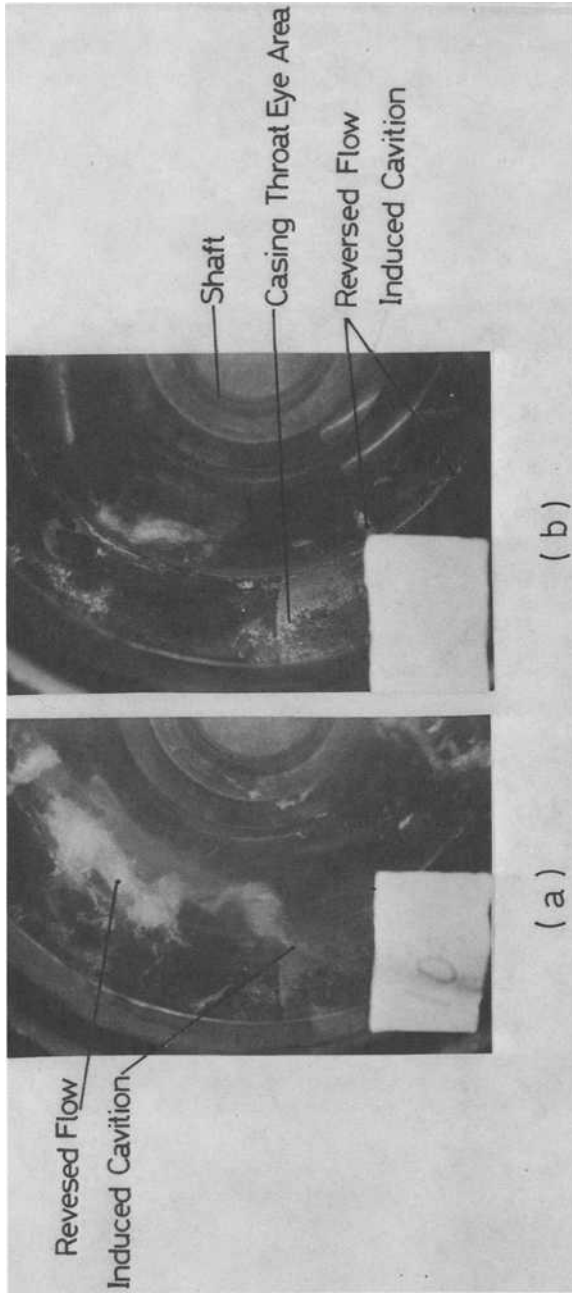


FIG. 4—Generation of reversed flow induced cavitation: (a) 10 percent Q, and (b) 40 percent Q.

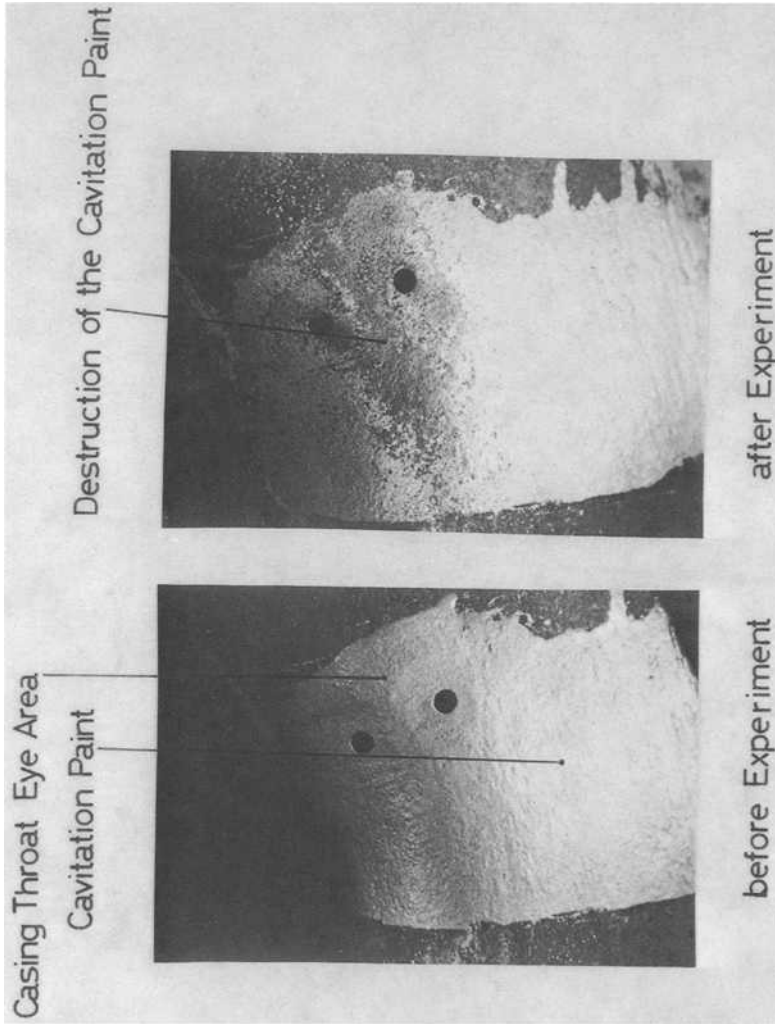


FIG. 5—Destruction of the cavitation paint and generation of small pits after partial flow operation of 910 min.

TABLE 1—Corrosion parameters obtained from the full polarization curves.

Flow Quantity, % Q	Throat-Eye Area			Suction Throat			Discharge Casing		
	b_a , mV	b_c , mV	E_{corr} , mV versus SCE ^a	b_a , mV	b_c , mV	E_{corr} , mV versus SCE	b_a , mV	b_c , mV	E_{corr} , mV versus SCE
100	250	230	350	240	210	48.6	270	230	310
75	210	190	330	200	190	42.3	220	210	360
40	200	210	340	200	180	41.1	200	190	350
20	250	230	330	200	160	38.6	210	160	350
10	360	310	320	190	150	36.4	190	180	290

^a SCE = Saturated calomel electrode.

The polarization resistance, R_p , was calculated from the experimental polarization curve as the slope of the curve at E_{corr} [3]:

$$R_p = S \left(\frac{\partial E}{\partial I} \right) E_{\text{corr}} \quad (1)$$

where S is the geometric area of the specimen electrode.

The corrosion current density can be calculated as

$$i_{\text{corr}} = \frac{b_a b_c}{2.303 (b_a + b_c) S} \left(\frac{\partial I}{\partial E} \right) E_{\text{corr}} \quad (2)$$

$$= \frac{B}{R_p} \quad (3)$$

The constant B was calculated from the experimental Tafel slope b_a and b_c , and the corrosion current density (i_{corr}) was calculated from the values of the constant B throughout this study.

The corrosion current densities determined after exposure of 10 min at each flow quantity are plotted in Fig. 6. The corrosion current density de-

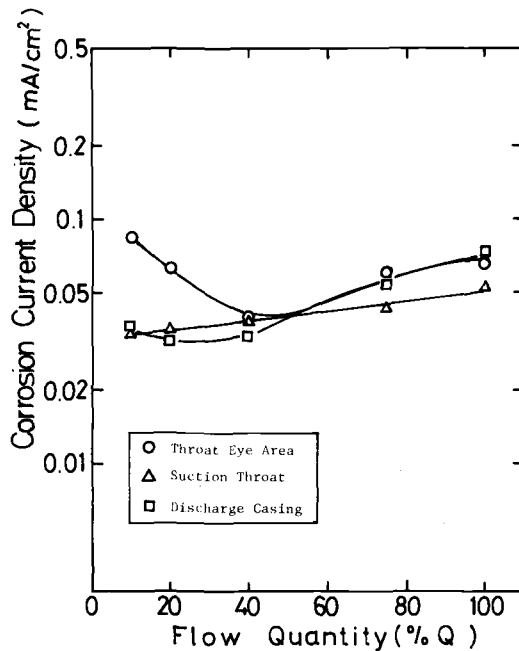


FIG. 6—Corrosion current density determined after exposure of 10 min as a function of flow quantity.

creased with decreasing flow quantity up to 40 percent Q , which would be expected as a result of decrease in flow velocity. A further decrease in flow quantity, however, resulted in an increase in i_{corr} for the throat-eye area of the suction casing. The increase in i_{corr} may be a result of the reversed flow originating from the impeller inlet. As described previously, the velocity of this reversed flow amounted to 15.5 m/s at 10 percent Q .

Figure 7 shows i_{corr} after exposure for 100 min at each flow quantity. At 10 percent Q , i_{corr} for the throat-eye area rose very sharply to 29 mA/cm². This behavior was not observed at the other locations.

Figure 8 describes the time behavior of i_{corr} for the throat-eye area at 10 percent Q . The corrosion current density decreased initially and increased very sharply after 60 min of exposure. This behavior coincides with the presence of the incubation period for cavitation.

During the cavitation test, however, only minor pitting damage was observed at the throat-eye area after prolonged exposure (910 min) between 50 and 0 percent Q , while the electrochemical measurement showed an i_{corr} of 29 mA/cm². This would correspond to a corrosion rate of 340 mm/year. Therefore, it is considered that the cavitation induced by the reversed flow under partial flow condition cannot explain the damage at the throat-eye

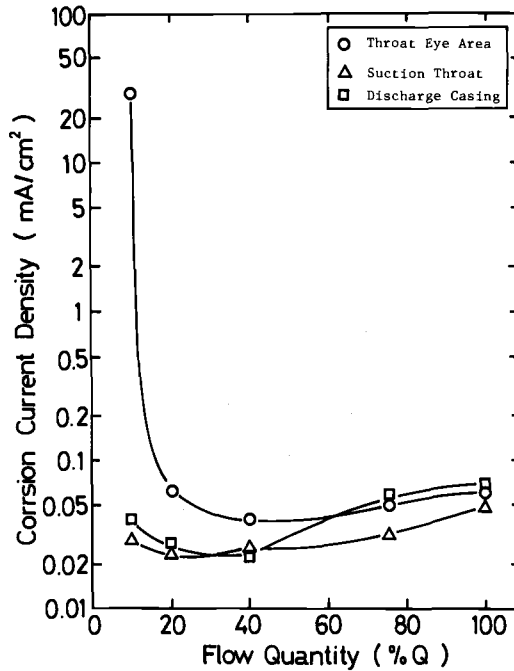


FIG. 7—Corrosion current density determined after exposure of 100 min as a function of flow quantity.

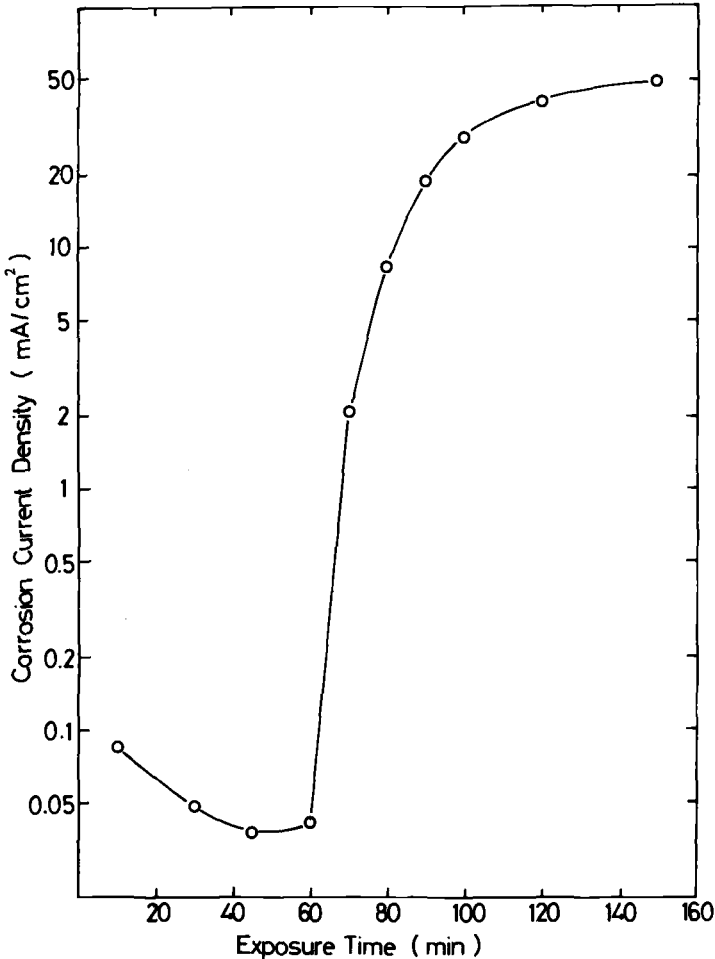


FIG. 8—Time behavior of corrosion current density for the throat-eye area at 10 percent Q .

area. The synergistic effect of cavitation and corrosion must be considered to explain this damage.

Figure 9 shows the i_{corr} decay of the freshly polished medium carbon steel surface measured using a tubular flow electrode at a velocity of 4 m/s. Extrapolation of this decay curve to 0.1 s yields an i_{corr} of 31 mA/cm², which coincides with the measured i_{corr} for the throat-eye area at 10 percent Q after exposure of 100 min. Moreover, the mass-transfer calculation on the basis of the Chilton-Colburn correlation [4] yields a maximum corrosion current density of 16.9 mA/cm² for the tubular flow electrode used. This lies in the order of the experimental data.

If we assume that this relation holds for higher velocity, for example, at the

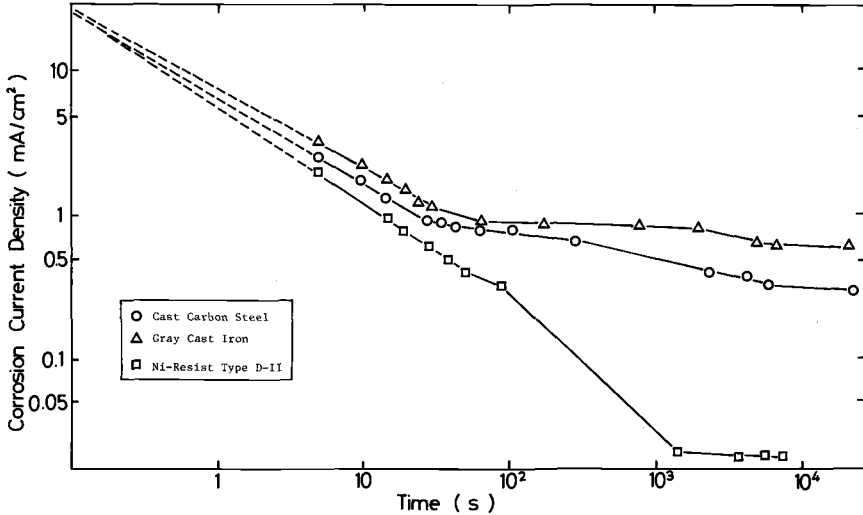


FIG. 9—Time behavior of corrosion current density for three different metals determined at 4 m/s using tubular flow electrodes.

reversed flow velocity of 15.5 m/s at 10 percent Q , we would expect a maximum i_{corr} of 51 mA/cm². This in turn agrees with the value measured for the throat-eye area at 10 percent Q after exposure for 150 min.

The corrosion current density measured for the throat-eye area before 60 min of exposure may be regarded as that of the oxide covered surface. When this surface layer is imploded with the reversed flow induced cavitation bubbles, this layer may be destroyed when the bubbles have sufficient intensity. It is considered that after the removal of this surface layer, the throat-eye area will be directly loaded by the bubbles. When the rate of the formation of the surface layer is higher than the destruction rate, the corrosion current would be determined by the diffusion rate of oxidizing agents to the surface or the rate of their electrochemical reduction at the surface. It appears that the result obtained at exposure less than 60 min can be discussed as the corrosion of electrode covered with corrosion products. In this period numerous pits were formed as a result of imploding bubbles (Fig. 10). After 60 min of exposure, turbulences created by the pits may decrease the average thickness of the surface layer and increase the intensity of cavitation. The locations of the implosions of the bubbles also increase as a result of the formation of the pits. After exposure of 100 min, the rate of destruction of the surface layer completely surpasses the rate of formation, and the corrosion current density approaches that of the complete bare surface.

The effect of cavitation on the metal surface can be classified as plastic deformation, which increases surface area and destruction and removal of the surface layer. Each effect causes enhancement of corrosion, so that elec-

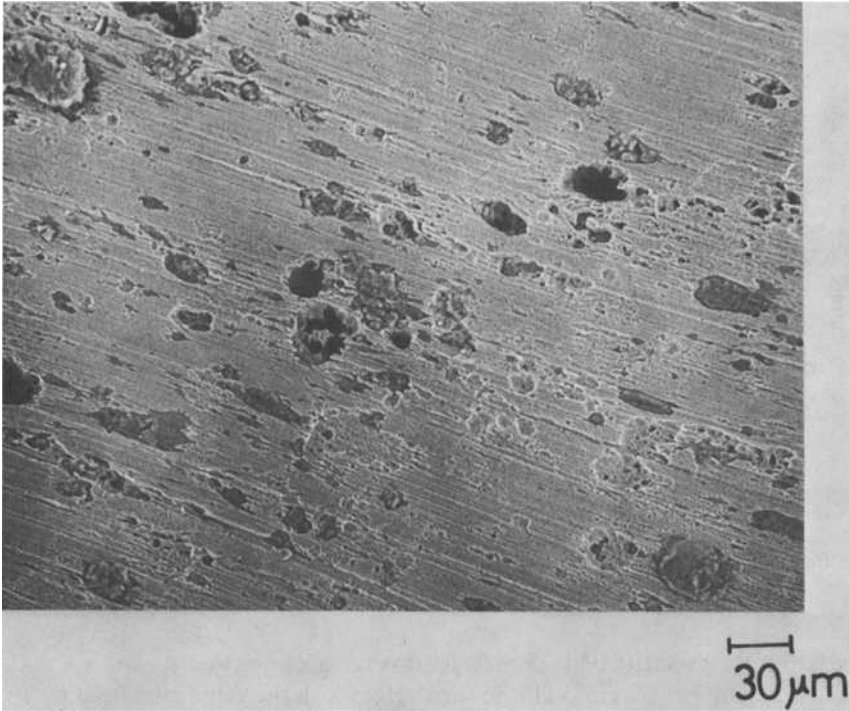


FIG. 10—Pitted electrode surface mounted at the throat-eye area.

trochemical measurements can integrate all these effects as well as the effect of dissolution of metals and the formation of the surface layer.

Figure 11 shows i_{corr} for the throat-eye area after exposure for 100 min at each flow quantity in a nonchlorinated water. In contrast to the result in the chlorinated water, no sharp increase in i_{corr} at 10 percent Q was observed, while numerous pits were observed on the test electrode after the measurement.

It may be premature to conclude that the absence of the sharp rise in the corrosion current density at the reduced flow quantity is correlated to the absence of chlorine in the water. It has been observed, however, that chlorine in the water enhanced both anodic and cathodic reaction, especially at higher flow velocity, thus resulting in localized corrosion acceleration [5]. It therefore appears reasonable to assume that chlorine aids the localized dissolution of the covered surface and causes localized disturbances such as pits. These result in a shortening of the incubation period for cavitation to result in the bare metal surface being exposed to the corrosive environment.

Even though it is not possible to separate the events taking place during cavitation bubble implosion, it may be concluded that the electrochemical

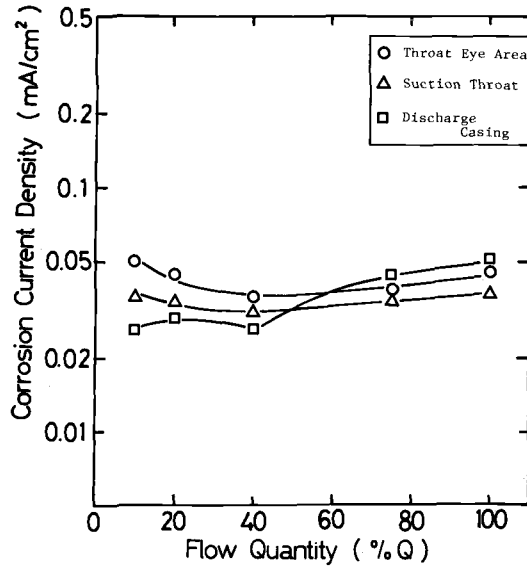


FIG. 11—Corrosion current density determined after exposure of 100 min as a function of flow quantity in the nonchlorinated water.

technique is a useful tool in determining the role of cavitation and corrosion in cavitation-corrosion.

Conclusions

Electrochemical measurements were applied for determination of the roles of cavitation and corrosion in pump-casing damage. It was found that cavitation induced from the reversed flow, originating from the impeller inlet under partial flow conditions, resulted in very high corrosion current density (50 mA/cm^2) for the throat-eye area of the suction casing.

This high corrosion current density is considered to be brought by the conjoint action of corrosion and cavitation, in which cavitation brings the metal surface into the oxide-free surface and corrosion takes place at this oxide-free surface.

References

- [1] Murakami, M. and Heya, N., *Transactions, Japanese Society of Mechanical Engineers*, Vol. 31, 1965, p. 1060.
- [2] Toyokura, T., *Transactions, Japanese Society of Mechanical Engineers*, Vol. 26, 1960, p. 1069.
- [3] Mansfeld, F. in *Advances in Corrosion Sciences and Technology*, Vol. VI, Plenum Press, New York, 1976, p. 163.
- [4] Postlethwaite, J. and Hurp, D. R., *Corrosion Science*, Vol. 7, 1967, p. 435.
- [5] Ishikawa, Y. and Ozaki, T., submitted to *Corrosion Engineering (Boshoku Gijutsu)*.

A Method of Evaluating Polarization Curves for Stainless Steel via a Simple Passivation Model

REFERENCE: Bernhardsson, S.-O. and Mellström, Rolf, "A Method of Evaluating Polarization Curves for Stainless Steel via a Simple Passivation Model," *Electrochemical Corrosion Testing. ASTM STP 727*, Florian Mansfeld and Ugo Bertocci, Eds., American Society for Testing and Materials, 1981, pp. 352-364.

ABSTRACT: If it is assumed that the passivation process of stainless steels in acid solutions follows Langmuir's adsorption isotherm, a relatively simple function is obtained that describes the form of an anodic polarization curve. This function has been adapted to experimental results obtained with stainless steels in sulfuric acid in order to study the effect of alloying elements on the rate of different partial reactions. Adjustment to experimental data can be effected by nonlinear regression analysis or by a simpler manual method. The results show that, among other things, chromium in concentrations ≥ 12 percent accelerates anodic dissolution and passivation, while nickel and molybdenum have the contrary effect.

KEY WORDS: stainless steels, electrochemical kinetics, passivation, corrosion

Measurement of polarization curves for stainless steels in acids is a commonly applied method. Often the purpose of such measurements is to obtain a relative measure of the resistance of a steel to a particular solution and to examine the effect of alloying elements or the effect of variations in the composition of the solution on the form of the polarization curve. Some parameters studied in these cases are the maximum current density, i_{\max} , and the passivation potential E_{pp} . In certain cases a closer analysis of the form of the polarization curve is desirable in order to arrive at a better understanding of the corrosion processes that take place.

Efforts have been made at a relatively early stage to evaluate polarization curves more accurately [1],² though with a limited amount of success. More recently, alternative methods have been indicated for evaluating stainless steel polarization curves [2]. More detailed consideration is given to these methods and their applications in the present report.

¹ Manager, Product Development of Stainless Steels, and head, Wet-Corrosion Laboratory, respectively, Sandvik AB, Sandviken, Sweden.

² The italic numbers in brackets refer to the list of references appended to this paper.

Experimental

Table 1 shows the composition of the alloys investigated. The alloys were forged and quench-annealed at 1050°C/20 min (austenitic alloys) or 820°C/20 min (ferritic alloys). Their structures were consistently single phased. Diffusion annealing was performed to eliminate segregations.

The test surface in the stationary or rotating disk electrode was vertical so as to avoid accumulations of hydrogen bubbles. The test surface was diamond polished and then washed with ethanol and distilled water. The test solutions were made from distilled and de-ionized water together with sulfuric acid (H_2SO_4) and sodium sulfate (Na_2SO_4) *pro analysi*. A mercury/mercury sulfate (Hg/Hg_2SO_4) electrode served as reference electrode. The counter (platinum) electrode was placed in a special electrode compartment connected to the cell via a glass filter. The solutions were de-aerated for 1 h before the measurements; during the measurements they were de-aerated with argon purified in pyrogallol. Before the measurements the specimen was freely corroding in the solution for 1 min, after which it was activated for 5 min at -600 mV saturated calomel electrode (SCE) for austenitic alloys and -750 mV SCE for ferritic alloys. All measurements were made at room temperature.

Passivation Mechanism

There are essentially two mechanisms for the anodic passivation of metals and alloys [3]: (1) chemisorption (solid-state reaction), and (2) dissolution-precipitation. Investigations have shown that chemisorption applies to chromium [4] and nickel [5] in acid solutions (contradictory results have been obtained for nickel [6]). Armstrong [3] has suggested that investigations with a rotating disk electrode (RDE) can be used to distinguish between chemisorption and dissolution. If the RDE is made to rotate faster, the transport of metallic ions away from the surface increases. Therefore, if dissolution-precipitation applies, the shape of the polarization curve must be influenced by a change in the speed at which the RDE rotates; if chemisorption applies, the curve will not be influenced in this way.

To ascertain the passivation mechanism of stainless steels in sulfuric acid solutions, AISI 304 and 316 were tested in 1 M H_2SO_4 at a sweep rate of 20 mV/min and at rotation speeds between 1 to 60 rps. The speed of rotation did not significantly influence the shape of the polarization curves of any of the alloys. The tests were also conducted at a constant potential equal to the passivation potential at different rotation speeds. Variations in the speed of rotation did not have any effect in this case either.

Therefore none of the anodic partial reactions occurring in these steels in 1 M H_2SO_4 is mass transport controlled. This implies that passivation occurs without the metallic ions that form the passive film escaping into the solution. The first layer of the passive film is thus formed between metallic

TABLE 1—Composition of alloys investigated, percentages by weight.

Alloy No.	Grade	C	Si	Mn	P	S	Cr	Ni	Mo	N	Cu
1	AISI 316L	0.03	0.6	1.7	0.030	0.030	17.5	13.5	2.7
2	15.7Cr	0.003	≤0.02	≤0.05	0.007	≤0.003	15.7	≤0.10	≤0.03	0.003	≤0.005
3	23.6Cr	0.003	≤0.02	≤0.05	0.006	≤0.003	23.6	≤0.10	≤0.03	0.003	≤0.005
4	15.6Cr-10.1Ni	0.003	≤0.02	≤0.05	0.007	≤0.003	15.6	10.1	≤0.03	0.003	≤0.005
5	15.7Cr-15.4Ni	0.003	≤0.02	≤0.05	0.007	≤0.003	15.7	15.4	≤0.03	0.002	≤0.005
6	17.4Cr-14Ni-0.78Si	0.014	0.78	1.7	0.005	0.010	17.4	13.95	0.03	0.029	0.016
7	17.8Cr-13.4Ni-3.9Si	0.014	3.9	0.73	0.010	0.008	17.8	13.4	0.04	0.033	0.017
8	15.8Cr-19.8Ni-0.17Mo	0.003	≤0.02	≤0.05	0.006	0.003	15.8	19.8	0.17	0.002	≤0.005
9	15.6Cr-19.8Ni-4.05Mo	0.003	≤0.02	≤0.05	0.013	0.003	15.6	19.8	4.05	0.002	≤0.005

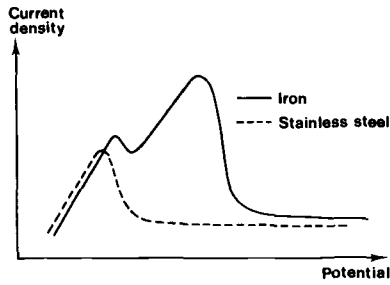


FIG. 1—Schematic polarization curves for iron and stainless steel.

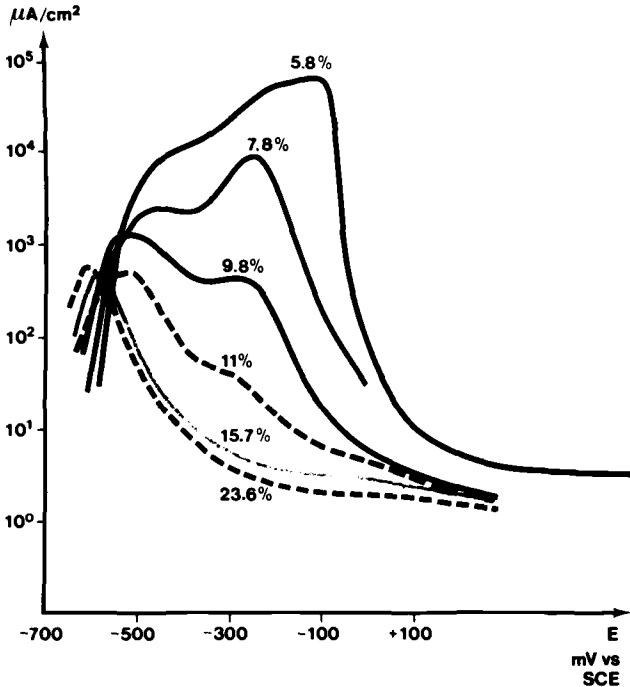


FIG. 2—Polarization curves of FeCr alloys in 0.01 M H_2SO_4 + 0.99 M Na_2SO_4 , 20 mV/min.

According to this sequence, a kinetic model for stainless steels should assume a simpler form than the one for iron. The following factors however, complicate the situation:

1. Certain alloying elements can be enriched on the surface both in metallic and in oxide form.

2. The alloying components can influence the mechanism or RDS, which may therefore differ from one alloy to another.

3. Since different types of atoms have different reactivities, the addition of different alloying elements can affect the active sites where the reactions normally occur.

These problems will not be dealt with at any great length in the present discussion.

The Langmuir isotherm has been chosen to describe the passivation process. The Temkin isotherm has been applied in one case, but has not yielded any substantial improvement as regards the adjustment of experimental data to the model obtained. The reason for this result may be that the error in the measurement of the polarization curves is of the same magnitude as the error in the model if not larger.

The total anodic current density, i_T , for a stainless steel can be written as [13]

$$i_T = (i_a + i_{ox}) \cdot (1 - \theta) \quad (3)$$

where

- i_a = partial current density originating from anodic dissolution,
- i_{ox} = partial current density from anodic passivation, and
- θ = degree of coverage of $M(OH)_{3ads}$.

The Langmuir isotherm can be formulated as

$$C \cdot \frac{d\theta}{dt} = k_{ox} \cdot (1 - \theta) - k_D \cdot \theta \quad (4)$$

where k_{ox} ($\text{mol}/\text{cm}^2 \cdot \text{s}$) is potential dependent, and k_D ($\text{mol}/\text{cm}^2 \cdot \text{s}$) is potential independent. k_D is presumed to be equally large for the primarily formed passive film and the thicker passive film at higher potentials. C (mol/cm^2) is a measure of the amount of species adsorbed to the surface. In the steady state

$$C \cdot \frac{d\theta}{dt} = 0 \quad (5)$$

that is,

$$\theta = \frac{k_{ox}}{k_{ox} + k_D} \quad (6)$$

Multiplication by $Z \cdot F$, where Z , the charge-transfer valence, is assumed to be the same both for k_D and for k_{ox} , and F is Faraday's constant, gives

$$\theta = \frac{i_{ox}}{i_{ox} + i_D} \quad (7)$$

Combining Eqs 1 and 7 leads to

$$i_T = \frac{i_D \cdot (i_a + i_{ox})}{i_D + i_{ox}} \quad (8)$$

i_a and i_{ox} are expressed as

$$i_a = A_a \cdot \exp(B_a \cdot E) \quad (9)$$

$$i_{ox} = A_{ox} \cdot \exp(B_{ox} \cdot E) \quad (10)$$

where E is the potential,

$$A_i = i_i^0 \cdot \exp(-B_i \cdot e_i^0) A / \text{cm}^2 \text{ versus } E_{\text{ref}} \quad (11)$$

and

$$B_i = 2.303/b_i \text{ mV}^{-1} \quad (12)$$

where

b_i = Tafel slope,

i_i^0 = exchange current density, and

e_i^0 = single equilibrium potential.

It should be noted here that the value of A_i depends on the reference potential chosen. Equation 8 can thus be written as

$$i_T = \frac{i_D [A_a \cdot \exp(B_a \cdot E) + A_{ox} \cdot \exp(B_{ox} \cdot E)]}{i_D + A_{ox} \cdot \exp(B_{ox} \cdot E)} \quad (13)$$

i_T is a function describing the form of a polarization curve with one maximum. It is easily shown that i_T is dependent, to a greater or lesser degree, on all parameters in Eq 13. Ebersbakh et al [13] have discussed the implications and validity of Eq 13, though formulated in a somewhat different way. A certain set of parameter values gives the results shown in Fig. 3.

Evaluation Methods

Equation 13 can be used to simulate polarization curves and thus increase the understanding of the importance of different processes. But more valuable is the fact that it can be used to further evaluate polarization curves.

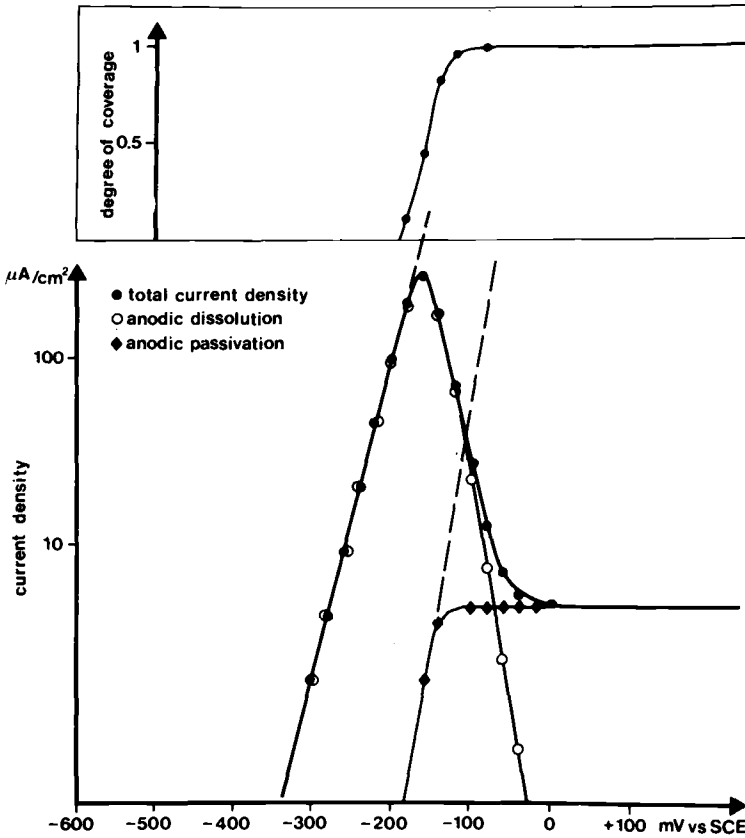


FIG. 3—Calculation of total current density, partial current densities, and degree of coverage with Eq 13.

Two evaluation methods can be used: (1) a manual method, and (2) adjustment by nonlinear regression.

Manual Method

Figure 3 shows that the only reaction which, according to the model, occurs at lower potentials is anodic dissolution. This means that A_a and B_a can be determined from this portion of the curve. Figure 3 also shows that in the potential area where i_T decreases with increasing potential

$$i_a \gg i_{ox} \gg i_D \quad (14)$$

For this area, therefore, Eq 13 can be rewritten as

$$i_T = \frac{i_D \cdot A_a \cdot \exp(B_a \cdot E)}{A_{ox} \cdot \exp(B_{ox} \cdot E)} \quad (15)$$

or

$$i_T = i_D \cdot \frac{A_a}{A_{ox}} \exp[E(B_a - B_{ox})] \quad (16)$$

Logarithmically we obtain

$$\log i_T = \log \left(i_D \cdot \frac{A_a}{A_{ox}} \right) + E \cdot (B_a - B_{ox}) \cdot 2.303 \quad (17)$$

Since

$$\frac{\sigma \log i_T}{\delta E} = (B_a - B_{ox}) \cdot 2.303 \quad (18)$$

B_{ox} can be determined from this portion of the curve (compare Fig. 4) while i_D is taken as the lowest current density in the passive range, whereupon A_{ox} can be calculated with the aid of Eq 16. In this way the rate constants in Eq 13 can be determined using a ruler and calculator.

In the acidic solutions in which polarization curves for stainless steels are often measured, hydrogen is generated at high rate at lower potentials. Sometimes, therefore, it can be difficult to determine A_a and B_a simultaneously with acceptable accuracy because the cathodic reaction and the anodic dissolution reaction overlap and i_{max} is small. In these cases B_a is taken to equal 0.0575 mV^{-1} , which corresponds to a Tafel slope of 40 mV/decade; this has proved a good average in many studies in our laboratory.

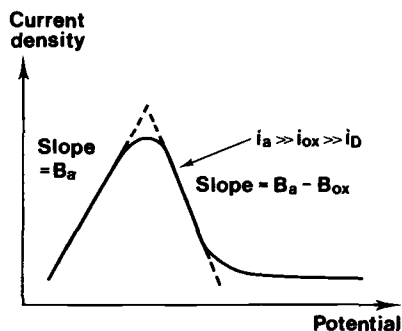


FIG. 4—Manual Tafel slope determination from polarization curves.

Adjustment by Nonlinear Regression Method

Experimental data have been adjusted to Eq 13 by using a method based on the Gauss-Newton method [14] and also by means of LETAGROP [15].

The Gauss-Newton method, as it is applied here, does not allow more than two parameters to be adjusted simultaneously because otherwise a divergency is very liable to be obtained. Usually, therefore, the parameters A_a and B_a have been determined from four measuring points on the first part of the curve, i_D has been taken as i_{\min} , and adjustment has then been carried out by the Gauss-Newton method to determine A_{ox} and B_{ox} .

LETAGROP has the advantage of being more flexible. A larger number of parameters is permissible with this program, negative additions to the constants sought for are avoided, and, if a divergency occurs, conjectural parameter values can be adjusted. If, however, the initial value of the parameters is far removed from the values sought, convergence can be very slow. It is therefore advisable to supplement LETAGROP with a linear search method, or else to begin calculations with the initial values from the manual method.

Applications

The evaluation methods described previously have been used on a large number of alloys. The nonlinear regression methods have been used particularly often, the manual method in fewer cases.

Efforts made to obtain an analytical expression containing the sweep rate showed that this is not possible. Because steady-state measurements are difficult to carry out in practice, evaluation has been based on curves recorded at sweep rates of 2 to 20 mV/min under the assumption that these rates will give conditions close to steady state.

Table 2 shows the results from the evaluation of the polarization curve for AISI 316L, measured in 1 M H_2SO_4 , with a sweep rate of 2 mV/min at room temperature. The results obtained from the two different methods agree fairly well. Figure 5 compares experimental and calculated values for AISI 316L for the case when the Gauss-Newton method was used.

TABLE 2—Rate constants for partial anodic reactions on AISI 316L in 1 M H_2SO_4 , room temperature, 2mV/min. A_a , A_{ox} are given versus SHE.^a $i_D = 0.45 \mu A/cm^2$.

	Manual Method	Gauss-Newton Method
Anodic dissolution, A_a	0.26 mA/cm ²	0.26 mA/cm ²
Anodic dissolution, B_a	0.064 mV ⁻¹	0.064 mV ⁻¹
Tafel slope	(=36.3 mV/decade)	(=36.2 mV/decade)
Anodic passivation, A_{ox}	0.051 mA/cm ²	0.069 ± 0.019 mA/cm ²
Anodic passivation, B_{ox}	0.087 mV ⁻¹	0.092 ± 0.001 mV ⁻¹
Tafel slope	(=26.4 mV/decade)	(=25.1 ± 0.2 mV/decade)

^aSHE = standard hydrogen electrode.

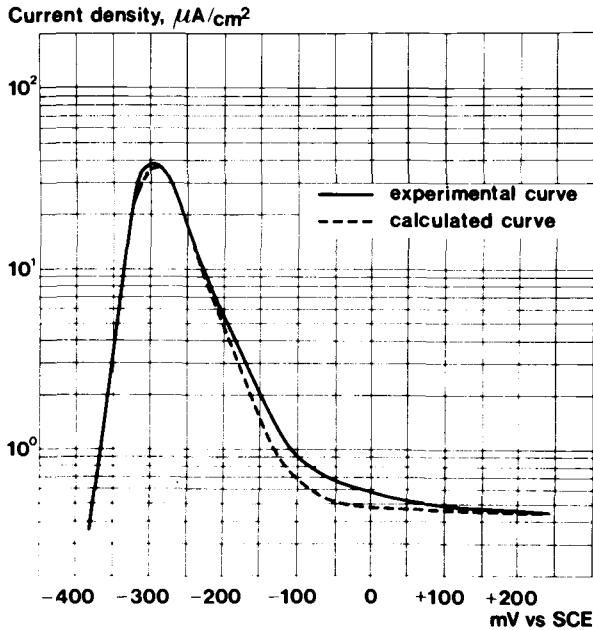


FIG. 5—Comparison between experimental and calculated polarization curves for AISI 316L.

The Gauss-Newton method has also been applied to other alloys. The results given in Table 3 show that the addition of chromium increases the rates of anodic dissolution and passivation parameters, and that nickel has the opposite effect. Silicon has a weak effect on the rate constants, while molybdenum decreases A_u very much, but in contrast to nickel, molybdenum does not change A_{ox} to any great extent. It can be seen that B_{ox} often assumes a value between 0.09 to 0.10. This agrees with what is expected from the proposed mechanism (Eq 2), since the theoretical value for a rate determining step (RDS) preceded by two charge-transfer steps and with $Z = 3$ would be 0.096 mV^{-1} .

Conclusions

The assumption that the passivation process follows the Langmuir adsorption isotherm gives a function that well describes the polarization curves for stainless steels in sulfuric acid. By using this function, polarization curves can be evaluated to give an increased understanding of the influence of alloy and solution composition on the passivation behavior of stainless steels. The evaluation can be made either by a manual method (using a ruler and calculator) or by a nonlinear regression method.

TABLE 3—Rate constants for partial anodic reactions for different alloys in sulfuric acid (ambient temperature). A_a , A_{ox} are given versus SHE.^a

Alloy Composition, wt. %	Solution	Sweep Rate	i_{max} , mA/cm ²	E_{pp} , mV SCE ^c	A_a , mA/cm ²	B_a , mV ⁻¹	A_{ox} , mA/cm ²	B_{ox} , mV ⁻¹	iD , μ A/cm ²
15.7Cr	1 M H ₂ SO ₄	10 mV/5 min ^b	23.1	-400	2.2 · 10 ⁶	0.0575	2.0 · 10 ⁴	0.098	0.45
23.6Cr	1 M H ₂ SO ₄	10 mV/5 min ^b	18.2	-455	8.6 · 10 ⁶	0.0575	2.6 · 10 ⁷	0.12	0.23
15.6Cr-10.1Ni	1 M H ₂ SO ₄	10 mV/5 min ^b	1.3	-340	1.4 · 10 ⁴	0.0575	2.7 · 10 ²	0.090	1.1
15.7Cr-15.4Ni	1 M H ₂ SO ₄	10 mV/5 min ^b	1.1	-300	2.5	0.0575	0.06	0.098	0.34
17.4Cr-14Ni-0.78Si	1 M H ₂ SO ₄	20 mV/min	8.4	-261	88	0.0575	0.04	0.097	1.9
17.8Cr-13.4Ni-3.9Si	1 M H ₂ SO ₄	20 mV/min	5.7	-264	85	0.0575	0.04	0.091	1.5
15.8Cr-19.8Ni-0.17Mo	2 M H ₂ SO ₄	20 mV/min	5.8	-230	1.57	0.0575	6.9 · 10 ⁻⁴	0.094	1.2
15.6Cr-19.8Ni-4.05Mo	2 M H ₂ SO ₄	20 mV/min	0.074	-164	0.01	0.0575	1.2 · 10 ⁻⁴	0.075	1.3

^aSHE = standard hydrogen electrode.

^bPotentiostatically.

^cSCE = saturated calomel electrode.

References

- [1] Mueller, W. A., *Journal of the Electrochemical Society*, Vol. 107, 1960, p. 157.
- [2] Bernhardsson, S., *Extended Abstracts*, 25th International Society of Electrochemistry meeting, Brighton, 1974.
- [3] Armstrong, R. D., *Corrosion Science*, Vol. 11, 1971, p. 693.
- [4] Armstrong, R. D., *Journal of Electroanalytical Chemistry and Interfacial Electrochemistry*, Vol. 35, 1972, p. 119.
- [5] Ebersbakh, U., Schwabe, K., and König, P., *Electrochimica Acta*, Vol. 15, 1969, p. 773.
- [6] Bockris, J. O. M., Reddy, A. K. N., and Rao, B., *Journal of the Electrochemical Society*, Vol. 113, 1966, p. 1133.
- [7] Nord, H. and Bech-Nielsen, G., *Electrochimica Acta*, Vol. 16, 1971, p. 849.
- [8] Bech-Nielsen, G., *Electrochimica Acta*, Vol. 21, 1976, p. 627.
- [9] Miligy, A. A., Geana, D., and Lorenz, W. I., *Electrochimica Acta*, Vol. 20, 1975, p. 273.
- [10] Bessone, J., Karakaya, L., Lorbeer, P., and Lorenz, W. I., *Electrochimica Acta*, Vol. 22, 1977, p. 1147.
- [11] Oftedal, T. A., *Electrochimica Acta*, Vol. 18, 1973, p. 401.
- [12] Vetter, K. I. and Gorn, F., *Electrochimica Acta*, Vol. 18, 1973, p. 321.
- [13] Ebersbakh, U., Schwabe, K., and Ritter, K., *Electrochimica Acta*, Vol. 12, 1967, p. 927.
- [14] Karlsson, F. and Westin, R., *Chemica Scripta*, Vol. 2, 1972, p. 207.
- [15] Sillén, L. G., *Acta Chemica Scandinavica*, Vol. 16, 1962, p. 11.

Effect of Large Voltage Modulations on Electrodes Under Charge-Transfer Control

REFERENCE: Bertocci, Ugo and Mullen, J. L., "Effect of Large Voltage Modulations on Electrodes Under Charge-Transfer Control," *Electrochemical Corrosion Testing, ASTM STP 727*, Florian Mansfeld and Ugo Bertocci, Eds., American Society for Testing and Materials, 1981, pp. 365-380.

ABSTRACT: The experimental test of the validity of a mathematical treatment of the effect of large a-c voltage modulations on the behavior of electrodes under charge-transfer control was carried out for the case of the hydrogen evolution reaction. A frequency analysis of the resulting current showed that both d-c and a-c components of the faradaic current were in quantitative agreement with the predictions of the mathematical model. Deviations from the calculated values, which were observed in certain conditions (particularly at higher frequencies), were explained as the effect of the ohmic-drop error.

KEY WORDS: alternating current enhanced corrosion, alternating current modulation, charge transfer control, frequency analysis, hydrogen evolution

In a large number of practical situations metallic structures are subjected to alternating voltages that cause currents to flow into ionic conductors (the most common of which is soil) that are in contact with them. These currents might flow because of failure of insulation, but there are also cases where the metals are exposed without protection. There is therefore a substantial interest in understanding what role an alternating signal can play in affecting the kinetics of an electrode, so as to be able to predict when and to what extent corrosion can be caused by the effect of alternating currents [1-5].²

As a part of research carried out at the National Bureau of Standards (NBS) concerning the corrosion of copper concentric neutral cables, the conditions under which a-c enhanced corrosion could be expected were examined; consequently, a mathematical treatment was developed that described the current response of an electrode under charge-transfer control to a large sinusoidal modulation of the voltage. The possibility of measuring

¹Research chemist and chemist, respectively, Chemical Stability and Corrosion Division, Center for Material Science, National Bureau of Standards, Washington, D.C. 20234.

²The italic numbers in brackets refer to the list of references appended to this paper.

separately the faradaic and the capacitive components of the current was also examined. This led to the identification of the conditions necessary for such a separation [6].

The theoretical treatment showed the potential usefulness of frequency analysis for the recovery of information concerning the mechanism and rate of the electrode reaction, as well as data concerning the enhancement of the corrosion process.

The principal points of the mathematical treatment are briefly reviewed in this paper. The effects of ohmic-drop error on current measurements are discussed. Frequency analysis techniques are applied to an electrode under charge-transfer control, and the experimental results are compared with the theoretical predictions.

Mathematical Analysis

Faradaic Current

We will present here in a simplified form some of the results of the analysis that has been given in detail elsewhere [6]. For an electrode under charge-transfer control, the partial anodic or cathodic current can be expressed as

$$i_{dc} = I_0 \exp(AE) \quad (1)$$

where I_0 and A are positive for anodic processes and negative for cathodic ones. E is the electrode potential taken with respect to some convenient reference value. As is well known, Eq 1 can be used to express the total current in the so-called Tafel region, that is, when the partial current of opposite sign is very small.

If the voltage is sinusoidally modulated, so that

$$E = E_0 + V \sin \omega t \quad (2)$$

the expression for the faradaic current can be obtained, and by harmonic analysis the current can be separated into a constant (or dc as customarily called) component and into the various harmonics (of angular frequency ω , 2ω , . . . , $n\omega$) of the modulating signal.

It can be shown that the amplitude coefficients of each of these components can be expressed in the form

$$i_{f,n} = I_0 \exp(AE_0) \cdot F_n(A, V) \quad (3)$$

which can be rewritten as

$$i_{f,n} = i_{dc} * F_n(A, V) \quad (4)$$

because, in the absence of a modulating signal Eq 2 becomes $E = E_0$ and therefore

$$i_{dc}^* = I_0 \exp(AE_0) \quad (5)$$

Introduction of Eq 5 into Eq 3 gives Eq 4. The root means square (rms) value of each of these sinusoidal components of the faradaic current is

$$(i_{f,n})_{rms} = \sqrt{\frac{(i_{f,n})^2}{2}} \quad (6)$$

Equation 4 shows that every frequency component of the faradaic current is proportional to the current in the absence of modulation i_{dc}^* multiplied by an adimensional coefficient whose value depends only on the kinetic parameter A (which determines the Tafel slope) and on the amplitude V of the sinusoidal modulation. The index n indicates the order of the harmonics; zero designates the dc term. An obvious consequence of Eq 4 is that all frequency components of the faradaic current, when plotted against the electrode potential E_0 on a semilogarithmic scale, will exhibit the same Tafel slope as i_{dc}^* .

Additional information can be derived from the analysis of the phase relationships among the various current components. It can be shown that the components of the faradaic current of odd order ($\omega, 3\omega, 5\omega, \dots$) bear alternately a 0 or $\pm\pi$ phase relationship with the modulating signal, while the phase of the even ($2\omega, 4\omega, 6\omega, \dots$) components is shifted by $\pm\pi/2$ with respect to the modulating signal.

Reflecting the fact that the relaxation times for charge-transfer are extremely short, the factors F_n do not depend on the frequency of the signal, and therefore the amplitude of all the current components is independent of the frequency. It can also be shown that F_0 , the factor for the d-c component of the faradaic current, is always greater than 1, so that a sinusoidal modulation of the voltage produces a rectified current that increases the rate of the electrode reaction.

As is well known, the coefficient A is related to the Tafel slope b by the equation $A = \ln 10/b$. Therefore, since the factors F_n depend on A , if the anodic and cathodic Tafel slopes differ so will the cathodic and anodic F_n factors. In such a case the effect of a sinusoidal voltage modulation will be different on the anodic and cathodic d-c partial currents, and consequently the intersection of the Tafel lines, which determines the potential at which no direct current flows, will be shifted.

Capacitive Current

For the analysis of the effect of an alternating voltage on an electrode it is necessary to consider the capacitive current i_c as well, since the electrode-

solution interface constitutes a circuit with a capacitance and resistance in parallel. Therefore the total current is

$$i = i_f + i_c \quad (7)$$

The electrode capacitance in general varies with potential; it is strongly affected by adsorption phenomena, some of which can be rather slow, so that relaxation times can be large compared with variations in electrode potential.

In many instances, however, the capacitance is only a function of potential, and often its variations can be relatively minor within certain potential ranges. The analysis has shown that if the electrode capacitance is a function of potential only, a sinusoidal modulation as in Eq 2 does not cause any d-c component of i_c . Moreover, it can be shown that its odd harmonic components ($\omega, 3\omega, 5\omega, \dots$) are shifted by $\pm \pi/2$ with respect to the modulating signal, while the even components are shifted by 0 or π .

Comparison of these phase shifts with those of the faradaic current shows that when the hypotheses employed in this analysis are applicable, it is possible to separate the faradaic and capacitive components of the current, provided that phase information is available.

Ohmic-Drop effects

The theoretical treatment assumes that no ohmic-drop error, R_Ω , is included into the circuit to which the voltage given by Eq 2 is applied. In practice, however, R_Ω is never zero; this can substantially affect the values measured experimentally, which causes a frequency dependence when, according to the theory, none should be found. A careful analysis of the effects of the ohmic drop is therefore necessary in order to examine to what extent it can explain some apparent discrepancies between theoretical predictions and experimental results.

The response of the working electrode to the voltage signal E given by Eq 2 can be described (neglecting the phase relationships between different frequency components) by the equivalent circuit of Fig. 1, to which a new voltage signal $E' = E_0 + V \sum_{1k}^\infty \sin(k\omega t)$ is applied. Each frequency component of the current is then separated by a tuned filter F before dividing into a faradaic component through a resistor R_n (with n indicating the order of the harmonics) and a capacitive component through a capacitance C_n . The constant, or d-c, component obviously has no capacitive counterpart. All current components will flow through the ohmic-drop resistor R .

The value of the resistances R_n can be obtained from Eq 3, since R_n is the derivative of E_0 with respect to $i_{f,n}$.

$$R_n = \frac{dE_0}{di_{f,n}} = \frac{1}{Ai_{f,n}} = \frac{1}{AI_0 \exp(AE_0)F_n(A, V)} = \frac{R_0^*}{F_n(A, V)} \quad (8)$$

where R_0^* is the charge-transfer resistance for the electrode at the potential E_0 in the absence of sinusoidal voltage modulation.

The values of C_n depend on how the double-layer capacitance varies with potential. If we assume that its variation in the range of potentials investigated is negligible, then

$$C_1 = C_{dl} \tag{9}$$

while all other C_n , for $n > 1$, are equal to zero.

Experimental observations on the electrode employed for this work have shown that C_n for $n > 1$ are small, and that Eq 9 is a good approximation.

Once the values to be assigned to the components in the circuit of Fig. 1 are calculated, it is possible to calculate the in-phase and out-of-phase components of the current at angular frequency $n\omega$. Calling

$$\alpha = 1 + (n\omega C_n R_n)^2 \tag{10}$$

$$\beta = R_\Omega (1 + [n\omega C_n R_n]^2) + R_n \tag{11}$$

$$\delta = n\omega C_n R_n^2 \tag{12}$$

we have

$$(i'_{n\omega})_{\text{rms}} = \frac{V}{\sqrt{2}} \frac{\alpha\beta}{\beta^2 + \delta^2} \tag{13}$$

and

$$(i''_{n\omega})_{\text{rms}} = \frac{V}{\sqrt{2}} \frac{\alpha\delta}{\beta^2 + \delta^2} \tag{14}$$

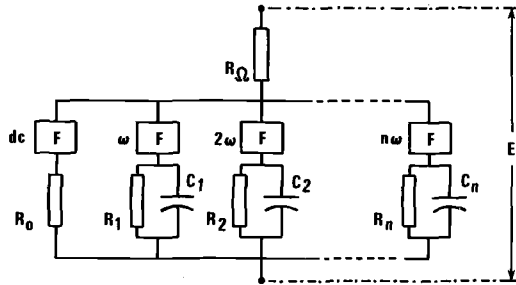


FIG. 1—Equivalent circuit of the electrode/electrolyte system under large sinusoidal voltage modulation.

It is easy to show that if the ohmic-drop resistance goes to zero Eqs 13 and 14 revert to the theoretical values $(i'_{n\omega})_{\text{rms}} = V/\sqrt{2}R_n$ and $(i''_{n\omega})_{\text{rms}} = n\omega C_n V/\sqrt{2}$.

It is also interesting to evaluate the effect of varying the average electrode potential E_0 , upon which, as shown by Eq 8, R_n depends exponentially. At high overvoltages, that is, for values of E_0 such that the direct-current density i_{dc}^* is large and R_n is small with respect to R_Ω , Eq 13 and 14 become

$$\lim_{R_n \rightarrow 0} (i'_{n\omega})_{\text{rms}} = \frac{V}{\sqrt{2}R_\Omega} \quad (15)$$

and

$$\lim_{R_n \rightarrow 0} (i''_{n\omega})_{\text{rms}} = \lim_{R_n \rightarrow 0} \frac{n\omega C_n R_n^2 V}{\sqrt{2}R_\Omega} = 0 \quad (16)$$

The current becomes independent of R_n and is limited only by the ohmic-drop resistance. On the other hand, when E_0 is shifted to values where the current density is small, R_n becomes larger, so that $(n\omega C_n R_n)^2 \gg 1$. Then

$$\lim_{R_n \rightarrow \infty} (i'_{n\omega})_{\text{rms}} = \frac{V}{\sqrt{2}} \frac{(n\omega C_n)^2 R_\Omega}{[1 + (n\omega C_n R_n)^2]} \quad (17)$$

and

$$\lim_{R_n \rightarrow \infty} (i''_{n\omega})_{\text{rms}} = \frac{V}{\sqrt{2}} \frac{n\omega C_n}{[1 + (n\omega C_n R_n)^2]} \quad (18)$$

These current values are proportional to the admittance of an RC series circuit, where the resistance is the ohmic-drop resistance R_Ω .

At both limits the in-phase current, instead of varying with E_0 on a Tafel slope, becomes constant, depending only on the ohmic drop R_Ω . One of the effects of an ohmic-drop error is that it introduces a phase shift in the current so that the identity between faradaic current and in-phase component is no longer true. This also introduces an additional dependence of the current components on frequency, which can be calculated from Eqs 13 and 14 by varying ω at constant E_0 .

In the next section it will be shown that the effects of the ohmic-drop resistance described here account well for the deviations from the theoretical behavior observed.

Experimental

Purpose of the Experimental Work

The distortion of the faradaic current that leads to an increase of the d-c current and can cause enhanced corrosion is not dependent on special conditions concerning the electrode surface, such as the presence of a rectifying semiconductor film, but is a consequence only of the nonlinearity of the current-voltage characteristics of the electrode, and therefore should be observed in a large class of electrode-electrolyte systems. The effect is graphically illustrated by the waveforms shown in Fig. 2, which are experimental recordings. The lower trace shows the sinusoidal voltage signal applied to the electrode; the upper trace is the current response, which shows the high degree of distortion that is the cause both of the rectification and of the appearance of harmonics of the modulating frequency.

The particular quantitative mathematical treatment employed here was developed for a specific case of kinetics (charge-transfer control), but should maintain a fair degree of applicability for the prediction of the behavior of electrodes having a more complex kinetics.

The main purpose of this work was verifying the validity of the mathematical model as quantitatively as possible. For this reason it was more convenient to choose an electrochemical system that was known to be under charge-transfer control over as wide a range of current densities as possible.

Experimental Methods

Experiments aimed at testing the validity of the theoretical model have been carried out on the hydrogen evolution reaction. The electrode material was OFHC copper, and the solution composition was $0.5 M Na_2SO_4$ (sodium sulfate) + $0.1 M H_2SO_4$ (sulfuric acid). By minimizing other cathodic reactions (in particular, oxygen reduction by bubbling argon in the cell) and favoring transport in solution by means of vigorous stirring, it was possible to obtain a straight cathodic Tafel plot with a slope of 120 mV/decade over a potential range larger than 300 mV .

As a further test of the applicability to the electrode under study of the hypothesis used in the mathematical analysis, the electrode impedance was measured by applying a very small ($< 2 \text{ mV}$) modulating signal about in the middle of the (d-c) potential range where a straight Tafel slope was obtained. The results are given in Fig. 3, where the imaginary component Z'' of the electrode impedance (for unit surface area) is plotted versus the real component Z' . The plot is approximately a semicircle, which indicates that there is no detectable contribution of transport to the electrode kinetics. From the plot the ohmic-drop error is found to be about $6 \Omega \cdot \text{cm}^2$, while the charge-transfer resistance is more than $400 \Omega \cdot \text{cm}^2$.

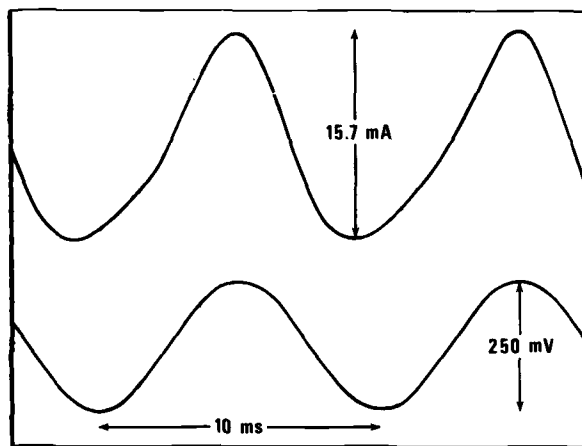


FIG. 2—Voltage input signal and current response for copper in $0.5 \text{ M Na}_2\text{SO}_4 + 0.1 \text{ M H}_2\text{SO}_4$.

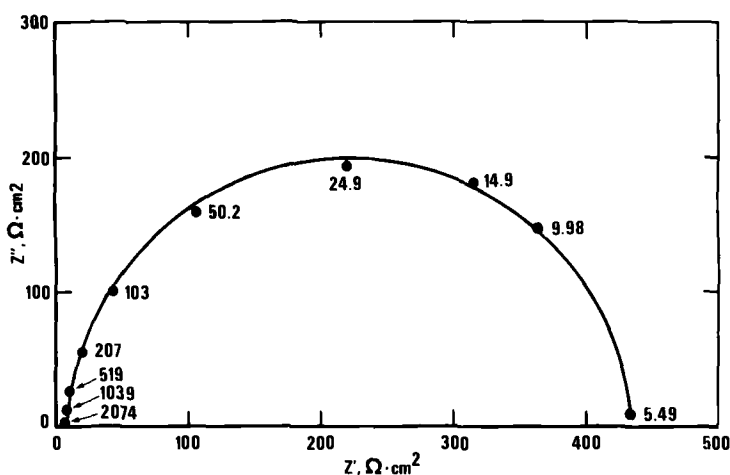


FIG. 3—Imaginary impedance Z'' versus real impedance Z' for copper in $0.5 \text{ M Na}_2\text{SO}_4 + 0.1 \text{ M H}_2\text{SO}_4$. $E_0 = -506 \text{ mV}$ versus NHE. Frequency as parameter.

The circuit employed for the measurements is schematically shown in Fig. 4. Two voltages, a constant one (E_0 of Eq 2) and a pure sinewave (of amplitude V), where higher harmonics had been minimized by filtering, were added and applied to the control voltage input of the potentiostat. A phase-sensitive lock-in amplifier measured the amplitude of the current both at frequency ω of the modulation and at twice that frequency, each one divided into the component in phase and the component in quadrature with the modulating signal. By means of the low-pass filters the d-c components of the

voltage (E_0) and of the current (i_{dc}) could be recorded. With the filters switched off, the total current and voltage signal could be stored in the digital oscilloscope and successively reproduced on the X-Y recorder in the form illustrated in Fig. 2. Inputs and outputs of the measuring system, with the symbols used here, are given in Table 1.

In a few instances the current signal was fed to a 200-channel spectrum analyzer. In this way the amplitude of higher-order harmonics could be ob-

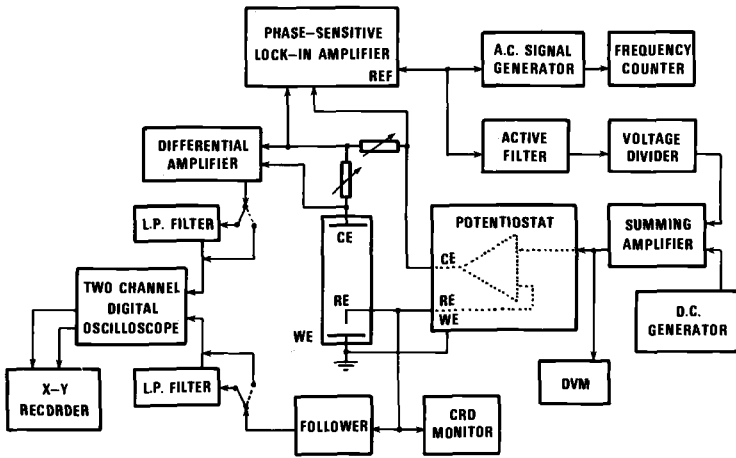


FIG. 4—Schematic diagram of the circuit used for the measurements.

TABLE 1—Input and output quantities.

Input Quantities			
E_0	V	$\omega = 2\pi\nu$	
d-c component of electrode potential	amplitude of modulating voltage	angular frequency of modulating voltage	
Output Quantities			
Constant (D-C)	Components	In Phase with Modulating Voltage	$\pm \pi/2$ with Respect to Modulating Voltage
i_{dc}^*	i_{dc}	i'_ω	i''_ω
current density for $V = 0$	current density for $V > 0$	current density at frequency ω	current density at frequency ω
		$i'_{2\omega}$	$i''_{2\omega}$
		current density at frequency 2ω	current density at frequency 2ω

tained. All phase information was lost, however, and only the absolute value of the current density of angular frequency $n\omega$ was obtained:

$$|i_{n\omega}| = \sqrt{(i'_{n\omega})^2 + (i''_{n\omega})^2}$$

Results and Discussion

Current-potential measurements in the absence and in the presence of a modulating sinusoidal voltage were carried out. Figure 5 shows the Tafel plot of i_{dc} in both conditions, as well as i'_{ω} , i''_{ω} , and $i''_{2\omega}$. The solid lines represent the theoretical values for the various components of the faradaic current calculated from the experimental values of i_{dc}^* by means of Eq 3. The factors $F_n(A, V)$ were calculated in accordance with the formulae given in Ref 6.

Linear Tafel behavior is exhibited by the d-c current between -350 and -650 mV versus normal hydrogen electrode (NHE). Above -350 mV the cathodic current becomes approximately independent of potential, the reaction being the reduction of the residual oxygen. Below -650 mV the deviations are caused by concentration polarization. When the modulating signal was applied, i_{dc} was larger than i_{dc}^* by a factor in good agreement with the theoretical one. The capacitive component i''_{ω} is largely independent of potential, which indicates that the electrode capacitance remains nearly constant in the range studied. In agreement with this conclusion the term $i'_{2\omega}$ was found to be negligibly small, which suggested that all higher harmonics of the current are almost exclusively faradaic.

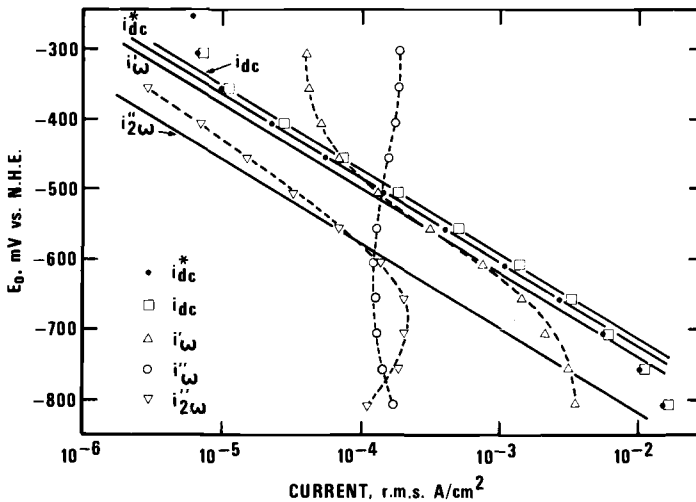


FIG. 5—Root mean square current density versus electrode potential for copper in 0.1 M $H_2SO_4 + 0.5 M Na_2SO_4$, with and without voltage modulation ($V = 50$ mV, $\nu = 25$ Hz). Solid lines are calculated values.

The current signal was also examined with a spectrum analyzer for a value of E_0 of -506 mV versus NHE, and a modulation at 25 Hz of 35.4 mV rms. The output values recorded during the spectrum analysis, as well as those obtained from the spectrum analyzer, are reported for comparison in Table 2, which also gives theoretical and experimental ratios between the various current components and the current density i_{dc}^* in the absence of modulation.

The values reported in Table 2 confirm that the capacitive currents at 2 ω and 3 ω are negligibly small, which is equivalent to saying that the double-layer capacitance varies very little in the electrode potential range (100 mV) covered by the modulation. The ratios are also in excellent agreement with the theory.

The spectrum is shown in Fig. 6 along with the spectrum obtained by substituting a pure resistor for the cell and passing a current of the order of 100 μ A rms at 25 Hz. The harmonic distortion is extremely small; the amplitude of the 50-Hz harmonics is below the detection limits (about 10^{-7} A), and could be measured at about $4 \cdot 10^{-8}$ A only after filtering out the large 25-Hz signal. As Fig. 6 shows, the only spurious signal detected was a 60-Hz peak at $5 \cdot 10^{-7}$ A. The small peak at about 20 Hz that can be seen on the side of the 25-Hz peak of the electrode current is caused by the magnetic stirrer and could be eliminated by shutting it off.

Another Tafel plot, for a larger modulation of 88.3 mV rms. ($V = 125$ mV) at 100 Hz, is shown in Fig. 7. The behavior of the d-c component is close to the theoretical prediction over a range of about 300 mV, but significant distortions can be seen in the other frequency components.

The main reason for the deviation from the theoretical behavior is the ohmic-drop error (discussed in a preceding section). The deviations can be accounted for quantitatively, as shown in Fig. 8, which reproduces in detail part of Fig. 7. Figure 8 shows the direct-current density, i_{dc}^* , in the absence of modulation and the experimental values of the a-c components of the current at the frequency of modulation ω . The dashed lines represent the theoretical values of i'_{ω} (from Eq 3) and of i''_{ω} (assuming a double-layer capacitance of 52 μ F/cm²) in the absence of ohmic-drop error. The dot-dashed lines are

TABLE 2—Values obtained from circuit in Fig. 2 and from spectrum analyzer. $E_0 = -506$ mV versus NHE.^a $V = 35.4$ mV rms at 25 Hz. Current density values in μ A/cm² rms.

	i_{dc}^*	i_{dc}	i'_{ω}	i''_{ω}	$/i_{\omega}/$	$i'_{2\omega}$	$i''_{2\omega}$	$/i_{2\omega}/$	$/i_{3\omega}/$
Circuit	186	238	152	161	221	0.1	32	32	...
Spectrum analyzer	215	31	7.3
Ratios		i_{dc}/i_{dc}^*		i'_{ω}/i_{dc}^*		$i'_{2\omega}/i_{dc}^*$		$i'_{3\omega}/i_{dc}^*$	
Theoretical		1.24		0.76		0.176		0.0276	
Found		1.28		0.82		0.17		0.039	

^aNHE = normal hydrogen electrode.

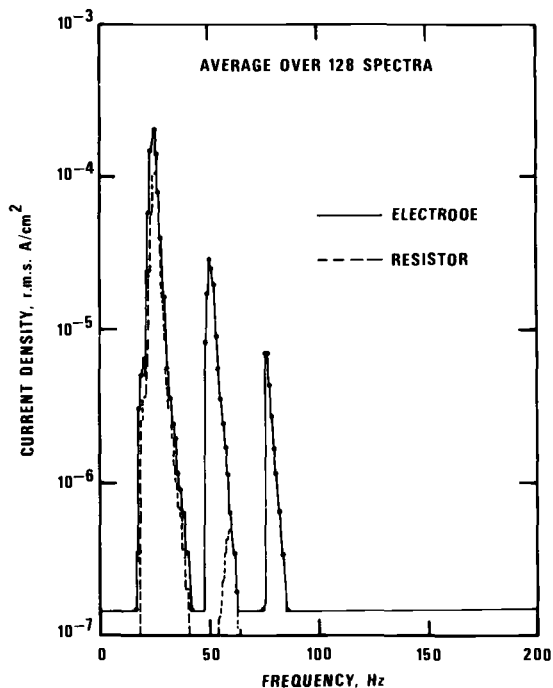


FIG. 6—Solid line: frequency spectrum of current density for a copper electrode in 0.1 M H_2SO_4 + 0.5 M Na_2SO_4 . $E_0 = -506$ mV versus NHE, $V = 50$ mV, $\nu = 25$ Hz. Scale is log (rms A/cm²) versus Hz. Average over 128 spectra. Dotted line: spectrum of current through resistor. Scale is log (rms A) versus Hz. Average over 128 spectra.

calculated from Eqs 13 and 14 for an ohmic-drop resistance of 6 Ω ; the value is obtained from the high-frequency end of the semicircle in Fig. 3. As Fig. 8 shows, the experimental values fall quite close to the calculated lines. It should be pointed out that no empirical, adjustable parameters enter these calculations once the Tafel slope for the current density in the absence of modulation (here shown as a solid line) is drawn through the experimental points.

Comparisons between the predictions of the amplitude of the faradaic components and the experimental values are summarized in Fig. 9. This shows the experimental ratios of i_{dc} , i'_{ω} , and $i''_{2\omega}$ to i_{dc}^* , and the theoretical lines. The agreement is very good for amplitudes V up to about 200 mV. Beyond that the current density caused by the modulation was less than predicted, because the electrode potential was being driven outside the linear Tafel range.

The effect of the frequency of the modulating signal has been also examined. Fig. 10 shows the ratio between the direct current i_{dc} and i_{dc}^* . The

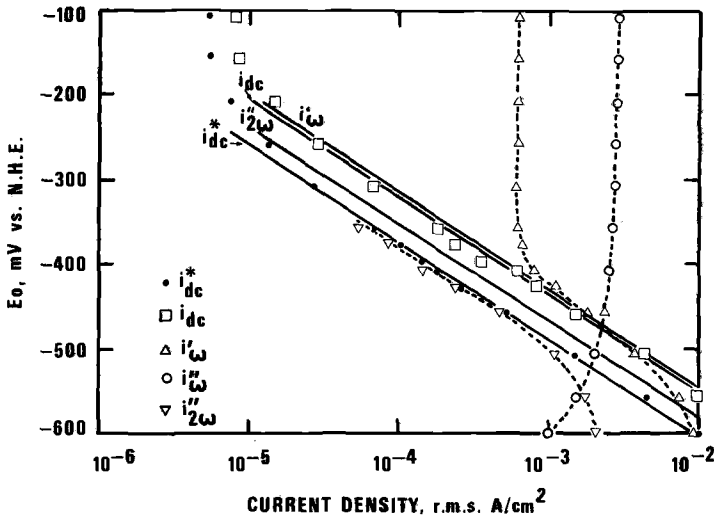


FIG. 7—Root mean square current density versus electrode potential for copper in 0.1 M $H_2SO_4 + 0.5 M Na_2SO_4$, with and without voltage modulation ($V = 125 mV, \nu = 100 Hz$). Solid lines are calculated values.

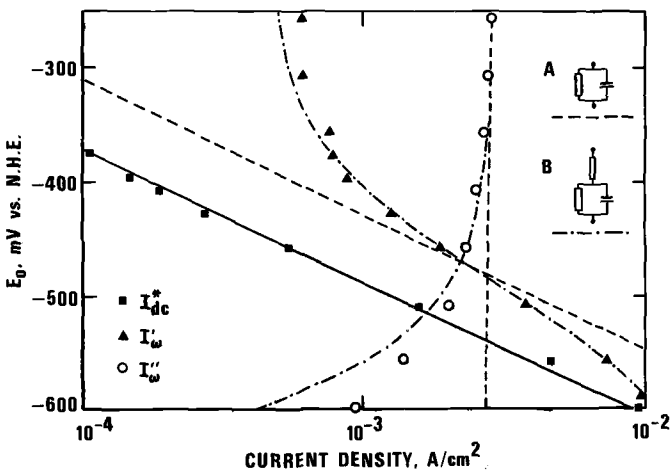


FIG. 8—Current density in the absence of modulation i_{dc}^* , and in-phase (i'_{ω}) and out of phase (i''_{ω}) components of the current density at the modulation frequency ($\nu = 100 Hz$). Dashed lines are calculated without ohmic drop (equivalent circuit shown in inset A). Dash-dot lines calculated with an ohmic-drop error of 6Ω (equivalent circuit shown in inset B).

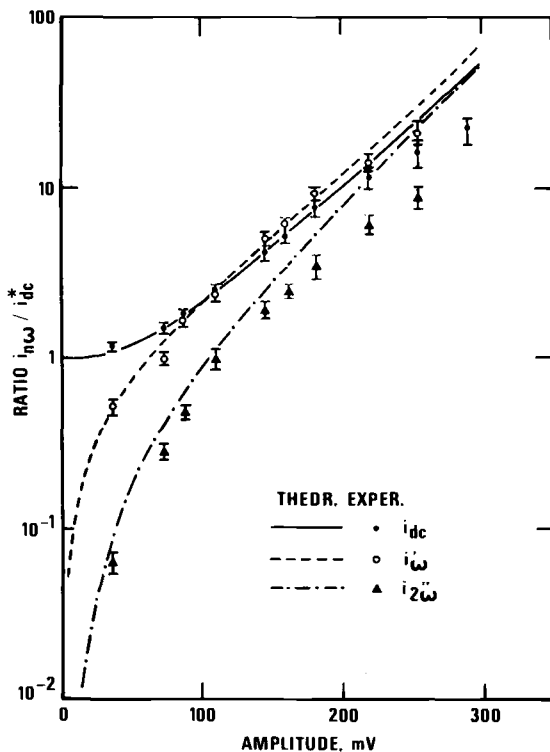


FIG. 9—Ratio between various components of the faradaic current and direct current in the absence of modulation i_{dc}^* as a function of the amplitude of modulation. $\text{Cu}/\text{H}_2\text{SO}_4 + \text{Na}_2\text{SO}_4$, $E_0 = -506$ mV versus NHE, $\nu = 103.3$ Hz.

measurements were carried out at the same potential ($E_0 = -456$ mV versus NHE) and at the same modulating amplitude ($V = 100$ mV) at frequencies ranging from 25 Hz to 10 kHz. As expected, the deviations caused by the ohmic-drop error become quite large when the frequency is increased. The results shown pertain to two different cell configurations having different ohmic-drop resistance. With $R_\Omega = 6 \Omega$, significant deviations from the theoretical behavior begin at about 300 Hz, while reducing R_Ω to about 0.8Ω increases the frequency of the beginning of the deviations by a factor of 10, to around 3 kHz. The effect of the ohmic-drop error is even more pronounced on the current components at the modulation frequency.

Figure 11 shows the values of i'_ω and i''_ω as a function of frequency, together with the lines calculated from Eqs 13 and 14, assuming a d-c capacitance of $48 \mu\text{F}$ and $R_\Omega = 0.7 \Omega$. The agreement is satisfactory, which indicates again that the greatest part of the deviations from the theoretical behavior is due to the ohmic-drop error. It should be noted that in its absence i'_ω would be independent of frequency.

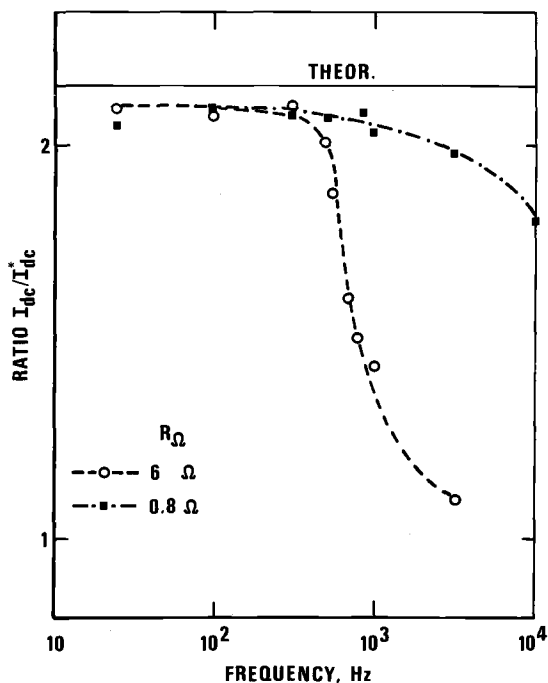


FIG. 10—Ratio between direct current in the absence and in the presence of modulation as a function of frequency for two values of the ohmic-drop resistance. $\text{Cu}/\text{H}_2\text{SO}_4 + \text{Na}_2\text{SO}_4$. $E_0 = -456 \text{ mV}$ versus NHE. $\nu = 100 \text{ mV}$. Solid line indicates theoretical value.

Conclusions

The experimental results presented here show conclusively that the mathematical analysis previously published [6] predicts accurately the current response to a sinusoidal voltage of an electrode under charge-transfer control, and can be therefore used as a basis for the understanding of the effect of alternating current on corrosion. It also shows that frequency analysis holds promise to be an important tool for the study of electrodes undergoing corrosion. Since the model employed does not involve special properties of the electrode surface in order to produce the effect called faradaic rectification [7], it is to be expected that an increase in the corrosion rate due to a-c leakage is a widespread phenomenon with considerable practical implications.

Acknowledgments

This work has been performed as part of Contract E(49-1)3800 with the Department of Energy, whose financial support is gratefully acknowledged.

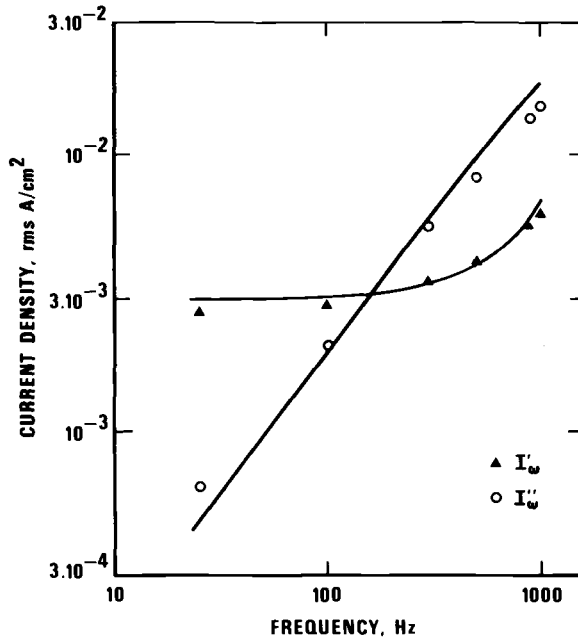


FIG. 11—In phase (i'_{ω}) and out-of-phase (i''_{ω}) components of the current density as a function of the frequency of modulation. Constant amplitude $V = 100$ mV. Solid lines are calculated for $R_{\Omega} = 0.7 \Omega$ and $C = 48 \mu F/cm^2$.

References

- [1] McCollum, B. and Ahlborn, G. H., Technical Paper BST72, National Bureau of Standards, 1916.
- [2] Compton, K. G., Research Report Project 265, International Copper Research Association, 1977.
- [3] Chin, D. T., Fu, T. W., Kamrowski, G. F., and Pookote, S., 1978 Research Conference, National Association of Corrosion Engineers, Houston, 1978.
- [4] Nesslage, D. J., Paper No. 762, *Corrosion 78*, National Association of Corrosion Engineers, 1978.
- [5] Bertocci, U. and Mullen, J. L., Paper No. 242, *Corrosion 79*, National Association of Corrosion Engineers, 1979.
- [6] Bertocci, U., *Corrosion*, Vol. 35, 1979, p. 211.
- [7] Breyer, B. and Bauer, H. H., *Alternating Current Polarography and Tensammetry*, Wiley-Interscience, New York, 1963.

H. A. Newborn,¹ D. C. Bratlie,¹ and C. R. Crowe¹

Progress in Mini-Potentiostat Development for Corrosion Testing

REFERENCE: Newborn, H. A., Bratlie, D. C., and Crowe, C. R., "**Progress in Mini-Potentiostat Development for Corrosion Testing**," *Electrochemical Corrosion Testing, ASTM STP 727*, Florian Mansfeld and Ugo Bertocci, Eds., American Society for Testing and Materials, 1981, pp. 381-389.

ABSTRACT: There is considerable interest in developing mini-potentiostats to perform both long-term and multispecimen corrosion tests. Various options utilizing state-of-the-art electronic components were tested with both resistive loads and actual electrochemical cells to compare their performances. Attention was then focused on a particular design that was economically competitive and performed adequately over a wide range of effective cell resistance. Accuracy must be maintained despite large cell resistance variations occurring in corrosion studies.

KEY WORDS: corrosion, laboratory instrumentation, operational amplifiers, potentiostats

The corrosion research community has a need for miniature inexpensive potential control devices. Commercially available instrumentation is for the most part multi-purposed, requiring complex circuitry and accessories. A large investment (several thousand dollars) is presently required for each potentiostat. Since it is necessary for a corrosion scientist or engineer to run multispecimen experiments and tests requiring long times at a constant preset potential, inexpensive mini-potentiostats provide an economic answer. Various designs using state-of-the-art electronic circuitry have been built and tested at the Naval Surface Weapons Center (NAVSWC) [1] and at other laboratories [2,3]. The goal was to design an electronically stable unit to provide control under specific test conditions.

In our laboratory the need exists for low-cost potentiostats operating at high currents (≥ 500 mA) with potential control to ± 1 mV. Applications include potential control for battery discharge experiments, potential control for the simultaneous testing of large specimens (such as tensile, fracture-toughness, and flat-plate specimens), and potential control for highly reac-

¹Metallurgist, electrical engineer, and metallurgist, respectively, Naval Surface Weapons Center, White Oak, Silver Springs, Md. 20910.

²The italic numbers in brackets refer to the list of references appended to this paper.

tive anodes. In these applications, control units that can be dedicated to the test specimens for long periods of time are required. Most low-cost potentiostatic instruments appearing in the literature do not meet our ≥ 500 -mA output current (with control to ± 1 mV) requirement.

A bibliography of potentiostat design published in 1972 [4] lists 94 references spanning 35 years of research and development. Basic designs are also reviewed in many electrochemistry textbooks. An excellent section in Gileadi et al [5] forms the basis for some of the conceptual designs and test procedures to be described. Design work up to the time of publication has also been surveyed; germane references are cited in this paper.

The function of a potentiostat is to deliver the required current to maintain the potential of the so-called "working electrode" (the specimen to be studied) at a preset level with respect to a reference electrode. A three-electrode electrochemical cell containing a working electrode, a reference electrode (such as a saturated calomel electrode), and a counter (or auxiliary) electrode acting as a current source or sink is required.

The development of operational amplifiers (op-amps) has led to a conceptual simplification of the function of a potentiostat, and a reduction in the number and cost of necessary active components. An op-amp has two inputs, denoted V_+ and V_- , and one output, V_{out} . The ideal op-amp performs the following functions (in dc applications):

1. If ΔV ($\Delta V = V_- - V_+$) is zero, V_{out} is zero ($V_{out} = A\Delta V$).
2. If ΔV is finite, V_{out} is infinite [gain (A) = infinity].
3. The current through the inputs is zero (input impedance = infinity).
4. The output current is independent of the characteristics of the amplifier (output impedance \approx zero).

An ideal op-amp would make an excellent potentiostat with the reference voltage and the preset control voltage (for the working electrode) as the two inputs, and with the counter electrode connected to the output. Since the reference electrode must remain electrically isolated from the working cell, infinite input impedance is desired. The amplifier sends current through the counter electrode until the input voltages are equal.

A comprehensive review [6] of the use of op-amps in electrochemical instrumentation cites progress to 1972. Trade-offs in the current design of op-amps make some properties approximately ideal, while other properties are not optimal. For instance, the RCA CA3160 amplifier has an input resistance rating of $1.5 \times 10^{12} \Omega$. However, its output impedance is 500Ω , and its offset voltage (error in ΔV) can be as high as 15 mV. A considerable amount of progress has been made in regard to op-amps that can handle high currents without external booster transistors. Currents up to 1 A can be driven with a National Semiconductor LH0021CK device.

In general, a potentiostat can be thought of as an amplifier driving an external load. The topic of which parameters of the potentiostat should be op-

timized to have the minimum effect on the load is next discussed (refer to Fig. 1). I_R must be very small to avoid large errors in the reference voltage. Devices are available that have very high input impedances ($> 10^{10} \Omega$ for the National Semiconductor LM 310) which are sufficient to prevent polarization of the reference electrode.

An analysis of the effect of gain and output resistance on potentiostat performance shows that the following equations hold:

$$V_C = A(V_S - V_R) - I_{\text{appl}} r$$

$$V_P = A(V_S - V_R) = I_{\text{appl}} (r - R_{\text{cell}})$$

To minimize the effect of the potentiostat on the electrochemical cell, r must be designed to be as small as possible. V_P remains constant with current variation, but V_C does not. Further analysis shows that the gain, A , should be large to force the differential input to be very small.

Because a-c response is important in electrochemical experiments, it is desirable to have a wide frequency response. However, a cell having a large capacitive load can cause the potentiostat to oscillate; to prevent this a compensation network must be selected to achieve stability. The simplest way to achieve stability is to introduce a -6 dB/octave (-20 dB/decade) frequency rolloff. This is done by adding a capacitor to the internal circuitry. The size of this capacitor is determined by the desired range of frequency response and the capacitive load of the cell. For wide bandwidth, the capacitor should be small. For stable operation with large capacitive loads, however, the capacitor should be large. Most general amplifier circuits will oscillate when capacitive loads near 1000 pF are driven.

Circuit Design

Greene et al [7] have illustrated the utility of a mini-potentiostat for corrosion experiments. A reproduction of the curve illustrated in ASTM Recom-

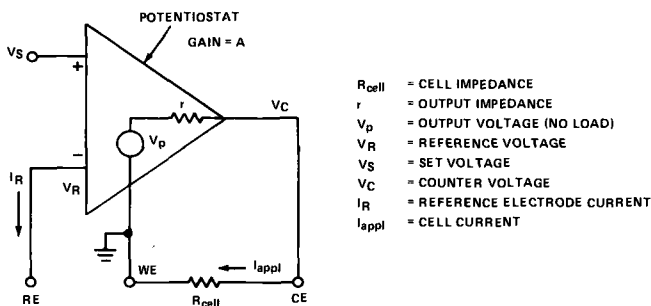


FIG. 1—General potentiostat.

mended Practice for Standard Reference Method for Making Potentiostatic and Potentiodynamic Anodic Polarization Measurements (G 5-78) was used as a gauge of mini-potentiostat performance. A stringent test established for the devices was the maintenance of an electrode potential within 1-mV deviation from a preset value over a wide range of applied currents. The range of 1 mA to 1 A of output current was chosen. Tests of various design options were made using variable resistor and more complex cell analogs. The DH (author's designation) potentiostat design was shown to have adequate regulation and was then used in an actual anodic polarization experiment. Its response was compared with that of a commercial Princeton Applied Research (PAR) potentiostat.

Since a fundamental principle underlying op-amp performance is their ability to hold voltages at the plus and minus inputs nearly equal, a few configurations were attempted using a single op-amp. The set voltage was entered at the plus input of the amplifier, whereas the minus input was associated with the potential across the load resistor. Two of the variations attempted utilized high input impedance RCA CA3160 operational amplifiers connected with high-gain power transistors to the output for current boosting. These variations were designated "Darlington" and "Emitter Follower." Figure 2 is a schematic representation of these designs. Although there are several wiring variations, it should be noted that most simple op-amp potentiostats utilize this basic type of circuit.

The voltage regulation of these units met the specification for output current of up to 40 mA. Recently, Baboian [2] has developed similar circuitry utilizing a single op-amp design. This circuit uses a new BIFET operational amplifier. The device utilizes junction field-effect transistors for very high input impedance and bipolar transistors to develop high gain and low distortion. The design is meant to supply 10 mA.

Figure 3 is a schematic diagram of a potentiostat designed by Mansfeld [3]. The DH potentiostat developed at NAVSWC is shown in Fig. 4. Both units were tested with good results. The Mansfeld circuit utilizes LH0044 low-noise op-amps with power transistors wired to their output for current boosting. The DH circuit uses LH 0021 op-amps (1-A capability), which eliminates the need for additional high-gain transistors. Both units require buffering to minimize input currents through the reference electrode.

The data for the voltage error (ΔV) plotted against output current (I_{appl}) (Fig. 5) for the options described indicate that a linear relationship exists between ΔV and I_{appl} , as predicted by Eq 1. At 500 mA, ΔV (Mansfeld) = 9 mV, independent of the set voltage V_S , whereas ΔV (DH) = 4 mV, also independent of V_S . The DH potentiostat has a 1-mV error associated with its set potential at approximately 150 mA; the Mansfeld unit, at around 80 mA. The data indicate that the DH unit is better suited to high-current operation. At low current (about 20 mA), both units remained in specification (less than 1-mV error).

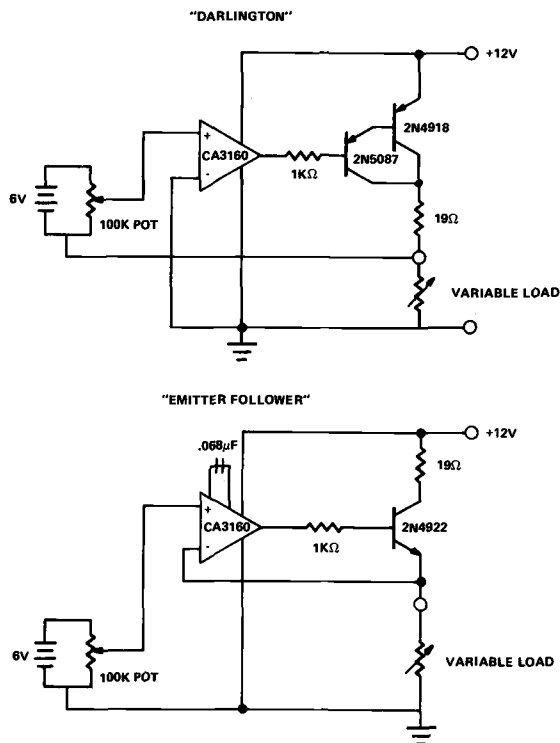


FIG. 2—Schematics of the "Darlington" and "Emitter Follower" options.

Additional data was taken across a resistive load using a PAR 173 commercial potentiostat. Only after adapting the unit by shortening its standard leads was a 1-mV error specification obtained; as is, the unit performed comparably to the DH potentiostat. The maximum output current (that is, the current at which regulation is totally lost) was found to be 600 mA for the Mansfeld unit, and 1 A for both the DH and PAR units.

In addition, all units were tested with a pulse generator for response time in a shift of output current (analogous to a quick lowering of the effective electrochemical cell resistance, as is known to occur upon pit initiation). All units responded well with the stable current at 50 mA and pulsed current of 500 mA. The response times were approximately 30 μ s for all units. The errors in the set potential were identical to those measured at steady-state current of 500 mA.

It was felt that the improvement in accuracy could be attributed not only to the larger-capacity operational amplifiers, but to the lower effective output resistance existing in the DH unit ($r = 0.009 \Omega$ as opposed to 0.020Ω for the Mansfeld potentiostat). This allowed the unit to track more accurately, as

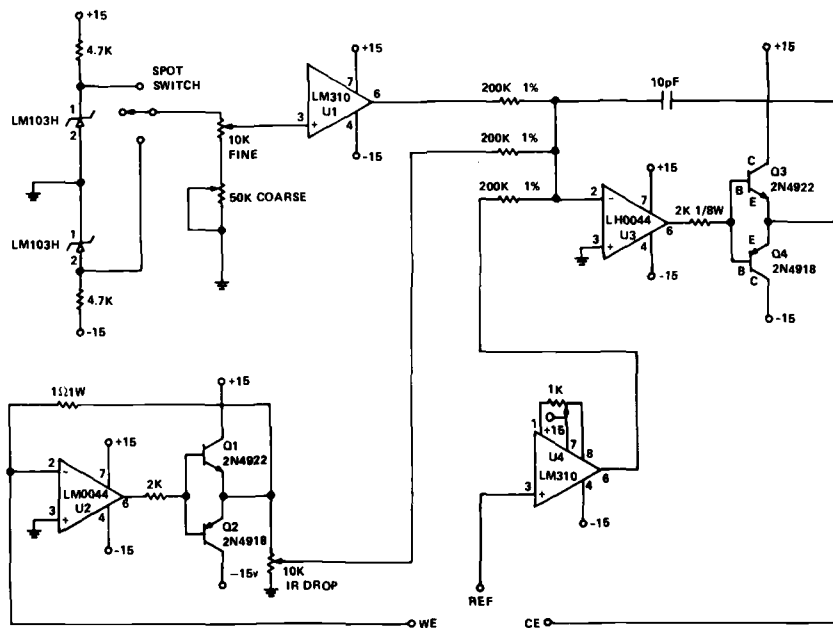


FIG. 3—Schematic of the Mansfeld potentiostat.

was grossly exhibited in the shortening of the electrode leads on the commercial PAR unit.

The DH potentiostat was then used in conjunction with an actual electrochemical cell. Evaluation was made of the ability of the DH model to perform the standard ASTM G 5 anodic polarization curve. The apparatus consisted of a Greene-type cell with an ASTM Type 430 stainless steel specimen exposed to 1 *N* sulfuric acid (H_2SO_4) solution at 30°C. The performance of the DH model was compared with that of the commercial PAR potential control unit (Model 173) both potentiostatically and potentiodynamically at various scan rates. Figure 6 illustrates good agreement between the PAR and DH runs, and the ASTM G 5 standard curve at various test conditions.

Since it is desirable to see the current variation over many decades, conversion to log scale is required. The PAR has a log converter module (Model 376) to perform this task. An external Moseley log converter with interface circuitry was used with the DH.

There were differences in the plots due to different system noises. The PAR with its log converter produced very smooth curves, agreeing closely with the standard. The DH also produced curves that followed the standard, but with increasing noise with decreasing scan rates. The curves show slight deviations from the standard. It is felt that most of these deviations result from use of the Moseley log converter. As a check, the linear current output

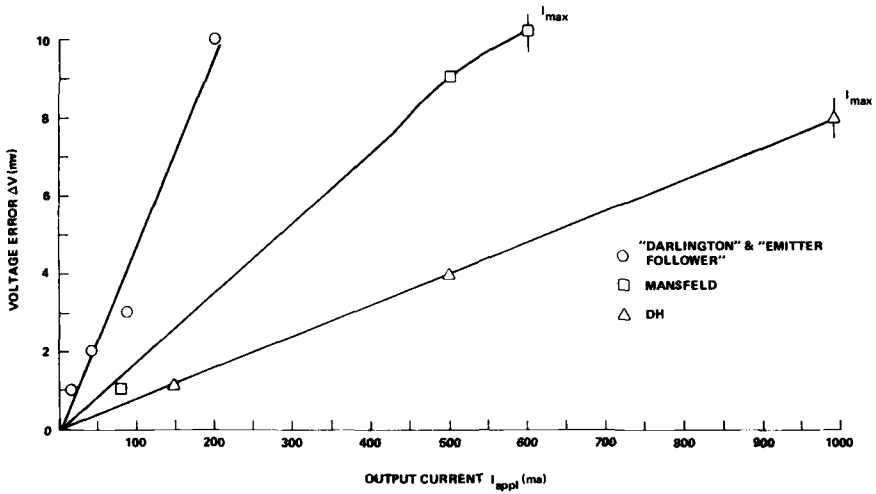


FIG. 5—Plot of voltage error versus output current for various design options.

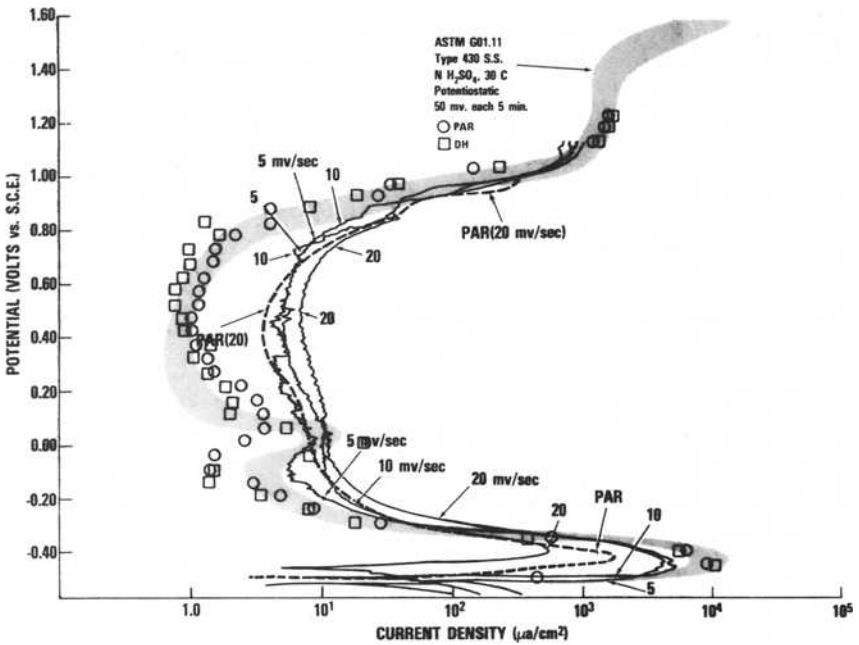


FIG. 6—ASTM standard curve versus PAR and DH data.

of the PAR was hooked to the Moseley log converter and a run was made. The same types of noise and deviations were present.

We deduce from Eq 1 that the gain of a potentiostat should be as high as possible to keep ΔV very small. This is fine for pure d-c operation, but stability for a-c applications would be marginal. The d-c gain of the DH unit is approximately 320 000, but it is presently compensated to have a unity gain crossover frequency of 28 kHz. In comparison, the commercial Wenking 70HP10 potentiostat has a unity gain crossover frequency of 300 kHz. By an adjustment of the feedback capacitance, C , the crossover frequency can be varied in the DH unit (Fig. 5).

Since the reference electrode and associated circuitry are a very high impedance network, it is important to have the reference electrode and the input stage close together. Long leads at this high impedance can easily pick up enough stray electromagnetic interference to cause faulty operation. Either an external buffer amplifier should be used or else the potentiostat should be very close, physically, to the cell.

Improvements for the DH Potentiostat

One improvement for the DH potentiostat is a revision of the ± 6.2 -V regulators. The Zener diodes can be replaced with integrated circuit regulators less sensitive to temperature variations and current fluctuations. The ± 6.2 -V supplies are used for the potential set supply. If any drift occurs in the supply voltage, it will be noticed in the set potential.

Another improvement would be the construction of a low-cost log conversion circuit for current measurement and plotting. If a log converter could be built cheaply enough, each potentiostat could have one included in its circuitry; otherwise, a multiplexer would be needed to deliver each current in turn to a converter.

References

- [1] Newborn, H. A. and Bratlie, D. C., "Analysis of Mini-Potentiostat Design Options for Corrosion Research," NSWC/WOL TR 78-129, 1 Sept. 1978.
- [2] Baboian, R., "Modern Electronics' Effect on Corrosion Technology," part of the educational lecture presented 12 Mar 1979 at Corrosion/79, National Association of Corrosion Engineers, Atlanta, Ga.
- [3] Mansfeld, F. and Inman, R. V., *Corrosion*, Vol. 35, No. 1, 1979, p. 21.
- [4] Gabe, D. R., "Bibliography of Potentiostat Design," *British Corrosion Journal*, Vol. 7, 1972, p. 236.
- [5] Gileadi, E., Kirowa-Eisner, E., and Penciner, J., *Interfacial Electrochemistry*, (Addison-Wesley, Reading, Mass., 1975, pp. 151-205.
- [6] Mattson, J. S., et al, Eds., *Electrochemistry: Calculations Simulations, and Instrumentation*, Vol. 2, Marcel Dekker, New York, 1972, Chapter 10, pp. 263-350.
- [7] Greene, N. D., Moebus, G. A., and Baldwin, M. H., *Corrosion*, Vol. 29, No. 6, 1973, p. 234.

W. M. Peterson¹ and Howard Siegeman¹

A Microprocessor-Based Corrosion Measurement System

REFERENCE: Peterson, W. M. and Siegeman, Howard, "A Microprocessor-Based Corrosion Measurement System," *Electrochemical Corrosion Testing, ASTM STP 727*, Florian Mansfeld and Ugo Bertocci, Eds., American Society for Testing and Materials, 1981, pp. 390-406.

ABSTRACT: An instrument for the performance of electrochemical corrosion measurements has been developed, which includes a 16-bit built-in microprocessor. Electrochemical corrosion measurements, by their very nature, benefit by being placed under microprocessor control. These measurements include pretimed equilibration periods, examination of corrosion potentials for stability, initiation of scans at potentials relative to the corrosion potential, and reversal of scans at selected potentials or current densities or both. Similarly, the calculations usually performed on electrochemical corrosion rate data can be performed and even optimized through the use of a built-in microprocessor. The instrument described here utilizes the microprocessor as completely as possible—to define the measurement, perform the experiment, and replay the data in a format that is most meaningful to the operator.

This paper will describe in detail how the microprocessor is utilized to set up an experiment, acquire, validate, and store the experimental data, and then recall all, or selected portions, of that data. Typical applications of the instrument will be described in detail showing how the device can be used for the evaluation of potentiodynamic polarizations, cyclic polarizations, Tafel plots, polarization resistance plots, galvanic corrosion measurements, corrosion behavior diagrams, sensitization tests, and current integration measurements of a number of typical alloys in a variety of corrosive environments. The advantages enjoyed by a microprocessor-based device as compared to an analog instrument will be described.

Electrochemical corrosion measurements are sufficiently intricate that incorporation of a microprocessor into the measuring device can prove beneficial—beneficial for both the operator and the data. A "smart" instrument expands the capability of the corrosion scientist, relieves operator tedium, and improves the accuracy of the data acquired during the experiment. For greatest efficiency the microprocessor should be utilized as completely as possible—to define the measurement, acquire, validate, and store experimental data and recall all or selected portions of the data in a format that is most meaningful to the operator. The success of the microprocessor in car-

¹Application group leader and marketing manager, respectively, EG&G Princeton Applied Research Corporation, Princeton, N.J. 08540.

rying out the desired experimental scheme, such as to mimic human operation as closely as possible, is obviously a function of the program under which the microprocessor operates. The purpose of this paper is to examine the advantages of a dedicated microprocessor-controlled corrosion-measurement instrument from the standpoint of experimental optimization and operator convenience. Also, the method of interaction between the user and a commercially available instrument will be described.

Typical Measurements

A typical electrochemical corrosion measurement involves a number of discrete operations:

1. Pretreatment—Specimen surfacing and preparation.
2. Experimental Definition—Specification of experimental operating parameters.
3. Specimen Conditioning—Equilibration of the specimen with the environment and measurement of corrosion potential.
4. Data Acquisition—Application of a potential scan and measurement of resultant current and potential data.
5. Data Analysis—Calculation of corrosion rates, peak currents, integrals, corrosion potentials, etc.

Except for the pretreatment step the remainder of the measurement scheme can be automated and placed under the control of the microprocessor. Steps 2 through 5 involve many decision points that can be implemented by the microprocessor.

Experimental Definition

In the definition of the experiment a number of questions must be answered:

What kind of experiment is to be performed?

What are the initial and final limits of the potential scan?

Is the scan to be reversed at a particular potential, current, or current density?

What is the geometric area of the specimen?

The microprocessor can aid the user in defining the measurement by requesting the appropriate set of parameters for any given experiment. If the operating program contains preset limits for experimental parameters, inadvertent errors and wasted effort can be avoided.

Specimen Conditioning

Conditioning the specimen prior to the actual data acquisition is an extremely important step in the procedure and usually involves delaying initia-

tion of the scan until a given time interval has elapsed, or until the change in corrosion potential with time reaches an acceptably low rate—functions that an automated device incorporating a microprocessor can perform routinely.

Data Acquisition

It is during data acquisition that the availability of microprocessor control becomes essential if continuous operator attention during the measurement is to be avoided. The inclusion of a potential scan in the typical experiment described previously classifies the measurement as part of the family of potentiodynamic studies. The microprocessor can be instructed to acquire each data point (that is, each pair of current and potential points) during the scan under stringently controlled conditions. Each current measurement can be compared by the microprocessor to the set of three preceding data points and examined for validity. If a noise spike should invalidate a particular current measurement (as can happen when measurements of extremely low currents are perturbed by random line noise transients) the microprocessor can discard the invalid data. The microprocessor can control the digital conversion of the measurement data, and then smooth and store that data.

Data Analysis

For the analysis of the data the microprocessor is again extremely valuable to the corrosion scientist. The microprocessor can attend to scaling the data appropriately so that it can be replayed from memory. During data analysis corrosion rates are calculated and all pertinent data are labelled on the recorder chart.

Practical Implementation

The foregoing discussion has been rather general. The concepts described earlier have been implemented in the form of the EG&G Princeton Applied Research Model 350 Corrosion Measurement Console (Fig. 1). This commercial instrument incorporates a 16-bit microprocessor to perform a wide variety of corrosion investigations.

A block diagram (Fig. 2) shows the interaction of the various hardware subassemblies (central processing unit, memory, potentiostat, etc.) An operational flowchart (shown in Fig. 3) describes in general terms the software subroutines that control the operation of the instrument. The operating program for this instrument resides in 10 000 "words" of nonvolatile Programmable Read Only Memory (PROM); that is, the program information is retained when the instrument power is turned off. Experimental data from a single polarization scan are stored in 2000 words (equivalent to 2000 data points) of Random Access Memory (RAM) which *is* volatile, that is, the data

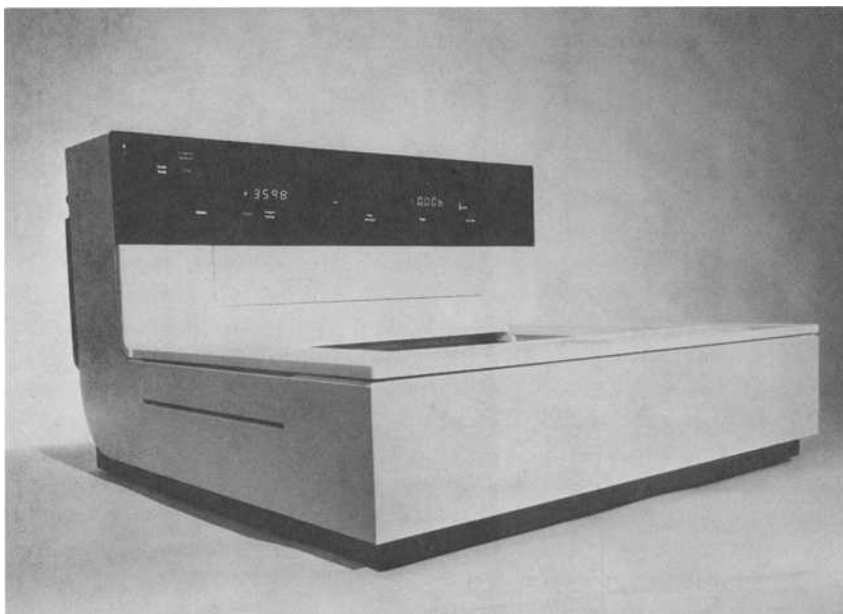


FIG. 1—*Microprocessor-controlled measurement system.*

are lost when power to the instrument is removed. Since it is often necessary or desirable to retain such experimental data, a curve storage option has been developed which permits storage of 50 polarization curves on a single tape cartridge.

The ability of this device to replay stored data from even a single polarization scan can save much time and avoid the need to repeat certain measurements. In conventional, nonmicroprocessor-based corrosion experiments, the user selects the anticipated current and potential ranges of the experiment and arranges calibration of the X - Y recorder axes so that the measurement of interest appears on the chart. Often, while the experiment is underway, or after it has been completed, the investigator realizes that an additional measurement will be required because the current or potential limits are incorrect for the experiment at hand, or because a portion of the main curve must be studied in greater detail (that is, at higher current sensitivity or with the potential axis amplified). Since the microprocessor can be connected to an eight-decade autoranging current-to-voltage converter (with log functions accomplished more efficiently in software than in hardware), the time saved in making additional, unnecessary measurements is significant. Also with a microprocessor-based instrument, the need to repeat the

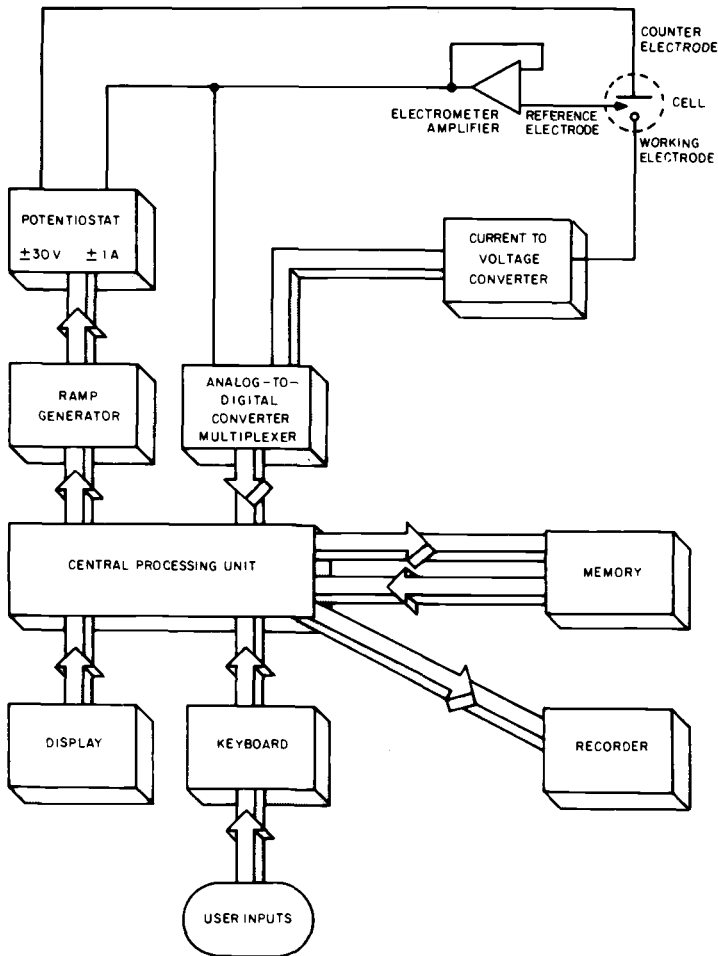


FIG. 2—Block diagram.

experiment merely to study a portion of the main curve in greater detail can often be avoided since the device can be instructed to replay a portion of the stored curve such that the area of interest is expanded to full scale. This can be valuable, since for a series of similar experiments, it is often difficult to prepare the specimen surface as reproducibly as one would like.

A microprocessor-based instrument does not relieve the corrosion scientist of the responsibility of repeating experiments to verify data and establish confidence limits on the data. If anything, however, data comparison with a microprocessor-based instrument is simplified because of the ease of data storage, recall, and manipulation.

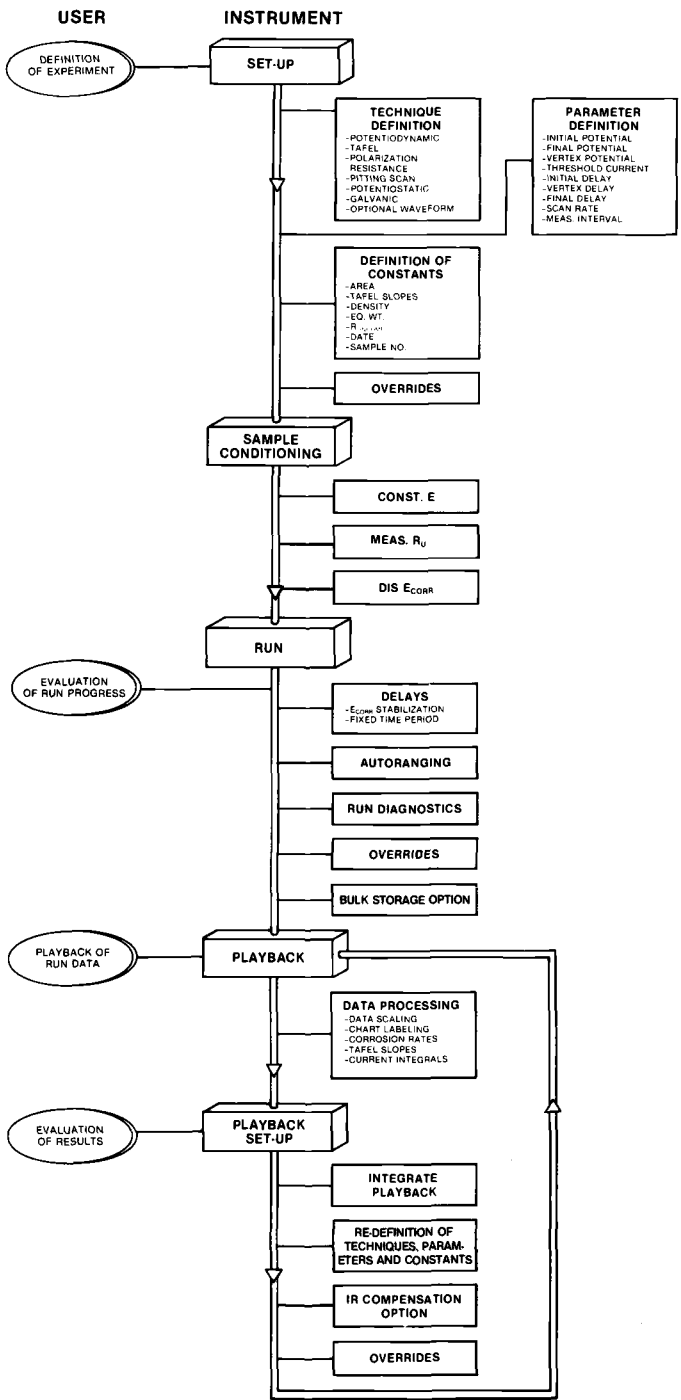


FIG. 3—Operational flow chart.

The potentiostatic circuitry of the instrument is optimized for corrosion measurements. Electrochemical corrosion experiments are typically performed with scan rates of about 0.1 mV/s. The combination of a large time constant in the current measurement circuit and a dual-slope analog-to-digital converter filters experimental data very effectively. As a result, currents as low as 10 nA may be reliably measured. This type of signal conditioning limits the scan rate to a maximum of 100 mV/s.

Potentiodynamic Techniques

The corrosion experiment is defined by using the keyboard (Fig. 4) in association with the display panel (Fig. 5). The experimental procedure set-up is accessed by pressing the pushbutton labelled SET-UP. The available techniques are POTENTIODYNAMIC, TAFEL PLOT, POLARIZATION RESISTANCE, PITTING SCAN, POTENTIOSTATIC, GALVANIC CORROSION, and EXTERNAL WAVEFORM. The first four techniques are potentiodynamic in nature; that is, current is measured as a function of potential. These techniques are in most general use and will be discussed in detail.²

Since the corrosion potential can be measured and stored in the memory of the microprocessor, the instrument can be programmed to apply an initial potential that is defined relative to the corrosion potential. This is especially convenient since the corrosion potential must be allowed to stabilize before the experiment is begun. Regardless of the amount the corrosion potential drifts before it stabilizes, the desired potential range about the corrosion potential can conveniently be obtained.

The POTENTIODYNAMIC mode is the most versatile. The initial potential may be specified relative to the corrosion potential or as an absolute voltage. Since this mode is usually used with rather large potential ranges, the final potential may be specified only as an absolute voltage. The POTENTIODYNAMIC mode may also be used to perform cyclic polarization studies. This is done by informing the microprocessor that it should request a vertex potential, that is, a potential at which the scan direction is reversed. One may also specify a threshold current, which must be exceeded before the scan direction is reversed. This is the same waveform that is used in the PITTING SCAN. The initial potential in the PITTING SCAN mode, how-

²It is assumed that the reader is familiar with the techniques and terminology of electrochemical corrosion testing. The following applicable ASTM documents may be found in Part 10 of the *Annual Book of ASTM Standards: Recommended Practice for Conventions Applicable to Electrochemical Measurements in Corrosion Testing (G 3-74)*, *Recommended Practice for Standard Reference Method for Making Potentiostatic and Potentiodynamic Anodic Polarization Measurements (G 5-78)*, *Definitions of Terms Relating to Corrosion and Corrosion Testing (G 15-79a)*, *Practice for Conducting Potentiodynamic Polarization Resistance Measurements (G 59-78)*, and *Practice for Conducting Cyclic Potentiodynamic Polarization Measurements for Localized Corrosion (G 61-78)*.

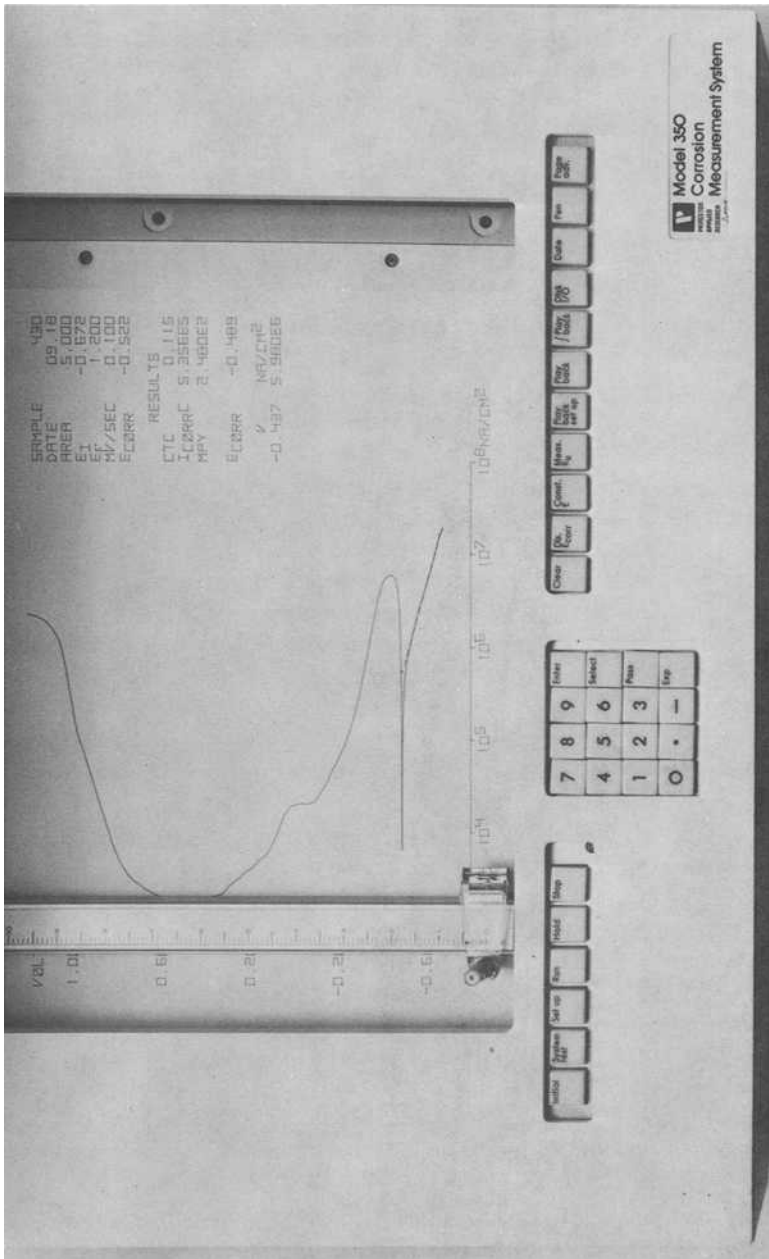


FIG. 4—Keyboard.

ever, is limited to the measured corrosion potential. In the TAFEL PLOT and POLARIZATION RESISTANCE modes both the initial and final potentials may be entered relative to the corrosion potential.

For all potentiodynamic modes, the potential is displayed on the *Y*-axis and the logarithm of the current is displayed on the *X*-axis during "real-time" data acquisition. The instrument measures the current and the microprocessor scales the recorder accordingly with no adjustment required by the operator. The *X*-axis of the recorder is calibrated to display five decades of current. The instrument can, however, measure accurately eight current decades from 10 nA to 1A. Currents between 1 and 10 nA are measured with low accuracy and are, therefore, not specified. If the current should reach the lower or higher limit of the recorder during data acquisition, the recorder will "fold-over" three decades and data acquisition will continue. When PLAYBACK is implemented following the completion of a scan, the data will be scaled to fit the graph paper and the axes will be labelled. During PLAYBACK, the data for POLARIZATION RESISTANCE is plotted in an *E* versus *i* format. For all other potentiodynamic modes, an *E* versus log *i* format is used.

After the desired technique is selected, the instrument requests the parameters necessary to perform the experiment. The scan rate is selected as SLOW (0.1 mV/s), FAST (1 mV/s), or USER-SPECIFIED, which can be any value between 0.001 and 100 mV/s. If the selected scan rate is greater than 1 mV/s, the potential is varied by an analog ramp generator. For scan rates equal to or less than 1 mV/s, the potential is varied with a staircase waveform (see Fig. 6). The potential is changed by a specific step size, and that potential is applied to the specimen for a measured duration, after which it is stepped again. The current is measured for 16.7 ms immediately prior to the step. The effective scan rate is the step size divided by the duration of the step. For example, if the potential is stepped 2 mV every 10 s, the effective scan rate is 0.2 mV/s.

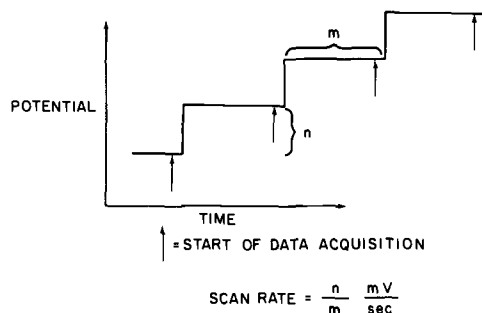


FIG. 6—Staircase waveform used for scan rates equal to or less than 1 mV/s.

The step size selected by the instrument is not simple, and requires explanation. It is governed by two considerations. First, one would like maximum data density, that is, smallest step size, in the region of the corrosion potential where corrosion currents are measured. Secondly, one would like to utilize as many of the 2000 data registers as possible during an experiment to obtain maximum resolution of the data. The Model 350, therefore, automatically sets the step size at 0.5 mV whenever the experiment is initiated within 250 mV of the measured corrosion potential. When the applied potential exceeds $E_{\text{corr}} \pm 250$ mV during the potential scan, the microprocessor divides the voltage range yet to be scanned by the number of vacant data registers to obtain the optimum step size. The step can remain 0.5 mV, or be changed to 2 mV, or any multiple of 2 mV.

There is one exception to the step-size calculation. In the case of a PITTING SCAN with a specified vertex potential and threshold current, there is some uncertainty regarding the potential at which the scan is reversed. This is because that potential depends upon the actual cell current. In this case, the microprocessor arbitrarily increases the calculated step size by 50 percent to avoid a situation where all available data registers are utilized before the experiment is completed.

In most potentiodynamic experiments, the corrosion potential must be allowed to stabilize before the experiment is begun. This can be accomplished in two ways. The experiment can be delayed a programmed time period before the scan is initiated. Alternatively, one may require that the experiment not commence until the corrosion potential has stabilized to less than a programmed "drift rate". The instrument will measure the corrosion potential and store that value in memory once every 10 s for 200 s. After this initial period, the microprocessor subtracts the "first" E_{corr} from the "last" E_{corr} , and divides that difference by 200 s to calculate the drift rate. If the measured drift rate is less than the programmed drift rate, the scan will begin. If the measured drift rate is too high, the instrument will continue to measure the corrosion potential every 10 s, simultaneously deleting the "first" corrosion potential from the memory. In this way, a sliding set of measured E_{corr} values taken over a 200-s interval is always in the memory. The experiment begins only when the measured drift rate becomes less than the entered value. The resolution of the potentiometer is 2 mV. The lowest measurable drift rate, therefore, is 0.01 mV/s.

If a specimen area is entered during the set-up procedure, the measured current will be divided by the area in software and reported as current density. If no area is entered, data will be reported as current.

The instrument will also request values for the anodic and cathodic Tafel constant. The instrument will measure these values from the automatic extrapolation of the linear region of the Tafel plot, or the operator can enter values for the Tafel constant if they are known or can be inferred from the literature.

If automatic corrosion-rate calculations are to be performed, the operator must enter numerical values for the density and equivalent weight of the specimen.

At this point, the experiment can be initiated. It is important to realize that because the instrument can (1) calculate a drift rate of E_{corr} , (2) specify an initial potential relative to E_{corr} , (3) automatically autorange the current, and (4) measure threshold currents, operator attention is not required. Also, the recorder is completely under microprocessor control, and requires no calibration by the user.

After the experiment is completed, the operator presses the button labelled **PLAYBACK**. The instrument then automatically scales the data to fit the chart paper, labels the axes, and prints setup information along with the results of the calculation performed on the data (see Fig. 7).

The operator may then wish to examine in closer detail a portion of the scan. This can be accomplished by using the **PLAYBACK SET-UP** button. In this mode the operator has the opportunity to redefine the initial and final potentials. If these differ from the values originally selected, the microprocessor automatically scales both axes to the new values and replots the stored data within the new limits over as much of the chart as possible.

In **PLAYBACK SETUP**, the technique may be changed, for example, to evaluate the linear current response rather than the logarithmic current signal. After altering these parameters, another **PLAYBACK** can be initiated to output data on the recorder. For example, the polarization resistance curve in Fig. 8 is data replotted from Fig. 7.

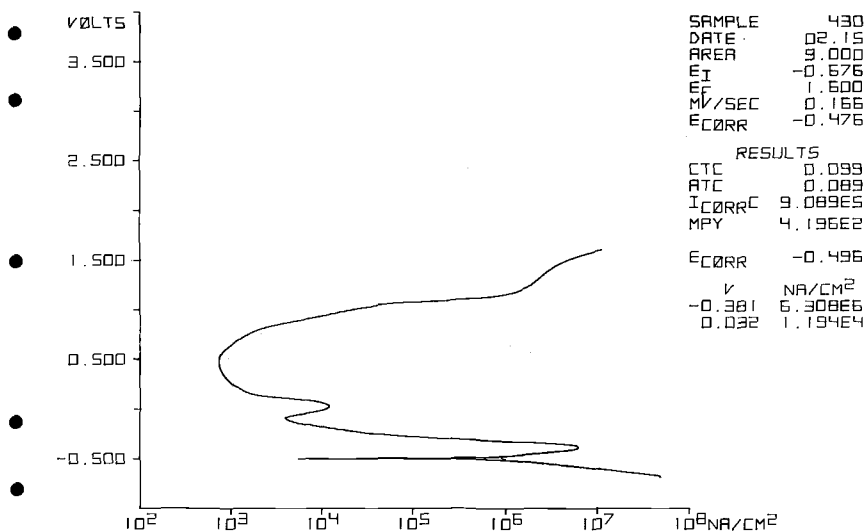


FIG. 7—Potentiodynamic polarization plot of 430 stainless steel in 1 N H₂SO₄.

If the INTEGRATE PLAYBACK feature is accessed, the current is integrated between the specified initial and final potentials, and the resulting coulombs are printed on the chart (Fig. 9). This feature is valuable for performance of sensitization tests to determine grain boundary grooving.

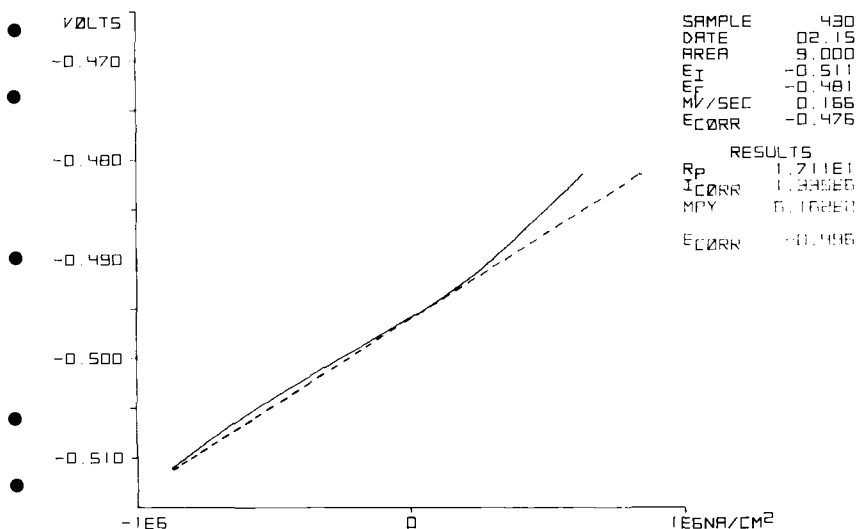


FIG. 8—Data from Fig. 7 replotted as polarization resistance.

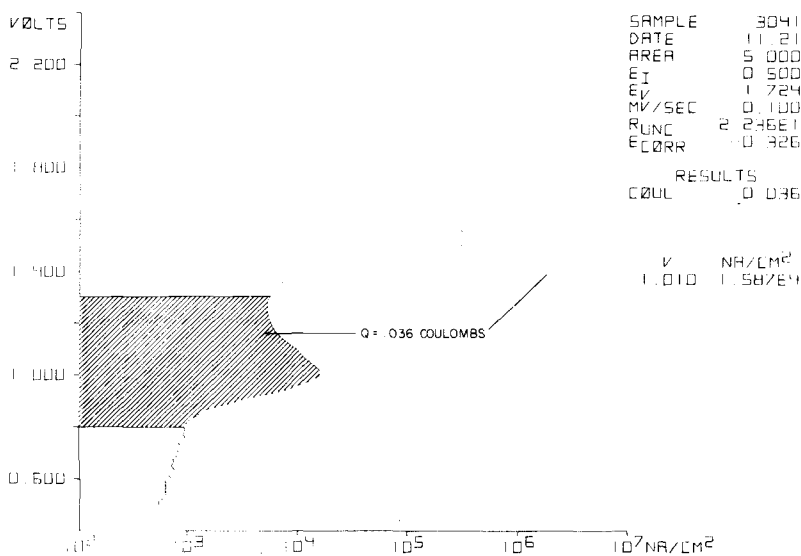


FIG. 9—PLAYBACK illustrating INTEGRATE capability.

As mentioned previously, the instrument will maximize resolution of an experiment, and therefore will only store the results of one experiment. Since one may wish to examine several experiments overlaid on identical axes, provision for manual scaling is provided. The operator defines the Y -axis by specifying initial and final potentials. The X -axis is defined by specifying the number of current decades and the maximum decade for a log i format, and the full-scale current for a linear format.

iR Compensation

The effect of uncompensated resistance is known to significantly alter the results of corrosion experiments.^{3,4} The resistance of the solution between the surface of the specimen and the reference electrode (Luggin probe) may lead to an error in the actual potential of the specimen. The magnitude of this error is proportional to the cell current. With analog potentiostatic circuitry, this effect is best compensated by positive feedback of a signal derived from the cell current into the input of the potentiostat. However, real-time compensation of the cell resistance with analog circuitry is inconvenient and its accuracy is suspect.

The EG&G Princeton Applied Research Corporation Model 356 *iR* Compensation Option, designed to be used in conjunction with the Model 350 console, can correct experimental polarization data for the solution resistance between the specimen and the reference electrode. The Model 356 (see Fig. 10) is installed between the Model 350 and the electrometer (the latter placed in close proximity to the cell). A 2.2-kHz a-c current is applied to the specimen and a phase-sensitive detector in the Model 356 measures the in-phase component of the resulting voltage. The in-phase potential is directly proportional to the cell resistance. The actual resistance, calculated from the

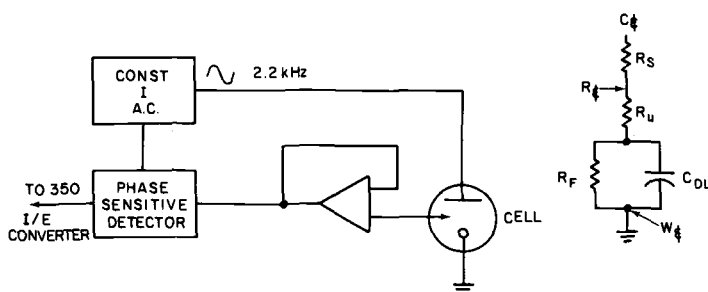


FIG. 10—Block diagram of *iR* compensation module.

³Mansfeld, F., *Corrosion*, Vol. 32, 1976, p. 143.

⁴Britz, D., *Journal of Electroanalytical Chemistry*, Vol. 88, 1978, p. 309.

measured voltage and the known controlled current, is presented on the display panel.

The polarization experiment is performed as usual with the actual compensation accomplished in software during **PLAYBACK**. The measured cell current is multiplied by the cell resistance to yield the potential due to "iR drop", which is subtracted from the applied potential.

An example of iR compensation is shown in Fig. 11. The measured resistance of the 430 Stainless Steel specimen in 0.02 *N* sulfuric acid (H_2SO_4) was 2.93 Ω . The uncompensated cathodic Tafel constant was 0.190 V/decade while the Tafel constant of the compensated curve was 0.106 V/decade. It is apparent from Fig. 11 that a seemingly negligible cell resistance can have a rather dramatic effect on calculated results.

This method of data correction is not a "real-time" approach for correction of experimental data, as is the positive feedback IR approach. However, the latter technique suffers from the possibility that the entire experiment may be invalidated by incorrect adjustment of the degree of positive feedback supplied to the analog potentiostat. Also, with positive feedback IR there is no possibility of collecting and examining uncorrected data. Both approaches assume that the solution resistance remains invariant during the course of the measurement. While such an assumption may be unwarranted in certain circumstances, for example, film formation, adsorbed gas layers on the specimen surface, there is no known instrumental method available which can simultaneously apply a polarizing potential to the specimen and independently measure the solution resistance resulting from such polarization.

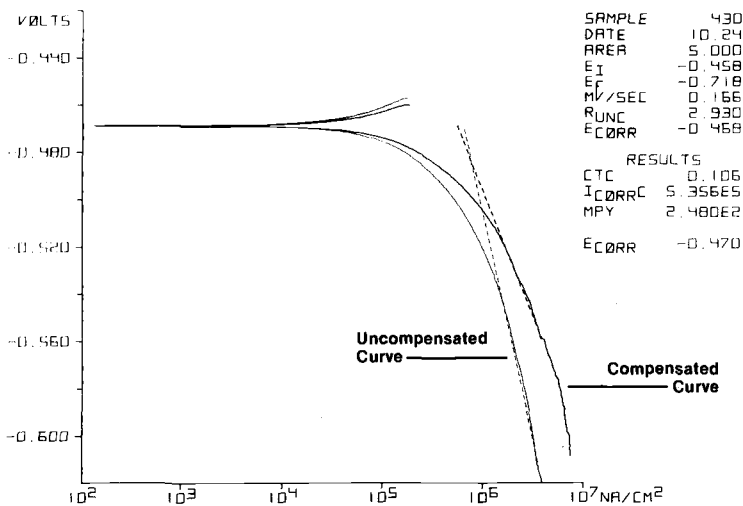


FIG. 11—Tafel plot with and without iR compensation.

Other Techniques

The POTENTIOSTATIC mode allows the imposition of a controlled potential to the test specimen while the current is measured versus time. One may also step from the initial potential to another potential during the experiment. The instrument must be informed of the time interval between current measurements and the time after the experiment is begun when the potential step should be applied. The instrument requests these parameters from the operator through the display panel during SET-UP.

In the GALVANIC CORROSION mode, the instrument monitors the current and potential (if desired) of a galvanic cell consisting of two dissimilar metals. The instrument does not control any parameter of the galvanic cell but, instead, functions as a zero resistance ammeter and potentiometer. The time between measurements is the only information the instrument requires from the operator.

When PLAYBACK is implemented the instrument plots both the current and potential versus time (Fig. 12).

The EXTERNAL WAVEFORM technique allows the operator to input a signal from an external source into the back-panel of the instrument, and the instrument will apply that waveform to the cell and measure the resulting current.

The EXTERNAL WAVEFORM mode also allows the operator to perform a Corrosion Behavior Diagram^{5,6} under automatic instrument control. No external devices are required to perform Corrosion Behavior Diagrams.

Calculations

Microprocessors are often utilized in instruments for their "number crunching" capability. In the Model 350, corrosion rates are calculated by the microprocessor using (1) constants for area, equivalent weight, and density keyed in by the operator, (2) Tafel slopes either keyed in by the operator or measured by the instrument, and (3) a value of the corrosion current density calculated from the measured polarization curve by the instrument.

If the experiment being run is a potentiodynamic-polarization plot or a Tafel plot, the microprocessor examines the data on both the anodic and cathodic sides of the first corrosion potential to find the semilog straight-line segment which will yield a Tafel constant. If a line segment is found which is linear for 0.2 decades of current, the slope of that segment will be reported as the Tafel constant in volts per decade. The straight-line segment is then extrapolated to intersect the corrosion potential and the resultant value of corrosion current density is utilized in the calculations.

⁵Morris, P. E. and Scarberry, R. C., *Corrosion*, Vol. 26, 1970, p. 169.

⁶Morris, P. E. and Scarberry, R. C., *Corrosion*, Vol. 28, 1972, p. 444.

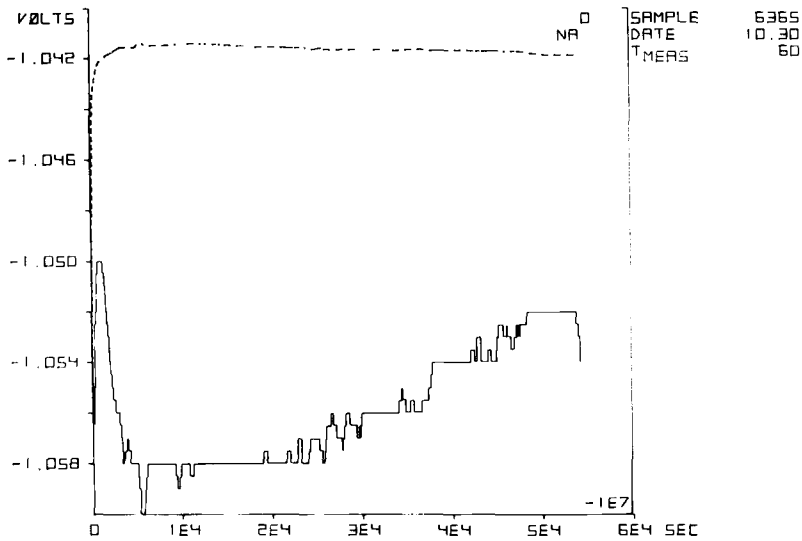


FIG. 12—PLAYBACK of galvanic corrosion experiment. Solid line is potential.

If a polarization-resistance experiment is run, the calculation of corrosion current density differs from the preceding procedure. The linear polarization data is processed to find the first derivative value at the corrosion potential. The polarization resistance thus calculated is multiplied automatically by the appropriate constants to yield the corrosion current density value.

Summary

The papers collected in this volume cover several aspects of the use of electrochemical methods for the study of corrosion. They can be broadly divided into three groups. The first contains papers where electrochemical techniques, many of them having some degree of novelty, have been applied to the examination of specific materials or phenomena. A second group contains papers where the emphasis is on discussing or proposing electrochemical techniques rather than on their application to specific systems. The last group is composed of papers mostly concerned with describing electrochemical instruments for corrosion testing. There is, of course, a considerable degree of overlapping between these groups, so that the subdivision is rather arbitrary, but they nevertheless provide a rough indication of the main point of the various contributions.

To the first group belong the work of Toušek on pitting in iron, that of Lee also dealing with localized corrosion, and the paper by Tong correlating electrochemical measurements and corrosion behavior in a series of iron-nickel-chromium alloys. Two papers, by Amzallag and co-workers and by Kessler and Kaesche, combine mechanical testing with electrochemical techniques for the study of stress corrosion cracking and fatigue in stainless steels. The corrosion of dental alloys has been studied by Sarkar, and Ishikawa and co-workers have presented two papers dealing with the galvanic corrosion of copper alloys and the effects of cavitation on pump casings. Finally, the paper by Chen and Theus reports on corrosion studies of iron in molten salts.

Some of the papers are more difficult to classify since they not only focus on some particular aspect of corrosion, such as atmospheric or underground corrosion, but evaluate or discuss some specific technique. One example is the work by Smyrl concerning the corrosion of copper in acidic solutions, but whose main contribution is a description of an automated system for carrying out digital faradaic impedance measurements. A similar intermediate position between the first and the second group could be assigned to the contributions of Mansfeld and of Kucera and Gullman, where a systematic and thorough evaluation is made of the results of applying electrochemical measurements to the monitoring of atmospheric corrosion. The paper by Bertocci and Mullen, although discussing frequency analysis, has as a main purpose the study of corrosion enhancement caused by alternating current in underground structures.

In the second group are several papers dealing with the use of a-c techniques for the measurement of the electrode impedance; two presentations

which cover the whole field are the very extensive review by Macdonald and McKubre and that by the late Professor Epelboin and his group in Paris. The inclusion of these two papers together with the contributions by Haruyama and Tsuru, Scantlebury, and Smyrl make this book an important benchmark for the assessment of the relevance and usefulness of a-c techniques in the area of corrosion.

Other papers concerned principally with experimental techniques are those by DeLuccia and Berman for determining hydrogen in metals, and that by Postlethwaite, measuring corrosion rate controlled by the oxygen diffusion. The paper by Isaacs and Vyas describes an elegant typographic method using a scanning reference electrode for the detection of localized corrosion. This group also includes the important report by Baboian and Haynes on the results of round-robin tests done by members of ASTM Subcommittee G01.11 on Electrochemical Measurements in Corrosion Testing.

There are also overlaps between the first two groups and the third (the one emphasizing the description of instrumentation). Examples are the aforementioned papers by Haruyama and Tsuru and by DeLuccia and Berman, but many others include detailed descriptions and discussions of electrochemical instruments used in corrosion studies. An exhaustive account of a microprocessor-based commercial instrument is given in the paper by Peterson and Siegeman, and Newborn and co-workers present a review of potentiostats employed in corrosion testing.

Florian Mansfeld

Rockwell International Science Center, Thousand Oaks, Calif. 91360; symposium chairman and co-editor

Ugo Bertocci

National Bureau of Standards, Washington, D.C. 20234; symposium vice-chairman and co-editor

INDEX

A

A-c impedance, 110, 150, 167, 187, 198
 A-c induced corrosion, 365
 A-c modulation, 365
 Admittance, 303
 Alloying, 352
 Aluminum alloys, 150, 163, 238, 243
 Anodic oxide films, 150
 Atmospheric corrosion, 215, 238

B

Barnacle electrode, 256, 260
 Bode diagram, 169, 172, 173
 Brass, 328
 Breakdown potential, 34
 Bronze, 328

C

Carbon steel, 238, 242, 339
 Cavitation, 339
 Cell factor, 215
 Charge transfer resistance, 150, 155, 161
 Chloride solutions, 15, 30, 35, 71, 84, 172, 183, 187, 210, 226, 274, 303
 Copper, 15, 198, 206, 238, 283, 327, 365, 372
 Corrosion fatigue, 69, 75
 Corrosion mechanism, 150, 203
 Corrosion monitor, 167, 174, 177, 215
 Corrosion rate, 57, 104, 150, 180, 298, 309, 319, 330, 345, 363

Crack growth rate, 69
 Crack initiation, 84
 Crevice corrosion, 43, 49, 54, 63, 274
 Cyclic depassivation, 69
 Cyclic polarization, 132, 134, 137, 274

D

Dental amalgams, 285
 Digital signal analysis, 198

E

Electroplating, 256, 267
 Equivalent circuit, 113, 115, 137, 169, 178, 192, 195, 207, 369, 403
 Erosion, 399

F

Faradaic impedance, 150, 202
 Fast Fourier transform, 200
 Flow system, 293, 329, 339
 Fracture properties, 84
 Frequency analysis, 365
 Frequency domain measurement, 118
 Frequency response, 150
 Fused salt, 303

G

Galvanic corrosion, 234, 327, 396, 406

H

High-strength steels, 256, 262, 264
 Hydrogen embrittlement, 256
 Hydrogen evolution, 365
 Hydrogen permeation, 256

I

Immersion test, 180, 187
 Impedance diagram, 114, 117, 137,
 147, 156, 162, 163, 164, 172,
 173, 175, 191, 193, 194, 196,
 206, 208, 211, 235, 372
 Inhibition, 150, 160, 179
 Intergranular corrosion, 3, 19
 Iron, 34, 150, 160, 172

L

Localized corrosion, 3, 34, 43, 167,
 274
 Low-cycle fatigue, 77

M

Magnesium chloride, 84
 Metallurgical studies, 107
 Microprocessor, 390
 Mixed potential theory, 167

O

Ohmic drop, 253, 368, 403
 Operational amplifiers, 381
 Organic coatings, 162, 187
 Outdoor exposure, 215
 Oxidation, 283
 Oxygen reduction, 290

P

Passivation, 274, 352
 Pitting, 3, 14, 34, 167, 274

Pitting potential, 34, 274
 Polarization curves, 26, 34, 65, 88,
 99, 274, 280, 281, 283, 307,
 356, 374, 388
 Polarization resistance, 6, 110, 146,
 150, 156, 161, 169, 188, 207,
 229, 303, 309, 330, 346, 402
 Potential/ pO_2 diagram, 303, 311,
 319
 Potentiodynamic polarization, 274,
 283, 396, 401
 Potentiostats, 126, 381, 383, 385-387
 Protection potential, 43, 63, 274, 280

R

Reduction, 283
 Relative humidity, 219

S

Salt-spray test, 150
 Scanning technique, 3, 9
 Seawater, 43, 48
 Sensitization, 22
 Silver, 283
 Stainless steel, 3, 17, 43, 50, 79, 84,
 96, 181, 274, 352
 Strain rate, 69, 84
 Stress corrosion cracking, 3, 28, 84
 Sulfuric acid, 20, 96, 156, 160, 164,
 172, 205, 226, 356, 371
 Surface morphology, 26, 92, 108, 211
 Sustained load testing, 256

T

Tafel plot, 396
 Tafel slope, 303, 309, 342, 360
 Temperature effects, 43, 99
 Time-of-wetness, 215, 221, 238, 247,
 252

Tin, 283
Thin-layer studies, 215, 225
Transfer function analysis, 140
Transfer function analyzer, 154, 189,
233

W

Warburg impedance, 116, 171, 195
Weathering steel, 238, 242

Weight-loss data, 215, 226, 244, 247,
249, 297, 309, 330
Welding, 3, 24, 270

Z

Zinc, 227, 238

